Pedro João Figueiredo Aparício

Jesus College,
Systems Biology Doctoral Training Centre,
Department of Engineering Science

Supervisors

Paul N. Watton
Mark S. Thompson

Modelling Signalling Pathways and Cellular Dynamics in Vascular Mechanobiology:

A Theoretical, Experimental and Computational Study

A thesis submitted for the degree of Doctor of Philosophy

Trinity 2016

This work is dedicated to my parents,
Ana Bela Viegas Figueiredo and António Manuel Matos Aparício,

and grandparents,
Maria de Matos Boa, Manuel Augusto Aparício,
João Fernandes Figueiredo and Mariana Maria Machado Viegas Figueiredo,

for believing in the value of education.

Deo gratias.

A thesis submitted for the degree of Doctor of Philosophy.

Modelling Signalling Pathways and Cellular Dynamics in Vascular Mechanobiology: A Theoretical, Experimental and Computational Study

By Pedro João Figueiredo Aparício, Jesus College.

Submitted Trinity 2016.

Abstract

Blood vessels are dynamic structures whose properties are continuously adapted by resident vascular cells. Existing mechanobiological models tend to ignore regulatory signalling and cell population dynamics, both key determinants of arterial growth and remodelling (G&R). In this D.Phil., a combined theoretical, experimental and computational approach is used to formulate, refine and implement a novel model of the arterial wall that includes vascular mechanics, microstructure, biochemical metabolism and signalling, and cell phenotype and population dynamics.

A mathematical chemo–mechano–biological (CMB) model is formulated by coupling a biomechanical model of the arterial wall as a cylindrical nonlinear elastic membrane to a system of biologically–informed evolution laws governing fibroblast cell–mediated, transforming growth factor (TGF)-β–regulated collagen metabolism. Model simulation of inflammatory aneurysm development suggests that increasing TGF-β levels promotes a cell–driven profibrotic response leading to aneurysm stabilisation, illustrating the model's ability to couple chemo–biological processes to tissue–level mechanical evolution.

To inform the theoretical framework experimentally, a recent mouse model of post–developmental disruption of medial smooth muscle TGF-β signalling is for the first time subjected to hypertension, and characterised by biaxial mechanical testing and (immuno)histological staining. Increased adventitial TGF-β levels following perturbation are associated with strong profibrotic responses (increased cellularity, collagen deposition, thicker walls) altering tissue mechanics (lower biaxial stress, higher structural stiffness).

Simulation of realistic arterial geometries is enabled by coupling the 1D CMB model to a three–dimensional structural solver. Heterogeneous spatial distributions of mechanical, microstructural and chemo–biological variables determining the evolution of complex saccular aneurysm geometries can be simulated with this 3D implementation.

A novel chemo–mechano–biological model of vascular cell dynamics and regulatory signalling governing arterial G&R is formulated, informed by specifically–generated experimental data, and implemented in an advanced 3D computational framework. This will allow for virtual investigation of therapies acting on chemo–biological agents of arterial G&R, with potential benefits for vascular disease patients.

Statement of Originality

I hereby declare that this submission is my own work and to the best of my knowledge it contains no materials previously published or written by another person, or substantial proportions of material which have been accepted for the award of any other degree or diploma at the University of Oxford or any other educational institution, except where due acknowledgement is made in the thesis.

Any contribution made to the research by others, with whom I have worked at the University of Oxford or elsewhere, is explicitly acknowledged in the thesis.

I also declare that the intellectual content of this thesis is the product of my own work, except to the extent that assistance from others in the project's design and conception or in style, presentation and linguistic expression is acknowledged.

Pedro João Figueiredo Aparício.
October 2, 2016.

Acknowledgements

I would like to express sincere appreciation to the principal investigators that have guided my research over these last four years. First and foremost to Dr Paul Watton for his guidance and support, as well as for the many opportunities for scientific, academic and professional development Paul kindly offered me since the very beginning of the D.Phil. project. I would also like to thank Dr Mark Thompson for his continuous supervision. I am also greatly indebted to Prof Jay Humphrey for the opportunity to visit his Continuum Biomechanics Laboratory for an extended period of time, which allowed me to receive training, perform experiments, and generate and analyse the comprehensive data set that constitutes an important part of the D.Phil work; the many fruitful discussions held with Prof Humphrey contributed to shape many other aspects of this thesis.

I am also extremely thankful to all the members of the research group I have been a part of during my D.Phil. project. A special thanks to Dr Katia Mandaltsi and Dr Jack Hornsby for their friendship and support in the office and in conferences throughout the world. Thanks also to Dr Alisa Selimovic, Dr John Vardakis (Prof Ventiko's Fluids and Biocomplexity group) for sharing their scientific knowledge and academic experience, as well as to Dr Haoyu Chen, Mr I-Tung Chan, Mr Shaktidhar Dandapani, Ms Christobel Gondwe, Ms Catherine Wong (Dr Watton's Theoretical Mechanobiology group), and Dr Nazri Bajuri (Dr Thompson's Mechanobiology group) for all the companionship and productive scientific discussion.

I am truly indebted to all the members of Prof Humphrey's Continuum Biomechanics lab, not only for the patience helpfulness during my training and data collection periods, but above all for their generosity and team spirit at all times. Special thanks to Dr Matthew Bersi, Dr Jacopo Ferruzzi, Dr Paolo Di Achille, Dr John Wilson, Dr Manuel Rausch, Dr Chiara Bellini, Ms Ramak Khosravi and Ms Arina Korneva.

I am also thankful to Dr Namrata Gundiah for the opportunity to visit her Biomechanics Laboratory, and for the many stimulating scientific exchanges. Thanks also to Mr Ankur Kulkarni, Mr Siddhartha Jaddivada and all the present and past members of Dr Gundiah's lab I interacted with.

I would also like to thank the faculty and my colleagues at the Doctoral Training Centre (DTC) for jointly making this a vibrant and rich scientific community. My special thanks to Prof Elspeth Garman, Systems Biology DTC programme director (2012-13), to Ms Samantha Miles, DTC centre administrator, and my colleagues Dr Jonathan Brooks-Bartlett, Dr Dhruva Raman, Dr Lukas Hutter and all the other DTC members I had the pleasure of working alongside.

This thesis template was based on template created by Brett Tully (2010; *'Allostasis of Cerebral Water: Modelling the Transport of Cerebrospinal Fluid'*, PhD Thesis, University of Oxford), which I am thankful for.

This work was funded by the PhD studentship granted to Pedro Aparício by the Engineering and Physical Sciences Research Council (EPSRC); this support is greatly acknowledged.

A particular word of thanks to all my friends in the UK, USA, Portugal, Italy, The Netherlands, France, Germany and elsewhere — you have made these four years at Oxford a truly remarkable journey.

Finally, I would like to express my deepest gratitude to my parents and girlfriend without whose loving presence, wholehearted support and unwavering dedication nothing in this D.Phil. project could have been accomplished.

Dissemination

Peer-Reviewed Journal Papers

1. **Aparicio P**, Thompson MS, Watton PN. (2016) A novel chemo-mechano-biological model of arterial tissue growth and remodelling. *Journal of Biomechanics*. 49:2321–2330.
2. **Aparicio P**, Mandaltsi K, Boamah J, Selimovic A, Bratby M, Uberoi R, Ventikos Y, Watton PN. (2014) Modelling the Influence of Endothelial Heterogeneity on Abdominal Aortic Aneurysm Evolution. *International Journal of Numerical Methods in Biomedical Engineering*. 30(5):563-586.

Peer-Reviewed Conference Proceedings

1. **Aparicio P**, Gundiah N, Thompson MS, Watton PN. (2016) *Modelling the Chemo-Mechano-Biology of Arterial Growth and Remodelling: a 3-Dimensional, Fluid-Solid-Growth Simulation*. European Congress on Computational Methods in Applied Sciences and Engineering (ECCOMAS). 5-10 June 2016, Crete Island, Greece.
2. **Aparicio P**, Thompson MS, Watton PN. (2016) *Vascular cells as dynamic integrators-actuators: A multiscale theoretical framework applied to fibroblast differentiation in aneurysm development*. 11th International Symposium on Biomechanics in Vascular Biology and Cardiovascular Disease. 2-3 May 2016, Atlanta, GA, USA.
3. **Aparicio P**, Thompson MS, Watton PN. (2015) *Workers, scaffolds and megaphones - or why vascular cells matter*. Second Workshop of the Multiscale Biology Network. 1 December 2015, University of Sheffield, Sheffield, UK.
4. **Aparicio P**, Watton PN. (2015) *A Chemo-Mechano-Biological Model of Arterial Tissue Growth and Remodeling: Signaling Pathways governing Myofibroblast Persistence underlying Vascular Pathology*. Vasculata 2015, 3-6 August 2015, Charlottesville, VA, USA.
5. **Aparicio P**, Rahman T, Thompson MS, Watton PN. (2015) *A Novel Chemo-Mechano-Biological Mathematical Model of Arterial Tissue Growth and Remodeling: Modelling of Signaling Pathways governing Adventitial Adaptive*

Response. 13th US National Congress on Computational Mechanics, 26-30 July 2015, San Diego, CA, USA.

6. **Aparicio P**, Mandaltsi A., Thompson MS, Watton PN. (2014) *Investigating the role of Cell Signalling on Intracranial Aneurysm Evolution: A novel chemo-mechanobiological mathematical model*. 7th World Congress of Biomechanics, 6-11 July 2014, Boston, USA.
7. Mandaltsi A, Chen H, **Aparicio P**, Hornsby J, Dickinson E, Eriksson T, Ventikos Y, Watton PN. (2014) *Modelling the mechanobiology of intracranial aneurysm evolution*. 7th World Congress of Biomechanics, 6-11 July 2014, Boston, USA.
8. Mandaltsi A, **Aparicio P**, Robertson A, Watton P. (2014) *Modelling the mechanobiology of intracranial aneurysm evolution*. Interdisciplinary Cerebrovascular Symposium IntraCranial Stent Meeting, 2-4 June 2014, Zurich, Switzerland.
9. **Aparicio P**, Boamah J, Chan I, Chen H, Dickinson E, Thomas E, Grytsan A, Hornsby J, Mandaltsi A, Penrose J, Watton P. (2014) *In silico modelling of the mechanobiology of soft-tissue*. INSIGNEO Showcase, University of Sheffield, 8 May 2014, Sheffield, UK.
10. **Aparicio P**, Thompson MS, Watton PN. (2013) *A computational model of arterial wall degeneration: Coupling signalling pathways to vascular mechanobiology*. 3rd International Conference on Computational and Mathematical Biomedical Engineering, 16-18 December 2013, Hong Kong.
11. **Aparicio P**, Mandaltsi A, Chen H, Watton PN. (2013) *Modelling the evolution of vascular disease: aneurysms*. Medical Engineering Centre Annual Meeting, 3-4 September 2013, London, UK.
12. **Aparicio P**, Mandaltsi A, Boamah J, Ventikos Y, Watton PN. (2013) *Modelling the Influence of Endothelial Cell Heterogeneity on Abdominal Aneurysm Evolution: a Patient-specific Simulation using a novel Fluid-Solid-Growth (FSG) Framework*. XXIV Congress of the International Society of Biomechanics, 4-9 August, Natal, Brazil.

CONTENTS

Contents ix

List of Figures xii

List of Tables xv

Acronyms xvi

1 Background and Motivation 1
- 1.1 Arteries in health and disease . . . 1
  - 1.1.1 Arterial microstructure and mechanobiology . . . 2
  - 1.1.2 Arterial pathobiology . . . 3
- 1.2 Adventitia, fibroblasts and TGF-β signalling . . . 5
  - 1.2.1 Adventitia layer . . . 5
  - 1.2.2 Fibroblasts . . . 6
  - 1.2.3 TGF-β mechanotransduction . . . 7
  - 1.2.4 TGF-β signalling in vascular disease . . . 10
- 1.3 Mechanobiological conceptual models . . . 11
  - 1.3.1 Arterial constitutive models . . . 11
  - 1.3.2 Arterial biomechanics growth and remodelling (G&R) models . . . 12
  - 1.3.3 Advanced Computational Frameworks . . . 16
  - 1.3.4 Models of TGF-β signalling . . . 17
- 1.4 Experimental Mechanobiological Models . . . 19
- 1.5 Thesis Structure . . . 21

2 CMB Theoretical Model 24
- 2.1 A novel CMB model of arterial tissue G&R . . . 25
  - 2.1.1 Methods: novel CMB model . . . 25
  - 2.1.2 Results: novel CMB model . . . 38
  - 2.1.3 Discussion: novel CMB model . . . 50
- 2.2 CMB Model Extensions . . . 56
  - 2.2.1 Model extension I: Collagen recruitment stretch remodelling coupled to arterial chemo–mechano–biology . . . 57
  - 2.2.2 Model extension II: modelling fibroblast differentiation dynamics . . . 63
  - 2.2.3 Model extension III: Modelling cell stiffness . . . 87

2.3 Conclusion . . . 101

3 Chemo–Mechano–Biological Experimental Study 102
3.1 Methods . . . 103
3.1.1 Study design . . . 103
3.1.2 Mechanobiological perturbations . . . 104
3.1.3 Animals, tissue harvesting and processing . . . 106
3.1.4 Mechanical data acquisition . . . 107
3.1.5 Histological staining . . . 114
3.2 Experimental results . . . 116
3.2.1 Biaxial mechanical data . . . 117
3.2.2 Microstructural data . . . 134
3.2.3 Biochemical and cellular data . . . 138
3.3 Discussion . . . 148
3.3.1 Study design and methods . . . 149
3.3.2 Comparison with previously published results . . . 152
3.3.3 Study insights . . . 156
3.3.4 Study limitations and future work . . . 168
3.3.5 Preliminary fit to 1D theoretical CMB model . . . 172
3.4 Conclusion . . . 182

4 CMB model update to 3 dimensions 183
4.1 Methods . . . 184
4.1.1 Arterial mechanics . . . 185
4.1.2 Arterial tissue growth and remodelling . . . 188
4.1.3 Computational implementation . . . 191
4.2 Results . . . 194
4.2.1 Saccular aneurysm development . . . 194
4.2.2 Investigating the outcomes of profibrotic therapy . . . 198
4.3 Discussion . . . 206
4.3.1 Comparison predictions 3D *vs.* 1D CMB models . . . 207
4.3.2 3D CMB Model insight . . . 211
4.3.3 Limitations and future work . . . 215
4.4 Conclusion . . . 218

5 Conclusions and Future Directions 219
5.1 Main findings . . . 220
5.1.1 Chapter 2: Conceptual 1D CMB model of arterial G&R . . . 220
5.1.2 Chapter 3: *In vivo* model of arterial chemo–mechano–biology . . . 222
5.1.3 Chapter 4: CMB model extension to 3 dimensions . . . 223
5.2 Limitations and Recommendations . . . 225
5.2.1 Chapter 2: Conceptual 1D CMB model of arterial G&R . . . 225
5.2.2 Chapter 3: *In vivo* model of arterial chemo–mechano–biology . . . 226
5.2.3 Chapter 4: CMB model extension to 3 dimensions . . . 228

5.2.4 Directions for Future Research 229
5.3 Final Note 232

References **233**

A Experimental Data Tables and Additional Experimental Plots **244**

List of Figures

1.1 Arterial Microstructure . . . 2
1.2 Computational frameworks I . . . 16
1.3 Computational frameworks II . . . 16

2.1 CMB Model Components . . . 25
2.2 Collagen stretch distributions PDF . . . 27
2.3 Initial CMB model: Signalling pathways diagram . . . 30
2.4 Elastin degradation . . . 36
2.5 CMB Simulation Loop . . . 37
2.6 Novel CMB model — mechanical variables . . . 39
2.7 Novel CMB model — biochemical Variables . . . 41
2.8 Additional parameter studies for the novel CMB model — mechanical variables I . . . 44
2.9 Additional parameter studies for the novel CMB model — biochemical variables I . . . 45
2.10 Additional parameter studies for the novel CMB model — mechanical variables II . . . 46
2.11 Additional parameter studies for the novel CMB model — biochemical variables II . . . 48
2.12 Additional parameter studies for the novel CMB model — mechanical variables III . . . 49
2.13 CMB coupling to the remodelling of recruitment stretch — parameter study on the rate of mechanotransduction . . . 59
2.14 Additional Parameter Studies for the CMB coupling to the remodelling of recruitment stretch — mechanical variables . . . 60
2.15 Additional Parameter Studies for the CMB coupling to the remodelling of recruitment stretch — biochemical variables . . . 61
2.16 Myofibroblast differentiation influencing arterial mechanobiology . . . 65
2.17 CMB model extension to capture myofibroblast differentiation — regulatory signalling pathways diagram . . . 67
2.18 CMB model extended to capture myofibroblast differentiation: parameter study on the basal rate of myofibroblast apoptosis — mechanical variables . . . 75
2.19 CMB Model extended to capture myofibroblast differentiation: Parameter study on the basal rate of myofibroblast apoptosis — biochemical variables . . . 77
2.20 Additional parameter studies on the CMB model extended to capture myofibroblast differentiation — mechanical variables I . . . 79
2.21 Additional parameter studies on the CMB model extended to capture myofibroblast differentiation — biochemical variables . . . 81

2.22 Additional parameter studies on the CMB model extended to capture myofibroblast differentiation — mechanical variables II . . . 83
2.23 Vascular cells as integrators–actuators: motivation for introduction of the concept of cell stiffness . . . 89
2.24 CMB model extended to include a representation of cell stiffness — parameter study on the rate of mechanotransduction . . . 96
2.25 CMB model extended to include a representation of Cell Stiffness — additional parameter studies . . . 97

3.1 Biaxial mechanical testing device . . . 108
3.2 Biaxial mechanical testing source images . . . 118
3.3 Load–deformation and stress–stretch curves from pressure–inflation tests of ATA — group comparison study . . . 119
3.4 Load–deformation and stress–stretch curves from axial force–stretching tests of ATA — group comparison study . . . 120
3.5 Accurate determination of in vivo stretch from axial force–stretch curves . . . 121
3.6 Representative fit to 4-fibre family constitutive model — stress–stretch responses . . 122
3.7 Representative fit to 4-fibre family constitutive model — loads–deformations responses 123
3.8 Linearisation of stress–stretch response . . . 124
3.9 Representative stored energy isocontours — ATA segment . . . 125
3.10 Representative stored energy isocontours — IAA segment . . . 126
3.11 Summary mechanical metrics — unloaded dimensions . . . 128
3.12 Summary mechanical metrics — loaded dimensions . . . 130
3.13 Summary mechanical metrics — stretch ratios . . . 131
3.14 Summary mechanical metrics — Cauchy stresses . . . 132
3.15 Summary mechanical metrics — linearised stiffnesses . . . 133
3.16 Summary mechanical metrics — energy metrics . . . 134
3.17 Picrosirius red staining for fibrillar collagen — source images . . . 135
3.18 Quantification of total collagen pixels and distribution of pixel colours from PSR images 136
3.19 Immunofluorescence tissue sections for biochemical and cellular quantification — source images at 14 weeks . . . 140
3.20 Immunofluorescence tissue sections for biochemical and cellular quantification — source images at 18 weeks . . . 141
3.21 Quantification of total counts and area density of MMP-2 pixels and cell nuclei from IF images . . . 143
3.22 Quantification of total pixel counts and area density for CD45 and α-SMA from IF images . . . 144
3.23 Quantification of pixel counts and area density for TGF-β and pSMAD-2 from IF images . . . 147
3.24 Gross morphology images — intramural haematoma in diseased IAA . . . 159
3.25 Gross morphology images — haematoma and atheroma in diseased ATA . . . 160
3.26 Exogenous TGF-beta source function . . . 175
3.27 Preliminary fit to 1D CMB model — mechanical and geometrical variables . . . 177
3.28 Preliminary fit to 1D CMB model — chemo–biological variables . . . 178

4.1 Fluid–Solid–Growth simulation framework 185
4.2 Definition simulation and elastin degradation domains 186
4.3 3D CMB modelling saccular aneurysm development — mechanical variables 195
4.4 3D CMB modelling saccular aneurysm development — biochemical variables 197
4.5 3D CMB model investigating profibrotic therapy on large saccular aneurysms — biochemical variables 199
4.6 3D CMB model investigating profibrotic therapy on large saccular aneurysms — mechanical variables 200
4.7 Geometry comparison between untreated *vs.* treated large saccular aneurysms 202
4.8 3D CMB model investigating profibrotic therapy on very large saccular aneurysms — biochemical variables 203
4.9 3D CMB model investigating profibrotic therapy on very large saccular aneurysms — mechanical variables 205
4.10 Geometry comparison between untreated *vs.* treated very large saccular aneurysms . 206
4.11 1D CMB model predictions for comparison with 3D CMB implementation 209

A.1 Load–deformation and stress–stretch curves from pressure–inflation tests of IAA — group comparison study 245
A.2 Load–deformation and stress–stretch curves from axial force–stretching tests of IAA — group comparison study 246

List of Tables

2.1 Initial CMB model: mechanical model, geometrical domain and simulation parameters 34
2.2 Initial CMB model: biochemical model parameters I 34
2.3 Initial CMB model: biochemical model parameters II 35
2.4 CMB model extended to capture myofibroblast differentiation — mechanical model, geometrical domain and simulation parameters 72
2.5 CMB Model extended to capture myofibroblast differentiation — biochemical model parameters I 73
2.6 CMB model extended to capture myofibroblast differentiation — biochemical model parameters II 74

3.1 Experimental groups and time points 104
3.2 Blood Pressure data 117
3.3 CMB model fitting to experimental results: modified parameter values 176

4.1 CMB coupling to FSG framework: model parameters 193

A.1 Summary mechanical variables 247
A.2 Comparison of mechanical data with Ferruzzi et al. (2015) 248
A.3 PSR histological quantification 249
A.4 IF quantification 250

ACRONYMS

1(3)D	One(Three)–Dimensional
α-SMA	α–Smooth Muscle Actin
AA	Arterial Aneurysm
AAA	Abdominal Aortic Aneurysm
AngII	Angiotensin-II
ATA	Ascending Thoracic Aorta
BCT	BrachioCephalic Trunk
CD45	Cluster of Differentiation 45
CFD	Computational Fluid Dynamics
CMB	Chemo–Mechano–Biology
CTGF	Connective Tissue Growth Factor
EC	Endothelial Cell
ECM	ExtraCellular Matrix
EDR	Energy Dissipation Ratio
EDS	Ehler–Danlos Syndrome
EMT	Epithelial–Mesenchymal Differentiation
eNOS	endothelial Nitric Oxide Synthase
ER	oEstrogen Receptor (binding site)
FA	Focal Adhesion
FAK	Focal Adhesion Kinase
FBE	Force Balance Equation
FEM	Finite Element Method
FL	axial Force–Length biaxial mechanical data
FSG	Fluid–Solid–Growth
FSI	Fluid–Solid–Interaction
FSP-1	Fibroblast–Specific Protein-1
G&R	Growth and Remodelling
GAG	GlycosAminoGlycan
GL	Green–Lagrange (strain)
HBSS	Hanks Balanced Salt Solution
IA	Inflammatory Aneurysm
IAA	Infra–renal Abdominal Aorta
ICA	Intracranial Aneurysm
IF	ImmunoFluorescence
IGF-1(2)	Insulin–like Growth Factor-1(2)
IHC	ImmunoHistoChemistry
KO	Knock–Out
LAP	Latency–Associated Peptide
LDS	Loeys–Dietz Syndrome
LLC	Large Latency Complex
L-NAME	NG-nitro-L-arginine methyl ester hydrochloride
LTBP	Latent TGF-β Binding Protein
MAP	Mean Arterial Pressure
MFS	Marphan Syndrome
MMP	Matrix MetalloProteinase
MSC	Mesenchymal Stem Cell
MYH	Myosin Heavy Chain
NE	NorEpinephrine
NO	Nitric Oxide
OSI	Oscillatory Shear Index
PD	Pressure–outer Diameter biaxial mechanical data
PDF	Probability Density Function
PG	ProteoGlycans
pSMAD-2(3)	phosphorylated SMAD-2(3)
PCR	Polymerase Chain Reaction
SA	Saccular Aneurysm
SEDF	Strain Energy Density Function
SEM	Standard Error of the Mean
SF	Stress Fibre
SLC	Small Latency Complex
TGF-β	Transforming Growth Factor–β
TAA	Thoracic Aortic Aneurysm
TGFBR1(2)	TGF-β receptor type I(II)
TIMP	Tissue Inhibitor of MetalloProteinases
(V)SMC	(Vascular) Smooth Muscle Cell
WSS	Wall Shear Stress

CHAPTER 1

BACKGROUND AND MOTIVATION

Arteries are complex structures (Sec. 1.1). Arterial wall material properties are dictated by their multi–layer, multi–constituent composition, which the resident vascular cell population dynamically adapts over time so as to maintain a preferred state of homoeostasis in the face of perturbations (Sec. 1.1.1). Several vascular pathologies arise as a result of compromised cell–mediated arterial metabolism (Sec. 1.1.2). The importance of the adventitial mechanobiological response has been increasingly recognised (Sec. 1.2), which assumes key importance in connective tissue pathologies where the inner layers become dysfunctional (Sec. 1.2.1). Fibroblasts are the main cell type populating this layer (Sec. 1.2.2). Fibroblast secretion and remodelling of fibrous matrix is extensively regulated by the transforming growth factor (TGF)-β signalling pathway (Sec. 1.2.3), which is found to be dysregulated in several instances of vascular disease (Sec. 1.2.4). So as to gain insight into arterial behaviour, several classes of mechanobiological models have been formulated (Sec. 1.3). Initially purely focusing on arterial material properties (Sec. 1.3.1), models were extended to predict changes in arterial geometry or mechanics over time (Sec. 1.3.2) and have been integrated into advanced computational frameworks for multi–physics, three–Dimensional simulations (Sec. 1.3.3). The importance of incorporating aspects of cell biology and regulatory signalling on these models has become increasingly recognised (Sec. 1.3.4). Computational models require experimental data sets for refinement, calibration and validation (Sec. 1.4); *in vivo* animal models have been developed to study arterial mechanobiology at different scales and when subject to different perturbations. This introduction sets the scene and presents the motivation for the novel work presented in the following chapters of this D.Phil. thesis, whose structure can be found in Sec. 1.5.

1.1 ARTERIES IN HEALTH AND DISEASE

Arteries are incredibly dynamic structures which are able to respond to perturbations so as to maintain a preferred *homoeostatic* condition. The necessary adaptations are brought about by the many cell types populating the different layers of the arterial wall, which are able to perceive the properties of their surrounding medium and act on this medium. Arterial disease is often caused by the inability of vascular cells to transduce deviations from homoeostasis, by their individually inadequate responses or by an uncoordinated response. Here, basic concepts on the microstructure, mechanobiology and pathology of arteries are introduced.

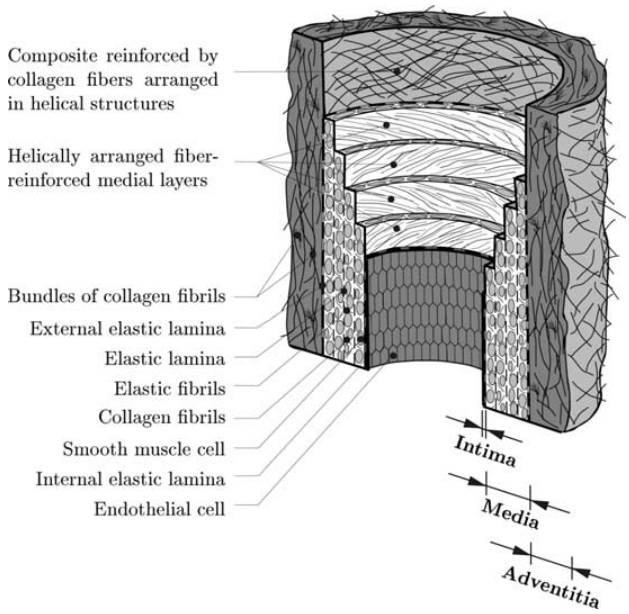

Figure 1.1: Microstructure of the different arterial layers (reproduced from (Holzapfel et al., 2000), with permission from Springer).

1.1.1 Arterial microstructure and mechanobiology

The living blood vessel is a highly dynamic structure with a complex microstructural and cellular composition. Arteries are composed of three layers (Holzapfel et al., 2000), Fig. 1.1. The *intima* is the innermost layer, where a sheet of endothelial cells (EC) covers the vessel lumen. Its direct contribution to load–bearing is negligible; however, it plays significant roles in sampling the mechanics of blood flow and its biochemical composition in nutrients, chemokines/cytokines, growth factors, hormones and immune cells. ECs mechanotransduce the intraluminal wall shear stress (WSS) exerted by the blood. EC regulation of luminal permeability is also tightly regulated, and its dysfunction may be implicated in diseases with an immune system component (Conway and Schwartz, 2012). The *media* is the intermediate layer, where concentric lamellae of elastin and collagen fibres and vascular smooth muscle cells (VSMC) give the artery its compliance and tonus. At physiological pressures and in healthy arteries, the media is the main load–bearing layer in the wall (Holzapfel et al., 2000). VSMC dysfunction has been linked to diseased states, e.g. VSMC apoptosis in aneurysms (López-Candales et al., 1997). The *adventitia* is the outmost arterial layer. It is rich in fibroblasts and thick collagen bundles, whose high stiffness prevent wall over–stretching following peaks in blood pressure (Holzapfel et al., 2000). Fibroblasts mediate collagen turnover and remodelling, and are also responsible for cyclic stress/strain mechanotransduction (Humphrey and Holzapfel, 2012). In diseased states in which the media has

significantly lost its load-bearing capacity, the adventitia is the primary load–bearer and prevents vessel mechanical failure (Humphrey, 2008a). In summary, the healthy arterial wall is a compliant bioviscoelastic solid with approximately linearly elastic behaviour at physiological pressures and increased stiffness and strength at higher pressures (Huang and Niklason, 2014).

1.1.2 Arterial pathobiology

Dysfunctional blood vessel wall growth and remodelling (G&R) processes are major contributors to prevalent forms of cardiovascular disease (CVD), one of the main causes of death in developed countries (30% of all deaths in the USA are attributable to CVD (NHLBI, 2013)).

Arterial aneurysms (AA) are permanent and localised dilations of the arterial wall which are irreversible and may be at increased risk of rupture (McGloughlin, 2011). Aneurysmal dilations can affect the entire arterial circumference (*fusiform* aneurysms) or only part of it (*saccular* aneurysms), and these can occur at many different sites along the vascular tree. Aneurysms in the abdominal aorta (aortic abdominal aneurysms, AAAs) have a prevalence as high as 8.9% among men, whereas thoracic aortic aneurysms (TAAs) may have an overall incidence of 10.4 per 100,000 per year (Sakalihasan et al., 2011). Aneurysm rupture takes place when the stresses acting on the wall exceed the strength of the wall (Phillippi et al., 2011); haemorrhage following AAA rupture is responsible for ca. 8,000 deaths in the UK and 15,000 deaths in the USA annually, which is expected to increase as the population ages (Sakalihasan et al., 2005). Abdominal aneurysms whose outer diameter reaches 5.0—5.5cm are considered to be at an elevated risk of rupture and can be treated electively, either by invasive surgery or by endovascular aneurysm repair. This "maximum diameter" criterion follows from the law of Laplace for the average circumferential wall stress $\sigma = (Pr_i)/h$ (P: transmural pressure, r_i inner radius, h wall thickness) (Humphrey, 2002), which ignores both the non–cylindrical geometry of most arteries and the (often anisotropic and time–varying) wall strength. For this reason, rupture can occur in up to 23% of the clinically "low–risk" cases with diameter inferior to 5.0cm (Vorp and Vande Geest, 2005). Aneurysm rupture seems to be greatly dependent on the (regionally–varying) micro–mechanical properties of the wall locally determining its mechanical strength (Raghavan and Simão da Silva, 2011). The aetiology of aneurysms is complex and site–specific, with marked differences between thoracic and abdominal AAs (Ruddy et al., 2008). Common findings include: wall weakening

with degradation of medial elastin fibres; decreased medial layer cellularity; increased adventitial collagen remodelling during aneurysm evolution; and increased protease:protease inhibitor ratios in ruptured aneurysms (Frösen et al., 2012). Immune cell infiltration is commonly present in aneurysmal tissue, in particular in the abdominal aorta (Rizas et al., 2009) and cerebral arteries (Frösen et al., 2012).

In *hypertension*, an excessive intraluminal load and increased pulsatility cyclically overstrains the arterial wall, which signals mural cells to increase extracellular matrix (ECM) turnover rates (Humphrey, 2008b). The resulting decrease in elastin (Eberth et al., 2010) and increase in collagen content (Wang and Chesler, 2012) and cross-linking (Wang et al., 2013) leads to a thicker and much stiffer arterial wall (Eberth et al., 2010) that increases pulmonary vascular resistance and may promote heart failure (Hall, 2010). Altered ECM remodelling resulting in sub–optimal mechanical properties is also characteristic of *vascular genetic hereditary syndromes*, in particular those associated with aneurysm development (Lindsay and Dietz, 2011). Marfan syndrome (MFS) is the most prevalent of these; a mutation to the ECM component fibrillin-1 gene results in reduced sequestration and excessive activity of the cytokine transforming growth factor (TGF)-β, leading to weakened walls (fragmented elastin, increased collagen content) with increased tortuosity and prone to aneurysm and dissection (Neptune et al., 2003; Doyle et al., 2012). Increased TGF-β signalling is also present in the Loeys-Dietz syndrome (LDS), however, here it is the mutation to TGF-β receptors that causes the disease (Loeys et al., 2005).

Common to all of the previously discussed arterial pathologies are the following points: (1) Dysfunctional G&R processes lead to blood vessel walls with sub-optimal microstructural, mechanical or geometrical characteristics, which can fail in catastrophic events such as aneurysm rupture; (2) Such G&R processes are always mediated by cells endogenous to the vascular wall (ECs, SMCs, fibroblasts), and often there is immune cell involvement; (3) Such mural cells modulate their phenotype in response to their biochemical (signalling cytokines, proteolytic load) and biomechanical (shear stress, cyclic strain) environment, and vascular pathology results from a downward spiral of maladaptation (e.g. pro–inflammatory EC phenotype in conjunction with synthetic VSMC phenotype leading to immune cell infiltration and wall degradation in inflammatory aneurysms) that ultimately leads to loss of function (e.g. stiffening in hypertension, wall weakening and rupture in arterial aneurysms).

1.2 ADVENTITIA, FIBROBLASTS AND TGF-β SIGNALLING

In light of the previous sections, it is clear that any model of vascular biology to be used in fundamental research or clinical decision–making must attempt to capture vascular cell response to mechanical loading, biochemical composition of the medium and interactions with other cells and surrounding ECM. The chemo–mechano–biological model of vascular connective tissue G&R formulated, implemented and analysed in Chapter 2 of this thesis focuses primarily on *adventitial fibroblast mechanobiology*.

1.2.1 Adventitia layer

Recent research has supported the central role of the adventitia in vascular physiology, well beyond the long–accepted passive "straight jacket" role in preventing arterial distension. Based on observations in the context of G&R of hypertensive arteries, Stenmark et al. (2006) regard the adventitia as a "biological processing centre" and the "principal injury–sensing tissue of the vessel wall". Unlike the media, which is not perfused and seems to be impermeable to non–medial cells under physiological conditions (Michel et al., 2007), the adventitia of large elastic arteries such as the human aorta is well perfused by a network of blood vessels, the *vasa vasorum*. In response to mechanical damage or secretion of inflammatory mediators, immune cells infiltrate the adventitia of these vessels, triggering pathological cascades by secreting ECM—degrading proteolytic enzymes and inflammatory mediators that activate adventitial fibroblasts. An "outside-in" hypothesis for vascular wall inflammation has been suggested (Maiellaro and Taylor, 2007), where immune cell infiltration starts in the adventitia and then progresses towards the intima, with adventitial fibroblasts being the first vascular cells to be activated, proliferate and up–regulate ECM deposition (Stenmark et al., 2006).

The significance of the collagenous adventitial layer is particularly clear in the setting of inflammatory aneurysms, where extensive loss of medial elastin and VSCMs and significantly increased collagen content and adventitial thickness (He and Roach, 1994) leave collagen as the only significant load–bearer in the arterial wall (Humphrey and Holzapfel, 2012); aneurysm expansion and rupture have experimentally been found to depend critically on the properties of arterial collagen (Dobrin and Mrkvicka, 1994). The fact that medial VSMC apoptosis and

endothelial denudation are very extensive in most advanced–stage intracranial and abdominal aneurysms (Frösen et al., 2012) also points to the crucial importance of adventitial fibroblasts/myofibroblasts in mediating collagen G&R, which may mediate aneurysm stabilisation or enlargement (Humphrey and Holzapfel, 2012; Wilson et al., 2013).

1.2.2 Fibroblasts

Unlike EC or VSMC, fibroblasts have received little attention in vascular research until recently (Humphrey and Holzapfel, 2012). However, fibroblasts are highly responsive to applied cyclic deformation, mechanotransducing both directly, via modulation of gene expression, and indirectly, via the production of autocrine and paracrine effectors such as TGF-β (Chiquet et al., 2003). Fibroblasts have broader functional capabilities than ECs or SMCs (Stenmark et al., 2006), and can respond to altered conditions by modulating proliferation and cell numbers, regulating secretion of ECM structural components and active molecules, and changing phenotype to VSMC–like cells, or myofibroblasts (Strauss and Rabinovitch, 2000). Fibroblasts are connective tissue cells of mesenchymal embryonic origin (McAnulty, 2007). In adult tissues in homoeostasis, fibroblasts are found in a low–proliferative, low–secretory, non–contractile state. In addition to proliferation of existing populations, fibroblasts can also originate from endothelial populations via epithelial–mesenchymal transition (EMT) (Kalluri et al., 2003), differentiation of precursor cells circulating in the blood (fibrocytes) (Schmidt et al., 2003; Dai et al., 2005a) or maturation of resident mesenchymal stem cell (MSC) populations (McAnulty, 2007).

Fibroblasts in adult connective tissues continuously secrete procollagen (McAnulty et al., 1991), a precursor of collagen with a short half–life; procollagen is then extracellularly proteolytically converted into collagen, a triple helix molecule that is organised into fibres with very high stiffness, mechanical strength and stability (Shoulders and Raines, 2009). Fibroblasts also secrete proteolytic enzymes, in particular matrix metalloproteinases (MMPs), which are responsible for the degradation of ECM components such as collagen or elastin, as well as for proteolytic activation of latent/immature biomolecules (Hobeika et al., 2007). MMPs are themselves secreted in an inactive zymogenic form that requires activation (Sinclair and Ryan, 1994). Different classes of MMPs have different targets and proteolytic capabilities (Siefert and Sarkar, 2012), and are secreted in response to specific stimuli and at specific times and rates (Rizas et al., 2009).

For example, in AAAs, both resident mural cells and infiltrating immune cells secrete proteases (Longo et al., 2002; Aziz and Kuivaniemi, 2008). Fibroblasts are also responsible for the secretion of tissue inhibitors of metalloproteinases (TIMPs), active inhibitors of MMP proteolytic action by the formation of irreversible inhibitory complexes with them (Brew et al., 2000). Imbalances in MMP:TIMP ratio favouring heightened proteolytic activity have been found in ruptured aneurysms (Brophy et al., 1991). Both *in vitro* (Grinnell, 2003) and *in vivo* (Chiquet et al., 2003) models consistently show that mechanically loading connective tissue leads to changes in fibroblast proliferation and secretion of ECM components or mediators of matrix metabolism; altered matrix turnover gradually changes matrix microstructural and mechanical properties.

1.2.3 TGF-β mechanotransduction

As the arterial wall is populated by fibroblasts and other cell populations that dynamically change phenotype, intercellular communication via paracrine signalling is a key determinant of arterial wall G&R processes and adaptation to altered environmental conditions. Among the large number of molecular species that act as regulatory and signalling mediators, transforming growth factor (TGF)-β has special importance. Long known to be "the most potent regulator of ECM formation and cell–ECM interaction" (Streuli et al., 1993), TGF-β is secreted by many cell types in virtually all connective tissues, modulating a large number of cellular phenomena (Akhurst and Hata, 2012). In vascular tissues, TGF-β isoforms 1–3 are produced by all resident cell types as well as by infiltrating immune cells (Roberts et al., 1986; Martin et al., 1992; Rizas et al., 2009) and degranulating platelets trapped in intraluminal or intramural thrombi (Tomasek et al., 2002), all of which secrete a non–functional (*latent*) form into the extracellular space. Latent TGF-β comprises the active TGF-β homodimer non–covalently associated with the latency–associated peptide (LAP), a prodomain–derived dimer that prevents interaction of the active form with its receptors, together forming the small latency complex (SLC) (Hyytiäinen et al., 2004). Upon secretion, this complex can associate with members of the latent TGF-β binding protein (LTBP) family, thus forming the large latent complex (LLC). Because LTBPs interact non–covalently with microfibril–associated fibrillins, the LLC is localised to the ECM, which acts as a reservoir of latent TGF-β.

TGF-β activation *in vivo* thus requires release of the active molecule from the latent com-

plex, which is a highly regulated process. One mechanism of TGF-β activation is proteolysis, in particular by plasmin, thrombospondin or gelatinases MMP-2,9 (Yu and Stamenkovic, 2000). Alternatively, TGF-β activation can be mediated by integrins, which bind to the RGD domain of the LAP (Munger and Sheppard, 2011; Henderson and Sheppard, 2013). Integrin $\alpha v\beta 8$ activates TGF-β indirectly, by binding and presenting the latent complex to the membrane bound protease MT1-MMP. In contrast, a traction–dependent mechanism dependent on a functional actin cytoskeleton seems to be required for latent TGF-β activation through integrins $\alpha v\beta 6$ (Keski-Oja et al., 2004; Shi et al., 2011), $\alpha v\beta 3$ and $\alpha v\beta 5$ (Wipff et al., 2007).

Once activated, TGF-β ligand signals through membrane receptor complexes comprising TGF-β type II (TGFBR2) and type I (TGFBR1) receptors with serine/threonine kinase activity (Weiss and Attisano, 2013) and a variable number of other co–receptors. TGF-β signalling proceeds intracellularly via two main axes (Akhurst and Hata, 2012; Doyle et al., 2012; Forte et al., 2010). When signalling through the *canonical* pathway, TGF-β receptors phosphorylate receptor R-SMADs (SMAD-2 and SMAD-3), which form heteromeric complexes with a common mediator co-SMAD (SMAD-4) that translocate to the nucleus and activate the expression of downstream genes; the signalling axis is inhibited by the inhibitory I-SMAD (SMAD-7). In addition to this well–defined axis, TGF-β may also activate a number of intracellular signalling pathways that are independent of R-SMAD, collectively designated *non–canonical* pathway(s): PI3K–AKT–mTOR axis; TAK1–JNK,p38 axis; RAS–ERK1/2 axis; RHO–ROCK axis; ALK1–Smad1/5/8 axis. The gene expression pattern adopted by the cell as a result of the integration of the previous signalling pathways dictates the phenotype it acquires, for example in terms of secretion of biomolecules, proliferation, differentiation, migration or matrix remodelling. Finally, important cross–talks have been identified between TGF-β and other signalling factors, in particular Angiotensin-II (AngII) upstream (Rosenkranz, 2004; Habashi et al., 2011) and connective tissue growth factor (CTGF) downstream (Leask and Abraham, 2006; Ruiz-Ortega et al., 2007). In spite of all the complexity above, it is broadly accepted that TGF-β is a crucial component of mechanotransduction, signalling and phenotypic regulation in the arterial wall — this is a *central hypothesis* to the work presented in this thesis. So as to substantiate this view, it is necessary to understand when cells produce TGF-β and its effects on cell phenotype.

Adventitial fibroblasts in normal adult arteries generally do not secrete TGF-β (Shi et al., 1996b). However, fibroblasts (Streuli et al., 1993; Lindahl et al., 2002) and VSMCs (Riser et al., 1998; Gutierrez and Perr, 1999; Li et al., 1998; O'Callaghan and Williams, 2000) cyclically strained *in vitro* greatly increase the transcription of the TGF-β gene and the secretion of the TGF-β protein. Once released into the medium, TGF-β acts both as an autocrine and paracrine signalling factor, by diffusing to different wall layers through the (fenestrated) elastic laminae (Michel et al., 2007). Being a promoter of ECM deposition (Streuli et al., 1993), interaction of TGF-β with its transmembrane receptors on fibroblasts leads to increased transcription and secretion of procollagen (Appling et al., 1989; O'Callaghan and Williams, 2000; Roberts et al., 1986; Akhurst and Hata, 2012; Li et al., 1998; Gutierrez and Perr, 1999; Lindahl et al., 2002; McAnulty et al., 1991), decreased transcription and secretion of collagenases (Edwards et al., 1987; Akhurst and Hata, 2012) and increased transcription and secretion of TIMP (Edwards et al., 1987; Akhurst and Hata, 2012), all of the previous having the joint effect of promoting ECM accumulation. TGF-β also promotes an increase in fibroblast numbers by increasing their rate of proliferation (Streuli et al., 1993; Lawrence, 1996; Schuster and Krieglstein, 2002; Yang et al., 2002; Akhurst and Hata, 2012) and promoting chemotaxis and differentiation of precursor cells such as fibrocytes and MSCs (Yang et al., 2002; Schmidt et al., 2003; McAnulty, 2007). Finally, TGF-β promotes the phenotypic switch of fibroblasts to highly secretory, contractile and migratory myofibroblasts (Tomasek et al., 2002; Jones et al., 2009b; Theruvath et al., 2012; Akhurst and Hata, 2012); these cells have higher rates of secretion of procollagen but also of MMPs (partial ECM degradation may facilitate their migration), which may increase the proteolytic load experienced by the matrix (Zalewski et al., 2002; Jones et al., 2009b).

TGF-β also promotes ECM deposition by VSMCs; however, induction of apoptosis has been consistently reported (Schuster and Krieglstein, 2002; Jones et al., 2009b; Theruvath et al., 2012; Hishikawa et al., 1999; Fukui et al., 2003) (note also the existence of contradicting evidence (Majesky et al., 1991; Nabel et al., 1993)). Finally, TGF-β acts as both a chemoattractant (Palladino et al., 1990; Sporn and Roberts, 1990; Rizas et al., 2009; Akhurst and Hata, 2012) and an immunosuppressor (Palladino et al., 1990; Sporn and Roberts, 1990; Lawrence, 1996; Akhurst and Hata, 2012) to infiltrating immune cells.

1.2.4 TGF-β signalling in vascular disease

Being such a key regulator of cell function in the arterial wall, it is hardly surprising that abnormal levels of TGF-β and dysfunctional TGF-β signalling have been consistently found across a broad spectrum of vascular conditions. In the case of *hypertension*, an excessive deposition of collagen leads to stiffening of the arterial wall and subsequent complications (Wang and Chesler, 2012); as expected, excessive production of TGF-β is a common finding (Stenmark et al., 2006), and loss of TGF-β signalling prevents chronic hypoxia–induced hypertension in a mouse model (Chen et al., 2006). In conditions where weakened arterial walls result from dysfunctional G&R, it would be expected that increasing TGF-β would be protective. This was reported for *inflammatory aneurysms*, generally associated with the abdominal aorta. These aneurysms are characterised by extensive immune cell infiltration, a hypocellular media (following VSMC apoptosis), increased collagen turnover and a large proteolytic load leading to elastin degradation (He and Roach, 1994; Sakalihasan et al., 2005). Experimental studies have revealed a protective role for TGF-β in these aneurysms: over–expression of TGF-β via endovascular gene therapy resulted in stabilisation of previously formed abdominal aortic aneurysm (AAA) (Dai et al., 2005b); systemic neutralisation of TGF-β enhanced immune cells infiltration, MMP activity and degradation of the vessel wall (Wang et al., 2010); TGF-β induction by cyclosporine A prevented aneurysm formation in two well–established aneurysm animal models (Dai et al., 2011). However, the opposite was found for a large class of aneurysms, those related to *Genetic Heritable Disorders*, and commonly associated with the thoracic aorta (Lindsay and Dietz, 2011). Due to different genetic mechanisms, there is persistently *increased* TGF-β signalling that is associated with elastin fragmentation and VSMC proliferation but little immune system involvement (Lindsay and Dietz, 2011); in this case the wall is mechanically weak and prone to tortuosity, aneurysm and dissection (Loeys et al., 2006). Consistent with the previous results, treatment of a MFS mouse model with an inhibitor of AngII signalling (upstream of TGF-β), losartan, decreased elastin fragmentation and arterial expansion (Habashi et al., 2006).

A possible explanation to this apparent paradox of TGF-β effects lies on the pathobiological mechanism of each lesion and its time of development (Wang et al., 2010). Reduced elastin content and poor elastin fibre organisation is observed in young children with MFS or LDS in the absence of inflammation, which suggests a defect in elastogenesis rather than post–developmental

elastin degradation (Loeys et al., 2005). Excessive TGF-β signalling would also contribute to the expansion of the fibroblast population and their differentiation into myofibroblasts with highly secretory profiles (including secretion of MMPs), which would jointly result in weak walls with degraded elastin and collagen deposits that can be observed in MFS or LDS (Loeys and Dietz, 2008). Elastin degradation in inflammatory aneurysms is clearly associated with immune cell infiltration and takes place during vascular maturity (Sakalihasan et al., 2005). Hypocellular (VSMC apoptosis) medias with low elastin content (immune cell–driven proteolysis) have reduced contribution to load–bearing, and thus TGF-β action on stimulating adventitial fibroblast collagen deposition would increase the mechanical strength of the wall. The immunosuppressive effect of this cytokine would also reduce the inflammatory reaction, with positive effects on the arterial wall.

1.3 MECHANOBIOLOGICAL CONCEPTUAL MODELS

Given the complexity of the arterial wall discussed above, there has been a considerable effort over the last decades to formalise the conceptual understanding of arterial behaviour through theoretical and computational *models* able to capture and predict the evolution of arterial material, microstructural, biochemical and cellular properties.

1.3.1 Arterial constitutive models

In terms of models of arterial tissue material response, two approaches can be found in the literature. The first model proposed considered the strain energy density function (SEDF) Ψ characterising the entire arterial wall to be a function of some combination of radial, circumferential and axial components of a particular strain tensor; the material parameters in such SEDFs are directly fit to a sets of tissue mechanical test results, and do not have any direct interpretation in terms of the properties of wall constituents (Holzapfel et al., 2000). The most widely used SEDF in such class was formulated by Fung et al. (1979); the 2D strain measure used is the Green–Lagrange tensor E, whose principal directions are assumed to coincide with the circumferential ($\theta\theta$) and axial (zz) directions, while the radial strain is neglected,

$$\Psi = \frac{c}{2}\exp\left[a_1\left(E_{\theta\theta}^2 - E_{\theta\theta}^{*2}\right) + a_2\left(E_{zz}^2 - E_{zz}^{*2}\right) + 2a_4\left(E_{\theta\theta}E_{zz} - E_{\theta\theta}^{*}E_{zz}^{*}\right)\right], \tag{1.1}$$

where $E^*_{\theta\theta}, E^*_{zz}$ are standard strains and c, a_1, a_2, a_4 are material constants.

The second class of constitutive models treats the arterial wall as a combination of fibre-reinforced composite structures (*layers*). Each such structure is described by a SEDF with terms accounting for the mechanical behaviour of their constituents, which can have very different properties. This latter class of models is microstructurally–motivated: each structure is identified with an arterial layer (generally only the media and adventitia are considered), and constituents include isotropic amorphous matrix (ground substance), neo-Hookean elastin fibres, exponential collagen fibre families and passive and active VSMC contributions (Bellini et al., 2014); the material parameters can thus be identified with the contributions to load–bearing (stiffness × mass fraction) of each constituent in each layer. A SEDF that has been extended and incorporated in most arterial constitutive models since its initial formulation by Holzapfel et al. (2000) is

$$\Psi_L = \frac{c_L}{2}\left(\bar{I}_1 - 3\right) + \left(\frac{k_{1L}}{2k_{2L}}\right)\sum_i \left\{\exp\left[k_{2L}\left(\bar{I}_{iL} - 1\right)^2\right] - 1\right\}, \tag{1.2}$$

where subscripts $L = M, A$ refer to the media and the adventitia, resp., $\bar{I}_1 = \bar{C} : I$ is the 1st invariant of the modified Cauchy–Green tensor $\bar{C}$, $\bar{I}_{iL} = A_{iL} : \bar{C}$ are invariants associated with fibre family i in layer L, A_{iL} are structure tensors, and c_L, k_{1L}, k_{2L} are material constants.

1.3.2 Arterial biomechanics growth and remodelling (G&R) models

Constitutive biomechanical models are important to study the material properties of arterial tissue samples given stress-strain data, or to predict stress distributions given strain data and patient–specific or population–averaged material properties. However, predicting the evolution of structural, mechanical and geometrical properties of arteries over time is significantly more relevant for the clinician (Wilson et al., 2013), and several computational biomechanics models of vascular evolution have been developed (Humphrey and Holzapfel, 2012).

Growth of soft tissues was initially modelled in the volumetric growth framework (Rodriguez et al., 1994), where the arterial evolution was decomposed into (fictitious) small parts that would grow independently, and an additional elastic deformation that would assure compatibility and continuity of the body,

$$F_{\text{eg}} = F_e\, F_g, \tag{1.3}$$

where F_{eg} is the observed growth deformation, F_g the growth deformation gradient and F_e the elastic deformation gradient. Residual stresses emerge naturally from this latter deformation. A different approach made use of the continuum theory of mixtures to model (multiphase) tissue growth as a summation of the growth of each of its constituents (Humphrey and Rajagopal, 2002),

$$\Psi = \sum_{L,k} \upsilon_L \cdot \phi_L^k \cdot \Psi_L^k \tag{1.4}$$

where $\upsilon_L := V_L/V$ are the volume fractions of each layer L, and $\phi_L^k = m_L^k/m_L$, Ψ_L^k the mass densities and SEDF, resp., of constituent k in layer L. The latter method is currently the most widely used, as tissue evolution emerges naturally from the dynamics of its constituents (in general, υ_L, ϕ_L and Ψ_L^k may be time–dependent) (Ateshian and Humphrey, 2012).

Classes of G&R governing laws

The problem of how to construct laws governing cell–mediated tissue G&R has been the subject of intense research in the last 15 years. It follows from experimental observations that vascular cells are responsive to their mechanical environment and change their secretory or contractile phenotype such that homoeostatic mechanobiological conditions are maintained (Humphrey, 2008a). However, it is not clear what the mechanical quantity of interest for cell mechanotransduction is (*stress*, *stretch*, ...), and different models make use of different metrics to drive arterial G&R (Humphrey and Holzapfel, 2012).

A second difference lies in the method of computation of the current levels of matrix constituents (Humphrey, 2008a). Some models follow the *integral* formulation formalised by Baek, Rajagopal, and Humphrey (2005), where the current levels of a particular constituent k in layer L are computed by integrating over the simulation time interval $]-\infty, t]$ the rates of mass production $\dot{m}_L^k(\tau)$ multiplied by the "survival function" $q_L^k(t-\tau)$. This formulation is particularly intuitive, as it clearly separates constituent production ($\dot{m}_L^k(t)$) from degradation ($q_L^k(t)$); however, it requires storage of a large number of values for the computation of the integral. A more computationally efficient approach is the *differential* formulation by Watton et al. (2004), which uses differential equations to compute the rate of change in the levels of matrix constituents (m_L^k, modelling *growth*) and collagen fibre stretches (modelling *remodelling*), with only the net effect (e.g. production/degradation) being explicitly represented. Numerical methods for ODEs can then be used to efficiently compute the current values of the variables of interest.

An example of a *stress*–based *integral* law by Baek et al. (2006) is

$$m_L^k(t) = \int_{-\infty}^{t} \dot{m}_L^k(\tau) \cdot q_L^k(t-\tau)\, d\tau \quad (1.5) \qquad \dot{m}_L^k(\tau) \propto \frac{m_L(t)}{m_{\mathrm{L0}}} \left[k\left(\sigma_L^k(t) - \sigma_{L,\mathrm{hom}}^k\right) + f_{\mathrm{hom}} \right], \quad (1.6)$$

where σ_L^k are scalar measures of the Cauchy stresses experienced by constituent k in layer L, hom are their homoeostatic values, f_{hom} is the baseline rate of production, c is a material constant and $m_L(t)$, m_{L0} are the masses of layer L at $t = t_0$. In contrast, an example of a *stretch*–based *differential* formulation by Watton et al. (2004) is

$$\frac{\partial m_L^k}{\partial t}(t) \propto \left(\epsilon_L^k(t) - \epsilon_{L,\mathrm{hom}}^k\right), \quad (1.7)$$

where ϵ_L^k are scalar measures of Green-Lagrange strains experienced by constituent k in layer L.

Existing arterial mechanobiological G&R models

Several mechanobiological models of arterial G&R can be found in the computational vascular biomechanics literature, which incorporate constituent–specific material properties and G&R laws, and are applied to modelling different pathobiological entities such as aneurysm development, hypertension, flow–induced arterial adaption or vasospasm.

Most models follow (even if partially) the theoretical framework of Humphrey (1999) in modelling tissue evolution as a result of continuous deposition and degradation of load–bearing constituents in different reference configurations. Gleason et al. (2004a) used a rule–of–mixtures approach to compute the passive contributions of collagen, elastin and smooth muscle cells to load–bearing, as well as a flow–dependent active stress term modelling tonus adaptation to prescribed changes in intraluminal flow. Baek et al. (2005) followed a similar formulation and uses an integral approach with mass deposition coupled to wall stress exceeding a homoeostatic threshold to model arterial G&R underlying saccular aneurysm formation. Baek et al. (2007b) extended the previous formulation by considering a survival function coupled to fibre tension (thus modelling fibre damage), and the quasi–static solution of the governing mechanical equations implemented in axisymmetrical membranes with prescribed wall damage is applied to study cerebral vasospasm and its resolution.

A conceptually similar approach is taken by Kroon and Holzapfel (2007, 2008), who define the rate of collagen mass deposition to be proportional to a scalar measure of domain deforma-

tion derived from the right Cauchy-Green tensor C; the total fibre family SEDF is then computed as an integral of the rate of mass production by a "life cycle function" similar to the survival function mentioned above. The geometrical domain used is an idealised cylindrical membrane, aneurysm development is kicked-off by a step degradation in the medial layer, and the mechanical equilibrium equation is iteratively solved quasi-statically. Watton et al. (2004) use a differential, stretch–based formulation to model adaption of collagen mass density and remodelling of collagen recruitment to load–bearing as a result of deviation from homoeostatic ("attachment") values of collagen fibre stretch. Abdominal aneurysm development is triggered by prescribing an axisymmetrical loss of elastin. This model has been used to generate predictions consistent with clinical observations (Watton and Hill, 2009), and to predict the development of saccular cerebral aneurysms (Watton and Ventikos, 2009).

Other models exist. Chatziprodromou et al. (2007) prescribe a linear decrease in the Young's modulus of a small arterial wall region to drive aneurysmal expansion (implicitly modelling dysfunctional loss of smooth muscle tone), without explicitly modelling any G&R process. Aneurysm formation as a result of damage is modelled by Li and Robertson (2009), where elastin damage — "mechanical" (maximum strain, accumulated strain) and "enzymatic" (WSS and its spatial gradient) — perturbs the system; no collagen G&R is considered. Finally, Volokh and Vorp (2008) coupled Volokh's softening hyperelastic constitutive model predicting arterial wall failure by means of a "maximum work before failure" material constant (Volokh, 2008) to a non-microstructurally–based constitutive model where mass density is linked to wall Cauchy stress, stiffness is coupled to mass density, and wall strength is coupled to stiffness.

In spite of being biologically–motivated, most of the models above are essentially phenomenological, i.e. the coupling between mechanical stimuli and the observed changes in vessel microstructure and/or material properties do not explicitly take into account the cellular and biochemical mediators of such responses. The D.Phil. project presented here aims at improving the biochemical and biological understanding of vascular mechanobiology informing arterial G&R conceptual models.

1.3.3 Advanced arterial G&R computational frameworks

Some of the mechanobiological models of arterial G&R discussed above have recently been integrated in advanced computational frameworks for the multi–physics simulation of solid and fluid mechanics in complex 3–Dimensional (3D) geometries.

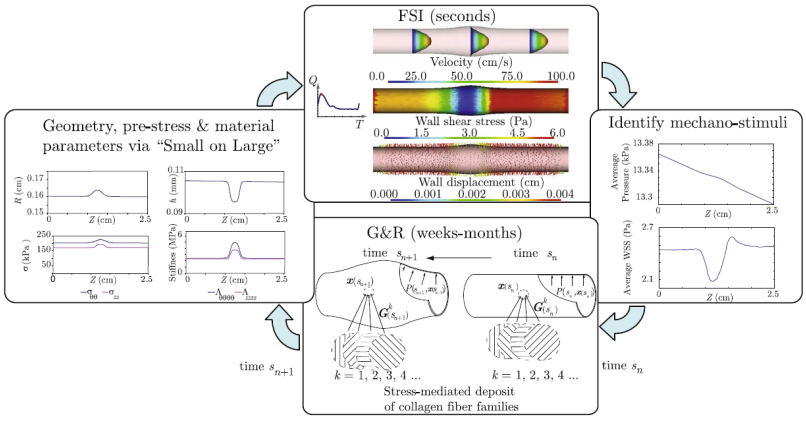

Figure 1.2: Figueroa et al. (2009) computational framework (reprinted from Figueroa et al. (2009), with permission from Elsevier).

The vascular G&R model of Baek et al. (2005) was integrated in a Fluid–Solid–Growth (FSG) loop (Figueroa et al., 2009), which makes use of (i) a coupled momentum method for the computation of fluid flow in deformable arteries, (ii) a linearised arterial wall constitutive response (theory "small on large") and (iii) a Fluid–Solid–Interaction (FSI) computational framework to solve both the 3D haemodynamics and the solid mechanics characterising an axisymmetrical membrane wall, Fig. 1.2. The influence of such mechanical quantities on long–term arterial G&R was implemented by coupling both wall Cauchy stress σ and blood shear stress to collagen deposition (implicitly modelling EC signalling); the initial insult triggering aneurysm development was a prescribed degradation of elastin and VSMC (the latter fully phenomenological). This framework was then applied to simulate the development of abdominal aortic aneurysms with realistic geometries (Sheidaei et al., 2011).

A similar approach is taken by Watton et al. (2009a), who couple the G&R model of Watton et al. (2004) to a quasi–static, rigid–wall FSG loop for the computation of both fluid and solid mechanics driving aneurysm evolution after an initially prescribed elastin degradation in a non–axisymmetrical geome-

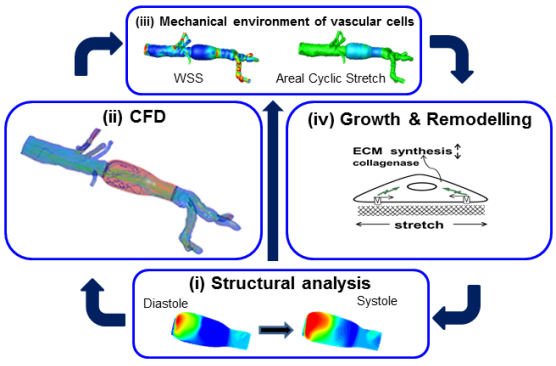

Figure 1.3: Watton et al. (2011) computational framework (reproduced from Aparício et al. (2014), Copyright ©2014 John Wiley & Sons, Ltd.).

try domain. Differential, stretch–based G&R laws are used to compute rates of collagen growth and recruitment stretch remodelling (phenomenologically capturing fibroblast mechanotransduction), and further elastin degradation is coupled to low WSS values (phenomenologically capturing immune cells infiltration following increased EC permeability). This model has subsequently been used to simulate the stabilisation of a saccular aneurysm in the internal carotid artery (Watton et al., 2011), and it has been implemented in thick–wall (Schmid et al., 2010, 2013) and patient-specific (Aparício et al., 2014) domains, Fig. 1.3. The 3D implementation of the theoretical model of arterial G&R discussed in Chapter 4 follows the work of Watton and colleagues.

1.3.4 Existing mechanobiological models of (TGF-β) regulatory signalling

Given the importance of the TGF-β signalling pathway as a regulator and coordinator of vascular cell–mediated G&R of the arterial wall in health and disease, Sec. 1.2.3 and Sec. 1.2.4, it is important to review the extent to which existing models of (arterial) connective tissue mechanobiology have explicitly incorporated components of this pathway. Several mathematical models have focused on capturing the dynamics of TGF-β receptor–ligand interaction and intracellular signalling by means of compartmental model–type systems of coupled ODEs based on the law of mass action. Vilar et al. (2006) predict the duration of cell responses to TGF-β to be a function of the kinetics of ligand–induced receptor degradation. Zi and Klipp (2007) formulate a comprehensive model of TGF-β receptor binding, receptor internalisation and intracellular signalling through the canonical TGF-β pathway. A similar model is formulated by Vizán et al. (2013), who applied it to investigate the cell sensitivity to TGF-β stimulation as a result of receptor–ligand dynamics. Warsinske et al. (2015) couple a simplified model of TGF-β receptor–ligand interaction to a model of α–Smooth Muscle Actin (α-SMA) secretion; this model is applied to the investigation of fibroblast differentiation in the context of TGF-β–induced fibrosis, however without any explicit representation of tissue microstructure or mechanics.

A different group of models focuses less on TGF-β ligand–receptor and intracellular signalling and more on the TGF-β–induced phenotypic changes and their consequences on cell–mediated ECM remodelling. Dale et al. (1996) use a system of coupled constant–rate ODEs to model fibroblast–mediated collagen tissue metabolism under the influence of TGF-β regulation in skin wounds; the model is used to investigate the influence of administering exogenous TGF-β

on the composition of the tissue in terms of different types of collagen, however without explicitly modelling microstructure or biomechanics. Cell–mediated collagen matrix deposition and alignment under the control of TGF-β in the context of wound healing is modelled by Dallon et al. (2001); McDougall et al. (2006). The authors use an agent–based approach to track each fibroblast cell, which migrates along and remodels a continuous field of collagen fibre directions and densities; the effects of a spatially–uniform but time–varying concentration of TGF-β on cell proliferation, motility, reorientation and collagen production are investigated, however without accounting for mechanical loads or the overall deformation of the tissue. Other authors have considered the chemoattractant and pro–fibrotic effect of TGF-β indirectly, without explicitly modelling these signalling pathways: Rouillard and Holmes (2012), for example, include a "chemical guidance cue" in their agent–based model of fibroblast migration in the context of healing myocardial infarcts, however without specifying which chemokine is involved. Purely continuum models integrating some aspects of TGF-β signalling as a mechanotransduction mediator have also been developed. Sáez et al. (2013) model collagen turnover in the context of vascular hypertension by allowing collagen mass density to evolve under the influence of a simplified representation of the TGF-β signalling pathway: the authors assume that TGF-β and TIMP density are positively correlated with vascular smooth muscle cell tone, and that collagen turnover rate is a function of the levels of these two molecules (collagen degradation by MMPs being directly correlated to TIMP levels). Lacking a specific focus on TGF-β signalling, important components of the pathway are not included, such as the influence of TGF-β on the dynamics of vascular cells, or the competition between MMPs and TIMPs that dictates the proteolytic load in the wall.

The need to predict continuum spatio–temporal distributions of active biomolecules (MMP, TIMP, cytokines), cell populations (ECs, VSMCs, (myo)fibroblasts) and cell–matrix interactions (matrix remodelling) in the developing and diseased tissue has been established in the literature (Humphrey, 2008b; Humphrey and Holzapfel, 2012; Wilson et al., 2013). In light of the previous works, there seems to be room for improving the representation of the biochemical mediators of vascular connective tissue mechanobiology under the influence of the TGF-β regulatory signalling pathway, and further to integrate these models in multi–scale, multi–physics computational frameworks that are able to predict vascular disease progression under realistic conditions (Ho et al., 2010). Model guidance, calibration and validation require integrative approaches: the-

oretical and computational tools are used to design experiments, which generate data sets that are able to inform model development, iteratively.

1.4 EXPERIMENTAL MECHANOBIOLOGICAL MODELS

Computational mechanobiological models are extremely important to test mechanistic hypotheses, identify parameters or quantities that crucially determine system behaviour, predict evolution based on current information or estimate values for quantities that cannot be experimentally derived. However, experimental data is essential to validate, calibrate, continuously refine and extend the experimental model formulated. For this reason, experimental models have increasingly been used alongside theoretical approaches in arterial mechanobiology research. Human sample scarcity, availability of tissue specimens only at end stages of aneurysm development (when aneurysms become elective for surgery or rupture), poor control and monitoring of the arterial conditions and the impossibility to subject patients to most perturbations prompted the development of experimental model systems.

In vivo animal models, in particular, can be ethically used to study the effects of genetic, microstructural, biochemical or mechanical perturbations to arterial mechanobiology, and are closer to human arteries than cell culture *in vitro* models. Animal models featuring cell type–specific deletion (*knock–out*, KO) or reduced (*knock–down*) expression of genes encoding for components of the TGF-β signalling pathway have been extensively used, in particular those related to extracellular regulation of TGF-β (fibrillin-1,2; fibulin-4,5; fibronectin-1), TGF-β latency (LTBP-1,2,4) and activation (integrin units β8, β6, αV), TGF-β ligands (isoforms 1,2,3) and receptors (TGFBR1,2 and auxiliary receptors endoglin and betaglycan) and intracellular signalling (SMAD-1,2,3,4,5,7 and TGF-β activated kinase 1) (Dijke and Arthur, 2007).

Blood vessels' mechanical function as conduits of blood with adequate material properties is determined by their microstructure, itself continuously remodelled and adapted by vascular cells under the control of regulatory signalling pathways. Therefore, the application of animal models to study vascular pathology arising from genetic perturbations becomes particularly powerful when (a) combined with other types of perturbations (e.g. mechanical), and/or (b) used to generate multi–dimensional data sets characterising arterial geometry, microstructure, cellular activity

and/or biochemical environment. Ju et al. (2014) overlay on a mouse model of Marphan syndrome (fibrillin-1 hypomorphism) a knock–out of proinflammatory cytokine interleukin (IL)-6 to study the importance of the IL-6 — helper T cell 17 recruitment — macrophage recruitment axis in MFS–associated thoracic aortic dilatations; arterial geometry is monitored *in vivo* by ultrasound, arterial wall microstructure is visualised by multiphoton microscopy (MPM), and the levels of inflammatory cytokines are visualised by immunohistochemistry (IHC) and quantified by quantitative real–time PCR (qt-PCR). Wu et al. (2014) use a mouse model of both mechanical (AngII infusion–induced hypertension) and genetic (knock out of T cell receptors CD4 and CD8, recombinating enzyme RAG-1 and cytokine IL-17) perturbations to arterial wall homoeostasis to study the involvement of T cell–mediated inflammation in arterial stiffening; vessel geometry and blood pressures are used to compute average mechanical quantities, and the levels of load–bearing fibres and inflammatory cells are quantified. A specific component of the TGF-β signalling pathway is knocked-down by Tan et al. (2013), namely SMAD-3, in the context of inflammatory aortic aneurysms; gene expression was visualised by Western Blot and quantified by qt-PCR, cell markers were visualised by IHC and immunofluorescence (IF), collagen microstructure was visualised by Scanning Electron Microscopy (SEM) and vessel mechanics were analysed by uniaxial tensile tests (passive mechanics) and small vessel myography (contractile function).

A more comprehensive biomechanical characterisation of perturbed vessels was performed by Bersi et al. (2014); the authors used a biaxial pressure–inflation and axial stretch mechanical testing device and a four–fibre family microstructurally–motivated constitutive model to characterise the stress–strain behaviour of vessels from several genetic mouse models, in particular fibrillin (FBN)-1 hypomorphism, Fibulin (FBLN)-5 KO, α-SMA KO, dystrophin KO, sarcoglycan–delta (SGCD) KO and AngII–infused Apolipoprotein E (ApoE) KO. Similar biaxial mechanical characterisation of FBLN-5 KO mice was performed by Ferruzzi et al. (2015), who also characterised the microstructure of the vessel wall by histological staining for elastin, collagen, mural cells and glycosaminoglycans (GAGs). Bellini et al. (2015) challenged a mouse model of dysfunctional VSMC contractile function (myosin heavy chain (MYH) gene missense mutation) with pharmacologically–induced hypertension; the vessels were characterised both mechanically by biaxial mechanical testing and microstructurally by several histological stains.

The experimental study presented in Chapter 3 makes use of a novel *in vivo* genetic animal

model of arterial disease, with tissue samples being characterised by biaxial mechanical testing, Picrosirius red collagen staining and Immunofluorescence.

1.5 THESIS STRUCTURE

The present D.Phil. project aims at developing a biologically–centred vascular mechanobiological model that couples a rigorous description of arterial wall microstructure, material properties and biomechanics to a model of the influence of cell population dynamics and regulatory biochemical signalling. The resulting Chemo–Mechano–Biological (CMB) framework can then be applied to provide novel insight into the processes underlying arterial tissue G&R in health and disease. As discussed in the following chapters, the added modelling capabilities open up new lines of research sitting at the heart of mechanobiology, at the interface between cell biology, biochemical signalling, tissue microstructure and vascular mechanics. In particular, questions such as the influence of cellular population dynamics on the ability of the vessel wall to maintain homeostasis or the virtual investigation of the outcomes of pharmacological therapy on the evolving mechanobiological properties of the arterial wall over the course of disease progression can now start to be addressed.

An integrative theoretical, experimental and computational approach was taken in this project. Initially, a conceptual mathematical model of arterial chemo–mechano–biology focusing on the fibroblast–mediated adventitial G&R response was developed (Chapter 2). An *in vivo* animal model of vascular perturbation was then used to generate a multi–dimensional data set (Chapter 3). The signalling pathways and vascular cell biology model initially developed was finally incorporated into an advanced computational framework for 3D simulation of arterial chemo–mechano–biology (Chapter 4). The D.Phil. thesis is structured as follows:

Chapter 1: The scientific context framing the D.Phil. project work is presented. Fundamental concepts on arterial structure, cellular composition and arterial disease are introduced. Detail is provided on the mechanobiological properties of the adventitial layer and of resident vascular cells, as well as on TGF-β signalling in mechanotransduction and dysregulation in disease. Existing computational models of arterial constitutive response and G&R are reviewed, as well as their integration into advanced computational frameworks and their

coupling to certain aspects of the TGF-β signalling pathway. *In vitro* systems used to study connective tissue mechanobiology are reviewed, and animal models of arterial aneurysm are discussed. Thesis structure is presented.

Chapter 2: A novel mathematical model of the chemo–mechano–biology of the arterial wall is formulated in 1D, coupling the biomechanical model of Watton et al. (2009b) with the TGF-β–regulated, cell–mediated collagen metabolism model of Dale et al. (1996). The computational implementation of the model is detailed, and simulation results illustrating the application of the model to predict inflammatory aneurysm evolution and to investigate the effects of profibrotic therapy are shown; this work was published in Aparício et al. (2016). A comprehensive set of additional parameter studies is performed to investigate the behaviour of the model. Three important model extensions are then discussed. Firstly, some aspects of arterial chemo–biology are coupled to the dynamics of cell–mediated remodelling of the collagen fibre natural configuration; illustrative results are shown. Secondly, the CMB model is extended to capture fibroblast to myofibroblast cell differentiation, and the effects of vascular cell dynamics on the G&R behaviour of a perturbed artery are investigated. Thirdly, a cell stiffness variable is added, thus modelling remodelling of sub–cellular structures. Chapter sections close with discussions on the importance of augmenting mechanobiological models with explicit representations of (i) biochemical mediators of matrix metabolism, (ii) the dynamics of vascular cell populations and (iii) mechanically–active intracellular structures.

Chapter 3: An experimental study using an *in vivo* animal model of perturbation to the aortic artery and focusing on generating an integrated biomechanical / microstructural / cellular / biochemical data set is discussed. Details on the design of the study (study groups, study time points) are given, as well as details on the animal model used (conditional disruption of signalling through TGF-β receptor type 2 in the vascular smooth muscle cells of mature mice concurrently subjected to hypertension). The methods used for biaxial mechanical testing of tissue samples and mechanical data fitting to a microstructurally–motivated constitutive model, as well as for histological staining (Picrosirius red for fibrillar collagen, immunofluorescence for cellular and biochemical markers) and imaging, are given. Multi–dimensional results for each study group are then presented, in particular: pressure–

outer diameter and axial force–length data and corresponding continuum average quantities; stored elastic energy isocontours and summary mechanical metrics; quantification of total and types of fibrillar collagen; and quantification of total and density of cellular and biochemical markers. Finally, a few of the previous experimental data are used to perform a preliminary fit to the CMB model in Chapter 2, which prompts a discussion on how experimental data can inform conceptual model development.

Chapter 4: A 3–Dimensional Fluid–Solid–Growth (FSG) computational framework previously developed (Aparício et al., 2014) is enriched by incorporating the signalling pathways–regulated, cell–mediated collagen metabolism model developed in Chapter 2. Details on the 3D implementation and coupling with the CMB model are provided. The 3D CMB implementation is then applied to simulating saccular aneurysm development and to investigate the effect of applying a profibrotic stimulus to aneurysms developing at different rates. The chapter closes with a consistency check between the 1D and the 3D implementations of the model for a particular case.

Chapter 5: The D.Phil. work is overviewed and future directions of research are identified. The main findings generated by the theoretical, experimental and computational tools used, extended or developed in this project are summarised. Some study limitations are identified, which sets the scene for discussing future directions of research, in particular: coupling the CMB model focusing on adventitial collagen metabolism by (myo)fibroblasts with models of other layers and cell populations (luminal ECs, medial VSMCs); performing a rigorous determination of the conditions of mechanobiological stability predicted by the model, as well as the thermodynamic consistency of the model; performing a rigorous fit of the CMB model to the multi–dimensional experimental data collected; coupling haemodynamic variables computed by the FSG loop to specific arterial chemo–mechano–biological mechanisms; applying the CMB model to describe TGF-β–regulated mechanobiology in other systems such as the heart, musculoskeletal system or the skin.

CHAPTER 2

CHEMO–MECHANO–BIOLOGICAL THEORETICAL MODEL OF ARTERIAL G&R

Conceptual models of vascular mechanobiology are important tools to further our understanding of arterial growth and remodelling (G&R) processes in health and disease. In this chapter, a novel chemo–mechano–biological (CMB) model of arterial connective tissue metabolism is formulated (Sec. 2.1). Based on the view that vascular cells are responsive to both mechanical and biochemical cues, and remodel the vascular matrix accordingly, a CMB model coupling a simple description of the biomechanics of an artery as a pressurized and axially stretched 1D nonlinear elastic membrane to a representation of cell–mediated collagen turnover under the control of the Transforming Growth Factor (TGF)-β signalling pathway was formulated (Sec. 2.1.1). The coupled CMB model was computationally implemented and used to study inflammatory aneurysm evolution and its response to a virtual collagen–promoting therapy (Sec. 2.1.2), prompting a discussion on the merits and limitations of this approach (Sec. 2.1.3). The initial model formulation is further developed to capture important aspects of arterial chemo–mechano–biology (Sec. 2.2). Firstly, the evolution of adventitial collagen fibre configurations is coupled to the levels of vascular cells and metabolically–active biomolecules (Sec. 2.2.1). Secondly, fibroblast differentiation into mechanically–active myofibroblasts is modelled (Sec. 2.2.2). Thirdly, cell–level mechanical maturation involving the development of intracellular stress generating and transmitting elements is modelled by introducing a theoretical cell stiffness variable (Sec. 2.2.3). The chapter closes with a summary of conceptual developments and numerical results, which are linked to the experimental and computational work presented in other chapters (Sec. 2.3).

Arterial growth and remodelling (G&R) is mediated by vascular cells in response to their environment, Sec. 1.1. Mechanical and biochemical factors tend to be modelled separately, which ignores their complex interplay in modulating vascular cell phenotype, Sec. 1.3. In this chapter, a novel Chemo–Mechano–Biological (CMB) model of arterial G&R is formulated, and then extended to capture additional features of cell–mediated arterial mechanobiology. CMB model formulation and numerical results were published in Aparício et al. (2016).

2.1 A NOVEL CMB MODEL OF ARTERIAL TISSUE G&R

In the first section of this chapter, the initial formulation of the Chemo–Mechano–Biological (CMB) model of arterial connective tissue G&R is introduced, simulated and discussed.

2.1.1 Methods: novel CMB model

2.1.1.1 Chemo–mechano–biological (CMB) modelling framework

The theoretical CMB model presented here integrates two published mathematical models, i.e. Watton et al. (2009b) and Dale et al. (1996), Fig. 2.1. The biomechanical model of Watton et al. (2009b) captures the biomechanics of cylindrical membranes with a constitutive response similar to that of arteries, and subject to axial pre–stretch and intraluminal pressurization, Fig. 2.1 *right*. Changes in collagen mass are directly coupled to deviations from strain homoeostasis, and thus this model does not include an explicit representation of the cell biology or biochemical regulatory signalling involved. The biomechanical component formulated in Sec. 2.1.1.2, and its extension in Sec. 2.1.1.3, are based on this existing model. The biochemical model of Dale et al. (1996) focuses on the temporal variation of cellular and molecular species relevant to collagen synthesis and degradation in the context of wound healing, however, without accounting for the influence of system biomechanics on cell response. The signalling pathways biochemical component formulated in Sec. 2.1.1.4 is an adaptation and extension of this model, Fig. 2.1 *left*.

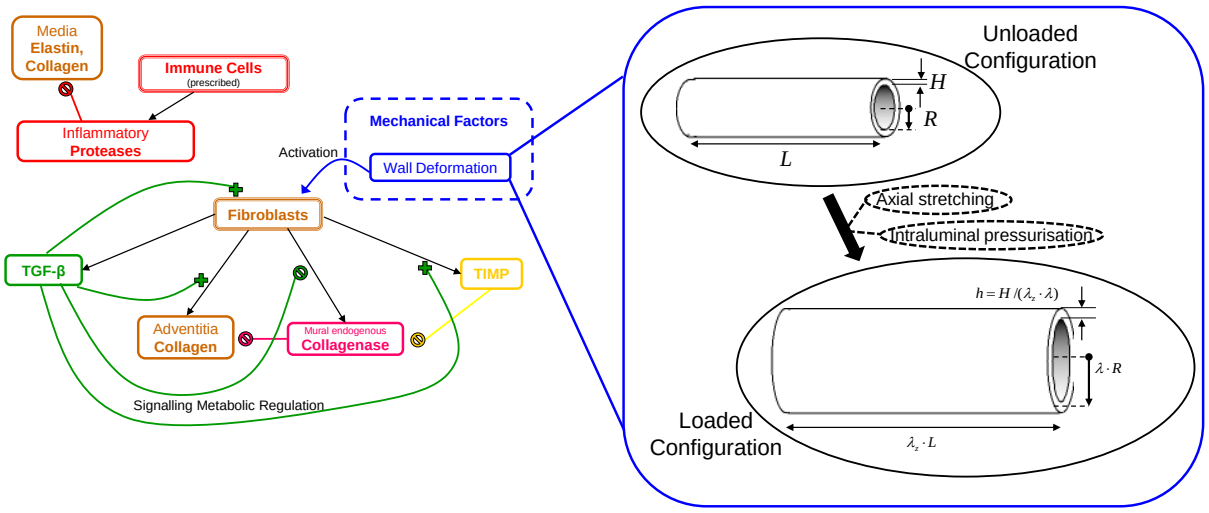

Figure 2.1: **CMB Model Components.** Regulatory signalling pathways biochemical model component, *left*, interfacing with the biomechanical model component, *right*.

2.1.1.2 Biomechanical model component

The artery is modelled as a two–layered cylindrical non–linear elastic membrane. The derivation of the force–balance equation (FBE) governing the system's mechanics follows Watton et al. (2009b). Let subscripts $L = M, A$ denote medial and adventitial layers, resp., and let superscripts $p = E, C$ denote elastin and collagen constituents, resp. Considering as the only load–bearing constituents elastin and collagen in the media and collagen in the adventitia, it follows that

$$p = \frac{1}{R\,\lambda\,\lambda_z}\left[H_{\mathrm{M}}\cdot\left(P^E_{\mathrm{M}}(\lambda) + P^C_{\mathrm{M}}(\lambda^C_M)\right) + H_{\mathrm{A}}\cdot P^C_{\mathrm{A}}(\lambda^C_A)\right], \tag{2.1}$$

where R is the unloaded inner radius; H_M, H_A the unloaded layer thicknesses; λ_z, λ the axial and circumferential stretches, resp.; p the internal pressure; and P^p_{L} the 1^{st} Piola–Kirchhoff stress term for constituent p in layer L. The medial elastinous constituent is modelled as a neo-Hookean material and thus

$$P^E_{\mathrm{M}}(\lambda) = m^E_{\mathrm{M}}\cdot K^E_{\mathrm{M}}\cdot\lambda\cdot\left(1-\frac{1}{\lambda_z^2\cdot\lambda^4}\right), \tag{2.2}$$

where K^E_m is a stiffness–like material constant and $m^E_{\mathrm{M}}(t)$ is the (dimensionless) normalised mass density which is used to simulate elastin degradation.

Following Chen (2014), it is assumed that collagen fibres have a distribution of recruitment, and that each fibre has a linear mechanical response, i.e.

$$\tilde{\Psi}^C_L(\lambda^C_L) = \begin{cases} 0 & \lambda^C_L < 1 \\ \frac{K^C_L}{2}\cdot\left(\lambda^C_L - 1\right)^2 & \lambda^C_L \geq 1 \end{cases}, \tag{2.3}$$

where K^C_L are stiffness–like material constants. Here and for simplicity, it is assumed that all collagen fibres are aligned along the circumferential direction. The Strain Energy Density Function (SEDF) for the entire collagenous tissue is obtained by integrating the fibre SEDF over the distribution of recruitment stretches of load–bearing fibres,

$$\Psi^C_L(\lambda) = \int_1^{\lambda}\tilde{\Psi}^C_L(\lambda^C_L)\cdot\rho\left(\lambda^R_L\right)d\lambda^R_L, \tag{2.4}$$

where circumferential (λ), collagen fibre (λ^C_L) and collagen recruitment (λ^R_L) stretches are related by $\lambda = \lambda^C_L\cdot\lambda^R_L$; and $\rho\left(\lambda^R_L\right)$ is the probability density function (PDF) characterising the distribution of collagen recruitment stretches in the population of fibres. A triangular distribution function is

used here, see Fig. 2.2 *right*,

$$\rho\left(\lambda_L^R\right) = \begin{cases} 0 & \lambda_L^R < \lambda_L^{R,\min} \\ \frac{2\left(\lambda_L^R - \lambda_L^{R,\min}\right)}{\left(\lambda_L^{R,\max} - \lambda_L^{R,\min}\right)\left(\lambda_L^{R,\mathrm{mode}} - \lambda_L^{R,\min}\right)} & \lambda_L^{R,\min} < \lambda_L^R < \lambda_L^{R,\mathrm{mode}} \\ \frac{2\left(\lambda_L^{R,\max} - \lambda_L^R\right)}{\left(\lambda_L^{R,\max} - \lambda_L^{R,\min}\right)\left(\lambda_L^{R,\max} - \lambda_L^{R,\mathrm{mode}}\right)} & \lambda_L^{R,\mathrm{mode}} < \lambda_L^R < \lambda_L^{R,\max} \\ 0 & \lambda_L^R > \lambda_L^{R,\max} \end{cases}. \tag{2.5}$$

where $\lambda_L^{R,min}$ and $\lambda_L^{R,max}$ define the minimum and maximum collagen recruitment stretches for the distribution, i.e. minimum/maximum factors for which the tissue must be stretched for collagen fibres of maximum/minimum undulation to begin to bear load; $\lambda_L^{R,mode}$ relates to the modal recruitment stretch of the distribution.

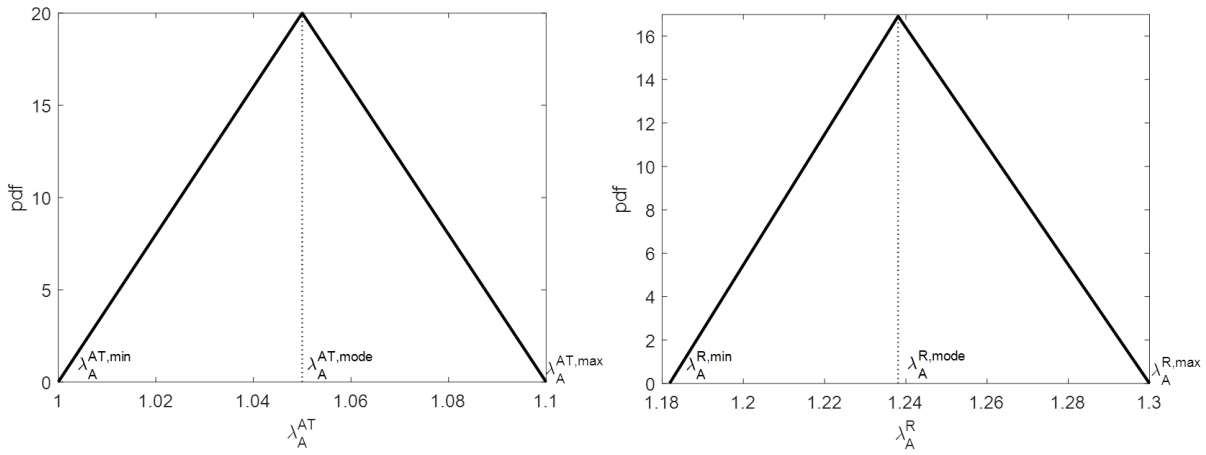

Figure 2.2: Illustrative triangular PDF for collagen attachment stretch λ_A^{AT} (*left*) and corresponding recruitment stretch λ_A^R (*right*) in the adventitia assuming a systolic circumferential stretch of 1.3.

The standard multiplicative decomposition $\lambda = \lambda_L^C \cdot \lambda_L^R$ (Watton and Hill, 2009) is updated to the distribution framework,

$$\lambda_L^{C,\max} \cdot \lambda_L^{R,\min} = \lambda_L^{C,\min} \cdot \lambda_L^{R,\max} = \lambda_L^{C,\mathrm{mode}} \cdot \lambda_L^{R,\mathrm{mode}} = \lambda. \tag{2.6}$$

The stress term for the entire population of collagenous fibres in layer L is obtained by differentiating the SEDF (Eq. (2.4)) with respect to λ and multiplying by the respective normalised mass density term,

$$P_L^C(\lambda_L^C) = m_L^C \cdot \frac{\partial \Psi_L^C}{\partial \lambda} = m_L^C \cdot \left(\frac{\partial}{\partial \lambda} \int_1^{\lambda} \tilde{\Psi}_L^C(\lambda) \cdot \rho\left(\lambda_L^R\right) d\lambda_L^R \right), \tag{2.7}$$

where m_L^C denotes collagen normalised mass densities in layer L. As derived by Aparício et al. (2016), the closed–form expression for the 1st Piola–Kirchhoff stress term P_L^C is

$$P_L^C(\lambda) = \begin{cases} 0 & \lambda < a \\ m_L^C K_L^C \zeta \left[\frac{1}{c-a} \cdot \left((a+\lambda) \ln\left(\frac{\lambda}{a}\right) + 2a - 2\lambda \right) \right] & a \leq \lambda < c \\ m_L^C K_L^C \zeta \left[\frac{1}{c-a} \left((a+\lambda) \ln\left(\frac{c}{a}\right) + a - c + \left(\frac{a-c}{c}\right)\lambda \right) - \frac{1}{b-c} \left((b+\lambda) \ln\left(\frac{\lambda}{c}\right) + b + c - \left(\frac{b+c}{c}\right)\lambda \right) \right] & c \leq \lambda < b \\ m_L^C K_L^C \zeta \left[\frac{1}{c-a} \left((a+\lambda) \ln\left(\frac{c}{a}\right) + a - c + \left(\frac{a-c}{c}\right)\lambda \right) - \frac{1}{b-c} \left((b+\lambda) \ln\left(\frac{b}{c}\right) - b + c - \left(\frac{b-c}{c}\right)\lambda \right) \right] & \lambda \geq b, \end{cases} \tag{2.8}$$

where $a = \lambda_L^{R,min}$, $b = \lambda_L^{R,max}$, $c = \lambda_L^{R,mode}$, and $\zeta := 2/(b-a)$ is a constant. The normalised mass densities of the structural constituents medial elastin m_M^E and collagen m_M^C, and adventitial collagen m_A^C are computed by Eq. (2.15), Eq. (2.19), in the signalling pathways model component.

2.1.1.3 Adaption of collagen attachment stretch distribution: a biologically-informed law

Vascular cells compact newly deposited collagen into a strained state (Alberts et al., 2014), the "attachment" (Watton et al., 2004) or "deposition" (Baek et al., 2005) stretch. The existence of a distribution of collagen fibre wavinesses (reference configurations) (Schrauwen et al., 2012) implies the existence of a distribution of attachment stretches; in this work and for simplicity, this distribution of attachment stretches is modelled by a piecewise linear triangular PDF entirely similar to Eq. (2.5) (substitute $\lambda_L^{R,min}$, $\lambda_L^{R,mode}$, $\lambda_L^{R,max}$ for $\lambda_L^{AT,min}$, $\lambda_L^{AT,mode}$, $\lambda_L^{AT,max}$) and plotted in Fig. 2.2 (*left*) for a particular case.

During aneurysm enlargement, the adventitial collagen matrix may change its role from a protective sheath to playing a load–bearing role. The evolution of this tissue–level property is necessarily mediated by vascular cells, which crawl along and remodel the collagen fibres they secrete (Alberts et al., 2014). Previous authors have modelled this cell–mediated change in adventitial load–bearing role. Chen (2014) prescribed the maximum adventitial attachment stretch to evolve according to a sigmoidal simplified Richards' growth function, and considers possible narrowing and skewing of the entire attachment stretch distribution. Here, and for the first time, the evolution of the attachment stretch distribution is computed as a function of the evolution of system variables, rather than being phenomenologically prescribed. It is assumed that: (1) fibroblast cells continuously transduce the mechanical state of the collagen fibres (Chiquet et al., 2003); (2) fibroblast cell properties gradually change in response to changes in the mechanical properties

of their surroundings; and (3) cells have a finite memory, and thus the history of change in the mechanical condition of their surrounding tissue will influence their properties back to a certain time. Modelling the maximum attachment stretch as a running temporal average of the maximum collagen fibre stretch is thus a natural choice,

$$\lambda_A^{AT,max}(t) = \frac{1}{T_{AT}} \cdot \left(\int_{t-T_{AT}}^{t} \lambda_A^{C,max}|_s(\tau) d\tau \right), \tag{2.9}$$

where T_{AT} is the time interval over which the maximum adventitial collagen fibre stretch (at systole), $\lambda_A^{C,max}|_s$, is averaged. Similarly, the minimum attachment stretch is modelled to evolve according to

$$\lambda_A^{\mathrm{AT,min}}(t) = \left[\frac{1}{T_{AT}} \cdot \left(\int_{t-T_{AT}}^{t} \lambda_A^{C,min}|_s(\tau) d\tau \right) \right] + f_{narrow}^{min}(t), \tag{2.10}$$

where $f_{narrow}^{min}(t)$ relates to the width of the attachment stretch distribution, which may narrow over time. Lastly, the modal attachment stretch evolves as

$$\lambda_A^{\mathrm{AT,mode}}(t) = \left[\frac{1}{T_{AT}} \cdot \left(\int_{t-T_{AT}}^{t} \lambda_A^{C,mode}|_s(\tau) d\tau \right) \right] + f_{skew}^{mode}(t), \tag{2.11}$$

where $f_{skew}^{mode}(t)$ relates to the skew of the distribution, which may also evolve over time. It is further required that, as the system evolves, $\lambda_A^{\mathrm{AT,mode}}(t) < \lambda_A^{\mathrm{AT,max}}(t)$ and $\lambda_A^{\mathrm{AT,mode}}(t) > \lambda_A^{\mathrm{AT,min}}(t)$. In the examples presented in here, and for simplicity, the evolving narrowing/skewing functions are considered to be

$$f_{narrow}^{min}(t) = k_{narrow}^{min} \cdot \left[\max\left\{ \left(\frac{\lambda_A^{\mathrm{C,max}}(t) - \lambda_A^{\mathrm{AT,max}}(t)}{\lambda_A^{\mathrm{AT,max}}(t)} \right), 0 \right\} \right], \tag{2.12}$$

$$f_{skew}^{mode}(t) = k_{skew}^{mode} \cdot \left[\max\left\{ \left(\frac{\lambda_A^{\mathrm{C,max}}(t) - \lambda_A^{\mathrm{AT,max}}(t)}{\lambda_A^{\mathrm{AT,max}}(t)} \right), 0 \right\} \right], \tag{2.13}$$

where $k_{narrow}^{min}, k_{skew}^{mode}$ are constants. The attachment stretch distribution in the media is not re-modelled.

2.1.1.4 Signalling pathways biochemical model component

The temporal evolution of cellular and molecular species involved in arterial connective tissue degeneration is modelled in this signalling pathways biochemical model component, Fig. 2.3. Simplifying assumptions followed in formulating all the equations governing the cellular number

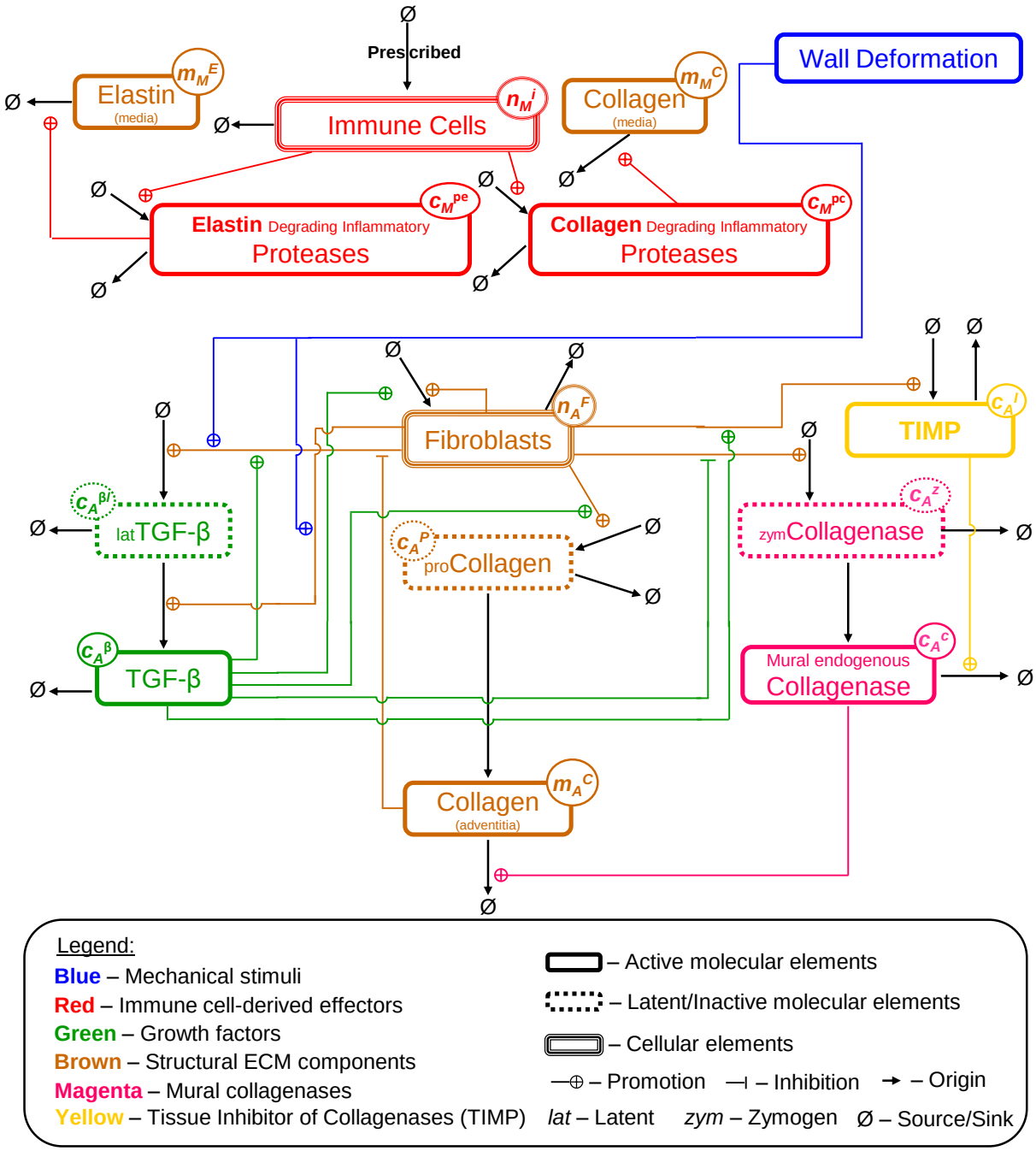

Figure 2.3: **Signalling pathways biochemical model diagram.** All links between species included are based in published experimental observations. Variable symbols used in the governing equations can be found within circles next to the name of each species in the diagram. See text for details.

densities n, molecular concentrations c and mass densities m normalised to the beginning of simulation (hereafter "normalised densities") include: (i) spatial homogeneity, (ii) non–saturating enzyme kinetics, and (iii) very rapid enzyme–substrate interactions. The arterial wall is reduced biochemically to two compartments: the media, constituted of fibrillar elastin and collagen; and the adventitia, where collagen metabolism is mediated by resident fibroblasts and the active molecular species they secrete. The evolution of these species is described by a system of coupled

non–linear constant rate ODEs. Parameter definitions, values and supporting references can be found in Table 2.1—Table 2.3.

Medial degeneration Infiltrating immune cells are common findings within the arterial wall of aneurysms Rizas et al. (2009). The level of immune cells $n_M^i(t)$ in the model is prescribed,

$$n_M^i(t) = \begin{cases} i_0 & t < t_{i0} \\ i_0 + \left(\frac{t-t_{i0}}{k_i+(t-t_{i0})}\right) \cdot i_{\max} & t \geq t_{i0} \end{cases}. \tag{2.14}$$

The inflammatory response mediated by these cells is involved in the degradation of medial elastin (m_M^E) and collagen (m_M^C) ((Frösen et al., 2012)). These processes are captured in the model by the dependence on immune cell–produced elastin–degrading elastases c_M^{pe} and collagen–degrading collagenases c_M^{pc} in the sink terms of the governing ODEs below,

$$\frac{dm_M^E}{dt} = -r_e \cdot c_M^{pe} \cdot m_M^E, \qquad \frac{dm_M^C}{dt} = -r_{cm} \cdot c_M^{pc} \cdot m_M^C. \tag{2.15}$$

The governing ODEs for protease concentration are

$$\frac{dc_M^{pc}}{dt} = r_{pc_1} \cdot n_M^i - r_{pc_2} \cdot c_M^{pc}, \qquad \frac{dc_M^{pe}}{dt} = r_{pe_1} \cdot n_M^i - r_{pe_2} \cdot c_M^{pe}. \tag{2.16}$$

Adventitial collagen growth Some of the mechanobiological processes responsible for adventitial collagen metabolism discussed in Sec. 1.2 are now mathematically formalised. The main cells responsible for collagen maintenance in the adventitia are fibroblasts; their normalised number density is denoted n_A^F. Fibroblasts produce (adventitial) procollagen c_A^P and zymogen c_A^z which are subsequently converted into active forms, i.e. collagen m_A^C and collagenase c_A^{ca}, respectively (Shoulders and Raines, 2009). Tissue inhibitors of metalloproteinases (TIMPs), denoted c_A^I, are common collagenase inhibitors secreted by fibroblasts, which form an irreversible inhibitory complex with the enzymes and suppress their action (Brew et al., 2000). Collagen maintenance is a tightly regulated process. For instance, TGF-β is a signalling molecule with a collagen–promoting (i.e., *profibrotic*) action in the adventitia: it promotes procollagen synthesis (Lindahl et al., 2002); it stimulates fibroblast population growth via increased migration (Martin et al., 1992), proliferation (Akhurst and Hata, 2012) and differentiation (McAnulty, 2007); it suppresses zymogen secretion and upregulates TIMP secretion (Akhurst and Hata, 2012). TGF-β is secreted by fibroblasts in an inactive latent form $c_A^{\beta l}$, which is then activated to c_A^{β}. The system of

ODEs governing collagen metabolism is:

$$\frac{dn_A^F}{dt} = \left(r_{f_1} + r_{f_2} \cdot c_A^{\beta}\right) \cdot n_A^F - r_{f_3} \cdot n_A^F \tag{2.17}$$

$$\frac{dc_A^P}{dt} = \left(r_{p_1} + r_{p_2} \cdot c_A^{\beta}\right) \cdot n_A^F - r_{p_3} \cdot c_A^P \tag{2.18}$$

$$\frac{dm_A^C}{dt} = r_{c_1} \cdot c_A^P - r_{c_2} \cdot c_A^{ca} \cdot m_A^C \tag{2.19}$$

$$\frac{dc_A^z}{dt} = \left(\frac{r_{z_1}}{1 + r_{z_2} c_A^{\beta}}\right) \cdot n_A^F - r_{z_3} \cdot c_A^z \tag{2.20}$$

$$\frac{dc_A^{ca}}{dt} = r_{ca_1} \cdot c_A^z - \left(r_{ca_2} + r_{ca_3} \cdot c_A^I\right) \cdot c_A^{ca} \tag{2.21}$$

$$\frac{dc_A^I}{dt} = \left(r_{I_1} + r_{I_2} c_A^{\beta}\right) \cdot n_A^F - \left(r_{I_3} + r_{I_4} \cdot c_A^{ca}\right) \cdot c_A^I \tag{2.22}$$

TGF-β Regulatory signalling TGF-β is one of the most significant regulators of collagen metabolism and matrix deposition in the arterial wall (Streuli et al., 1993). There is no baseline production of latent TGF-β by adventitial fibroblasts (Shi et al., 1996a). Instead of being continuously present, it transiently acts as a link in fibroblast mechanotransduction pathways by coupling deviations from mechanical homoeostasis to altered collagen metabolism (Lindahl et al., 2002). The latent ($c_A^{\beta l}$) and active (c_A^{β}) forms of TGF-β are modelled by

$$\frac{dc_A^{\beta l}}{dt} = \left(\frac{r_{\beta l_1} \cdot c_A^{\beta} + r_{\beta l_2} \cdot f\left(\lambda^F\right)}{1 + r_{\beta l_3} \cdot m_A^C}\right) \cdot \; n_A^F - \left(r_{\beta l_4} + r_{\beta l_5} \cdot f\left(\lambda^F\right) \cdot n_A^F\right) \cdot c_A^{\beta l} \tag{2.23}$$

$$\frac{dc_A^{\beta}}{dt} = \left(r_{\beta_1} + r_{\beta_2} \cdot f\left(\lambda^F\right) \cdot n_A^F\right) \cdot c_A^{\beta l} - r_{\beta_3} \cdot c_A^{\beta} \tag{2.24}$$

TGF-β–mediated mechanotransduction is considered to take place at two levels. First, increased stretch of fibroblast cells above homoeostatic values ($\lambda^F > \lambda_h^F$) leads to the increased production of latent TGF-β (O'Callaghan and Williams, 2000). Secondly, latent TGF-β is activated not only by endogenous and immune cell–driven proteolysis but also by a stretch–dependent mechanism (Shi et al., 2011). To simulate this, and for illustration, consider $f\left(\lambda^F\right) = (\lambda^F - \lambda_h^F)/\lambda_h^F$ and, here, further assume that: (i) the stretch fibroblasts transduce and respond to is equal to the stretch of the surrounding collagen fibres, and in particular $\lambda^F = \lambda_A^{C,max}$; (ii) the homoeostatic stretch target for fibroblasts λ_h^F is equal to the stretch target for the collagen fibres they remodel, the attachment stretch, $\lambda_h^F = \lambda_A^{AT,max}$.

Collagen remodelling: the recruitment stretch distribution The collagen recruitment distribution in the adventitia, $\rho\left(\lambda_A^R\right)$, evolves to return the collagen stretch distribution towards the collagen attachment stretch distribution. Following Watton et al. (2004), the rate of evolution of minimum, mode and maximum recruitment stretches is driven by deviations of collagen stretch from homoeostatic attachment values (which are dynamic, c.f. Eq. (2.9)—Eq. (2.11)),

$$\frac{d\lambda_{\mathrm{A}}^{R,\mathrm{min}}}{dt} = \alpha_{\mathrm{A}}^{C} \cdot \left(\frac{\lambda_{\mathrm{A}}^{C,\mathrm{max}}|_s - \lambda_{\mathrm{A}}^{\mathrm{AT,max}}}{\lambda_{\mathrm{A}}^{\mathrm{AT,max}}} \right), \tag{2.25}$$

$$\frac{d\lambda_{\mathrm{A}}^{R,\mathrm{max}}}{dt} = \alpha_{\mathrm{A}}^{C} \cdot \left(\frac{\lambda_{\mathrm{A}}^{C,\mathrm{min}}|_s - \lambda_{\mathrm{A}}^{\mathrm{AT,min}}}{\lambda_{\mathrm{A}}^{\mathrm{AT,min}}} \right), \tag{2.26}$$

$$\frac{d\lambda_{\mathrm{A}}^{R,\mathrm{mode}}}{dt} = \alpha_{\mathrm{A}}^{C} \cdot \left(\frac{\lambda_{\mathrm{A}}^{C,\mathrm{mode}}|_s - \lambda_{\mathrm{A}}^{\mathrm{AT,mode}}}{\lambda_{\mathrm{A}}^{\mathrm{AT,mode}}} \right), \tag{2.27}$$

where α_{A}^{C} is a rate constant. The collagen recruitment stretch distribution in the media follows similar G&R laws (rate constant α_{M}^{C}).

2.1.1.5 Computational implementation

Parameter value selection Parameter definitions and values can be found in Table 2.1—Table 2.3. The simulation time scale (inflammation starting at $t_{i0} = 40$ years and simulation run until $t_{sim} = 90$ years) loosely resembles the life time of a human being. The model was geometrically and microstructurally parametrised to the human abdominal aorta, Table 2.1. Parameters controlling the G&R dynamics of the system (α_M^C, α_A^C, T_{AT}) are determined such that mechanical and biochemical variables achieve physiologically consistent steady states, e.g. $2 \leq \lambda^s \leq 4$ and $\lambda_A^{C,max} \leq 1.1$ at final steady state. Parameter values for the biochemical model, Table 2.2 and Table 2.3, are illustrative and loosely motivated by literature observations. Infiltrating immune cell properties and secreted molecules were based on Rizas et al. (2009). TGF-β secretion, activation and regulation of fibroblast phenotype was based on Streuli et al. (1993), Martin et al. (1992), McAnulty (2007), Shi et al. (2011) and Akhurst and Hata (2012). Collagen properties were informed by Shoulders and Raines (2009). Collagen metabolism mediated by matrix metalloproteinases (MMPs) was based on Hobeika et al. (2007) and Siefert and Sarkar (2012), while the action of TIMPs was informed by Brew et al. (2000). Finally, two biologically–informed rate constant inequalities, i.e. active collagenase degradation (r_{ca_2}) slower than zymogenic collage-

Table 2.1: **Initial CMB model mechanical parameters.** Symbols, definitions, values and references.

Parameter	Definition	Value [unit]	Notes and References
R_0	Physiological luminal arterial radius, unloaded configuration	10 [mm]	Physiological human infra-renal aortic radius 7.5–12mm (McGloughlin, 2011)
H_0	Physiological arterial wall thickness, unloaded configuration	2 [mm]	Human abdominal aortic wall thickness 0.23–4.26mm in abdominal aortic aneurysms (Raghavan et al., 2006)
H_M^{factor}	Ratio {media layer : total wall} thickness	2/3	(Gao et al., 2006)
L	Physiological arterial length	0.2 [m]	Length of human descending aorta (Dotter et al., 1950)
p^s	Systolic blood pressure	120 [mmHg]	(Guyton and Hall, 2006)
K_{factor}	Adventitial:medial stiffness factor	4	Adventitia stiffer than media once overstretched (Holzapfel et al., 2000)
$P_{m,0}^{E:C}$	Ratio of load initially borne by medial elastin to medial collagen	0.8	Elastin main load–bearer in healthy arteries (McGloughlin, 2011)
λ_z	Arterial axial stretch ratio	1.3	(Watton et al., 2011)
α_M^C	Baseline rate of medial collagen recruitment stretch remodelling	1.2 [year^{-1}]	
α_A^C	Baseline rate of adventitial collagen recruitment stretch remodelling	1.2 [year^{-1}]	
T_{AT}	Collagen stretch averaging time period for attachment stretch remodelling	10 [years]	
k_{skew}^{mode}	Factor for adventitial collagen attachment stretch distribution skewing	2	
k_{narrow}^{min}	Factor for adventitial collagen attachment stretch distribution narrowing	2	
t_{sim}	Total simulation time	90 [years]	Analogous to maximum lifespan of healthy human
t_{Treat}	Time for treatment with TGF-β step increase	45 [years]	
β_{step}	Magnitude of TGF-β step increase	2	
β_a^C	Adventitial collagen growth rate	1 [year^{-1}]	Watton et al. (2009b) model
$t_{ElD,0}$	Time for onset of medial elastin degradation	40 [years]	Watton et al. (2009b) model; equal t_{i0}
$t_{CmD,0}$	Time for onset of medial collagen degradation	40 [years]	Watton et al. (2009b) model; equal t_{i0}
Δt_{ED}	Time interval for complete medial elastin degradation	10 [years]	Watton et al. (2009b) model
Δt_{CmD}	Time interval for complete medial collagen degradation	10 [years]	Watton et al. (2009b) model
$m_{M,min}^E$	Minimum level of medial elastin	1×10^{-8}	Watton et al. (2009b) model
$m_{M,min}^C$	Minimum level of medial elastin	1×10^{-8}	Watton et al. (2009b) model

Table 2.2: **Initial CMB model biochemical parameters I.** Symbols, definitions, values and references.

Parameter	Definition	Value [unit]	Notes
r_e	Elastin degradation rate by immune cell proteases	1 [year^{-1}]	
r_{cm}	Medial collagen degradation rate by immune cell proteases	1 [year^{-1}]	
t_{i0}	Time for onset of immune cell infiltration	40 [years]	
i_0	Initial level of immune cells in vessel wall	0	
i_{max}	Maximum level of immune cells in vessel wall	1	
k_i	Time for immune cell levels to reach half of maximum level	1.25 [years]	
r_{pc_1}	Collagenase secretion rate by immune cells	1 [year^{-1}]	
r_{pc_2}	Baseline immune cell collagenase degradation rate	1 [year^{-1}]	
r_{pe_1}	Elastase secretion rate by immune cells	1 [year^{-1}]	
r_{pe_2}	Baseline immune cell elastase degradation rate	1 [year^{-1}]	
r_{f_1}	Baseline fibroblast migration and proliferation rate	1 [year^{-1}]	
r_{f_2}	Fibroblast population dynamics sensitivity to TGF-β	0.5 [year^{-1}]	combined chemotactic and growth factor effects
r_{f_3}	Fibroblast cell death rate	1 [year^{-1}]	
r_{p_1}	Baseline procollagen secretion rate by fibroblasts	1 [year^{-1}]	
r_{p_2}	Fibroblast procollagen secretion sensitivity to TGF-β	0.5 [year^{-1}]	
$r_{p_3} = r_{p_3}^d + r_{p_3}^m$	Combined baseline degradation ($r_{p_3}^d$) and modification ($r_{p_3}^m$) rates	0.5+0.5 [year^{-1}]	
r_{c_1}	Baseline adventitial procollagen modification rate	0.5 [year^{-1}]	equal $r_{p_3}^m$
r_{c_2}	Adventitial collagen degradation rate by collagenases	0.5 [year^{-1}]	

Table 2.3: **Initial CMB model biochemical parameters II.** Symbols, definitions, values and references.

Parameter	Definition	Value [unit]	Notes
r_{z_1}	Baseline zymogen secretion rate by fibroblasts	1 [year^{-1}]	
r_{z_2}	Fibroblast zymogen secretion sensitivity to TGF-β (repressor)	0.5	
$r_{z_3} = r^d_{z_3} + r^m_{z_3}$	Combined baseline zymogen degradation ($r^d_{z_3}$) and modification ($r^m_{z_3}$) rates	0.5+0.5 [year^{-1}]	
r_{ca_1}	Baseline zymogen modification rate	0.5 [year^{-1}]	equal r^m_{caz3}
r_{ca_2}	Baseline active collagenase degradation rate	0.25 [year^{-1}]	active collagenase degradation (r_{ca_2}) slower than zymogenic collagenase degradation ($r^d_{z_3}$)
r_{ca_3}	Collagenase inactivation rate by collagenase inhibitors	0.25 [year^{-1}]	Formation of inhibitor / collagenase complex
r_{I_1}	Baseline collagenase inhibitor secretion rate	1 [year^{-1}]	
r_{I_2}	Fibroblast collagenase inhibitor secretion sensitivity to TGF-β (promoter)	0.5 [year^{-1}]	
r_{I_3}	Baseline collagenase inhibitor degradation rate	0.75 [year^{-1}]	
r_{I_4}	Collagenase inactivation rate by inhibitor	0.25 [year^{-1}]	equal r_{ca4}
$r_{\beta l_1}$	Fibroblast latent TGF-β secretion sensitivity to active TGF-β (promoter)	0.1 [year^{-1}]	
$r_{\beta l_2}$	Fibroblast latent TGF-β secretion sensitivity to deviations from mechanical homoeostasis	5 [year^{-1}]	default value
$r_{\beta l_3}$	Fibroblast latent TGF-β secretion sensitivity to collagen levels (repressor)	1	
$r_{\beta l_4} = r^d_{\beta l_4} + r^m_{\beta l_4}$	Combined baseline degradation ($r^d_{\beta l_4}$) and modification ($r^m_{\beta l_4}$) rates	0.5+0.5 [year^{-1}]	
$r_{\beta l_5}$	Latent TGF-β modification rate by stretch–dependent mechanism	1 [year^{-1}]	
$r_{\beta 1}$	Baseline latent TGF-β activation rate	0.5 [year^{-1}]	equal $r^m_{\beta l_4}$
$r_{\beta 2}$	Modification rate by stretch–dependent mechanism	1 [year^{-1}]	equal $r_{\beta l_5}$
$r_{\beta 3}$	Baseline degradation rate	1 [year^{-1}]	active TGF-β degradation (r_{β_3}) faster than latent TGF-β degradation ($r^d_{\beta l_4}$)

nase degradation ($r^d_{z_3}$), and active TGF-β degradation (r_{β_3}) faster than latent TGF-β degradation ($r^d_{\beta l_4}$), were based on Dale et al. (1996).

Initial conditions for the mechanical variables are as follows. Circumferential stretch at systole λ^s_0 is initialised to 1.3 and the axial stretch is taken to be $\lambda_z = 1.3$. The initial attachment stretch distributions are prescribed; this implies initial values for the recruitment stretch distributions according to Eq. (2.6), with $\lambda^C_L(t=0) = \lambda^{AT}_L(t=0)$. More specifically, the adventitia is assumed to bear no load at systole, $\lambda^{AT,max}_A = 1$. Furthermore, the distribution is assumed to be symmetric and with width $w(t) = 0.1$, so that $\lambda^{AT,min}_A = 0.9$ and $\lambda^{AT,mode}_A = 0.95$. It is assumed that the medial collagen bears load during the cardiac cycle, and further that $\lambda^{AT,max}_M = 1.1$; $\rho(\lambda^{AT}_M)$ is assumed to be symmetric and with width $w(t) = 0.1$, so that $\lambda^{AT,min}_M = 1$ and $\lambda^{AT,mode}_M = 1.05$. Determination of other material constants follows Watton et al. (2004). The densities of cellular and molecular species are normalised to their initial value. However, for species that are absent from normal arteries under baseline conditions, i.e. both forms of TGF-β ($c^{\beta l}_A$,c^{β}_A) and infiltrating

immune cells (n_M^i), the initial values are set to zero.

Watton et al. (2009) Model So as to allow comparison with previously existing, phenomenological models, the biomechanical model of Watton et al. (2009b) is adapted and implemented here. The degradation of medial elastin and collagen is prescribed according to

$$m_{\mathrm{m}}^E = \begin{cases} m_{\mathrm{m},0}^E & t < t_{\mathrm{ED},0} \\ m_{\mathrm{m},0}^E \cdot \left(\frac{m_{\mathrm{m,min}}^E}{m_{\mathrm{m},0}^E} \right)^{\frac{t - t_{\mathrm{ED},0}}{\Delta t_{\mathrm{ED}}}} & t_{\mathrm{ED},0} \leq t < t_{\mathrm{ED},0} + \Delta t_{\mathrm{ED}} \\ m_{\mathrm{m,min}}^E & t \geq t_{\mathrm{ED},0} + \Delta t_{\mathrm{ED}} \end{cases}, \tag{2.28}$$

$$m_{\mathrm{M}}^C = \begin{cases} m_{\mathrm{M},0}^C & t < t_{\mathrm{CmD},0} \\ m_{\mathrm{M},0}^C \cdot \left(\frac{m_{\mathrm{M,min}}^C}{m_{\mathrm{M},0}^C} \right)^{\frac{t - t_{\mathrm{CmD},0}}{\Delta t_{\mathrm{CmD}}}} & t_{\mathrm{CmD},0} \leq t < t_{\mathrm{CmD},0} + \Delta t_{\mathrm{CmD}} \\ m_{\mathrm{M,min}}^C & t \geq t_{\mathrm{CmD},0} + \Delta t_{\mathrm{CmD}} \end{cases}, \tag{2.29}$$

where $t_{\mathrm{ED},0}$, $t_{\mathrm{CmD},0}$ are onset times for elastin and medial collagen degradation, resp.; Δt_{ED}, Δt_{CmD} time intervals for such degradation; $m_{\mathrm{M},0}^E$, $m_{\mathrm{M},0}^C$ their normalised densities at $t = 0$; and $m_{\mathrm{M,min}}^E$, $m_{\mathrm{M,min}}^C$ their ("minimum") normalised densities after completion of degradation. So as to allow for comparison between models, model parameters governing elastin degradation kinetics in both the novel CMB model and the model of Watton et al. (2009b) were selected such that the kinetics of elastin degradation predicted by either model were similar, c.f. Fig. 2.4.

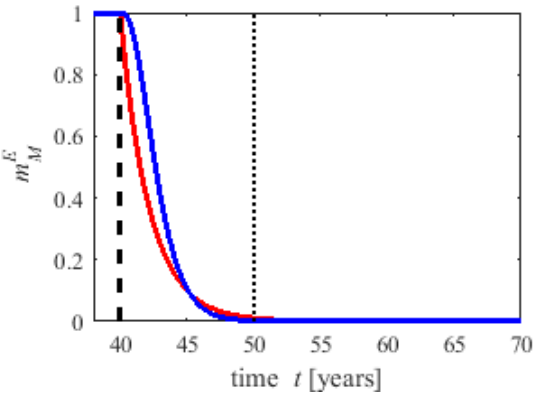

Figure 2.4: Kinetics of elastin degradation predicted by the novel CMB model (blue) *vs.* the previously existing model of (Watton et al., 2009b) (red). For both models elastin starts degrading at $t_{i0} = 40$ years (black dashed line), and degradation is almost complete at $t_{end}^{ElDeg} = 50$ years (black dotted line).

The normalised mass density of adventitial collagen in Watton et al.'s model is biologically motivated but phenomenologically coupled to the deviation from mechanical homoeostasis,

$$\frac{dm_{\mathrm{A}}^C}{dt} = \beta_{\mathrm{A}}^C \cdot m_{\mathrm{A}}^C \cdot \left(\frac{\lambda_{\mathrm{A}}^{\mathrm{C,max}} - \lambda_{\mathrm{A}}^{\mathrm{AT,max}}}{\lambda_{\mathrm{A}}^{\mathrm{AT,max}}} \right). \tag{2.30}$$

The remodelling of medial and adventitial recruitment stretches is similar to the model formulated, Eq. (2.25)—Eq. (2.27). Finally, the remodelling of the adventitial collagen attachment stretch follows the same laws as the CMB model, Sec. 2.1.1.3.

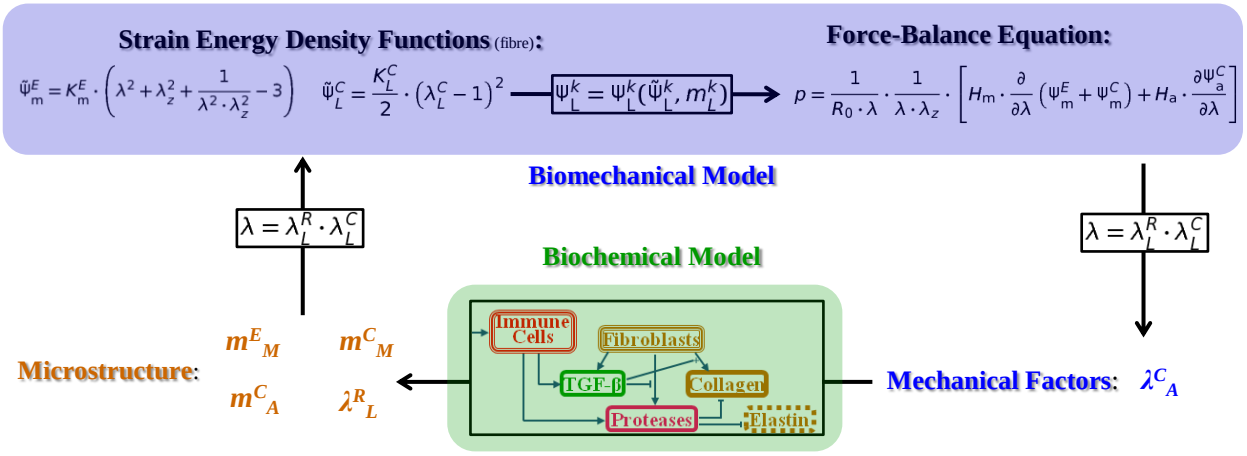

Figure 2.5: CMB model computational simulation loop.

Simulation Loop The general CMB model was implemented in Matlab R2013a (The Mathworks, Nattick, MA, USA). The system of coupled equations was iteratively solved by a fully explicit approach: the system of coupled ODEs, Eq. (2.14)—Eq. (2.24) and Eq. (2.25)—Eq. (2.27), were solved by a backward finite differences Euler method using a fixed step length of 0.0069 years (at which step independence was achieved), while the algebraic force–balance equation (FBE), Eq. (2.1), was solved by Matlab–native function `fzero`. Once system variables are initialised, the simulation is started. The SEDFs for each elastin and collagen fibre $\tilde{\Psi}^k_L$ are computed, which and then integrated over the distribution of load–bearing fibres and multiplied by the respective normalised mass densities m^k_L to obtain the SEDFs for each fibre population Ψ^k_L. These functions are then passed to the FBE, Eq. (2.1), which is solved for the systolic intraluminal pressure. The stretch ratio computed is resolved to collagen fibre stretch λ^C_A, which is passed to the mechanotransduction functionals used to generate updated estimates of the cellular and biochemical variables (such as those of the load–bearing constituents m^E_M, m^C_M, m^C_A) and collagen fibre recruitment (λ^R_L) and attachment (λ^{AT}_L) stretch distributions by means of the signalling pathways set of coupled ODEs. The updated estimates for the masses of load–bearing constituents and collagen recruitment stretches are fed back into the SEDFs, which are input to the FBE for updated solution, iteratively, Fig. 2.5.

2.1.2 Results: novel CMB model

The CMB model is applied to simulate the evolution of inflammatory aneurysms (IAs), Sec. 2.1.2.1; and the effects of a collagen–promoting drug on the development of this disease, Sec. 2.1.2.2. IAs, such as most AAAs, are a class of aneurysms where immune cells infiltrate into the arterial wall and secrete proteolytic enzymes which degrade load–bearing elastin, resulting in arterial expansion (Sakalihasan et al., 2005). A model of an initially healthy artery is subjected to prescribed immune cell infiltration according to Eq. (2.14). Immune cell infiltration starts at $t_{i0} = 40$ and results in elastin degradation, which is almost complete at $t_{End}^{ElDeg} = 50$, Fig. 2.4. The ability of the model to simulate return to a stable state is then assessed. Different values of rate constant $r_{\beta l_2} = \{0.1, 1, 5, 10\}$ in Eq. (2.23) are used to simulate different rates of fibroblast mechanotransduction. Finally, the predictions generated by the CMB model (in blue) are compared with the Watton et al. (2009b) model (in red).

2.1.2.1 Modelling inflammatory aneurysm evolution

Mechanical variables Fig. 2.6(a)—(c) display the mechanical evolution of an idealised aneurysm in response to a prescribed infiltration of immune cells starting at $t = 40$ years. The production of proteolytic enzymes by these infiltrating cells, Eq. (2.16), results in elastin degradation in the media and arterial enlargement, as can be seen by the increase in circumferential stretch, Fig. 2.6(a). Increasingly more of the load previously borne by medial elastin is now being borne by adventitial collagen, leading to an increase in adventitial collagen stretch, Fig. 2.6(c). The adventitia responds to this aneurysmal expansion of the artery by *growth*, increasing collagen mass (Fig. 2.6(b)), and *remodelling*, a change in attachment stretch distribution. This adaptive response of the adventitia slows down the enlargement of the artery, c.f. the reducing slope of each curve in Fig. 2.6(a) during years 50—70. At the end of the simulation, the circumferential stretch increases by a factor of 2 to 4 (Fig. 2.6(a)), and the collagen density increases by up to 50% (Fig. 2.6(b)). Notably, the adventitia changes its role from a protective sheath to bearing load (Fig. 2.6(c)), i.e. $\lambda_A^{C,max} = 1$ at $t = 0$ shifts to $\lambda_A^{C,max} > 1$ as the aneurysm converges to a new homoeostasis. This adventitial adaptation was a result of the collagen attachment stretch law implemented in the model, Eq. (2.9), and emerges naturally from the underlying evolution of the collagen stretch distribution.

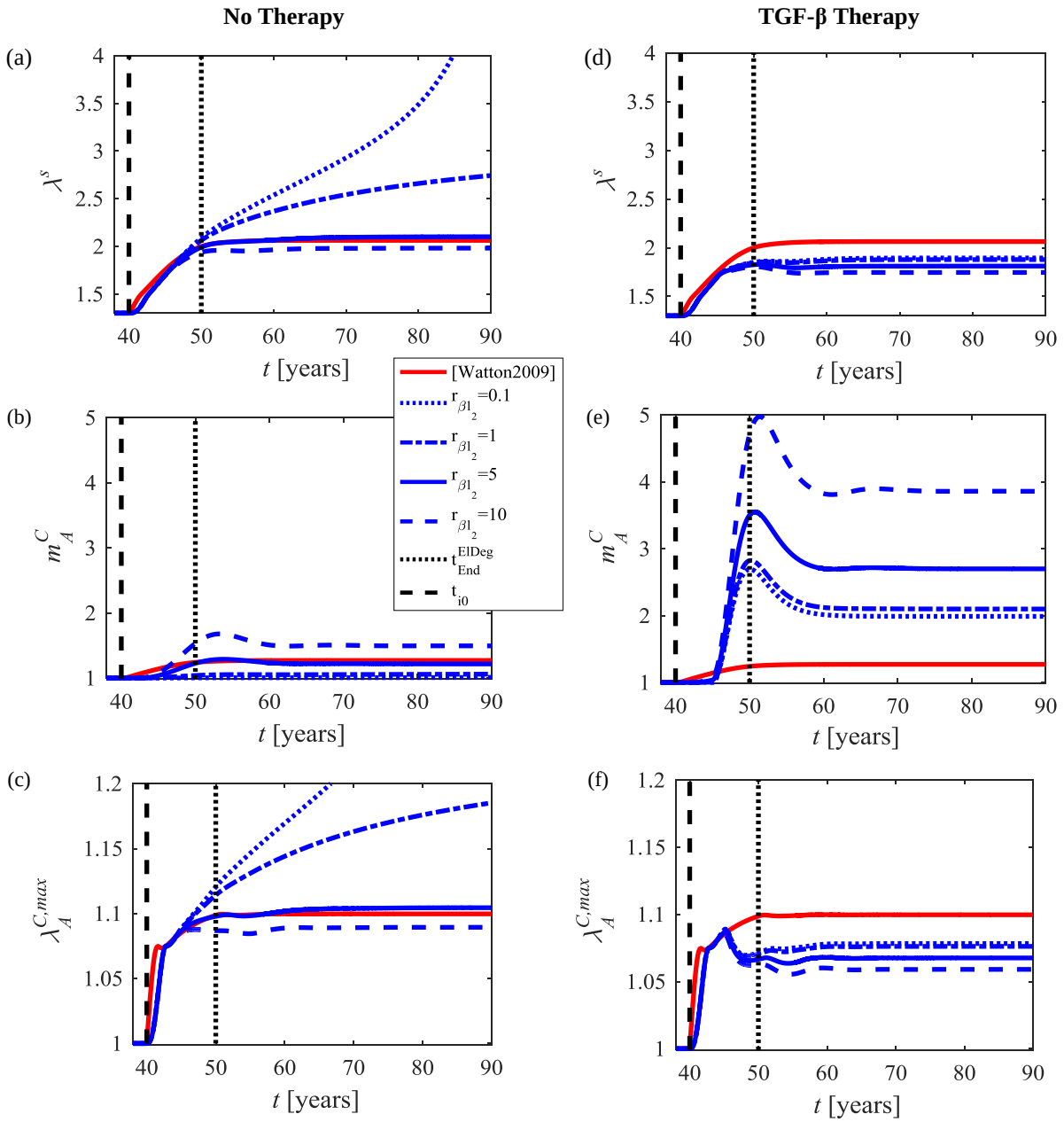

Figure 2.6: **Novel CMB model simulation results — mechanical variables**. Parameter study on the rate of mechanotransduction $r_{\beta l_2}$ for the IA development case (*left*) *vs.* TGF-β therapy case (*right*).

Target behaviours Different rates of mechanical to biochemical mechanotransduction (directly correlated to mechanotransduction *sensitivity*) were simulated for the coupled CMB model. Each blue line in Fig. 2.6(a)—(c) corresponds to a different value of rate constant $r_{\beta l_2}$ in Eq. (2.23), the rate of production of latent TGF-β by fibroblasts as a result of a deviation of collagen fibre stretch from its homoeostatic target (the *attachment stretch*). It is clear that faster rates of mechanotransduction (solid and dashed lines) lead to faster and ultimately larger collagen production as a result of arterial expansion, Fig. 2.6(b). Such fast re–enforcement of the adventitia halts further expansion, and results in stable domains (later time points in Fig. 2.6(a), Fig. 2.6(c)). On the other hand, in the two slower mechanotransduction cases (dotted and dashed–dotted lines) there are

only very modest collagen increases in the adventitia, Fig. 2.6(b), which cannot stop the continuous enlargement of the artery, accelerating for the slowest rate of mechanotransduction $r_{\beta l_2} = 0.1$ and approx. linear for $r_{\beta l_2} = 1$ (later time points in Fig. 2.6(a), Fig. 2.6(c)). The CMB model is thus able to capture two distinct characteristic behaviours of aneurysmal arteries — stabilisation *vs.* continual growth.

Consistency with pre–existing model The evolution of the mechanical quantities predicted by the CMB model (blue curves) for the faster mechanotransduction cases is very similar to the behaviour predicted by the conceptually simpler model of Watton et al. (2009b) (red curve), Fig. 2.6(a)—(c). However, the CMB model additionally predicts the biological condition of the wall, i.e. estimates of the levels of different cell types and biomolecules directing the observed mechanical changes, Fig. 2.7(a).

Cellular and molecular variables Fig. 2.7(a) displays the predicted evolution of the cellular and biomolecular variables for simulation case $r_{\beta l_2} = 5$. The rates of change of these species are given by the equations in Sec. 2.1.1.4, a mathematical implementation of the biochemical network in Fig. 2.3. The prescribed infiltration of immune cells (thick red line) is followed by a similar increase in proteases (thin red line). These proteolytic enzymes lead to degradation of medial elastin and collagen (dot–dashed brown line), and the artery enlarges. Adventitial fibroblasts respond via TGF-β signalling, increasing the levels of the latent form (dashed green line) that is then converted into the active form (solid green line). As described in Sec. 2.1.1.4, TGF-β promotes collagen deposition by its multiple actions on fibroblasts: increase in fibroblast numbers (thick brown line), down–regulation in endomural collagenases (solid magenta line) and increase in inhibitors of collagenases or TIMPs (yellow line). The overall effect is an increase in collagen (thin brown line), also seen in Fig. 2.6(b); such significant *growth* in collagen leads to aneurysm stabilisation. This new mechanical homoeostasis is perceived by fibroblasts, which reduce TGF-β secretion. In its absence, all the remaining biomolecules achieve new steady states: approx. 50% increase in fibroblasts, inhibitors, and immature collagen and collagenase; approx. 25% increase in mature collagen and collagenase; and a return of TGF-β levels to zero, which thus behaves as a transient mechanotransducer.

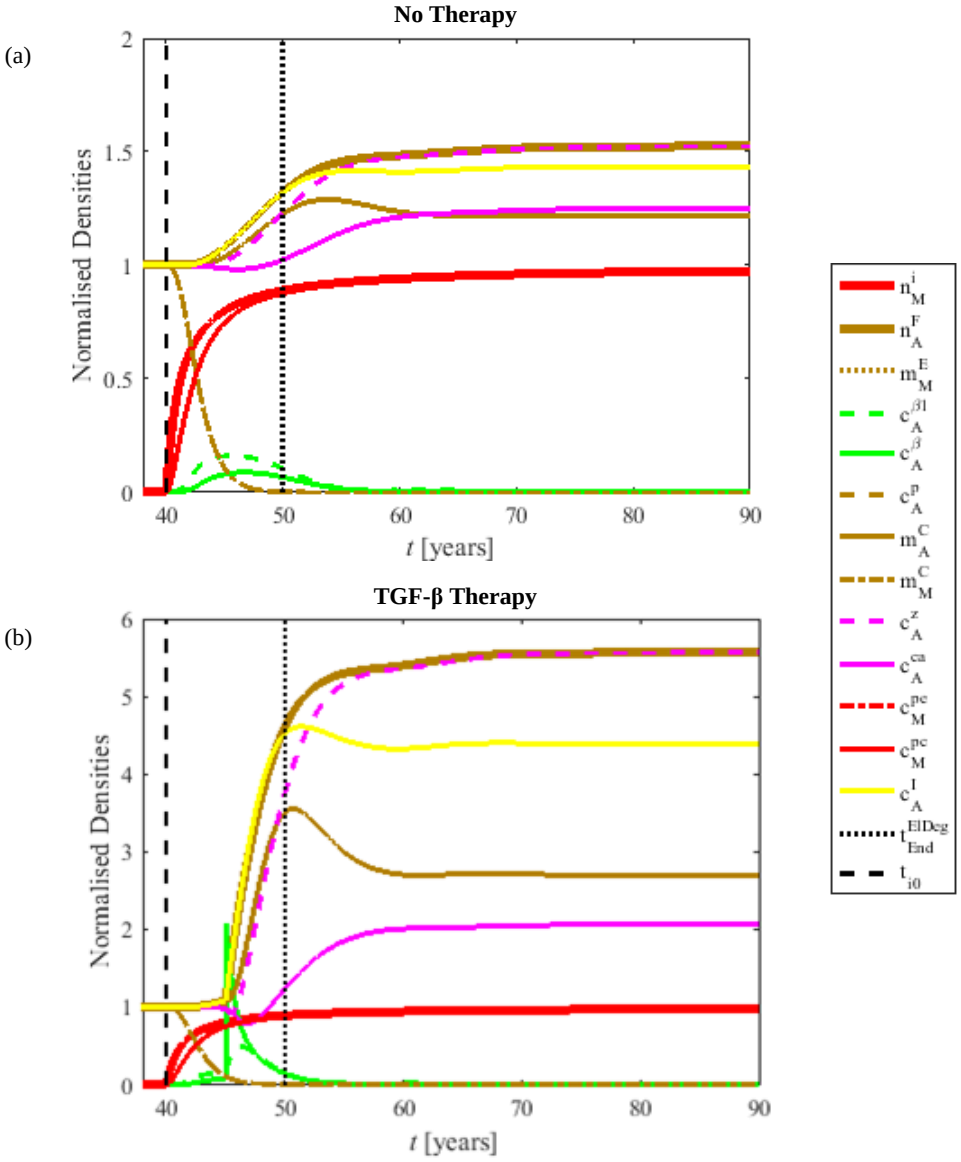

Figure 2.7: **Novel CMB model simulation results — biochemical and cellular variables**. IA development case (a) *vs.* TGF-β therapy case (b). $r_{\beta l_2} = 5$ for both cases. Note different vertical scales

2.1.2.2 Investigating the outcomes of pharmacological therapy

This study is identical to the previous, except that a step increase in active TGF-β levels is introduced at $t_{Treat} = 45$ years. Simulation results are shown in Fig. 2.6(d)—(f) and Fig. 2.7(b).

Mechanical variables Introduction a TGF-β step has a dramatic effect on the evolution of system mechanical and microstructural variables, Fig. 2.6(d)—(f). Shortly after TGF-β is supplied at $t = 45$ years, there is a very large increase in collagen levels, Fig. 2.6(e), which over–shoot and then converge to 2—4 times the initial levels. This large additional increase in adventitial collagen significantly constrains the expansion of the artery, with all simulation cases reaching stabilisation, Fig. 2.6(d), at much lower collagen stretches, Fig. 2.6(f). When compared to the previous

study, Fig. 2.6 *left*, the coupled CMB model seems to suggest that a pharmacological collagen–promoting therapy leads to stabilisation of otherwise enlarging arteries (slower mechanotransduction cases), and faster stabilisation at lower stretches of already stabilising arteries (faster mechanotransduction cases).

Cellular and biochemical variables Fig. 2.7 shows the predicted evolution of the cellular and biochemical quantities. As in the previous study, the increase in immune cells is prescribed (thick red curve), leading to increased proteolytic enzymes (thin red curve) and elastin degradation (dot–dashed brown curve). A step increase in active TGF-β is introduced at $t = 45$ years (vertical solid green curve). The collagen–promoting actions of this signalling molecule take place as in the "no therapy" case, but to a much larger extent: fibroblast numbers increase significantly (thick brown curve), and these cells are stimulated to secrete larger quantities of collagen (thin solid brown curve) and collagenase inhibitors (yellow curve). Each fibroblast also reduces its secretion of collagenases (magenta curve), but overall collagenase levels are nonetheless increased due to the large increase in fibroblast numbers. As mechanical homoeostasis is quickly reached, Fig. 2.6(d), active TGF-β levels drop back to zero, confirming its action as a transient mechanotransducer. A biochemical steady–state follows, characterised by a particularly large density of fibroblasts (5.5 times), inhibitors (4.5 times) and collagen (2.5 times) as expected in a fibrotic tissue. Interestingly and as observed clinically (Barbour et al., 2007), collagenase levels are also higher than at baseline (2 times); however, the ratio inhibitors:collagenases is higher than initially (2.25 *vs.* 1), which represents lower enzymatic activity.

2.1.2.3 Model exploration: additional parameter studies

So as to further explore the behaviour of the model in different regions of the parameter space, a comprehensive set of parameter studies has been performed. In each of the studies below, a single parameter has been assigned values higher and lower than its default value (as shown in Table 2.1—Table 2.3); no TGF-β therapy is applied. The effects of such variation on system mechanics (Fig. 2.8, Fig. 2.10 and Fig. 2.12) and biochemistry/cell biology (Fig. 2.9 and Fig. 2.11) are then plotted; as for the illustrative parameter study above, the mechanical results predicted by the model of Watton et al. (2004) are plotted in red for comparison.

TGF-β secretion In addition to the $r_{\beta l_2}$ parameter whose effects on system dynamics were investigated above, another term related to TGF-β secretion is controlled by parameter $r_{\beta l_3}$ and captures the repressor effect of the formation of a mature collagen matrix on TGF-β secretion by fibroblasts (Streuli et al., 1993), Eq. (2.23). Different values were assigned to this parameter, $r_{\beta l_3} = \{0.1, 1(\text{default}), 5, 10\}$, and the effect of such variation on system mechanics can be seen in Fig. 2.8(a). It is clear that increasing the gain of this feedback mechanism results in slower increases in collagen deposition m_A^C resulting in ultimately larger arterial enlargements λ^s; for the highest value of $r_{\beta l_3} = 10$ the system never attains stabilisation, and linear growth is still visible at the end of simulation. Conversely, a lower value of $r_{\beta l_3} = 0.1$ promotes very fast collagen increase and stabilisation at lower domain stretches. By comparing the temporal evolution of biochemical and cellular variables in this case, Fig. 2.9(a), with default $r_{\beta l_3} = 1$, Fig. 2.7(a), it becomes clear that the increase in collagen deposition is mediated by an over 2 times larger increase in latent TGF-β, which after following activation fosters a larger profibrotic response.

TGF-β downstream effects As discussed above, TGF-β regulates arterial mechanobiology through its profibrotic actions on fibroblast phenotype. One important action is an hypothesised positive feedback loop, term $r_{\beta l_1}$ in Eq. (2.23), whereby active TGF-β would promote latent TGF-β secretion. The parameter study $r_{\beta l_1} = \{0.1, 0.5(\text{default}), 1, 2\}$ in Fig. 2.8(b) shows that the effect of this hypothesised mechanism is very small until a certain threshold is reached — for the largest value of $r_{\beta l_1} = 2$ there is a continuous increase in collagen mass m_A^C, which results in a continuous reduction in domain circumferential stretch λ^s. The mechanism behind the observed behaviour can be seen in Fig. 2.9(b): when the gain factor in the TGF-β positive feedback loop is too strong, the secretion of its latent form is excessive and persistent, thus resulting in a continuous increase in the levels of the biochemical species regulated by this pathway. This parameter study is important to establish a bound on the value of $r_{\beta l_1}$, which should be below 2 to avoid unphysiological results.

TGF-β is known to promote increased fibroblast numbers both via increased migration (Martin et al., 1992) and proliferation (Akhurst and Hata, 2012). This effect is jointly included in the CMB model via term r_{f_2} in Eq. (2.17). Parameter study $r_{f_2} = \{0.1, 0.5(\text{default}), 1, 2\}$ makes clear how sensitive the behaviour of the model is to fibroblast dynamics: increasing this parameter value promotes a very large increase in fibroblast numbers, Fig. 2.9(c), which deposit

significantly larger amounts of collagen, thus promoting arterial stabilisation at lower domain stretches, Fig. 2.8(c). In contrast, the model seems to be less sensitive to the profibrotic actions of TGF-β on each fibroblast cell, i.e. promoting procollagen deposition (r_{p_2} in Eq. (2.18)), reduc-

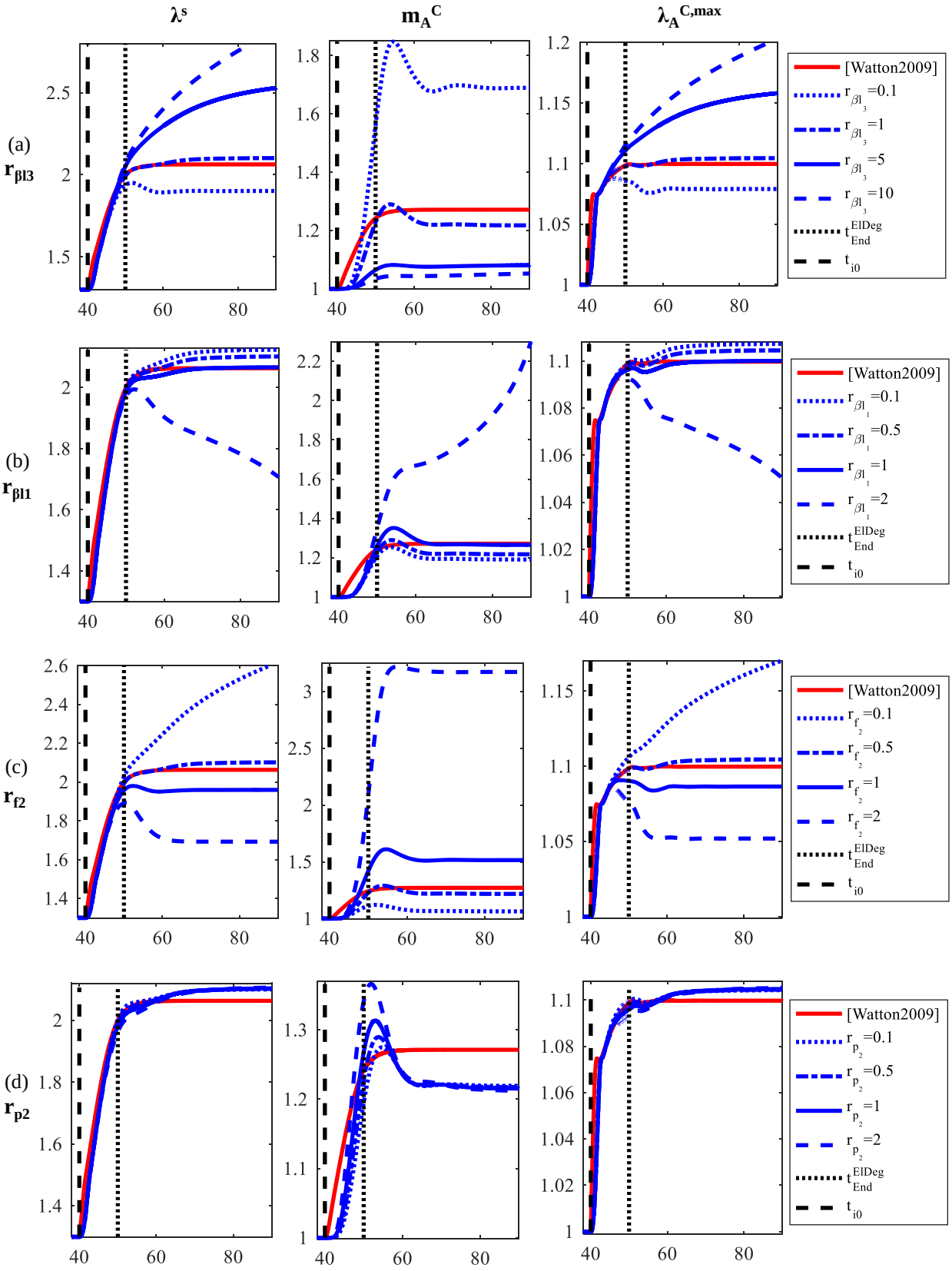

Figure 2.8: **Additional parameter studies for the novel CMB model — mechanical variables I.** Parameter studies on $r_{\beta l_3}$ (a), $r_{\beta l_1}$ (b), r_{f_2} (c), r_{p_2} (d). Horizontal axes refer to time [years].

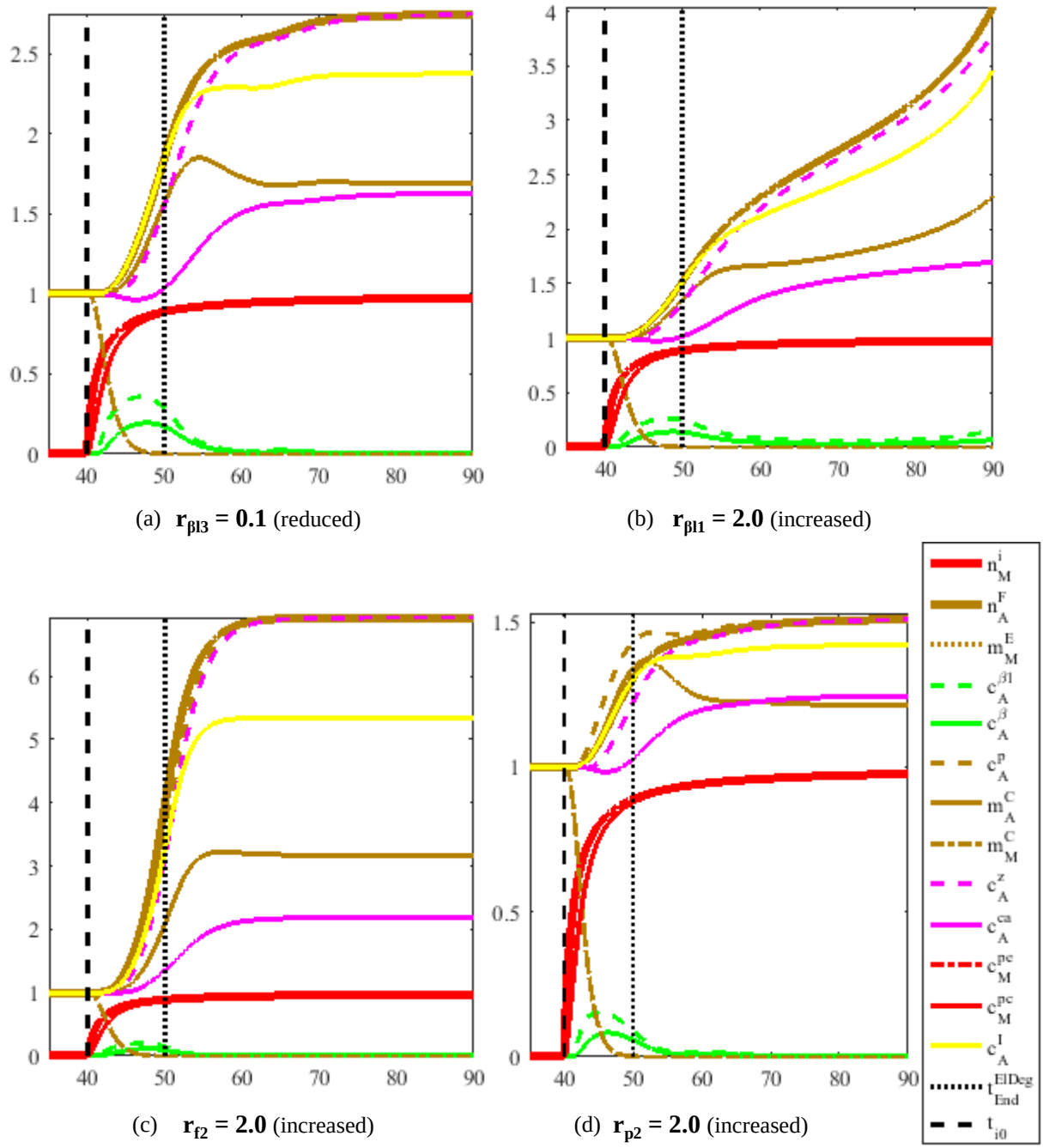

Figure 2.9: **Additional parameter studies for the novel CMB model — biochemical variables I.** Simulation with $r_{\beta l_3} = 0.1$ (a), $r_{\beta l_1} = 2$ (b), $r_{f_2} = 2$ (c), $r_{p_2} = 2$ (d). Horizontal axes refer to time [years].

ing collagenase synthesis (r_{z_2} in Eq. (2.20)) and promoting TIMP secretion (r_{I_2} in Eq. (2.22)). A parameter study on the rate of procollagen secretion in response to increased TGF-β levels, $r_{p_2} = \{0.1, 0.5(\text{default}), 1, 2\}$, shows only transient effects on the initial peak of procollagen and collagen (Fig. 2.9(d)), which has only a negligible effect on system mechanics at steady state (Fig. 2.8(d)). Similar effects were observed for r_{z_2} and r_{I_2} (*results not shown*), which led to a transient decrease in collagenase levels or increase in TIMPs, respectively, but without changing the final steady–state.

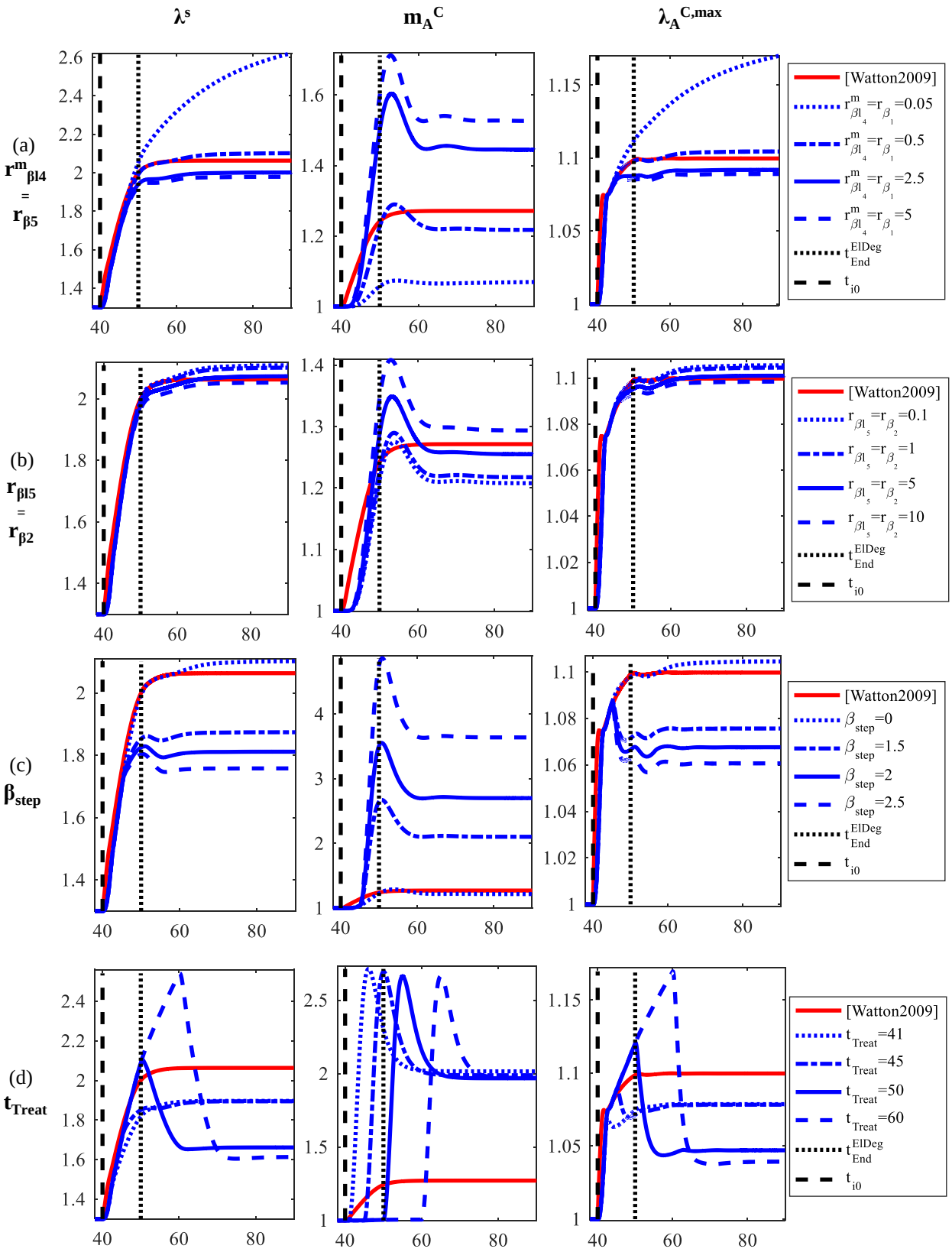

Figure 2.10: **Additional parameter studies for the novel CMB model — mechanical variables II.** Parameter studies on $r^m_{\beta l_4} = r_{\beta_1}$ (a), $r_{\beta l_5} = r_{\beta_2}$ (b), β_{step} (c), t_{Treat} (d). Horizontal axes refer to time [years].

TGF-beta activation Because TGF-β is secreted in an inactive form but its profibrotic action is carried out by the active form, studying the influence of the different mechanisms of TGF-

β activation becomes important. A parameter study on the baseline rate of TGF-β activation $r^m_{\beta l_4} = r_{\beta_5} = \{0.05, 0.5(\text{default}), 2.5, 5\}$ in Eq. (2.23) and Eq. (2.24), Fig. 2.10(a), reveal that faster TGF-β activation rate leads to much larger collagen deposition, which results in stabilisation of the domain at lower domain stretches (however, without reduction in domain stretch after initial increase). As expected, the mechanism behind this increase in collagen involves a large activation of latent TGF-β (note the almost absence of the latent TGF-β peak and the larger peak in active TGF-β in Fig. 2.11(a)), which promotes a stronger fibrotic response.

In contrast, a parameter study on the integrin–mediated, deformation–dependent mechanism of TGF-β activation, term $r_{\beta l_5} = r_{\beta_2} = \{0.1, 1(\text{default}), 5, 10\}$ in Eq. (2.23) and Eq. (2.24), showed only small increases in collagen deposition secondary to faster TGF-β activation, Fig. 2.10(b), which led to only small changes in the steady state levels of λ^s. The smaller changes observed were dependent on a slightly larger conversion of latent into active TGF-β and the elicited profibrotic response, c.f. Fig. 2.11(b). In this case, the model seems to suggest that the baseline mechanism of latent TGF-β activation leads to larger differences in the final steady states of enlarged domains than the integrin–mediated, tension–dependent mechanism; this observation holds as long as a steady–state is reached at all — the more transient effect of the latter mechanism could become more significant in cases of continuous growth.

TGF-beta therapy In this section, the influence of parameter values related to the application of a TGF-β profibrotic stimulus is investigated. Larger levels of the TGF-β step $\beta_{step} = \{0, 1.5, 2(\text{default}), 2.5\}$ result in stronger profibrotic responses downstream, Fig. 2.11(c), which leads to initially faster and ultimately larger collagen deposition and domain stabilisation at lower stretch values, Fig. 2.10(c). A more interesting result is obtained by varying the time for applying the TGF-β stimulus, $t_{Treat} = \{41, 45(\text{default}), 50, 60\}$. Fig. 2.11(d) shows that the predicted increase in collagen levels is similar regardless of time of application of the profibrotic stimulus; however, the effect of this increase in collagen on the final steady state of the arterial circumferential stretch is more dramatic the later the stimulus is applied, Fig. 2.10(d). This effect is likely due to the increasingly important role of the adventitia as a load–bearer as a result of medial degradation: a large increase in collagen mass density early on will have a small effect on the mechanical equilibrium of the domain, as initially very few collagen fibres are responsible for load–bearing, whereas later on many collagen fibres are deposited in a state of pre–stretch, and

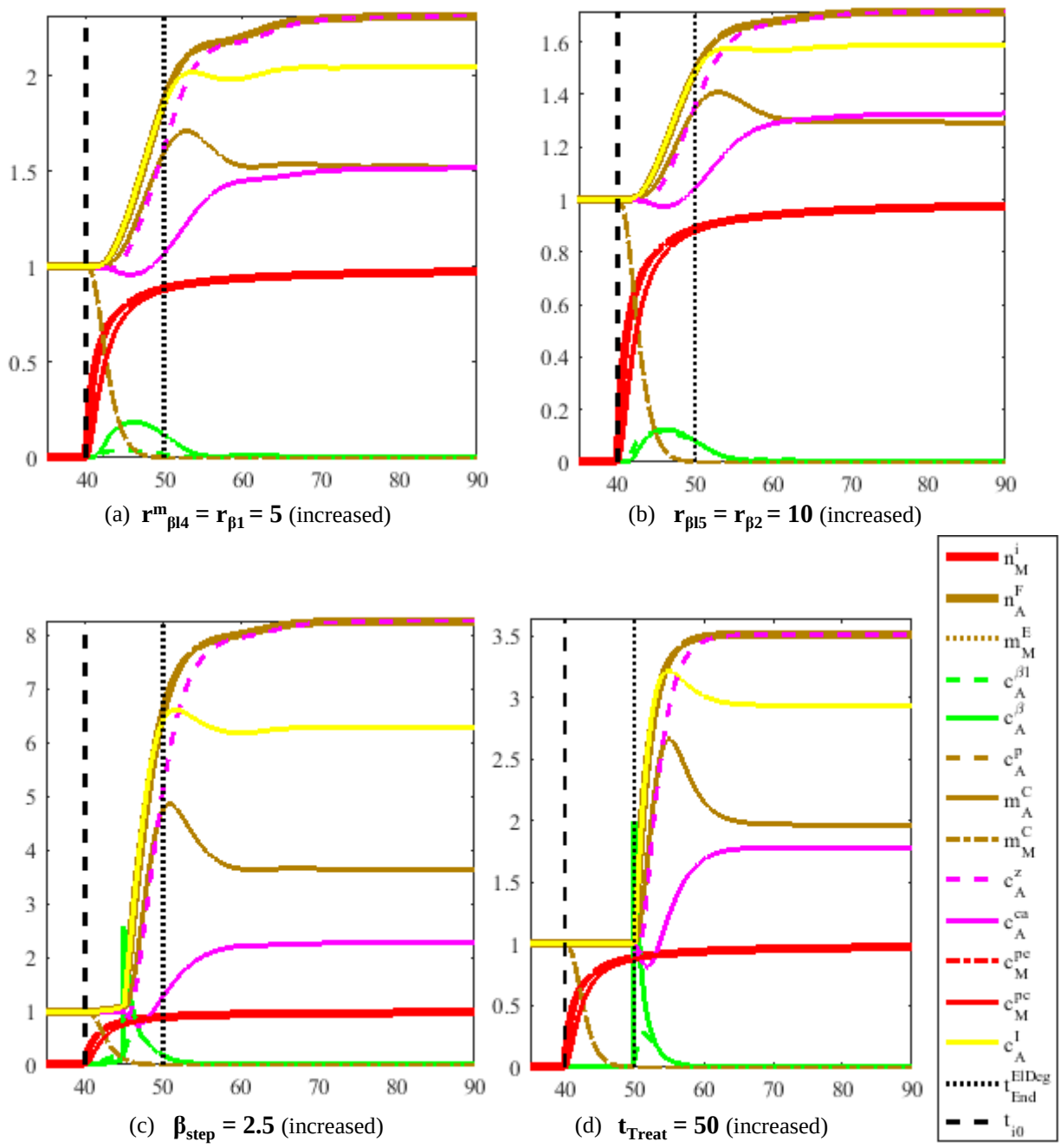

Figure 2.11: **Additional parameter studies for the novel CMB model — biochemical variables II.** Simulation with $r^m_{\beta l_4} = r_{\beta_1} = 5$ (a), $r_{\beta l_5} = r_{\beta_2} = 10$ (b), $\beta_{step} = 2.5$ (c), and $t_{Treat} = 50$ (d). Horizontal axes refer to time [years].

thus changing the mass density of this collagen population will have much more significant effects on the mechanical equilibrium predicted. It will only be possible to assess the mechanobiological significance of this result when specifically–designed experiments are carried out.

Recruitment stretch remodelling Long–term aneurysm development is mainly due to the gradual deposition of new collagen fibres with a progressively longer reference length, which is captured in the CMB model by the remodelling of collagen recruitment stretches, Eq. (2.25)—Eq. (2.27). As expected, a parameter study on the rate of collagen recruitment stretch remodelling as a func-

tion of perturbations to collagen stretch homoeostasis, $\alpha_M^C = \alpha_A^C = \{0.5, 1, 1.2(\text{default}), 1.5\}$, shows that larger rates of remodelling result in faster and ultimately larger expansions of the arterial domain, which require larger increases in collagen levels to attain stabilisation, Fig. 2.12(a).

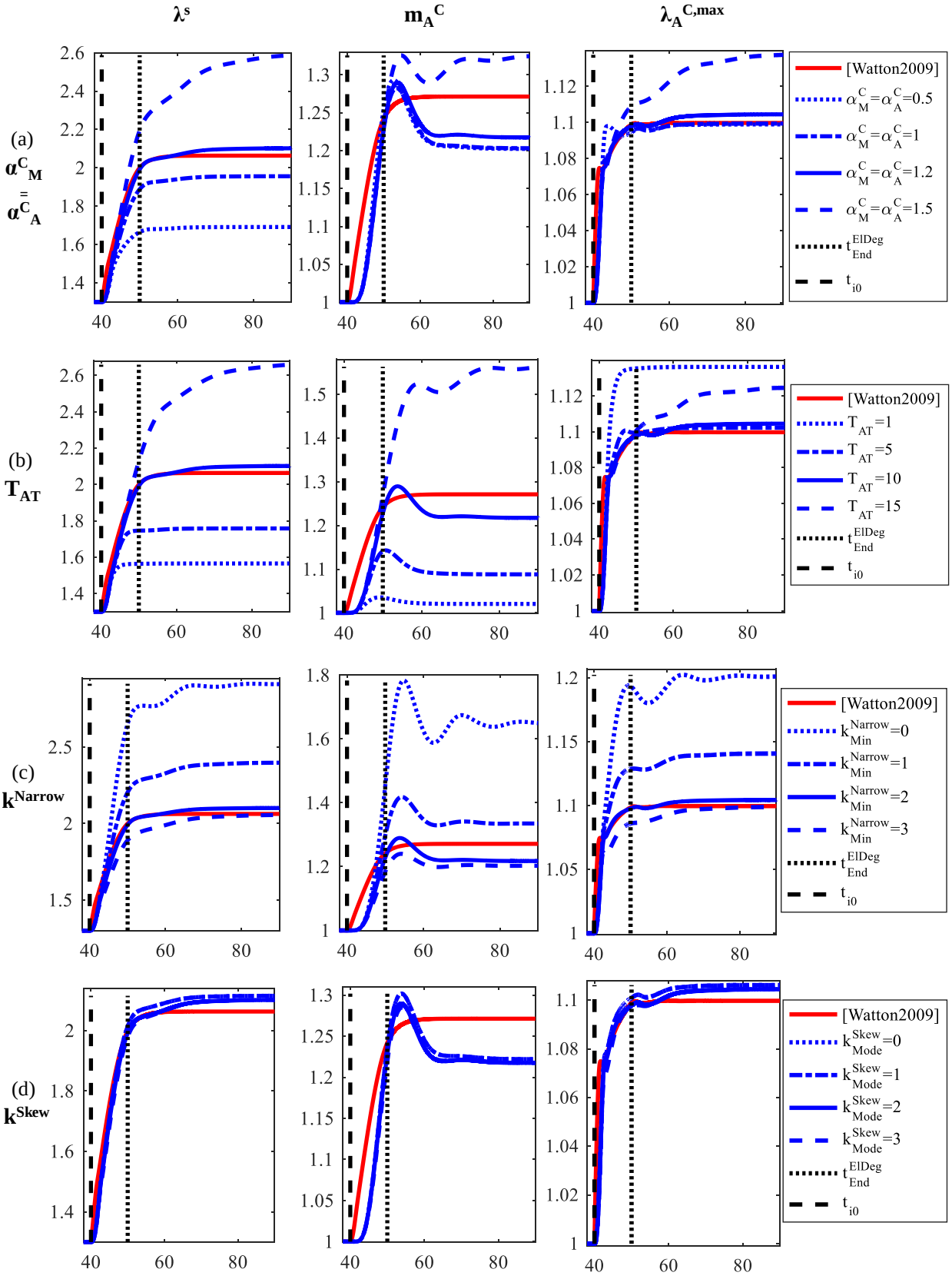

Figure 2.12: **Additional parameter studies for the novel CMB model — mechanical variables III.** Parameter studies on $\alpha_M^C = \alpha_A^C$ (a), T_{AT} (b), k_{min}^{Narrow} (c), k_{mode}^{Skew} (d). Horizontal axes refer to time [years].

Attachment Stretch Remodelling An important novel feature introduced in this CMB model was modelling the evolving role of the adventitia from an initially protective straitjacket to being the main load–bearer over the course of medial degradation; the underlying rightward shift of the attachment stretch distribution is not prescribed, but rather arises from the evolution of the collagen fibre stretches, Eq. (2.9)—Eq. (2.11). Here, the influence of some parameters related to the evolution of this distribution is numerically investigated.

A parameter study on the period over which collagen fibre stretches were averaged for evolving the salient points of the attachment stretch distribution, $T_{AT} = \{1, 5, 10(\text{default}), 15\}$, shows the importance of this parameter, Fig. 2.12(b). Short averaging periods result in fast attainment of a steady state collagen fibre stretch, which promotes faster stabilisation of the domain at lower circumferential stretches requiring a small increase in collagen density. Conversely, larger T_{AT} values result in slower system responses, thus promoting larger increases in domain stretches requiring a larger increase in collagen mass for stabilisation. The influence of two other parameters modulating attachment stretch evolution was numerically investigated, i.e. the factors coupling deviations from stretch homoeostasis to distribution narrowing, $k_{Min}^{Narrow} = \{0, 1, 2(\text{default}), 3\}$ in Eq. (2.12), and skewing, $k_{Mode}^{Skew} = \{0, 1, 2(\text{default}), 3\}$ in Eq. (2.13). Fig. 2.12(c) shows that the system is quite sensitive to the narrowing factor : large values of k_{Min}^{Narrow} promote domain stabilisation at much lower circumferential and collagen fibre stretches, and requiring smaller increases in collagen density. On the other hand, factor k_{Mode}^{Skew} has only a negligible influence on system behaviour, Fig. 2.12(d).

2.1.3 Discussion: novel CMB model

2.1.3.1 Model insight

Model innovations and their relevance A novel chemo–mechano–biological (CMB) model of arterial G&R has been developed by coupling and extending the conceptual aneurysm model of Watton et al. (2009b) with the biochemistry model of Dale et al. (1996). This enables the coupled model to capture the bidirectional interaction between arterial mechanics and biochemistry. The underlying biological mechanisms included in the biochemical model component, Sec. 2.1.1.4, all of which are supported or informed by experimental observations, have as their most significant components: (a) active molecules responsible for collagen metabolism (proteases and

enzymatic inhibitors); (b) TGF-β, a potent regulator of fibroblast phenotype and matrix deposition that acts as a mechanotransducing signal by vascular cells; (c) fibroblasts, the dominant cell population in the adventitia and responsible for collagen metabolism; and (d) infiltrating immune cells, commonly found within the arterial wall in inflammatory aneurysms.

A significant development in the mechanical model component (Sec. 2.1.1.2, Sec. 2.1.1.3) was related to modelling the stretches at which fibroblasts deposit collagen fibres, or *attachment stretches*. Based on the observation of fast fibroblast–mediated collagen turnover in the vasculature (half–life of 3–90 days), Humphrey (1999) modelled the process of connective tissue evolution as resulting from cell–mediated deposition and degradation of tissue constituents with different reference configurations. Building on this work, Humphrey and Rajagopal (2002) hypothesised the deposition of such constituents in a state of stress(strain); in the arterial adventitia, this process might be mediated by fibroblasts tugging on and loading the collagen fibrils they secrete (Alberts et al., 1994). Since then, many computational studies have implemented some description of collagen attachment stretch influencing arterial G&R (Watton et al., 2004; Baek et al., 2006; Kroon and Holzapfel, 2009). Experimental observations have provided some support to the view that fibroblast–mediated collagen deposition (under stretch) and degradation mediates vascular G&R processes: rapid and extensive adventitial adaption to (mechanical) perturbation characterised by fibroblast proliferation and differentiation (Stenmark et al., 2011); "hand–over–hand" mechanism for collagen fibre deformation and loading by fibroblasts (Meshel et al., 2005); fibroblast–mediated (elastic) fibril orientation and stretching upon deposition (Czirok et al., 2006). However, experimental quantification of collagen attachment stretches is still an open question, which has recently motivated the development of novel experimental systems (Hill et al., 2012).

$\lambda_A^{AT}(t)$ was modelled in this study to evolve as a result of the predicted evolution of the system, rather than being prescribed as previously (Chen, 2014). The choice of the particular evolution laws, Eq. (2.9)—Eq. (2.11), was guided by the principle that vascular cells continuously transduce the properties of their surroundings, which dynamically influence their phenotype (Regan and Aird, 2012). In implementing this principle in the stretch–based formulation followed here after Watton et al. (2009b), a temporal average of collagen stretch was taken as a natural choice: on the one hand, each individual cell is continuously influenced by its environment, with its current

state resulting from the composition of past states, up to a certain point (finite memory system). On the other, the cell population as a whole is dynamically changing as a result of cell death and proliferation, with the current state of the population being a composition of the states of younger cells programmed at more recent time points with those of older cells programmed earlier, up to a certain point (finite cell lifespan).

Including the additional biological complexity above allows the CMB model to simulate arterial aneurysm evolution governed by mechanisms that are closer to reality, Sec. 2.1.2.1, with arterial properties dynamically emerging from the close coupling between mechanics and chemo–biology. The potential of this type of model to predict the effect of pharmacological therapy on the mechanical and biochemical condition of diseased arteries was investigated, Sec. 2.1.2.2, and a comprehensive set of parameter studies was run to further characterise system behaviour predicted by the CMB model in different regions of the parameter space, Sec. 2.1.2.3.

Predicted arterial evolution Aneurysms are known to display two distinct behaviours: stabilisation *vs.* enlargement (which sometime alternate over time) (Sakalihasan et al., 2005). Understanding which arteries stabilise and should be left untreated *vs.* which vessels progressively enlarge and require intervention is of great clinical relevance. As was seen in Fig. 2.6 *left* and Fig. 2.7(a) in Sec. 2.1.2.1, the CMB model was able to capture both a return to a mechanical and biochemical steady state (*stabilisation*), and a continuous enlargement for different rates of mechanotransduction. Aneurysm enlargement is extremely complex and multi–factorial; in any case, both computational (Wilson et al., 2013) and experimental (Frösen et al., 2012) studies suggest that the dynamics of collagen G&R and those of aneurysm enlargement are closely related. Furthermore, the new steady state achieved after the prescribed perturbation (immune cell infiltration) was characterised by trends qualitatively consistent with those seen in aneurysmal tissue: increased immune cell (Rizas et al., 2009) and (myo)fibroblast (Maiellaro and Taylor, 2007) numbers; reduced medial elastin (Sakalihasan et al., 2005) and increased adventitial collagen (Sakalihasan et al., 2005; Hobeika et al., 2007); increased TGF-β levels (Ruddy et al., 2008; Rizas et al., 2009); increased collagenase levels (Hobeika et al., 2007; Rizas et al., 2009); and increased TIMP concentration (Ruddy et al., 2008).

Promisingly, the model predicts that introducing a pharmacological collagen–promoting

"therapy", Fig. 2.6 *right* and Fig. 2.7(b) in Sec. 2.1.2.2, i.e. applying a step increase in active TGF-β, acts to stabilise enlarging aneurysms; this is consistent with some experimental observations in animal models of aneurysm (Dai et al., 2005b, 2011). This interesting result could be simulated by previously existing models; however, it would not emerge from the predicted arterial dynamics. The ability to capture the evolution of active biomolecules and their therapeutic effects on arterial mechanobiology is a valuable insight offered by the CMB model.

An extensive set of parameter studies was also performed to explore different regions of the parameter space, Sec. 2.1.2.3. System behaviour was found to be very sensitive to the dynamics of TGF-β secretion in response to deviations from stretch homoeostasis, parameter $r_{\beta l_2}$ (Fig. 2.6 *left*, Fig. 2.7(a)), and of the repressor effect of the formation of a mature collagen matrix, parameter $r_{\beta l_3}$ (Fig. 2.8(a), Fig. 2.9(a)), but less so to active TGF-β promotion of latent TGF-β secretion, parameter $r_{\beta l_1}$ (Fig. 2.8(b), Fig. 2.9(b)), as long as this parameter value was below a certain threshold, beyond which a sustained signalling response would be triggered. Increased TGF-β levels resulting from faster baseline TGF-β activation were also found to significantly impact the system, parameter $r^m_{\beta l_4} = r_{\beta_1}$ (Fig. 2.10 (a), Fig. 2.11 (a)), whereas latent TGF-β activation via the tension–dependent mechanism (Shi et al., 2011), parameter $r_{\beta l_5} = r_{\beta_2}$ (Fig. 2.10 (b), Fig. 2.11 (b)), was found to have only a small effect on the final steady–state, provided that stabilisation was attained and TGF-β signalling was only transient. Regarding downstream TGF-β profibrotic actions, the most significant effect was the increase in fibroblast numbers, parameter r_{f_2} (Fig. 2.8(c), Fig. 2.9(c)), whereas the modulation of fibroblast secretion of active biomolecules, parameters r_{p_2} (Fig. 2.8(d), Fig. 2.9(d)), r_{ca_2}, r_{I_2}, was found to produce only a transient effect and contribute very little to the final steady–state.

The dynamics of collagen fibre remodelling were found to be very important for system evolution. As expected, larger rates of collagen fibre recruitment stretch remodelling as a result of deviations from stretch homoeostasis, terms α^C_M, α^C_A, Fig. 2.12(a), led to domains stabilising at higher stretches, while smaller averaging periods T_{AT}, Fig. 2.12(b), promoted faster evolution of the collagen attachment stretch distribution, and domain stabilisations at lower domain stretches and requiring smaller increases in collagen normalised density. In addition to a rightward shift of the distribution of adventitial collagen attachment stretches, it was found that distribution narrowing, parameter k^{Narrow}_{Min}, Fig. 2.12(c), had a stronger effect on domain evolution than distribution

skewing, k_{Mode}^{Skew}, Fig. 2.12(d). Once more experimental data on TGF-β regulation of fibroblast–mediated adventitial G&R *in vivo* becomes available, it will be possible to judge the correctness of some of the assumptions and particular choices made during model formulation and that gave rise to the system behaviours previously discussed. The experimental data set detailed in Chapter 3 is part of this effort.

2.1.3.2 Particular choices, limitations and future directions

Biomechanical model component The arterial wall was modelled as a bilayered non–linear elastic cylindrical membrane. The choice of parameter values used in the numerical studies in Sec. 2.1.2.1—Sec. 2.1.2.2 was illustrative to reproduce different target behaviours of arterial tissue evolution (stabilisation *vs.* enlargement), subject to conditions for realistic results. Extension to a full 3–Dimensional model of the arterial wall following the work of Aparício et al. (2014) and Grytsan et al. (2015) is a natural development, which will be presented in Chapter 4.

Several particular choices were made when coupling arterial mechanics to biochemistry. First, distributions of collagen recruitment (λ^R) and attachment (λ^{AT}) stretch were modelled by triangular PDFs, Eq. (2.5). This mathematically convenient formulation is consistent with the experimentally observed unimodal distributions of collagen waviness (Schrauwen et al., 2012); alternative functionals, e.g. gamma distributions (Hill et al., 2012), could easily be incorporated in the model if they are found to be preferable. Second, the attachment stretch distribution was made to evolve according to Eq. (2.9)—Eq. (2.11). This was based on the observations that the adventitia progressively assumes the role of main load–bearer, and that fibroblasts depositing and stretching collagen are highly plastic cells (Stenmark et al., 2006; McAnulty, 2007). Here and for the first time, the hypothesised change in collagen attachment stretch was computed from the evolution of system variables according to running temporal averages of collagen fibre stretch; alternative governing laws could be explored in this framework. Third, deviations from mechanical homoeostasis were coupled to fibroblast mechanotransduction by the stretch–based functional $f(\lambda_A^{C,max})$; alternative, e.g. stress–based (Baek et al., 2005), functionals could be accommodated by the model. Fourth, collagen fibres were considered to align with the circumferential direction, and no fibre re–orientation was modelled. In reality, medial and adventitial collagen fibres generally align (with some dispersion) along two principal directions, which can change in disease

(Holzapfel, 2017); coupling a representation of (non–symmetric) collagen fibre dispersion to the present CMB model could be pursued in the future.

Biochemical model component Biochemical and cellular variables were described by means of the signalling pathways biochemical model component, Sec. 2.1.1.4. Biochemical complexity was simplified by grouping together many different biomolecular species into a few representative variables: the only signalling molecule considered was TGF-β1, the most significant regulator of ECM deposition (Ruiz-Ortega et al., 2007); c_A^I specifically represents TIMP-1 levels; over 30 different types of vascular collagenases (Rizas et al., 2009) were grouped into three representative categories; fibrillar collagen types I and III were treated together. Given the still considerable number of cellular and biochemical system variables (thirteen) and related parameters (thirty one), further simplification may be advisable, which can be achieved by ignoring immature procollagen c_A^P and zymogen c_A^z species, and/or by grouping together immune cell–secreted collagenases c_M^{pc} and elastases c_M^{pe} into a single variable. Furthermore, not all actions of the biomolecules modelled were included. In particular, TGF-β is an important regulator of inflammation: it is secreted by infiltrating immune cells, acting on them by increasing their migration and promoting protease secretion (Rizas et al., 2009; Akhurst and Hata, 2012). Simplifications and extensions to the biochemical component of the CMB model is introduced in Sec. 2.2.2.

From the many cell types populating the arterial wall, the model presented above only considers fibroblasts (which populate the increasingly important adventitial layer (Humphrey and Canham, 2000)), and infiltrating immune cells. Other cell types are also present in the arterial wall. Intimal endothelial cells (ECs) transduce wall shear stress, thus regulating both luminal permeability to immune cells (Conway and Schwartz, 2012) and wall tonus by influencing medial vascular smooth muscle cells (VSMCs) active stress generation (Humphrey et al., 2007). An interesting non–mechanistic model for VSMC stress generation coupled to EC vasoconstrictor/-vasodilator activity exists in the literature, (Baek et al., 2007b); coupling this EC/VSCM model to the adventitial fibroblast–centred CMB model above would be relatively straightforward, thus providing a comprehensive and integrated description of arterial wall mechanobiology. Finally, in the presence of TGF-β and mechanical tension, fibroblasts may differentiate into myofibroblasts, a highly secretory, contractile and migratory cell type implicated in the progression of vascular disease, in particular aneurysms (Forte et al., 2010). Model extension to include this coupled

chemo–mechanical cell differentiation process is also introduced in Sec. 2.2.2.

A major shortcoming of this model is the lack of validation, which is partially due to the current lack of experimental data suitable to fit mechanobiological models. Model development and refinement requires data generated from *in vitro* (Bai et al., 2014) and animal (Li et al., 2014) experimental models of vascular pathobiology. The multi–dimensional data set presented in Chapter 3 is part of the research programme to address this shortcoming.

2.2 CMB Model Extensions

The following sections detail three important extensions to the original formulation of the CMB model of arterial tissue G&R. Collectively, these extensions aim at improving the range of mechanobiological processes included in the CMB model above, as well as illustrating the potential of the model to answer a variety of research questions related to cell–mediated arterial mechanobiology. In Sec. 2.2.1 remodelling of collagen fibre natural configurations, i.e. collagen recruitment stretch distribution, is coupled to some system variables characterising the chemo–mechano–biological state of the system. Extended model behaviour is then numerically assessed, and venues for future model development are identified. Sec. 2.2.2 describes CMB model non–dimensionalisation, simplification and extension to capture some important components of arterial tissue G&R under the control of the TGF-β signalling pathway, in particular the links between TGF-β signalling and the infiltrating immune cells, and the TGF-β–dependent fibroblast differentiation into mechanically–active myofibroblasts. This extended model is then used to predict the effect of long myofibroblast permanence times, producing results consistent with hypotheses found in the literature. Describing cell–level mechanical maturation processes is the focus of Sec. 2.2.3, where stress fibres and focal adhesions are jointly represented in the model by a "cell stiffness" variable. The importance of different mechanisms in determining the evolution of this quantity in response to perturbation is then numerically investigated.

2.2.1 Model extension I: Collagen recruitment stretch remodelling coupled to arterial chemo–mechano–biology

Fibroblasts are the resident cells in the adventitia, and responsible for the maintenance of its collagenous matrix, Sec. 1.2. Fibroblasts not only secrete (pro)collagen but also MMPs, enzymes responsible for collagen degradation (McAnulty, 2007). Predicting collagen *growth* (change in mass) as a result of the TGF-β–regulated balance between collagen secretion and maturation, collagenase secretion, and TIMP (collagenase inhibitor) secretion was the focus of the biochemical model component formulated in Sec. 2.1.1.4 above. In addition to secreting collagen, fibroblasts are also responsible for *remodelling* the resulting collagenous matrix, i.e. continuously changing its microstructural properties (Alberts et al., 2014). An important remodelling mechanism involves fibroblasts continuously laying down collagen fibres in reference configurations different from the reference configurations of previously deposited collagen fibres that are continuously degraded over time (Humphrey and Rajagopal, 2002).

Following the stretch–based framework of Watton et al. (2004), the reference configuration of each collagen fibre is described here by the stretch required for each fibre to uncrimp and start bearing load, the *recruitment* stretch. In response to perturbations from mechanical equilibrium, the recruitment stretch evolves to restore the collagen fibre stretch towards its homoeostatic levels, Eq. (2.25)—Eq. (2.27). Even though the previous equations capture the overall change in collagen recruitment stretch distribution as a result of perturbations to material equilibrium, they are still phenomenological in the sense that they do not take into account the chemo–biological species responsible for such changes. In Sec. 2.2.1.1 below, Eq. (2.25)—Eq. (2.27) are updated to include explicit representations of some key mediators of collagen turnover that are computed by the biochemical model component in Sec. 2.1.1.4.

2.2.1.1 Methods: functional formulation

It is hypothesised that remodelling of collagen recruitment stretch results from continuous deposition and degradation of collagen fibres at different reference (i.e. recruitment) configurations. As such, the evolution of recruitment variables will depend on the (a) proportion of fibroblast cells remodelling collagen fibres to the levels of collagen fibres being remodelled, and (b) the

levels of collagen fibres and collagenases jointly describing collagen turnover. It follows that the rate of remodelling of adventitial collagen in Eq. (2.25)—Eq. (2.27) α_A^C is not constant, but rather depends on the proportion of fibroblast normalised number density to collagen fibre mass density (general function $f(n_A^F, m_A^C)$), and on the levels of collagen mass density together with collagenases concentration (general function $g(m_A^C, c_A^{ca})$):

$$\alpha_A^C = \text{const.} \quad \rightarrow \quad \alpha_A^C = \alpha_A^C(n_A^F, m_A^C, c_A^{ca}) = \alpha_{A_0}^C \cdot f(n_A^F, m_A^C) \cdot g(m_A^C, c_A^{ca}), \tag{2.31}$$

where $\alpha_{A_0}^C$ is a constant. Here and for simplicity, the following particular choices are made: $f(n_A^F, m_A^C)$ is taken as the ratio between the levels of fibroblasts (which remodel the tissue) to collagen being remodelled; $g(m_A^C, c_A^{ca})$ is taken as the geometric mean of the levels of mural collagenases (metabolising collagen) and collagen being metabolised. The equations describing adventitial collagen recruitment stretch remodelling thus become Eq. (2.25)—Eq. (2.27) with

$$\alpha_A^C(n_A^F, m_A^C, c_A^{ca}) = \alpha_{A_0}^C \cdot \left(\frac{n_A^F}{m_A^C}\right) \cdot \sqrt{m_A^C \cdot c_A^{ca}}. \tag{2.32}$$

The collagen recruitment stretch distribution in the media follows the same G&R laws, with corresponding parameter $\alpha_M^C = \alpha_{M_0}^C$ being constant, as collagen, collagenase and fibroblasts levels are not modelled in this layer.

2.2.1.2 Results

To assess the significance of introducing the previous changes to the functions used to compute collagen recruitment stretch evolution, the numerical study simulating the development of inflammatory aneurysms, Sec. 2.1.2.1, is run again with exactly the same laws and parameters, except with Eq. (2.32) replacing α_A^C in Eq. (2.25)—Eq. (2.27) ($\alpha_{A,0}^C = 1.2$, as before).

Comparing Fig. 2.13 with Fig. 2.6 *left*, it is clear that a similar overall behaviour is predicted by either version of the model: fast rates of latent TGF-β secretion by fibroblasts in response to deviation from mechanical homoeostasis allow for sufficiently fast increases in collagen mass density, Fig. 2.13(b), resulting in domain stabilisation, Fig. 2.13(a), at reasonably low domain stretches, Fig. 2.13(c). The chemo–biological mechanism behind such adaptive response is transient TGF-β signalling, Fig. 2.13(d), which promotes profibrotic increases in fibroblast number density (1.5 times baseline), collagen mass density (1.25) and TIMP concentration (1.5) to levels very similar to the ones predicted by the previous model (c.f. Fig. 2.7(b)). A closer look

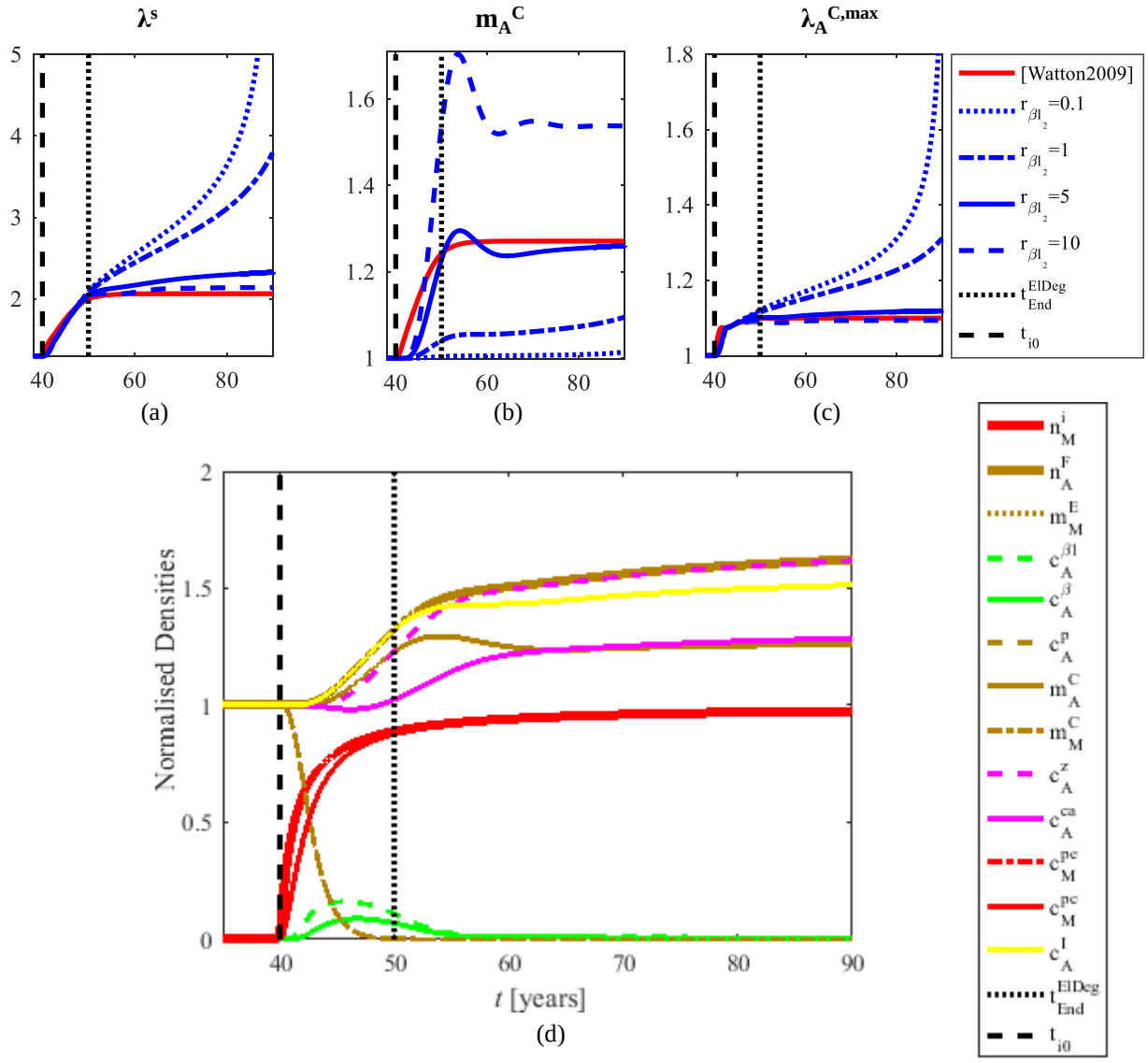

Figure 2.13: **CMB coupling to the remodelling of collagen recruitment stretch — consistency study**. Parameter study on the rate of mechanotransduction $r_{\beta l_2}$ displaying the evolution of both mechanical and biochemical variables ($r_{\beta l_2} = 5$). Compare with the initial model in Fig. 2.6 *left* and Fig. 2.7(b).

at the results further reveals that stabilisation seems to be more difficult to attain when collagen attachment stretch remodelling is coupled to the levels of some biochemical species. Fig. 2.13(a) shows that the rate of enlargement for the smallest value of $r_{\beta l_2} = 0.1$ accelerates faster than in the previous model, and that the second to slowest rate of mechanotransduction $r_{\beta l_2} = 1$ leads to accelerating rather than linear enlargement, as previously.

To further investigate the origin of this slightly less stable behaviour, two additional parameter studies are run, both of which related to the dynamics of collagen fibre remodelling, Fig. 2.14 and Fig. 2.15. A parameter study on the baseline rate of collagen recruitment stretch remodelling in both layers, $\alpha^M_{C,0} = \alpha^A_{C,0} = \{0.5, 1, 1.2(\text{default}), 1.3\}$ in Eq. (2.32), Fig. 2.14(a), shows that, unlike the previous model (Fig. 2.12(a)), very fast rates of recruitment stretch re-

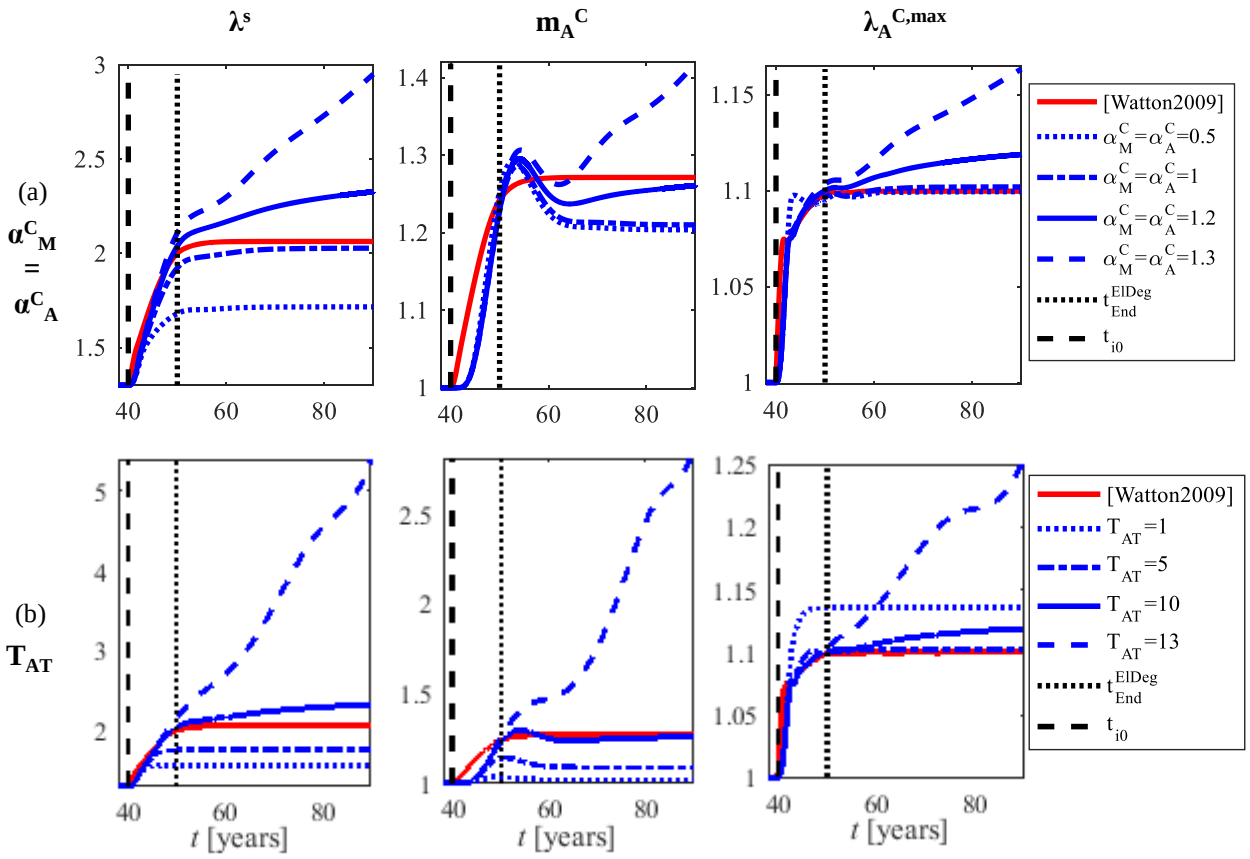

Figure 2.14: **Additional parameter studies for the CMB coupling to the remodelling of collagen recruitment stretch — mechanical variables**. Parameter studies on $\alpha_M^C = \alpha_A^C$ (a) and T_{AT} (b). Compare with Fig. 2.12(a),(b).

modelling lead to aneurysms displaying approx. linear continuous growth ($\alpha_C^M = \alpha_C^A = 1.3$, dashed curve); the resulting increase in collagen is not sufficient wall reinforcement conducive to stabilisation. Similarly, a parameter study on the averaging time period for computation of the evolution of the salient points of the attachment stretch distribution in the adventitia, $T_{AT} = \{0.5, 1, 1.2(\text{default}), 1.3\}$ in Eq. (2.9)—Eq. (2.11), Fig. 2.14(b), shows that, unlike for the previous model (Fig. 2.12(b)), the largest averaging period T_{AT} capturing the slowest adaption of the attachment stretch distribution results in aneurysms growing approx. linearly. The collagen density plot shows that this system's ability to reinforce the wall by increasing collagen mass density is not sufficient to halt aneurysm expansion.

Taking a look at the predicted evolution of the biochemical and cellular variables for fast rates of collagen recruitment stretch remodelling, Fig. 2.15(a), and slow attachment stretch adaption (large averaging periods), Fig. 2.15(b), reveals that for both cases there is a large and sustained growth in fibroblast numbers (thick brown curves), which promotes a continuous increase in the levels of all the biomolecules secreted by this cell type, namely collagen (thin brown curve),

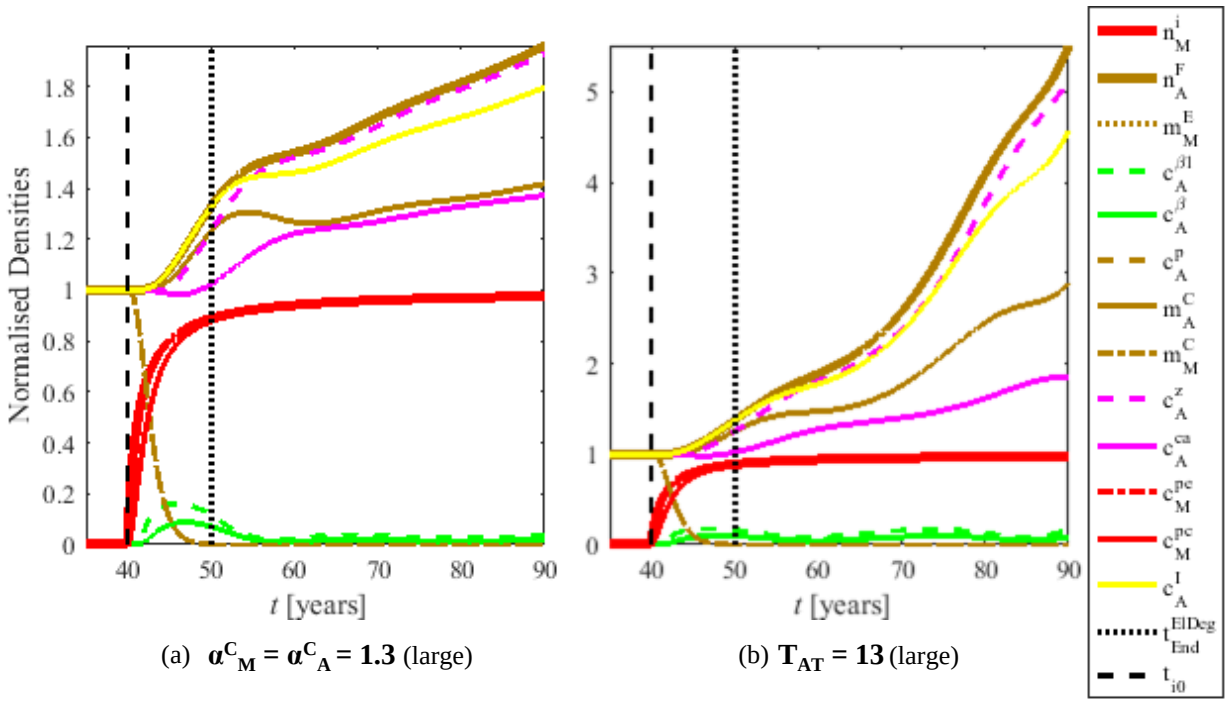

(a) $\boldsymbol{\alpha^C_M = \alpha^C_A = 1.3}$ (large) (b) $\boldsymbol{T_{AT} = 13}$ (large)

Figure 2.15: **Additional parameter studies for the CMB coupling to the remodelling of collagen recruitment stretch — biochemical variables**. Parameter studies on $\alpha^C_M = \alpha^C_A$ (a) and T_{AT} (b).

zymogenic collagenase (dashed magenta curve) and collagenase inhibitors (yellow curve). Note also that the levels of latent and active TGF-β (green curves) never fully return to baseline, which is particularly evident in Fig. 2.15(b). Because TGF-β acts as a transient mechanotransducer signalling deviation from mechanobiological homoeostasis and prompting cell–mediated G&R, persistently elevated TGF-β levels indicate that these systems never fully re–attain homoeostasis; compare for example with Fig. 2.7(a), where the system reaches a new mechanobiological steady state, which results in a return of TGF-β levels to baseline.

2.2.1.3 Discussion

Predicted behaviour The results shown in the previous section reveal that the CMB model extended to couple collagen fibre remodelling to the levels of some of the chemo–biological mediators of this process, Eq. (2.32), mostly predicts system behaviours similar to the previous model, Fig. 2.13; however, in some regions of the parameter space, accelerating growth is predicted where the previous model would predict stabilisation or approx. linear growth. The numerical studies in Fig. 2.14 and Fig. 2.15 suggest that this different behaviour may be due to distinct dynamics of collagen recruitment and attachment stretch evolution.

In order to understand the origin of such contrasting behaviour, it is instructive to consider

the full equation governing the remodelling of one of the salient points of the recruitment stretch distribution in the new formulation, e.g. for $\lambda_A^{R,\max}$:

$$\frac{d\lambda_A^{R,\max}}{dt} = \underbrace{\alpha_{A_0}^C \cdot \left(\frac{n_A^F}{m_A^C}\right) \cdot \sqrt{m_A^C \cdot c_A^{ca}}}_{\alpha_A^C(n_A^F, m_A^C, c_A^{ca})} \cdot \left(\frac{\lambda_A^{C,min}|_s - \lambda_A^{AT,min}}{\lambda_A^{AT,min}}.\right) \tag{2.33}$$

Aneurysm stabilisation *vs.* continuous enlargement in this model is predicted to result from the competition between two processes (Watton et al., 2004): the deposition of collagen fibres at progressively larger reference configurations (*recruitment stretches*) promotes expansion, while increase in collagen mass density shifts the mechanical equilibrium towards lower domain stretches. For this reason, faster rates of recruitment stretch remodelling result in larger domain expansions and require larger increases in collagen density for stabilisation, Fig. 2.12(a). Allowing the distribution of adventitial collagen to adapt also plays a role in this competition between collagen growth and remodelling (Chen, 2014): a rightward shift in $\rho(\lambda_A^{AT})$ modelling the increasingly load–bearing role of the adventitia over disease progression (computed here *via* the integral laws in Eq. (2.9)—Eq. (2.11)) reduces the difference between attachment and collagen fibre stretches away from equilibrium, which reduces the rate of collagen recruitment stretch remodelling (Eq. (2.33)) and promotes arterial domain stabilisation at lower stretches and requiring smaller increases in collagen mass, c.f. Fig. 2.12(b).

In this extended CMB model, not only collagen *growth* (increase in mass density) but also collagen *remodelling* (change in natural configuration) are coupled to the dynamics of chemo–biological species. As can be seen in the parameter study for the rate of increase in fibroblast numbers as a result of TGF-β signalling r_{f_2}, Fig. 2.8(c), the strongest component of the TGF-β profibrotic action predicted by this model is its upregulation of fibroblast numbers, which enables the secretion of increasingly more (pro)collagen, thus reinforcing the wall and promoting stabilisation. However, in coupling collagen stretch remodelling to the density of fibroblasts remodelling it, Eq. (2.32), the situation changes: the large increase in fibroblast numbers necessary for a significant increase in collagen mass density for domain stabilisation also increases factor n_A^F/m_A^C in Eq. (2.33), because only a fraction of the secreted procollagen is modified into load–bearing collagen (c.f. Eq. (2.18), Eq. (2.19)); increasing this factor increases the rate of collagen recruitment stretch remodelling, which if the baseline rate $\alpha_{A_0}^C$ is very large or if the adaption

of the attachment stretch distribution is very slow, results in unstable, continuously growing domains, as can be seen in Fig. 2.14, Fig. 2.15.

Modelling assumptions and future development Several assumptions were involved in this model extension and are (partially) responsible for the predicted behaviours. Firstly, non–saturating kinetics are assumed for all species, which allow for unbound growth in fibroblast numbers in case of a persistently elevated (TGF-β) stimulus (c.f. Eq. (2.17)); using saturating functions such as the Gompertz function to describe the temporal evolution of a fibroblast population that saturates at very large values (e.g. due to competition for nutrients) may be necessary when fibroblast population dynamics are very far away from the linear, non–saturating regime (Edelstein-Keshet, 2005). Secondly and following Dale et al. (1996), first order kinetics are assumed for the conversion of procollagen into load–bearing collagen, and the rate of procollagen degradation is taken to be equal to the rate of procollagen modification (c.f. Eq. (2.18), Eq. (2.19)); additional experimental data on the kinetics of collagen maturation would inform more realistic laws. Finally and more importantly, the rate of remodelling of collagen attachment stretch was taken to be proportional to a simplistic ratio of ($f(n_A^F, m_A^C) = n_A^F / m_A^C$ factor in Eq. (2.31)); alternative functional forms could be used instead, which would predict a different influence of the fibroblast population dynamics on the rate of remodelling of collagen recruitment stretch. In particular, considering functional forms that predict bounded remodelling rates is advisable, in particular for systems that are perturbed very far away from homoeostasis.

2.2.2 Model extension II: modelling fibroblast differentiation dynamics

2.2.2.1 Motivation: myofibroblast differentiation

Arterial wall G&R refers to a complex set of interrelated mechanisms that enable arterial wall adaptation to perturbation (Humphrey, 2008a). If this adaptive response fails to restore the wall to a preferable (*homoeostatic*) healthy condition, vascular diseases such as aneurysm (Sakalihasan et al., 2005), atherosclerosis (Montecucco and Mach, 2009) or dissection (Schriefl et al., 2012) may develop. To understand and intervene in these processes, it is critical to consider the populations of vascular cells residing in the arterial wall. In addition to intimal endothelial cells and medial vascular smooth muscle cells, long–term arterial evolution is determined by adventi-

tial fibroblasts, the main cell type populating the outermost layer and responsible for the turnover of collagen fibres, Sec. 1.2. Immune cell infiltration also takes place in many vascular conditions with an inflammatory component, such as atherosclerosis, hypertension and aneurysm (Maiellaro and Taylor, 2007).

Several existing models of arterial mechanobiology have incorporated some aspects of cell–driven arterial G&R. Wall mechanics influencing the rates of fibroblast and VSMC collagen production have been incorporated in models of aneurysm growth (Watton et al., 2004; Baek et al., 2005). EC transduction of blood wall shear stress regulating SMC–generated tonus was modelled (Baek et al., 2007b), as well as EC–regulated luminal permeability to immune cell infiltration (Aparício et al., 2014). In all the previous models, cell–driven G&R mechanisms are fixed: the algorithms used to describe cellular responses are the same at all times. This implicitly assumes an unchanging vascular cell population, whose response to perturbation is similar at all disease stages. However, abundant evidence demonstrates that the relative amount and action of different cell types populating the vessel wall dynamically change over the course of disease progression. During aneurysm development, for example, the vascular endothelium may completely disappear or become dysfunctional (Frösen et al., 2012); medial VSMCs may undergo extensive apoptosis resulting in reduced cell density (López-Candales et al., 1997); and adventitial fibroblasts, in the presence of mechanical tension and certain growth factors such as TGF-β, differentiate into activated myofibroblasts (Tomasek et al., 2002), Fig. 2.16.

Myofibroblasts are highly secretory, depositing abundant collagen (Hinz and Gabbiani, 2010), but also highly migratory, thus secreting proteolytic enzymes required for matrix degradation and cell migration (Shi et al., 1999; Jones et al., 2009b). Medial SMC apoptosis and the rise in myofibroblast numbers suggest a shift in the populations of vascular cells in the walls of abdominal (Sakata et al., 2007) and thoracic (Jones et al., 2009a) aneurysms. Aneurysm progression has been suggested in the literature to correlate with increased proteolytic loads resulting from myofibroblast permanence (Jones et al., 2009b). Therefore, modelling vascular cell dynamics over disease progression is essential to correctly predict the development of these conditions, and to develop therapies targeting particular cell types.

In this section, the CMB model formulated in Sec. 2.1 and extended in Sec. 2.2.1 is adimensionalised, simplified and extended to model fibroblast to myofibroblast differentiation under

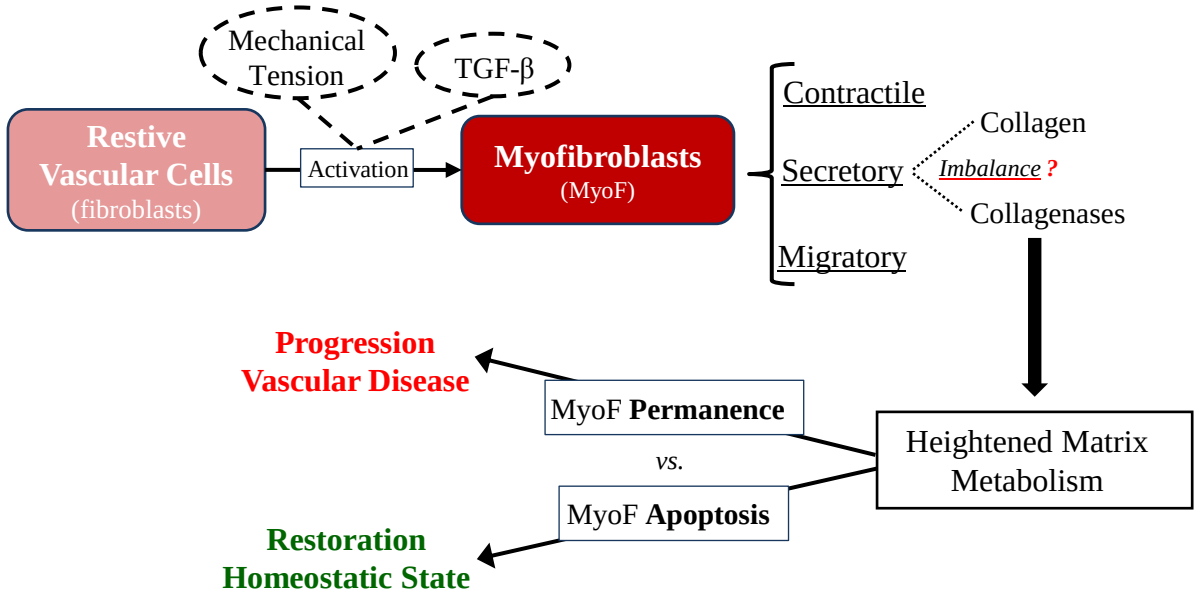

Figure 2.16: **Myofibroblast differentiation influencing arterial mechanobiology**. Mechanisms depicted are supported by Jones et al. (2009b); Forte et al. (2010); Hinz and Gabbiani (2010).

the control of TGF-β. In addition, the revised CMB model also includes terms for the important coupling between TGF-β and infiltrating immune cells, Sec. 2.2.2.2. Following an initially prescribed degradation of the media *via* immune cell infiltration, the extended model simulates the evolution of some of the mechanical and biochemical variables characterising arterial wall condition, Sec. 2.2.2.3. Explicitly modelling both types of variables is necessary, as myofibroblast differentiation simultaneously requires growth factors and mechanical tension. As the artery enlarges, the extended CMB model predicts the emergence of a small myofibroblast population, which is consistent with experimental observations. The numerical results also highlight the importance of modelling the dynamics of this cell population: progression towards stabilisation *vs.* continuous accelerating enlargement depends on a single parameter, the rate of myofibroblast cell death. This bifurcation behaviour is consistent with mechanisms proposed in the literature that correlate aneurysm development with myofibroblast persistence, Sec. 2.2.2.4. Finally, the dependence of system behaviour on a set of key parameters is explored, in particular those related to myofibroblast differentiation and apoptosis, myofibroblast secretion of active molecules and myofibroblast remodelling of the matrix.

2.2.2.2 Methods: model development

The CMB model formulated here follows the initial model formulation in Sec. 2.1.1, coupling a biochemical model governing cell–driven collagen metabolism under the control of TGF-β

signalling with a 1D biomechanical model of arterial mechanical response.

Biomechanical model The biomechanical component of the CMB model is similar to the one in Sec. 2.1.1.2. Briefly, the artery is modelled as a cylindrical non–linear elastic membrane with elastin (E) and collagen (C) contributing to load–bearing in the media (M), and collagen being the only load–bearing constituent in the adventitia (A). The resulting force–balance equation governing mechanical equilibrium is Eq. (2.1) as in Sec. 2.1.1.2. Medial elastin is modelled as a neo–Hookean material. Each collagen fibre in either layer is modelled as linearly elastic. The mechanical contribution of the entire population of fibres in either layer is then obtained by integrating the strain energy density function for each fibre over the distribution of fibre recruitment stretches $\rho(\lambda_L^R)$ ($L = M, A$), multiplied by the collagen normalised mass density in that layer. Triangular distribution functions describe stretch distributions (Chen, 2014), with the minimum ($\lambda_L^{R,min}$), mode ($\lambda_L^{R,mode}$) and maximum ($\lambda_L^{R,max}$) points as figures of merit. Medial elastin (m_M^E) and collagen (m_M^C) and adventitial collagen (m_A^C) normalised mass densities are computed by the extended signalling pathways model below.

Signalling pathways biochemical model The biochemical component of this extended model, Fig. 2.17, builds on the model formulated in Sec. 2.1.1.4. As before, this extended model component uses a system of non–linear ODEs to compute the temporal evolution of cellular number densities (n), molecular concentrations (c) and mass densities (m) normalised to the beginning of the simulation ("normalised densities").

Adventitial collagen growth. Fibroblasts (n_A^F) are the resident cell population in the adventitia, primarily responsible for mediating adventitial collagen turnover (McAnulty, 2007). This is a highly regulated process, with fibroblasts not only secreting adventitial collagen (m_A^C) but also enzymes responsible for its degradation (collagenases, c_A^{ca} (Shoulders and Raines, 2009)), and their inhibitors (Tissue Inhibitors of MetalloProteinases or TIMPs, c_A^I (Brew et al., 2000)).

TGF-β. If mechanical loads on the wall are increased (as in hypertension (Stenmark et al., 2006)) or if load–bearing capacity is reduced (as in aneurysm (Frösen et al., 2004)), the resulting wall over–straining is perceived by fibroblasts, which upregulate the secretion of active agents signalling this perturbation. The most important of these agents is TGF-β, which is secreted in an inactive form ($c_A^{\beta l}$) and then activated into the functional molecule (c_A^{β} (O'Callaghan and Williams,

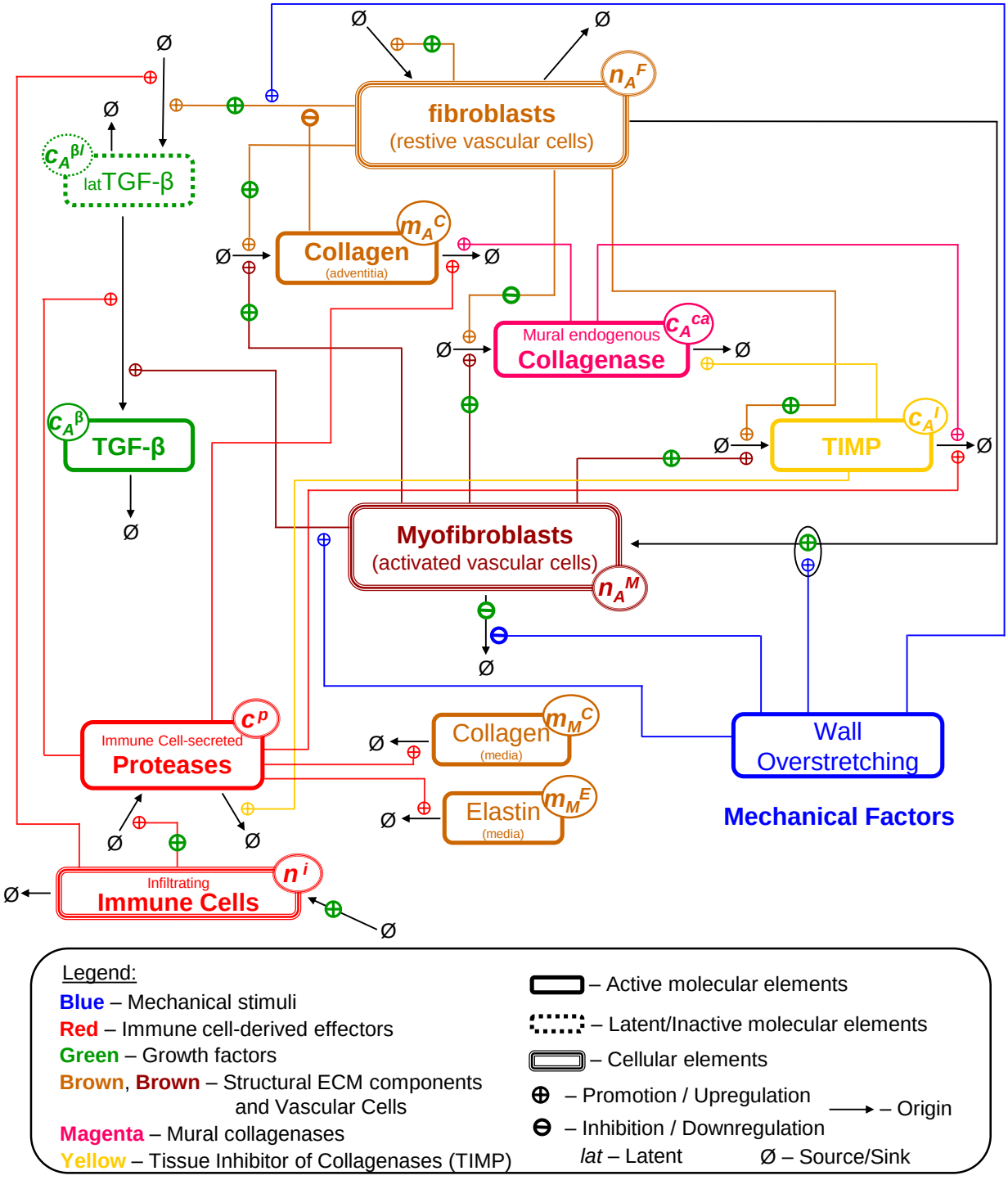

Figure 2.17: **CMB model extension to capture myofibroblast differentiation — regulatory signalling pathways diagram.** All links between species included are based on published experimental observations. Variable symbols used in the governing equations can be found within circles next to the name of each species in the diagram. For details see text.

2000)). TGF-β exerts a matrix–promoting (*profibrotic*) action on fibroblasts themselves, stimulating fibroblast proliferation, upregulating collagen and TIMP secretion and downregulating collagenase (Akhurst and Hata, 2012).

Myofibroblasts. In addition to those effects, in the presence of mechanical tension TGF-β also

promotes fibroblast differentiation into an active cell type, the myofibroblast (Vaughan et al., 2000). Myofibroblasts are highly secretory, promoting very fast matrix turnover by producing large quantities of collagen, collagenase and inhibitors (Kirk et al., 1995). In addition to being highly contractile (Tomasek et al., 2002), it seems that under certain conditions myofibroblasts are also highly migratory, producing large amounts of proteolytic enzymes (Shi et al., 1999). Myofibroblast apoptosis (i.e. programmed cell death) has been found to be downregulated by TGF-β (Hinz and Gabbiani, 2010), as well as by lack of stress–shielding due to a poorly organised or dysfunctional matrix (Forte et al., 2010). Myofibroblasts have been identified in abdominal (Sakata et al., 2007) and thoracic (Jones et al., 2009a) aortic aneurysmal tissue, and it has been recently suggested in the literature that the appearance and persistence of a migratory myofibroblast population may be related to aneurysm development (Forte et al., 2010; Jones et al., 2009b). Finally, myofibroblast contraction has been identified to activate latent TGF-β via an integrin–dependent mechanism (Wipff et al., 2007).

Medial degradation. Immune cells (n^i) are commonly found infiltrating the wall of aneurysms (Frösen et al., 2012). Once inside the wall, these cells secrete large quantities of proteolytic enzymes (*proteases*, c^p) that degrade load–bearing elastin (m_M^E) and collagen (m_M^C) in the media and collagen in the adventitia (Rizas et al., 2009). Medial degradation following immune cell infiltration (and smooth muscle cell apoptosis) is believed to trigger initial aneurysmal expansion. Interestingly, TGF-β is also secreted by some immune cells (Rizas et al., 2009), and acts back on these cells by promoting their migration towards the inflammation site (Akhurst and Hata, 2012) and by upregulating secretion of proteases (Mantovani et al., 2013; Pickup et al., 2013).

The previously discussed vascular biology was modelled here by a system of non–linear ODEs, Eq. (2.34)—Eq. (2.44). These equations are based on those in Sec. 2.1.1.4 with the following modifications, which were based on some important discussion points raised in Sec. 2.1.3:

Simplifications: (a) Immature species (procollagen c_A^P and zymogenic collagenase c_A^z in the previous model) are removed, and collagen m_A^C and collagenase c_A^{ca} are modelled to be directly secreted by fibroblasts; (b) Different types of immune cell–secreted proteases (c_M^{pc} and c_M^{pc} in the previous model) are grouped into a single variable, c^p, which degrades elastin and collagen in both layers

Extensions: (a) TGF-β–dependent fibroblast n_A^F to myofibroblast n_A^M differentiation is now modelled according to Eq. (2.34) and Eq. (2.40) below; (b) The levels of inflammatory cells infiltrating the entire arterial wall n^i are not prescribed but are rather governed by the ODE in Eq. (2.41); in addition, the bi–directional interaction between TGF-β and immune cells is now included, Eq. (2.38), Eq. (2.39), Eq. (2.41) and Eq. (2.42) below

Modification: The time variable is now adimensional, with $\Delta t = 1$ being the characteristic time period for degradation of half of medial elastin ($m_M^E \simeq 0.5$, 2.5 years in the previous formulations), or equivalently $\Delta t = 2$ corresponding to the time for degradation of most medial elastin ($m_M^E \simeq 0.1$); all rate constants are now adimensional (N.B. normalised densities and deformation metrics were already adimensional)

The system of governing equations for the levels of cellular and biochemical species is:

$$\frac{dn_A^F}{dt} = (r_{f_1} + r_{f_2} \cdot c_A^\beta) \cdot n_A^F - (r_{f_3} + r_{f_4} \cdot f(\lambda^F) \cdot c_A^\beta) \cdot n_A^F \tag{2.34}$$

$$\frac{dm_A^C}{dt} = (r_{c_1} + r_{c_2} \cdot c_A^\beta) \cdot n_A^F + (r_{c_3} + r_{c_4} \cdot c_A^\beta) \cdot n_A^M - (r_{c_5} \cdot c^p + r_{c_6} \cdot c_A^{ca}) \cdot m_A^C \tag{2.35}$$

$$\frac{dc_A^{ca}}{dt} = \left(\frac{r_{ca_1}}{1 + r_{ca_2} \cdot c_A^\beta}\right) \cdot n_A^F + (r_{ca_3} + r_{ca_4} \cdot c^\beta) \cdot n_A^M - (r_{ca_5} + r_{ca_6} \cdot c_A^I) \cdot c_A^{ca} \tag{2.36}$$

$$\frac{dc_A^I}{dt} = (r_{I_1} + r_{I_2} \cdot c_A^\beta) \cdot n_A^F + (r_{I_3} + r_{I_4} \cdot c_A^\beta) \cdot n_A^M - (r_{I_5} + r_{I_6} \cdot c_A^{ca} + r_{I_7} \cdot c^p) \cdot c_A^I \tag{2.37}$$

$$\frac{dc_A^{\beta l}}{dt} = \left(\frac{r_{\beta l_1} c_A^\beta + r_{\beta l_2} f(\lambda^F)}{1 + r_{\beta l_3} \cdot m_A^C}\right) \cdot n_A^F + r_{\beta l_4} \cdot n^i - (r_{\beta l_5} + r_{\beta l_6} \cdot c^p + r_{\beta l_7} \cdot f(\lambda^F) \cdot n_A^M) \cdot c_A^{\beta l} \tag{2.38}$$

$$\frac{dc_A^\beta}{dt} = (r_{\beta_1} + r_{\beta_2} \cdot c^p + r_{\beta_3} \cdot f(\lambda^F) \cdot n_A^M) \cdot c_A^{\beta l} - r_{\beta_4} \cdot c_A^\beta \tag{2.39}$$

$$\frac{dn_A^M}{dt} = (r_{m_1} \cdot f(\lambda^F) \cdot c_A^\beta) \cdot n_A^F - \left(\frac{r_{m_2}}{1 + r_{m_3} \cdot f(\lambda^F) + r_{m_4} \cdot c_A^\beta}\right) \cdot n_A^M \tag{2.40}$$

$$\frac{dn^i}{dt} = r_{i_1} \cdot c_A^\beta - r_{i_2} \cdot n^i \tag{2.41}$$

$$\frac{dc^p}{dt} = (r_{p_1} + r_{p_2} \cdot c_A^\beta) \cdot n^i - (r_{p_3} + r_{p_4} \cdot c_A^I) \cdot c^p \tag{2.42}$$

$$\frac{dm_M^E}{dt} = -r_e \cdot c^p \cdot m_M^E \tag{2.43}$$

$$\frac{dm_M^C}{dt} = -r_{cm} \cdot c^p \cdot m_M^C \quad , \tag{2.44}$$

where $f(\lambda^F)$ is a mechanotransduction functional that couples arterial mechanics to several (myo)fibroblast–mediated processes: fibroblast stretch to production of latent TGF-β, Eq. (2.38); fibroblast to myofibroblast differentiation, Eq. (2.34) and Eq. (2.40); stretch–

dependent, myofibroblast–mediated latent TGF-β activation, Eq. (2.38) and Eq. (2.39); and suppression of myofibroblast apoptosis by loss of matrix stress shielding, Eq. (2.40). To simulate this coupling, for illustration and following the same choice as in Sec. 2.1.1.2, consider $f(\lambda^F) = (\lambda^F - \lambda^F_h)/\lambda^F_h$ and, here, further assume that the fibroblast stretch is equal to the maximum fibre stretch of the collagen matrix, i.e. $\lambda^F = \lambda^{C,max}_A$, and that its homoeostatic target is equal to the corresponding collagen attachment stretch, $\lambda^F_h = \lambda^{AT,max}_A$.

Adventitial collagen attachment stretch. Similarly to Sec. 2.1.1.3, the changing role of the adventitial layer from a protective sheath to becoming a significant load–bearer is modelled by an adaptive, time–dependent attachment stretch distribution, $\rho\left(\lambda^{AT}_A\right)$. Eq. (2.9)—Eq. (2.11) are also used here to model the rightward shift, narrowing and skewing of this distribution. Informed by the observation that myofibroblasts are more contractile than fibroblasts and can generate significantly more force, the averaging period T_{AT} is now made a decreasing function of the ratio of myofibroblasts to total mural cells (fibroblasts + myofibroblasts),

$$T_{AT}(n^M_A, n^F_A) = T^F_{AT} - (T^F_{AT} - T^M_{AT}) \cdot \left(\frac{n^M_A}{n^M_A + n^F_A}\right) \quad , \tag{2.45}$$

where T^F_{AT}, T^M_{AT} are fibroblast and myofibroblast–specific collagen attachment stretch adaption time periods, resp., and $T^F_{AT} > T^M_{AT}$.

Collagen recruitment stretch. Similarly to the initial CMB model formulation in Sec. 2.1.1.2, the distribution of collagen recruitment stretches in the adventitia, $\rho\left(\lambda^R_A\right)$, evolves such that the minimum, mode and maximum points of the collagen stretch distribution evolve towards their corresponding attachment stretch homoeostatic targets,

$$\frac{d\lambda^{R,\min}_A}{dt} = \alpha^C_A \cdot \left(\frac{\lambda^{C,max}_A - \lambda^{AT,max}_A}{\lambda^{AT,max}_A}\right), \tag{2.46}$$

$$\frac{d\lambda^{R,\max}_A}{dt} = \alpha^C_A \cdot \left(\frac{\lambda^{C,min}_A - \lambda^{AT,min}_A}{\lambda^{AT,min}_A}\right), \tag{2.47}$$

$$\frac{d\lambda^{R,mode}_A}{dt} = \alpha^C_A \cdot \left(\frac{\lambda^{C,mode}_A - \lambda^{AT,mode}_A}{\lambda^{AT,mode}_A}\right), \tag{2.48}$$

where, building on the first model extension in Sec. 2.2.1, $\alpha^C_A(n^F_A, n^M_A, m^C_A, c^{ca}_A)$ is a rate parameter proportional to: the ratio of the levels of fibroblasts n^F_A and myofibroblasts n^M_A (which remodel the tissue) to adventitial collagen m^C_A being remodelled; and the geometric mean of the levels of

mural collagenases c_A^{ca} (metabolising collagen) and collagen being metabolised,

$$\alpha_A^C = \alpha_{A0}^C \cdot \left(\frac{n_A^F + k_{M:F}^{Rem} \cdot n_A^M}{m_A^C} \right) \cdot \sqrt{m_A^C \cdot c_A^{ca}}, \tag{2.49}$$

where α_{A0}^C is a rate constant and $k_{M:F}^{Rem} > 1$ denotes the ratio of the rates of collagen remodelling by (highly dynamic) myofibroblasts to fibroblasts. The collagen recruitment stretch distribution in the media follows similar laws (rate constant α_{M0}^C), however without linking to the levels of collagenase or (myo)fibroblasts, which are not modelled in this layer.

Computational Implementation Model implementation closely follows Sec. 2.1.1.5.

Parameter value selection. Definitions, values and supporting references for all model parameters can be found in Table 2.4—Table 2.6. Values for the geometrical and mechanical parameters are very similar to Table 2.1; only those differing from previous values are shown in Table 2.4. Parameters controlling system dynamics (α_M^C, α_A^C, T_{AT}^F, T_{AT}^M, $k_{M:F}^{Rem}$) were chosen such that biomechanical and biochemical steady states are physiologically realistic, e.g. $\lambda_A^{C,max} \leq 1.15$ and $\lambda^s \leq 2$ for a final non–aneurysmal steady state following adaptive response to initial perturbation. Biochemical parameter values were chosen to balance source and sink terms in unperturbed conditions, subject to biologically–informed inequalities. In particular, myofibroblast rates of secretion were made much larger that those of fibroblasts ($r_{c_3} >> r_{c_1}$; $r_{ca_3} >> r_{ca_1}$; $r_{I_3} >> r_{I_1}$), and matrix degradation required for myofibroblast migration was modelled by an elevated rate of collagenase secretion by these cells ($r_{ca_3} > r_{c_3}, r_{I_3}$).

Initial conditions. Initial conditions for the mechanical variables are identical to Sec. 2.1.1.5. The densities of most cellular and molecular species are normalised to one at the onset of simulation; species that are absent from unperturbed mature arteries (active and latent TGF-β, myofibroblasts, immune cells and proteases) have their initial values set to zero.

Simulation loop. The general CMB model was implemented in Matlab R2013a. The system of coupled equations was iteratively solved by a fully explicit approach: the system of coupled ODEs (Eq. (2.34)—Eq. (2.44) and Eq. (2.46)—Eq. (2.48)) is solved by a backward finite differences Euler method, while the algebraic force–balance equation (Eq. (2.1)) is solved by `fzero`. After variable initialisation, the simulation is started. The arterial system is initially perturbed at $t = 1$ by prescribing a small 5% reduction in the normalised density of medial elastin and collagen, and a small increase of 0.05 in the number density of infiltrating immune cells. System

Table 2.4: **CMB model extended to capture myofibroblast differentiation — mechanical parameters.** Symbols, definitions, values and references.

Parameter	Definition	Value	Notes and References
α^{C}_{M0}	Baseline rate of medial collagen recruitment stretch remodelling	5	
α^{C}_{A0}	Baseline rate of adventitial collagen recruitment stretch remodelling	5	
$k^{Rem}_{m:f}$	Ratio of myofibroblast to fibroblast rates of collagen stretch remodelling	2	*Biologically–Informed Inequality*: Myofibroblasts highly dynamic (Tomasek et al., 2002), $k^{Rem}_{m:f} > 1$
T^{F}_{AT}	Collagen stretch averaging time period for attachment stretch remodelling by fibroblasts	1	
T^{M}_{AT}	Collagen stretch averaging time period for attachment stretch remodelling by myofibroblasts	0.5	*Biologically–Informed Inequality*: Myofibroblasts highly dynamic (Tomasek et al., 2002), $T^{f}_{AT} > T^{m}_{AT}$
k^{mode}_{Skew}	Factor for adventitial collagen attachment stretch distribution skewing	1	
k^{min}_{Narrow}	Factor for adventitial collagen attachment stretch distribution narrowing	1	
t_{sim}	Total simulation time	15	
t_{pert}	Time for onset of system perturbation	1	Small immune cell infiltration
n^{i}_{pert}	Initial step increase in immune cell levels	0.05	Small immune cell infiltration
$m^{E}_{M,pert}$	Initial step decrease in medial elastin	0.95	Small medial degradation
$m^{C}_{M,pert}$	Initial step decrease in medial elastin	0.95	Small medial degradation
λ_{thresh}	"Excessive enlargement" stretch threshold	5	Simulation stopped if threshold reached

mechanical response is predicted by the biomechanical model component, which solves the FBE to compute the domain stretch at systolic pressure; this value is then passed to the biochemical model component, which updates the levels of active biomolecules and cell types; updated normalised mass densities and collagen recruitment stretch distribution are then fed back to the biomechanical model component, iteratively, until the end of simulation is reached, or until an "excessive enlargement" threshold on the circumferential stretch ratio is reached (*Exc. Enlarg.*), at which point the simulation is stopped. In this new adimensional framework, an illustrative simulation time span of 15 adimensional time units is used, which is within the range of previous theoretical studies (Watton et al., 2004, 2009b) and allows for visualisation of interesting model behaviour with sufficient detail. For comparison, the conceptual biomechanical model of Watton et al. (2009b) is also implemented, Sec. 2.1.1.5. The time course of medial elastin and collagen degradation is fed into this model from the results of the extended CMB model.

2.2.2.3 Results

The numerical studies shown in this section display the arterial evolution predicted by the extended CMB model in response to the initially prescribed perturbation (medial degradation and immune cell infiltration) and according to different sets of parameter values. The evolution of both

Table 2.5: **CMB model extended to capture myofibroblast differentiation — biochemical parameters I** Symbols, definitions, values and references.

Parameter	Definition	Value	Notes and References
r_{f_1}	Baseline fibroblast migration and proliferation rate	1	
r_{f_2}	Fibroblast population dynamics sensitivity to TGF-β	10	Combined TGF-β chemotactic and growth factor effects (McAnulty, 2007; Streuli et al., 1993; Martin et al., 1992)
r_{f_3}	Baseline fibroblast cell death rate	1	Equal r_{f_1}; balancing source/sink terms at homoeostasis
r_{f_4}	Rate of TGF-β and tension–driven fibroblast to myofibroblast differentiation	100	Mechanical tension and TGF-β both required for myofibroblast differentiation; Myofibroblasts fast stress–response cells (Tomasek et al., 2002)
r_{m_1}	Rate of TGF-β and tension–driven fibroblast to myofibroblast differentiation	100	Equal to r_{f_4}, cellular species conversion
r_{m_2}	Rate of baseline myofibroblast cell death (including apoptosis)	1	
r_{m_3}	Rate of ECM stress-shielding–dependent myofibroblast apoptosis suppression	1	Return of ECM to original mechanical properties provides stress–shielding to endomural cells and induces myofibroblast apoptosis (Forte et al., 2010)
r_{m_4}	Rate of TGF-β–dependent myofibroblast apoptosis suppression	1	TGF-β1 inhibiting myofibroblast apoptosis via PI3K-AkT pathway (Hinz and Gabbiani, 2010)
r_{i_1}	Rate of immune cell chemotaxis in response to active TGF-β	0.1	TGF-β increasing immune cell (macrophage) chemotaxis (Akhurst and Hata, 2012)
r_{i_2}	Baseline immune cell death rate	1	
r_{p_1}	Rate of baseline immune cell protease secretion	1	
r_{p_2}	Rate of TGF-β–driven increase in immune cell protease secretion	1	TGF-β inducing immune cells (neutrophils and macrophages) to switch to type II phenotype, with increase MMP-9 secretion (Pickup et al., 2013)
r_{p_3}	Rate of baseline immune cell protease degradation	1	Equal r_{p_1}; balancing source/sink terms at homoeostasis
r_{p_4}	Rate of TIMP–mediated immune cell protease inhibition	0.5	Equal r_{I_7}; TIMPs inhibiting proteases secreted by immune cells (Rizas et al., 2009)
r_e	Elastin degradation rate by immune cell proteases	100	fast elastin degradation necessary for substantial medial degradation following small step in immune cells
r_{cm}	Medial collagen degradation rate by immune cell proteases	1	
r_{c_1}	Rate of baseline collagen deposition by fibroblasts	1	
r_{c_2}	Rate of TGF-β–driven increase in collagen deposition by fibroblasts	1	
r_{c_3}	Rate of baseline collagen deposition by myofibroblasts	10	*Biologically–Informed Inequality*: myofibroblasts highly secretory, $r_{c_3} >> r_{c_1}$ (Shi et al., 1996a)
r_{c_4}	Rate of TGF-β–driven increase in collagen deposition by myofibroblasts	2	*Biologically–Informed Inequality*: myofibroblasts highly secretory, $r_{c_4} >> r_{c_2}$ (Shi et al., 1996a)
r_{c_5}	Rate of immune cell protease–driven collagen degradation	1	
r_{c_6}	Rate of endomural collagenase–driven collagen degradation	1	Equal r_{c_1}, balancing source/sink terms at homoeostasis

biochemical/cellular and biomechanical variables is plotted; results computed with the biomechanical model of (Watton et al., 2009b) also plotted for comparison.

Myofibroblast permanence and arterial wall pathology Following differentiation, myofibroblast permanence time is determined by the rate of myofibroblast cell death (*apoptosis*). Here, a parameter study on this rate is performed, $r_{m_2} = \{0, 0.1, 1, 5, 10\}$, with the resulting evolution of mechanical and cellular/biochemical variables displayed in Fig. 2.18 and Fig. 2.19, resp.

The arterial system (initially in homoeostasis) is perturbed by a small degradation of medial elastin and collagen of 5% and immune cell infiltration of 0.05 at $t = 1$. Proteolytic enzymes secreted by infiltrating immune cells result in a rapid degradation of medial elastin for all simu-

Table 2.6: **CMB model extended to capture myofibroblast differentiation— biochemical parameters II** Symbols, definitions, values and references.

Parameter	Definition	Value	Notes and References
r_{ca_1}	Rate of baseline collagenase secretion by fibroblasts	1	
r_{ca_2}	Rate of TGF-beta–driven down–regulation in collagenase secretion by fibroblasts	1	
r_{ca_3}	Rate of baseline collagenase secretion by myofibroblasts	30	*Biologically–Informed Inequalities*: myofibroblasts highly secretory, $r_{ca_3} >> r_{ca_1}$, and migratory, $r_{ca_3} > r_{c_3}, r_{I_3}$ (Shi et al., 1999)
r_{ca_4}	Rate of TGF-β–driven up–regulation in collagenase secretion by myofibroblasts	2	Increased MMP-9 secretion by myofibroblasts in response to TGF-β (Jones et al., 2009b; Theruvath et al., 2012); *Biologically–Informed Inequality*: myofibroblasts highly secretory, $r_{ca_4} > r_{ca_2}$ (Shi et al., 1996a)
r_{ca_5}	Rate of baseline endomural collagenase degradation	0.5	Equal $r_{ca_1} - r_{ca_6}$; balancing balancing source/sink terms at homoeostasis
r_{ca_6}	Rate of TIMP–mediated endomural protease inhibition	0.5	Formation of inhibitor/collagenase complex (Brew et al., 2000); Equal $r_{ca_1} - r_{ca_5}$; balancing balancing source/sink terms at homoeostasis
r_{I_1}	Rate of baseline TIMP secretion by fibroblasts	1	
r_{I_2}	Rate of TGF-β–driven increase in TIMP secretion by fibroblasts	1	
r_{I_3}	Rate of baseline TIMP secretion by myofibroblasts	10	*Biologically–Informed Inequality*: myofibroblasts highly secretory, $r_{I_3} >> r_{I_1}$ (Shi et al., 1996a)
r_{I_4}	Rate of TGF-β–driven increase in TIMP secretion by myofibroblasts	2	*Biologically–Informed Inequality*: myofibroblasts highly secretory, $r_{I_4} > r_{I_2}$ (Shi et al., 1996a)
r_{I_5}	Rate of baseline TIMP degradation	0.5	Equal $r_{I_1} - r_{I_6}$; balancing source/sink terms at homoeostasis
r_{I_6}	Rate of formation of TIMP–endomural protease inhibitory complex	0.5	Equal r_{ca_6} and $r_{I_1} - r_{I_5}$; balancing source/sink terms
r_{I_7}	Rate of formation of TIMP—immune cell protease inhibitory complex	0.5	Equal r_{p_4}
$r_{\beta l_1}$	Rate of active TGF-β–driven increase in latent TGF-β secretion by fibroblasts	0.1	TGF-β auto–induction (Akhurst and Hata, 2012)
$r_{\beta l_2}$	Rate of latent TGF-β secretion by fibroblasts in response to deviations from mechanical homoeostasis of the wall	1	
$r_{\beta l_3}$	Rate of collagen–driven suppression in latent TGF-β secretion by fibroblasts	1	Negative feedback loop (Streuli et al., 1993)
$r_{\beta l_4}$	Rate of latent TGF-β secretion by immune cells	1	TGF-β secreted by infiltrating macrophages in its latent form (Rizas et al., 2009)
$r_{\beta l_5} = r^d_{\beta l_5} + r^c_{\beta l_5}$	Combined baseline endogenous degradation ($r^d_{\beta l_5}$) and conversion into active form ($r^c_{\beta l_5}$) rates	0.5+0.5	
$r_{\beta l_6}$	Rate of proteolytic activation of latent into active TGF-β by immune cell proteases	1	
$r_{\beta l_7}$	Rate of tension–dependent, integrin–mediated latent into active TGF-β activation by myofibroblasts	1	Highly contractile myofibroblasts (Tomasek et al., 2002) responsible for mechanical tension and integrin–mediated TGF-β activation (Hinz and Gabbiani, 2010; Wipff et al., 2007)
r_{β_1}	Rate of baseline latent into active TGF-β conversion	0.5	Equal $r^c_{\beta l_5}$
r_{β_2}	Rate of proteolytic activation of latent into active TGF-β by immune cell proteases	1	Equal $r_{\beta l_6}$
r_{β_3}	Rate of tension–dependent, integrin–mediated latent into active TGF-β activation by myofibroblasts	1	Equal $r_{\beta l_7}$
r_{β_4}	Rate of baseline active TGF-β degradation	1	*Biologically–Informed Inequality*: Active TGF-β degradation faster than latent TGF-β degradation, $r_{\beta_4} > r^d_{\beta l_5}$ (Sporn and Roberts, 1990)

lation cases, which falls to almost zero at $t = 4$, Fig. 2.18(a). In response to this almost complete loss of medial elastin (and of its contribution to load–bearing), the pressurised artery expands and its circumferential stretch increases up to $t = 4$, Fig. 2.18(b). After this time point, different simulation cases display very distinct behaviours, which is a direct result of the different cellular responses elicited: low rates of myofibroblast cell death ($r_{m_2} = \{0, 0.1\}$, red curves) lead to

continuous and accelerating aneurysmal enlargement; faster rates of myofibroblast disappearance ($r_{m_2} = \{1, 5, 10\}$, green curves) result in late re–stabilisation, with λ^s reaching similar steady states for each case, all under 2 (non–aneurysmal).

Collagen *growth* response, i.e. change in collagen normalised mass density, can be seen in Fig. 2.18(c). Following prescribed medial degradation, a small increase in collagen mass can be seen around $t = 1$; as discussed below, this is due to an initial rise in fibroblast numbers, which have a pro–fibrotic action. Following this initial rise, most simulation cases display a dip in adventitial collagen density, which goes below its initial value. Simulation cases for which myofibroblast apoptosis rate is very low have the greatest decreases (red curves), reaching as low as 70% of its initial value before the simulation is stopped due to excessive enlargement (red crosses). This observation points to the fact that the proteolytic action of (migratory) myofibroblasts that persist leads to an unbalance between adventitial collagen deposition and degradation, favouring the latter, which results in weaker walls that continue enlarging. For the stabilisation cases (green curves), note that larger rates of myofibroblast disappearance result in lower

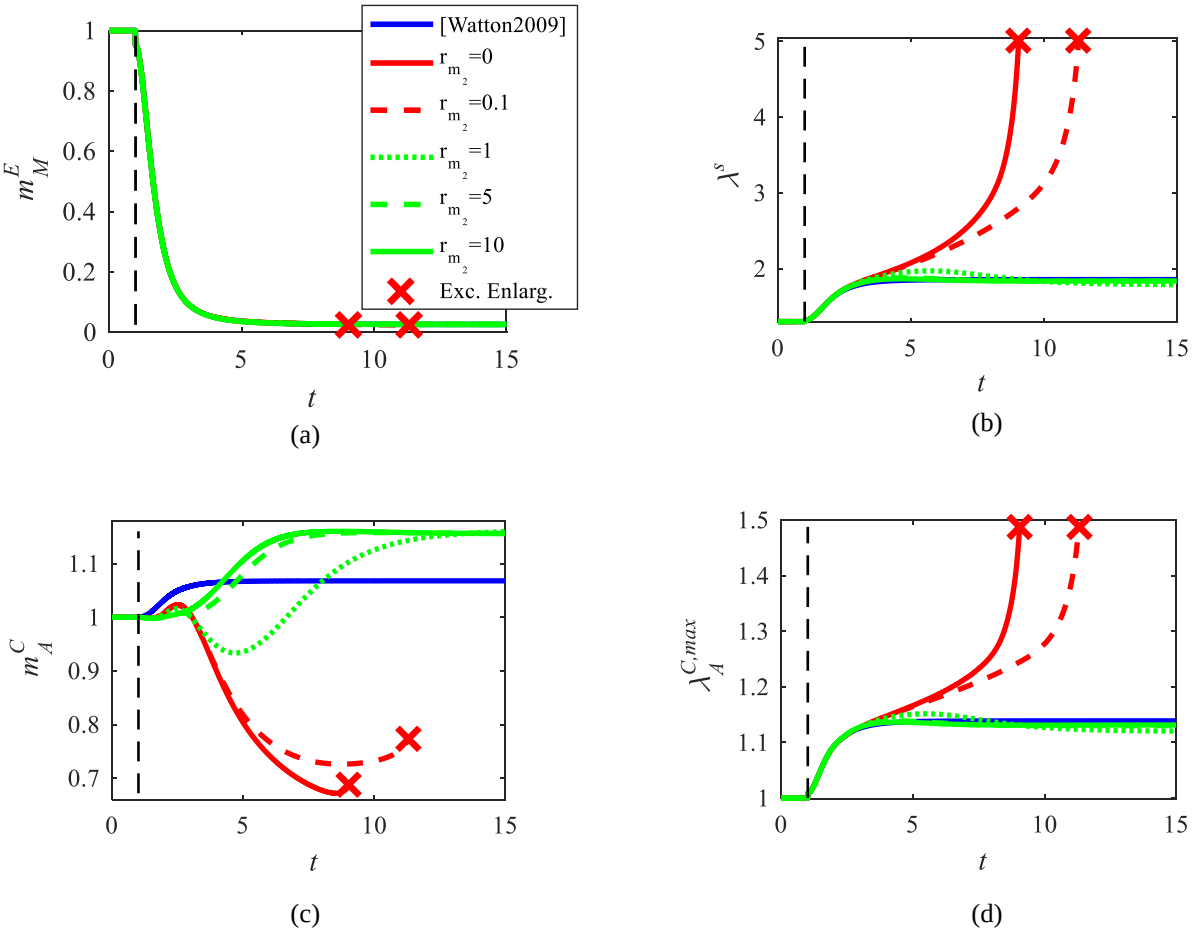

Figure 2.18: **CMB model extended to capture myofibroblast differentiation — mechanical variables.** Parameter study on the basal rate of myofibroblast cell death r_{m_2}.

intermediate reduction in adventitial collagen density and faster final convergence to the same steady–state, around 15% higher than its initial value.

Maximum adventitial collagen stretch, Fig. 2.18(d), follows a similar trend to the circumferential stretch discussed above, with initial expansion being followed by either accelerating continuous growth (slow myofibroblast apoptosis, red curves) or stabilization (faster myofibroblast apoptosis, green curves). Increasing rates of myofibroblast apoptosis lead to lower intermediate increases in collagen stretch, but slightly higher final steady states. Collagen stretch can be used to infer the arterial wall *remodelling* response, i.e. change in collagen reference configuration. From being initially a protective straitjacket bearing no load ($\lambda_A^{C,max}(t_0) = 1$), the adventitia progressively becomes load–bearing ($\lambda_A^{C,max}(t > t_0) > 1$). Note that for the stabilisation cases, following medial elastin degradation the adventitial layer becomes a significant load–bearer, with its collagen fibres being stretched to 10—15%.

The levels of chemo–biological variables over time for three simulation cases are shown in Fig. 2.19. Each row in this figure shows a different simulation case, with the first two being stabilisation cases ($r_{m_2} = \{1, 10\}$, green lines in Fig. 2.18) and the last one being an excessive enlargement case ($r_{m_2} = 0.1$, red line in Fig. 2.18). For each simulation case, the plot in the right column focusing on the levels of TGF-β ($c_A^{\beta l}$, c_A^{β}), immune species (n^i) and myofibroblasts (n_A^M) is a zoomed–in version of the plot in the left column, which shows elastin (m_M^E), collagen (medial m_M^C, adventitial m_A^C), collagenases (c_A^{ca}), TIMPs (c_A^I) and fibroblasts (n_A^F).

Note that for the stabilisation cases, the final steady states of all cellular and biochemical species are similar. In Fig. 2.19(a), the initial large medial elastin degradation (brown dotted curve) is clear (c.f. Fig. 2.18(a)), as well as a small medial collagen degradation (brown dashed curve). The most visible effect of the adventitial response is the increase in profibrotic species, in particular fibroblasts (thick brown solid line), collagenases (magenta line), TIMPs (yellow line) and collagen (brown solid line). The additional adventitial collagen content increases arterial load–bearing capacity, halting further arterial enlargement. The new chemo–mechano–biological steady state that follows is characterised by a more collagenous adventitia (15% increase), with collagenases being perfectly balanced by their inhibitors (both increase 30%, final ratio 1:1) and increased fibroblast numbers (50% increase).

Some of the biological mechanisms underlying these changes can be appreciated in the zoomed–in Fig. 2.19(a)*right*. The initially prescribed small step in immune cell levels of 0.05 (thick red curve) decreases over time, which corresponds to a gradually resolving immune cell process. Even so, the transient increase in inflammatory proteases (thin red curve) promotes me-

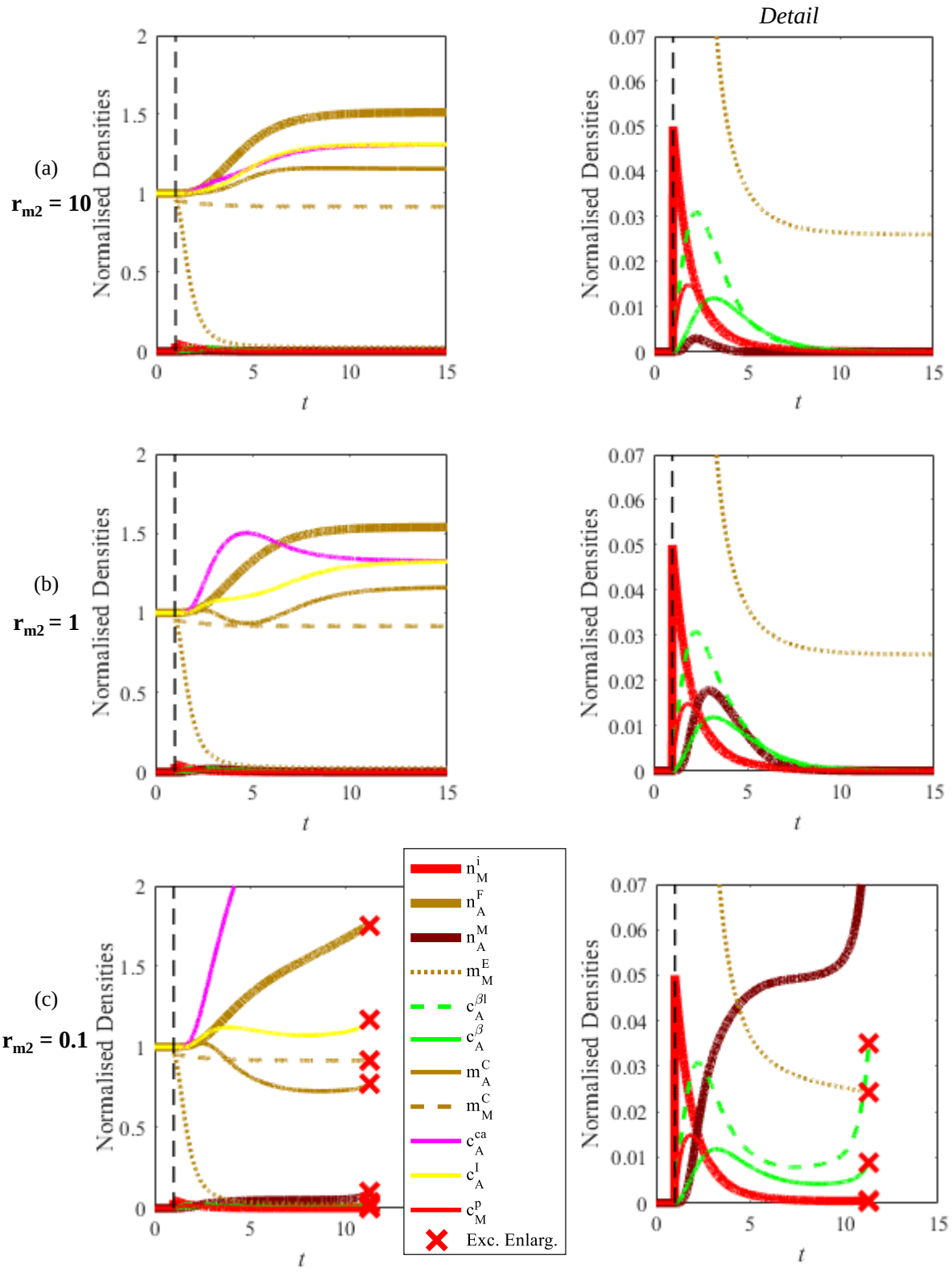

Figure 2.19: **CMB Model extended to capture myofibroblast differentiation — biochemical variables.** Parameter study on the basal rate of myofibroblast cell death r_{m_2}.

dial elastin degradation to very small values (0.025, dotted brown line). This loss in load–bearing capacity and resulting aneurysmal enlargement is perceived and transduced by adventitial fibroblasts, which secrete the mechanotransducer latent TGF-β (dashed green line), then converted to active TGF-β (solid green line); note that the peak in latent TGF-β is followed shortly after by the peak in active TGF-β. TGF-β promotes the previously–described pro–fibrotic response in fibroblasts, which allows for arrest of domain expansion and re–attainment of a mechanobiological steady state. Once this state is reached, TGF-β levels drop to zero, confirming the action of this signalling molecule as a transient mechanotransducer.

The next two rows in Fig. 2.19 correspond to simulation results from systems with gradually lower myofibroblast basal apoptosis rates r_{m_2}. The smaller this parameter value, the higher the initial increase in myofibroblast levels (which differentiate from fibroblasts under the effect of TGF-β and mechanical loading), and the longer the time before the myofibroblast population returns to zero (myofibroblast *permanence time*), c.f. dark brown thick curves in Fig. 2.19(a) and Fig. 2.19(b)*right*. Being a migratory species, myofibroblasts secrete large amounts of collagenases (magenta curves), whose rate of initial increase is correlated to the rate of initial increase in myofibroblast levels and thus inversely correlated with r_{m_2}, c.f. magenta curves in Fig. 2.19(a) and Fig. 2.19(b)*left*. Higher collagenase levels resulting from longer myofibroblast permanence times lead to larger adventitial collagen degradation. In the limit $r_{m_2} = 0$, Fig. 2.19(c), the rise in myofibroblast numbers stops being transient and a myofibroblast population persists (thick dark brown curve in Fig. 2.19(c)*right*). The direct effect of this myofibroblast permanence is a sustained increase in collagenase levels (magenta curve in Fig. 2.19(c)*left*) due to the very fast rate of collagenase secretion by these migratory cells, Sec. 2.2.2.2. The resulting adventitial collagen degradation (thin brown curve in Fig. 2.19(c)*left*) is excessively large, thus greatly reducing wall load–bearing capacity; this condition ultimately leads to accelerating aneurysmal enlargement, as seen in Fig. 2.18(b).

Model exploration: additional parameter studies Inducing myofibroblast persistence by decreasing the rate of myofibroblast basal cell death r_{m_2} was shown to result in excessive collagen degradation promoting continuous aneurysmal enlargement. In this paragraph, the mechanisms underlying this finding and involving a close coupling between tissue–level mechanical equilibrium

and cell–mediated matrix turnover will be investigated through numerical studies on a number of key parameters regulating myofibroblast secretion and remodelling of the collagenous matrix, and myofibroblast population dynamics.

Imbalance in myofibroblast secretion of collagenase and collagen. Firstly, the effect of the imbalance between the rates of collagen (r_{c_3}, Eq. (2.35)) and collagenase (r_{ca_3}, Eq. (2.36)) secretion by myofibroblasts is studied. Initially and informed by the observation that myofibroblasts are highly migratory and (at least under some conditions) secrete large amounts of collagenases (Jones et al., 2009b), the rate of collagenase production by these cells was

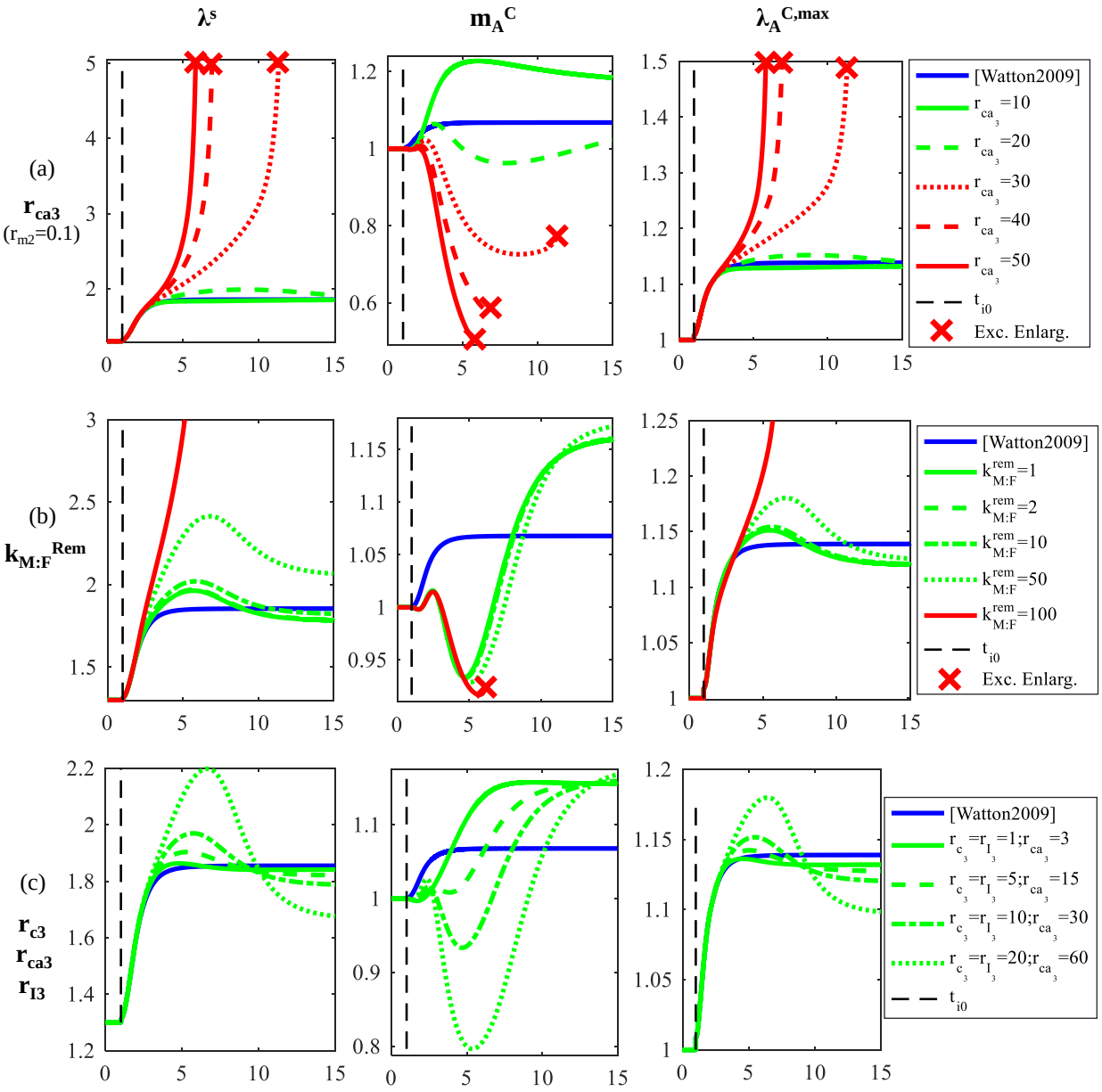

Figure 2.20: **Additional parameter studies on the CMB model extended to capture myofibroblast differentiation — mechanical variables I**. Parameter studies on r_{ca_3} (a) (for the case $r_{m_2} = 0.1$), $k_{M:F}^{Rem}$ (b), and $r_{ca_3} = 3r_{c_3} = 3r_{I_3}$ (c). Horizontal axes refer to adimensional time.

taken to be 3 times larger than their rate of collagen and TIMP secretion. Here it is studied $r_{ca_3} = \{1,2,3(\text{default}),4,5\} \cdot r_{c_3} = \{10,20,30(\text{default}),40,50\}$, for the case $r_{m_2} = 0.1$ where, as was seen in Fig. 2.18 and Fig. 2.19(b), the system was unstable but on the verge of stability. Fig. 2.20(a) shows that the imbalance between the rates of collagen and collagenase secretion has a strong effect on the predicted tissue evolution: as the difference between these two rate constants increases, adventitial collagen m_A^C is degraded to a lower level following initial perturbation, which results in continuous growth in λ^s for $r_{ca_3} \geq 3 \cdot r_{c_3}$ (for $r_{m_2} = 0.1$). Looking at the evolution of cellular and biochemical mediators for a large $r_{ca_3} = 50$, Fig. 2.21(a), it becomes clear that faster increases in collagenase secretion following the appearance of a sizeable myofibroblast population result in a significant collagen degradation, which pushes the system further out of mechanical equilibrium. This is perceived by fibroblasts, which secrete larger amounts of TGF-β, promoting increased differentiation into myofibroblasts, whose numbers now grow approx. linearly rather than stabilising (c.f. Fig. 2.19(a)). The resulting accelerating increase in collagenases configures a cyclic maladaptation feedback loop that explains the observed system instability. $r_{m_2} = 1$ is considered as default hereafter.

Enhanced myofibroblast remodelling rate. A different mechanism whereby the rising of a myofibroblast population may lead to unstable aneurysmal growth is investigated in a parameter study on the ratio of myofibroblast to fibroblast rates of collagen recruitment stretch remodelling, $k_{M:F}^{Rem} = \{1,2(\text{default}),10,50,100\}$ in Eq. (2.49). Increasingly larger values of $k_{M:F}^{Rem}$ promote faster remodelling of adventitial collagen, which leads to faster increases in domain stretch, Fig. 2.20(b). If the rate of remodelling of recruitment stretch consistently exceeds a certain threshold, here due to the rise of the myofibroblast population and to a large value of $k_{M:F}^{Rem} = 100$, collagen cannot be deposited sufficiently fast to balance domain expansion, and stabilisation cannot be attained (red curve).

Enhanced myofibroblast secretory rate. In addition to being highly contractile and possibly remodelling collagen faster than fibroblasts, myofibroblasts are also highly secretory, secreting collagen, collagenases and TIMPs faster than fibroblasts, Sec. 2.2.2.1. To understand the importance of this enhanced secretory ability, the rates of secretion by this cell type are varied, $r_{ca_3} = 3 \cdot r_{c_3} = 3 \cdot r_{I_3} = 3 \cdot \{1,5,10(\text{default}),20\}$. As expected, jointly increasing the rate of secretion of active molecules by myofibroblasts while retaining the imbalance between the secretion

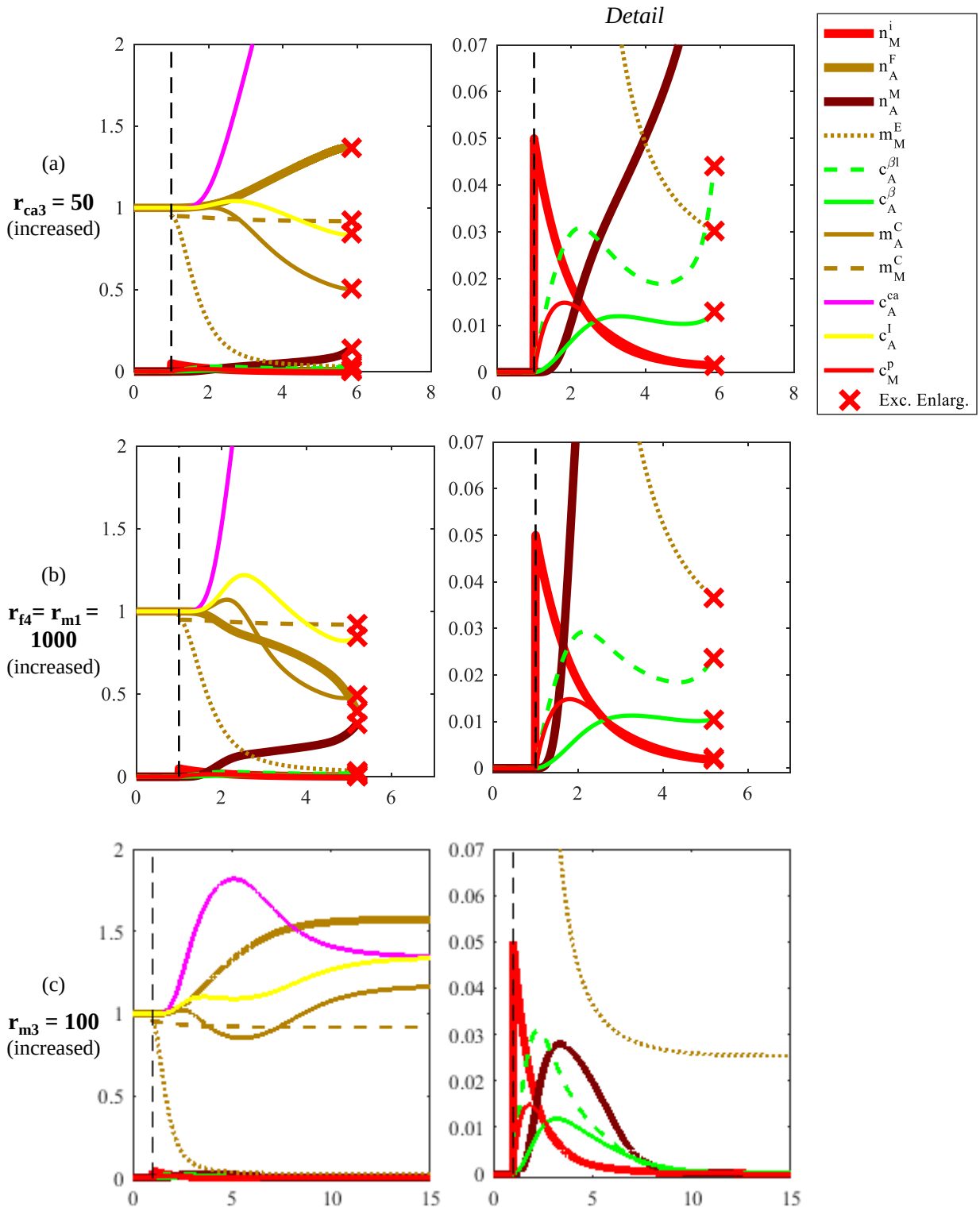

Figure 2.21: **Additional parameter studies on the CMB model extended to capture myofibroblast differentiation — biochemical variables**. Simulation with $r_{ca_3} = 50$ (a), $r_{f_4} = r_{m_1} = 1000$ (b), and $r_{m_3} = 100$ (c). Horizontal axes refer to adimensional time.

of collagen and collagenase by these cells results in a heightened initial degradation in adventitial collagen and a larger initial expansion of the artery, Fig. 2.20(c). Note that the differences are much more significant during and shortly after the initial "transient" period, during which sizeable myofibroblast population is present. Because the dynamics and stability properties of

the system seem to be highly dependent on the evolution of the myofibroblast population, it becomes important to study the influence of parameters controlling myofibroblast appearance (by differentiation from fibroblasts) and resolution (by apoptosis).

Fibroblast to myofibroblast differentiation rate. Increasing rates of myofibroblast differentiation, $r_{f_4} = r_{m_1} = \{0, 10, 100(\text{default}), 1000\}$ in Eq. (2.34), Eq. (2.40), results in increasing collagen degradation following the formation of a large myofibroblast population, which in the extreme case $r_{f_4} = r_{m_1} = 1000$ promotes continuous aneurysm enlargement, Fig. 2.22(a). As expected, Fig. 2.21(b), an increased rate of myofibroblast differentiation promotes a fast increase in the myofibroblast population (thick dark brown curve), whose fast rate of secretion of collagenases (magenta curve) promotes collagen degradation (thin brown curve).

Inhibition of myofibroblast apoptosis. Two mechanisms of inhibition of myofibroblast apoptosis were included in the model. A parameter study on the rate of TGF-β–mediated repression of myofibroblast apoptosis, $r_{m_3} = \{0, 1, 10(\text{default}), 100\}$ in Eq. (2.40), shows that choosing larger values of this parameter increases the initial peak and overall permanence time of the myofibroblast population, Fig. 2.21(c), which results in large increases in collagenase levels contributing to collagen degradation (c.f. Fig. 2.21(c) *vs.* Fig. 2.19(b)). As previously, an increasingly large collagen degradation promotes an increasingly large initial expansion of the artery, Fig. 2.22(b). Even though all the parameter values studied here still allow for the system to achieve a new steady state, the trend displayed here is similar to previous studies, and it is expected that further increasing this value will result in unstable systems. A similar parameter study on the factor coupling repression of myofibroblast apoptosis to deviations from mechanical homoeostasis, r_{m_4} in Eq. (2.40), shows similar trends (*not shown*).

2.2.2.4 Discussion

In this section, the CMB model initially formulated in Sec. 2.1 was extended to capture the dynamics of some of the cell types populating the arterial wall over the course of aneurysm enlargement. The extended model is the first arterial mechanobiological model to successfully incorporate fibroblast to myofibroblast differentiation under the influence of both biochemical regulatory signalling (TGF-β pathway) and mechanical loading (wall stretch), Sec. 2.2.2.2. In addition, the important bidirectional coupling between infiltrating immune cells and TGF-β is

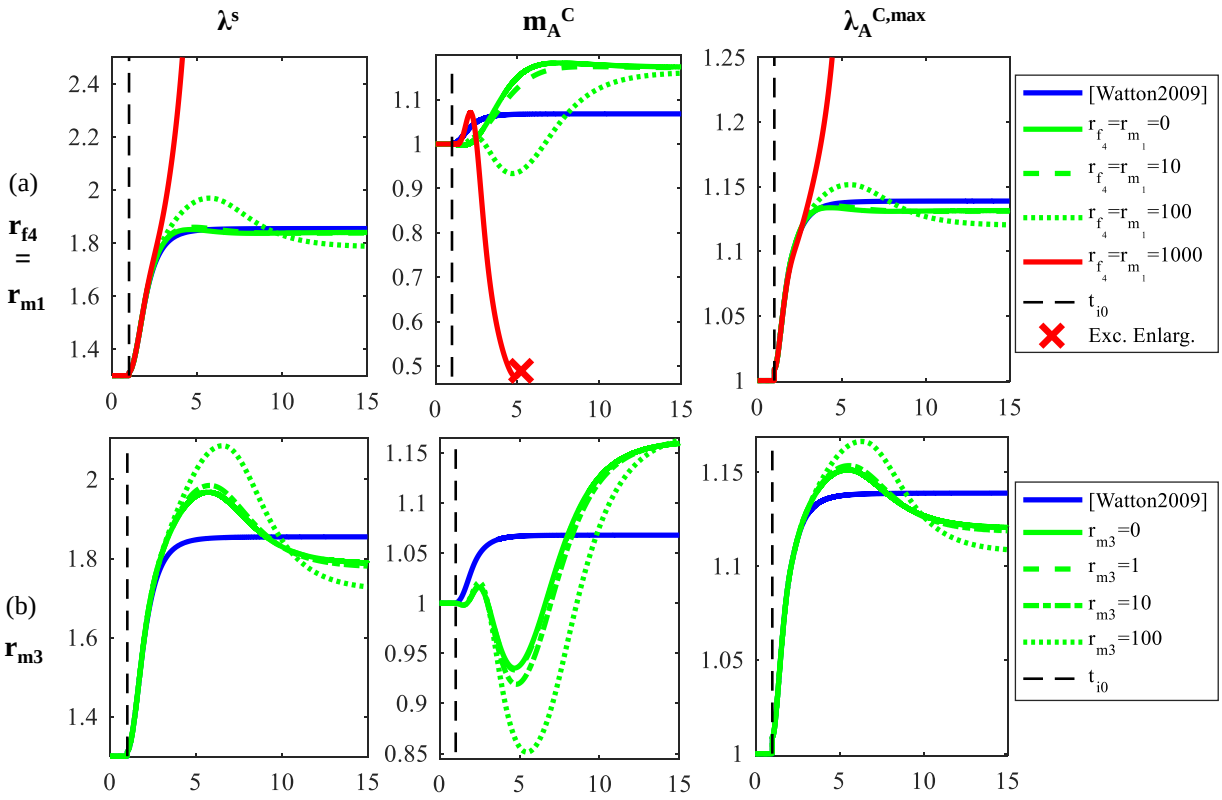

Figure 2.22: **Additional parameter studies on the CMB model extended to capture myofibroblast differentiation — mechanical variables II**. Studies on $r_{f_4} = r_{m_1}$ (a) and r_{m_3} (b).

also included. Simulation results support the importance of modelling myofibroblast population dynamics in predicting aneurysm development.

Model Insight Arterial evolution predicted by the CMB model including cell population dynamics was investigated by a comprehensive set of numerical parameter studies, Sec. 2.2.2.3.

In the first of these studies, a single parameter value was varied, the baseline rate of myofibroblast cell death, r_{m_2}. As expected, the model predicts that the myofibroblast population reaches higher peak values and longer "residence times" (loosely defined as the time during which myofibroblast number density is larger than zero) the lower r_{m_2} becomes, Fig. 2.19 *right*. The consequences of different myofibroblast population dynamics to aneurysm expansion and biomechanics are rather striking, Fig. 2.18. Slower myofibroblast cell death leads to a larger initial reduction in load–bearing adventitial collagen, and to larger initial increases in collagen fibre and circumferential stretch. Past a certain critical threshold, which for the combination of parameters in the study lies in $r_{m_2} \in]0.1, 1[$, the arterial domain does not converge to a new, slightly enlarged steady state (green curves), but rather displays accelerating expansion (red curves). This interesting bifurcation behaviour between stabilisation and continuous enlargement, two important

behaviours displayed by aneurysms (Sakalihasan et al., 2005), was a direct consequence of the different cellular compositions of the arterial wall for each simulation case, as only parameter r_{m_2} was varied.

The CMB model also provides some insight into the biomolecular mechanisms underlying the predicted behaviours. Fig. 2.19 *left* shows that the lower the rate of myofibroblast cell death r_{m_2}, the larger the initial increase in collagenases following myofibroblast differentiation (magenta curves), and the more pronounced the dip in adventitial collagen becomes (solid thin brown curves). An increased proteolytic load has been correlated with fibroblast activation in the adventitia of damaged arteries (Shi et al., 1999). Excessive collagenase secretion by myofibroblasts was suggested in the literature to be necessary for these cells to breach their surrounding matrix during migration (Jones et al., 2009b); this mechanism was included in the model by assigning a rate of myofibroblast collagenase secretion larger than the rates of secretion of either collagen or TIMPs ($r_{ca_3} > r_{c_3}, r_{I_3}$ in Eq. (2.36)—Eq. (2.37)).

Myofibroblasts are an active cell type with high secretory, migratory and contractile activity (Shi et al., 1996a). Commonly described in the context of wound healing (Tomasek et al., 2002), myofibroblasts have been identified in a number of other settings. In vascular disease, myofibroblasts have been identified in the walls of arteries of thoracic (Jones et al., 2009a) and abdominal (Sakata et al., 2007) aortic aneurysms, re–stenosis (Forte et al., 2010) and fibrotic disease (Hinz and Gabbiani, 2010). Because these cells are very active and because other cell populations undergo apoptosis (VSMCs (López-Candales et al., 1997)) or differentiation (fibroblasts (Forte et al., 2010)), myofibroblasts may have a disproportionate influence in driving the progression of vascular disease (Jones et al., 2009b). As previously mentioned, the numerical simulation discussed above seems to supports this hypothesis.

In addition to the numerical study on r_{m_2}, several other parameter studies were run to further investigate model behaviour. Regarding the mechanisms behind myofibroblast persistence being responsible for unstable aneurysm expansion, it was seen that (a) an imbalance between the rate of collagen (r_{c_3}) and collagenase (r_{ca_3}) secretion by these cells was necessary, Fig. 2.20(a); and (b) increasing the rate of myofibroblast remodelling of collagen fibre recruitment stretch ($k_{M:F}^{Rem}$) drives continuous expansion of systems that would otherwise stabilise, Fig. 2.20(b). The latter effect resonates the findings in Sec. 2.2.1, where it was seen that coupling collagen recruitment

stretch remodelling to the levels of the cells remodelling it according to a functional of the form of Eq. (2.32) gives rise to the existence of a threshold rate of remodelling beyond which the system cannot compensate for an excessively fast collagen remodelling with additional collagen deposition, and the system becomes unstable. The two–fold mechanism underlying the observed instability behaviour highlights the importance of modelling the coupling between regulatory biochemistry and cell–driven matrix metabolism both in terms of growth (i.e., change in mass) and remodelling (i.e., change in natural configuration).

Other aspects of myofibroblast population dynamics beyond rate of apoptosis were also investigated. Unsurprisingly, it was found that parameter combinations that increased myofibroblast residence time and peak levels, either by faster differentiation ($r_{f_4} = r_{m_1}$), Fig. 2.22(a), or by downregulating apoptosis (r_{m_3}, r_{m_4}), Fig. 2.22(b), result in stronger proteolytic loads, more extensive matrix degradation, and more expanded (and possibly unstable) arteries. These parameter studies collectively makes clear that modelling the coupling between vascular cell action and tissue–level aneurysm evolution requires an understanding of both the dynamics of cell populations, and of their individual actions on the vascular matrix.

In this section, and for the first time, fibroblast to myofibroblast differentiation under the control of mechanical and biochemical stimuli is modelled. More generally, the CMB modelling framework enables, for the first time, the study of how dynamic cellular populations influence arterial response to perturbation and the progression of vascular disease; how changing mechanical and biochemical conditions influence the dynamics of such cell populations; and how specific components of signalling pathways regulate cell response. Targeting cell–specific active agents, for example those promoting myofibroblast differentiation in fibrotic diseases (Hinz and Gabbiani, 2010), has been suggested as a promising therapeutic strategy with high efficacy and reduced side effects. Modelling is an invaluable tool to explore prospective therapeutic strategies, and the CMB modelling approach developed here is well–equipped for this task, as was explored in relation to the virtual investigation of the effects of pro–fibrotic therapy on aneurysm expansion, Sec. 2.1 above.

Limitations and research directions Only fibroblasts and myofibroblasts were comprehensively modelled in this extended version of the CMB model; some of the actions of infiltrating *native*

immune cells (neutrophils, macrophages), such as protease secretion and regulation by TGF-β, were also included. Many immune cell types are present in diseased arterial tissues. These cells, in particular *adaptive* immune cells (T and B lymphocytes), have diverse actions coordinated by signalling factors such as TGF-β (Rizas et al., 2009). Including other cell types in the model formulated here is straightforward and may be valuable for modelling specific vascular pathologies. Moreover, endothelial cells lining the lumen, as well as stress–generating medial VSMCs, were not included in the model; this simplification was informed by the observation that the contribution of those cell types to arterial mechanobiology becomes smaller over the progression of some forms of arterial disease such as aneurysm, where complete loss or dysfunction of the endothelium (Frösen et al., 2012) and extensive VSMC apoptosis (López-Candales et al., 1997) are observed in later stages of the disease. However, modelling EC and VSMC mechanobiology may be very important to capture earlier stages of aneurysm progression, or to study other diseases.

Myofibroblast biology is complex and not yet fully understood; in this extended CMB model, some of the processes identified in the literature were not modelled. First, myofibroblast cell response seems to change over time, from a highly secretory and migratory cell type, the *proto–myofibroblast*, to a highly contractile species, the *differentiated myofibroblast*, characterised by newly formed prominent stress fibres and large adhesion complexes (Tomasek et al., 2002). The transition between these states seems to depend on the development of a "mechanically–resistive" stiff matrix (Vaughan et al., 2000). TGF-β is also required, and it seems that this peptide promotes a continuum of cell differentiation from basal (fibroblast) to secretory and migratory (proto–myofibroblast) to contractile (differentiated myofibroblast). In the model formulated above, only two points on this differentiation continuum, i.e. restive fibroblasts and migratory myofibroblasts, were included via two separate system variables. In the future, it may be more reasonable to model this differentiation process using a single system variable whose properties change over the differentiation process (e.g. time–varying rate constants); Sec. 2.2.3 below introduces a continuum variable for the extent of cellular mechanical maturation.

Second, myofibroblasts can derive not only from fibroblasts, but from a number of other cell sources (Forte et al., 2010): endothelial cells, by endothelial mesenchymal transition (EMT); circulating precursors (fibrocytes); smooth muscle cells, by de–differentiation; and resident precursor cells, such as mesenchymal stem cells. The importance of each cell source is likely to be

context–dependent; in large artery pathology, adventitial fibroblasts are currently considered to be the most significant cell source (Maiellaro and Taylor, 2007; Jones et al., 2009a). Third, myofibroblast de–differentiation into restive fibroblasts upon disease resolution has been observed *in vitro* (Wipff et al., 2007); however, it does not seem to be an important mechanism *in vivo*, where myofibroblast apoptosis is observed (Forte et al., 2010). Myofibroblast de–differentiation was therefore not included in the extended CMB model.

As discussed above, vascular cell biology and its regulation by biochemical signalling is highly complex and context–dependent. The extended CMB model presented here is only a first step, and highlights the importance of having an improved representation of cell biology to modelling vascular mechanobiology. Interesting experimental questions are suggested by this model, such as the existence of a critical rate of myofibroblast apoptosis below which accelerating arterial expansion develops. Conversely, experimental data is essential to refine model formulation, for example by demonstrating in a condition– and site–specific manner what is the most important cell of origin for myofibroblast differentiation, or what is the size of each cell population. One important finding from the experimental study using an animal model of vascular perturbation, Chapter 3, was that following mechanical perturbation to mice arteries with deficient TGF-β signalling, the emergence of a large population of adventitial cells displaying markers of myofibroblast phenotype could be observed. This finding was indeed a strong motivation behind the development of this model extension.

2.2.3 Model extension III: Modelling cell stiffness

2.2.3.1 Motivation: dynamics of stress fibres and focal adhesions

Arteries are highly dynamical structures, which in face of perturbation are able to adapt their microstructural, biomechanical and geometrical properties to attain a preferred state of homoeostasis, Sec. 1.1 and Sec. 1.2. Arterial adaption is mediated by vascular cells, which populate the arterial wall and dynamically transduce changes in the properties of their surrounding environment such as concentrations of signalling molecules, mechanical loads and/or biophysical and biochemical properties of the ECM. Such mechanical and biochemical *inputs* are *integrated* by vascular cells, which adapt their structure (cytoskeleton, cell membrane) and biochemistry (intracellular signalling) accordingly. As a result of changes in cell properties in response to changes in

their environment, cell behaviour (*phenotype*) also changes, in terms of secretion of signalling or structural molecules, proliferation, (de–)differentiation into other cell types, contractility, motility, etc. Changes in cell phenotype result in changes in the way cells *act* on their surrounding ECM, in particular by modulating matrix mass density (*growth*), its structural properties such as fibre reference configurations (*remodelling*), or its biochemical composition (*maturation*). In view of the previous observation, the conceptual framework that regards vascular cells as *dynamic integrators–actuators* naturally arises, whereby perturbations to arterial homoeostasis are perceived by vascular cells, whose structural adaptation supports functional adaptations that impact cell–driven matrix G&R, thus changing tissue–level properties in an attempt to restore homoeostasis, Fig. 2.23.

(Myo)fibroblasts are important mechanical *dynamic integrator–actuator* cells. When the matrix they populate is subject to mechanical tension, fibroblasts orient along principal directions of stress and develop axial bundles of filamentous actin in the cytosol, the stress fibres (SF) (Tomasek et al., 2002). Cells in this initial stage of mechanical maturation, also known as *proto–myofibroblasts*, display high motility and, as they migrate, deposit large amounts of collagen and (ED-A) fibronectin. For connecting intracellular SFs to ECM components, proto–myofibroblasts develop attachment complexes in their cell membranes composed of large clusters of transmembrane integrin proteins, the focal adhesions (FA).

If mechanical tension, a "mechanically–resistive" stiff substrate (elastic modulus of over 20kPa) and TGF-β1 are simultaneously present, proto–myofibroblasts further mature into *differentiated myofibroblasts* (Hinz, 2010). These cells are characterised by *de novo* expression of α-smooth muscle actin (α-SMA), which localises to thick SFs and enables them to generate over 4 times as much stress as non–α-SMA fibres (Tomasek et al., 2002). Differentiated myofibroblasts seem to be fairly stationary, and the additional contractile force generated by their thick SFs is converted into isometric tension used to remodel the surrounding ECM (Pellegrin and Mellor, 2007). Large stress generation by differentiated myofibroblasts seems to promote the formation of "supermature" FAs, of large size (8–30μm long) and specific molecular composition (tensin, FAK) (Goffin et al., 2006). The myofibroblast fibronexus composed of thick α-SMA SFs in the cytosol, large supermature FAs in the membrane and a stiff (ED-A fibronectin– and collagen–rich) ECM allows for the transmission of large amounts of force contributing to extensive matrix

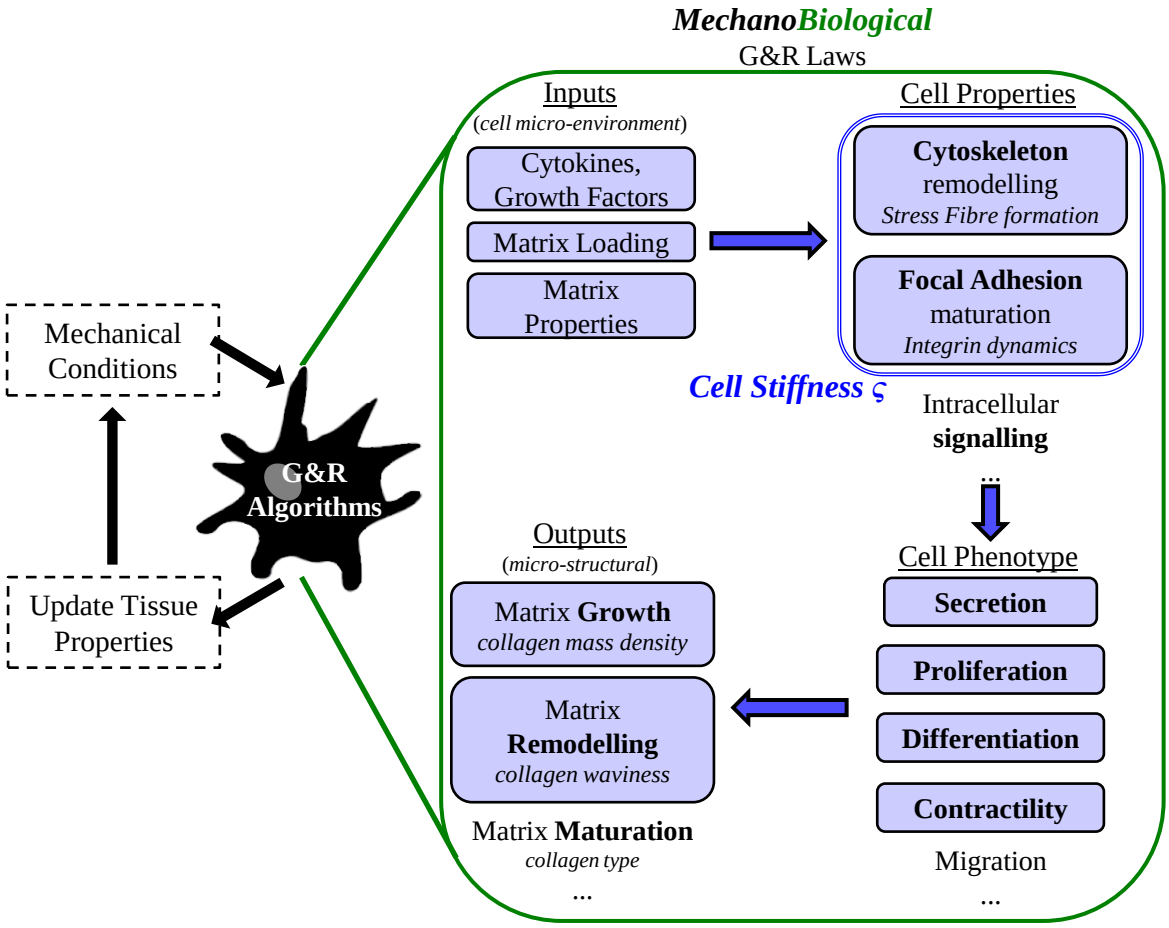

Figure 2.23: **Vascular cells as integrators–actuators.** Motivation for introduction of the concept of cell stiffness ς. Processes and/or components modelled are shaded in blue.

remodelling (Hinz, 2010). For as long as there is a population of fully differentiated myofibroblasts, a positive feedback loop exists, whereby myofibroblast contraction leads to matrix stiffening, which promotes sustained myofibroblast phenotype and force generation; this may result in skin contractures (Tomasek et al., 2002) or excessively thickened and stiff vessels in hypertension (Stenmark et al., 2006).

The molecular mechanisms behind the observed mechanical maturation of fibroblasts are extremely complex. FA and SF formation seems to be regulated by the small GTP–binding protein RhoA (Burridge and Chrzanowska-Wodnicka, 1996); there are several modes of activation of this signalling axis, including growth factors (such as TGF-β) via receptor tyrosine kinase, cell–to–cell adhesion via CAMs or adherens junctions, or matrix loading via integrins or proteoglycans (Sastry and Burridge, 2000). In particular, TGF-β seems to increase the size and area of FAs and promote α-SMA expression that localises to thick SFs (Dugina et al., 2001). Increased rho signalling promotes stress fibre formation via myosin light chain phosphorylation, and actin–myosin cycling promotes SF force generation, which is transmitted to the FAs where these fibres are an-

chored (Burridge and Chrzanowska-Wodnicka, 1996). The dynamics of SFs and FAs are not only related, but they influence each other. Goffin et al. (2006) observe that FA maturation (increase in area) determines tension generation by the cell, which itself determines the dynamics of α-SMA recruitment of SFs and their growth and thickening. Conversely, integrin clustering underlying FA assembly is positively correlated to cytoskeletal contractility, which is enhanced by the maturation of SFs (Chen et al., 2003). Finally, mature FAs are key components of many intracellular and extracellular signalling pathways, in particular the Focal Adhesion Kinase (FAK) axis, which is involved in modulating cell motility, cytoskeletal tension, matrix assembly and cell fate (Romer et al., 2006).

Several models have attempted to capture some features of the cellular mechanical maturation process involving SFs and FAs. Shemesh et al. (2005) model FA formation and growth as a result of traction–driven reduction in the chemical potential of integrin clusters in a thermodynamically–consistent framework. Nicolas and Safran (2006) model FA growth as a result of a stretch–dependent mechanotransduction process by the integrin cluster in the framework of elasticity theory. Giannone and Sheetz (2006) model FA–based signalling as a result of conformational changes of single mechano–sensing molecules within the FA. Deshpande et al. (2008) model integrin diffusion in the cell membrane and couple membrane stretch to the chemical potential of activated, high–affinity integrins able to bind ligands and cluster into FAs. Pathak et al. (2011) couple the previous model of integrin dynamics and FA formation with a model of intracellular mechanotransduction signalling cascades (FAK signalling promoting formation of diffusible IP_3) and calcium–dependent SF activation, thus integrating FA formation, intracellular signalling and cytoskeletal contraction.

The model extension discussed here supplements the CMB model with a description of cell–level mechanical maturation processes. To do so, it includes features of the SF and FA formation and maturation processes mentioned above, integrating them in the existing conceptual description of myofibroblast differentiation and action on matrix G&R. Rather than being a definitive model of SF/FA maturation in the context of myofibroblast differentiation, this model extension simply aims at illustrating future directions for model development while raising interesting conceptual questions relative to the processes being modelled.

2.2.3.2 Methods: model development

As discussed above, vascular cells transduce their environment, changing their properties such that their actions on the surrounding substrate result in re–attainment of tissue–level homoeostasis. In "wound–like environments" where mechanical homeostasis is lost, connective tissue cells such as fibroblasts develop cytoskeletal (stress fibres) and membrane (focal adhesions) structures that render them mechanically active, i.e. able to generate more contractile force and transmit it to the ECM being remodelled (Sastry and Burridge, 2000). Further, it seems that there is a positive feedback loop in the process of mechanical maturation: triggered by mechanical and/or biochemical stimuli, FAs form, which promote SF maturation (by localization of α-SMA) and thickening, which in turn allow for more force generation, promoting FA growth and maturation, further promoting SF development.

Cell stiffness Given that SF maturation and FA growth are directly related in a positive feedback loop, a single variable describing the state of cellular mechanical maturation is introduced. *Cell stiffness* ς^{cell} is a cell property describing both cellular tension generation (SFs) and transmission (FAs) elements. Cell stiffness is expected to be low in mechanically–immature cells such as basal fibroblasts, and to increase over fibroblast mechanical activation, reaching large values for mechanically–active cells such as myofibroblasts. Here, it is considered that cell stiffness can change as a result of three distinct mechanisms:

$$\varsigma^{cell} = f\left(\lambda^{ECM}, \lambda^{cell}, c^{sig}\right). \tag{2.50}$$

Loss of ECM mechanical homeostasis by over– or under–straining, which is related to matrix stretch λ^{ECM}, is known to promote fibroblast differentiation by SF formation and FA maturation (Tomasek et al., 2002). The constitutive response of fibroblasts is highly non–linear (Fernández et al., 2006), and direct cell stretch λ^{cell} also seems to be able to modulate α-SMA protein expression and thus SF properties. Finally, signalling and growth factors (concentration c^{sig}) are known to modulate RhoA signalling and thus contractility–induced SF and FA formation and maturation. In the following, a multiplicative decomposition is considered,

$$\varsigma^{cell} = \varsigma_0^{cell} \cdot f_{ECM}\left(\lambda^{ECM}\right) \cdot f_{cell}\left(\lambda^{cell}\right) \cdot f_{sig}\left(c^{sig}\right), \tag{2.51}$$

where ς_0^{cell} is the initial level of cell stiffness.

It is now necessary to formulate specific functional forms for each function f; let us first consider the ECM–dependent term f_{ECM}. Mechano–sensitive cells such as fibroblasts are known to be responsive to stretching of their surrounding matrix; a collagenous–only adventitia is considered here, and thus $\lambda^{ECM} = \lambda^{C}_{A}$. It is assumed that fibroblasts are able to continuously gauge the stretch state of their surrounding matrix against a reference, which is considered to be the collagen stretch ratio at $t = 0$, $\lambda^{C}_{A,0}$. Instantaneous collagen matrix stretches $\lambda^{C}_{A}(t)$ are averaged over the long matrix remodelling time scales by a running time average, and thus

$$f_{ECM}\left(\lambda^{ECM}\right) = f_{ECM}\left(\lambda^{C}_{A}\right) = 1 + k_{ECM} \cdot \left(\left\langle \lambda^{C}_{A} \right\rangle_{T_\varsigma} - \lambda^{C}_{A,0}\right) = 1 + k_{ECM} \cdot \left[\left(\frac{1}{T_\varsigma}\int_{t-T_\varsigma}^{t} \lambda^{C}_{A}(\tau)\, d\tau\right) - \lambda^{C}_{A,0}\right], \quad (2.52)$$

where k_{ECM} is a weighting parameter and $< \cdot >_{T_\varsigma}$ denotes averaging with time period T_ς.

When stretched past a certain point, fibroblasts display a stress–stiffening constitutive response, which likely arises from their actin cytoskeleton (Fernández et al., 2006); it has also been observed that, over time, application of direct stretch to fibroblasts promotes α-SMA–positive SF assembly (Hinz, 2010). This implies a cellular non–linear stress–stretch response, which implies that cell stiffness ς^{cell} is positively correlated to cell stretch λ^{cell}. Assuming that fibroblast cells are attached to the collagen fibres they remodel (Alberts et al., 2014), stretching collagen fibres away from their homoeostatic configurations will result in cell stretch, and thus $\lambda^{cell} \propto (\lambda^{C}_{A} - \lambda^{C}_{A,hom})$, with $\lambda^{C}_{A,hom} = \lambda^{AT}_{A}$. Finally, and for simplicity, a normalised difference between collagen fibre and attachment stretch is considered,

$$f_{cell}\left(\lambda^{cell}\right) = f_{cell}\left(\lambda^{C}_{A} - \lambda^{C}_{\text{hom}}\right) = 1 + k_{cell} \cdot \left(\frac{\lambda^{C}_{A}(t) - \lambda^{C}_{A,hom}(t)}{\lambda^{C}_{A,hom}(t)}\right) = 1 + k_{cell} \cdot \left(\frac{\lambda^{C}_{A}(t) - \lambda^{AT}_{A}(t)}{\lambda^{AT}_{A}(t)}\right), \quad (2.53)$$

where k_{cell} is a weighting parameter.

Many biochemical signalling factors can trigger SF formation and FA maturation, in particular via activation of the RhoA signalling axis (Sastry and Burridge, 2000). Here, only the influence of TGF-β is considered, and thus $c^{sig} = c^{\beta}_{A}$. Increasing levels of this cytokine promote α-SMA SF formation. The simplest linear functional form for f_{sig} is chosen,

$$f_{sig}\left(c^{sig}\right) = f_{sig}\left(c^{\beta}_{A}\right) = 1 + k_{sig} \cdot c^{\beta}_{A}, \quad (2.54)$$

where k_{sig} is a weighting parameter.

Cell phenotype and action Changing cellular properties such as cell stiffness ς^{cell} leads to changes in cell phenotype, which are reflected in cellular G&R action on their surrounding matrix. Let superscript $cell = F, M$ in ς^{cell} denote fibroblast and myofibroblast cell stiffness. Here,

it is assumed that fibroblast differentiation into myofibroblasts requires fibroblast cell stiffness to reach a minimum threshold stiffness, which is taken as the initial myofibroblast stiffness ς_0^M. Building on Eq. (2.34) and Eq. (2.40),

$$\frac{dn_A^F}{dt} = \left(r_{f_1} + r_{f_2} \cdot c_A^\beta\right) \cdot n_A^F - \left(r_{f_3} + r_{f_4} \cdot \left(\frac{\lambda_A^C - \lambda_A^{AT}}{\lambda_A^{AT}}\right) \cdot c_A^\beta \cdot u\left(\varsigma^F - \varsigma_0^M\right)\right) \cdot n_A^F, \tag{2.55}$$

$$\frac{dn_A^m}{dt} = \left(r_{m_1} \cdot \left(\frac{\lambda_A^C - \lambda_A^{AT}}{\lambda_A^{AT}}\right) \cdot c_A^\beta \cdot u\left(\varsigma^F - \varsigma_0^M\right)\right) \cdot n_A^F - \left(\frac{r_{m_2}}{1 + r_{m_3} \cdot \left(\frac{\lambda_A^C - \lambda_A^{AT}}{\lambda_A^{AT}}\right) + r_{m_4} \cdot c_A^\beta}\right) \cdot n_A^M, \tag{2.56}$$

where $u(x) = 0, x < 0 \wedge u(x) = 1, x \geq 0$ is the Heaviside step function.

The stiffness levels of fibroblasts and myofibroblasts change their matrix G&R action because stiffer cells have thicker SFs capable of generating more contractile force, and larger FAs able to transmit this force to the ECM being remodelled. Adaption of the adventitial collagen attachment stretch distribution is computed, as in previous sections, by

$$\lambda_A^{AT,max} = \left\langle \lambda_A^{C,max} \right\rangle_{T_{AT}} = \frac{1}{T_{AT}} \int_{t-T_{AT}}^{t} \lambda_A^{C,max}(\tau)\, d\tau, \tag{2.57}$$

and the corresponding equations for $\lambda_A^{AT,mode}$ and $\lambda_A^{AT,min}$. However, time period T_{AT} is now a function of evolving fibroblast and myofibroblast cell stiffnesses,

$$T_{AT} = \frac{T_{AT,0}}{\left(\frac{\varsigma^F}{\varsigma_0^F}\right) \cdot u\left(n_A^F\right) + \left(\frac{\varsigma^M}{\varsigma_0^M}\right) \cdot u\left(n_A^M\right)}. \tag{2.58}$$

Remodelling of adventitial collagen recruitment stretch is governed, as in previous sections, by Eq. (2.25)—Eq. (2.27). The rate factor α_A^C in Eq. (2.49) is now extended to account not only for the levels of (myo)fibroblasts remodelling the tissue, but also their stiffnesses,

$$\alpha_A^C = \alpha_{A0}^C \cdot \left(\frac{\varsigma^F \cdot n_A^F + \varsigma^M \cdot n_A^M}{m_A^C}\right) \cdot \sqrt{m_A^C \cdot c_A^{ca}}, \tag{2.59}$$

where α_{A0} is a rate constant. Note that cells are not load–bearing elements, and thus cellular mechanical maturation as described by the cell stiffness variable ς^{cell} does not directly influence the mechanical equilibrium computed by the biomechanical component of the CMB model; its influence is indirect, manifesting over long periods of time *via* cell action on G&R of adventitial collagen mass density and recruitment/attachment stretch distributions.

Model implementation and parameter selection The final CMB model extended in this section to model cellular mechanical maturation is similar to the model in the previous Sec. 2.2.2, except for the modifications mentioned above in relation to the computation of cell stiffness and its influence in cell differentiation and cell–mediated matrix remodelling. In particular, the mechanical component of the CMB model is the same as in Sec. 2.2.2.2. In the biochemical model component, fibroblast and myofibroblast cell stiffness levels are computed at each iteration step by Eq. (2.50). The equations governing the levels of cellular and biochemical species are Eq. (2.34)—Eq. (2.44) as in Sec. 2.2.2.2, except for the equations for fibroblast and myofibroblast levels, Eq. (2.34) and Eq. (2.40), which are replaced by Eq. (2.55) and Eq. (2.56) above. The equations governing the time evolution of the distribution of adventitial attachment stretch are Eq. (2.25)—Eq. (2.27) as previously, however with T_{AT} computed by Eq. (2.57) above. Finally, time evolution of collagen recruitment stretch distribution is computed by Eq. (2.25)—Eq. (2.27), however with α_A^C given by Eq. (2.59) above (and α_M^C being constant).

All of the previous parameters take the same values as previously in Sec. 2.2.2, which can be found in Table 2.4—Table 2.6, with one exception: the basal rate of collagenase secretion by myofibroblasts r_{ca_3} is taken to be equal to their rate of secretion of collagen $r_{c_3} = 10$, which is justified by the focus of this section on fully differentiated myofibroblasts, which are fairly stationary and thus are not expected to secrete as much collagenase as migratory (proto–)myofibroblasts. The values for the parameters in the newly formulated Eq. (2.50)—Eq. (2.58) above are only illustrative, and follow biologically–informed inequalities. Given that myofibroblasts are intrinsically stiffer than fibroblasts due to their thicker SFs and mature FAs, it is required that $\varsigma_0^M > \varsigma_0^F$; $\varsigma_0^F = 1$ and $\varsigma_0^M = 1.1$, such that the predicted increase in fibroblast stiffness allows for myofibroblast differentiation. For the same reason, $k_{cell}^M > k_{cell}^F$, and in particular $k_{cell}^M = 2k_{cell}^F = 1$. Thick SFs and supermature FAs allow myofibroblasts to generate more isometric tension. This may enable them to better sense and respond to variations in ECM stretch, implying $k_{ECM}^M > k_{ECM}^F$, and in particular $k_{ECM}^M = 2k_{ECM}^F = 2$; it also enables myofibroblasts to exert more force on the matrix they remodel, and thus $T_\varsigma^M < T_\varsigma^F$, in particular $T_\varsigma^F = 2T_\varsigma^M = 1$. TGF-$\beta$ promotes α-SMA SF assembly, a defining feature of myofibroblasts, and thus $k_{sig}^M > 0 \wedge k_{sig}^F = 0$; in particular, $k_{sig}^M = 1$. $T_{AT,0} = 1.3$ was chosen to meet the numerical target $\lambda_A^{AT} \approx 1.1$ at the new steady state.

Similar to the numerical studies presented in Sec. 2.2.2.3, a perturbation (small decrease in

medial elastin and collagen to 0.95, and small increase in infiltrating immune cells to 0.05) is introduced at $t_{i0} = 1$, and system response predicted by the extended CMB model is plotted for 4 different parameter values (in blue) until $t = 15$. The results predicted by the biomechanical model of Watton et al. (2009b) are also plotted in red for comparison.

2.2.3.3 Results

Evolution of vascular cell stiffness A parameter study on the rate of mechanotransduction $r_{\beta l_2} = \{0.1, 1, 5(\text{default}), 10\}$ in Eq. (2.38), Fig. 2.24, is run so as to check consistency with previous model formulations, in particulars the initial model formulation (Fig. 2.6*left* in Sec. 2.1.2.1) and the model extension coupling chemo–biology to collagen recruitment stretch remodelling (Fig. 2.13 in Sec. 2.2.1.2). Consistent with previous studies, it is observed that following initial domain expansion as a result of medial degradation, $1 < t < 3$ in Fig. 2.24(a), there is a fibrotic increase in collagen density, Fig. 2.24(b), which promotes domain stabilisation, $t > 3$ in Fig. 2.24(a), and a similar stabilisation or even small reduction in collagen fibre stretches, Fig. 2.24(c). Also consistent with previous observations, increasing the rate of mechanotransduction $r_{\beta l_2}$ results in initially faster and later larger increases in collagen density, which promote stabilisation of the arterial domain at lower domain and collagen fibre stretches.

Fig. 2.24(d) shows the predicted evolution in the cell stiffness of adventitial fibroblasts. Initially ($1 < t < 3$) there is a fast stiffening of fibroblasts, which results from the compounded effect of ECM stretch (factor f_{ECM}), cell stretching away from its preferred state (factor f_{cell}) and biochemical signalling via the TGF-β pathway (factor f_{sig}). Because fibroblast cell stiffness becomes larger that the threshold ς_0^M, myofibroblast differentiation takes place (Eq. (2.55), Eq. (2.56)). Following this initial transient perturbed period, collagen deposition promotes arterial stabilisation (or even a small reduction in stretch). Once the collagenous fabric is back to stretch homoeostasis, cells are assumed to return to an unstretched state (factor f_{cell} when $\lambda_A^C \to \lambda_{A,hom}^C$), and cell stiffness reduces accordingly. Analogously, a return to mechanobiological equilibrium is perceived by cells, which reduce their secretion of TGF-β; a reduction in TGF-β signalling leads to a reduction in the stimulus for forming thick α-SMA fibres, thus reducing cell stiffness (factor f_{sig} when $c_A^\beta \to 0$) . As a result of these two mechanisms, there is a reduction in ς_A^F around $t = 5$, whose extent is positively correlated to the rate of mechanotransduction $r_{\beta l_2}$. Note that fibrob-

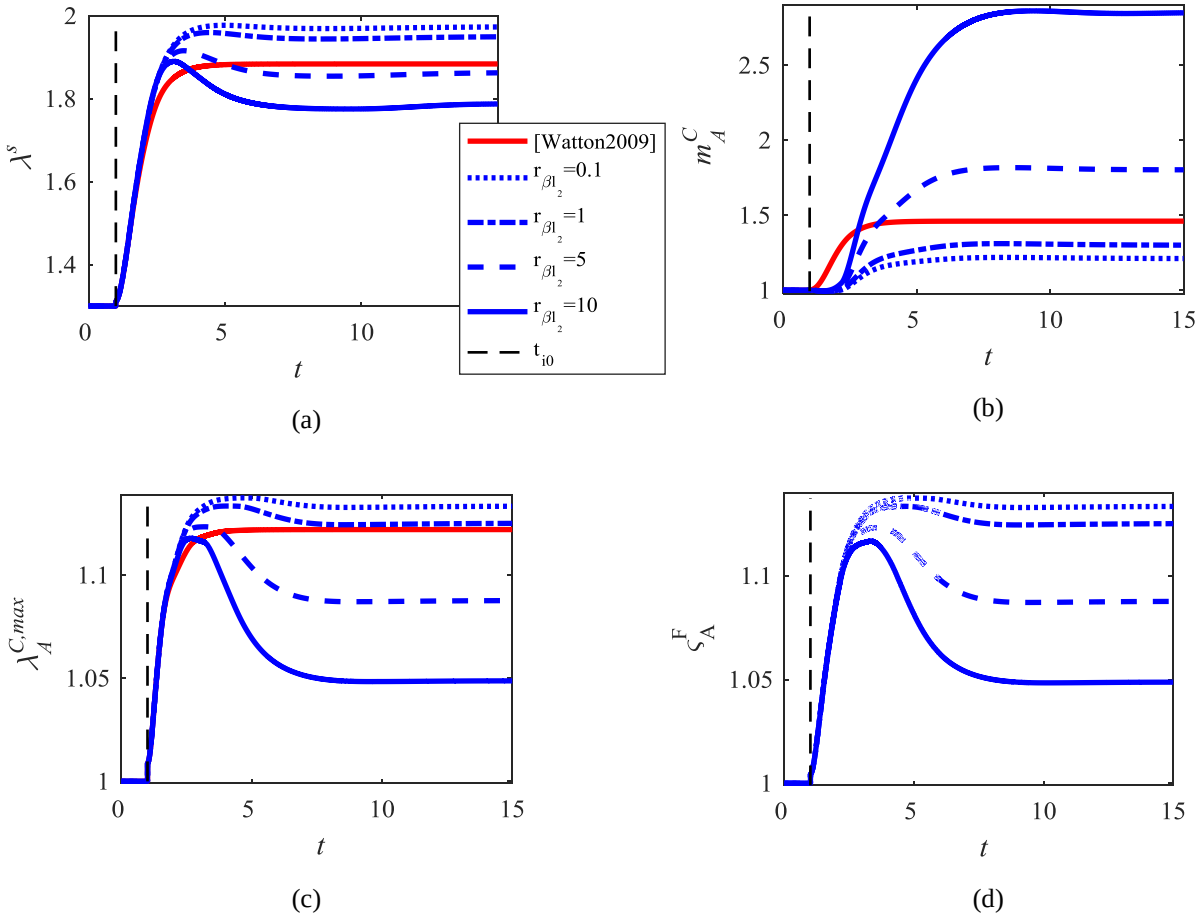

Figure 2.24: **CMB model extended to include a representation of cell stiffness.** Parameter study on the rate of mechanotransduction $r_{\beta l_2}$.

last cell stiffness does not return to basal levels after re–attainment of mechanical homoeostasis. The increasingly load–bearing role of the adventitia implies that a significant proportion of the collagen fibres are permanently stretched. Fibroblast cell stiffness captures this increasing load–bearing role of the tissue via factor f_{ECM}, which remains permanently elevated because the new steady state value of λ_A^C is larger than $\lambda_A^C(t=0)$, corresponding to a "mechanically passive" tissue.

Model exploration: additional parameter studies Additional parameter studies are run to investigate the influence of each of the three mechanisms governing the evolution of cell stiffness. Fig. 2.25(a) shows the influence of the parameter weighting the contribution of cell stretch, $k_{cell}^M = 2k_{cell}^F = \{0.2, 1(\text{default}), 2, 3\}$. Increasing this factor promotes an initially faster increase in fibroblast cell stiffness ς_A^F, which results in slightly larger steady–state values. These cell stiffness dynamics lead to initially faster but ultimately lower levels of adventitial collagen m_A^C. On the other hand, increasing the parameter weighting the contribution of matrix stretching, $k_{ECM}^M = 2k_{ECM}^F = \{0.2, 1, 2(\text{default}), 4\}$, Fig. 2.25(b), influences the final steady state of fibroblast cell stiffness rather than its initial rate of increase, with larger k_{ECM}^F resulting in ultimately

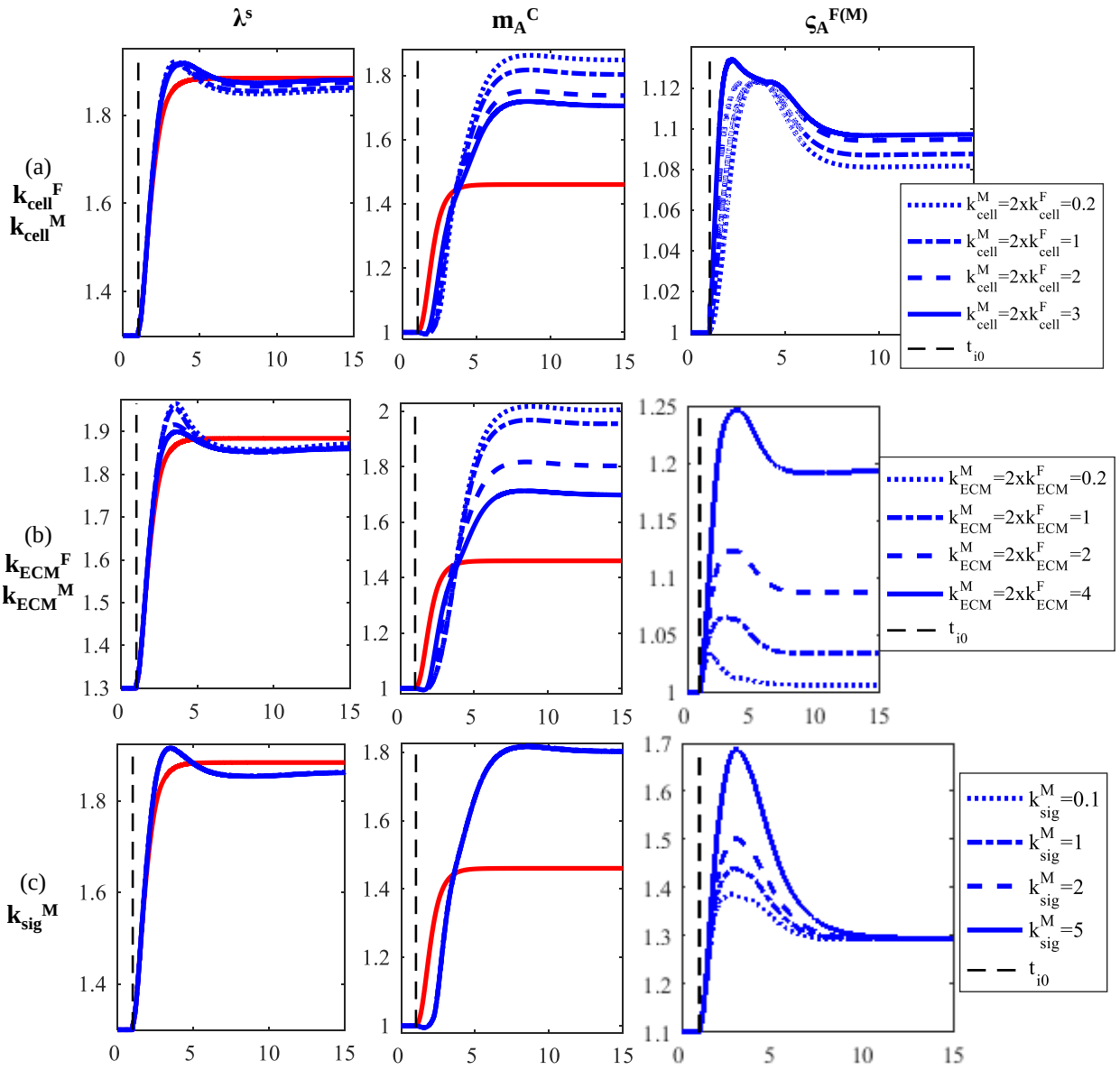

Figure 2.25: **Additional parameter studies on the CMB model extended to include a representation of cell stiffness.** Parameter studies on $k^M_{cell} = 2k^F_{cell}$ (a), $k^M_{ECM} = 2k^F_{ECM}$ (b) and k^M_{sig} (c). Horizontal refer to adimensional time. The last plot in each row shows ς^F_A in (a) and (b), and ς^M_A in (c).

larger ς^F_A values. The resulting initially faster rate of collagen deposition m^C_A reduces the initial increase in stretch λ^s, and domain stabilisation requires less collagen mass increase than otherwise. Finally, increasing the weighting parameter for the influence of active TGF-β levels on myofibroblast cell stiffness, $k^M_{sig} = \{0.1, 1(\text{default}), 2, 5\}$, Fig. 2.25(c), promotes a larger peak in ς^M_A, which then converges to the same final steady state. The effect of different myofibroblast cell stiffness dynamics on tissue–level collagen density m^C_A or stretch λ^s is very small.

2.2.3.4 Discussion

Model formulation and insight Based on the paradigm regarding vascular cells as *dynamic integrators–actuators*, Sec. 2.2.3.1, a simple mathematical description of cell–level mechanical properties was coupled both to environmental stimuli (the *inputs*) and to the dynamics of cell population change and their remodelling action on the ECM (the *outputs*), Sec. 2.2.3.2.

To elaborate, a single *cell stiffness* variable ς^{cell}, Eq. (2.50), was introduced to jointly describe the development of intracellular contractile structures (cytoskeletal stress fibres (Pellegrin and Mellor, 2007)) and membrane anchorage complexes able to transmit the forces generated by cell contraction to the surrounding matrix (integrin–based focal adhesions (Burridge and Chrzanowska-Wodnicka, 1996)), thus modelling the maturation of mechanically–active cells. Based on observations from the literature (Goffin et al., 2006; Hinz, 2010), fibroblast cell stiffness was made to depend on three distinct stimuli: matrix stretch, Eq. (2.52), cell stretch, Eq. (2.53), and the concentration of biochemical signalling factors, Eq. (2.54). Different aspects of cell behaviour were coupled to cell *stiffening* (i.e., mechanical activation): a minimum stretch threshold was required for fibroblast to myofibroblast differentiation, Eq. (2.55), Eq. (2.56); and cell contractility was assumed to be positively correlated to cell stiffness, which influenced the predicted dynamics of cell–mediated matrix remodelling. Higher cell stiffness was thus coupled to a faster adaption of the attachment stretch distribution, Eq. (2.57) and Eq. (2.58), as well as to a higher rate of remodelling of collagen fibre recruitment stretch distribution, Eq. (2.59).

The model was implemented to predict arterial response to perturbation as a result of vascular cell transduction, phenotypic change and ECM remodelling, Sec. 2.2.3.3. Model results are consistent with previous formulations (compare $r_{\beta l_2}$ parameter studies in Fig. 2.6*left* with Fig. 2.24). In addition to the system dynamics previously predicted, the CMB model developed here is able to compute the time evolution in cell stiffness, a structural–functional descriptor of cell mechanical maturation. Fig. 2.24(d) shows that following an initial perturbation setting off aneurysmal enlargement, there is an initially fast increase in cell stiffness, which plateaus and for some cases decreases to a new steady state larger than baseline.

To investigate how each of the three mechanisms included in the model extension contribute to the observed dynamics of ς^{cell}, additional parameter studies were run, where a range of values

was assigned to the weighting factors of each mechanism. Fig. 2.25(a) shows that cell stretch (functional f_{cell}) is primarily responsible for the initial rate of increase in fibroblast cell stiffness. This result is not surprising: direct cell stretching as a result of matrix deformation is expected to be very significant immediately after the initial perturbation, but to reduce over time as fibroblasts break and establish new connections to the ECM they remodel (Chiquet et al., 2003); this is included in the model by functional f_{cell}, Eq. (2.53), which reduces over time as the collagen stretch converges back towards the homoeostatic attachment stretch. On the other hand, matrix stretch (functional f_{ECM}) determines to a large extent the final steady–state of ς_A^F, Fig. 2.25(b). This permanent contribution to cell stiffness follows from the fact that the collagenous matrix remains permanently over–stretched in this system, in the sense that the adventitia becomes a structural load–bearer following medial layer (partial) degradation. Fibroblasts are assumed to be able to experience this permanently over–stretched state (possibly through a sustained increase in local matrix material stiffness (Hinz, 2010)), which is captured in the mathematical model by the difference between average collagen fibre stretch and its baseline level in functional f_{ECM}, Eq. (2.52). Finally, Fig. 2.25(c) shows that increasing the weight of the concentration of TGF-β on the evolution of myofibroblast cell stiffness increases its initial peak but not its final steady–state, which matches the evolution of the levels of this biomolecule. This transient effect is consistent with the transient nature of both TGF-β signalling and the myofibroblast population.

It is interesting to note that even though all the simulation cases in Fig. 2.25 displayed different cell stiffness dynamics (right column), the effect of such cell–level properties on collagen density evolution was small (centre column), and the effect of both growth and remodelling actions on the evolution of arterial stretch was even smaller (left column), whereas different rates of mechanotransduction $r_{\beta l_2}$ led to significantly different levels of collagen, Fig. 2.24(b), and stretch ratios, Fig. 2.24(a). A possible explanation for this observation is that, for the default combination of parameter values chosen, the mechanical equilibrium is determined to a large extent by the dynamics of collagen deposition governed by the signalling pathways component of the CMB model, which are not greatly affected by the evolution of cell stiffness, which is considered here to be related to cell contractility and to cell action on the distributions of recruitment and attachment stretches. Performing further parameter studies in much larger regions of the parameter space is thus advisable.

Limitations, particular choices and future directions Several particular choices were made when formulating the model extension introduced here. Firstly, a single *cell stiffness* variable was used to describe the development of both tension–generating (stress fibres) and tension–transmitting (focal adhesions) elements, which was based on the observation that there is a positive feedback loop on the formation and maturation of these structures (Goffin et al., 2006); in the future, modelling contractile and attachment elements separately such as in Pathak et al. (2011) may be more adequate. Secondly, cell stiffness evolution was made a function of only three distinct variables, two of them mechanical (λ^{ECM}, λ^{cell}) and one biochemical (c^{sig}); in reality, a very large range of biochemical, mechanical and cellular stimuli can activate different intracellular pathways involved in mechanical maturation (Sastry and Burridge, 2000). Thirdly, the influence of matrix stretch was modelled by functional f_{ECM} in Eq. (2.52), which considered the difference between the average value of collagen fibre stretch and a reference value of stretch (taken as the initial value of stretch); as mentioned above, a description based on local matrix stiffness could be preferable, as it is known that myofibroblast differentiation is heavily dependent on substrate stiffness (Hinz, 2010), and there are significant variations in wall stiffness in diseased arteries (Vorp and Vande Geest, 2005). Fourthly, fibroblasts and myofibroblasts were described by two separate system variables governed by ODEs with coupled terms modelling cell differentiation (Eq. (2.55) and Eq. (2.56)). In reality, there seems to be a differentiation continuum from restive fibroblasts to intermediate migratory proto–myofibroblasts to stationary and highly contractile differentiated myofibroblasts (Hinz, 2010); in particular, it may be important to introduce a dependence of fibroblast cell stiffness on TGF-β concentration by prescribing $k^F_{sig} > 0$ in Eq. (2.54), thus modelling intermediately–activated fibroblasts.

Taking into account the overwhelming biological complexity involved in the processes related to cellular mechanical maturation, the present CMB model extension is but a first step towards modelling mechanical maturation of vascular cells regarded as *dynamic integrators–actuators*. Simulation results above show that the model formulation chosen allows for fine–tuning the dynamics of cell stiffness evolution, in particular its initial rate of increase, peak value and final steady state. A thorough investigation of the parameter space should be performed to further study model behaviour, in particular related to the coupling between cell stiffness evolution and cell–mediated G&R of the collagen ECM. Many related cell processes were left out and may

become important in different research contexts, such as focal adhesion–based intracellular signalling or the dependence of cell migration and proliferation on the development of a functional fibronexus (Romer et al., 2006). The modelling framework presented here is flexible enough to be applied in the future to study other mechanisms.

Model development will benefit from data generated in specifically designed experiments in highly controlled and closely monitored *in vitro* models. Because cell stiffness describing cellular mechanical maturation is correlated with the levels of SFs and FAs, histological staining of tissue sections or cell cultures for specific markers such as α-SMA (SFs) or tensin (FAs) (Hinz, 2010) could be used to calibrate the theoretical model. Advanced experimental systems could be used in this regard, in particular those where fibroblast morphology and cell–matrix interactions are studied in biochemically–conditioned 3D matrices under loading (Grinnell, 2003), and those assessing the molecular basis of cell contractility and force transmission to a deformable substrate by traction force microscopy (Legant et al., 2013).

2.3 Conclusion

A theoretical model of cell–mediated arterial G&R capturing the close couplings between vascular biochemistry, biomechanics and cell biology was formulated, implemented and analysed in this chapter. This conceptual model is innovative in integrating important mechanisms of arterial mechanobiology, including cell–matrix interaction, regulatory signalling, cell population dynamics and cell–level mechanical maturation. As with any theoretical model, guidance from experimental studies is key for model refinement and (qualitative) validation; Chapter 3 details the generation of a mechanical, biochemical and cellular data set from an *in vivo* animal model of signalling and mechanical perturbation to vascular homoeostasis. In addition to experimental guidance, it is essential to generate realistic computational predictions; updating the 1D CMB model developed here to a 3D framework able to simulate solid (and fluid) mechanics in complex geometries is addressed in Chapter 4.

CHAPTER 3

AN *in vivo* EXPERIMENTAL ANIMAL MODEL OF ARTERIAL CHEMO–MECHANO–BIOLOGY

Experimental guidance is critically necessary to expand our understanding of fundamental arterial mechanobiological processes in health and disease, which is the foundation for the development and refinement of conceptual models. In this chapter, an animal model of signalling and mechanical perturbation to vascular homoeostasis is used to generate a comprehensive and multi–dimensional data set characterising arterial chemo–mechano–biological response (Sec. 3.1). The properties of two distinct aortic segments were assessed at several time points for two experimental groups against controls (Sec. 3.1.1): in one, TGF-β signalling was conditionally disrupted post–development by knock–out of TGF-β receptor type 2 (TGFBR2); in another, hypertension was induced pharmacologically in addition to TGFBR2 disruption (Sec. 3.1.2). Following tissue harvesting and processing (Sec. 3.1.3), the biomechanical properties of the ascending thoracic aortic and infrarenal abdominal aortic segments were quantified by biaxial mechanical testing (Sec. 3.1.4), collagen microstructure was visualised by the Picrosirius red assay and biomolecular and cellular markers were visualised by immunofluorescence (Sec. 3.1.5); custom–developed data processing pipelines allowed for biomechanical, microstructural and biochemical/cellular quantities to be computed over time (Sec. 3.1.5.3). The results of this study show dramatic changes in the properties of perturbed arteries over time (Sec. 3.2). Mechanical data show that, following perturbation, arteries tended to display larger structural stiffness but lower linearised material stiffness, higher thickness, lower biaxial stretches and Cauchy stresses *in vivo*, lower distensibility and extensibility, and lower stored elastic energy (Sec. 3.2.1.1). Collagen quantification revealed increased levels of total collagen in the wall, and suggested an evolving distribution of collagen fibre thickness and packing (Sec. 3.2.2). Immunohistochemistry revealed layer and vessel segment–specific patterns of evolution of several cellular and biochemical markers, with overall increased cell numbers (specifically those of immune and contractile cells) and increased levels of proteolytic enzymes and TGF-β signalling mediators (Sec. 3.2.3). Study design and results are then discussed (Sec. 3.3), focusing in particular on the methods used to introduce signalling and mechanical perturbations to the arterial wall (Sec. 3.3.1), on the consistency of study results with previously published work (Sec. 3.3.2), on the novel insights this study generated (Sec. 3.3.3), and on the specific limitations of the study pointing towards interesting future work (Sec. 3.3.4). The CMB model developed in Chapter 2 is then applied to capture some features of the experimental data set, which suggests venues for both theoretical model development and experimental investigation (Sec. 3.3.5). The main findings of this experimental study are then summarised, and their relevance to other components of this D.Phil. thesis is considered (Sec. 3.4).

Genetic mouse models have been increasingly used to study how different arterial properties (geometry, microstructure, cellular composition and action, regulatory biochemistry and

metabolism, biomechanics) change in response to different types of perturbations (genetic, pharmacological, mechanical), Sec. 1.4. In this chapter, an animal model of post–developmental genetic and mechanical perturbation to the TGF-β signalling pathway is characterised biomechanically, microstructurally and biochemically.

3.1 METHODS

3.1.1 Study design

The goal of this study is to characterise different aspects (biomechanics, biochemistry, microstructure, cellularity) of arterial mechanobiological response to different types of perturbations. The TGF-β–mediated profibrotic adventitial fibroblast response to vessel dilatation was of particular interest, both because of the increasingly recognised role of the adventitia in vascular pathology (Humphrey and Holzapfel, 2012), and because the experimental results could be correlated with predictions generated by the CMB model formulated in Chapter 2.

An overview of the experimental groups, time points and observations is shown in Table 3.1. An animal model of genetically–induced disrupted cellular signalling through the TGF-β pathway was used (Li et al., 2014), which allowed for conditional knock-out of the TGF-β receptor type 2 (TGFBR2) gene in VSMCs (*details bellow*). In this model, vascular pathology (dissection, aneurysmal enlargement) was triggered by TGF-β signalling perturbation in medial VSMCs, while the adventitial response should still be mediated by normal fibroblasts. Similarly to Li et al. (2014), TGFBR2 disruption was performed post–weaning so as to ensure a certain degree of vascular maturity, but induction only started at 6 weeks (2 weeks later than in the previous study), so as to reduce the incidence of aortic dissection (see Figure 2B *bottom* therein).

The study of Li et al. (2014) showed that aneurysmal enlargement would still take place in the absence of dissection, however it would only develop to significant levels at very late time points (30 weeks of age, Figure S3 therein). Given that hypertension is a risk factor for both thoracic and abdominal aortic aneurysm development (Sakalihasan et al., 2011), it was hypothesised that elevating the blood pressure would accelerate aneurysm development in cases where the aneurysm wall was dysfunctional and prone to aneurysmal enlargement. Mice were subject

Table 3.1: **Experimental Design.** Experimental groups (*rows*) and time points (*columns*).

o - Observation	**6 weeks**		**12 weeks**		**14 weeks**		**18 weeks**
Control (not induced) ***Ctrl***	**o**		**o**		**o**		**o**
TGFβR2 Disruption ***Dis***	***Dis***		**o**		**o**		**o**
TGFβR2 Disruption + Hypertension ***Dis+HT***	***Dis***		***HT***		**o**		**o**

to a systemic, non-invasive hypertensive stimulus with minimal cross–over with inflammatory pathways (*details below*), such that the confounding immune reaction was as reduced as possible. This stimulus was applied at 6 weeks after TGFBR2 disruption (12 weeks of age), when it was considered there was a sufficient convergence towards a new vascular homoeostatic state (Li et al. (2014) reported a stabilisation in the percentage of aortic dissections past this point, Figure 2B *top* therein). In addition to observations at time of TGFBR2 disruption (6 weeks) and hypertension stimulus (12 weeks), there were observations at 14 and 18 weeks, corresponding to a "short" and a "long" time (2 and 6 weeks, resp.) after induction of hypertension (N.B. Kopkan and Majid (2005) report stabilisation in increased systolic blood pressure 2 weeks after hypertension induction using similar methods).

To summarise, three experimental groups were considered, Table 3.1: TGRBR2 disruption ("Dis"); TGFBR2 disruption and overlaid hypertension ("Dis+HT"); and unperturbed control ("Ctrl"). So as to cover a large range of arterial phenotypes, both the ascending thoracic aorta (ATA) and the infra–renal abdominal aorta (IAA) were analysed for each animal, as these segments display significant heterogeneity (Ruddy et al., 2008). Observations were made for the relevant groups at 6, 12, 14 and 18 weeks of age, and three mice were studied per observation, making up a total of 27 animals (54 segments). All animal procedures, including breeding, euthanising, post–weaning TGFBR2 disruption and pharmacologically–induced hypertension were approved by the Institutional Animal Care and Use Committee of Yale University.

3.1.2 Mechanobiological perturbations

In this study, post–developmental arterial homoeostasis was perturbed by genetically–induced disruption of TGF-β signalling and pharmacologically–induced hypertension.

3.1.2.1 Disruption of signalling through TGF-beta Receptor II

Following (Li et al., 2014), TGFBR2 was conditionally knocked-out in the smooth muscle cells of *Myh11-CreER^{T2}.Tgfbr2$^{f/f}$* mice of strain C57BL/6. These are male mice homozygous for the TGFBR2 gene, where one of the coding segments (exon 2) was flanked by *loxP* sites, and whose expression of the enzyme Cre recombinase fused with a modified oestrogen receptor–binding site (ER^{T2}) is under the control of a myosin heavy chain (MYH)11 promoter, specifically activated in smooth muscle cells. Upon injection of the synthetic oestrogen tamoxifen, Cre activity is induced in VSMCs, leading to *Tgfbr2* disruption in these cells.

In this study, each mouse in the *Dis* and *Dis+HT* groups was given every day for 5 days an intraperitoneal injection of 0.1mL of a solution of 10mg tamoxifen per mL of corn oil (i.e., 1mg/day of tamoxifen). An approximate 3cm end section of the tail of each animal sacrificed was frozen at -80°C, and later homogenized and used for PCR identification of both *Tgfbr2 loxP* and *Myh11–Cre* sites following standard protocols; the few (2) animals not expressing either molecule were not included in the analysis. Finally, Li et al. (2014) reported excellent selectivity and robustness of *Tgfbr2* deletion in medial VSMCs of mice expressing *Tgfbr2* loxP and *Myh11–Cre* transgenes after treatment with tamoxifen.

3.1.2.2 Hypertensive Stimulus

Similarly to Bellini et al. (2015), hypertension was induced in mice in the *Dis+HT* group by supplementation of drinking water with 3g/L of NG-nitro-L-arginine methyl ester hydrochloride (L-NAME), and a high salt chow (8% NaCl, Harlan TD.92012). L-NAME is a blocker of the endothelial–derived nitric oxide synthase (eNOS), required for synthesising the vasodilator nitric oxide (NO), thus increasing peripheral resistance, while a high–salt diet promotes increased osmotic pressure and blood volume, both contributing to increased blood pressure (Rodriguez-Iturbe et al., 2005). L-NAME inhibition of eNOS is also related to increased oxidative stress and some immune cell activation, which may result in kidney damage and further salt retention (Kitamoto et al., 2000). In spite of inducing some inflammatory processes, L-NAME–induced hypertension has a much smaller immune component than AngII–induced hypertension (Wu et al., 2014); it does not directly influence arterial wall remodelling unlike norepinephrine (NE)–induced hypertension (Dao et al., 2001); and it is not invasive unlike aortic banding (Hibuse

et al., 2009) or even AngII or NE–induced hypertension, which generally require subcutaneous implantation of osmotic pumps (Bersi et al., 2013).

Blood pressure was measured at baseline, 2 and 6 weeks of L-NAME and high salt diet in four female littermates of the male mice used in the study and by means of standard non–invasive tail–cuff methods (Eberth et al., 2009). Briefly, mice were placed in clear acrylic nose cone holders measurement tubes and heated until the temperature in their tails reached approx. 34°C (measured with an infrared thermometer). 60 cuff inflation cycles were then run, with cuff operation and data acquisition performed by a CODA tail–cuff blood pressure system (Kent Scientific Corporation, Torrington, CT, USA). After removal of outliers, systolic, diastolic and mean arterial pressures (MAP) were averaged for each mouse and then for the mouse group. Blood pressure results are shown in Table 3.2 in Sec. 3.2.

3.1.3 Animals, tissue harvesting and processing

Several breeding pairs of *Myh11-CreER^{T2}.Tgfbr2$^{f/f}$* mice were kindly supplied by Prof George Tellides (Yale School of Medicine) and used to generate enough male mice for the study. At designated times, each mouse was euthanised by intraperitoneal injection of approx. 0.3 mL of a 1:10 Beuthanasia-D solution (active substances: pentobarbital, phenytoin). Following removal of the ribcage, exsanguination was performed by cardiac perfusion of Hanks balanced salt solution (HBSS). The heart, aortic arch (down to just before the first intercostal branch), brachiocephalic trunk (BCT) and the initial segments of the left common carotid and left subclavian arteries were gently dissected out and placed in HBSS (room temperature); similarly, an abdominal incision allowed for the abdominal aorta (from just above the coeliac artery to just after the iliac bifurcation) to be excised and placed in HBSS. Each excised segment was then manually cleaned of excess perivascular tissue and prepared for further testing.

In terms of the thoracic segment, the heart was removed, thus exposing the aortic root; the BCT was cut on the right subclavian artery / right common carotid artery bifurcation; double–knots using thin suture were used to close off the left common carotid, left subclavian and the aorta itself just distal to the left subclavian branch; the segment of the thoracic aorta distal to the applied suture was cut and fixed in 4% formalin overnight, followed by storage in 70% ethanol prior to embedding in paraffin for sectioning ($5\mu m$ section thickness) and histological or im-

munofluorescence (IF) staining; the remaining vessel was temporarily stored in HBSS at 4°C, and then cannulated to glass cannulae in the biaxial mechanical testing device (*details below*). The abdominal segment was also processed: small side branches to the abdominal aorta just distal to the left renal artery were ligated; the abdominal aorta was sectioned at the iliac bifurcation and just distal to the left renal artery; the "renal" segment was fixed in formalin in preparation for histology, while the IAA segment was temporarily stored in HBSS at 4°C for mechanical testing. From collecting the mouse to the last step in tissue preparation for histology or mechanical testing, the experimental protocol lasted approx. 4 hours.

3.1.4 Mechanical data acquisition

The workflow for biaxial mechanical testing, data processing and analysis follows closely the methods of Ferruzzi et al. (2013) for biomechanical phenotyping of mouse central arteries.

3.1.4.1 Biaxial mechanical testing

Following dissection, cleaning and side branch ligation, ATA and IAA segments were sequentially mechanically tested in a custom–built biaxial pressure–inflation, axial force–stretch testing device (Gleason et al., 2004b), Fig. 3.1. Each segment is secured to the hatched conical tips of custom–made 90° glass cannulae using thick 6-O suture in a double knot configuration. Vessel wall integrity is then assessed by gently running HBSS through the lumen of each vessel, which is then pressurised to reveal the existence of tears or holes in the vessel that result in fluid leaking. The mounted specimen is place in an outer ("adventitial") HBSS bath, which is heated by an external ("thermal") circulating bath at 37°C; HBSS is used, as it has been shown that it does not promote VSMC contractility and thus ensures passive behaviour (Bersi et al., 2013). The glass cannulae are connected to an inner ("luminal") HBSS flow, with both inner and outer baths being circulated by a Masterflex L/S peristaltic pump.

Pressure–inflation tests require control of the intraluminal pressure, which is carried out by 10% CO_2 pressurization of the luminal flow under the control of a PC-5PSIG-D/BP Alicat Scientific pressure controller. In series with the luminal flow tubing, two pressure transducers are placed directly before and after the cannulae, which allow for computation of the average pressure in the vessel by a Living Systems PM-4 pressure monitor. Vessel position and external diameter

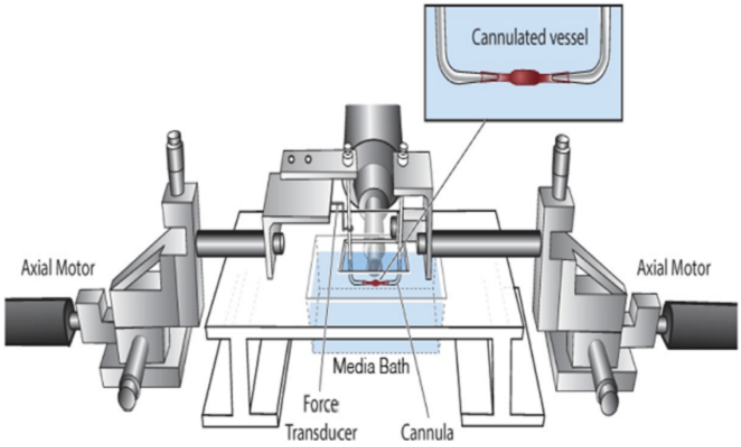

Figure 3.1: Pressure–inflation, axial force–stretch mechanical test device (reprinted from Udelsman et al. (2014), with permission from Elsevier).

are visualised by an InfiniVar CFM video microscope coupled to a Sony XC-ST50 monochrome CCD camera mounted horizontally and at the same height and longitudinal position of the cannulated vessel. Lighting is provided by an adjustable fibre optic light source.

So as to perform axial force–stretch tests, the positions of the left and right platforms (supporting distal and proximal cannulae, resp.) are regulated by two CMA-12CCCL Newport Corp. linear actuators, themselves controlled by a Newport ESP301 motion controller. A 50g load cell (31,S/N 1260079 Honeywell force transducer) is then attached to the left supporting platform, with the measurement hook gently attached to the vertical section of the distal glass cannula by melted paraffin wax. Data from the pressure transducers, optical microscope, load cell and motion controller is fed into a desktop computer via SCB-68 National Instruments data acquisition (DAC) board, which also passes control signals back to the motion and pressure controllers. A custom control program in LabVIEW 2015 (National Instruments, Austin, TX, USA) quantifies, displays and stores vessel diameter, axial force, intraluminal pressure and axial position, and allows for user regulation of the last two.

Once the vessel is mounted and the biaxial mechanical testing system is assembled, the unloaded geometry is initially estimated by performing small steps (0.01—0.02mm) of extension and compression of the vessel and determining the vessel configuration at which one further extension would lead to stretching of the arterial wall by visualising overall vessel geometry and uncrimping of fibre bundles. The vessel is then equilibrated and reacclimated at 90mmHg intraluminal pressure and with approx. 18mL/min HBSS adventitial and luminal flows for 30mins. Following equilibration the vessel is preconditioned by four pressurization–depressurization cycles

between 10 and 140mmHg, followed by re–estimation of unloaded length. *In vivo* axial stretch ($\lambda_{z,est}^{i.v.}$) is then estimated by slowly increasing the axial stretch of the sample while pressurizing it 60—120mmHg and monitoring the force at the transducer — $\lambda_{z,est}^{i.v.}$ is defined as the axial stretch at which the measured axial forces remain nearly constant in response to changes in luminal pressure, which is reasonable on energetic grounds (Weizsäcker et al., 1983). An automated biaxial mechanical testing programme is then run. Three pressure–inflation tests are performed by cyclic pressurization 10—140mmHg at three different values of stretch, i.e. $\lambda_z^{i.v.}$ and $\lambda_z^{i.v.} \pm 5\%$. Four axial force–length tests are then performed by stretching 0—44.13mN (ATA) or 0—24.52mN (IAA) at four different intraluminal pressures, 10, 60, 100 and 140mmHg (Ferruzzi et al., 2015). Pressure–inflation and axial force–stretch data are automatically stored in CSV format, ready for processing and visualisation. Finally, the system is disassembled and the vessel decannulated. Unloaded wall thickness is measured by cutting an approx. 0.5mm long ring–shaped section from the middle of the ATA or IAA segments, suspending it in HBSS solution and imaging the cross section.

3.1.4.2 Biaxial data processing

Vessel outer diameter is measured online during the biaxial test for the unloaded configuration (unloaded outer diameter, D_o) and for loaded configurations at specific intraluminal pressures and axial lengths ($d_o(P, l_z)$). Unloaded thickness H is measured by running a custom MATLAB–based manual segmentation and smoothing script on the images of the vessel ring suspended in HBSS. Unloaded inner radius and loaded outer radius are then given by $R_i = (D_o - 2H)/2$ and $r_o = d_o/2$, resp. The remaining loaded dimensions are computed by assuming that the vessel cross–section remains approximately circular upon pressurization and axial stretch, and that transient loading of the blood vessel (i.e., without growth and remodelling) is isovolumetric (incompressibility assumption) (Humphrey, 2013). Given unloaded axial length L_z, thickness H and outer radius $R_o = D_o/2$, the mean unloaded volume is $\bar{V} = \pi \left(R_o^2 - (R_o - H)^2\right) L_z$. Loaded inner radius r_i and thickness h are then given by

$$r_i = \sqrt{r_o^2 - \frac{\bar{V}}{\pi l_z}}, \qquad h = r_o - r_i. \tag{3.1}$$

Mean biaxial stretch ratios (i.e., circumferential stretch ratio and mid–thickness and global axial stretch ratio) are then given by

$$\lambda_\theta = \frac{r_i + h/2}{R_i + H/2}, \qquad \lambda_z = \frac{l_z}{L_z}. \tag{3.2}$$

Based on the observation that residual stresses in the arterial wall lead to approx. homogeneous through–thickness stress distributions at physiological conditions (Ferruzzi et al., 2013), experimentally–inferred mean values of the in–plane biaxial circumferential (σ_θ^{exp}) and axial (σ_z^{exp}) Cauchy stresses are used to characterize the stress states of the samples. Following from force balance considerations and assuming axisymmetrical deformations,

$$\sigma_\theta^{exp} = \left\langle \sigma_{\theta\theta}^{exp} \right\rangle = \frac{P_v^{exp} r_i}{h}, \qquad \sigma_z^{exp} = \left\langle \sigma_{zz}^{exp} \right\rangle = \frac{F^{exp}}{\pi h \left(2r_i^2 + h\right)}, \tag{3.3}$$

where $P_v^{exp} = P_d + k(P_p - P_d)$ is the intraluminal pressure at the cannulated vessel computed from the pressures measured by the proximal (P_p) and distal (P_d) pressure transducers (k is a fitting parameter); and $F^{exp} = F_T^{exp} + \pi r_i^2 P_v^{exp}$ is the force applied to the ends of the cannulated vessel (F_T^{exp} is the force measured at the force transducer). Finally, a rigorous determination of the *in vivo* axial stretch $\lambda_z^{i.v.}$ is performed by computing the stretch value at which the axial force–stretch curves for different pressures cross over (Van Loon, 1976), see Fig. 3.5.

3.1.4.3 Fitting to constitutive model

Solid mechanics framework Passive biaxial mechanical behaviour can be rigorously analysed by computing the planar components of a stress tensor as a function of an appropriate strain tensor (i.e., referring to the same configuration and having the same basis and objectivity transformation). Here the Cauchy stress $\boldsymbol{\sigma}$ and the left stretch $\boldsymbol{V}$ tensors are considered (note that $\boldsymbol{V}$ is computed from the deformation gradient tensor $\boldsymbol{F}$ by the polar decomposition $\boldsymbol{F} = \boldsymbol{V}\boldsymbol{R}$, where $\boldsymbol{R}$ is the rotation tensor (Holzapfel, 2000)). In the 2D biaxial problem of axisymmetrical inflation and extension of a thin–wall arterial segment, $\boldsymbol{F} = \mathrm{diag}(\lambda_r, \lambda_\theta, \lambda_z)$, while by incompressibility $\lambda_r = 1/\lambda_\theta\lambda_z$. Therefore, mechanical characterisation of the system simply requires the computation of $\sigma_\theta = \sigma_{\theta\theta}(\lambda_\theta, \lambda_z)$ and $\sigma_z = \sigma_{zz}(\lambda_\theta, \lambda_z)$.

Constitutive material model The stress–stretch constitutive relations above require modelling the material properties of the tissue. Following Holzapfel et al. (2000), the arterial wall is considered

to be a fibre–reinforced hyperelastic composite material. A microstructurally–motivated four–fibre family strain energy density function (SEDF) Ψ taking into account the contributions of an elastin–dominated isotropic matrix and of four parallel and mechanically nonlinear collagen fibre families (1: axial, 2: circumferential, 3,4: symmetric diagonal) is used to describe the passive mechanical behaviour of the arterial tissue (Ferruzzi et al., 2010, 2013),

$$\Psi\left(\boldsymbol{C},\boldsymbol{M}^i\right)=\frac{c}{2}\left(I_1-3\right)+\sum_{i=1}^{4}\frac{c_1^i}{4c_2^i}\left[e^{c_2^i\left(I_4^i-1\right)^2}-1\right], \tag{3.4}$$

where c, c_1^i, c_2^i are material parameters; $\boldsymbol{C}=\boldsymbol{F}^T\boldsymbol{F}$ is the right Cauchy–Green deformation tensor; $\boldsymbol{M}^i=\{0,\sin\alpha_0^i,\cos\alpha_0^i\}$ is a directional unit vector characterising the orientation α_0^i of each of the ith collagen fibre families with respect to the axial direction in the undeformed configuration; and I_1, I_4 are the 1st and 4th deformation invariants given by

$$I_1=\mathrm{tr}\boldsymbol{C}=\lambda_\theta^2+\lambda_z^2+\frac{1}{\lambda_\theta^2\lambda_z^2},\qquad I_4=\boldsymbol{M}^i\cdot\boldsymbol{C}\boldsymbol{M}^i=(\lambda^i)^2=\lambda_\theta^2\sin^2\alpha_0^i+\lambda_z^2\cos^2\alpha_0^i, \tag{3.5}$$

where $\mathrm{tr}(\cdot)$ is the trace operator and λ^i is the stretch of the ith collagen fibre family.

Using the previously defined SEDF and assuming a planar state of stress, the theoretically–computed circumferential (σ_θ^{th}) and axial (σ_z^{th}) components of the Cauchy stress tensor are given as a function of the corresponding stretch ratios by

$$\begin{aligned}\sigma_\theta^{th}=&c\left(\lambda_\theta^2-\frac{1}{\lambda_\theta^2\lambda_z^2}\right)+c_1^1\left(\lambda_\theta^2-1\right)e^{c_2^1\left(\lambda_\theta^2-1\right)^2}\lambda_\theta^2\\&+2c_1^{3,4}\left[\left(\lambda_\theta^2\sin^2\alpha_0+\lambda_z^2\cos^2\alpha_0\right)-1\right]e^{c_2^{3,4}\left[\left(\lambda_\theta^2\sin^2\alpha_0+\lambda_z^2\cos^2\alpha_0\right)-1\right]^2}\lambda_\theta^2\sin^2\alpha_0,\end{aligned} \tag{3.6}$$

$$\begin{aligned}\sigma_z^{th}=&c\left(\lambda_z^2-\frac{1}{\lambda_\theta^2\lambda_z^2}\right)+c_1^1\left(\lambda_z^2-1\right)e^{c_2^1(\lambda_z^2-1)^2}\lambda_z^2\\&+2c_1^{3,4}\left[\left(\lambda_\theta^2\sin^2\alpha_0+\lambda_z^2\cos^2\alpha_0\right)-1\right]e^{c_2^{3,4}\left[\left(\lambda_\theta^2\sin^2\alpha_0+\lambda_z^2\cos^2\alpha_0\right)-1\right]^2}\lambda_z^2\cos^2\alpha_0.\end{aligned} \tag{3.7}$$

Constitutive model fitting Estimation of the eight parameter values (c, c_1^1, c_2^1, c_1^2, c_2^2, $c_1^3=c_1^4$, $c_2^3=c_1^4$, $\alpha_0^3=-\alpha_0^4$) characterising arterial tissue passive material behaviour, Eq. (3.4), is performed by nonlinear least squares minimization of an error function e measuring the normalised difference between experimentally estimated (*exp*) and theoretically predicted (*th*) applied loads (i.e., intraluminal pressure P and axial force F),

$$e=\sum_{i=1}^{N}\left[\left(\frac{P_v^{th}-P_v^{exp}}{\bar{P_v}^{exp}}\right)_i^2+\left(\frac{F^{th}-F^{exp}}{\bar{F}^{exp}}\right)_i^2\right], \tag{3.8}$$

where N is the number of samples; overbars signify values averaged over the entire group of samples; and theoretical loads are computed from theoretical stresses in Eq. (3.6), Eq. (3.7) through Eq. (3.3). Eq. (3.8) has been shown to produce reasonably good fits at both low and high load ranges (Ferruzzi et al., 2013).

In this study, data fitting by minimization of the error function e was done using MATLAB–native `lsqnonlin` function. Initial guesses for the parameter values were randomly selected in the range $[0,1]$, and constraints $c, c_1^i, c_2^i \geq 0$ and $0° \leq \alpha_0^i \leq 90°$ were enforced during regression. Due to different parameter value initialisation and in order to avoid reaching relative minima of e, 30 fitting runs were performed for each mouse's biaxial mechanical data set; the results from each fitting run were then checked, and the "best fit" was selected taking into account both the root mean square of the fitting error ($RMSE = \sqrt{e/N}$) and visual inspection of the predicted *vs.* experimentally measured pressure–diameter and axial force–length curves.

So as to simulate average loads–deformations and stress–strain data from the theoretical SEDF with best–fit parameter values, it is necessary to determine λ_θ for each loaded configuration characterised by intraluminal pressure P and axial stretch λ_z. For each pair (P, λ_z), a Newton–Raphson algorithm is used to solve Eq. (3.3) *left*,

$$P - \frac{\sigma_\theta(\lambda_\theta, \lambda_z) \cdot h(\lambda_\theta, \lambda_z)}{r_i} = 0 \tag{3.9}$$

for r_i, with $h(\lambda_\theta, \lambda_z)$ computed using incompressibility, $\sigma_\theta(\lambda_\theta, \lambda_z)$ given by the constitutive relation Eq. (3.6) with best–fit parameter values, and $\lambda_\theta = \lambda_\theta(r_i, h)$ by Eq. (3.2) *left*. The inner radius computed is then used to calculate loaded thickness by Eq. (3.1), biaxial stretch ratios by Eq. (3.2), elastic stored energy by Eq. (3.4) and circumferential and axial biaxial stresses by Eq. (3.6), Eq. (3.7). Biaxial mechanical tests can thus be simulated for a range of (P, λ_z) pairs.

Stress–strain linearisation The theory of small on large of Baek et al. (2007a) is used to linearise the constitutive response of arteries subjected to small motions. In general, the Cauchy stress tensor $\boldsymbol{\sigma}$ for a hyperelastic material in 3D under isovolumetric motions is computed by

$$\boldsymbol{\sigma} = -p\boldsymbol{I} + 2\boldsymbol{F}\frac{\partial \Psi}{\partial \boldsymbol{C}}\boldsymbol{F}^T, \tag{3.10}$$

where p is a Lagrange multiplier enforcing incompressibility, $\boldsymbol{I}$ is the identity matrix, $\boldsymbol{C} = \boldsymbol{F}^T\boldsymbol{F}$ is the right Cauchy–Green deformation tensor and $(\cdot)^T$ is the transpose operator. Let the overall

deformation $\boldsymbol{F}$ be decomposed into a large finite deformation from reference to intermediate configuration (such as driven by long–term G&R) $\boldsymbol{F}^0$, and a small deformation (such as over cardiac cycle) $\boldsymbol{F}^*$, such that $\boldsymbol{F} = \boldsymbol{F}^*\boldsymbol{F}^0$. Baek et al. (2007a) show that the equivalent changes in Cauchy stress $\boldsymbol{\sigma} = \boldsymbol{\sigma}^* + \boldsymbol{\sigma}^0$ can be written in tensor components as

$$\boldsymbol{\sigma}_{ij} = -p^*\delta_{ij} + \underbrace{\sigma^0_{ij}}_{\sigma_{\text{pre}}} + \underbrace{\mathscr{C}_{ijkl}\epsilon_{kl}}_{\sigma_{\text{lin}}} + \mathscr{D}_{ijkl}\Omega_{kl}, \tag{3.11}$$

where ϵ_{kl} and Ω_{kl} are the components of the small strain and small rotation tensors, resp.; superscripts ^{0},* have the same meaning as above; the Einstein summation convention is used (δ_{ij} is a Kronecker delta); σ_{pre} and σ_{lin} are the prestress and the linearised stress, resp..

Furthermore, the *linearised stiffness matrix* $\mathscr{C}_{ijkl}$ characterising infinitesimal deformations around a finitely deformed state is given by

$$\mathscr{C}_{ijkl} = \delta_{ik}\sigma^0_{lj} + \sigma^0_{il}\delta_{jk} + 4F^0_{iA}F^0_{jB}F^0_{kP}F^0_{lQ}\frac{\partial^2\Psi}{\partial C_{AB}\partial C_{PQ}}\bigg|_{C^0}. \tag{3.12}$$

The linearised *circumferential* and *axial stiffness* discussed below are the corresponding in–plane components of the linearised stiffness matrix, i.e. $\mathscr{C}_{\theta\theta\theta\theta}$ and $\mathscr{C}_{zzzz}$, resp.

By following a similar approach to the one described in the last paragraph of the previous section, it is possible to simulate several mechanical quantities of interest at *in vivo* conditions. Given an accurately computed *in vivo* axial stretch $\lambda_z^{i.v.}$ and a small range of pressures around group–specific mean arterial pressure (MAP), numerical solution of Eq. (3.9) can be used to compute loaded inner radius, then used to calculate loaded thickness (Eq. (3.1) *right*), biaxial stretch ratios (Eq. (3.2)), stored elastic energy (Eq. (3.4)), biaxial stresses (Eq. (3.6), Eq. (3.7)) and biaxial linearised material stiffness (Eq. (3.12)) at the *in vivo* configuration.

Energetic considerations Following Ferruzzi et al. (2015), energy dissipation over biaxial loading and unloading cycles was assessed. Let superscripts $K = L, U$ denote loading and unloading, resp. The strain energy associated with either deformation is given by

$$\Psi^K = \underbrace{\sum_{i=1}^{3}\left(\int_{E_{\theta\theta,min}}^{E_{\theta\theta,max}} S_{\theta\theta}\,dE_{\theta\theta}\right)_i^K}_{\text{pressure–inflation tests}} + \underbrace{\sum_{j=1}^{4}\left(\int_{E_{zz,min}}^{E_{zz,max}} S_{zz}\,dE_{zz}\right)_j^K}_{\text{axial force–stretch tests}}, \tag{3.13}$$

where $\boldsymbol{S} = \boldsymbol{F}^{-1}\boldsymbol{\sigma}\boldsymbol{F}^{-T}$ is the second Piola–Kirchhoff stress tensor, $E_{\theta\theta}$,E_{zz} the planar circumferential and axial components of the Green–Lagrange strain tensor $\boldsymbol{E} = (\boldsymbol{C} - \boldsymbol{I})/2$ (N.B. $\boldsymbol{S}$ and $\boldsymbol{E}$

are work conjugates), and $(\cdot)^{-1}$ the inverse operator. Integration is performed numerically by a trapezium rule, with strain limits of integration evaluated at limit pressures and forces: $E_{\theta\theta,min} = E_{\theta\theta,min}(P = 10mmHg)$, $E_{\theta\theta,max} = E_{\theta\theta,max}(P = 140mmHg)$, $E_{zz,min} = E_{zz,min}(F = 0mN)$, and $E_{zz,max} = E_{\theta\theta,min}(F = F_{max})$, with $F_{max} = 44.13mN$ for ATAs and $F_{max} = 24.52mN$ for IAAs, as previously. Following the computation of loading and unloading strain energies, their normalised difference or *energy dissipation ratio* (EDR) is computed to assess energy losses,

$$EDR(\%) = \frac{\Psi^L - \Psi^U}{\Psi^L} \times 100. \tag{3.14}$$

Summary geometrical and mechanical metrics (loaded dimensions, Cauchy stresses, linearised stiffnesses and stored elastic energy) at individual *in vivo* stretch and group–specific mean arterial pressures were computed for each arterial segment and then averaged for each observation group. Similarly, the EDR over biaxial loading/unloading cycle was computed for each arterial segment and then used to compute group averages. In addition to computing $\Psi(\lambda_\theta(P^{MAP}), \lambda_z^{i.v.})$, maps of the SEDF as a function of $(\lambda_\theta, \lambda_z) \in [0.8, 2.4]$ pairs were computed from Eq. (3.4) and using best–fit parameter values; these SEDF maps were then plotted as stored energy isocontours.

3.1.5 Histological staining

Formalin–fixed, paraffin–embedded samples were sectioned ($5\mu m$ thickness) and stained by the Yale Pathology Tissue Services (School of Medicine, Yale Universities). Some of these tissue sections were then imaged and processed to quantify arterial wall microstructure, cellular composition and biochemical environment.

3.1.5.1 Picrosirius red (PSR) for fibrillar collagen

So as to visualise collagen fibres (collagen types I and III), tissue sections from the 14 and 18 weeks time points in each experimental group were stained with Picrosirius red (PSR) using standard protocols (Udelsman et al., 2014; Bersi et al., 2016). Stained slides were then imaged under polarised light at 20x magnification by an Olympus BX/51 microscope (CellSens Dimension); the distribution of birefringent collagen fibre colours correlates with collagen fibre diameter, with thick fibres (predominantly type I) showing as orange/red and thin fibres (predominantly type III) showing as yellow/green (Dayan et al., 1989). Each slide was imaged twice with different

exposure times: a "low exposure" time of 20ms was used to image densely packed collagen fibres in the adventitia, followed by a "high exposure" time of 200ms to image the less dense collagen fibres in the media.

A custom MATLAB script was then used to process the acquired images (Bersi et al., 2013, 2016). Several partial images for each tissue section were stitched together to produce cross sectional images with 1360x1024 resolution. A global thresholding routine was used for background removal, and manual segmentation routines were used to isolate medial and adventitial sections. The code then computed total collagen pixels and distribution of collagen pixel colours in each layer. Estimation of medial and adventitial cross–sectional areas for computation of biochemical and cellular area densities (*details below*) was also based on the PSR images. Given the apparent cohesiveness of the media, total number of medial pixels was taken from the mask applied to this image during manual segmentation ("Segment." label). In contrast, the adventitia displayed much less structural integrity; based on the observation that most of the this layer is composed of fibrillar collagen (Humphrey, 2002), the total number of adventitial pixels was made equal to the total number of collagen–positive pixels in this layer after background exclusion ("Coll. Pxls" label). Area was computed from pixel counts according to the calibration factor $645 \times 645\text{nm}^2$ per pixel, and averaged for each group.

3.1.5.2 Immunofluorescence (IF) for cellular and biochemical markers

Several markers of biomolecules and cell types were visualised by immunofluorescence (IF). Tissue sections were deparaffinised, rehydrated and blocked for nonspecific binding. Sections were then incubated overnight with primary antibodies against: MMP-2 (Millipore AB19167, 1:500), a gelatinase with collagenolytic activity mainly secreted by mural VSMCs and (myo)fibroblasts but also by infiltrating macrophages (Hobeika et al., 2007; Ruddy et al., 2008); TGF-β1,2,3 (Abcam ab66043, 1:500), signalling peptides regulating inflammatory and ECM metabolic processes (Akhurst and Hata, 2012); pSMAD-2 (Millipore AB3849-I, 1:100), an intracellular signalling mediator in the TGF-β "canonical" (profibrotic, immunosuppressor) pathway (Doyle et al., 2012); α-SMA (Abcam ab5694, 1:100), a contractile protein expressed by smooth muscle cells and differentiated myofibroblasts (Beamish et al., 2010); and CD45 (BD Pharmingen 550539, 1:100), a transmembrane protein expressed by a large range of immune cells, including lymphocytes, gran-

ulocytes and macrophages (Abbas et al., 2014). Species–specific Alexa Fluor 594–conjugated secondary antibodies (Invitrogen) were then used to visualise primary antibody binding. Following mounting and ProLong Gold antifade reagent with 4',6-diamidino-2-phenylindole (DAPI, Invitrogen) for counter–staining of cell nuclei, sections were imaged by an Olympus BX/51 microscope and associated Olympus DP70 digital camera.

Images taken of each tissue section were then stitched, thresholded, manually segmented and used to extract layer–specific pixel counts for each marker by means of a custom–built MATLAB script. Cross sectional images with visible staining or sectioning artefacts (e.g. adventitia pulled to cover the medial layer during sectioning) were excluded from analysis. Area densities of markers and cells (extracted from pSmad-2 images) were computed using the previously calculated layer–specific cross–sectional areas for each observation group.

3.1.5.3 Data analysis

Individual geometrical, mechanical and histological/IF measurements were averaged for each observation group (i.e., experimental group observed at a particular time point); the mean and standard error of the mean $SEM = s/\sqrt{N}$ (s: standard deviation, N: number of samples) are reported. In addition to the absolute values, fold–changes of the perturbed (*Dis* and *Dis+HT*) groups with respect to the control group were also computed by taking the ratio between each perturbed observation group average and a baseline value. 12wks *Ctrl* group averages were taken as baselines for the mechanical summary metrics (vascular mechanical maturity is reached at 6–8 weeks (Ferruzzi et al., 2016)), while 14wks *Ctrl* group averages were taken as baselines for PSR and IF quantification (very small differences between 12 and 14 weeks groups in pilot studies were observed). Note that due to the low number of samples available, statistical tools could not be used to compute the statistical significance of the differences observed between observation groups, Sec. 3.3.4. The present study should thus be regarded as exploratory, with the results reported below supporting the relevance of further experimental work with this model.

3.2 RESULTS

Blood pressure measurements in mice undergoing high salt and L-NAME diet for induction of hypertension are displayed in Table 3.2. An approx. 10% increase from baseline (12wks of age)

to 2 weeks of hypertension (14wks of age) in systolic, MAP and diastolic pressure is observed. Between 2 and 6 weeks of hypertension (18wks of age) there is only a small (1%–3%) increase in blood pressure, which may indicate stabilisation or very slow further blood pressure increase.

Table 3.2: Blood Pressure data. *HT* stands for salt and L-NAME–induced hypertension.

Time point		**Baseline**		**2 weeks HT**		**6 weeks HT**	
Number of samples		3		3		3	
Metric		mean	SEM	mean	SEM	mean	SEM
Systolic	absolute value (mmHg)	126.98	10.42	138.24	13.69	139.91	11.10
	fold-change from baseline	1.00	0.00	1.09	0.03	1.10	0.00
MAP	absolute value (mmHg)	105.71	10.01	115.46	14.48	117.18	9.00
	fold-change from baseline	1.00	0.00	1.09	0.04	1.11	0.04
Diastolic	absolute value (mmHg)	95.53	9.87	104.55	14.89	106.34	8.12
	fold-change from baseline	1.00	0.00	1.09	0.05	1.12	0.06

3.2.1 Biaxial mechanical data

Gross appearance of vessels mounted on the mechanical testing device and vessel rings cut for unloaded thickness determination are shown in Fig. 3.2 for each group at 14 and 18 weeks.

Vessels from both perturbed groups display a larger calibre at loaded *in vivo* (group–specific MAP and vessel–specific $\lambda_z^{i.v.}$) and particularly at unloaded configurations when compared with the corresponding controls (compare 18wks ATAs and IAAs from each perturbed group); calibres of vessels from each group are similar at 14wks (Fig. 3.2(a)) and 18wks (Fig. 3.2(b)). Thickening of the vessel wall is also clearly seen in the rings cut from perturbed vessels, which also display a slightly larger inner diameter when unloaded (compare 18wks ATA rings from each group). Consistent with the previous observation, perturbed arteries also seem to display accumulations of fibrotic tissue on the outer surface, with the adventitia appearing less smooth and more opaque (compare in particular 14wks ATAs from perturbed *vs.* control groups); this tissue accumulation may be attributed to adventitial fibrosis, perivascular tissue deposition and (more likely) a combination of the two. Interestingly, note also that the 14wks ATA *Dis+HT* segment appears less stretched at the estimated *in vivo* loaded configuration than the corresponding *Dis* or *Ctrl* vessels, which suggests a lower *in vivo* axial stretch.

Accurate quantification of unloaded and loaded dimensions following mechanical data processing can be found in Table A.1 in Appendix A (absolute values) and Fig. 3.11, Fig. 3.12 in Sec. 3.2.1.4 (fold–changes from control).

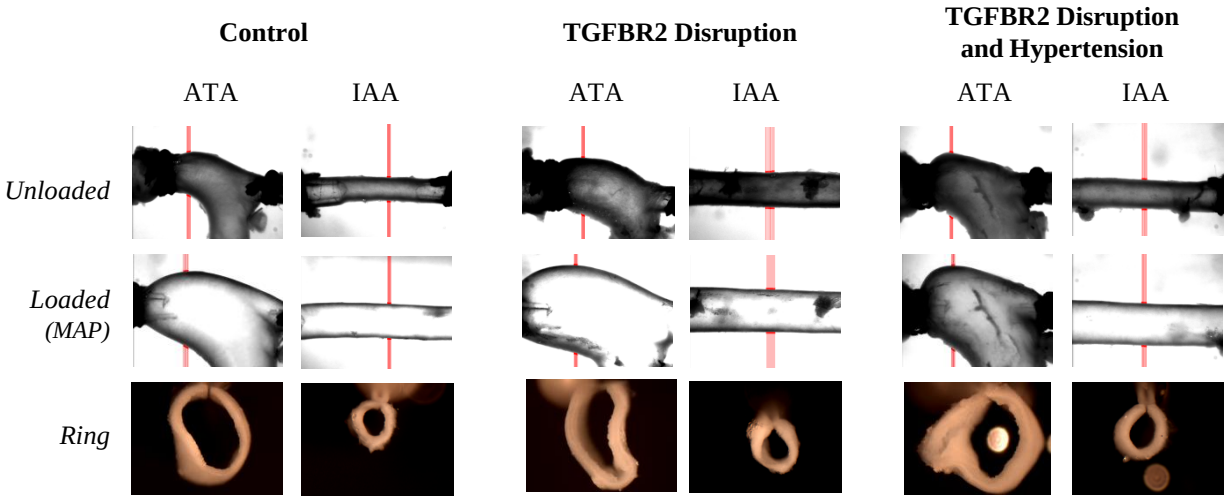

(a) Representative vessel segments at 14 weeks

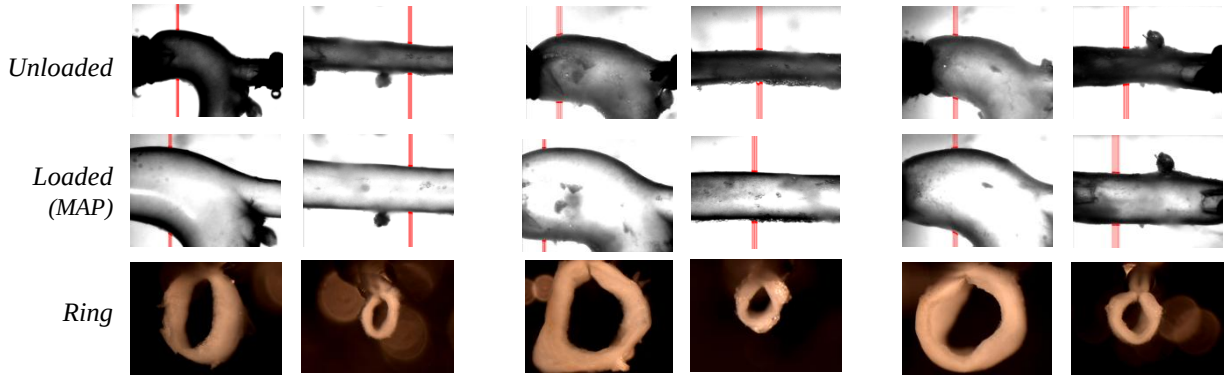

(b) Representative vessel segments at 18 weeks

Figure 3.2: **Biaxial mechanical testing source images.** Representative images showing vessel mounting on biaxial mechanical testing device and vessel ring for unloaded thickness measurement at 14 weeks (a) and 18 weeks (b).

3.2.1.1 Experimentally acquired mechanical data

In this section, comprehensive set of curves from biaxial pressure–inflation, axial force–stretch tests are plotted. Pressure–inflation behaviour is characterised by pressure–outer diameter (P–d_o) and axial force–pressure (F_z–P) curves directly acquired from biaxial testing, as well as by the processed curves circumferential Cauchy stress–stretch (σ_θ–λ_θ) and axial Cauchy stress–circumferential stretch (σ_z–λ_θ), as computed by Eq. (3.2) and Eq. (3.3). Similarly, axial force–stretching behaviour is characterised by unprocessed outer diameter–axial stretch (d_o–λ_z) and axial force–stretch (F_z–λ_z) curves, as well as by the continuum relations circumferential stretch–axial stretch (λ_θ–λ_z) and axial Cauchy stress–stretch (σ_z–λ_z) given by Eq. (3.2) and Eq. (3.3). For each of the previous relations, different groups are plotted against each other for each experimental group, allowing for the effect of different perturbation on arterial mechanical properties to be inferred ("group comparison"). Each set of 8 plots (P–d_o, F_z–P, σ_θ–λ_θ, σ_z–λ_θ, d_o–λ_z, F_z–λ_z, λ_θ–λ_z, σ_z–λ_z) for three time points is plotted for both ATA and IAA segments.

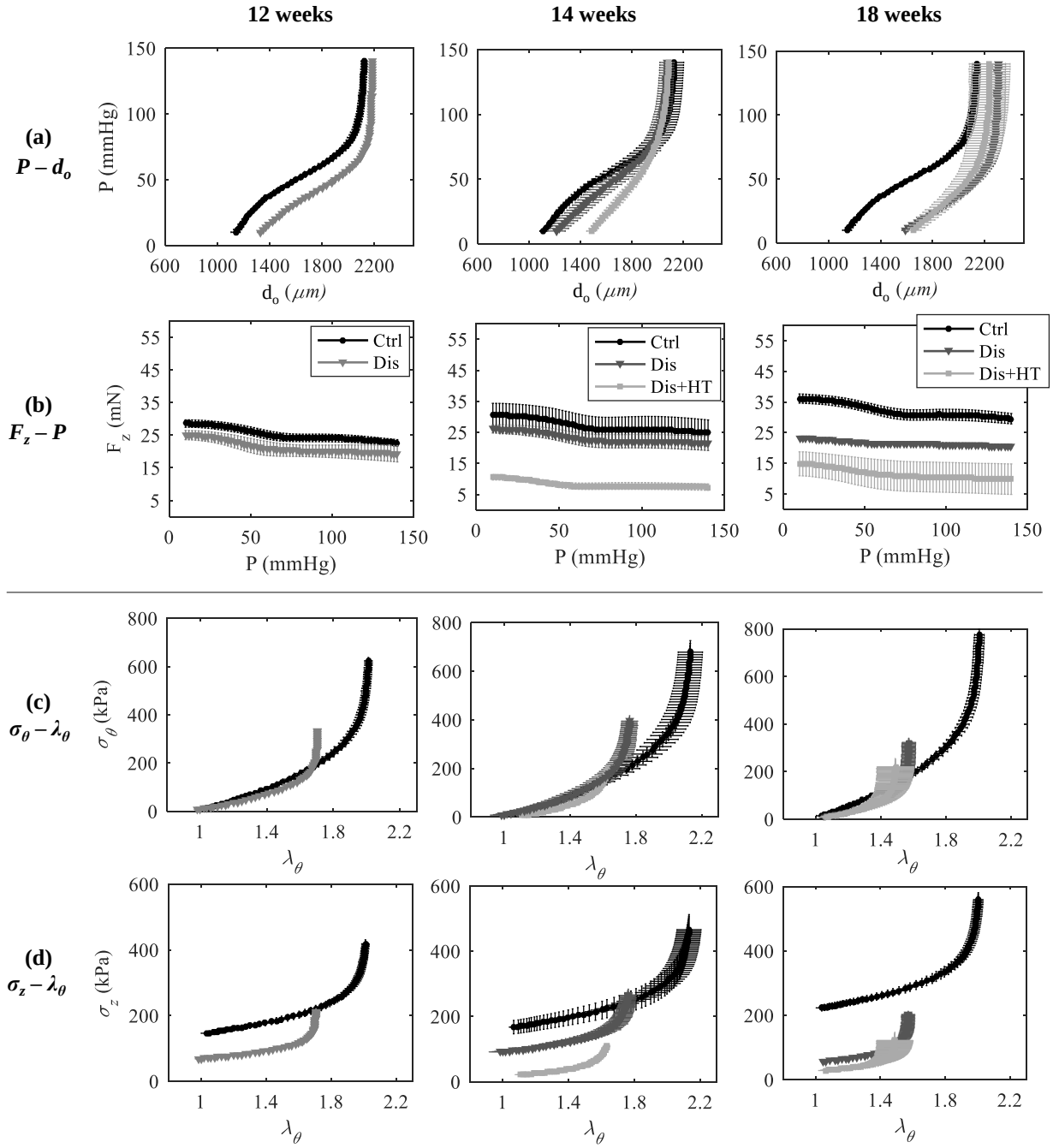

Figure 3.3: **Group comparison study for ATAs subject to pressure–inflation tests.** Load–deformation and stress–stretch curves from pressure–inflation tests. Means (dots) and SEMs (horizontal and vertical bars) are depicted for each curve. Pressure–inflation tests were performed at vessel–specific $\lambda_z^{i.v.}$.

Fig. 3.3 and Fig. 3.4 compare average load–deformation and stress–stretch curves for ATAs of different experimental groups at each time point. Fig. 3.3(a) shows a tendency towards larger outer diameters on the low pressure (P<80mmHg) range for arteries from perturbed groups, tendency which accentuates over time. Analogously, Fig. 3.4(b) shows that, for a given pressure, arteries subjected to further perturbations (i.e. *Ctrl vs. Dis vs. Dis+HT* groups) display decreased axial stretches (in particular *in vivo* stretches), trend which accentuates over time. These results make clear that perturbed arteries are larger (by increased calibre, thickening or both)

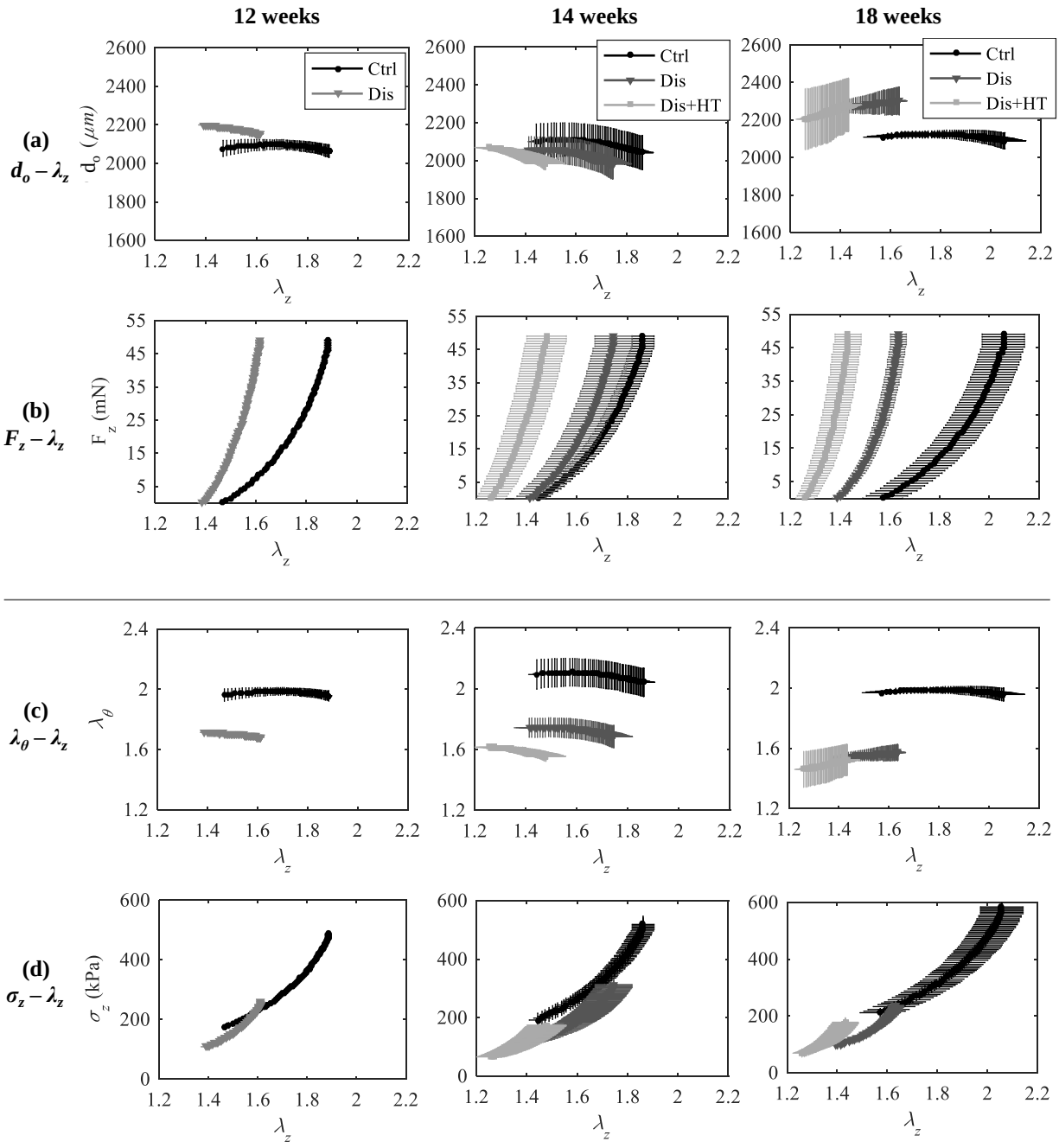

Figure 3.4: **Group comparison study for ATAs subject to axial force–stretching tests.** Load–deformation and stress–stretch curves from axial force–stretching tests of ATA. Means (dots) and SEMs (horizontal and vertical bars) are depicted for each curve. Axial force–stretching tests were performed at intraluminal P=100mmHg.

and less stretched axially at their *in vivo* configuration. Biaxial stress–stretch behaviour, σ_θ–λ_θ in Fig. 3.3(c) and σ_z–λ_z in Fig. 3.4(d), show increasingly reduced maximum stresses and stretches with increased perturbation in an almost step–wise fashion, i.e. maximum stress/stretch in *Dis+HT* group lower than in *Dis* group lower than in *Ctrl* group. Given that the same loads (intraluminal pressure and axial force) were applied to all vessels, these results may be explained by an increase in structural stiffness, possibly due to increased wall thickness (c.f. Sec. 3.2.1.4). Biaxial stretch plots λ_θ–λ_z, Fig. 3.4(c), show a trend towards lower ranges of axial stretch at

lower circumferential stretches for vessels subjected to further perturbations. This clear loss in extensibility is consistent for all time points. Fig. A.1 and Fig. A.2 in Appendix A display a group comparison of load–deformation and stress–stretch curves at different time points for the IAA segment.

Accurate determination of *in vivo* stretch The axial stretch at the *in vivo* configuration $\lambda_{z,est}^{i.v.}$ was initially estimated before biaxial testing by performing cycles of pressurization at constant stretch and determining the value of stretch at which the F_z–P curve was approx. flat, Sec. 3.1.4.2. A more accurate determination of this quantity was based on the results of biaxial testing, by computing the intersection point of F_z–λ_z curves at different pressures. Fig. 3.5 shows the graphical calculation of the *in vivo* axial stretch after biaxial testing for a representative sample (12wks IAA in the *Ctrl* group). $\lambda_z^{i.v.}$ corresponds to the intersection of axial force–stretch curves obtained from axial force–stretching tests at 60, 100 and 140mmHg. In this sample, the value of the axial stretch computed after testing, $\lambda_z^{i.v.} = 1.618$, was close but larger than the initially estimated value of $\lambda_{z,est}^{i.v.} = 1.53$. This was a consistent trend in most vessels tested, with $\lambda_z^{i.v.}$ being 3.94±0.32% and 5.44±0.52% larger than $\lambda_{z,est}^{i.v.}$ in Ctrl ATAs and IAAs, resp.

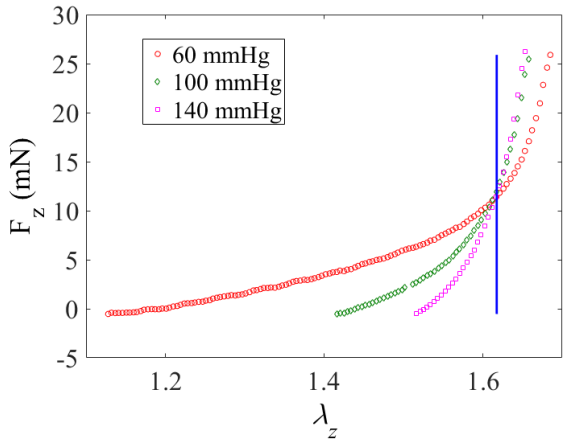

Figure 3.5: **Accurate determination of *in vivo* axial stretch.** $\lambda_z^{i.v.}$ in blue corresponds to the intersection of axial force–stretch curves at three different pressures.

3.2.1.2 Fit to 4-Fibre Family Constitutive Model

The experimental data from biaxial pressure–inflation, axial force–stretching tests were fit to the microstructurally–motivated four–fibre family constitutive model and then linearised according to the procedure described in Sec. 3.1.4.3. In this section, quality of fit is illustrated for a representative data set (12wks *Ctrl* IAA) by plotting experimentally–acquired load–deformation and stress–stretch curves against those predicted theoretically by fitting the SEDF to experimental data. In addition, the linearisation of the stress–strain response for the same vessel is shown.

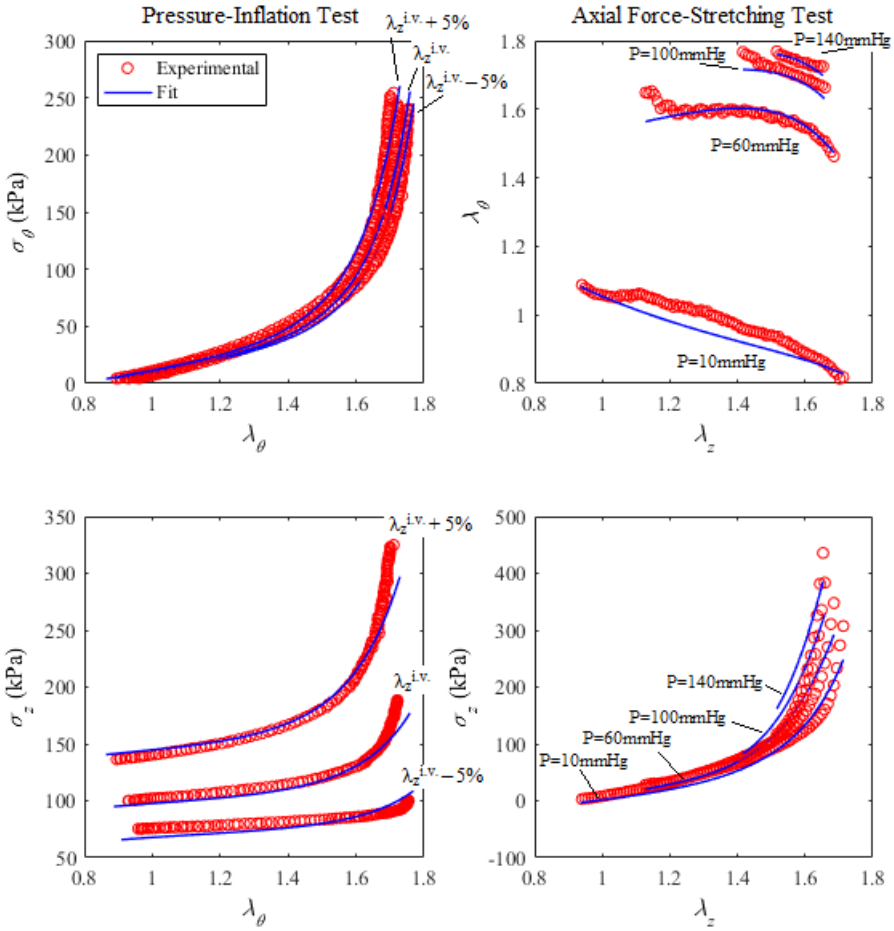

Figure 3.6: **Representative fit to 4-fibre family constitutive model.** Predicted (blue curves) *vs.* experimental (red circles) average stress–stretch responses. Pressure–inflation tests (*left*) were run at fixed $\lambda_z^{i.v.}$,$\lambda_z^{i.v.}$ ±5% stretch, while axial force–stretching (*right*) were run at fixed P=10, 60, 100, 140mmHg.

Representative fit Fig. 3.6 display the pressure–inflation (*left*) and axial force–stretch (*right*) stress–strain curves for both experimentally–acquired ("Experimental") data and those generated via the SEDF in Eq. (3.4) with best–fit parameter values ("Fit"). Note that all three pressure–inflation curves together with all four axial force–stretch curves were jointly used to compute best fit parameter values by nonlinear least squares minimization of the error function, Eq. (3.8). A good match between experimentally–acquired and theoretically–computed data can be seen in σ_θ–λ_θ, σ_z–λ_θ and λ_θ–λ_z plots; however, a slightly worse fit can be seen in the σ_z–λ_z plot, with theoretically–generated curves diverging significantly from the experimental data at larger pressure values (top two curves, P=100 and 140mmHg). Worse theoretical predictions for the σ_z–λ_z curves were consistently observed after data fitting.

By means of Eq. (3.3), theoretically computed average biaxial stresses could be converted into global loads (i.e., pressure and axial force). Fig. 3.7 shows a comparison between experimental and theoretical loads–deformations curves. Similarly to what was observed in the stress–stretch

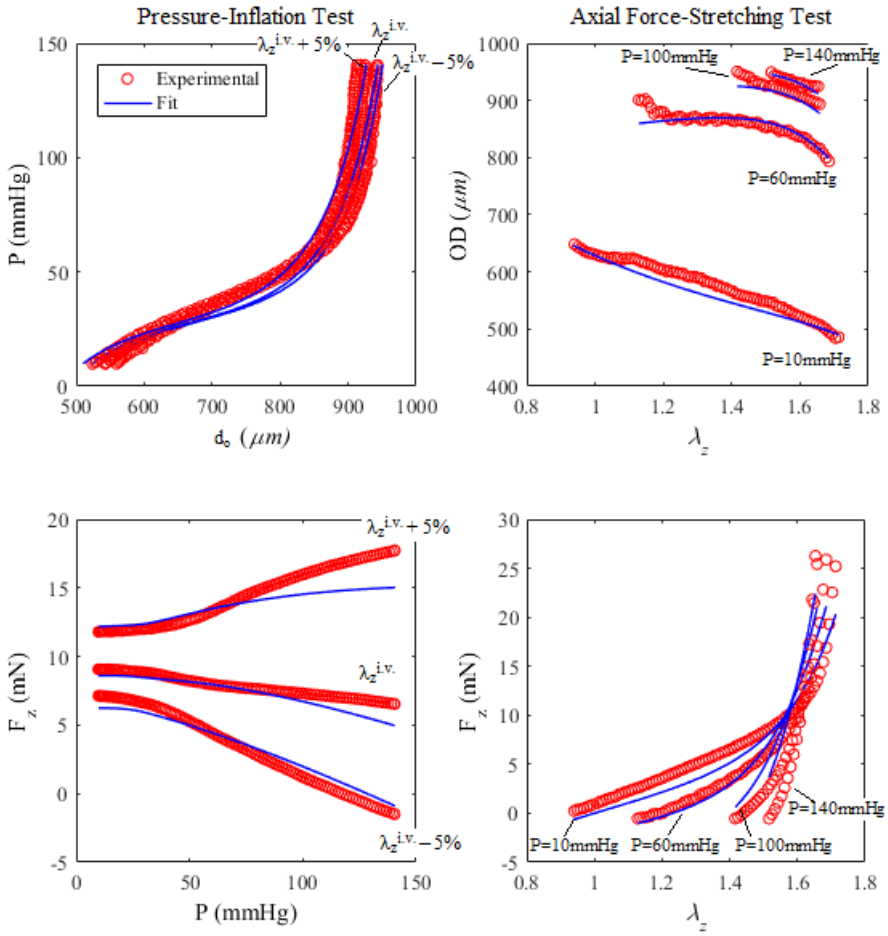

Figure 3.7: **Representative fit to 4-fibre family constitutive model.** Predicted (blue curves) *vs.* experimental (red circles) loads–deformations responses. Pressure–inflation tests (*left*) were run at fixed $\lambda_z^{i.v.}$,$\lambda_z^{i.v.} \pm 5\%$ stretch, while axial force–stretching (*right*) were run at fixed P=10, 60, 100, 140mmHg.

plots, the best–fit constitutive model allowed for reasonably good fits for the P–d$_o$, F$_z$–P and d$_o$–λ_z curves. Divergences between experimental data and theoretical predictions can be seen in the low pressure ranges of the P–d$_o$ curves and at the high pressure regions of the F$_z$–P curves with higher stretches. Theoretical predictions are more distant from experimental data for the F$_z$–λ_z case, which is particularly clear for axial force–stretch curves at higher pressures. Interestingly, the abscissa of the theoretically–predicted intersect between these curves, i.e. the theoretically–predicted *in vivo* stretch, is smaller than the experimentally–determined $\lambda_z^{i.v.}$, and thus closer to the initially estimated $\lambda_{z,est}^{i.v.}$. The previously noted divergences between experimental and theoretical curves were present to some extent in most of the fittings performed, having resulted in small yet significant RMSE values of around 10% (12.7% in this example).

Linearisation of the stress–strain behaviour around the *in vivo* configuration The microstructurally–motivated SEDF with best–fit parameters was used to generate a pressure–inflation curve at $\lambda_z^{i.v.}$, which was linearised around group–specific MAPs (see Table 3.2). Fig. 3.8

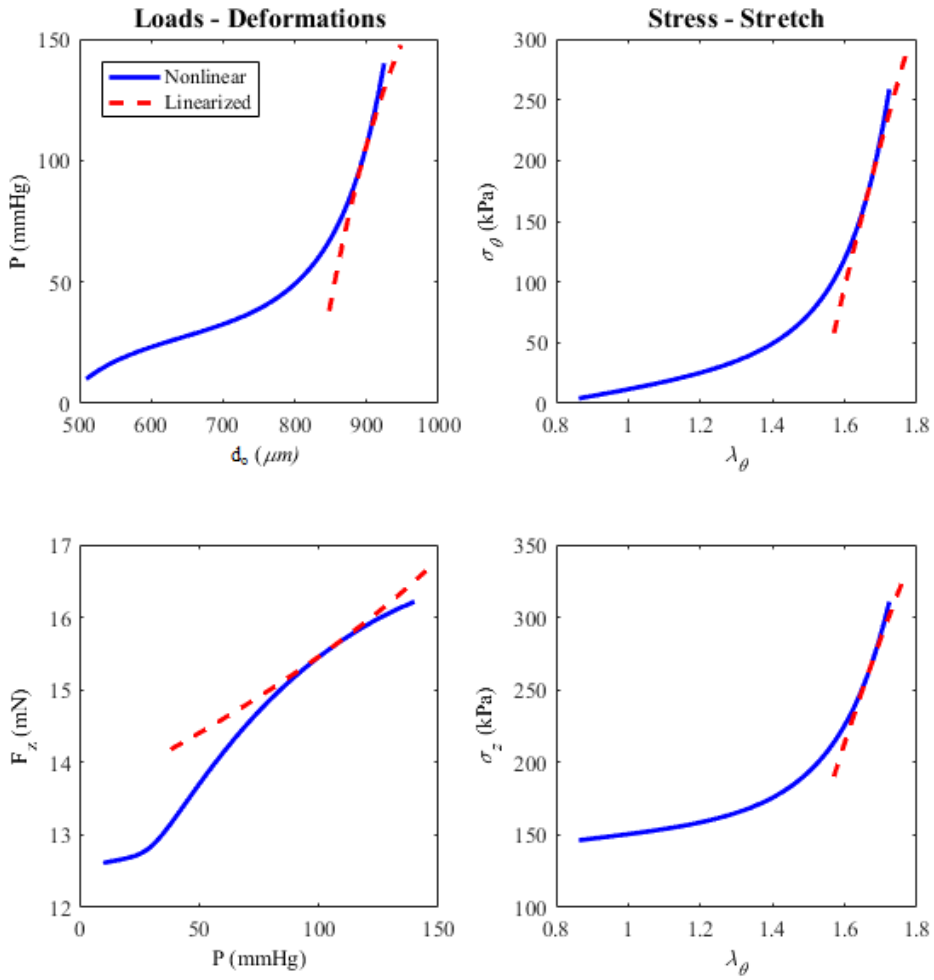

Figure 3.8: **Linearisation of stress–stretch response at *in vivo* configuration.** Linearisation (dashed red curve) was performed around MAP and at $\lambda_z^{i.v.}$ for the simulated loads–deformations (*left*) and stress–stretch (*right*) responses to pressure–inflation test using best–fit parameters for the SEDF.

shows loads–deformations (*left*) and stress–stretch (*right*) relations from such a theoretically–simulated pressure–inflation test, as well as its linearisation around *in vivo* conditions. The linearisation is locally tangent to the non–linear relation at the *in vivo* configuration, and then slowly diverges as loads are increased or decreased; note that the computed linearisation is still close to the non–linear curve for stresses up to 40–70kPa above and 20–30kPa below.

3.2.1.3 Representative Stored Elastic Energy Isocontours

After fitting SEDF parameter values to the biaxial mechanical data, the stored elastic energy Ψ was computed as a function of circumferential and axial stretch pairs. $\Psi(\lambda_\theta, \lambda_z)$ isocontours were then plotted, allowing for a graphical examination of the dependence of stored elastic energy on biaxial stretching.

Fig. 3.9 shows $\Psi(\lambda_\theta, \lambda_z)$ isocontours for representative ATA segments of each experimental group at 14 and 18 weeks (black circles indicating *in vivo* properties). As expected, ATAs from

the *Ctrl* group, Fig. 3.9(a), display very small variation over time, with their *in vivo* stored energy being very similar at 14 and 18 weeks. The introduction of TGFBR2 disruption, Fig. 3.9(b), clearly results in more asymmetric energy isocontours with respect to the diagonal $\lambda_\theta = \lambda_z$, which is correlated to an increased degree of anisotropy. A significant decrease in *in vivo* stored energy (black circles) is also present in this group, which is further aggravated over time ($\Psi^{i.v.}$ lies in the $[100, 250]$kPa region for *Ctrl* ATAs, while for the *Dis* it is situated on the 60kPa iscontour at 14wks and on the 40kPa isocontour at 18wks). Moreover, in this group the tendency towards particularly dense isocontours in the λ_θ direction becomes clear at 18wks, which points towards a significant loss in vessel distensibility.

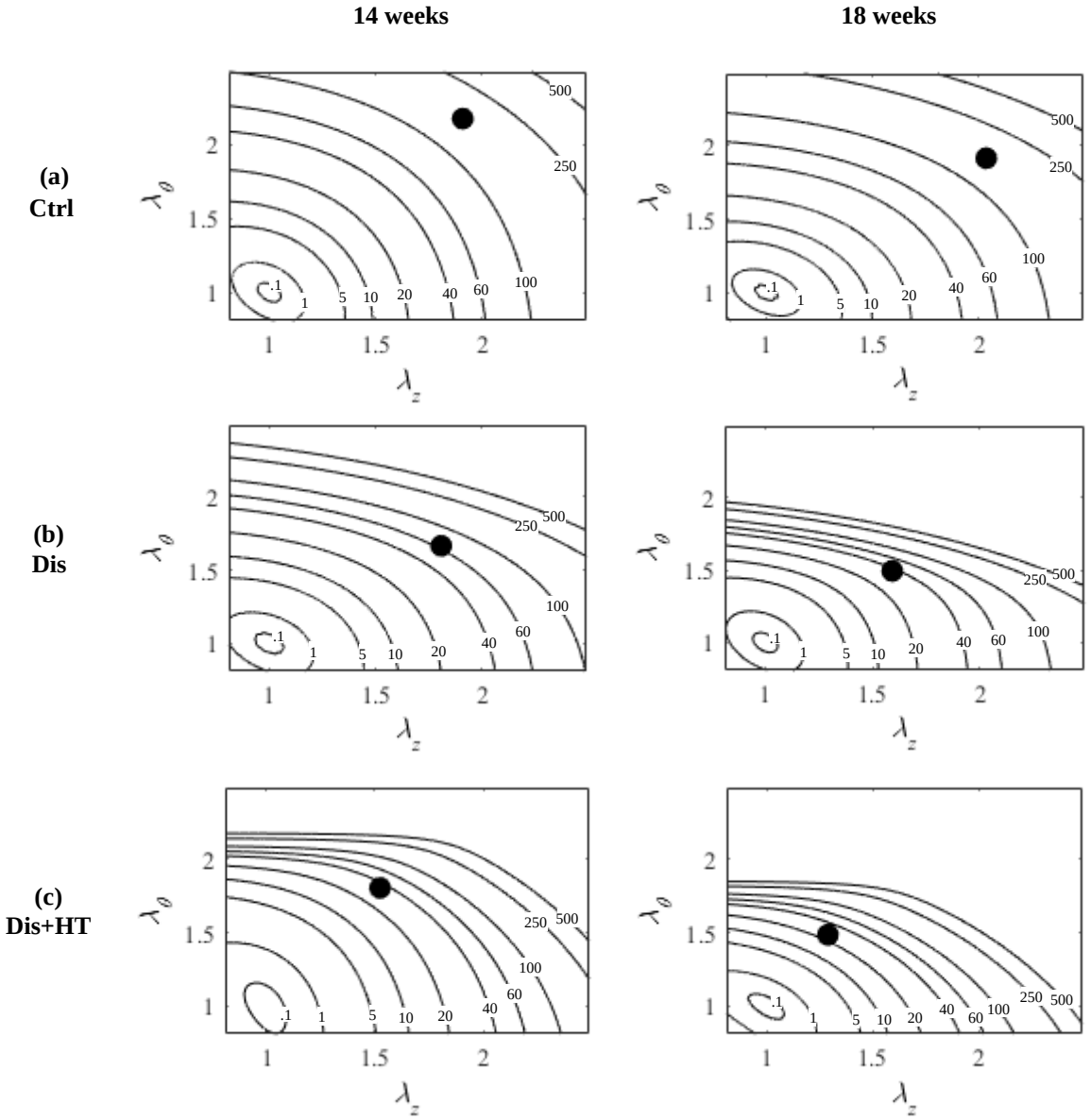

Figure 3.9: **Representative stored elastic energy isocontours in ATAs.** Energy isocontours for ATA segments representative of each experimental group at 14 and 18 wks. Isocontours have associated energies {0.1, 1, 5, 10, 20, 40, 60, 100, 250, 500}kPa (or J/m^3) in all plots. Black circles denote *in vivo* conditions, i.e. group–specific MAP and vessel–specific $\lambda_z^{i.v.}$.

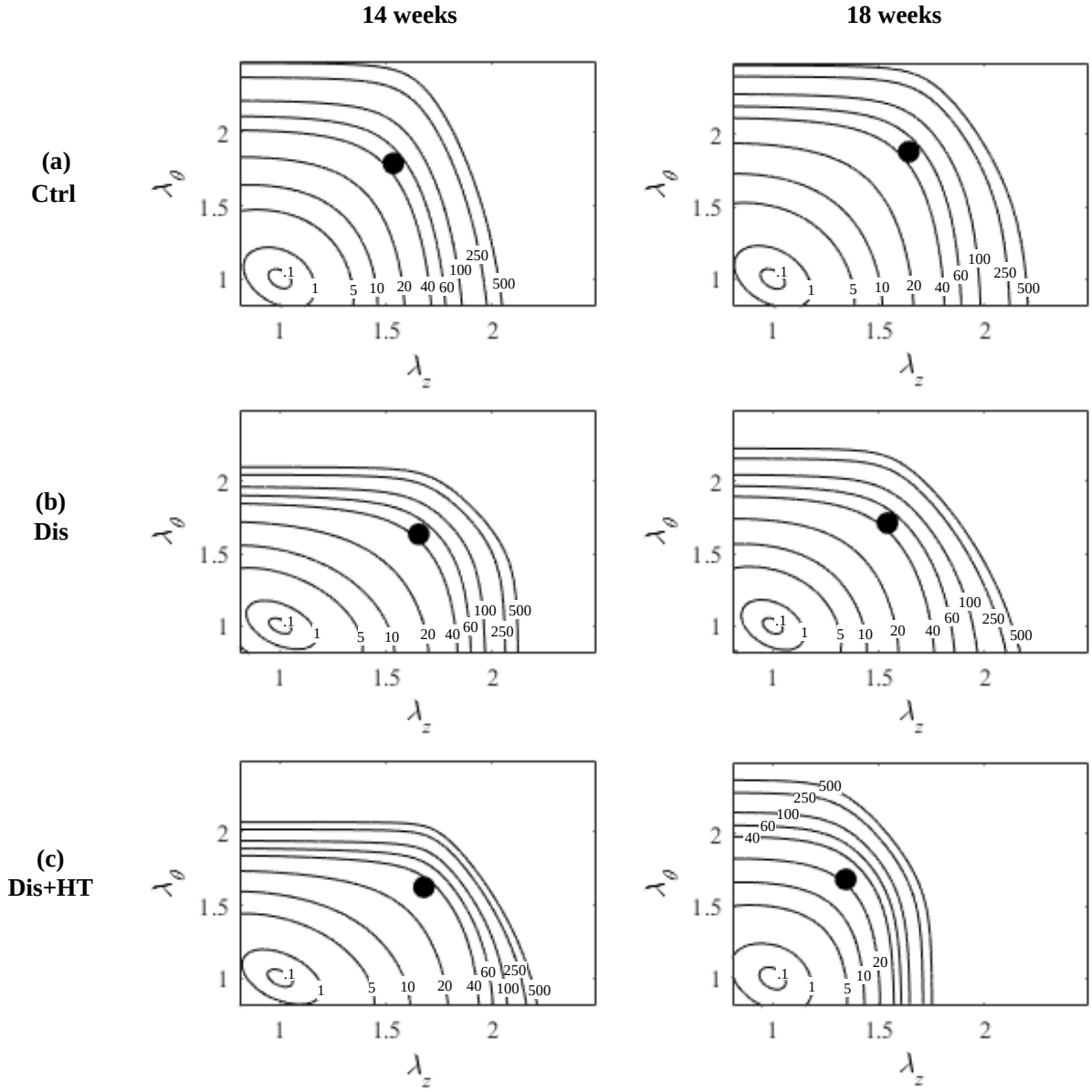

Figure 3.10: **Representative stored elastic energy isocontours in IAAs.** Energy isocontours for IAA segments representative of each experimental group at 14 and 18 wks. Isocontours have associated energies {0.1, 1, 5, 10, 20, 40, 60, 100, 250, 500}kPa (or J/m^3) in all plots. Black circles denote *in vivo* conditions, i.e. group–specific MAP and vessel–specific $\lambda_z^{i.v.}$.

Inducing hypertension in addition to disrupting TGF-β signalling through TGFBR2, Fig. 3.9(c), also leads to more dense energy isocontours (i.e., higher nonlinearity in the constitutive response) and reduced *in vivo* stored energy. Decreases in distensibility (i.e., increases in $\partial\Psi/\partial\lambda_\theta$) also take place in the *Dis+HT* group but are larger than for the representative ATAs in the *Dis* group at both 14 and 18 weeks. In addition, decreases in extensibility (i.e., increases in $\partial\Psi/\partial\lambda_z$) become more significant especially at 18wks; interestingly, the significant reduction in both extensibility and distensibility result in more isotropic behaviour than in the *Dis* group. Note also that the reduction in *in vivo* stored energy is greater: ca. 40kPa at 14 weeks, and on the region between 20 and 40kPa at 18wks.

Analogously, Fig. 3.10 shows the stored energy isocontours computed for representative IAA segments of each experimental group at 14 and 18 weeks. IAA Ψ maps are quite distinct from those characterising the ATA segments for the *Ctrl* group, Fig. 3.10(a). This observation points to very different constitutive responses of each segment, with the ATA being more distensible and extensible than the IAA; this is unsurprising given the significant axial extension of the ATA during cardiac cycle (the aortic root moves with the heart, which displays vertical motion), while the IAA is tethered axially by the renal arteries (Humphrey, 2002).

Challenging IAA segments with disruption of TGF-β signalling, Fig. 3.10(b), leads to a clear reduction in distensibility at 14wks but almost no change in axial properties. Interestingly, there seems to be a small recovery in distensibility at 18wks. Note also that the *in vivo* stored energy $\Psi^{i.v.}$ (black circles) remains unchanged from *Ctrl*. Inducing hypertension in animals with TGFBR2 knocked–out leads to more significant changes, Fig. 3.10(c). Energy isocontours at 14wks are quite similar to those in the *Dis* group, with a significant reduction in distensibility. However, note that the *in vivo* stored energy is now reduced from the $[40, 60]$kPa to the $[20, 40]$kPa range, which is further reduced to approx. 20kPa at 18wks. At this later time point there can also be seen a recovery in distensibility, however coinciding with a very large reduction in extensibility, which renders the vessel significantly anisotropic.

3.2.1.4 Summary Mechanical Metrics

The arterial wall biomechanical state following perturbation to TGF-β signalling and induced hypertension was assessed in each observation group. In addition to the unloaded dimensions, several geometrical and mechanical metrics were computed at the "*in vivo* configuration" obtained by loading the vessel with group–specific MAP (baseline for *Ctrl* and *Dis*, 2 and 6 weeks of hypertension for *Dis+HT*) and stretching it to vessel–specific $\lambda_z^{i.v.}$:

Unloaded dimensions: outer diameter (D_o), wall thickness (H), inner diameter (D_i), inner radius (R_i), thickness to inner radius ratio ($H : R_i$), *in vitro* axial length (L_z)

***In vivo* loaded dimensions (at MAP and $\lambda_z^{i.v.}$):** outer diameter ($d_o^{i.v.}$), wall thickness ($h^{i.v.}$), inner diameter ($d_i^{i.v.}$), inner radius ($r_i^{i.v.}$), thickness to inner radius ratio ($h^{i.v.} : r_i^{i.v.}$), circumferential stretch ($\lambda_\theta^{i.v.}$), *in vivo* axial stretch ($\lambda_z^{i.v.}$)

***In vivo* Cauchy stresses (at MAP and $\lambda_z^{i.v.}$):** circumferential ($\sigma_\theta^{i.v.}$), axial ($\sigma_z^{i.v.}$)

***In vivo* linearised stiffnesses (at MAP and $\lambda_z^{i.v.}$):** circumferential ($\mathscr{C}_{\theta\theta\theta\theta}^{i.v.}$), axial ($\mathscr{C}_{zzzz}^{i.v.}$)

Energy metrics: Elastic energy stored *in vivo* ($\Psi^{i.v.}$), energy dissipation ratio (EDR)

Absolute values for the observation group averages of the previous quantities can be found in Appendix A Table A.1. So as to make clear how perturbed groups diverge from vascular homoeostasis over time, some of the previous quantities in each perturbed group at 12, 14 and 18 weeks were normalised to the corresponding averages for the 12 weeks group, at which point vascular mechanical maturity was fully attained. Fold–changes were then plotted over time for each segment (ATA, IAA) and perturbed group (*Dis*, *Dis+HT*).

Fig. 3.11 shows the temporal variation of some unloaded dimensions as fold–changes of the *Dis* and *Dis+HT* groups from baseline. Both segments display an increase in loaded inner radius

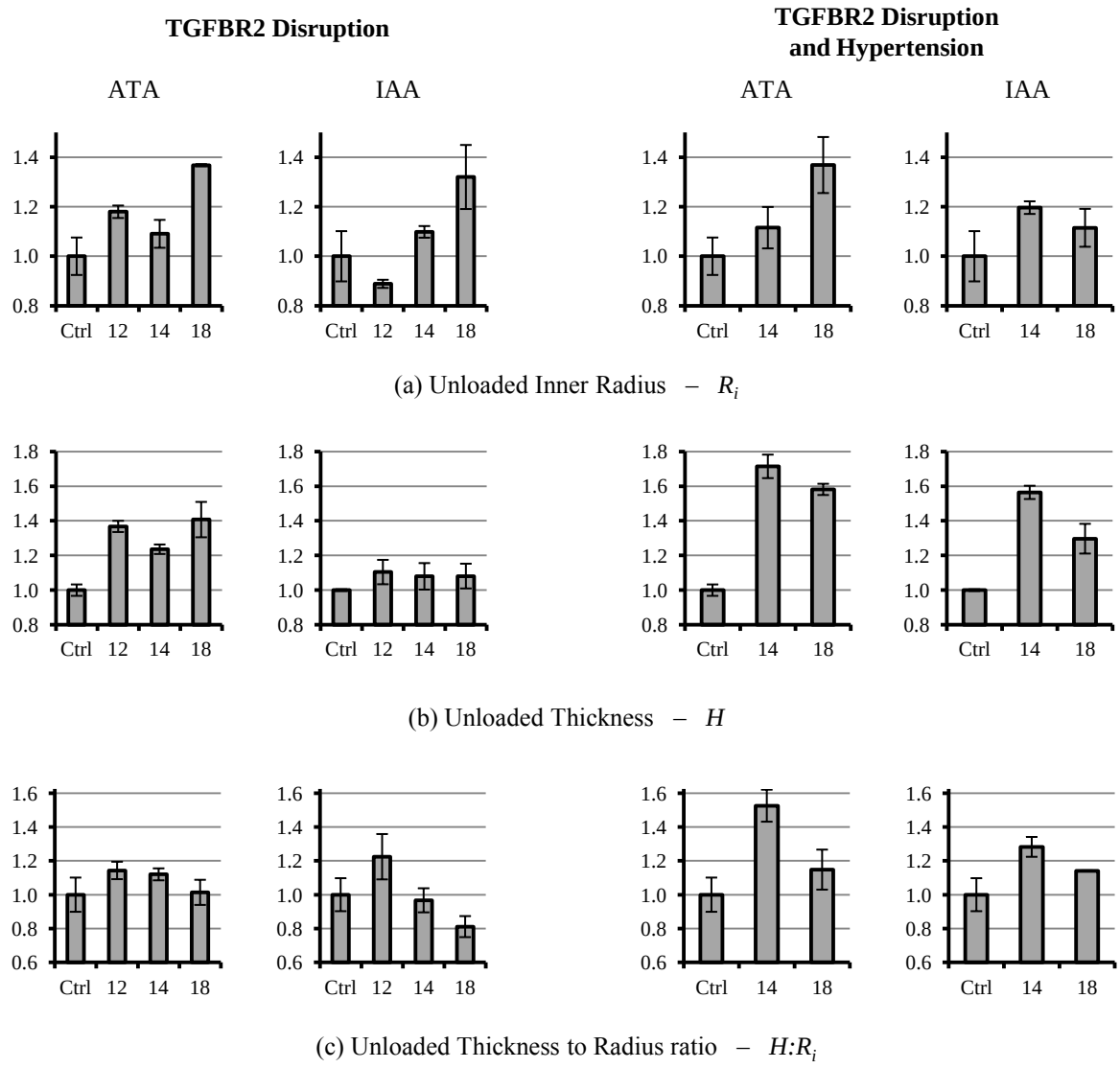

Figure 3.11: **Summary metrics I — Unloaded dimensions.** Horizontal axes refer to mice age in weeks of perturbed groups *vs.* control, while vertical axes refer to fold–changes from baseline (12wks *Ctrl*).

over time in both perturbed groups, Fig. 3.11(a), with the largest diameters (around 1.4 times baseline) present at the later time point of 18 weeks (with the exception of *Dis+HT* IAA). Note that the observed arterial dilation was rather similar in ATA segments of either perturbed group (compare 14 and 18 weeks time points only), but induction of hypertension seems to have resulted in a significant reduction of arterial calibre for IAAs at 18 weeks.

Thickness in the unloaded configuration was also increased by the applied perturbations, Fig. 3.11(b). TGFBR2 disruption promotes significant thickening of the arterial wall of ATAs, which reaches approx. 1.4 times baseline; the increase in IAA thickness is much smaller, approx. 1.10 times baseline, and stabilises at 12wks. Inducing hypertension in addition to disruption of TGF-β signalling promotes a much more extensive thickening of the arterial wall (1.7 and 1.6 times baseline for ATA and IAA at 14wks, resp.), which reduces from 14 to 18 weeks, thus pointing to an initial overshoot in wall thickness followed by a slow reduction (possibly towards a new homoeostatic state). Consistent with the previous reasoning, the ratio of unloaded thickness to unloaded inner radius, Fig. 3.11(c), generally displays a maximum value of 1.2—1.5 times baseline at 12–14 weeks, followed by a decrease at 18wks.

Fig. 3.12 shows three important geometric measures characterising arteries loaded at group–specific MAP and vessel–specific *in vivo* axial stretch (the "*in vivo* configuration"). Increases in loaded inner radius following perturbation, Fig. 3.12(a), are much more modest than for unloaded inner radius for both segments and groups, which reach only 1.1–1.15 times baseline at 18wks. Note also the small decrease (0.95–0.98 times baseline) in loaded inner radius for both ATA and IAA in the *Dis* group and ATA in the *Dis+HT* group at 14wks.

In contrast, loaded thickness, Fig. 3.12(b), increases more than the corresponding unloaded quantities (Fig. 3.11(b)), with the increases being particularly significant in the ATAs of hypertensive mice (2.7 *vs.* 1.6 times baseline at 18 weeks). In any case, temporal evolution of this quantity is similar to the corresponding unloaded quantity: arteries in the *Dis* group display increased loaded thickness over time, with stabilisation (IAA) or further increase (ATA) from 14 to 18 weeks; arteries in the *Dis+HT* group display a large increase in thickness at 14 weeks followed by a small decrease or stabilisation at 18 weeks. For both *Dis* and *Dis+HT* groups, the changes are more significant in ATAs (up to 2 and 2.8 times baseline, resp.) than in IAAs (up to 1.15 and 1.7 times baseline, resp.).

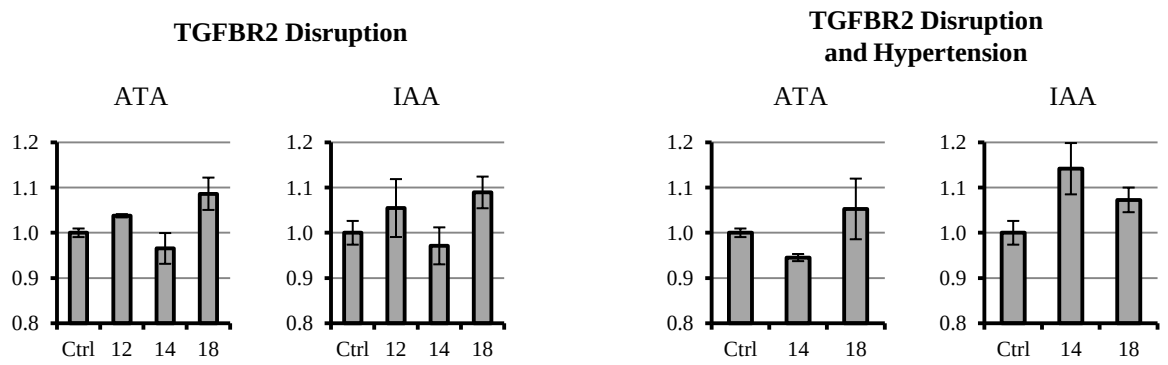

(a) *In vivo* Loaded Inner Radius (at MAP and $\lambda_z^{i.v.}$) – $r_i^{i.v.}$

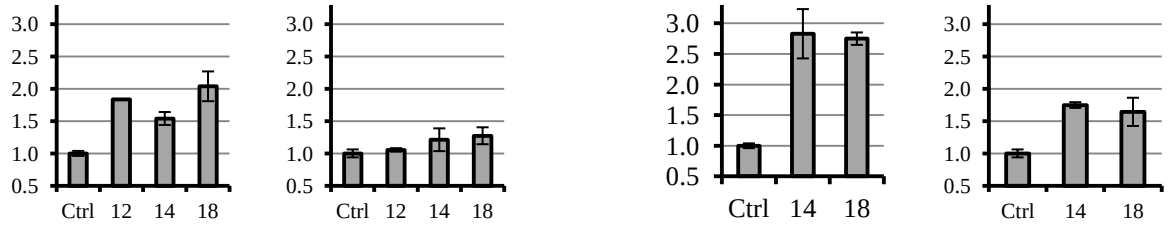

(b) *In vivo* Loaded Thickness (at MAP and $\lambda_z^{i.v.}$) – $h^{i.v.}$

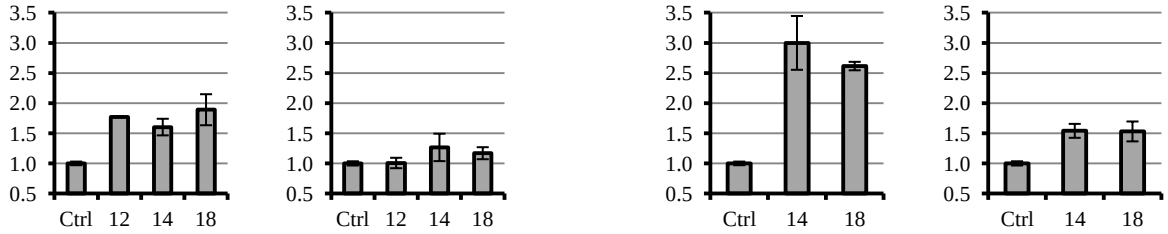

(c) *In vivo* Loaded Thickness to Radius ratio (at MAP and $\lambda_z^{i.v.}$) – $h^{i.v.}:r_i^{i.v.}$

Figure 3.12: **Summary metrics II — Loaded dimensions.** Horizontal axes refer to mice age in weeks of perturbed groups *vs.* control, while vertical axes refer to fold–changes from baseline (12wks *Ctrl*).

The fact that loaded thickness increases more than unloaded thickness may partially explain the observation that loaded inner radius increases less than unloaded inner radius in perturbed groups. Supporting this reasoning, Fig. 3.12(c) shows that increases in loaded thickness to loaded inner diameter ratios are much larger than the corresponding unloaded quantities (Fig. 3.11(c)), with ATAs in the *Dis+HT* group at 14 weeks displaying 1.5 (unloaded) *vs.* 3 (loaded) times baseline, for example. Therefore, the results suggest that a very large increase in thickness which persists in loaded configurations results in a small increase (and in some cases a small decrease) of inner radius with respect to baseline. Note also that introducing hypertension leads to larger increases in $h^{i.v.} : r_i^{i.v.}$ for both ATA (2 *vs.* 2.6 times baseline at 18 weeks) and IAA (1.2 *vs.* 1.6 times baseline) segments.

Fig. 3.13 displays biaxial stretch ratios for the perturbed groups over time. "*In vivo*" cir-

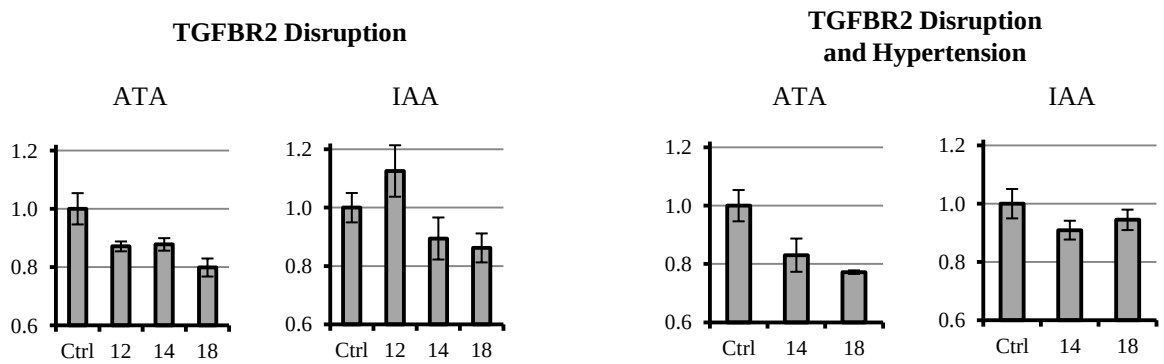

(a) *In vivo* Circumferential Stretch Ratio (at MAP and $\lambda_z^{i.v.}$) – $\lambda_\theta^{i.v.}$

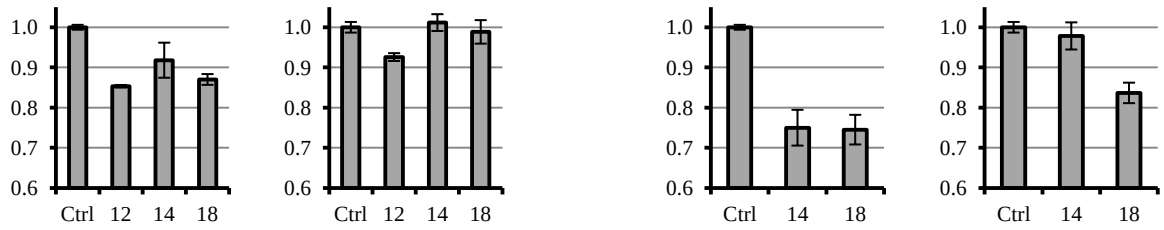

(b) *In vivo* Axial Stretch Ratio – $\lambda_z^{i.v.}$

Figure 3.13: **Summary metrics III — Biaxial stretch ratios.** Horizontal axes refer to mice age in weeks of perturbed groups *vs.* control, while vertical axes refer to fold–changes from baseline (12wks *Ctrl*).

cumferential stretches are computed mid–wall by Eq. (3.2) (*left*) at the "*in vivo* configuration", while *in vivo* axial stretches are computed from the intersection of F_z–λ_z curves, as explained in Sec. 3.1.4.2. Fig. 3.13(a) shows a tendency towards reduction in circumferential stretches following perturbation to TGF-β signalling, and that a further induction of hypertension promotes a small further decrease in $\lambda_\theta^{i.v.}$ in ATAs but a small increase in IAAs. Note that in both disrupted groups the ATA is more affected than the IAA. A reduction in the value of *in vivo* axial stretch following arterial perturbation is also observed, Fig. 3.13(b). Induction of hypertension promotes a further decrease in this quantity: $\lambda_z^{i.v.}$ for 18wks *Dis* ATAs(IAAs) is approx. 0.88 (0.99), while for *Dis+HT* ATAs(IAAs) at the same time it is 0.75 (0.84).

Fig. 3.14 shows average biaxial Cauchy stresses for the perturbed groups with respect to the *Ctrl* baseline. A trend towards decreasing stresses over time, in particular for the ATA segment, which is worsened by induction of hypertension is present in both circumferential (Fig. 3.14(a)) and axial (Fig. 3.14(b)) stresses. A small reduction in the biaxial stresses experienced by 18wks IAAs in the *Dis* group of around 0.85 ($\sigma_\theta^{i.v.}$) and 0.72 ($\sigma_z^{i.v.}$) is intensified in the *Dis+HT* group to 0.74 and 0.52, resp. In comparison, 18wks ATAs see their biaxial stresses much more reduced to 0.56 ($\sigma_\theta^{i.v.}$) and 0.43 ($\sigma_z^{i.v.}$) times baseline, and further reduced by the application of hypertension to 0.4 and 0.3, resp. Taking into account the previous results, reductions in biaxial stresses are not

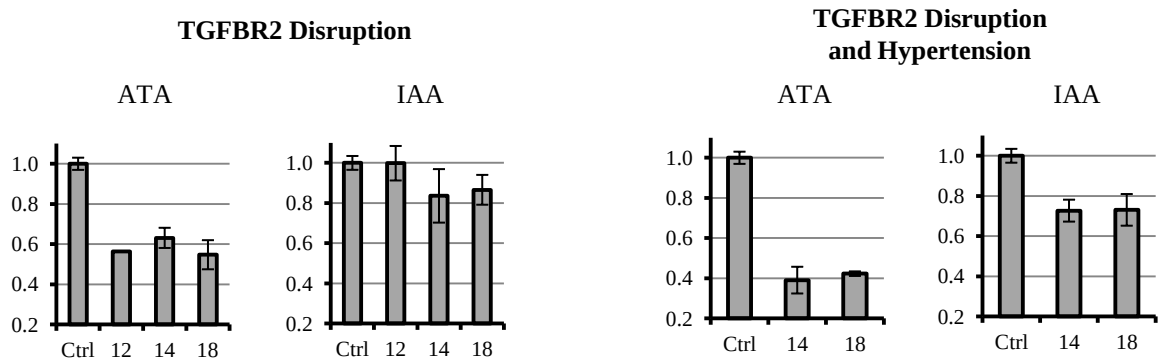

(a) *In vivo* Circumferential Cauchy Stress (at MAP and $\lambda_z^{\text{i.v.}}$) – $\sigma_\theta^{i.v.}$

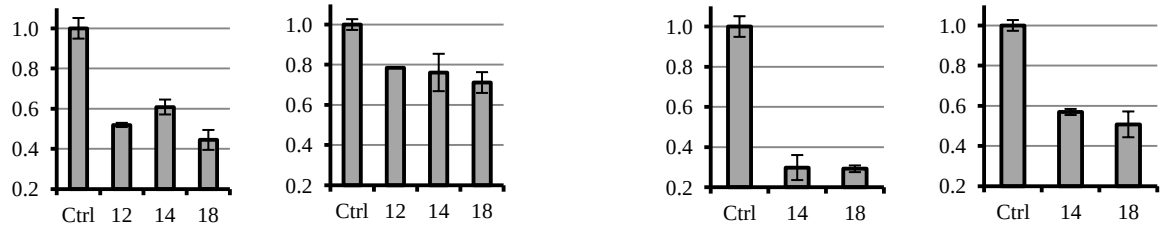

(b) *In vivo* Axial Cauchy Stress (at MAP and $\lambda_z^{\text{i.v.}}$) – $\sigma_z^{i.v.}$

Figure 3.14: **Summary metrics IV — Biaxial Cauchy stresses.** Horizontal axes refer to mice age (wks) of perturbed groups *vs.* control, while vertical axes refer to fold–changes from baseline (12wks *Ctrl*).

surprising. Consider that average circumferential and axial Cauchy stresses are proportional to r_i/h and $r_i^2/(h(2r_i^2+h))$, resp. , Eq. (3.3). The significantly increased $h^{i.v.}:r_i^{i.v.}$ ratio observed in Fig. 3.12, in particular for the *Dis+HT* ATAs, will lead to low circumferential stresses and even lower axial stresses (at the same intraluminal pressure and axial force), which is particularly true for *Dis+HT* ATAs, as expected.

The variations in (material) stiffness linearised around the *in vivo* configuration (i.e. at MAP and $\lambda_z^{i.v.}$) can be seen in Fig. 3.15. Fig. 3.15(a) shows some fluctuation of the circumferential linearised stiffness over time for the *Dis* group, which still returns to baseline at 18wks for both segments. Inducing hypertension in addition to TGFBR2 disruption results in a significant reduction in this quantity, which reaches 0.6 times baseline at 14 weeks for the ATA segment and approx. 0.8 times baseline for IAAs. In contrast, a large and progressive reduction in axial linearised stiffness can be seen in TGFBR2 disruption–only mice, Fig. 3.15(b), with the lowest value of 0.53 and 0.72 being achieved at 18wks for the ATA and IAA, resp. Once again, inducing hypertension leads to further reductions in $\mathscr{C}_{zzzz}$, which reduces suddenly to around 0.4 times baseline at 14wks for the ATA segment, and progressively reduces in IAAs to 0.68 at 18wks. Note that the decrease in both circumferential and axial material stiffness reported for the *Dis+HT* group takes

place in parallel with a seeming increase in structural stiffness, as judged by the steepening and leftward shift of the P–d_o (circumferential) and F_z–λ_z (axial) curves for both ATA (Fig. 3.3(a), Fig. 3.4(b)) and IAA (Fig. A.1(a), Fig. A.2(b)) at 18 weeks.

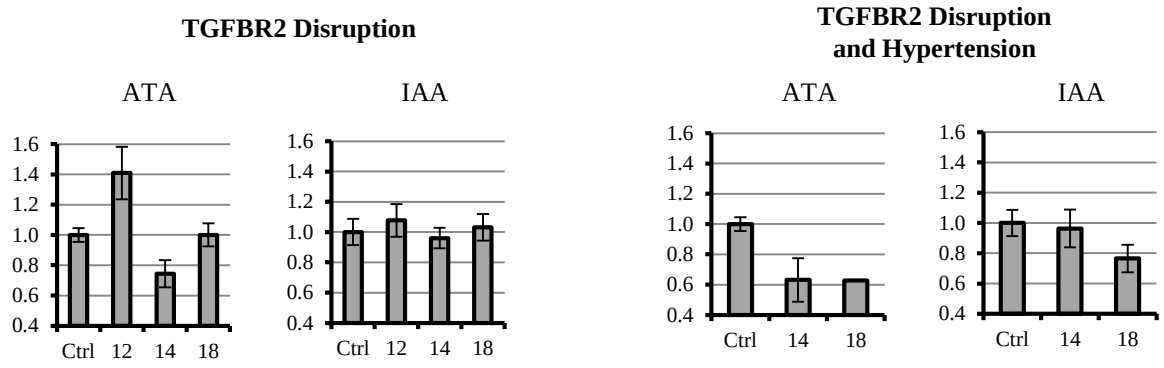

(a) *In vivo* Circumferential Linearised Stiffness (at MAP and $\lambda_z^{i.v.}$) – $\mathcal{C}_{\theta\theta\theta\theta}{}^{i.v.}$

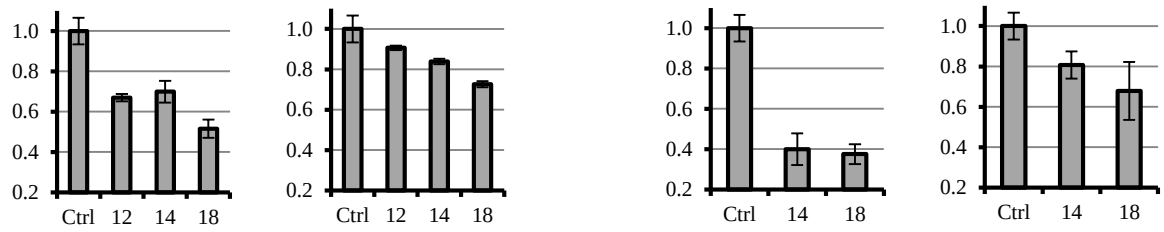

(b) *In vivo* Axial Linearised Stiffness (at MAP and $\lambda_z^{i.v.}$) – $\mathcal{C}_{zzzz}{}^{i.v.}$

Figure 3.15: **Summary metrics V - Biaxial linearised stiffness.** Horizontal axes refer to mice age (wks) of perturbed groups *vs.* control, while vertical axes refer to fold–changes from baseline (12wks *Ctrl*).

The effects of introducing perturbations to TGF-β signalling and blood pressure to arterial wall elastic energy storage can be seen in Fig. 3.16. The elastic energy stored at "*in vivo*" configuration is reduced in all perturbed groups, Fig. 3.16(a). As previously observed, ATAs seem to be more affected than IAAs (0.34 *vs.* 0.8 times baseline for the *Dis* group at 18wks, resp.), and induction of hypertension leads to further reduction in stored energy, to approx. 0.2 and 0.53 times baseline for ATA and IAA at 18wks, resp. Note that a particularly low value of 0.2 was reached for *Dis+HT* ATAs already at 14 weeks, while TGFBR2 disruption–only mice had a larger but still rather low value of 0.53 at the same time point; this observation suggests that changes in the arterial wall secondary to disruption of signalling through TGFBR2 are primarily responsible for arterial energy storage (in particular in ATAs), and that these arterial walls are vulnerable to further perturbation such as by induced hypertension.

Finally, the energy biaxially dissipated over the cardiac cycle is quantified by the energy dissipation ratio (*EDR*), Fig. 3.16(b). This dissipation is mainly due to viscoelastic dissipation,

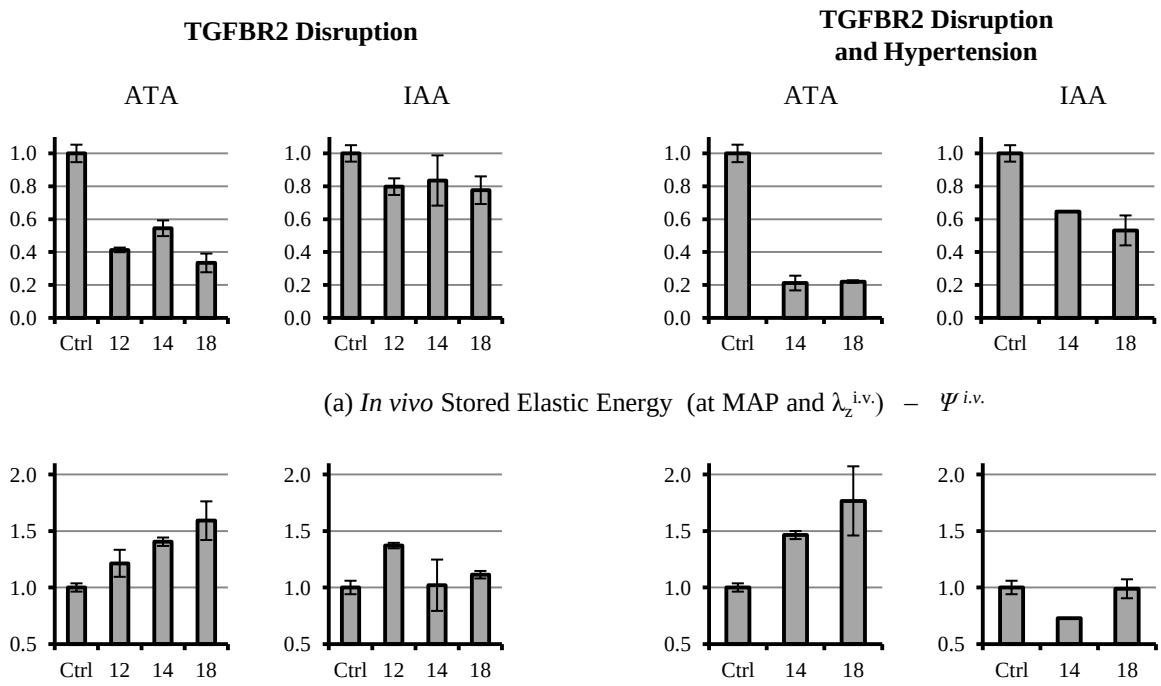

(a) *In vivo* Stored Elastic Energy (at MAP and $\lambda_z^{i.v.}$) – $\Psi^{i.v.}$

(b) Energy Dissipation Ratio *EDR*

Figure 3.16: **Summary metrics VI — Energy metrics.** Horizontal axes refer to mice age in weeks of perturbed groups *vs.* control, while vertical axes refer to fold–changes from baseline (12wks *Ctrl*).

and is correlated with loss of energy storage functionality in large elastic arteries such as the ATA (Ferruzzi et al., 2015). The results show progressive, step–wise increases in the EDR of ATAs in the *Dis* group, which reach 1.5 times baseline at 18 weeks. Induction of hypertension promotes even larger increases in EDR, which increases to over 1.75 times baseline at 18 weeks. Note also that at this later time point a large variability in animal phenotype is present, c.f. large error bar. Finally, the EDR of perturbed IAAs in either disruption group oscillates around baseline values, and returns to baseline levels at 18 weeks.

3.2.2 Microstructural data

Arterial wall microstructure was assessed by staining tissue sections with Picrosirius red, an histological technique commonly employed to visualise fibrillar collagen I and III, Sec. 3.1.5.1. Fig. 3.17 shows low (20ms) and high (200ms) exposure images used to delineate adventitial and medial collagen, resp., in ATAs and IAAs of each observation group at 14 and 18 weeks.

Comparing different experimental groups at 14 weeks, Fig. 3.17(a), it becomes clear that TGF-β disruption promotes a small increase in adventitial collagen (*low exposure* images), and that further induction of hypertension leads to much more significant adventitial collagen accu-

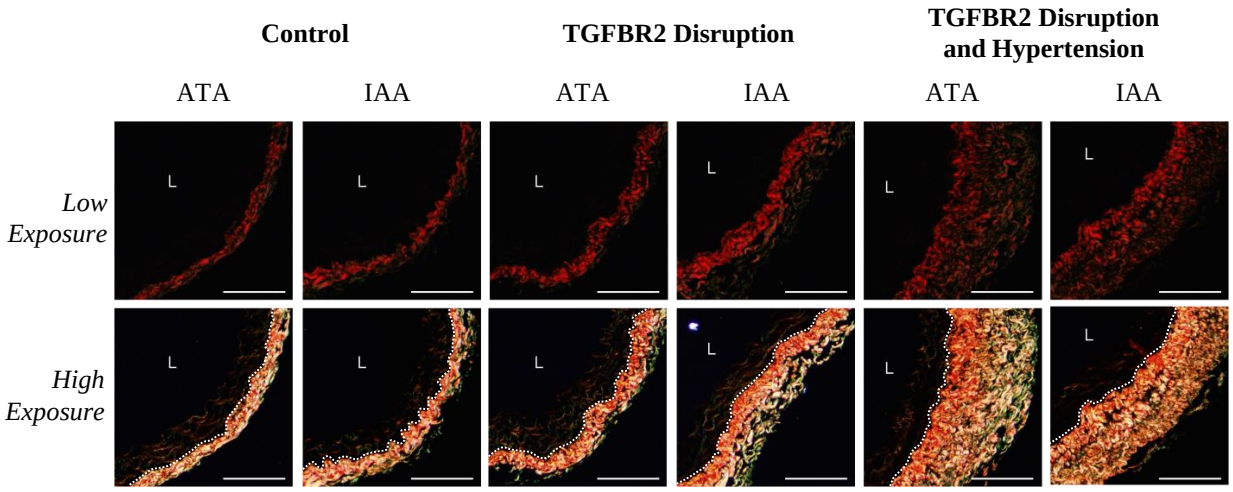

(a) Representative PSR tissue sections at 14 weeks

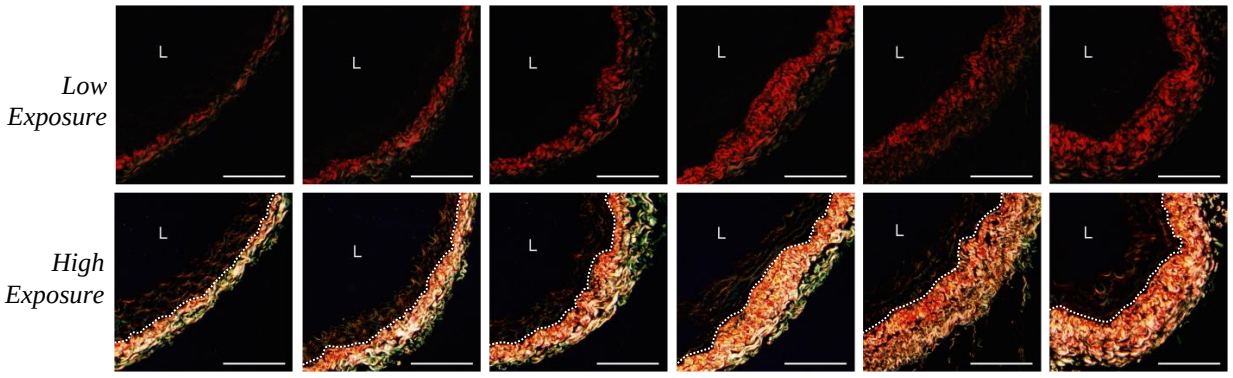

(b) Representative PSR tissue sections at 18 weeks

Figure 3.17: **PSR fibrillar collagen staining source images.** Representative images showing PSR–stained tissue sections from each observation group at 14wks (a) and 18wks (b). Each section was exposed to polarised light for 20ms (*low exposure*) or 200ms (*high exposure*) for delineation of adventitial and medial collagen, resp., and imaged at 20× magnification. L: lumen; scale bar is 100μm. The media (inner) / adventitia (outer) boundary in the *High Exposure* images is marked by the white dashed line (N.B. only the adventitia is visible in the *Low Exposure* images).

mulation, in particular in the ATA segment. Note also a change in the distribution of collagen pixel colours between groups (*high exposure* images): accumulation of thin, loosely–packed yellow/green collagen fibres on the outer side of the vessel is present in *Dis* IAA, while adventitial thickening in IAA of the *Dis+HT* group seems to be mostly due to the accumulation of thick, densely–packed red/orange collagen fibres; and an intermediate situation is seen in *Dis+HT* ATAs, which display a large orange transition band between red collagen pixels in the inner adventitial and yellow/green pixels in the outer adventitia. Finally, changes in the medial layer following arterial perturbation are not visible in the PSR images.

PSR–stained tissue sections at 18 weeks show some temporal variation in the microstructure of perturbed arteries, Fig. 3.17(b). Segments from the *Dis* group appear to display slightly thicker adventitias made up of a combination of red/orange and yellow/green pixels (*low exposure* images), with possibly the IAA displaying a majority of red/orange pixels. The ATA from the

Dis+HT group displays reduced thickness when compared to the 14wks vessel; however, most of it is composed of thick, densely–packed red collagen fibres plus some loose perivascular tissue (*high exposure* image). The IAA segment, on the other hand, seems to be as thick as the 14wks segment, and equally rich in red collagen pixels (*high exposure* image).

In this study, total number of collagen–positive pixels and distributions of pixel colours following illumination of tissue samples with polarised light were separately quantified for the media and adventitial layers of ATA and IAA segments in each observation group at 14 and 18 weeks using custom–built MATLAB scripts. Absolute values of group–averaged pixel numbers and percentages can be found in Appendix A Table A.3. As in the previous section, values in the perturbed groups were normalised to the corresponding baseline values, in this case 14 weeks *Ctrl* (pilot studies showed no significant differences between 12wks and 14wks *Ctrl* vessels). Fig. 3.18 shows fold–changes from baseline control values for total pixel counts and distributions of pixel colours in each layer.

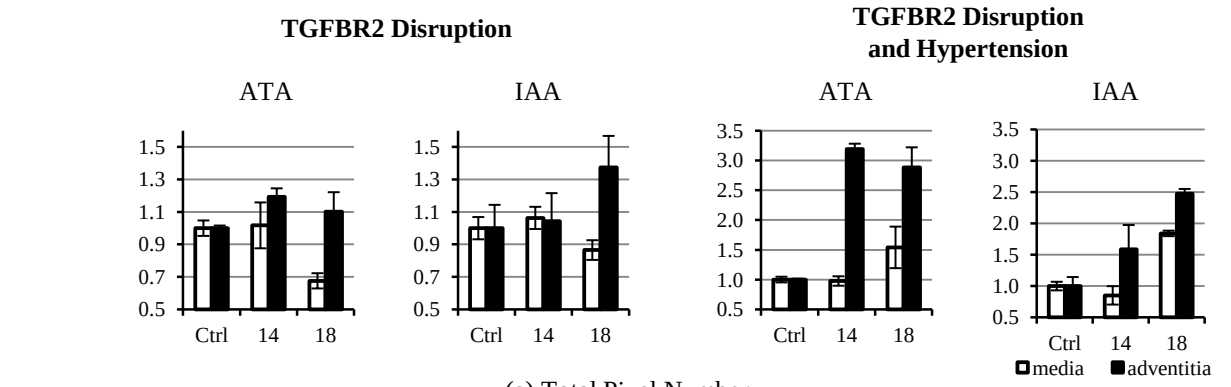

(a) Total Pixel Number

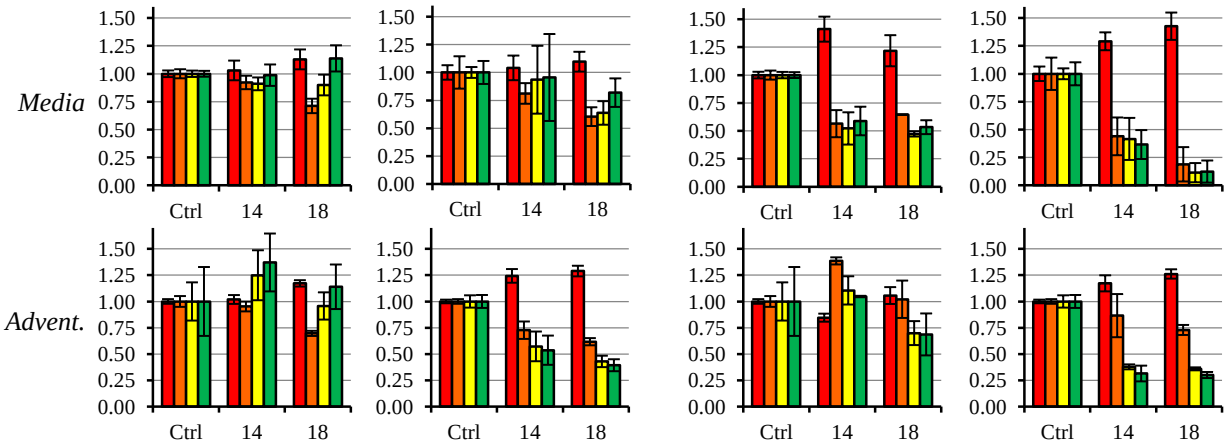

(b) Distribution of Pixel Colours

Figure 3.18: **Collagen quantification from PSR images.** Quantification of total collagen pixels and distribution of pixel colours from PSR images. Horizontal axes refer to age of mice in weeks of perturbed groups *vs.* control group, while vertical axis refer to fold–changes from baseline (14 weeks *Ctrl*).

Total collagen pixel counts, Fig. 3.18(a), show large changes in the adventitial layers of perturbed arteries. TGFBR2 disruption leads to a small increase (1.1–1.2 times baseline) in the total collagen pixel counts in ATA segments, and a significant increase in the total collagen pixels in the IAA at 18wks (just under 1.4 times baseline), which is consistent with observations made in the source images, Fig. 3.17(b). Further induction of hypertension leads to a very large increase in total adventitial collagen in both segments, with ATAs showing a large increase of 3.2 times baseline at 14 weeks followed by a small reduction at 18 weeks, and IAAs displaying a continuous increase to 2.5 times baseline at 18wks; this large thickening (followed by a small thinning in ATAs) is also consistent with Fig. 3.17. The evolution of medial collagen is rather different for each perturbed group: both segments in the *Dis* group display almost no changes at 14wks, followed by a large reduction at 18 weeks (under 0.7 times baseline for 18wks ATAs); segments in the *Dis+HT* group, on the other hand, show no variation (ATA) or a small decrease (IAA) in medial content at 14 weeks, followed by a considerable increase of this quantity at 18 weeks (1.5 and 1.85 times baseline for ATAs and IAAs, resp.). These results seem to suggest that inducing hypertension promotes both medial and adventitial collagen deposition in TGFBR2 KO mice.

Layer–specific distributions of pixel colours for each observation group quantified are plotted in Fig. 3.18(b). Group–specific distributions of medial collagen pixels are strikingly different, Fig. 3.18(b)*top*. TGFBR2 disruption leads to very small changes in medial collagen, with an increase in both red (thick, dense fibres) and green (thin, loose fibres) collagen pixels in the ATA and only a small increase in red pixels in the IAA at 18wks. In contrast, vessels in the *Dis+HT* group display a clear increase in red medial collagen pixels and a decrease in the remaining colours at 14wks, with ATAs seeing a small decrease in red pixels at 18wks, and IAAs displaying the opposite trend; the levels of orange, yellow and green pixels are particularly low in IAAs at 18wks, whose medial layers are mostly composed of red collagen pixels.

Unlike medial collagen, adventitial collagen pixel colour distribution varies significantly over time for each experimental group, Fig. 3.18(b)*bottom*. ATAs in the *Dis* group show a large increase in yellow/green pixels at 14 weeks (i.e., loosely–packed thin collagen fibres), which is replaced by red pixels (i.e., thicker and more densely packed collagen fibres) at 18wks. In contrast, *Dis* group IAAs always show a large proportional increase in red pixels and a corresponding decrease in orange, yellow and green pixels, which slightly accentuates at 18wks. A very simi-

lar trend is present in the IAAs of the *Dis+HT* group, however with larger proportions of thick, densely packed red and orange pixels. The evolution of collagen pixel distribution in the ATAs of the *Dis+HT* group is particularly interesting: at 14wks there is a small reduction in red pixels, a large increase in orange pixels and a small increase in yellow and green pixels; 4 weeks later, the proportion of orange pixels decreases but the proportion of red pixels returns to baseline, while the proportion of yellow and green pixels drops to under 0.75 times baseline. This observation is consistent with the representative tissue sections in Fig. 3.17.

This last observation points to a process of collagen maturation: thick but immature (less densely packed) collagen (orange) is initially deposited in the inner adventitia at 14wks, as well as loose thin collagen (yellow and green) in its outer section. At 18wks, however, the wall changes in collagen composition, with orange (less dense/thick) and yellow/green (loosely packed/thin) collagen pixels giving way to red pixels characteristic of thick and densely–packed collagen. Given the distributions of collagen pixel colours shown in Fig. 3.18(b)*bottom*, it becomes clear that the large increase in total collagen in the *Dis+HT* group, Fig. 3.18(b)*top*, is mostly due to thick and densely–packed red collagen in IAAs, and a combination of dense (red) and intermedially–packed (orange) thick collagen in ATAs.

3.2.3 Biochemical and cellular data

Tissue sections of ATA and IAA segments from each experimental group at 14 and 18 weeks were stained and visualised via immunofluorescence (IF) techniques using primary antibodies targeting MMP-2, TGF-β1,2,3, pSMAD-2, CD45 and α-SMA proteins, c.f. Sec. 3.1.5.2.

3.2.3.1 Source images

Fig. 3.19 and Fig. 3.20 display a representative set of sections from such cross–sectional images at 14 and 18 weeks, resp. For all the images shown, note that differences in elastin autofluorescence (in green) are due to the fixing and embedding procedure, and are not correlated with actual variation in the elastin fibre content of different vessels.

Representative source images at 14 weeks, Fig. 3.19, show significant differences in biochemical and cellular markers between observation groups, in particular for *Ctrl vs. Dis+HT* groups. MMP-2, Fig. 3.19(a), is present both in the media and adventitia of *Ctrl* ATA and IAA,

as expected for a collagenase secreted by mural cells (medial VSMCs and adventitial fibroblasts). Induction of TGFBR2 disruption alone seems to change MMP-2 protein content little; however, adventitial thickening promoted by hypertension induction (as was seen in Fig. 3.17(a)) promotes a large increase in MMP-2 expression in this layer (red/magenta signal outside medial external elastic lamellae in green). The presence of TGF-β ligand isoforms 1,2,3, Fig. 3.19(b), is more significant in the media of *Ctrl* arteries, which seems to be slightly reduced following disruption of TGF-β signalling. Further induction of hypertension leads to a very large increase in TGF-β in the thickened adventitia, in particular for the ATA. Note also the large break in the elastin lamella in the *Dis+HT* IAA tissue section. Greatly increased signalling downstream of TGF-β is also present following hypertension: pSMAD-2, Fig. 3.19(c), which is expressed in the media of *Ctrl* vessels, is present to a large extent in the thickened adventitias of the *Dis+HT* group, in particular in the thoracic segment.

Cellular changes also take place following vascular perturbation. Immune cell marker CD45, Fig. 3.19(d), is almost absent from *Ctrl* and *Dis* arteries; in the *Dis+HT* group, however, CD45–positive red pixels can be seen almost exclusively in the adventitia of both ATA and IAA segments. Mostly expressed by contractile VSMCs and myofibroblasts, α-SMA is unsurprisingly present almost exclusively in the media of unperturbed arteries, Fig. 3.19(e). TGFBR2 disruption induces small changes, with α-SMA signal appearing slightly reduced in the media of IAA segments. Induction of hypertension clearly results in the appearance of α-SMA–positive cells in the adventitia layers of both ATAs and IAAs.

Representative IF images for experimental groups at 18 weeks are shown in Fig. 3.20, which allow for identification of group–specific changes over time. Little change is seen in the *Ctrl* segments stained for MMP-2, Fig. 3.20(a), as well as in the *Dis* segments, where a small increase in MMP-2 signal may be present (compare IAA sections at 14 and 18 weeks). The hypertensive ATA at 18 weeks is less thick than at 14 weeks, but with a possibly higher signal intensity in the adventitia than at the earlier time point; no changes are visible for the IAA *Dis+HT segment*. TGF-β signal seems to be slightly increased in both *Dis* vessels from 14 to 18 weeks, Fig. 3.20(b). *Dis+HT* ATA adventitia is thinner than at 14 weeks but possibly displays a slightly larger signal intensity (thicker red/magenta shapes in the outer section of the arterial wall), while the IAA adventitia seems slightly thicker but displaying lower signal intensity than at 14 weeks (note the

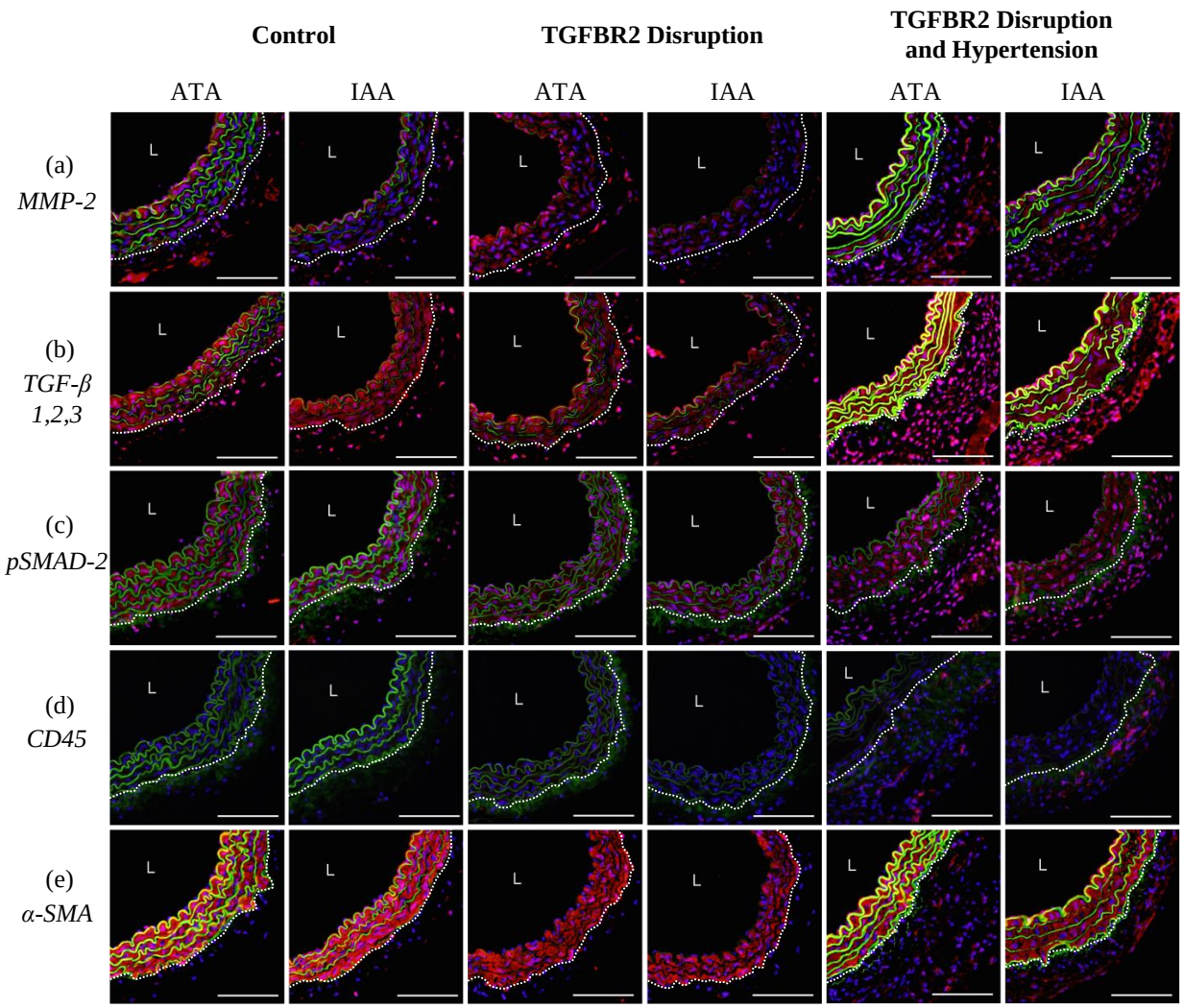

Figure 3.19: **Source IF images for visualisation of biochemical and cellular markers at 14wks.** Sections from representative source images for visualisation of MMP-2 (a), TGF-β1,2,3 (b), pSMAD-2 (c), CD45 (d) and α-SMA (e) markers (in red) and cell nuclei (DAPI, in blue) for each segment and experimental group at 14 weeks. Elastin fibre autofluorescence can be seen in green. Images were taken at 20× magnification. L stands for vessel lumen, and the scale bar is 100μm. The boundary between the media (inner) and the adventitia (outer) is marked by the white dashed line.

large outer red section in the *Dis+HT* IAA at 14 weeks, Fig. 3.19(b)). The representative images for pSMAD-2 staining, Fig. 3.20(c), show a clear reduction in adventitial thickness and adventitial pSMAD-2 signal in both ATA and IAA of the hypertensive group from 14 to 18 weeks, with little change for the remaining groups.

Similarly reduced is the immune cell marker CD-45 in the adventitia of both ATA and IAA segments of the *Dis+HT* group at 18 weeks, with CD-45–positive signal being almost completely absent from these images, Fig. 3.20(d); no changes can be seen from 14 to 18 weeks in the remaining observation groups. As expected, contractile cell marker α-SMA distribution shows little temporal change for the *Ctrl* segments, Fig. 3.20(e). *Dis* ATAs display a slightly more intense signal at 18 weeks than at the previous time point, while changes are not visible for

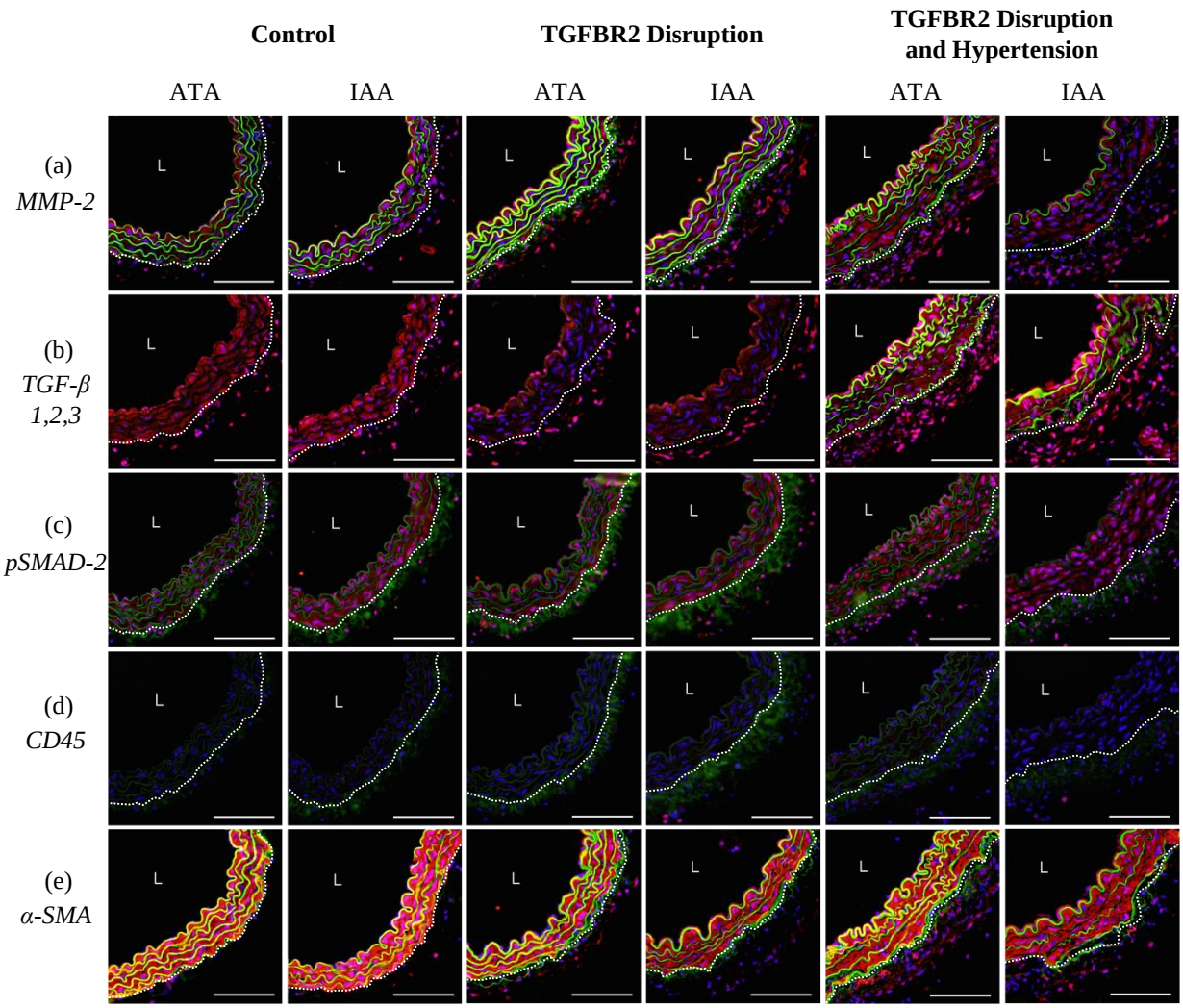

Figure 3.20: **Source IF images for visualisation of biochemical and cellular markers at 18wks.** Sections from representative source images for visualisation of MMP-2 (a), TGF-β1,2,3 (b), pSMAD-2 (c), CD45 (d) and α-SMA (e) markers (in red) and cell nuclei (DAPI, in blue) for each segment and experimental group at 18 weeks. Elastin fibre autofluorescence can be seen in green. Images were taken at 20× magnification. L stands for vessel lumen, and the scale bar is 100μm. The boundary between the media (inner) and the adventitia (outer) is marked by the white dashed line.

the corresponding IAA segment. Absolute adventitial α-SMA expression appears smaller in the thinner *Dis+HT* ATA segment from 14 to 18 weeks, while α-SMA signal intensity is reduced from 14 to 18 weeks in the corresponding IAA segment (note the presence of α-SMA–positive red bands at 14 weeks, Fig. 3.19(e), which are absent at 18 weeks).

3.2.3.2 Biochemical and cellular quantification

Each IF image was processed using custom–built MATLAB scripts enabling medial and adventitial manual segmentation, computation of total pixel number positive for a particular biochemical or cell marker, and total cell number count by automatic segmentation of DAPI–positive cell nuclei; for pSMAD-2 in particular, which translocates to the cell nucleus upon formation of re-

ceptor complexes with SMAD-4 (Dijke and Arthur, 2007), pixel counts were further categorized into "nuclear" when there was overlap between pSMAD-2 marker and DAPI, or "matrix" otherwise. Pixel area densities for each layer were also calculated by dividing layer–specific pixel counts by the area of each layer computed from manual segmentation of the PSR images (media) or total collagen pixels (adventitia). Absolute values of cross–sectional areas, pixel and nuclei counts and area densities for each layer, segment and observation group, as well as number of samples used to calculate each quantity, can be found in Appendix A Table A.4. Similarly to previous sections, pixel/nuclei numbers and area densities characterising perturbed groups were normalised by the corresponding baseline quantities characteristic of 14wks vessels in the *Ctrl* group (pilot studies showed no significant differences in IF images of 12 *vs.* 14 wks *Ctrl* vessels). Fig. 3.21—Fig. 3.23 display the time evolution of such normalised quantities *vs.* baseline control for the media and adventitia of each perturbed group.

Fig. 3.21(a) displays the temporal variation in total counts (*top*) and area density (*bottom*) of MMP-2–positive pixels. TGFBR2 disruption leads to a small increase in both total count and area density of adventitial MMP-2 pixels (black bars), which is already attained at 14wks for ATAs but is only visible at 18wks for IAAs. Medial pixel densities (white bars) change much less than adventitial densities, with ATAs displaying an elevated level at 14 weeks but returning to baseline at 18wks, and IAAs displaying a small increase only at 18wks. Introducing hypertension in addition to TGFBR2 disruption promotes much more significant changes in MMP-2–positive pixel numbers, which continuously increase to a maximum level of 9.7 times baseline for ATAs at 18wks, and is elevated to approx. 6 times baseline at 14wks but then returns to approx. baseline for IAAs. Medial pixel numbers display similar trends but to a much smaller extent (maximum increase of 2.3 and 2 times baseline for ATAs and IAAs, resp.). Changes in medial MMP-2 pixel density are similar but to a smaller extent. Taken together these results suggest that perturbation of TGF-β signalling promotes slightly increased MMP-2 protein expression in both ATAs and IAAs (but with different time courses), and that further induction of hypertension leads to even larger increases in MMP-2 total levels and area density, which are continuous for ATAs and transient for IAAs, and particularly significant in the adventitia. This last observation is consistent with the large increase in medial and particularly adventitial collagen levels shown in Fig. 3.18(a), as well as the qualitative observations drawn from Fig. 3.19 and Fig. 3.20.

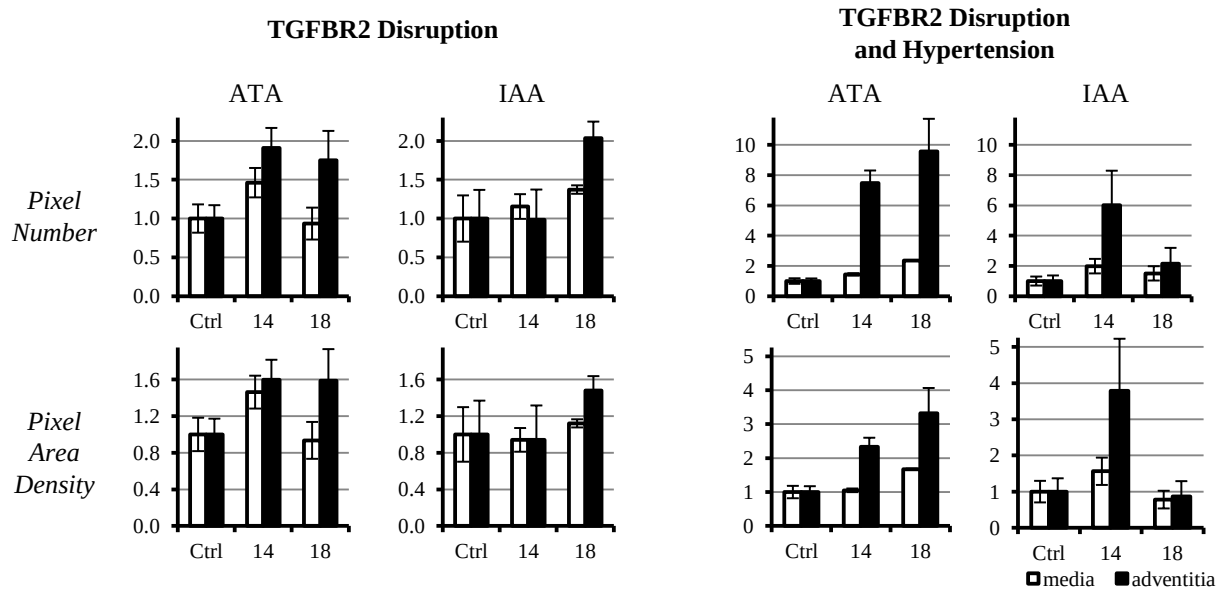

(a) MMP-2

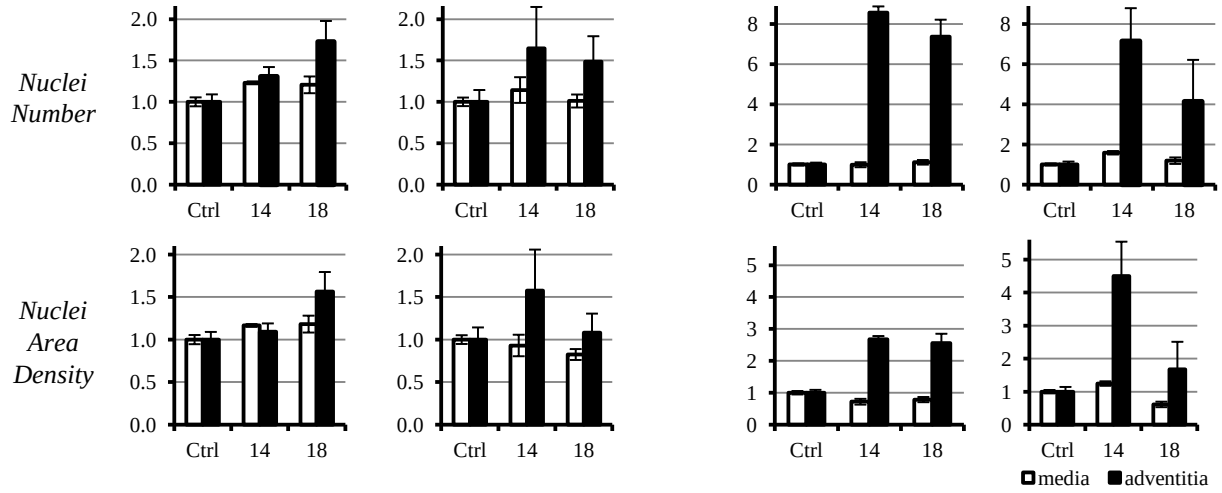

(b) Cell Nuclei

Figure 3.21: **MMP-2 and cell nuclei quantification from IF images.** Quantification of total counts and area density of MMP-2 pixels (a) and cell nuclei (b). Horizontal axes refer to mice age in weeks of perturbed groups *vs.* control, while vertical axis refer to fold–changes from baseline (14wks *Ctrl*).

Collagen deposition and MMP-2 secretion are mediated by vascular cells, in particular VSMCs in the media, fibroblasts in the adventitia and infiltrating immune cells throughout the wall when inflammation is present. Total nuclei number counts (*top*) and nuclei area density (*bottom*) are shown in Fig. 3.21(b); these correspond to total cell counts and densities, and are not specific to a particular cell type. ATAs in the *Dis* group show a continuous increase in total nuclei number and a corresponding small increase in nuclei density in the adventitia, which only becomes significant at 18wks. In contrast, IAAs in the same group show similar increases in total adventitial nuclei numbers and nuclei area densities at 14wks, followed by reductions towards baseline at 18wks. Medial quantities change very little in this group. More significant changes are present in *Dis+HT* vessels. Inducing hypertension promotes a very large increase in adven-

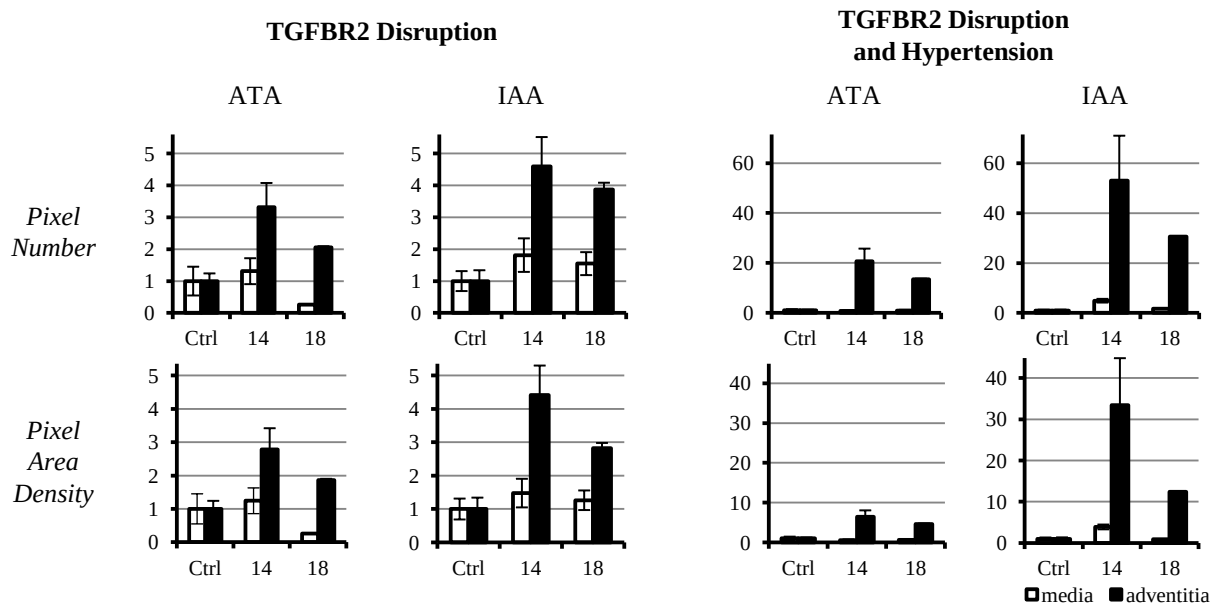

(a) CD45

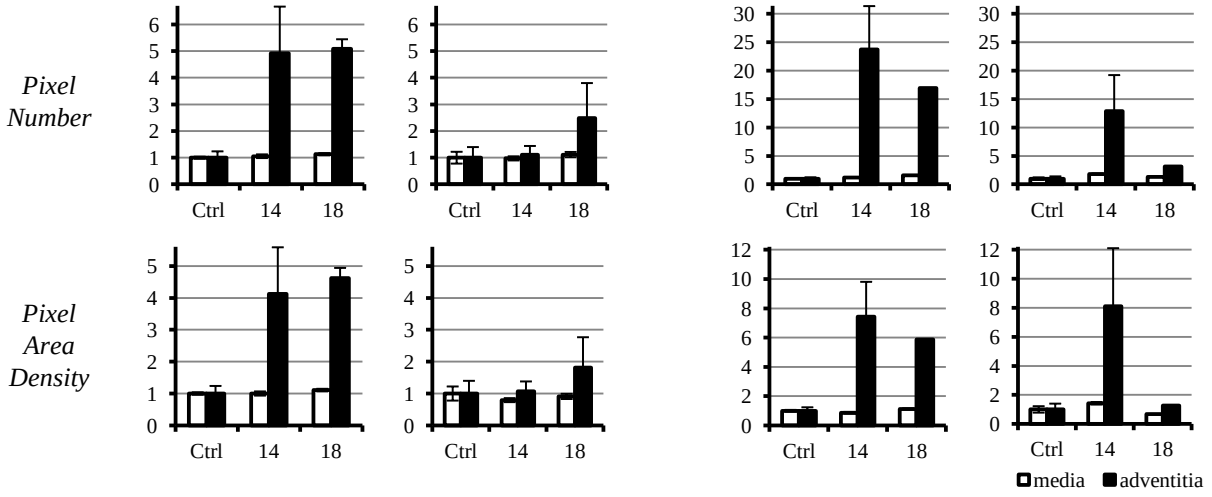

(b) α-SMA

Figure 3.22: **CD45 and α-SMA quantification from IF images.** Quantification of total pixel counts and area density for CD45 (a) and α-SMA (b). Horizontal axes refer to mice age in weeks of perturbed groups *vs.* control, while vertical axis refer to fold–changes from baseline (14wks *Ctrl*).

titial nuclei number and a reasonable increase in nuclei area density for both segments at 14wks, followed by a small reduction in ATAs and a large reduction in IAAs at 18wks. Compared with these changes, variations in medial quantities were very small. Similarly to MMP-2, the results show that inducing hypertension strongly intensifies trends already present to a small extent in TGFBR2 disruption–only adventitias, in this case a large increase in total nuclei counts and density, the latter to a smaller extent. Note also that ATAs and IAAs in each group display different patterns of evolution over time, with *Dis+HT* ATAs displaying increased nuclei density at 14wks which approximately persists at 18wks, while IAAs display a clear drop in the same quantity from 14 to 18 weeks.

So as to investigate which cell types might be related to such increases in nuclei numbers and densities, tissue sections were stained for inflammatory and contractile cell markers, Fig. 3.22. Fig. 3.22(a) shows quantification of IF staining for CD-45, a large spectrum immune cell marker expressed in particular by T cells and monocytes/macrophages. Disruption of TGF-β signalling promotes increases of total adventitial CD-45–positive pixel numbers and area densities at 14wks for both ATAs (approx. 3 times baseline) and IAAs (approx. 4.5 times baseline), followed by a decrease to approx. 2 (ATAs) and 3 (IAAs) times baseline at 18wks. Medial CD-45 levels increase at 14wks for both vessels, but then reduce to very small levels in ATAs and approx. stabilise for IAAs. Further induction of hypertension promotes much larger increases in adventitial total pixel levels and area densities for ATAs (approx. 20 and 8 times baseline, resp.) and especially for IAAs (over 50 and 30 times baseline, resp.) at 14wks, followed by a reduction at 18wks to levels that are still much larger than baseline. Variations in medial CD-45 levels are comparatively much smaller. These results are consistent with qualitative observations on the source images in Fig. 3.19 and Fig. 3.20, and support the hypothesis that TGFBR2 disruption is correlated with inflammatory processes that are significantly worsened by further perturbing the mechanical equilibrium with hypertension. Note also that the very large factors of increase for the total CD-45 pixel numbers of approx. 20 and 50 times baseline are partially due to very low levels at baseline, c.f. Table A.4.

α-SMA is a cytoskeletal contractile protein expressed in the vasculature by medial VSMCs and myofibroblasts (at least partially) originated from adventitial fibroblast differentiation. Fig. 3.22(b) shows layer–specific quantification of this protein for each experimental group. Firstly, note that both total pixel counts and area densities of medial α-SMA remain largely unchanged in all segments, times and observation groups, with the exception of small increases in total pixel numbers in both segments of the *Dis+HT* group, and a small reduction in α-SMA area density for *Dis+HT* IAAs at 18wks. This observation suggests that α-SMA–expressing VSMCs in the media remain largely unchanged, which is consistent with the very small variations in nuclei numbers and density observed in this layer in perturbed groups, c.f. Fig. 3.21(b). Significant changes, however, are seen in the adventitial levels of this protein. Vessels in the *Dis* group show increased α-SMA total pixel counts and densities, with ATAs displaying significant increases already at 14 weeks (approx. 5 and 4 times baseline, resp.) which then stabilise or slightly increase

at 18 weeks, and IAAs displaying smaller increases (2.5 and 2 times baseline, resp.) only at 18wks. Further induction of hypertension results in very large adventitial levels of this protein in both segments, which is followed by a small (ATAs) or very large (IAAs) reduction at 18wks; in particular, note that area density of adventitial α-SMA in *Dis+HT* IAAs has returned to baseline at 18wks. These results suggest that disruption of TGF-β signalling associated with mechanical perturbation by induction of hypertension lead to the appearance of a significant population of adventitial myofibroblasts expressing α-SMA, possibly differentiating from fibroblasts. This cell population is transient, increasing significantly immediately after perturbation (14wks) but then reducing over time (18wks). Furthermore, the perturbations introduced do not seem to affect medial VSMC expression of α-SMA. These considerations are consistent with what was observed in representative source images Fig. 3.19, Fig. 3.20.

To assess the influence of the TGF-β signalling axis on the microstructural, biochemical and cellular changes observed before, TGF-β ligand and p-SMAD2, an intracellular signalling mediator downstream of TGF-β, were quantified from IF images, Fig. 3.23. Continuous increases in both adventitial TGF-β pixel counts and area densities are seen in both segments of the *Dis* group, in particular in the IAA, Fig. 3.23(a). Induction of hypertension leads to even larger increases in these quantities, which reach large levels already at 14 weeks and then either stabilise (ATAs) or reduce towards baseline levels (IAAs). Medial TGF-β pixel counts and densities change comparatively little, with small increases seen in *Dis* IAAs at 18wks. The observation that levels of adventitial TGF-β ligand increase following disruption of TGFBR2 in medial SMCs is interesting, and may point towards intercompartmental communication, as suggested by Li et al. (2014). Both infiltrating immune cells and (myo)fibroblasts may be responsible for TGF-β secretion in the adventitia. Noting that CD-45–positive pixel counts and densities decrease from 14 to 18 weeks (Fig. 3.22(a)), but that both α-SMA (Fig. 3.22(b)) and TGF-β ligand (Fig. 3.23(a)) increase between these two time points, it is reasonable to hypothesise that increased levels of TGF-β ligand are secreted by differentiated myofibroblasts.

Upon binding to specific receptor complexes, TGF-β ligand activates several downstream intracellular pathways, in particular the canonical, SMAD–dependent pathway, which involves formation of complexes including pSMAD-2/3 that translocate to the nucleus and act as transcription factors to target genes. To infer activation of SMAD–dependent pathway, pSMAD-2–

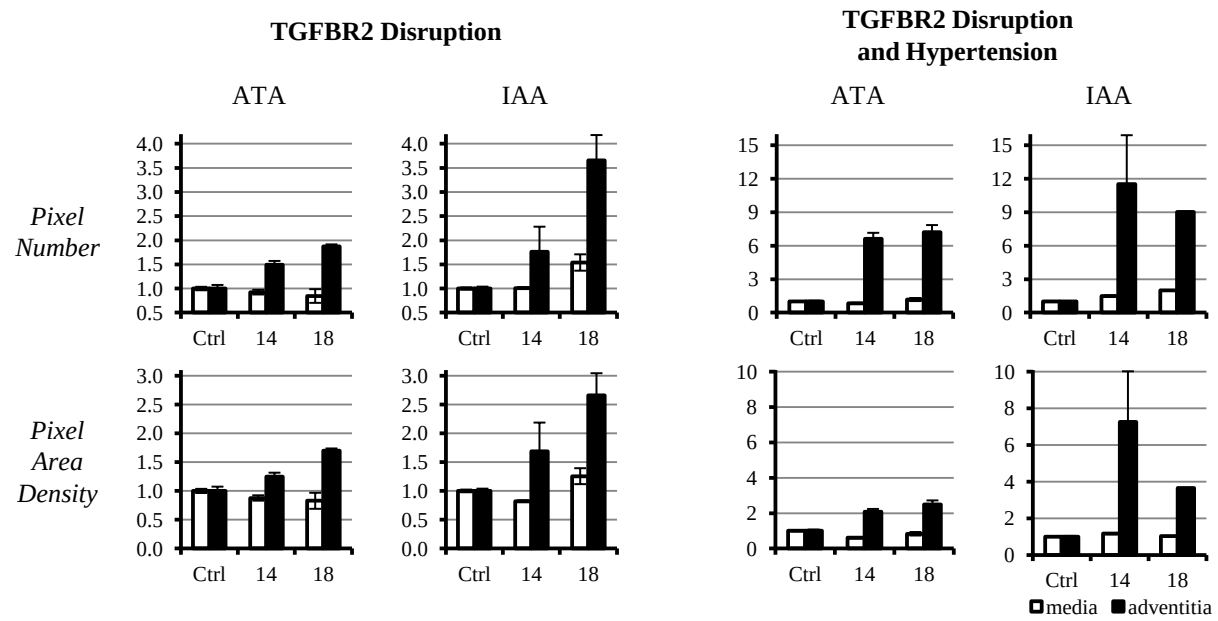

(a) TGF-β1,2,3

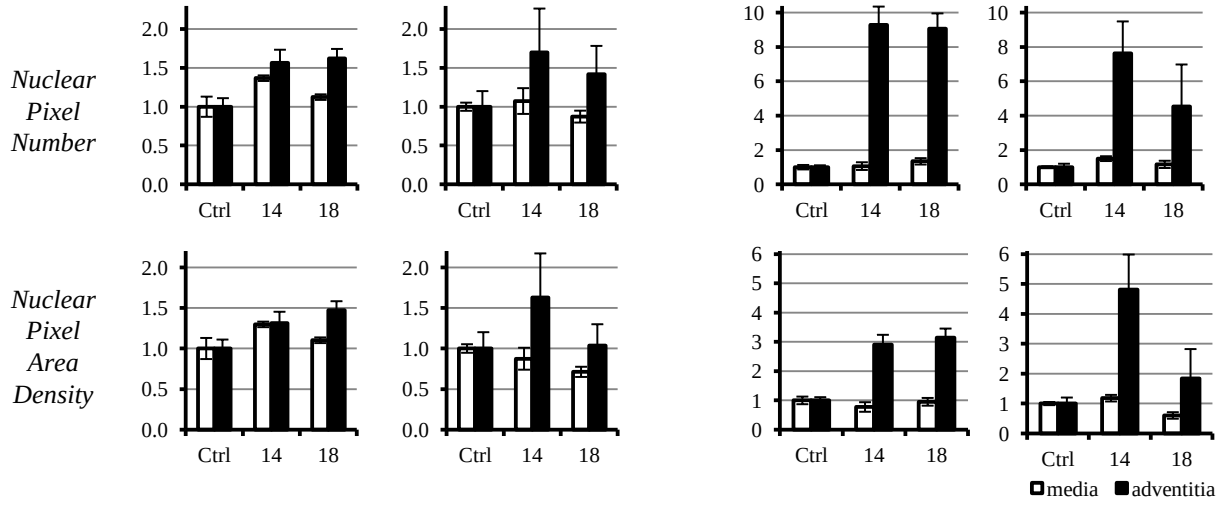

(b) pSMAD-2

Figure 3.23: **TGF-β and pSMAD-2 quantification from IF images.** Quantification of pixel counts and area density for TGF-β (total) (a) and pSMAD-2 (nuclear) (b). Horizontal axes refer to mice age (wks) of perturbed groups *vs.* control, while vertical axis refer to fold–changes from baseline (14wks *Ctrl*).

positive pixels overlapping with DAPI–stained nuclear pixels ("nuclear" pSMAD-2) were quantified, Fig. 3.23(b). TGFBR2 disruption in medial SMCs leads to interesting layer–specific changes in nuclear pSMAD-2 levels. In the adventitia of *Dis* ATAs there is a small increase in both pixel counts and density (1.5 times baseline), which can be partially explained by the small increase in TGF-β ligand (Fig. 3.23(a)). Interestingly, IAAs in this group show pSMAD-2 levels at 18wks that are lower than those at 14wks, even though TGF-β levels increase from 14 to 18 weeks. This observation could be explained by decreased sensitivity to TGF-β ligand and/or increased SMAD-2 inhibition (e.g. by inhibitory SMAD-7 (Akhurst and Hata, 2012)). Levels of pSMAD-2 in the media tend to slightly reduce over time in *Dis* IAAs, while slightly increasing at 14wks

and then reducing at 18wks for *Dis* ATA; this last observation is puzzling given that TGFBR2 was disrupted in these cells, and may point to cross–talks with other signalling pathways (e.g. AngII (Ruiz-Ortega et al., 2007)) or medial infiltration by TGFBR2–expressing immune cells (Fig. 3.22(a)). Further induction of hypertension leads to a large and sustained increase in adventitial pSMAD-2 nuclear pixel count and density in ATAs (10 and 3 times baseline, resp.), and a large increase at 14wks followed by a decrease at 18wks in IAAs; similar dynamics are observed for the TGF-β ligand (Fig. 3.23(a)). Changes in medial levels of pSMAD-2 in this group were comparatively much smaller, except for a reduction in density in *Dis+HT* IAAs at 18wks to 0.8 times baseline. Note that these considerations match qualitative observations in representative IF images, Fig. 3.19, Fig. 3.20.

3.3 Discussion: Experimental insight

In this chapter, a novel animal model of vascular perturbation was used to assess aortic tissue biomechanics, collagen microstructure and metabolism, and vascular cell composition following disruption of TGF-β signalling and further perturbation to mechanical equilibrium. TGF-β receptor type 2 (TGFBR2) was disrupted by inducible conditional knock–out in aortic VSMCs of post–weaning (6 weeks) mice, and in a group of these hypertension was later induced pharmacologically. Biaxial mechanical testing of excised ATA and IAA segments showed that TGFBR2 disruption resulted in dilated and significantly thickened vessels with higher circumferential and axial structural stiffness and lower in vivo stretch ratio; further induction of hypertension accentuated such trends. Fitting the experimental data to a microstructurally–motivated constitutive model revealed that disruption of TGF-β signalling tended to reduce distensibility and extensibility, decrease axial stress and material linearised stiffness, reduce elastic energy storage and increase (viscoelastic) energy dissipation. Induction of hypertension accentuated all the previous trends, in particular leading to largely reduced axial but also circumferential stresses and material stiffnesses, as well as largely decreased energy storage and largely increased energy dissipation.

Collagen staining revealed that TGFBR2 disruption increased the total amount of adventitial collagen but interestingly decreased the levels of medial collagen at later time points. Hypertensive arteries displayed a very large increase in adventitial collagen, as well as a small increase in

medial collagen. Colourimetric analysis also revealed segment–specific differences in collagen fibre thickness and packing, which evolved over time. Specific targeting of biomolecular and cellular markers revealed that perturbation to TGF-β signalling in *medial* VSMCs resulted in significant *adventitial* changes: levels of collagen–degrading MMP-2 were elevated; cell numbers were increased, in particular CD-45–positive inflammatory cells and α-SMA–positive contractile cells; levels of TGF-β ligand increased, even though levels of the intracellular mediator pSMAD-2 acting downstream of TGF-β only transiently. Induction of hypertension resulted in larger increases of all the previous quantities, in particular of total and CD-45– and α-SMA–positive cells, which evolved over time differently in ATAs *vs.* IAAs.

The comprehensive data set generated in this study allowed for mechanical, microstructural, cellular and biochemical characterisation of vascular cell–mediated mechanobiological response to perturbations of cell signalling and mechanical equilibrium. The results shed some light on different aspects of the chemo–mechano–biology of the arterial wall under the control of the TGF-β signalling axis, which motivate both novel experimental work and refinement of conceptual descriptions of arterial G&R.

3.3.1 Study design and methods

TGFBR2 disruption In this study, TGFBR2 was knocked–out in the VSMCs of post–weaning mice by a tamoxifen–inducible *loxP*–Cre recombinase system. This model was originally developed and applied to the study of arterial biology by Li et al. (2014), who reported highly reduced or even absent translation and expression of *Tgfbr2* in the isolated medial tissue and in medial SMCs harvested, expanded and sorted by flow cytometry following induction with the synthetic oestrogen tamoxifen (Figure 1(D–H) therein). In any case, the very high specificity and efficacy of *Tgfbr2* deletion was dependent on DNA inclusion of both *loxP* and *Myh11–Cre* sites, which was confirmed in this study by PCR; only two out of 27 tested animals were not expressing either sequence, which were removed from further analysis.

The novel animal model of perturbation to TGF-β signalling in VSMCs has been recently used in other studies. Gao et al. (2014a) disrupted TGFBR2 at 5wks of age and exposed the lumen of IAAs to porcine pancreatic elastase, a common model of AAA, (Thompson et al., 2006); the authors report that TGFBR2–disrupted arteries have a more stable medial VSMC population,

reduced immune cell infiltration, preservation of elastin and collagen and decreased aneurysm incidence and diameter. Gao et al. (2014b) use a very similar study design but, instead of elastase application, the left common carotid artery was partially ligated, thus increasing blood flow; it is reported that TGFBR2 disruption is associated with reduced VSMC proliferation, macrophage infiltration, MMP-9 proteolytic activity and medial thickening. However, none of the previous studies specifically quantifies TGF-β ligand or receptor. Given that Li et al. (2014) observed increased TGF-β ligand expression following tamoxifen treatment, it is not possible to exclude that the changes observed by Gao et al. may be secondary to a compensatory increase rather than to a decrease in TGF-β ligand, possibly acting on other wall layers.

Consistent with the previous reasoning are some of the findings of Hu et al. (2015), who use a very similar animal model (*loxP* sites in exon 4 rather than in exon 2) to show that TGFBR2 disruption at 6 weeks results in medial aortopathy (elastin breaks, macrophage infiltration) and adventitial compensatory response (increased cell proliferation and collagen deposition) mediated by significantly increased expression of TGF-β ligand 2 and 3. Finally, Ferruzzi et al. (2016) perform passive and active biaxial testing on mice with TGFBR2 disruption at 4 weeks, which were characterised by dysfunctional passive mechanical properties (*see below*), reduced contractile function and *in vitro* delaminations; treatment with rapamycin restores VSMC contractility but not passive properties. So as to investigate the influence of TGF-β signalling on the pathobiological processes described by other groups, the study here quantified levels of both TGF-β ligand (1,2,3) and downstream intracellular mediator pSMAD-2 in a layer–specific way.

As briefly mentioned in Sec. 3.1.2.1, it was decided to disrupt TGFBR2 at 6 weeks so as to reduce the incidence of dissections, which Li et al. (2014) reported to be under 25% for ATAs subject to tamoxifen treatment (Figure 2(B) therein). Even though some vessels in this study displayed intramural accumulation of red material, Sec. 3.3.3 below, no extensive dissections in the ATA were observed as in the previous study, which may be explained by the different endpoints in this and Li et al's studies (12wks *vs.* 26wks after TGFBR2 disruption, resp.). Note that most other studies apply TGFBR2 disruption to younger mice, of 4 (Li et al., 2014; Ferruzzi et al., 2016) or 5 (Gao et al., 2014a,b) weeks of age, which make direct comparison of findings between studies not straightforward. The first observation point of this study was taken at 6 weeks for *Ctrl* group arteries, Table 3.1. However, excessive enlargement of cannulated vessels

during biaxial testing and visible leaking at later stages of the test pointed to loss of vessel wall structural integrity upon testing. Given that the biaxial testing system and protocol followed has never been applied to arteries from mice less than 8 weeks of age (Bersi et al., 2014), and that arterial mechanical homoeostasis is reached between 6 and 8 weeks of age as estimated by elastin properties and mural stresses (Ferruzzi et al., 2016), it is reasonable to suggest that central arteries at 6 weeks are still fairly immature and cannot be tested with the methods employed here. Baseline values were then taken from 12 or 14 weeks *Ctrl* arteries, which displayed small differences.

Hypertensive stimulus Mice belonging to the *Dis+HT* group were induced hypertension at 12wks of age, i.e. 6 weeks after TGFBR2 disruption. Hypertension was pharmacologically induced by a combination of high–salt chow and eNOS blocking by supplementation of drinking water with L-NAME. This technique was chosen due to its systemic effects (elevating blood pressure in the ATA and IAA segments studied and on the tail artery, necessary for blood pressure measurement) and its non–invasiveness (when compared with techniques requiring surgery). Given that TGF-β is secreted by immune cells infiltrating the arterial wall (Rizas et al., 2009), that it acts as chemoattractant to these cells and regulates their phenotype (Akhurst and Hata, 2012), and that inflammatory immune cells can modulate arterial G&R (Ju et al., 2013; Tan et al., 2013), reducing inflammatory processes secondary to induction of hypertension was also an important consideration. Even though L-NAME is known to induce some inflammatory response by reactive oxygen production and local AngII induction (Kitamoto et al., 2000), it is reasonable to expect that L-NAME–induced inflammation will be less extensive than what would be the case if hypertension was induced by chronic administration of AngII, a potent inducer of vascular inflammation particularly studied in the context of atherosclerosis and aneurysm (Mehta and Griendling, 2007).

Blood pressure variation following induction of hypertension was monitored by a standard tail–cuff method. It is known that this pressure differs from the central blood pressure ATA and IAA segments experience; however, tail–cuff measurement is non-invasive and it does not require anaesthesia (unlike invasive catheter or ultrasound measurement), which is known to reduce central blood pressure (Janssen et al., 2004). Hypertension was induced in four 12 weeks female littermates of the male mice used for data generation in this study, and then measured 2 and 6

weeks later. Female mice were chosen due to the very limited number of (tamoxifen–inducible) male mice available for testing in the time line allocated to this project. Li et al. (2014) report a very small reduction in MAP following TGFR2 disruption, which justified using baseline values to analyse *Dis* group animals. Ferruzzi et al. (2015) report very small differences (well within error margins) for male *vs.* female wild–type mice of a similar strain to the one used in this study. Regardless, there may be gender–specific responses to the L-NAME and salt–induced hypertension, and the effect of combined TGFBR2 disruption and induced hypertension on blood pressure was not assessed (female mice are not tamoxifen–inducible). Ideally, blood pressure should be assessed in tamoxifen–induced male mice subject to hypertension.

Table 3.2 shows average blood pressure values following 2 and 6 weeks of hypertension. The results show a large initial variation of approx. 10mmHg (10%) in systolic, mean and diastolic pressures at 2 weeks of hypertension, and then a further small increase of approx. 2mmHg 4 weeks later. Bellini et al. (2015) used the same protocol for induction of hypertension (3g/L of L-NAME in drinking water and 8% NaCl chow), and used a similar tail–cuff method for monitoring blood pressure. The authors report that systolic and diastolic pressures were increased by approx. 40% (51mmHg and 36mmHg, resp.) after 18wks of hypertension stimulus. In addition to different endpoints (6 *vs.* 18 weeks of hypertension), other factors that may explain the significantly different values of blood pressure in this *vs.* Bellini et al.'s studies are mice gender (female *vs.* male, resp.), different strain of mice (C57BL/6 *vs.* C57BL/6J×129SvEv, resp.) and different age of mice at induction (12wks *vs.* 8–9wks, resp., with younger mice expected to be more susceptible to mechanical perturbations). Further studies will be necessary to fully characterise the effect of salt and L-NAME treatment on the blood pressure of C57BL/6 mice.

3.3.2 Comparison with previously published results

In this section, the consistency between the results of this study and literature findings using the same or similar models is assessed. Li et al. (2014) characterise ATA segments of 6wks old C57BL/6 mice following TGFBR2 disruption at 4wks in terms of vessel geometry, wall structure and gene expression. In spite of the different times of induction, many of their results are consistent with findings in this study: disrupted ATAs display adventitial fibrosis and mural thickening (even though at a very late time point of 30wks in the absence of dissection), which matches

the increased collagen quantity (Fig. 3.18(a)) and loaded thickness (Fig. 3.12(b)) observed here; increased (fibrillar) collagen I,III and TGF-β1,2,3 expression, which is consistent with the increased total collagen (Fig. 3.18(a)) and TGF-β protein levels (Fig. 3.23(a)) discussed above; increased cell proliferation (measured by BrdU incorporation) is also consistent with increases in cell number (Fig. 3.21(b)) in this study.

Some findings, however, are distinct. Li et al. (2014) report slightly reduced pSMAD-2 (in spite of larger SMAD-2) levels in 6wks ATAs following TGFBR2 disruption; Fig. 3.23(b), however, shows slightly increased total levels of pSMAD-2. The last observation time in this study (8wks *vs.* 2 wks post-induction) together with increased immune CD-45–positive cells in the media (Fig. 3.22(a)) may suggest that pSMAD-2–expressing cells were possibly present in the media when this protein was quantified, therefore increasing the value read. In addition, the authors report slightly decreased medial α-SMA levels 6 and 10 weeks post–disruption by IF analysis, while there are no significant changes in Fig. 3.22(b), even though source images appear to show a reduced signal intensity in *Dis* arteries when compared with *Ctrl* vessels (Fig. 3.19, Fig. 3.20). This observation suggests that the methods used here for quantification of α-SMA are not sensitive enough to small variations in signal intensity.

Hu et al. (2015) used a similar animal model (same mice strain, *loxP* targets in exon 4 of *Tgfbr2*) to disrupt TGFBR2 at 6wks (as in this study) and assess arterial condition at 10 and 20 weeks. Consistent with the findings in this study, the authors report post–TGFBR2 disruption aortic dilatation in ATAs and IAAs at unloaded configuration (c.f. inner radius measurements in Fig. 3.11(a)), medial elastin damage (c.f. elastin break in Fig. 3.19(b) *right*), increased (Mac-2) macrophage marker in all aortic segments (c.f. immune cell marker CD-45 levels in Fig. 3.22(a)), increased cell proliferation particularly in the adventitia (c.f. nuclei number counts in Fig. 3.21(b)), increased collagen accumulation in the adventitia (c.f. total collagen levels in Fig. 3.18(a)) and increased MMP-2 expression by medial VSMCs (c.f. MMP-2 protein levels in Fig. 3.21(a)). In addition, their study identified distinct marks of aortopathy in disrupted arteries, in particular penetrating ulcers, dissection and intramural haematoma; intramural accumulation of blood was also observed in some specimens analysed in this study, all belonging to the *Dis+HT* group (c.f. Fig. 3.24, Fig. 3.25 below).

Ferruzzi et al. (2016) used methods very similar to the ones employed here to assess tho-

racic aortic biaxial mechanical properties of Li et al.'s animal model of TGFBR2 disruption. Notwithstanding differences in tamoxifen induction and observation time points, the authors report changes in biaxial mechanical properties following tamoxifen induction that are consistent with the results of this study: increased collagen content and cross–sectional area (c.f. collagen pixel counts in Fig. 3.18(a) and unloaded wall thickness in Fig. 3.11(b)); rightward shift in the P-d_o curve, especially in the low pressure range (c.f. P-d_o in Fig. 3.3(a)); loss in distensibility (c.f. σ_θ–λ_θ curve in Fig. 3.3 (c) and increased $\partial\Psi/\partial\lambda_\theta$ in Fig. 3.9(b)); reduced *in vivo* axial stretch (c.f. Fig. 3.13(b)); and significant reduction in stored elastic energy *in vivo* (c.f. Fig. 3.16(a)). Note that Ferruzzi et al. (2016) separated tamoxifen–treated arteries in un–dissected and dissected groups, while no such division was performed here, which makes comparison of absolute values less straightforward.

The previous paragraphs show that many trends established in this study are consistent with previously published literature findings. In any case, it is still important to compare absolute values, in particular of mechanical quantities that, unlike tissue–level biomolecular quantification, are reported in physical units. Ferruzzi et al. (2015) performed a comprehensive mechanical characterisation of several aortic segments of wild–type (WT) and fibulin-5–deficient C57BL/6×129/SvEv mice at 20–22 weeks of age. Even though the previous study uses a mixed mouse background without *Myh11-CreER^{T2}.Tgfbr2$^{f/f}$* genetic constructs, it provides detailed mechanical information for both ATA and IAA segments at later age (when mechanical homoeostasis has been fully attained) than Ferruzzi et al. (2016), which contains data only for 8wks ATAs. A comparison between Ferruzzi et al. (2016) *Fbln$^{+/-}$* WT at 20–22wks and this study's *Ctrl* mechanical data at 18wks is presented in Table A.2 in Appendix A. Values are coloured red, green and blue when the average±2 SEM of each mechanical quantity in the study is above, (at least partially) within or below Ferruzzi et al.'s averages±2 SEM.

Table A.2 shows that average mechanical quantities characterising the IAA segment are consistent with values in the Ferruzzi et al.'s study, with only a lower outer diameter and axial linearised stiffness than previously reported. This is also the case for ATA's unloaded dimensions, except for the unloaded wall thickness, which is under what was previously reported. The remaining mechanical quantities for the ATA segment, however, are significantly different: loaded outer diameter and *in vivo* axial stretch are larger than previously reported, while wall thickness

is lower; *in vivo* Cauchy biaxial stresses are higher; circumferential linearised stiffness is higher, and axial stiffness lower; and stored elastic energy *in vivo* is higher. Possible causes for the differences observed fall into two categories. Firstly, those attributable to different animal models used. In this study, mice had a pure C57BL/6 background, while Ferruzzi et al. (2015) used mixed C57BL/6×129/SvEv mice. In addition, mice used in this study had oestrogen–inducible *Myh11–CreER*^{T2} in their genomes, and uninduced animals constitutively expressed the large, membrane–bound red fluorescent protein Tomato (Li et al., 2014); none of these genetic constructs was present in the mice used by Ferruzzi et al. (2015). Supporting the reasoning above, it has been observed that *Myh11-CreER*^{T2}.*Tgfbr2*$^{f/f}$ C57BL/6 mice have slightly different passive mechanical properties compared to wild–type C57BL/6 mice (Chiara Bellini, personal communication).

Secondly, the observed differences between the two mechanical data sets may be due to different testing protocols; this would explain the poor matching for ATA values, given the much more complex geometry of this segment when compared with the approximately cylindrical IAA. An independent observer was asked to compare representative mechanical data sets from either study, as well as images detailing biaxial mechanical testing and unloaded thickness measurement. Three differences were found. When cannulating the vessel for biaxial testing, more of the upstream brachiocephalic trunk (BCT) segment was left in this study than in Ferruzzi et al's (0.5 *vs.* 0.2mm); the BCT is known to be more compliant that the ATA, and thus leaving more of it in series with the ATA segment during testing may have resulted in over–estimation of (*in vivo*) axial stretches. Moreover, glass cannulae were placed co–axially in this study, which resulted in diameter measurements being made slightly off–plane (N.B. Ferruzzi et al.'s placed the cannulae slightly misaligned, such that the ATA segment where diameter was being measured was as close to horizontal as possible); consistently larger loaded outer diameters were estimated as a result, in particular for higher pressures. Finally, manual segmentation of the arterial wall for estimation of unloaded thickness seems to have excluded more perivascular tissue than in Ferruzzi et al.'s, with a measurable difference of approx. 5–10μm. Over–estimation of loaded outer diameter and *in vivo* axial stretch and under–estimation of unloaded thickness will have resulted in the over–estimation of loaded inner radius and under–estimation of loaded thickness *via* Eq. (3.1) and larger estimation of biaxial Cauchy stresses (average values being given by Eq. (3.3)), as is shown

in Table A.2. Over–estimated inner radius will have led to over–estimated circumferential stretch ratio via Eq. (3.2), which jointly with over–estimated *in vivo* axial stretch will have resulted in over–estimated stored energy at MAP, also shown in Table A.2.

In summary, the mechanical data generated in the study displays differences from previously published data, which may be due to different animal models and/or different testing techniques used. Even though the difference between animal models could affect different aortic segments to different extents, the much larger differences seen in the ATA than in IAA suggest that most of them should have arisen during mechanical testing. In any case, both animal model and biaxial testing methodologies including cannulation and arterial wall segmentation were consistent for all time points and observation groups in this study, so fold–changes between perturbed *Dis* and *Dis+HT* groups at different times and baseline *Ctrl* arteries should reveal real trends. This is supported by the many consistencies in the mechanical, structural, biochemical and cellular properties of TGFBR2–disrupted arteries and those reported by other studies, c.f. initial paragraphs in this section.

3.3.3 Study insights

In the previous section, the consistency of this study's data with previously published data was assessed. More than just being consistent with previous work, this study introduces four important novelties. First, each vessel in this study was characterised mechanically, microstructurally, biochemically and cellularly, which was meant to provide a clearer picture in terms of TGF-β–regulated, vascular cell–mediated arterial G&R response to perturbation; previous works have not characterised wall mechanics (Hu et al., 2015; Gao et al., 2014a,b), or have characterised arterial wall biochemistry/cellularity and mechanics in different animals (Li et al., 2014; Ferruzzi et al., 2016). Second, this study introduces for the first time a mechanical perturbation (induced hypertension) to the TGFBR2 disruption mouse model developed by Li et al. (2014); given that both microstructural and mechanical properties are disrupted following tamoxifen treatment, a further perturbation away from mechanical equilibrium was expected to significantly influence arterial G&R, which was in fact seen in the results. Third, this study is the first to evaluate arterial evolution in the IAA segment following TGFBR2 perturbation in the animal model of Li et al. (2014), which allows for comparison between ATA and IAA evolution; in addition, it is the

first one in which TGFBR2 disruption is performed at 6wks, and observations are made 6, 8 and 12 weeks later. Fourth, characterisation of cell markers, collagen and MMP-2 collagenase, and TGF-β signalling mediators is for the first time performed on a layer–specific basis by means of imaging techniques (PSR and IF). In this section, important features of the data set presented in Sec. 3.2 are discussed and related to other findings.

3.3.3.1 Arterial chemo–mechano–biology

Geometry and Stress Perturbing TGF-β signalling through TGFBR2, in particular when coupled to induced hypertension, led to significant changes in arterial tissue properties. Fig. 3.3(a), Fig. A.1(a) reveal increased outer diameter in pressure–inflation tests for disrupted groups (in particular for the lower range of pressures), which is consistent with inner radius at the *in vivo* and especially in the unloaded configurations (Fig. 3.12, Fig. 3.11, respectively). As mentioned in Sec. 3.2.1.4, vessel thickness seems to play a role in this pressure–dependent behaviour of r_i: both loaded and unloaded thicknesses are increased; however, unloaded thickness (Fig. 3.11(b)) is increased to a smaller extent than its loaded equivalent (Fig. 3.12(b)), and thickness to radius ratio is much larger at loaded configurations (Fig. 3.11(a) *vs.* Fig. 3.12(c)). This result may be partially explained by the significant reduction in axial stretch (Fig. 3.3(b), Fig. A.1(b)), in particular *in vivo* axial stretch (Fig. 3.13(b)): extension and pressurisation of arteries at lower values of axial stretch are expected to result in higher vessel thicknesses *via* Eq. (3.1) (akin to a Poisson's effect), which are then expected to display lower values of circumferential and axial stretch (see Eq. (3.3)), as the results show (Fig. 3.14).

Collagen deposition and structural stiffness Wall thickening seems to be largely due to adventitial thickening, as for example for the ATA segment there was a 5.5% increase in medial thickness but a 19.3% increase in adventitial thickness between *Ctrl* and *Dis* group at 14 weeks, Table A.4. Mostly composed of collagen, it is not surprising that increased adventitial areas are correlated to increases in total number of collagen pixels, Fig. 3.18. Related to this increase in collagen levels, total adventitial cell numbers (including collagen–remodelling fibroblasts (McAnulty, 2007)), Fig. 3.21(b)*top*, and MMP-2, a proteolytic enzyme secreted by fibroblasts and involved in collagen metabolism (Strauss and Rabinovitch, 2000), are also increased, Fig. 3.21(a)*top*. Vascular tissues with increased collagen content are known to be stiffer (Wang and Chesler, 2012). Collagen–

rich arterial walls in disrupted groups were correlated with increased biaxial structural stiffness, which can be seen in leftward shifts in the circumferential stress–stretch curves acquired during pressure–inflation tests (Fig. 3.3(c), Fig. A.1(c)) and axial stress–stretch curves acquired during axial force–stretching tests (Fig. 3.4(d), Fig. A.2(d)). Also consistent with biaxially stiffer walls, stored elastic energy contours of perturbed arteries displayed decreased extensibility ($\partial\Psi/\partial\lambda_z$) and distensibility ($\partial\Psi/\partial\lambda_\theta$) when compared with *Ctrl* arteries, Fig. 3.9, Fig. 3.10.

Linearised stiffness Interestingly, even though structural stiffness seems to be elevated in *Dis* and *Dis+HT* groups, linearised axial stiffness at *in vivo* configuration (a measure of material stiffness) is significantly reduced, Fig. 3.15(b), which was also observed by Ferruzzi et al. (2016) in ATAs following tamoxifen induction. A possible explanation for this paradox is a shift in mechanical operating point (i.e., *in vivo* configuration) in perturbed vessels: as previously discussed, both biaxial stretches at *in vivo* configuration are decreased in perturbed groups, Fig. 3.13, which results in a leftward shift in operating point (around which biaxial stiffness is linearised) on stress–strain curves; lower values of biaxial stretch are associated with lower values of linearised stiffness (this can be intuitively inferred by taking tangents to the circumferential and axial stress–stretch curves, Fig. 3.3(c), Fig. 3.4(d), and equivalent for IAA).

Energy metrics Stored elastic energy *in vivo* is also reduced in perturbed groups, Fig. 3.16(a), which can be partially attributed to shifts in operating point, c.f. left– and down–ward translation of black circles marking *in vivo* conditions in energy isocontour plots, Fig. 3.9 and Fig. 3.10. Shifts in *in vivo* configuration can be due to degradation of medial elastin fibres (note the large gap in a medial elastic lamella in Fig. 3.19(b)*left*), which are responsible for arterial prestresses that determine mechanical constitutive behaviour in particular at low pressures (Cardamone et al., 2009; Ferruzzi et al., 2011); note that the largest variations between *Ctrl* and perturbed groups took place at low pressures (vessel calibre, Fig. A.1, Fig. A.2) and at unloaded configuration (wall thickness and inner radius, Fig. 3.11(a),(b)). Note also that reduced energy storage may be also partially due to increased viscous dissipation, which is consistent with increased EDR in perturbed groups, Fig. 3.16(b). In face of similar findings, Ferruzzi et al. (2016) observe that accumulation of mucoid material within the arterial wall increased viscoelastic dissipation; increased deposition of glycosaminoglycans leads to intramural accumulation of mucoid material,

which has been found to alter arterial wall mechanical properties. In this study neither elastin nor glycosaminoglycans were quantified.

Intramural depositions Even without special staining it was possible to identify intramural accumulations of exogenous material in some tissue samples. Fig. 3.24 displays two views of the renal section of a 18wks *Dis+HT* abdominal aorta. The mouse supplying this artery appeared weak and died just after Beuthanasia-D injection. Tissue dissection revealed what appears to be an extensive intramural accumulation of blood surrounded by dense fibrotic tissue, which points to a long–term remodelling process. Blood accumulation can also be seen in Fig. 3.25, which displays a 18wks thoracic aorta (ascending and arch region) of the *Dis+HT* group. In addition to an intramural haematoma, the arterial wall in the ascending region also features accumulation of yellow fatty material that has the appearance of an atheroma. Intramural haematomas secondary to localised dissections have also been observed in other studies performed with this animal model (Li et al., 2014; Ferruzzi et al., 2016); in this study, however, the incidence of these pathological conditions was low, as intended.

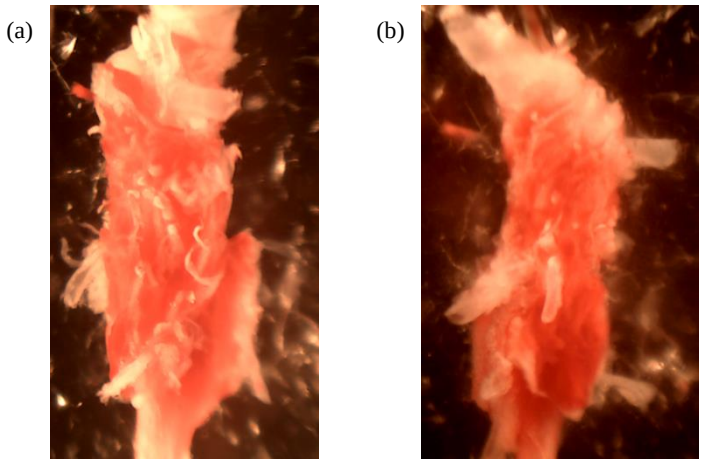

Figure 3.24: **Gross morphology of diseased vessels I.** An intramural haematoma surrounded by coherent (i.e., remodelled) fibrotic tissue can be seen in the renal section of a *Dis+HT* 18wks IAA in both dorsal/posterior (a) and ventral/anterior (b) views.

Matrix metalloproteinase 2 The previously observed changes in mechanics and collagen microstructure are mediated by changes in cellular and biochemical composition of the arterial wall, some of which were quantified. MMP-2 total amount and density tended to be increased in perturbed arteries, Fig. 3.21(a). This protease is constitutively secreted by medial VSMCs and adventitial fibroblasts (Barbour et al., 2007), and assumes particular importance in several vascular pathologies such as aneurysm, ischaemia or restenosis (Hobeika et al., 2007). MMP-2 is

(a) (b)

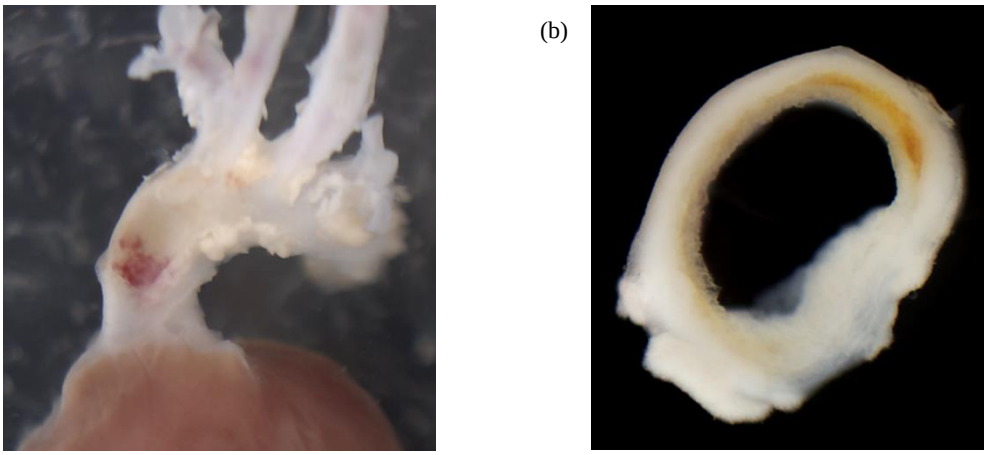

Figure 3.25: **Gross morphology of diseased vessels II.** Intramural accumulation of red and yellow material in the wall of a *Dis+HT* 14wks ATA, possibly corresponding to haematoma and atheroma regions, can be seen in an image of the excised ATA, aortic arches and branches (a), and in a cross–sectional image of a middle section of the ATA segment (b).

involved in collagen processing (elevated here), but it also has elastolytic activity (Rizas et al., 2009), which may result in elastin degradation and consequent change in constitutive properties, elastic energy storage and mechanical operating point discussed above.

Cellularity and CD-45 This study also showed significant increases in the cell number of perturbed adventitias, for almost no change in medial cellularity, Fig. 3.21(b). Adventitial increases in cell number are expected following injury to the adventitial wall (Maiellaro and Taylor, 2007); this is at least partially mediated by TGF-β–induced proliferation of mesenchymal cells (Akhurst and Hata, 2012), and adventitial TGF-β levels are elevated in this study (Fig. 3.23(a)). To understand which cell populations could be responsible for increased cell numbers, markers specific for two cell types were visualised by IF. The results show increased levels of CD-45, an immune cell marker, in particular in the adventitia, Fig. 3.22(a). The importance of adventitial inflammatory processes in vascular diseases has been receiving increasingly more attention, leading to the view that inflammatory processes may progress "outside–in" (i.e. from the adventitia towards the intima) in some conditions (Maiellaro and Taylor, 2007). Immune cells such as macrophages or T lymphocytes are commonly present in dysfunctional walls (Rizas et al., 2009), and their interactions with mural cells modulate arterial ECM remodelling in hypertension (Wu et al., 2014) and dissection (Ju et al., 2013).

α-SMA and collagen maturation α-SMA is an important molecular constituent of thick actin stress fibres, cytoskeletal components able to generate large contraction forces and isometric ten-

sion (Pellegrin and Mellor, 2007). In the normal aortic wall α-SMA is exclusively expressed by contractile medial VSMCs; over–loading of the arterial wall (secondary to medial degradation or increased intraluminal pressure) promotes fibroblast activation into highly contractile myofibroblasts expressing α-SMA; in this context, Jones et al. (2009a) observed the rise in a population of α-SMA–expressing myofibroblasts in thoracic aortic aneurysm as a result of differentiation from fibroblasts and a decrease in medial VSMCs. The results displayed in Fig. 3.22(b) show a large increase in α-SMA signal in the adventitia of perturbed arteries, thus suggesting fibroblast to myofibroblast differentiation. One important action of myofibroblasts is reorganising their surrounding ECM both by collagen fibre remodelling and by secreting specific types of collagen, thus modulating the distribution of collagen fibre undulation and content (Tomasek et al., 2002; Hinz, 2010). In addition to an increase in total collagen content, Fig. 3.18(a), the results show time–dependent changes in the distribution of collagen colours (correlated with collagen fibre diameter and packing), which is particularly suggestive in the adventitia, Fig. 3.18(b): ATAs in the *Dis* group show a large proportion of yellow/green pixels (thin/loosely packed collagen fibres) at 14 weeks, which are replaced by red pixels (thick/densely packed mature collagen fibres) at 18wks; ATAs in the *Dis+HT* group initially show a large proportion of orange pixels (thick but less densely packed collagen fibres), later replaced by red (thick and densely packed) collagen. As suggested by Eberth et al. (2009), changes in the distribution of collagen colours over time following mechanical perturbation may reveal (cell–mediated) collagen maturation processes, whereby some properties of the population of collagen fibres such as collagen type and/or packing coefficient. The results of this study seem to suggest that large amounts of thin, less packed ("immature") collagen fibres are deposited soon after perturbation, which are then gradually replaced by thicker and more packed ("mature") collagen fibres.

TGF-β signalling In addition to remodelling the vascular ECM, the forces applied by myofibroblasts on the matrix contribute to TGF-β activation (Wipff et al., 2007), which is consistent with the very large increases in adventitial TGF-β levels in perturbed groups that can be seen in Fig. 3.23(a); TGF-β is itself necessary for myofibroblast differentiation from fibroblasts (Tomasek et al., 2002). Latent TGF-β is activated not only be a traction–dependent, myofibroblast–mediated mechanism, but also by proteolytic degradation of the latency complexes quenching its signalling activity (Hyytiäinen et al., 2004). Matrix metalloproteinases such as

MMP-2 are responsible for such activation (Page-McCaw et al., 2007); elevated levels of MMP-2 in perturbed arteries, Fig. 3.21(a), are thus expected to contribute to the increased levels in TGF-β ligand. Conversely, TGF-β acts on adventitial fibroblasts and myofibroblasts through the non–canonical pathways to promote MMP-2 expression (Jones et al., 2009b), which may further contribute to the elevated MMP-2 levels observed. In addition to (myo)fibroblasts, TGF-β is secreted by infiltrating immune cells such as macrophages and T lymphocytes (Rizas et al., 2009) and acts on them as a chemoattractant (Akhurst and Hata, 2012); the positive feedback loop thus generated promotes an increase in immune cell numbers during vascular inflammation processes, which may have contributed to the significantly elevated CD-45–positive counts in the adventitias of perturbed arteries (Fig. 3.22(a)). Note also that TGF-β itself promotes macrophage switch to a highly secretory phenotype (Pickup et al., 2013), in particular of MMP-9, a protease with collagen and elastin degrading activity that has been found to synergise with MMP-2 in promoting aneurysm development (Longo et al., 2002; Theruvath et al., 2012).

pSMAD-2 signalling The three feedback loops involving TGF-β and myofibroblasts, MMP-2, infiltrating immune cells, resp., are likely to have contributed to the observed sustained increase in TGF-β levels in the adventitia of perturbed arteries. To further characterise the TGF-β signalling axis, the intracellular downstream mediator pSMAD-2 was quantified, Fig. 3.23(b). The first interesting observation is that in most cases increases in adventitial pSMAD-2 levels are smaller than increases in TGF-β ligand, and tend to level off before those of TGF-β. Several mechanisms could explain this observation (Doyle et al., 2012),(Akhurst and Hata, 2012): channelling of TGF-β signalling from the canonical (SMAD–dependent) pathway to other pathways such as RhoA/ROCK1, TAK1/JNK/p38/MAPK or RAS/ERK/MAPK; build-up of inhibitory SMAD-7, preventing nuclear translocation of pSMAD-2,3/SMAD-4 complex (N.B. only nuclear pSMAD-2 was considered); and/or saturation of the SMAD signalling pathway. Secondly, medial pSMAD-2 signalling slightly decreases in some observation groups following TGFBR2 disruption (as expected, given that SMAD-2,3 phosphorylation is carried out by membrane–bound TGF-β receptors integrating functional TGFBR2), but it also appears to increase in some experimental groups. Other than cryptic TGFBR1 phosphorylation in the absence of functional TGFBR2, two mechanisms can explain this observation. On the one hand, at the late time points observed (14 and 18 weeks) other cell types with functional TGFBR2 such as infiltrating immune cells

(Rizas et al., 2009) or migratory myofibroblasts (Maiellaro and Taylor, 2007) might be present in significant numbers in the media, thus changing pSMAD-2 readings. On the other, TGF-β–independent SMAD-2 phosphorylation has been reported, in particular under the control of AngII (Ruiz-Ortega et al., 2007). AngII is a pleiotropic signalling peptide regulating vascular cell contraction, growth, migration and ECM formation, and with extensive cross–talk with the TGF-β signalling pathway (Mehta and Griendling, 2007). As previously discussed, L-NAME may induce AngII signalling by promoting reactive oxygen species production (Kitamoto et al., 2000); the extent of L-NAME induced AngII signalling in this study is unknown.

3.3.3.2 Differences between perturbed groups

In this study and for the first time, the effect of inducing hypertension to a TGFBR2 disruption model was studied. In general, hypertensive disrupted arteries displayed trends that are similar to disruption–only arteries, but to a much larger extent. Unloaded thickness in *Dis+HT* arteries increases up to 45% more than for *Dis* arteries (Fig. 3.11(b)), and loaded thicknesses are up to 40% higher upon introduction of hypertension (Fig. 3.12(b)). As previously discussed, increases in adventitial collagen account for this result, with total collagen being up to 165% higher in hypertensive arteries than in TGFBR2 disruption–only arteries (Fig. 3.18(a)). In addition, hypertensive arteries tend to display more red/orange collagen pixels than *Dis* arteries (Fig. 3.18(b)), which shows that either thicker collagen is deposited, or it is remodelled and packed more efficiently in hypertensive arteries. Increased collagen content (Wang and Chesler, 2012), in particular of thick collagen type I, and increased collagen cross–linking (Wang et al., 2013) are common findings in hypertensive arteries.

Adventitial collagen deposition is carried out by (myo)fibroblasts. Hypertensive arteries were characterised by up to 5 times larger increases in adventitial cellularity when compared with *Dis* arteries (Fig. 3.21(b)), and up to 4.5 times larger increases in α-SMA signal (Fig. 3.22(b)). Animal models of hypertension show extensive proliferation of adventitial fibroblasts and associated large increases in (collagenous) ECM deposition, in parallel with fibroblast differentiation into α-SMA–expressing myofibroblasts that migrate towards the media (Stenmark et al., 2006). Associated with increased collagen turnover and possibly with myofibroblast migration, hypertensive models have shown increases in MMP-2 activity throughout the arterial wall (Jeffery and Mor-

rell, 2002), which is consistent with the up to 5 times larger increases in adventitial MMP-2 pixel counts following hypertension than in *Dis* arteries, Fig. 3.21(a). The presence of immune cells around vascular lesions secondary to hypertension, in particular of (CD-45–positive) T lymphocytes, has also been observed in hypertensive models, which is consistent with the significantly larger CD-45 signal in *Dis+HT* arteries when compared with those in the *Dis* group (up to 11 times larger, see Fig. 3.22(a)). Members of the TGF-β signalling family have also been shown to play important roles in hypertensive processes, in particular by promoting mesenchymal cell proliferation and ECM deposition (Humbert et al., 2004). The significantly larger levels of TGF-β ligands and downstream pSMAD-2 signalling in hypertensive arteries seen here (Fig. 3.23(a) and (b), resp.) certainly promoted the large increases in adventitial collagen (Fig. 3.18(a)) and cell numbers (Fig. 3.21(b)) seen, the latter both by increased mesenchymal cell proliferation and by chemoattraction of immune cells. Finally, note that genetic mutations leading to premature stop codons in the gene coding for TGFBR2 have been associated with a significant proportion (30%) of hypertension–induced plexiform lesions, which suggests that hypertension and disruption of TGF-β signalling may work synergistically to increase the severity of hypertensive maladaptation (Jeffery and Morrell, 2002).

This study also shows important changes in the biaxial mechanical properties of arteries following induction of hypertension. Hypertensive arteries displayed lower *in vivo* axial stretches (13% reduction, Fig. 3.13(b)), biaxial Cauchy stresses (68% reduction, Fig. 3.14) and biaxial linearised material stiffness, in particular axially (39% reduction, Fig. 3.15(b)), than TGFBR2 disruption–only arteries. In addition, hypertension promoted further reductions in ATA distensibility and extensibility (Fig. 3.10(c)), as well as a large decrease in IAA extensibility (Fig. 3.9(c)), which may have resulted from the large increase in collagen content. Eberth et al. (2009) quantified passive mechanical properties in the carotid arteries of a hypertension animal model; consistent with this study's results, the authors report increased collagen area fractions and wall thickness, and decreased *in vivo* axial stretch. Interestingly, the authors also report increased MCP-1, a chemoattractant of monocytes/macrophages, as well as intramural accumulations of glycosaminoglycans, which promote formation of mucoid deposits in the wall that increase viscoelastic energy dissipation (note that EDR computed in this study is larger for hypertensive ATAs than for *Dis*–only vessels at all time points, Fig. 3.16(b)). Reduced extensibility (leftward shift in

σ_z–λ_z curve) is also reported in the related study of Eberth et al. (2010).

3.3.3.3 Segment–specific changes

In addition to the induction of hypertension, this study also analysed differences between aortic wall segments, with the ATA being for the first time compared with the IAA. Different responses to perturbation were expected in these two segments given the large heterogeneity in their properties (Ruddy et al., 2008): embryologically, neural crest cells are the precursors for the ATA, whereas mesoderm cells give rise to the IAA; structurally, the media of the thoracic aorta has higher elastin content and larger number of lamellar units; mechanically, the abdominal aorta tends to be structurally stiffer and aneurysms in the abdominal aorta tend to display lower ultimate tensile stress; biochemically, metalloproteinase systems act differently in the thoracic and abdominal aorta, while TGF-β signalling seems to be deleterious in thoracic but protective in abdominal aortic aneurysms; vascular pathology is rather different in the two regions, with genetic syndromes being directly responsible for a large percentage of aneurysms in ATAs but not in the IAAs, and atherosclerosis being much more common in the abdominal than in the thoracic aorta.

The results show clear differences between these two segments. IAAs see smaller increases in thickness following perturbation (Fig. 3.11(b),Fig. 3.12(b)), which result in smaller decreases in biaxial Cauchy stresses (Fig. 3.14). Interestingly, note that *Dis* IAAs display larger increases of total adventitial PSR signal than ATAs (Fig. 3.18(a)), which may be due to higher levels of thick-/densely packed red collagen pixels deposited in this segment *vs.* in ATAs (Fig. 3.18(b)*bottom*). Larger increases in thick/densely packed (red) collagen fibres in IAAs, together with lower levels of elastin in the medial layer of the abdominal aorta, are consistent with the smaller decreases in biaxial material stiffness observed in this segment (Fig. 3.15), as well as lower decreases in *in vivo* stored elastic energy (Fig. 3.16(a)); EDR quantification is only meaningful for the ATA, which stores elastic energy during systole and converts it into work on the blood flow during the diastolic phase. Note also that IAAs are biaxially stiffer than ATAs at baseline (compare Fig. 3.9(a) with Fig. 3.10(a)), and that both extensibility ($\partial\Psi/\partial\lambda_z$) and distensibility ($\partial\Psi/\partial\lambda_\theta$) remain larger in perturbed IAAs than ATAs (Fig. 3.9(b),(c) *vs.* Fig. 3.10(b),(c)) at 14 weeks. Interestingly, there seems to be a recovery in distensibility from 14wks to 18wks in the IAA, while in the same period ATA distensibility decreases further.

This partial recovery in IAA distensibility from 14 to 18 weeks while ATA diverges further from baseline is consistent with trends shown in the chemo–biological mediators, which either take longer to increase in IAAs, decrease from 14 to 18 weeks in IAAs while remaining elevated for ATAs, or decrease further in IAAs than in ATAs. Adventitial MMP-2 levels in ATAs of the *Dis* group appear elevated already at 14 weeks, while IAA levels only reach similar levels at 18 weeks; following induction of hypertension, MMP-2 levels continuously increase in ATAs, while IAAs show a large reduction towards baseline from 14 to 18 weeks (Fig. 3.21(a)). A similar trend is observed in the adventitial cellularity levels in the *Dis* group. In the *Dis+HT* group, however, cell count seems to stabilise or decrease slightly at later time points in ATAs, while IAAs display a larger reduction in this quantity (Fig. 3.21(b)). A very similar trend is seen for α-SMA levels in the adventitia, which take longer to increase following TGFBR2 disruption in IAAs, and decrease much faster towards baseline levels in the hypertensive group (Fig. 3.22(b)). Interestingly, TGF-β signalling is larger and increases faster in *Dis* IAAs than ATAs, however there is a larger reduction in both TGF-β and pSMAD-2 adventitial levels from 14 to 18 weeks in hypertensive IAAs than in the corresponding ATAs (Fig. 3.23).

The previous observations suggest that faster and larger increases in adventitial TGF-β signalling, in particular through the canonical SMAD–dependent pathway, in IAAs promote a more efficient response to perturbation, with the deposition of more thick/densely packed collagen fibres. This results in smaller deviations from mechanical homoeostasis (e.g. Cauchy stresses, stored elastic energy) and faster convergence towards a new homoeostatic state characterised by biaxial mechanical properties closer to baseline and cellular numbers and levels of active biomolecules returning to baseline (note in particular the very low levels of adventitial α-SMA for *Dis+HT* IAAs, which are approx. back to baseline, suggesting the disappearance of a transient, "stress–response" myofibroblast population (Forte et al., 2010)).

3.3.3.4 Layer–specific changes

Imaging techniques together with computational image segmentation allowed for layer–specific microstructural, cellular and biochemical characterisation. The results shown in Sec. 3.2.2,Sec. 3.2.3 reveal important changes in both layers following perturbation, to a particularly large extent in the adventitia. TGFBR2 disruption resulted in increased total adventitial

collagen pixels, while medial collagen was decreased (Fig. 3.18(a)). Further induction of hypertension promoted adventitial collagen levels, as well as reversed decreasing medial collagen levels, which were actually higher in both segments at 18wks; these results suggest that medial VSMCs, responsible for collagen deposition in the media, can still transduce mechanical signals and increase their secretion of collagen even if TGF-β signalling through TGFBR2 is disrupted, possibly through local AngII secretion and TGF-β–independent SMAD signalling (Ruiz-Ortega et al., 2007). Note also that the evolution of the distribution of collagen pixel colours in the adventitia is significant in the ATA, where there is a progression between less organised (green, yellow, orange) collagen fibres towards thick and densely organised (red) fibres (Fig. 3.18(b)*bottom*), while in the media there is always a significant fraction of red pixels, and a small reduction in the percentage of other pixel types over time (Fig. 3.18(b)*top*).

Biochemical and cellular markers, Fig. 3.21—Fig. 3.23, generally display larger variations in the adventitia, which is particularly clear in the *Dis+HT* group. This is a very interesting observation for two reasons. Firstly, it supports the (relatively recent) view that the adventitia has a central role in sensing arterial wall injury and perturbation to its mechanical equilibrium (Stenmark et al., 2006). Consistent with this view, results show a large increase in adventitial cellularity (Fig. 3.21(b)), fibroblast activation (increase in α-SMA levels in the adventitia suggesting myofibroblast differentiation (Jones et al., 2009a), Fig. 3.22(b)) and presence of inflammation (Michel et al., 2007) (immune cell marker CD-45, Fig. 3.22(a)).

Secondly, results for arteries in the *Dis*–only group suggest that perturbation of medial VSMC signalling affects adventitial properties such as cellular composition (in particular of α-SMA–positive cells, Fig. 3.22(b)) and TGF-β signalling (TGF-β ligand levels, Fig. 3.23(a)). Li et al. (2014) hypothesise the existence of paracrine signalling mediators diffusing from the (disrupted) media to the adventitia, where they promote fibroblast activation; the authors suggest that insulin–like growth factor (IGF)-2 may be the mediator of medial–adventitial communication. This hypothesis of inter–compartmental communication is also supported by other studies: Kundi et al. (2009) observed that medial overexpression of SMAD-3 led to adventitial responses (myofibroblast differentiation, collagen deposition), while Goel et al. (2013) observed changes in collagen expression profile by cultured fibroblast cells exposed to medium conditioned by VSMCs exposed to TGF-β; the previous studies suggest that connective tissue growth factor (CTGF) or

IGF-2 may be signalling links between these layers. Finally, note that inter–compartment cell movement may also be taking place. Migration of adventitial (myo)fibroblasts towards the intima has been described in the context of hypertension (Humbert et al., 2004) and aneurysm (Jones et al., 2009b), which may partially explain the sustained medial levels of α-SMA and pSMAD-2 in disrupted arteries.

3.3.4 Study limitations and future work

Several gaps can be identified in the experimental design, methodology and data processing and analysis in this study; addressing them in future work will promote better characterisation of the animal model used, as well as improved understanding of arterial chemo–mechano–biology. Low numbers of mice were used in the study (n=3 per observation group, Table 3.1), which was due to the very limited time available to breed the mice (1 month gestation) and grow them up to the desired time points (1.5—4.5 months), as well as to the fact that only male mice could be used in the study (*Myh11–CreER^{T2}* was inserted in the Y chromosome). The number of samples whose data were analysed was even lower (c.f. Table A.1), which was due to no expression of the Cre recombinase in some mice (as confirmed by PCR), unsuccessful mechanical testing, and staining and sectioning artefacts (in some tissue sections the adventitia partially covered the media following sectioning, which rendered layer–specific quantification impossible); the *Dis+HT* group in IF quantification was particularly affected. In the future, increasing sample number per observation group should reduce group variability, and allow for the statistical significance of differences between groups to be computed.

Due to the limited number of inducible male mice available, monitoring of blood pressure at baseline *vs.* following induction of hypertension *via* high salt and L-NAME was performed in female littermates of the male mice used for data acquisition. As discussed in Sec. 3.3.1, this procedure was not entirely adequate: female mice are not tamoxifen–inducible (a small reduction in blood pressure following TGFBR2 disruption was reported by Li et al. (2014)); gender–specific differences exist (Bellini et al., 2015), and it is possible that male and female mice respond differently to mechanical perturbation; induction of hypertension in mice with dysfunctional TGFBR2 may lead to different values of blood pressure than in normal mice. An important future development is thus quantifying blood pressure evolution in male mice belonging to the *Dis* and *Dis+HT*

groups. Furthermore, the effects of induced hypertension were only studied here in conjunction with disruption of TGF-β signalling through TGFBR2. Teasing out the influence of hypertension *vs.* that of TGFBR2 requires a fourth, hypertension–only experimental group, which should be studied in the future.

Also related to vascular mechanics is the determination of a baseline homoeostatic state, which is related to the determination of vascular maturity. In this study, 6 weeks was initially chosen as the onset of vascular mechanical maturity (Cheng et al., 2013); however, biaxial mechanical tests using the system of Gleason et al. (2004b) resulted in tears developing during the test, and unreliable mechanical data (not shown). Supporting that 6wks was too early to establish vascular maturity, Wan and Gleason (2013) show variation in geometrical and mechanical properties in wild–type mice between 8 and 13 weeks, and Ferruzzi et al. (2016) mention unpublished observations that only at 9 weeks of age does the thoracic aorta reach over 85% of its final diameter, length and mass. In the future, it may be relevant to study in detail vascular evolution in the 6—12 week frame, so as to determine what is the most appropriate time point for baseline arterial chemo–mechano–biological levels.

The theoretical and computational tools used for biaxial mechanical data reduction and processing, in particular the algorithms for estimation of *in vivo* axial stretch, biaxial mechanical data fitting (microstructuraly–motivated SEDF Eq. (3.4), objective function Eq. (3.8)), were validated, published and extensively applied to the study of hundreds of vessel samples. In any case, continuous refinement of these tools may be necessary. In particular, note the less than optimal fits to the axial force–stretch data, Fig. 3.6—Fig. 3.7, as well as the possibility that the methods used to estimate the *in vivo* axial stretch may not be adequately applied to diseased arteries, which may not be able to optimize $\lambda_z^{i.v.}$ on energetic grounds.

Quantification of microstructure, biochemistry and cellular composition of the arterial wall was performed by PSR and IF staining of tissue sections taken from segments adjacent to the ones mechanically tested, i.e. the initial segment of the descending thoracic aorta just distal to the mechanically–tested ATA, and the renal portion of the abdominal aorta just upstream of the mechanically–tested IAA. This procedure was adopted as it was hypothesised that wall content in diffusible molecules (TGF-β ligand, MMP-2) and migratory cells (CD-45–positive immune cells) would be reduced following the mechanical testing protocol, and that it would be important to

correlate collagen levels to the levels of signalling regulators (TGF-β) and collagenases (MMP-2). However, recent observations showed that levels of proteases and immune cell markers were still elevated in perturbed arteries followed mechanical testing (M. Bersi and R. Khosravi, personal communication), so in the future it may be considered performing PSR and IF staining of vessels that were previously mechanically tested.

Being an extremely stable molecule, collagen turnover *in vivo* is a cell–mediated process (Humphrey, 2002). Therefore, the collagen maturation process hypothesised in Sec. 3.3.3 based on the observation of an evolving distribution of collagen pixel colours over time following perturbation, Fig. 3.18(b), necessarily involves the participation of vascular cells. However, the data presented in this study was not sufficient to determine the extent to which a deposition–(proteolytic) degradation mechanism and/or an adhesion–contraction remodelling mechanism contributed to the observed changes in the collagenous matrix properties. Cell–mediated collagen cross–linking is extremely important in determining the mechanical properties of the collagenous tissue, which may be altered in disease (Karsdal et al., 2013). Characterising collagen cross–linking in future studies using this animal model may provide important insight into cell–mediated collagen G&R processes.

In addition to MMP-2, CD-45, α-SMA, TGF-β1,2,3 and pSMAD-2, visualisation of several other important biochemical and cellular markers should be considered in the future. MMP-9 is a proteolytic enzyme capable of degrading elastin and collagen, and primarily secreted by infiltrating macrophages and neutrophils in perturbed arterial walls (Rizas et al., 2009). MMP-9 has been shown to act synergistically with MMP-2 in the context of aneurysm formation (Longo et al., 2002) and hypertensive arterial remodelling (Humbert et al., 2004), so quantifying the levels of this enzyme may be interesting in this animal model. Both MMP-2 and MMP-9 have elastolytic activity, and elastin degradation has been found to correlate with arterial constitutive behaviour and *in vivo* configuration (Cardamone et al., 2009; Ferruzzi et al., 2011). Quantifying elastin fibre content in the medial layer of perturbed arteries would thus contribute to establish a possibly interesting coupling between vascular mechanics and cellular/biochemical mediators; elastin quantification can be made by extracting black pixels in Verhoeff van Gieson (VVG) histological staining (Bersi et al., 2013), immunofluorescence or nonlinear optical imaging. Regulation of protease activity is carried out by tissue inhibitors of metalloproteinases (TIMPS), whose dynamics

have been associated with aneurysm (Ruddy et al., 2008) and hypertension (Jeffery and Morrell, 2002); quantifying isoforms TIMP-1 and TIMP-2, which form inhibitory complexes with MMP-9 and MMP-2 resp. (Brew et al., 2000), would allow for the estimation of the proteolytic activity of these enzymes.

Intramural accumulation of GAGs, often associated with a protein core to form proteoglycans (PGs), increases wall water content and viscoelastic dissipation, and have been associated with local delaminations conducive to large dissections in the thoracic aorta (Humphrey, 2012). Imaging intramural distributions of common PGs such as versican and/or GAGs such as hyaluronan would clarify their contribution to the increased energy dissipation (EDR, Fig. 3.16(b)) observed in perturbed ATAs. Finally, in this study it was possible to infer that the increased adventitial cellularity (DAPI–stained nuclei, Fig. 3.21(b)) occurred jointly with immune cell infiltration (CD-45, Fig. 3.22(a)) and myofibroblast differentiation (α-SMA, Fig. 3.22(b)). However, it was not possible to quantify the extent to which each cell type contributed because fibroblast population dynamics were not quantified separately; this limitation was mainly due to the absence of fibroblast markers with high specificity. Fibroblast–specific protein (FSP)-1 has been reported to be a good fibroblast marker in several fibroblast cultures (endothelium–derived (Iwano et al., 2002) and cancer–associated (Kalluri and Zeisberg, 2006)), and could be used in the future to quantify fibroblast numbers, which are expected to increase secondary to increased TGF-β levels (Akhurst and Hata, 2012). If adventitial fibroblasts in the aorta are found to express FSP-1, it might be interesting to develop an animal model analogous to the one used in this study, but where Cre recombinase would be under the control of an *Fsp1* (rather than *Myh11*) promoter (see Bhowmick et al. (2004)).

As discussed above, induction of hypertension by high salt diet and L-NAME administration has been correlated with AngII activation and induction of inflammation (Kitamoto et al., 2000). Ideally, induced inflammation should be minimal, so as to separate inflammatory–driven changes to the aortic wall from those due to TGFBR2 disruption and hypertension themselves. One possible strategy is to co–administer antioxidants that minimise L-NAME–driven reactive oxygen species production inducing AngII signalling. Usui et al. (1999) observe that administering antioxidants allopurinol, ebselen or N-acetylcysteine significantly reduces superoxide production while retaining L-NAME–induced hypertension in rats, which is confirmed for allopurinol by

Kasal et al. (2008); other studies show a reduction in (elevated) systolic blood pressure following administration of superoxide scavengers together with L-NAME (Kopkan and Majid, 2005), which may render this strategy impractical. Another strategy would be to block AngII signalling through angiotensin receptor type I (AT1) with losartan, which has been shown to attenuate aortic aneurysm progression in mice (Habashi et al., 2006). The problem with this strategy is that AngII signalling cross–talks with the TGF-β signalling axis (Habashi et al., 2011), thus might introduce further confounding factors. The best strategy in initial stages of research may simply be to monitor the levels of AngII, which is known to modulate both vascular inflammation and fibroblast–mediated adventitial remodelling (Tieu et al., 2011).

In this study, protein levels were quantified by processing IF–stained tissue sections. As discussed in Sec. 3.3.3, it is reasonable to hypothesise that soluble signalling molecules may be produced in one arterial layer and then diffuse to another according to a concentration gradient. So as to localise the transcription of genes encoding signalling proteins such as TGF-β, IGF or CTGF to a specific layer (and thus identify sources and gradients of such proteins), *in situ* hybridization (ISH) techniques could be used (e.g. Mori et al. (1999) used ISH to visualise layer–specific translation of CTGF following TGF-β stimulation).

3.3.5 Preliminary fit to 1D theoretical CMB model

In the previous sections, methods used and results obtained in this experimental study were discussed, compared with previously publish studies, correlated to other findings in the literature, and analysed in terms of limitations pointing to future work. In this section, the conceptual CMB model of cell–mediated and TGF-β–regulated arterial growth and remodelling (G&R) formulated in Chapter 2 is used to capture a few features of the data set generated in this experimental study. Rather than a rigorous fit, the work presented in this section is only meant to illustrate the ability of the CMB theoretical model to describe some of the processes taking place in the experimental animal model used, and to foster some discussion on possible synergies between theoretical and experimental approaches.

Simulation and qualitative fitting

The CMB model of cell–mediated and TGF-β–regulated arterial G&R extended to capture myofibroblast differentiation and TGF-β effects on infiltrating immune cells formulated in Sec. 2.2.2 was used to capture some features of the experimental study above. This formulation of the CMB model was chosen given the large increases in adventitial α-SMA–positive cells (suggesting the formation of a significant myofibroblast population), Sec. 3.1.5.2. As previously, the arterial wall is modelled as an axially stretched and pressurised bilayered membrane whose constitutive response is determined by the joint contributions of medial collagen and elastin and adventitial collagen; the resulting statement of mechanical equilibrium is Eq. (2.1). The turnover of adventitial collagen by adventitial (myo)fibroblasts is modelled by the chemo–biological model component, Sec. 2.2.2.2, with Eq. (2.34)—Eq. (2.44) governing the levels of adventitial cells, collagen, collagenases and collagenase inhibitors, as well as of latent and active TGF-β. Remodelling of adventitial collagen recruitment stretch is modelled by Eq. (2.46)—Eq. (2.48), with rate parameter α given by Eq. (2.49). Given that in the animal model used the medial layer is not extensively degraded (e.g. medial collagen is not greatly reduced, Fig. 3.18(a)) and thus the adventitial layer does not become the main load–bearer, adventitial attachment is not remodelled but fixed at its initial value.

All mechanical model parameter values and definitions can be found in Table 3.3. Mechanical parameter values were adapted to correspond to the IAA segment of normal C57BL/6 mice at 12 weeks (the baseline for experimental data analysis). Values for unloaded radius, unloaded thickness, medial to adventitial thickness ratio, systolic and diastolic blood pressures, unloaded axial length and loaded biaxial stretches were taken from 12wks *Ctrl* IAA values, Table A.1. Loaded wall thickness following cell–driven G&R was further computed by the CMB model for comparison with experimental measurements. Following Chen (2014), loaded thickness at systole is computed from the loaded biaxial stretch ratios λ_θ^s,λ_z using incompressibility, and considering a volumetric growth factor $V(t)/V_0$,

$$h^s = \frac{V(t)}{V_0} \cdot \frac{H}{\lambda_\theta^s \lambda_z}, \tag{3.15}$$

with $V(t)/V_0$ computed by assuming constant density of each layer by

$$\frac{V(t)}{V_0} = \frac{\left(\phi_M^E m_M^E + \phi_M^C m_M^C\right) V_{M,0} + m_A^C V_{A,0}}{V_{M,0} + V_{A,0}}, \tag{3.16}$$

where m_M^E, m_M^C, m_A^C are normalised mass densities, and the dry weight mass fractions of medial elastin and collagen (ϕ_M^E,ϕ_M^C) and the initial unloaded volumes of the media and adventitia ($V_{M,0}$,$V_{A,0}$) are given by

$$\phi_M^E = \frac{m_M^E}{m_M^E + m_M^C} \qquad \phi_M^C = \frac{m_M^C}{m_M^E + m_M^C}, \tag{3.17}$$

$$\begin{aligned} V_{M,0} =& \pi \left(R_{o,0}\, \lambda_{\theta,0}^s - \frac{H_{A,0}}{\lambda_{\theta,0}^s \lambda_z} \right)^2 \lambda_z L_z - \pi \left(R_{o,0}\, \lambda_{\theta,0}^s - \frac{H_0}{\lambda_{\theta,0}^s \lambda_z} \right)^2 \lambda_z L_z, \\ V_{A,0} =& \pi \left(R_{o,0}\, \lambda_{\theta,0}^s \right)^2 \lambda_z L_z - \pi \left(R_{o,0}\, \lambda_{\theta,0}^s - \frac{H_{A,0}}{\lambda_{\theta,0}^s \lambda_z} \right)^2 \lambda_z L_z, \quad \text{where} \quad H_{A,0} = \frac{1}{3} H_0. \end{aligned} \tag{3.18}$$

Parameter values for the rate constants in the ODEs governing the levels of cellular and biochemical levels were not altered (Table 2.5, Table 2.6), except for a small set that was modified such that the following experimental targets for the *Dis+HT* IAAs were reached:

Quantitative target: Predicted ratio between maximum remodelled thickness following the introduction of an hypertensive stimulus to the signalling perturbation group and initial thickness should be equal to the ratio of *in vivo* thickness of *Dis+HT* IAAs at 14 weeks to baseline (1.75, Fig. 3.12(b))

Qualitative targets: (i) predicted loaded thickness should display an increased value following introduction of hypertension, and then decrease (Fig. 3.12(b)); (ii) collagen levels should increase to large values during the simulated period (Fig. 3.18(a)); (iii) levels of collagenases and myofibroblasts should be initially increased and then return to approx. baseline (c.f. adventitial MMP-2 density, Fig. 3.21(a), and α-SMA density, Fig. 3.22(b)); (iv) TGF-β levels should be initially elevated and then only slightly reduced at the end of the study (c.f. concentration of TGF-β ligand in Fig. 3.23(a)).

To computationally simulate the perturbations to vascular homoeostasis applied in the experimental study, two strategies were employed. Firstly, the effects of perturbing TGF-β signalling in medial VSMCs by conditional disruption of TGFBR2 on the adventitia (whose chemo–mechano–biology is described by the CMB framework) are modelled by an exogenous source of active TGF-β to the adventitia. As discussed in Sec. 3.3.3, it is hypothesised that medial and adventitial cells communicate through diffusible signalling mediators (e.g. IGF-2, CTGF), which cross–talk with the TGF-β signalling axis and amplify its pro–fibrotic action (Leask and Abraham, 2006).

For simplicity and in the absence of specific data, this exogenous source of TGF-β signalling is mathematically modelled here by a Bateman function, which is commonly used in pharmacokinetics to describe the dynamics of a first order absorption, first order excretion process in a single compartment (Garrett, 1994). In particular,

$$c_A^{\beta,exog}(\tilde{t}) = c_0 \cdot \left(e^{-k_e \tilde{t}} - e^{-k_a \tilde{t}}\right), \tag{3.19}$$

where $\tilde{t} = t - t_0$ is the time after onset of application of exogenous TGF-β, and c_0, k_e, k_a were chosen such that a maximum level of $c_A^{\beta,exog} = 0.00025$ was present at an intermediate time ($t = 14$), followed by a small reduction at later time points (c.f. qualitative target above). The resulting concentration of exogenous TGF-β, Fig. 3.26, was added at each time point to the endogenous TGF-β levels governed by Eq. (2.38). Secondly, induced hypertension was modelled by prescribing a step increase in systolic blood pressure levels at $t = HT_{onset}$ to hypertensive levels (2wks of hypertension, Table 3.2), which was sustained until the end of simulation.

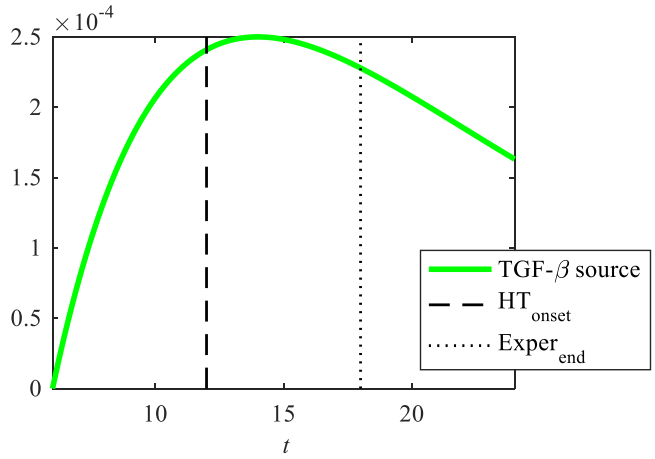

Figure 3.26: **Exogenous adventitial TGF-β source.** HT_{onset} refers to the onset of the hypertensive stimulus (12wks), while $\text{Exper}_{\text{end}}$ refers to the last time point in the experimental study (18wks).

Three simulation cases were considered: first, an exogenous adventitial TGF-β source according to Eq. (3.19) was introduced at the beginning of simulation, modelling the effects of TGFBR2 disruption alone (*Dis* experimental group); second, in addition to the prescribed exogenous TGF-β source, an hypertensive step was added to the exogenous TGF-β source at $t = HT_{onset}$ and held constant throughout simulation, modelling changes in *Dis+HT* vessels; third, an hypertensive step was applied as before but without introducing an additional source of TGF-β, thus modelling a fourth, hypertension–only group (not studied experimentally). Pilot parameter studies were run to determine a small set of parameters whose values should be adjusted to meet the simulation targets above, Table 3.3. So as to mimic the experimental timeline, simulation was started

Table 3.3: **CMB model fitting to experimental data.** Parameter symbols, definitions and values.

Parameter	Definition	Value [unit]	Notes
R_o	Unloaded outer radius	267.16 μm	computed from unloaded outer diameter of 12wks *Ctrl* IAA, Table A.1
H	Unloaded thickness	87.31 μm	12wks *Ctrl* IAA, Table A.1
$H_M : H$	Medial to total unloaded thickness ratio	2/3	
P^s	Baseline systolic blood pressure	126.98 mmHg	Table 3.2
P^s_{HT}	Hypertensive systolic blood pressure	138.24 mmHg	2 weeks post–HT induction, Table 3.2
L_z	Unloaded axial length	3.79 mm	12wks *Ctrl* IAA, Table A.1
$\lambda_z^{i.v.}$	*In vivo* axial stretch	1.66	12wks *Ctrl* IAA, Table A.1
$\lambda_{\theta,0}^{i.v.}$	Initial *in vivo* circumferential stretch		computed from unloaded and loaded outer diameters at 12wks *Ctrl* IAA, Table A.1
$\alpha^C_{A,0}$	Baseline rate of adventitial collagen recruitment stretch remodelling	0.5	adjustment to simulation time scale
T_{AT}	Collagen stretch averaging time period for attachment stretch remodelling	∞	No attachment stretch remodelling in either layer
r_{f_2}	Fibroblast population dynamics sensitivity to TGF-β	0.1	Avoiding excessive fibroblast proliferation
r_{f_4}	Rate of TGF-β and tension–driven fibroblast to myofibroblast differentiation	75	Avoiding excessive fibroblast proliferation
r_{m_1}	Rate of TGF-β and tension–driven fibroblast to myofibroblast differentiation	100	Formation of significant myofibroblast population
r_{c_2}	Rate of TGF-β–driven increase in collagen deposition by fibroblasts	0.5	To reach qualitative targets
r_{c_3}	Rate of baseline collagen deposition by myofibroblasts	20	To reach quantitative thickness target
r_{c_4}	Rate of TGF-β–driven increase in collagen deposition by myofibroblasts	10	To reach quantitative thickness target
r_{ca_2}	Rate of TGF-beta–driven down–regulation in collagenase secretion by fibroblasts	0.5	To reach qualitative targets
r_{ca_3}	Rate of baseline collagenase secretion by myofibroblasts	10	To reach quantitative thickness target
$r_{\beta l_2}$	Rate of latent TGF-β secretion by fibroblasts in response to deviations from mechanical homoeostasis of the wall	10	To reach qualitative targets
c_0	Scaling constant	0.0015895	
k_a	Absorption rate constant	0.153855	
k_e	Elimination rate constant	0.1	
t_0	Initial simulation time	6	
HT_{onset}	Time for onset of application of hypertensive stimulus	12	
$Exper_{end}$	Last time point in experimental model	18	
t_{sim}	Total simulation time	24	

at $t = t_0 = 6$ arbitrary time units (corresponding to experimental weeks), the hypertensive step was introduced at $t = HT_{onset} = 12$, the end of the experiment was marked at $t = Exper_{end} = 18$, and the simulation until $t = t_{sim} = 24$.

Theoretical predictions

Fig. 3.27 below displays the evolution of several structural and mechanical quantities predicted by the conceptual CMB model for the three simulation cases: TGF-β exogenous source only ("Dis", green), TGF-β source and hypertensive step ("Dis+HT", blue), and hypertensive step only ("HT", red). Adventitial collagen mass density increases for all simulation cases, Fig. 3.27(a). TGF-β signalling disruption alone leads to a sustained increase in adventitial collagen levels to approx. 50% baseline, which is likely due to the profibrotic action of TGF-β. The hypertension–only case displays a much smaller and transient increase in collagen mass. However, the combination

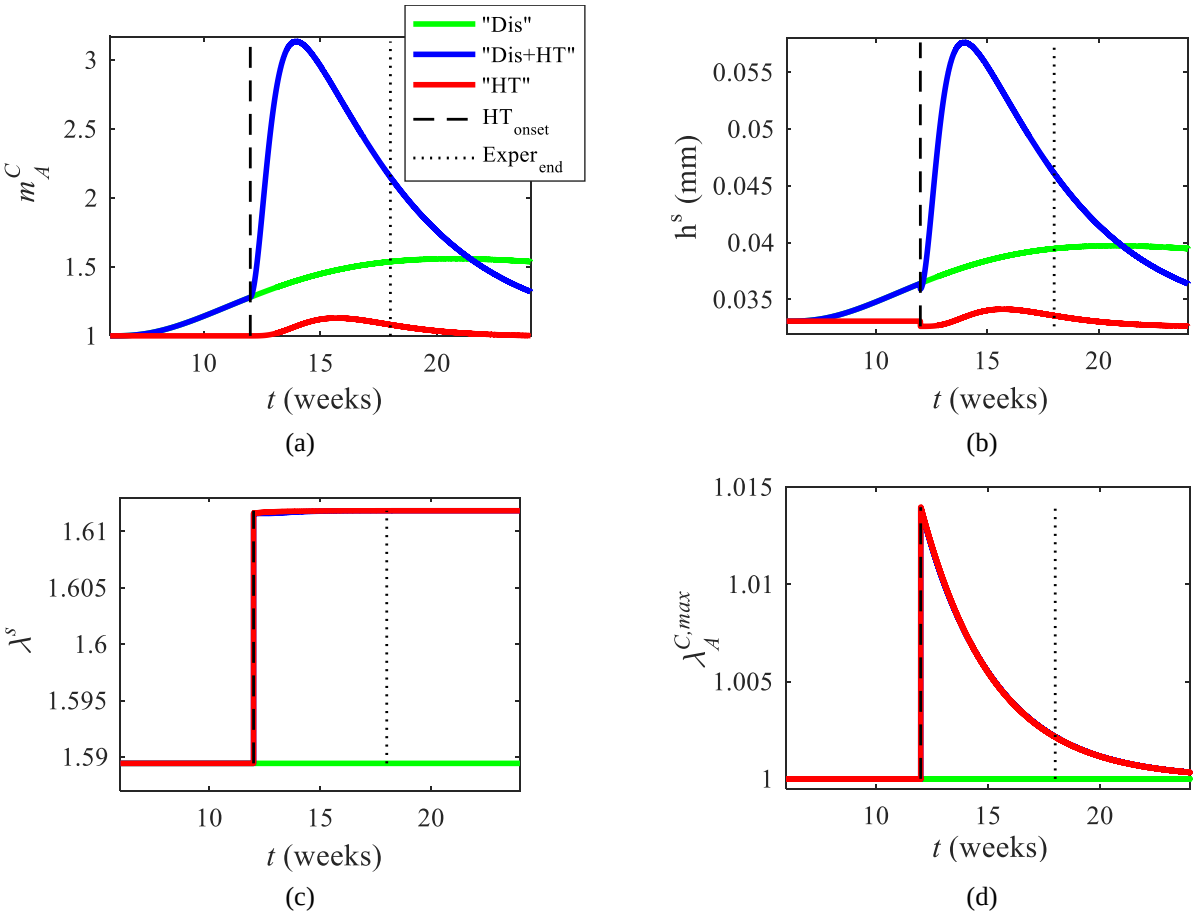

Figure 3.27: **Preliminary fit to 1D CMB model — Mechanical and geometrical variables.** 1D CMB model fitting some features of the experimental data set. Adventitial collagen normalised mass density m_A^C (a), loaded wall thickness at systole h^s (b), circumferential stretch ratio at systole λ^s (c) and maximum adventitial collagen fibre stretch at systole $\lambda_A^{C,max}$ (d) are plotted for TGFBR2 disruption–only (*Dis*, green curve), TGFBR2 disruption and hypertension (*Dis+HT*, blue curve) and hypertension–only (*HT*, red curve) cases. HT_{onset} refers to the onset of the hypertensive stimulus (12wks), while $\text{Exper}_{\text{end}}$ refers to the last time point in the experimental study (18wks).

of both increased adventitial TGF-β signalling and hypertension lead to a very large increase in collagen levels, which reduces at later time points. Loaded thickness at systole and $\lambda_z^{i,v.}$ display the same trends, Fig. 3.27(b), which is not surprising given that the remodelled thickness is a function of elastin and collagen mass densities by Eq. (3.15), and the levels of medial fibres do not change. In addition, note the small reduction in h^s the hypertension–only case at $t = 12$, which is due to the hypertensive step applied at this time period. Note also that the quantitative target of loaded thickness was met, with $\max\{h^s\} = (h^{MAP}_{IAA,Dis+HT}(14\text{wks})/h^{MAP}_{IAA,Ctrl}(12\text{wks})) \times h^s_0 = 1.75 \times 33\mu m \simeq 57\mu m$.

The CMB model predicts a step increase in circumferential stretch for the simulation cases where an hypertensive step was applied, Fig. 3.27(c) (N.B. the "Dis+HT" and "HT" curves almost overlap), while no change is visible in the TGF-β signalling disruption–only case. Moreover, in both cases involving stretching of adventitial collagen fibres ($\lambda_A^{C,max} > 1$) as a result of induced

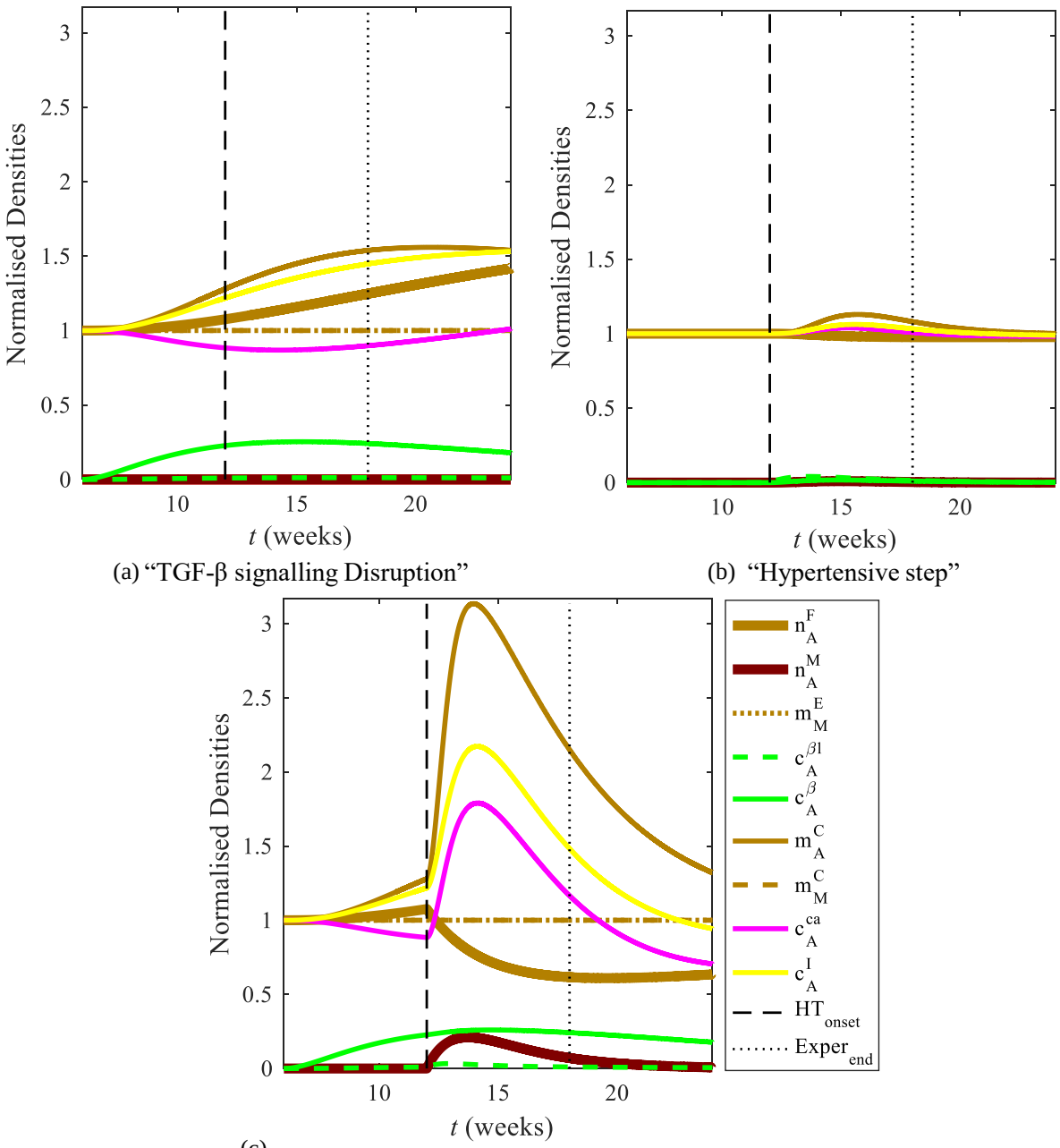

(a) "TGF-β signalling Disruption" (b) "Hypertensive step"

(c) "TGF-β signalling Disruption + Hypertensive step"

Figure 3.28: **Preliminary fit to 1D CMB model — chemo–biological variables.** 1D CMB model fitting some features of the experimental data set. Normalised mass, molar and number densities of cellular and biochemical species are plotted for TGFBR2 disruption–only (a), hypertension–only (b) and TGFBR2 disruption and hypertension (c) simulation cases. $\mathrm{HT}_{\mathrm{onset}}$ refers to the onset of the hypertensive stimulus (12wks), while $\mathrm{Exper}_{\mathrm{end}}$ refers to the last time point in the experimental study (18wks).

hypertension, the CMB model predicts that $\lambda_A^{C,max}$ returns to the homoeostatic value of $\lambda_A^{AT,max} = 1$ (N.B. the attachment stretch is not remodelled), Fig. 3.27(d); this follows from remodelling the recruitment stretch distribution via Eq. (2.46)—Eq. (2.48).

The evolution of the levels of biomolecular and cellular species predicted by the CMB model for the three simulation cases is shown in Fig. 3.28. In the TGF-β signalling disruption case, Fig. 3.28(a), the large and sustained increase in adventitial TGF-β (solid green curve) is clear,

which is promoted by the exogenous TGF-β source described by Eq. (3.19). TGF-β levels increased from baseline induce a profibrotic response, with increased fibroblast numbers (thick brown curve), increased adventitial collagen (thin solid brown curve), decreased collagenases (magenta curve) and increased inhibitors of collagenases (yellow curve). The hypertension–only case, Fig. 3.28(b), is also characterised by a profibrotic response (note the increased adventitial collagen density); however, this is transient and reaches a much smaller extent. Note also the small increase in latent TGF-β levels (dashed green curve), which shows that this profibrotic response was secondary to transduction of the hypertensive step by mural adventitial fibroblasts (rather than induced by exogenous TGF-β, as previously).

Levels of cellular and biochemical mediators predicted by the CMB model for the "Dis+HT" case are shown in Fig. 3.28(c). Firstly, it is clear that the adventitial response to the applied signalling and mechanical perturbations is much more significant than for either "Dis"– or "HT"–only cases, which suggests a synergistic action of these two stimuli. Fibroblast to myofibroblast differentiation may explain this observation. Myofibroblast differentiation requires the presence of both active TGF-β (which is elevated due to the exogenous source) and matrix straining (which is promoted by the hypertensive step) (Tomasek et al., 2002); the simultaneous presence of these stimuli in the "Dis+HT" case results in a significant increase in myofibroblast levels (thick maroon curve, qualitative target), and a corresponding decrease in their fibroblast cell source (thick light brown curve), which was included in the CMB model via terms r_{f_4} and r_{m_1} in Eq. (2.34) and Eq. (2.40), resp. Fully differentiated myofibroblasts extensively deposit collagen (Hinz, 2010); the CMB model captured this behaviour, with results showing a strong profibrotic response following the appearance of a sizeable myofibroblast population, including a large increase in collagen (thin brown curve, qualitative target) and collagenase inhibitors (yellow curve) levels, and a smaller increase followed by return to baseline of collagenase density (magenta curve, qualitative target). A transient profibrotic response is driven by a transient myofibroblast population, which increases following perturbation and then reduces to approx. baseline (qualitative target).

Remarks on preliminary fit to 1D CMB model

The CMB model of arterial G&R including TGF-β–regulated collagen metabolism and myofibroblast differentiation developed in Sec. 2.2.2 was applied to capture some features of the

experimental data set presented in this chapter. Disruption of TGF-β signalling in the media was assumed to promote increased TGF-β signalling in the adventitia (c.f. hypothesis of inter–compartmental communication proposed by Li et al. (2014)), and was modelled by a source of exogenous TGF-β in the adventitia governed by a Bateman function; hypertension was modelled by introducing a step increase in intraluminal blood pressure. A small set of model parameter values was then chosen such that model results following both perturbations would be consistent with experimental findings for IAAs in the *Dis+HT* group; this segment was chosen because its geometry is much closer to the idealised cylindrical geometry included in the mechanical component of the theoretical model.

CMB model predictions following biochemical and mechanical perturbations successfully match the set targets, in particular adventitial thickening (Fig. 3.27(b) *vs.* Fig. 3.12(b)), collagen levels (Fig. 3.27(a) *vs.* Fig. 3.18(a)) and densities of collagenase/MMP-2, α-SMA/myofibroblasts and active TGF-β ligand (Fig. 3.28(c) *vs.* Fig. 3.21(a), Fig. 3.22(b), Fig. 3.23(a), resp.). Moreover, the CMB model predicts an exuberant fibrotic response to a combination of increased TGF-β levels and wall overstretching secondary to hypertension, which is much larger than the summation of the effect of each perturbation. This predicted behaviour is consistent with the large effect of inducing hypertension in combination with TGFBR2 disruption observed experimentally (c.f. *Dis vs. Dis+HT* arteries). Furthermore, the CMB model suggests that this synergy between disrupted TGF-β signalling and induced hypertension in stimulating a strong adventitial fibrotic response is mediated by myofibroblast differentiation, which is consistent with large increases in adventitial α-SMA signal.

Rather than an accurate fit, this section only attempted to illustrate how the previously developed CMB model could be applied to successfully describe some features of the experimental data set. This exercise was important for two reasons. Firstly, it allowed for the identification of opportunities for CMB model development. Fig. 3.27(c) shows that systolic circumferential stretch is predicted to remain constant following hypertension–driven wall stretching. However, experimental results show that this quantity is slightly decreased 2 weeks after induction of hypertension, and then slightly recovers 4 weeks after (Fig. 3.13(a)); this reduction in loaded circumferential stretch was suggested to be related to a change in mechanical operating point following increased medial collagen deposition (Fig. 3.18(a)) and possibly medial elastin degra-

dation, Sec. 3.3.3. Turnover of medial elastin and collagen were not modelled here, as the CMB model was specifically developed for conditions where the media was degraded and the adventitia would take the dominant load–bearing role. This is not the case in this study, where medial lamellar structure is largely unchanged (see Fig. 3.19), and the initially unstretched adventitial collagen never becomes significantly load–bearing (note a collagen stretch following the hypertensive step of under 1.5%, Fig. 3.27(d)). In the future, specifically modelling VSMC–mediated medial collagen turnover under the influence of TGF-β signalling and immune cell action should be included in the model. In addition, the CMB model does not include any description of axial stretch remodelling, while this quantity is clearly reduced in this animal model (Fig. 3.13(b)); λ_z remodelling has been suggested to be an important strategy for arteries to reduce wall stress in response to perturbation (Humphrey et al., 2009). Note also that the CMB model mechanical component uses a nonlinear elastic membrane formulation for the arterial wall, which may not be adequate to describe the thickened IAAs in the *Dis+HT* group observed here, whose loaded thickness to inner radius ratio is over 10% (Table A.1 and Fig. 3.10).

In addition to suggesting important refinements to CMB model formulation, the modelling strategy presented here also suggests interesting applications for a combined experimental–theoretical approach. Further than running simulation cases to match experimental groups (*Dis* and *Dis+HT* cases), a theoretical model also allows for the simulation of alternative experimental conditions such as the "hypertension–only" case. As discussed in Sec. 3.3.4, this experimental group is essential to tease out the influence of disrupted TGF-β signalling from that of induced hypertension. The CMB model predicts that in this case only a minor adventitial fibrotic response will be elicited, and that it is the synergy of increased TGF-β signalling with hypertension–induced wall overstretching that gives rise to the large fibrotic response observed in the *Dis+HT* group. This result further supports the need for experimentation with a *HT* group. Not only can the theoretical model be used to predict alternative experimental conditions, it can also be used to infer what behaviour could be observed before, after or in between experimental time points; this was illustrated here by running the computational simulation for 6 "weeks" past the final experimental time point at $t = Exper_{end} = 18$. These interpolations/extrapolations should always be considered critically, but in any case they may suggest that interesting behaviour could be found at alternative time points, warranting experimental exploration.

3.4 CONCLUSION

The experimental study detailed in this chapter presents one of the only multi–dimensional data sets characterising arterial chemo–mechano–biological response to a combination of biochemical signalling and mechanical perturbations available in the literature. In addition to being consistent with previous work, this study sheds light on layer– and segment–specific changes secondary to the combination of TGFBR2 disruption and hypertension in two divergent aortic segments. Important processes underlying adventitial mechanobiological response were uncovered: increased adventitial TGF-β levels following disruption of medial TGF-β signalling; formation of a large α-SMA–positive cell population in the adventitia that is consistent with myofibroblast differentiation; and a strong synergy between increased TGF-β signalling (secondary to TGFBR2 disruption) and deviation from mechanical equilibrium (secondary to induction of hypertension) in promoting adventitial fibrotic response. In addition to its descriptive value, this experimental data set is invaluable to support the development and refinement of the CMB model formulated in Chapter 2 and upgraded to 3D in Chapter 4. A preliminary fit of the 1D CMB model to some features of the experimental data suggested that the model is well–suited to capture the evolution of biochemical mediators and cell populations mediating collagen metabolism and wall thickening. These results support the pursuit of an integrative theoretical–experimental approach to studying arterial chemo–mechano–biology.

CHAPTER 4

CMB MODEL UPDATE TO 3D: TOWARDS A CMB–FSG COMPUTATIONAL FRAMEWORK

Advanced 3D multi–physics computational frameworks for simulation of arterial mechanobiology have been developed, generally using non–mechanistic evolution laws. In this chapter, the 1D CMB model of arterial tissue G&R formulated in Chapter 2 is coupled to the 3D FEM–based structural solver of Watton et al.'s fluid–solid–growth (FSG) loop (Sec. 4.1). The arterial wall is described as a pressurised and axially stretched nonlinear elastic fibre–reinforced membrane (Sec. 4.1.1). Adventitial collagen mass density is computed by a system of ODEs modelling TGF-β profibrotic signalling and fibroblast–mediated matrix turnover, while collagen fibre recruitment and attachment configurations evolve according to biologically–informed laws (Sec. 4.1.2). The 3D CMB model is used to simulate saccular aneurysm development and response to profibrotic therapy (Sec. 4.1.3). Simulation results (Sec. 4.2) show that initially enlarging aneurysms can be stabilised by adventitial reinforcement and adaption to load–bearing (Sec. 4.2.1). Applying a "therapeutic" TGF-β step increases the magnitude of this adventitial response, which promotes earlier stabilisation of smaller aneurysms (Sec. 4.2.2). Modelling approach and results are then discussed (Sec. 4.3). The novel 3D implementation is an important improvement to the CMB model, as it allows for the computation of highly heterogeneous spatial distributions of mechanical, biochemical and cellular quantities in complex, non–axisymmetrical geometries (Sec. 4.3.2). Coupling haemodynamics to arterial mechanobiology, and modelling biomolecular transport should be pursued (Sec. 4.3.3). The 3D CMB model presented here is the first step towards the development of a fully coupled 3D CMB–FSG framework able to simulate arterial mechanobiological response to solid and fluid mechanical perturbations in health and disease (Sec. 4.4).

Several conceptual models of arterial growth and remodelling (G&R) have been implemented in advanced multi–physics computational frameworks for simulation of arterial wall fluid and solid mechanics in realistic 3D geometries, Sec. 1.3.3. In this chapter, the 1D CMB model of cell–mediated, TGF-β–regulated arterial wall G&R formulated in Chapter 2 is updated to 3 dimensions by coupling its chemo–biological component to the structural solver of Watton et al.'s Fluid–Solid–Growth (FSG) framework Watton et al. (2009a, 2011); Aparício et al. (2014).

4.1 METHODS: UPDATING THE CMB MODEL TO 3D

The FSG computational framework is a multi–physics platform that simulates arterial wall geometry, blood flow and microstructural composition, Fig. 4.1. The arterial wall is modelled as a pressurised and axially stretched nonlinear bilayered membrane. Displacement fields and surface geometries are computed at specific pressures by a custom–developed FEM structural analysis code, Fig. 4.1(A); loaded surface geometry (*solid domain*) is extracted. The simulation domain (yellow in Fig. 4.1(A)) is then integrated into a realistic (patient–specific) domain, and the intraluminal space (*fluid domain*) is automatically meshed with ANSYS ICEM (Canonsburg, PA, USA). Physiologically realistic and site–specific inlet flow rate and outlet pressure boundary conditions computed by software suite @neufuse are then applied to each flow surface, and the flow is simulated using ANSYS CFX, Fig. 4.1(B). Haemodynamic parameters on the flow domain surface are then interpolated at the nodal points of the solid domain mesh using Tecplot 360 (Bellevue, WA, USA). Fluid and solid mechanical quantities are thus available at each node, Fig. 4.1(C). These quantities are then passed to evolution laws governing the G&R of microstructural arterial constituents, Fig. 4.1(D). Updated levels of (load–bearing) arterial wall constituents influence the constitutive response of the wall, whose loaded geometry is re–computed; the FSG loop is then run iteratively, simulating arterial evolution.

In this study, the FSG simulation discussed above is supplemented by the chemo–biological model component developed in Chapter 2 (green section in Fig. 4.1). This conceptual description of cell–mediated, TGF-β–regulated collagen G&R replaces the biomechanics–based evolution equations previously used. The increased level of biological detail aims at expanding the range of mechanobiological processes included in the FSG loop, which can thus be used to predict the evolving spatial distributions of tissue properties that determine arterial evolution (possibly leading to catastrophic events) and its response to chemo–biological therapy. As a first step towards this goal, only the solid mechanical problem is considered here (note faded CFD box in Fig. 4.1). Coupling metrics of the fluid flow to the evolution of specific cellular and/or biochemical species is straightforward and should be explored in the future, especially with guidance from experimental studies.

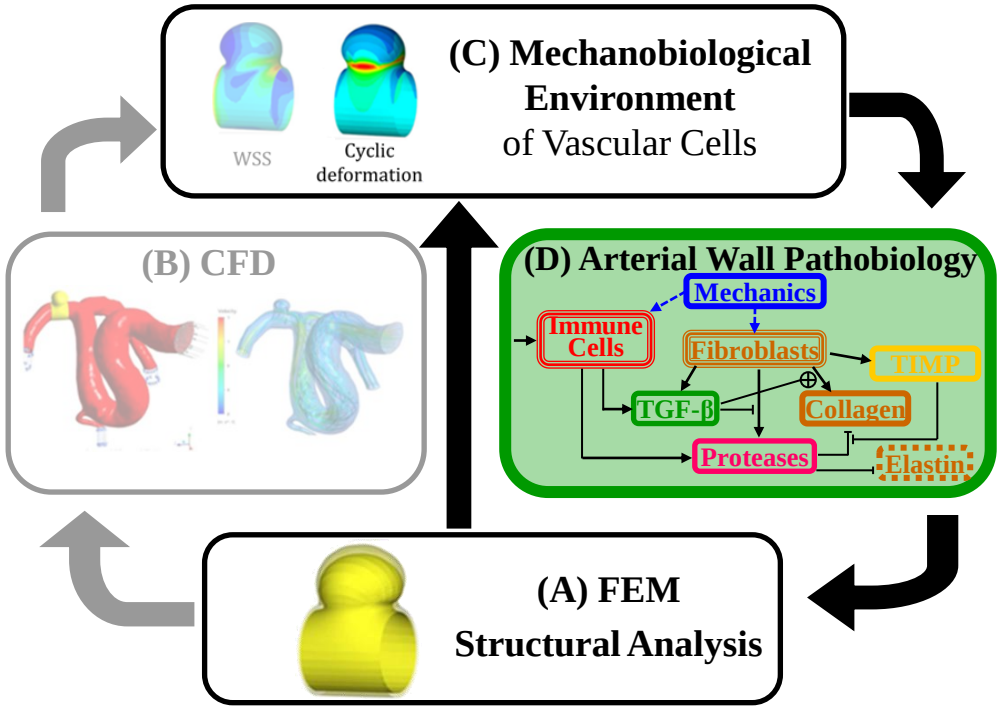

Figure 4.1: **FSG simulation framework for modelling arterial evolution in health and disease.** In this work, the chemo–biological model formulated in Chapter 2 replaces the previously formulated biomechanics–based collagen growth law (green box), and the fluid flow is not considered (faded box).

4.1.1 Arterial mechanics

The mechanical description of the arterial wall used here is based on the work of Watton et al. (2004) and later developed by Watton et al. (2011); Aparício et al. (2014); Chen (2014). The arterial wall is modelled as a bilayered nonlinear elastic membrane in 3D, which is initially cylindrical with radius R, thickness H and axial length L_1 and perimeter $L_2 = 2\pi R$; a material Lagrangian coordinate system is used, with $\theta_1 \in [0, L_1]$ and $\theta_2 \in [0, 2\pi R[$ being the axial and circumferential coordinates, resp., Fig. 4.2(a). The arterial wall is then internally pressurised to pressure P (in particular systolic P^s and diastolic P^d pressures), and axially stretched by factor λ_z; if arterial wall material properties are not changed, the loaded geometrical domain is still cylindrical, with loaded radius $r_P = \lambda^P R$, thickness $h^P = H/(\lambda_z \lambda^P)$ and length $l_1 = \lambda_z L_1$.

Mechanical equilibrium The displacement field of each lattice point is computed from static mechanical equilibrium by the principle of stationary potential energy (Holzapfel, 2000), which requires that at equilibrium the total potential energy Π (with contributions from both internal Π_{int} and external Π_{ext} potential energies) is stationary; in variational form,

$$\delta\Pi = \delta\Pi_{\text{int}} - \delta\Pi_{\text{ext}} = 0. \tag{4.1}$$

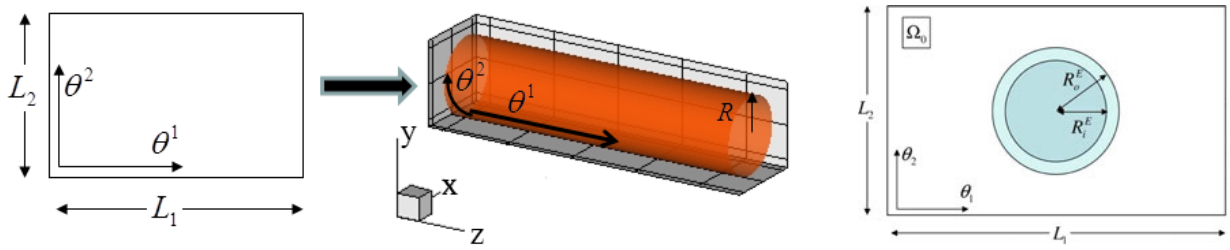

(a) (b)

Figure 4.2: **Simulation and elastin degradation domains.** Definition of (a) material Lagrangian coordinates (reproduced from Aparício et al. (2014), Copyright ©2014 John Wiley & Sons, Ltd.), and (b) elastin degradation domain (reproduced from Watton et al. (2011), with permission from Springer).

Watton (2002) showed that in a bilayered cylindrical artery (composed of media M and adventitia A) of small thickness subject to internal pressurisation Eq. (4.1) can be written as

$$\int_0^{2\pi R}\int_0^{L_1} \left[H_M\delta\Psi_M + H_A\delta\Psi_A - P(\boldsymbol{a}_1\times\boldsymbol{a}_2)\cdot\delta u_i\boldsymbol{A}_i\right] d\theta_1 d\theta_2 = 0, \tag{4.2}$$

where Ψ_M, Ψ_A are the strain energy density functions (SEDFs) characterising each layer, p is the intraluminal pressure, $\boldsymbol{A}_i, \boldsymbol{a}_i$ $(i = 1,2)$ are covariant basis vectors tangent to coordinate curves θ_i in the undeformed and deformed configurations, resp., and u_i is the midplane displacement along direction θ_i (N.B. it is assumed that the displacement field and thus SEDFs are constant through thickness). In this study, surface deformations are quantified by Green–Lagrange (GL) strains, which can be computed from the planar covariant basis vectors by

$$E_{ij} = \frac{1}{2}\left(\boldsymbol{a}_i\cdot\boldsymbol{a}_j - \boldsymbol{A}_i\cdot\boldsymbol{A}_j\right), \qquad i = 1,2. \tag{4.3}$$

Using the definition $\boldsymbol{E} = (1/2)(\boldsymbol{C} - \boldsymbol{I})$ ($\boldsymbol{C}$: right Cauchy–Green deformation tensor; $\mathbf{I}$: identity tensor) and taking into account that $C_{ii} = \lambda_i^2$ in pure stretch, it follows that stretches and GL strains of (collagen) fibres aligned along direction θ_i are related by $\lambda_i = \sqrt{2E_{ii}+1}$.

Constitutive model Following Watton et al. (2009b) and similarly to Sec. 2.1.1.2, the arterial wall is modelled mechanically as a bilayered nonlinear elastic membrane. Medial constitutive response is determined by both isotropic and linearly elastic elastin, which is modelled as a neo–Hookean material, and highly nonlinear collagen ECM (Holzapfel et al., 2000). Two collagen fibre families are considered, positively ($p = +$) and negatively ($p = -$)–wound fibres with angle $\gamma_{M_p} = \pm 30^\circ$ with respect to θ_2. Multiplying each term by the normalised mass densities of collagen and elastin in this layer, m_M^E and $m_{M_p}^C$, resp., the medial SEDF thus becomes

$$\Psi_M = m_M^E K_M^E(E_{11}+E_{22}+E_{33}) + \sum_{p=\pm;\ E_{M_p}^C>0} m_{M_p}^C \Psi_M^C\left(E_{M_p}^C\right), \tag{4.4}$$

where E_{ii} are the GL strains of elastin, $E^C_{M_p}$ the GL strains of medial collagen fibre families, k^E_M a material parameter, and $\Psi^C_M(E^C_{M_p})$ the SEDF for medial collagen. Adventitial constitutive response is determined by the highly nonlinear collagen matrix. Two double–helical collagen fibre families with angles $\gamma_{A_p} = \pm 45°$ are introduced, whose normalised mass densities $m^C_{A_p}$ are coupled to the chemo–biological model component below. The adventitial SEDF is

$$\Psi_A = \sum_{p=\pm;\ E^C_{A_p}>0} m^C_{A_p} \Psi^C_A\left(E^C_{A_p}\right), \tag{4.5}$$

where $E^C_{A_p}$ are the GL strains of adventitial collagen fibre families, and $\Psi^C_A(E^C_{A_p})$ is the SEDF for adventitial collagen.

Ψ^C_L $(L = M, A)$ formulation is similar to that in Sec. 2.1.1.2. Analogously to Eq. (2.3), each collagen fibre is assumed to have a linear stress–strain response, and thus a quadratic SEDF $\tilde{\Psi}^C_{L_p} = K^C_{L_p}(E^C_{L_p})^2$, where $K^C_{L_p}$ are material parameters. The distribution of collagen recruitment stretches is modelled by the triangular probability density function (PDF) $\rho(\lambda^R_{L_p})$ in Eq. (2.5), and the nonlinear constitutive response of the collagen matrix emerges as the result of gradual fibre recruitment,

$$\Psi^C_{L_p}\left(E^C_{L_p}\right) = \int_1^{\lambda_{L_p}} \underbrace{K^C_{L_p}\left(E^C_{L_p}\right)^2}_{\tilde{\Psi}^C_{L_p}} \rho(\lambda^R_{L_p}) d\lambda^R_{L_p}, \tag{4.6}$$

where $\lambda^C_{L_p} = \lambda_{L_p}/\lambda^R_{L_p}$ are collagen fibre stretches, $\lambda^R_{L_p}$ the corresponding recruitment stretch, and λ_{L_p} domain stretches resolved in the direction of collagen fibre families (c.f. Eq. (4.7)).

Deformation metrics Elastin GL strains E_{ij} $(i, j = 1, 2)$ refer to the unloaded configuration and are computed by solving Eq. (4.2) for $\boldsymbol{a}_1, \boldsymbol{a}_2$ and using Eq. (4.3). Resolving these strains in the directions of medial $(E_{M_p}(\theta_1, \theta_2, t))$ and adventitial $(E_{A_p}(\theta_1, \theta_2, t))$ collagen fibre families,

$$\begin{aligned} E_{M_p} &= E_{11}\sin^2\gamma_{M_p} + E_{22}\cos^2\gamma_{M_p} + 2E_{12}\sin\gamma_{M_p}\cos\gamma_{M_p}, \\ E_{A_p} &= E_{11}\sin^2\gamma_{A_p} + E_{22}\cos^2\gamma_{A_p} + 2E_{12}\sin\gamma_{A_p}\cos\gamma_{A_p}. \end{aligned} \tag{4.7}$$

Collagen fibre GL strains $E^C_{M_p}(\theta_1, \theta_2, t)$, $E^C_{A_p}(\theta_1, \theta_2, t)$ are computed with respect to the configuration at which collagen fibres are recruited to load bearing, and are thus given by

$$E^C_{M_p} = \frac{E_{M_p} - E^R_{M_p}}{1 + 2E^R_{M_p}}, \qquad E^C_{A_p} = \frac{E_{A_p} - E^R_{A_p}}{1 + 2E^R_{A_p}}, \tag{4.8}$$

where collagen recruitment strains are computed from their corresponding recruitment stretch ratios $\lambda^R_{M_p}(\theta_1,\theta_2,t)$, $\lambda^R_{A_p}(\theta_1,\theta_2,t)$ by

$$E^R_{M_p} = \frac{1}{2}\left(\left(\lambda^R_{M_p}\right)^2 - 1\right), \qquad E^R_{A_p} = \frac{1}{2}\left(\left(\lambda^R_{A_p}\right)^2 - 1\right). \tag{4.9}$$

4.1.2 Arterial tissue growth and remodelling

The chemo–biological model component developed in Chapter 2 is adapted here to model cell–mediated, TGF-β–regulated arterial G&R in 3D. In particular, the CMB model extended to capture myofibroblast differentiation, Sec. 2.2.2, is used; this choice was informed by the large increases in myofibroblast marker α-SMA observed in the adventitias of mechanically–perturbed arteries, Chapter 3. In the 1D model, the evolution of normalised densities of microstructural, biochemical and cellular species was governed by Eq. (2.34)—Eq. (2.44), remodelling of collagen recruitment stretch was modelled by Eq. (2.46)—Eq. (2.48), and adaption of the attachment stretch distribution was computed by Eq. (2.9)—Eq. (2.11). Some changes to the previous equations are introduced here to allow for their implementation and tractability in 3D.

Elastin degradation In this study, the arterial system initially at mechanobiological equilibrium is perturbed by prescribed elastin degradation. Extensive elastin degradation secondary to increased proteolytic load driven by immune cell infiltration is a common finding in late stage intracranial (Mehra et al., 2011) and abdominal (Sakalihasan et al., 2011) aneurysms. Modelling saccular aneurysm inception, elastin is prescribed to degrade in a circular patch with unloaded inner R^E_i and outer R^E_o radius, Fig. 4.2(b). In the inner region ($\theta_1 \in [0, L_1], \theta_2 \in [0, L_2[$: $(\theta_1 - L_1/2)^2 + (\theta_2 - L_2/2)^2 \leq (R^E_i)^2$), elastin normalised mass density evolves according to

$$m^E_M(\theta_1,\theta_2,t) = 1 - \left(1 - m^E_{M,\min}(t)\right)\cdot\left\{\exp\left[-\omega_1\left(\frac{\theta_1 - L_1/2}{L_1/2}\right)^2\right]\cdot\exp\left[-\omega_2\left(\frac{\theta_2 - L_2/2}{L_2/2}\right)^2\right]\right\}, \tag{4.10}$$

where parameters ω_1, ω_2 control the degree of localisation of the degradation function and $m^E_{M,\min}$ represents the minimum concentration of elastin at time t, which, by construction, is located at $(\theta_1,\theta_2) = (L_1/2, L_2/2)$. Following Watton et al. (2011), minimum elastin concentration decays exponentially according to

$$m^E_{M,\min}(t) = (m^E_{T_E})^{t/T_E} \qquad \text{for} \qquad 0 \leq t \leq T_E, \tag{4.11}$$

where $m^E_{T_E}$ is the final normalised concentration for $t \geq T_E$, and $m^E_{\min}(t = 0) = 1$. Outside the elastin degradation region $m^E_M = 1$ everywhere and at all times, and in the circular section

$(R_i^E)^2 < \theta_1 \in [0, L_1], \theta_2 \in [0, L_2[\ : \ (\theta_1 - L_1/2)^2 + (\theta_2 - L_2/2)^2 < (R_o^E)^2$ elastin concentration is interpolated linearly. Note that elastin normalised mass density is directly prescribed by Eq. (4.10), and thus ODEs governing levels of elastin (Eq. (2.43)), elastase–degrading enzymes (Eq. (2.42)) and immune cells (Eq. (2.41)) in the 1D CMB model are not used here.

Collagen growth In response to loss of elastin load–bearing capacity, the adventitial layer assumes an increasingly important load–bearing role. This process elicits microstructural adaptations, which involve cell–mediated deposition and degradation of adventitial collagen fibres under the regulation of signalling pathways such as TGF-β. In this initial 3D study and for simplicity, collagen is considered to grow in the adventitia only. Accordingly, the ODE in Eq. (2.35) governs the normalised mass density levels of adventitial collagen fibre families, which are assumed to vary together: $m_A^C := m_{A_+}^C = m_{A_-}^C$; medial collagen mass density does not change, and thus $m_M^C := m_{M_+}^C = m_{M_-}^C = 1, \forall\, t$ (Eq. (2.44) is not used here). The final set of ODEs governing the evolution of microstructural, cellular and biochemical variables is

$$\frac{dn_A^F}{dt}(\theta_1,\theta_2,t) = (r_{f_1} + r_{f_2}\cdot c_A^\beta)\cdot n_A^F - (r_{f_3} + r_{f_4}\cdot f(\lambda^{cell})\cdot c_A^\beta)\cdot n_A^F \tag{4.12}$$

$$\frac{dm_A^C}{dt}(\theta_1,\theta_2,t) = (r_{c_1} + r_{c_2}\cdot c_A^\beta)\cdot n_A^F + (r_{c_3} + r_{c_4}\cdot c_A^\beta)\cdot n_A^M - (r_{c_6}\cdot c_A^{ca})\cdot m_A^C \tag{4.13}$$

$$\frac{dc_A^{ca}}{dt}(\theta_1,\theta_2,t) = \left(\frac{r_{ca_1}}{1 + r_{ca_2}\cdot c_A^\beta}\right)\cdot n_A^F + (r_{ca_3} + r_{ca_4}\cdot c^\beta)\cdot n_A^M - (r_{ca_5} + r_{ca_6}\cdot c_A^I)\cdot c_A^{ca} \tag{4.14}$$

$$\frac{dc_A^I}{dt}(\theta_1,\theta_2,t) = (r_{I_1} + r_{I_2}\cdot c_A^\beta)\cdot n_A^F + (r_{I_3} + r_{I_4}\cdot c_A^\beta)\cdot n_A^M - (r_{I_5} + r_{I_6}\cdot c_A^{ca})\cdot c_A^I \tag{4.15}$$

$$\frac{dc_A^{\beta l}}{dt}(\theta_1,\theta_2,t) = \left(\frac{r_{\beta l_1}\cdot c_A^\beta + r_{\beta l_2}\cdot f(\lambda^{cell})}{1 + r_{\beta l_3}\cdot m_A^C}\right)\cdot n_A^F - (r_{\beta l_5} + r_{\beta l_7}\cdot f(\lambda^{cell})\cdot n_A^M)\cdot c_A^{\beta l} \tag{4.16}$$

$$\frac{dc_A^\beta}{dt}(\theta_1,\theta_2,t) = (r_{\beta_1} + r_{\beta_3}\cdot f(\lambda^{cell})\cdot n_A^M)\cdot c_A^{\beta l} - r_{\beta_4}\cdot c_A^\beta \tag{4.17}$$

$$\frac{dn_A^M}{dt}(\theta_1,\theta_2,t) = (r_{m_1}\cdot f(\lambda^{cell})\cdot c_A^\beta)\cdot n_A^F - \left(\frac{r_{m_2}}{1 + r_{m_3}\cdot f(\lambda^{cell}) + r_{m_4}\cdot c_A^\beta}\right)\cdot n_A^M. \tag{4.18}$$

Note that terms r_{c_5}, r_{I_7}, $r_{\beta l_4}$, $r_{\beta l_6}$, r_{β_2} are not included in the equations, but the numbering of the remaining rate constants is maintained for consistency. Note also that, according to Sec. 2.2.2.2, time is adimensional, with $\Delta t = 2$ being the characteristic time for degradation of most (over 90%) medial elastin. The mechanotransduction functional $f(\lambda^{cell})$ coupling deviations from mechanical homoeostasis to (myo)fibroblast cell response is

$$f(\lambda^{cell}) = f(\lambda^C - \lambda_{hom}^C) = f(\lambda^C - \lambda^{AT}) = \frac{\lambda_{A_+}^{C,\max}|_{\mathrm{MAX}} - \lambda_{A_+}^{AT,\max}}{\lambda_{A_+}^{AT,\max}}, \tag{4.19}$$

where $\lambda_{A_+}^{AT,\max} = \lambda_{A_+}^{C,\max}|_{\text{MAX}}(\theta_1,\theta_2,t=0)$ is the collagen attachment stretch and $\lambda_{A_+}^{C,\max}|_{\text{MAX}} = \max\left\{\lambda_{A_+}^{C,\max}|_{sys}, \lambda_{A_+}^{C,\max}|_{dias}\right\}$ denotes maximum collagen stretches evaluated in the systolic ($\lambda_{A_+}^{C,\max}|_{sys}$) and diastolic ($\lambda_{A_+}^{C,\max}|_{dias}$) configurations (collagen stretches are computed from collagen strains by $\lambda_{L_p}^{C} = \sqrt{2E_{L_p}^{C}+1}$, with $L = M, A; p = \pm$).

Remodelling of collagen recruitment stretch In addition to mediating collagen metabolism, mural cells also regulate collagen fibre properties that strongly influence collagenous tissue constitutive response. Remodelling of collagen fibre natural configuration for load–bearing is modelled here for each fibre family. Following Watton et al. (2004), it is assumed that recruitment stretches $\lambda^R = \lambda/\lambda^C$ are remodelled so as to allow collagen fibre stretches λ^C to return to their homoeostatic (or *attachment*) values $\lambda_{hom}^{C} := \lambda^{AT}$. Adapting the previous reasoning to a 3D framework, medial and adventitial ($L = M, A$, resp.) collagen fibre families are modelled to display distributions of recruitment stretches modelled by piecewise triangular PDFs; similarly to the 1D CMB model implementation (Eq. (2.46)—Eq. (2.48)), the minimum (min), mode (mode) and maximum (max) salient points of these distributions evolve according to

$$\frac{d\lambda_{L_p}^{R,\min}}{dt}(\theta_1,\theta_2,t) = \alpha\left(\frac{\lambda_{L_p}^{C,\max}|_{\text{MAX}} - \lambda_{L_p}^{\text{AT,max}}}{\lambda_{L_p}^{\text{AT,max}}}\right), \tag{4.20}$$

$$\frac{d\lambda_{L_p}^{R,\text{mode}}}{dt}(\theta_1,\theta_2,t) = \alpha\left(\frac{\lambda_{L_p}^{C,\text{mode}}|_{\text{MAX}} - \lambda_{L_p}^{\text{AT,mode}}}{\lambda_{L_p}^{\text{AT,mode}}}\right), \tag{4.21}$$

$$\frac{d\lambda_{L_p}^{R,\max}}{dt}(\theta_1,\theta_2,t) = \alpha\left(\frac{\lambda_{L_p}^{C,\min}|_{\text{MAX}} - \lambda_{L_p}^{\text{AT,min}}}{\lambda_{L_p}^{\text{AT,min}}}\right), \tag{4.22}$$

where $\lambda_{L_p}^{C,k}|_{MAX} = max\left\{\lambda_{L_p}^{C,k}|_{sys}, \lambda_{L_p}^{C,k}|_{dias}\right\}$, and $k = \min, \max, \text{mode}$. Unlike in Sec. 2.2.2, rate parameter α is a constant and does not depend on the levels of any cellular/biochemical species; this simplification was made to avoid instability effects, as discussed in Sec. 2.2.1.

Adaption of collagen attachment stretch The increasingly load–bearing role assumed by the adventitia as the media is degraded is modelled here by a rightwards shift in the distribution of adventitial collagen attachment stretches. Similarly to the 1D model (Eq. (2.9)—Eq. (2.11)), integral laws are used to compute the evolution of the salient points of the attachment stretch distribution as running averages of the corresponding collagen fibre stretches,

$$\lambda_{A_p}^{AT,\min}(\theta_1,\theta_2,t) = \frac{1}{T_{AT}}\cdot\left(\int_{t-T_{AT}}^{t}\lambda_{A_p}^{C,\min}|_{MAX}(\theta_1,\theta_2,\tau)d\tau\right), \tag{4.23}$$

$$\lambda_{A_p}^{AT,\text{mode}}(\theta_1,\theta_2,t) = \frac{1}{T_{AT}} \cdot \left(\int_{t-T_{AT}}^{t} \lambda_{A_p}^{C,\text{mode}} |_{MAX}\,(\theta_1,\theta_2,\tau) d\tau \right), \tag{4.24}$$

$$\lambda_{A_p}^{AT,\text{max}}(\theta_1,\theta_2,t) = \frac{1}{T_{AT}} \cdot \left(\int_{t-T_{AT}}^{t} \lambda_{A_p}^{C,\text{max}} |_{MAX}\,(\theta_1,\theta_2,\tau) d\tau \right), \tag{4.25}$$

where T_{AT} is the averaging time period (for simplicity, no dependence on (myo)fibroblast levels is included). The width and skew of the distribution are not altered (i.e., $f_{narrow}^{min} = f_{skew}^{mode} = 0$ in Eq. (2.10), Eq. (2.11)). So as to allow for the formation of a reasonably–sized aneurysm, Eq. (4.23)—Eq. (4.25) are only activated for $t \geq t_0^{AT}$, before which adventitial collagen attachment stretches are held fixed at their initial values. Angles γ_{L_p} are always defined in the unloaded configuration, and collagen fibre reorientation is not modelled.

Three different types of equilibrium are mentioned below. *Mechanical equilibrium* refers to static mechanical equilibrium governed by the force–balance equation in Eq. (4.2) and based on the principle of stationary potential energy. *Material equilibrium* refers to the (adventitial) collagen fibres being strained at their homoeostatic value, which implies that the collagen fibre stretch λ^C computed from Eq. (4.8) equals collagen fibre attachment stretch λ^{AT}, Eq. (4.23)—Eq. (4.25). *Chemo-mechano-biological equilibrium* refers to the densities of microstructural, biochemical and cellular quantities reaching steady state, or, equivalently, that all rates on the left hand–sides of Eq. (4.12)—Eq. (4.18) are zero.

4.1.3 Computational implementation

Parameter values Parameter symbols, values and definitions can be found in Table 4.1. Geometrical, material and microstructural parameter values closely follow Watton et al. (2011) and Chen (2014), with some adjustments for consistency with the previously formulated CMB model, c.f. Sec. 2.1.1.5. Briefly, systolic and diastolic pressures of 120mmHg and 80mmHg, resp., were initially prescribed. Material constants and collagen fibre families angles were informed by literature observations (Watton et al., 2009b) and further based on the assumptions that, under physiological conditions, only the media was load–bearing, and that in this layer elastin would bear 80% of the total load. Unloaded radius and thickness are consistent with human internal carotid artery dimensions (Watton et al., 2011). Initial values for recruitment and collagen fibre (i.e., attachment) stretches were computed similarly to Sec. 2.1.1.5. Medial collagen fibres are assumed to bear load during the cardiac cycle, i.e. $\lambda_{M_p}^{AT,\text{max}} > 1$; here, a symmetric triangular distribution with

$\lambda_{M_p}^{AT,\max} = 1.1$ and width 0.1 is considered, and thus $\lambda_{M_p}^{AT,\min} = 1.0$, $\lambda_{M_p}^{AT,\mathrm{mode}} = 1.05$. Adventitial collagen fibre families are prescribed to be initially deposited in a crimped state under physiological conditions, which requires $\lambda_{A_p}^{AT,\max}(t=0) \leq 1$; a symmetric triangular distribution of width 0.1 is assumed, and thus $\lambda_{A_p}^{AT,\min}(t=0) = 0.9$, $\lambda_{A_p}^{AT,\mathrm{mode}}(t=0) = 0.95$, and $\lambda_{A_p}^{AT,\max}(t=0) = 1.0$. Initial recruitment stretches for medial and adventitial collagen fibre families ($L = M, A$) are computed by

$$\lambda_{L_p}^{R,\min}(t=0) = \frac{\lambda_{L_p}|_{sys}(t=0)}{\lambda_{L_p}^{C,\max}(t=0)} = \frac{\sqrt{\left(\lambda_0^{sys}\right)^2 \cos^2\gamma_{L_p} + \lambda_z^2 \sin^2\gamma_{L_p}}}{\lambda_{L_p}^{AT,\max}(t=0)}, \tag{4.26}$$

$$\lambda_{L_p}^{R,\mathrm{mode}}(t=0) = \frac{\lambda_{L_p}|_{sys}(t=0)}{\lambda_{L_p}^{C,\mathrm{mode}}(t=0)} = \frac{\sqrt{\left(\lambda_0^{sys}\right)^2 \cos^2\gamma_{L_p} + \lambda_z^2 \sin^2\gamma_{L_p}}}{\lambda_{L_p}^{AT,\mathrm{mode}}(t=0)} \tag{4.27}$$

$$\lambda_{L_p}^{R,\max}(t=0) = \frac{\lambda_{L_p}|_{sys}(t=0)}{\lambda_{L_p}^{C,\min}(t=0)} = \frac{\sqrt{\left(\lambda_0^{sys}\right)^2 \cos^2\gamma_{L_p} + \lambda_z^2 \sin^2\gamma_{L_p}}}{\lambda_{L_p}^{AT,\min}(t=0)}. \tag{4.28}$$

Note that only adventitial attachment stretches are adaptive, and thus $\lambda_{M_p}^{AT}(t=0) = \lambda_{M_p}^{AT}, \forall\, t$.

Values of G&R parameters R_i^E, R_o^E, T_E, T_{AT}, t_0^{AT} and α are numerically determined to allow for the development of fairly large aneurysms that are still distant from the ends of the simulation domain $\{0, L_1\}$ to avoid boundary effects. All rate parameters included in the ODEs in Eq. (4.12)—Eq. (4.18) governing the evolution of biochemical and cellular quantities are given the same values as for the 1D CMB model in Sec. 2.2.2 (with the exception of $r_{f_4} = r_{m_1} = 1$, to prevent excessive myofibroblast differentiation); see Table 2.5 and Table 2.6. Initial conditions for these normalised densities are set to 1 for all species, except those initially absent from the wall (myofibroblasts and latent and active TGF-β), which are set to 0.

Simulation loop Following variable initialisation, the arterial surface geometry is meshed using $48 \times 72 = 3456$ rectangular elements. The displacement field of each surface node at systolic and diastolic pressures is computed by numerically solving the mechanical equilibrium, Eq. (4.2), using a custom–built FEM code in FORTRAN 77 (see Watton (2002); Watton et al. (2004) for details on the structural analysis computational routines and numerical solution). GL strains are then computed at each node by Eq. (4.3), from which strains of each collagen fibre family are computed via Eq. (4.7)—Eq. (4.8). Elastin degradation is computed in the elastin degradation region ($\theta_1 \in [0, L_1], \theta_2 \in [0, L_2[\ :\ (\theta_1 - L_1/2)^2 + (\theta_2 - L_2/2)^2 < (R_o^E)^2$) via Eq. (4.10)—Eq. (4.11). Collagen strains are converted to stretches and passed to the chemo–biological model compo-

nent, which computes the new levels of cellular and biochemical species determining the updated normalised mass density of adventitial collagen fibres, Eq. (4.12)—Eq. (4.18). Collagen recruitment stretch distributions for each collagen fibre family are updated via Eq. (4.20)—Eq. (4.22), and if $t \geq t_0^{AT}$ adventitial collagen attachment stretch distribution is updated using Eq. (4.23)—Eq. (4.25). Updated values of collagen recruitment strains and densities of load–bearing collagen and elastin are updated in the SEDF of each layer, Eq. (4.4) and Eq. (4.5). This locally altered

Table 4.1: **3D CMB model parameters.** Symbols, definitions and values.

Parameter	Definition	Value [unit]
Unloaded geometry		
R	Unloaded radius	1.5mm
H	Unloaded thickness	$R/5 = 0.3$mm
H_M	Medial layer unloaded thickness	$(2/3)H = 0.2$mm
H_A	Adventitial layer unloaded thickness	$(1/3)H = 0.1$mm
L_1	Unloaded axial length	12mm
L_2	Unloaded circumferential length (perimeter)	$2\pi R = 12.57$mm
Applied loads / deformations		
p^{sys}	Systolic pressure	120mmHg ≃ 16kPa
p^{dias}	Diastolic pressure	80mmHg ≃ 10.67kPa
l_1	Loaded axial length	16mm
λ_z	Axial stretch	1.3
Material parameters		
K_M^E	Medial new-Hookean material stiffness (elastin, VSMCs)	133.80kPa
K_M^C	Medial collagen fibre material stiffness	1.96kPa
K_A^C	Adventitial collagen fibre material stiffness	7.84kPa
Attachment stretches		
$\lambda_{M_\pm}^{AT,\min}$	Medial collagen, minimum	1.0 (constant)
$\lambda_{M_\pm}^{AT,\text{mode}}$	Medial collagen, mode	1.05 (constant)
$\lambda_{M_\pm}^{AT,\max}$	Medial collagen, maximum	1.1 (constant)
$\lambda_{A_\pm}^{AT,\min}(t=0)$	Adventitial collagen, minimum	0.9
$\lambda_{A_\pm}^{AT,\text{mode}}(t=0)$	Adventitial collagen, mode	0.95
$\lambda_{A_\pm}^{AT,\max}(t=0)$	Adventitial collagen, maximum	1.0
Recruitment stretches (t=0)		
$\lambda_{M_\pm}^{R,\min}(t=0)$	Medial collagen, minimum	1.16 (Eq. (4.26))
$\lambda_{M_\pm}^{R,\text{mode}}(t=0)$	Medial collagen, mode	1.22 (Eq. (4.27))
$\lambda_{M_\pm}^{R,\max}(t=0)$	Medial collagen, maximum	1.28 (Eq. (4.28))
$\lambda_{A_\pm}^{R,\min}(t=0)$	Adventitial collagen, minimum	1.28 (Eq. (4.26))
$\lambda_{A_\pm}^{R,\text{mode}}(t=0)$	Adventitial collagen, mode	1.35 (Eq. (4.27))
$\lambda_{A_\pm}^{R,\max}(t=0)$	Adventitial collagen, maximum	1.42 (Eq. (4.28))
G&R parameters		
R_i^E	Inner elastin degradation radius	$0.6L_1/2 = 4.8$mm
R_o^E	Outer elastin degradation radius	$0.8L_1/2 = 3.6$mm
T_E	Time for complete elastin degradation	4
$m_{T_E}^E$	Elastin density at $t = T_E$ in inner degradation region	0.01
$\omega_{1,2}$	Elastin degradation localisation parameters	1
α	Rate of collagen recruitment stretch remodelling	4.7
T_{AT}	Averaging period for adv. attachment stretch computation	$\{1, 5, 10\}$
t_0^{AT}	Onset time for adaption of collagen attachment stretch	3
Simulation parameters		
t_{end}	Final simulation time	8
Δt	Time increment between consecutive simulation steps	0.01
t_β	Time for application of TGF-β step (Sec. 4.2.2)	2
β_{step}	Magnitude of applied TGF-β step (Sec. 4.2.2)	0.1

constitutive response results in different wall displacement fields, which are again computed by structural analysis. This simulation loop is iteratively run at each simulation step (fixed increment Δt) until final simulation time t_{end} is reached.

4.2 Results: 3D CMB model numerical studies

The 3D implementation of the chemo–biological model coupled to the structural solver of Watton et al.'s FSG loop was described above. This 3D CMB model was then applied to model geometrical, microstructural, biochemical and cellular variables underlying saccular aneurysm development, Sec. 4.2.1, and their responses to the application of a profibrotic stimulus, Sec. 4.2.2. For all simulation cases, elastin degradation is prescribed in a circular patch, giving rise to a localised bulge on the arterial wall. G&R processes promote further enlargement (remodelling of collagen recruitment configuration), but also stabilisation (increased collagen density and adaption of adventitial collagen attachment stretch distribution). Re–attainment of chemo-mechano-biological equilibrium and thus aneurysm stabilisation is expected to depend strongly on how fast the adventitia adapts to load–bearing following medial degradation. Adventitial attachment stretch distribution is allowed to adapt for $t \geq t_0^{AT} = 3$, and three rates of adaption are studied: fast ($T_{AT} = 1$, Sec. 4.2.1), intermediate and slow ($T_{AT} = 5, 10$, resp., Sec. 4.2.2). To investigate *in silico* the effects of applying a profibrotic stimulus, a step in the concentration of active TGF-β of $\beta_{step} = 0.1$ is applied at $t_\beta = 2$ for the simulation cases in Sec. 4.2.2.

4.2.1 Saccular aneurysm development

In this section, the development and stabilisation of a saccular aneurysm is simulated. Fig. 4.3 shows the evolving distributions of mechanical and microstructural quantities at the arterial surface. Medial elastin is prescribed to degrade in a circular patch at the centre of the domain, Fig. 4.3(a), reaching near zero values at the centre of the domain at $t = 2$, which then extends to the edges of the domain at $t = 3$. Loss of medial load–bearing capacity results in larger displacements of the nodes in the elastin degradation region, which appears as a slight bulge in the loaded configuration. This increased deformation is quantified by the axial (E_{11}, Fig. 4.3(b)) and circumferential (E_{22}, Fig. 4.3(c)) components of the GL strain tensor, which in the elastin degradation region attain maximum values of approx. 2.3 and 3.6, resp., at $t = 3$; E_{11} and E_{22} remain constant

afterwards, which signals that stabilisation was attained.

The predicted adventitial G&R response following medial degradation impacts two microstructural properties of the wall. First, adventitial collagen fibre density increases, Fig. 4.3(d). Increases of up to 15% can be seen at $t = 4$, which promote wall reinforcement and aneurysm stabilisation; further increases of over 25% are seen at $t = 6$, and are necessary for chemo-mechano-

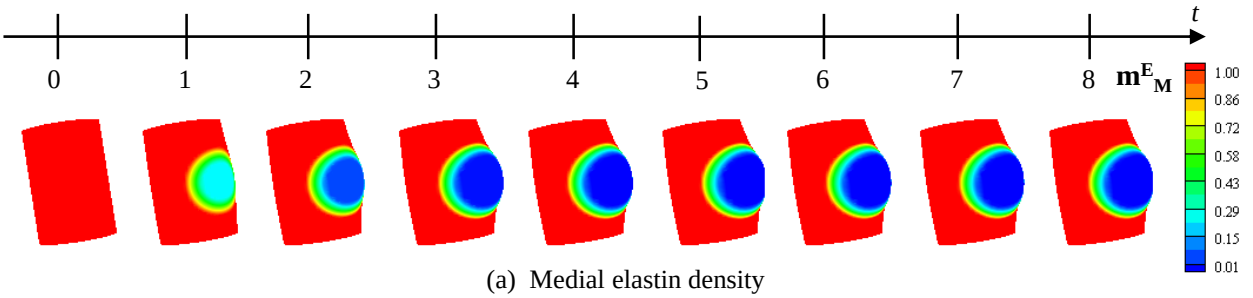

(a) Medial elastin density

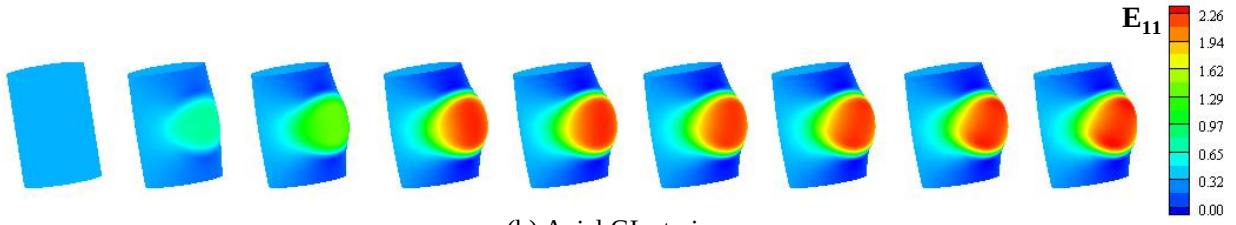

(b) Axial GL strain

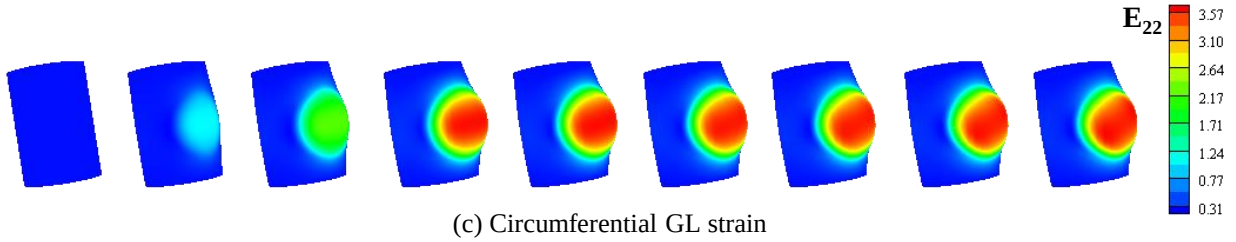

(c) Circumferential GL strain

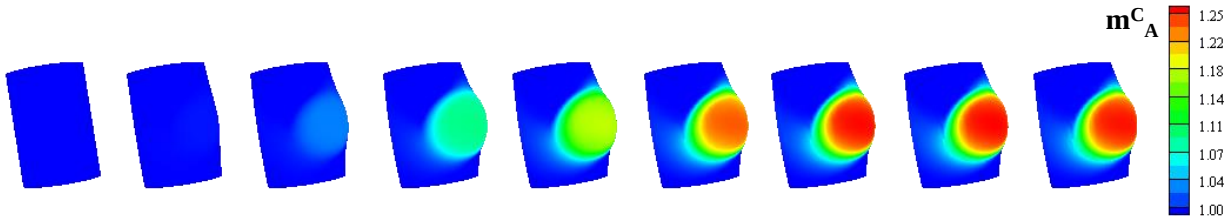

(d) Adventitial collagen density

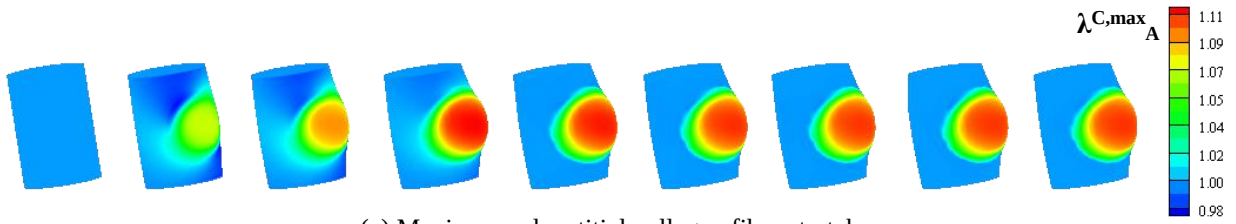

(e) Maximum adventitial collagen fibre stretch

Figure 4.3: **3D CMB modelling saccular aneurysm development — mechanical variables.** (a) Medial elastin density, (b) axial GL strain, (c) circumferential GL strain, (d) adventitial collagen density, and (e) maximum adventitial collagen fibre stretch.

biological equilibrium to be reached. Second, initially unstretched adventitial collagen fibres ($\lambda_A^{C,\max}(t=0)=1$) become load–bearing, reaching a (physiologically realistic) maximum value of approx. 1.11 at $t=3$, Fig. 4.3(e). From this point on, adventitial collagen stretch starts to decrease to its homoeostatic attachment stretch level, but then stabilises at under 1.10 for the later time points (i.e., material equilibrium is reached). The observation that $\lambda_A^{C,\max}>1$ at the new steady state captures the changing role of the adventitia to load–bearing, which was modelled here and for the first time by an adaptive collagen attachment stretch distribution governed by system dynamics, Eq. (4.25).

The temporal evolution of cellular and biochemical species underlying adventitial collagen growth response is shown in Fig. 4.4. Following elastin degradation and loss of medial load–bearing capacity ($0\leq t\leq 2$), fibroblasts are seen to respond to the resultant over–straining of the adventitia. Fibroblast density starts to increase visibly from $t=3$ onwards, reaching a maximum increase of approx. 80% with respect to baseline at $t=7$, Fig. 4.4(a). The larger fibroblast population is also responsible for an increased concentration of collagenases (c_A^{ca}, Fig. 4.4(b)) and collagenases inhibitors (c_A^I, Fig. 4.4(c)), which points to faster collagen metabolism. Note that at each time point collagenase levels are slightly smaller than those of their inhibitors (particularly clear at $t=6$), which points to a slightly reduced collagenolytic load; this effect, together with increased adventitial collagen production by fibroblasts, explains the increased collagen levels seen in Fig. 4.3(d).

Adventitial profibrotic response is regulated by the signalling factor TGF-β, whose latent form is secreted by adventitial fibroblasts following mechanical perturbation; upon activation, TGF-β regulates fibroblast phenotype. The model predicts a visible increase in latent TGF-β immediately after medial degradation and adventitial engagement, reaching its peak at $t=3$, Fig. 4.4(d). As material equilibrium is reached between $t=3$ and $t=4$ (i.e. collagen stretch converges to its homoeostatic attachment stretch target), Fig. 4.3(e), fibroblasts reduce the secretion of this signalling mediator, and its levels decay and reach zero at $t=6$. TGF-β activation slightly delays the rise and fall in active TGF-β levels, Fig. 4.4(e) (e.g. note that active TGF-β is still visible at $t=7$). Moreover, latent TGF-β degradation competes with its activation, which explains why active TGF-β levels are always lower than those of latent TGF-β (e.g. peak active TGF-β levels are over 2 times smaller than latent TGF-β peak levels). In any case, note that both forms of

TGF-β are only present transiently, which is consistent with TGF-β's role as a transient mechanotransducer. A comparison between system behaviour predicted by the 1D *vs.* 3D CMB model implementations will be presented in Sec. 4.3.1.

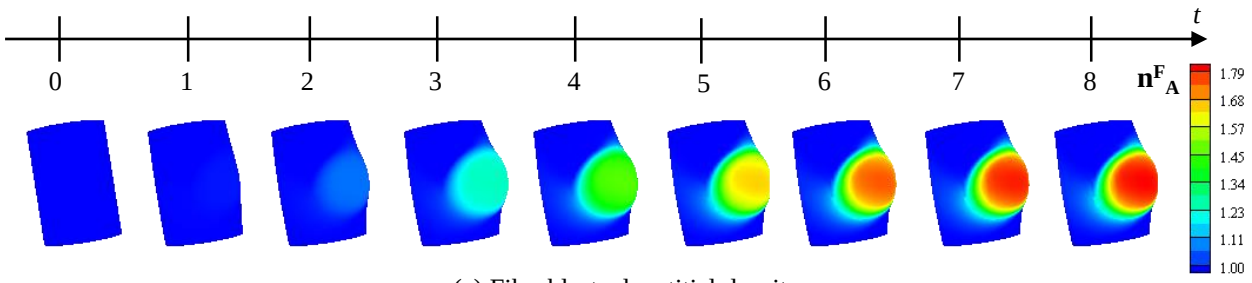

(a) Fibroblast adventitial density

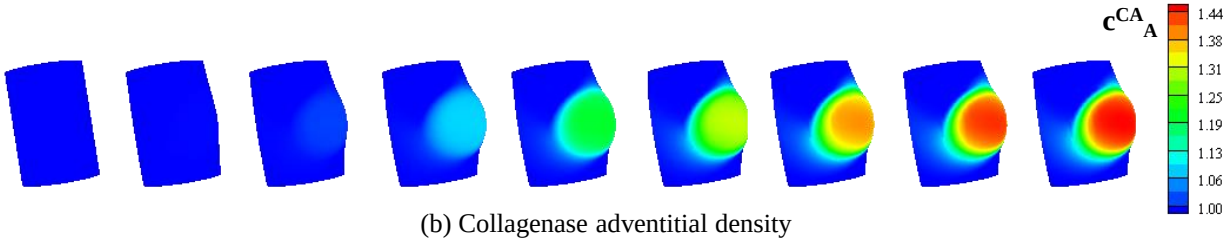

(b) Collagenase adventitial density

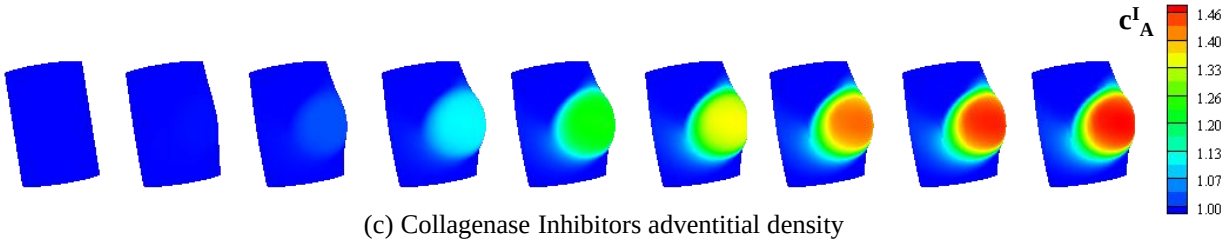

(c) Collagenase Inhibitors adventitial density

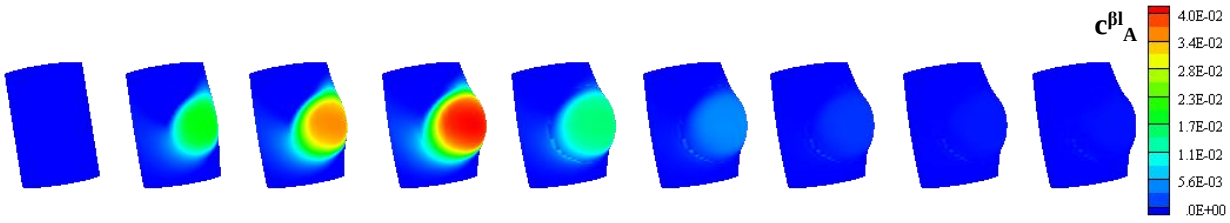

(d) Latent TGF-β adventitial density

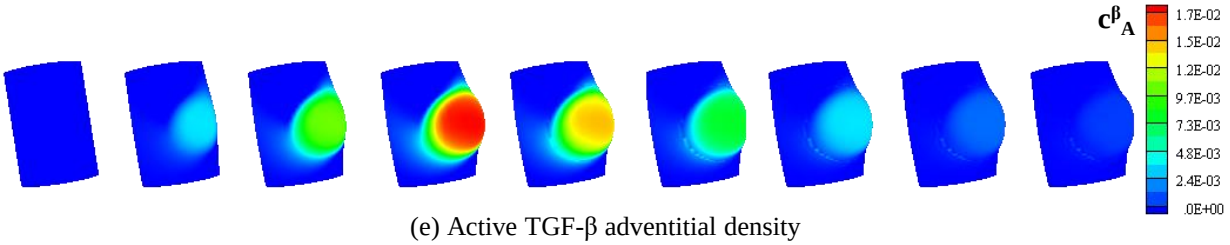

(e) Active TGF-β adventitial density

Figure 4.4: **3D CMB modelling saccular aneurysm development — biochemical variables.** Adventitial densities of (a) fibroblasts, (b) collagenases, (c) collagenase inhibitors, (d) latent and (e) active TGF-β.

4.2.2 Investigating the outcomes of profibrotic therapy

In this section, the development of larger aneurysms is simulated by decreasing the rate of adaption of adventitial attachment stretches to load–bearing. In addition, an adventitial profibrotic response is stimulated in the area where elastin degradation was prescribed by applying a step in TGF-β concentration of $\beta_{step} = 0.1$ at $t_\beta = 2$.

4.2.2.1 Large aneurysm development

A slower rate of adaption of adventitial collagen attachment stretch (larger averaging time period with illustrative value of $T_{AT} = 5$) is used here to simulate the development of a large saccular aneurysm. Fig. 4.5 shows the temporal evolution of some biochemical and cellular quantities at the aneurysm surface. Elastin degradation was prescribed to evolve as in the previous simulation case, thus reaching a steady state distribution at $t = 3$, Fig. 4.5(a). Note, however, that due to the slower adaption of adventitial collagen attachment stretch, a visibly larger saccular aneurysm develops (compare $t = 8$ frame in Fig. 4.3(a) *vs.* Fig. 4.5(b)). As a result of this deviation from material equilibrium, the TGF-β signalling pathway is activated, as can be inferred from the evolution in active TGF-β concentration, Fig. 4.5(b) *top*, which reaches a peak value larger than in the previous simulations. So as to assess the effect of applying a profibrotic "therapy", a step increase of 0.1 in c_A^β was applied at $t = 2$, Fig. 4.5(b) *bottom*. In both cases, it can be seen that active TGF-β levels return to baseline at later time points, which is consistent with the expected transient dynamics of this species.

TGF-β signalling changes the phenotype of adventitial cells in several important ways. Fig. 4.5(c) shows that fibroblast cell density increases as long as $c_A^\beta > 0$, which lasts until $t = 6$ for both treated and untreated cases. Note, however, that the application of an exogenous TGF-β step leads to much larger increases in fibroblast numbers, which are up to 2.5 times larger than in the no therapy case. Similar trends are seen for the densities of biomolecules secreted by fibroblasts, in particular collagenases and their inhibitors (not shown). In addition to increasing fibroblast numbers and their secretion of active molecules, TGF-β also promotes fibroblast differentiation into activated myofibroblasts, Fig. 4.5(d), whose population dynamics follow the evolution of active TGF-β levels with a delay. Applying a TGF-β step at $t = 2$ induces a fast and large increase in myofibroblast population ($t = 3$ frame in Fig. 4.5(d) *bottom*), which still transiently returns to

baseline when TGF-β signalling disappears.

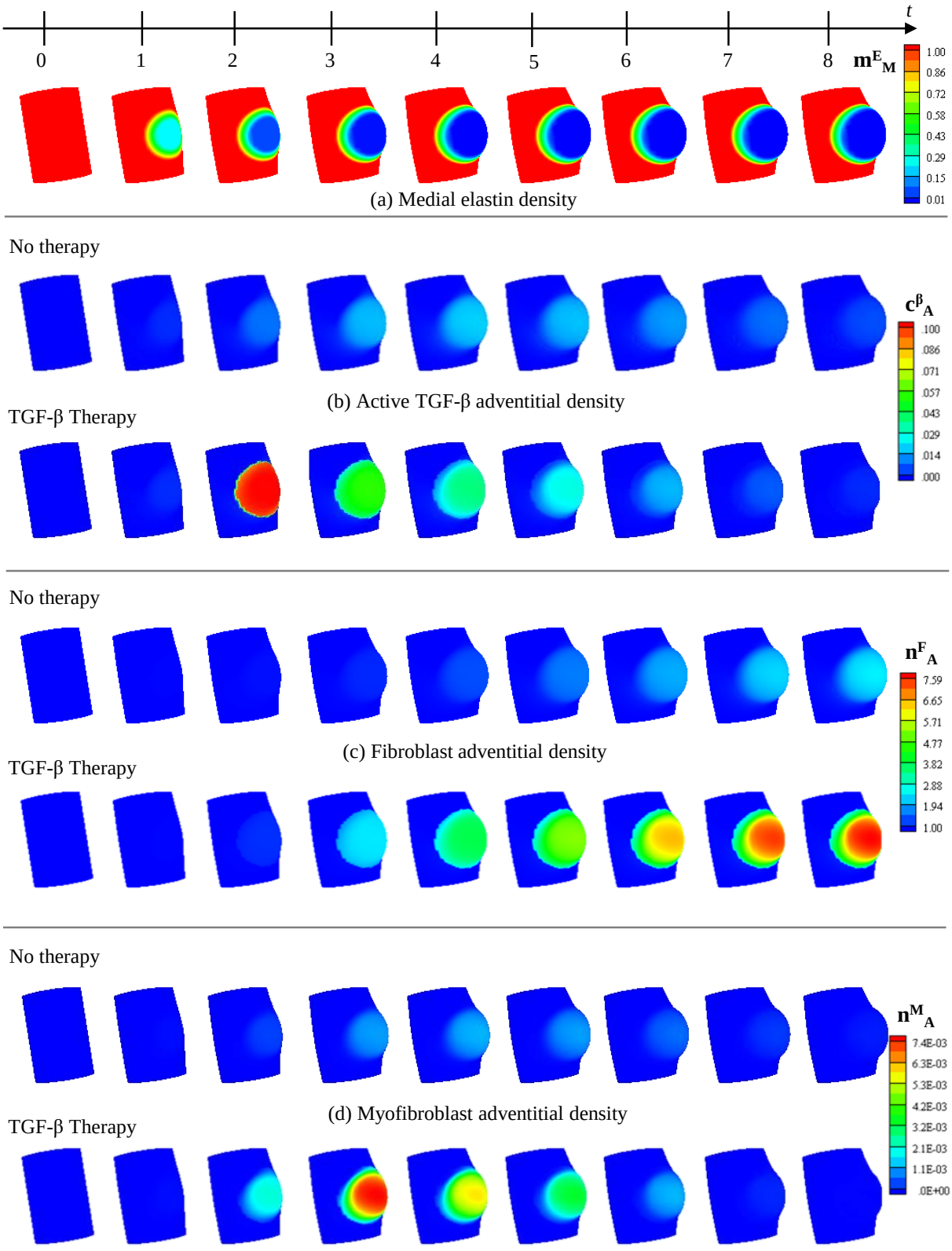

Figure 4.5: **3D CMB model investigating profibrotic therapy on large (T_{AT} = 5) saccular aneurysms — biochemical variables.** Untreated case (*No therapy*) is contrasted with treated case (*TGF-β therapy*) for each variable. (a) Medial elastin density (no therapy case), and adventitial densities of (b) active TGF-β, (c) fibroblasts and (d) myofibroblasts.

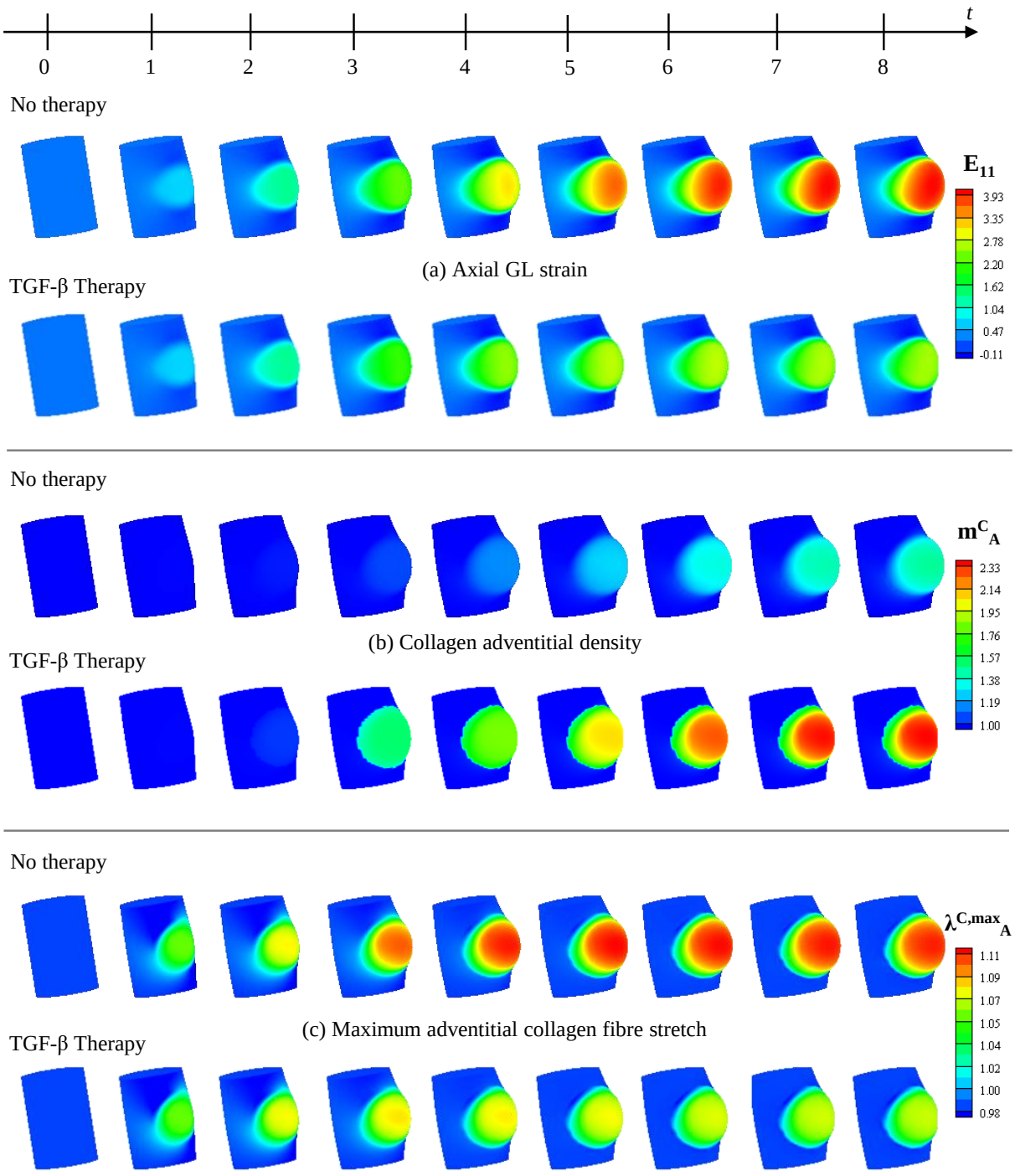

Figure 4.6: **3D CMB model investigating profibrotic therapy on large (T_{AT} = 5) saccular aneurysms — mechanical variables.** Untreated case (*No therapy*) is contrasted with treated case (*TGF-β therapy*) for each variable. (a) Axial GL strain, (b) adventitial collagen density, and (c) maximum adventitial collagen fibre stretch.

The effects of the previously observed medial degradation and adventitial profibrotic signalling on arterial wall deformation and collagen properties can be seen in Fig. 4.6. The larger expansion in the saccular aneurysm domain leads to higher GL strains, Fig. 4.6(a). Comparing with the previous simulation case, this larger aneurysm displays monotonic enlargement until $t = 6$ ($t = 3$ previously), which suggests that material equilibrium is not reached until later, and steady state values are up to 70% larger than previously observed, Fig. 4.6(a) *top*. The application

of a TGF-β step, however, promotes aneurysm stabilisation earlier ($t \simeq 4$) and at up to 30% less strain than in the untreated case, Fig. 4.6(a) *bottom*.

The protective action of TGF-β against aneurysmal development is due to its collagen–promoting action on adventitial fibroblasts. Fig. 4.6(b) shows that increases in adventitial collagen density secondary to medial degradation, Fig. 4.6(b) *top*, are boosted by TGF-β treatment, which promotes an early increase at $t = 3$ and the attainment of steady state values that are up to 55% larger than otherwise, Fig. 4.6(b) *bottom*; note in particular that collagen density right after application of the TGF-β step at $t = 3$ is larger than at the last time point for the untreated case. Aneurysm stabilisation following the application of a TGF-β step is also attained at lower adventitial collagen fibre stretches, Fig. 4.6(c). While in the untreated case $\lambda_A^{C,\max}$ increase up to over 1.11 at $t = 5$, Fig. 4.6(c) *top*, treated aneurysms achieve maximum adventitial collagen stretches of up to 1.08 around $t = 3$, then slightly reducing for late time points but remaining well over 1.0, Fig. 4.6(c) *bottom*. Note also that at $t = 8$ stabilised treated aneurysms have $\lambda_A^{C,\max}$ up to 5% lower than untreated aneurysms.

The effect of applying a TGF-β step to the geometry and surface deformation of enlarging saccular aneurysms can be seen in Fig. 4.7, which depicts wall distributions of axial (E_{11}, *left*) and circumferential (E_{22}, *right*) wall components of the GL strains for treated and untreated cases at $t = 8$ (when material and chemo-mechano-biological equilibrium was reached in both cases). The 3D CMB model predicts that applying a TGF-β profibrotic stimulus effectively reduces the dimensions of enlarging saccular aneurysms, which stabilise at up to 40% lower axial and circumferential GL strains than if no therapy was applied (N.B. GL strains are measures of overall arterial wall deformation — strains of collagen fibres differ significantly due to remodelling of their reference configurations).

4.2.2.2 Very large aneurysm development

To simulate the development of even larger saccular aneurysms, a slow rate of adventitial attachment stretch adaption (large averaging period $T_{AT} = 10$) was prescribed. The predicted evolution of some cellular and biochemical variables is shown in Fig. 4.8. Elastin degradation is prescribed, with elastin degradation patterns similar to those of the previous studies, Fig. 4.8(a). The much larger aneurysm dimensions at later time periods for the same elastin degradation clearly shows

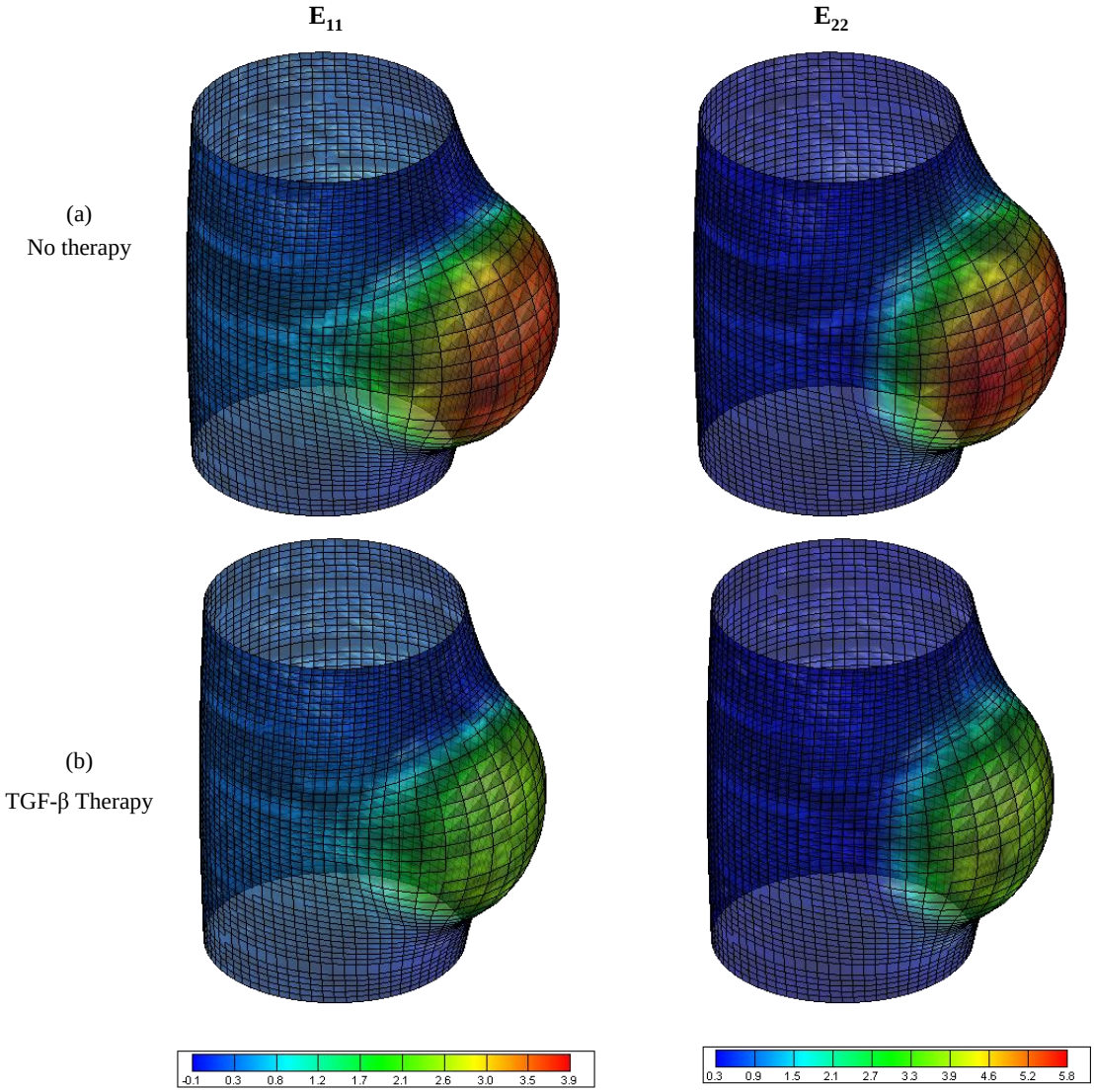

Figure 4.7: **3D CMB model investigating profibrotic therapy on large ($T_{AT} = 5$) saccular aneurysms — geometry comparison.** Systolic geometries of untreated (a) *vs.* TGF-β "treated" (b) aneurysms at $t = 8$. Axial (*left*) and circumferential (*right*) GL strain distributions are overlaid.

the importance of the dynamics of adventitial collagen attachment stretch adaption in determining aneurysm evolution. TGF-β levels are shown in Fig. 4.8(b). In the absence of exogenous supply, active TGF-β continuously increase and reach at $t = 6$ a peak value approx. 75% larger than for the previous simulation case, slowly starting to return to baseline in the last two time points, Fig. 4.8(b) *top*. In the treated case, shortly after the application of the TGF-β step at $t = 2$ there is a small reduction in c_A^β until $t = 4$, which then remains constant for the next three time points and then reduces again at the end of the simulation, Fig. 4.8(b) *bottom*. In both untreated and treated cases there is a reduction but never a return of TGF-β levels to baseline, which indicates that the system has not attained chemo-mechano-biological equilibrium by the end of the simulation.

Elevated TGF-β levels promote increases in fibroblast density, which continuously increases until the end of simulation for both cases, Fig. 4.8(c). Due to larger deviations from material

equilibrium in this very large aneurysm, final values of n_A^F in the untreated and treated cases are approx. 90% and 125% larger than the corresponding values in the previous study, resp., and the

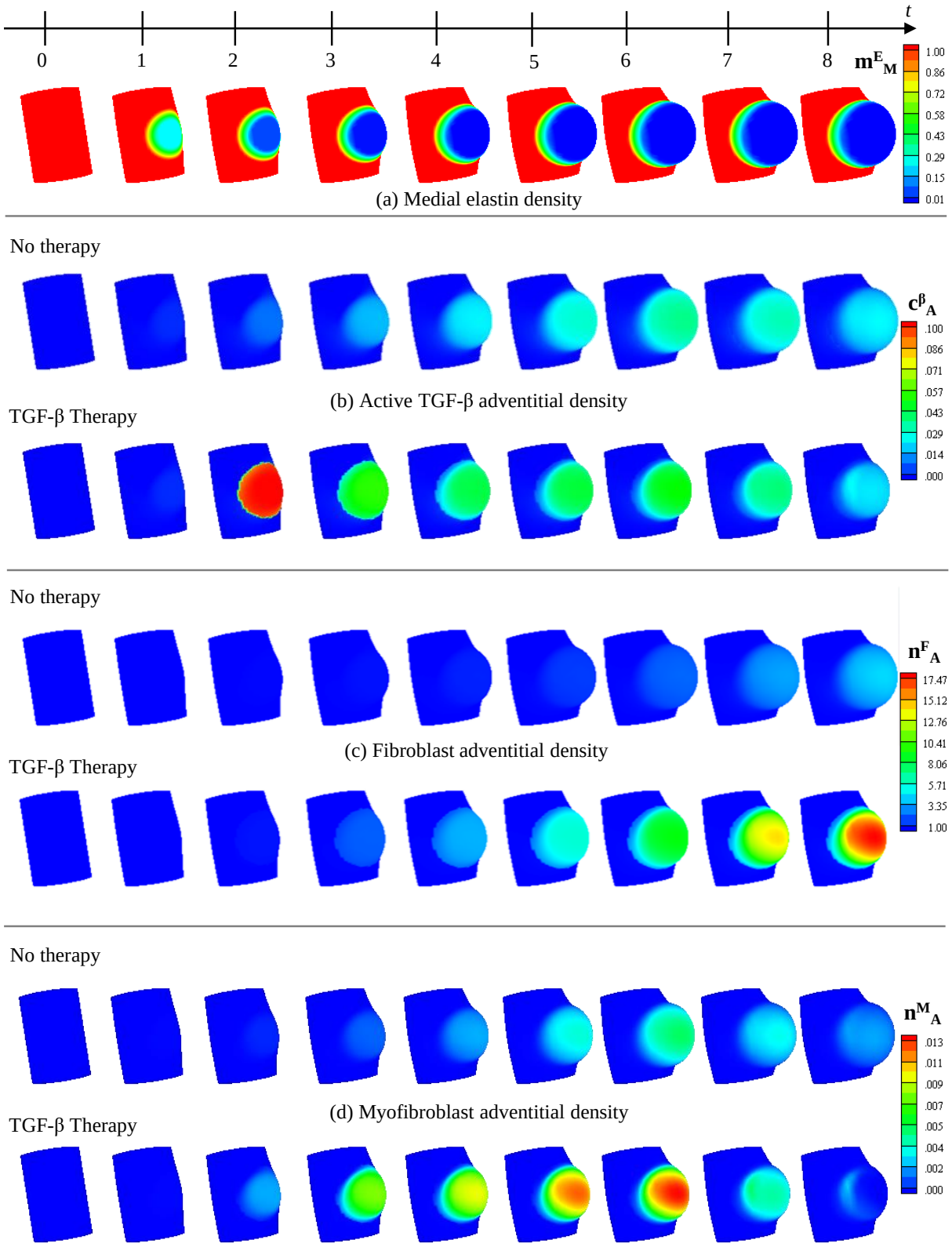

Figure 4.8: **3D CMB model investigating profibrotic therapy on very large (T_{AT} = 10) saccular aneurysms — biochemical variables.** Untreated case (*No therapy*) is contrasted with treated case (*TGF-β therapy*) for each variable. (a) Medial elastin density (no therapy case), and adventitial densities of (b) active TGF-β, (c) fibroblasts and (d) myofibroblasts.

ratio between final fibroblast densities in the treated to untreated cases in also larger than previously (3.9 *vs.* 2.5 relative to the initial configuration). Similar trends are seen in collagenases and collagenase inhibitors (*not shown*). Adventitial myofibroblast levels in both untreated and treated cases rise and fall, Fig. 4.8(d), their number density peaking for both cases at $t = 6$ and then slightly reducing towards baseline. In contrast to the previously simulated smaller aneurysm, myofibroblast levels in this study are approx. one order of magnitude larger, their peak value is attained later, and in neither case does it fully return to baseline (which took place at $t = 6$ in the previous study). The longer permanence time and later peaking time of the myofibroblast population in this study may explain the consistently increased levels of active TGF-β for $4 \leq t \leq 6$ seen in Fig. 4.8(b) *bottom*: myofibroblasts were modelled to increase TGF-β activation via an integrin–mediated, tension–dependent mechanism, Sec. 2.2.2.2, and thus an increasing myofibroblast population at $4 \leq t \leq 6$ may have sustained active TGF-β levels in spite of decreasing latent TGF-β levels.

Fig. 4.9 displays some deformation and microstructural metrics characterising the evolving aneurysmal wall. Unsurprisingly, the formation of a very large saccular aneurysm results in the development of large GL strains, whose axial component E_{11} in the untreated case reaches maximum values that are approx. 2 times larger than in the previous study ($T_{AT} = 5$), and 3.45 times larger than in the first study ($T_{AT} = 1$), Fig. 4.9(a) *top*. The introduction of a profibrotic TGF-β step leads to an even larger reduction in $E_{11}(t = 8)$, which is of approx. 55% here and was only 30% in the previous study.

Early aneurysm stabilisation at lower GL strains following the application of a TGF-β step is due to its profibrotic action, ultimately leading to increased collagen mass density, as clearly seen in Fig. 4.9(b): m_A^C in the treated case was approx. 2 times larger than for the no therapy case. This factor of increase in collagen density following TGF-β treatment is larger here than for the smaller aneurysm modelled in the previous study (only 55%). Note also that, unlike previously, collagen density does not reach steady state for the later time points, which, together with the previous observations for the cellular and biochemical variables, suggests that chemo-mechano-biological equilibrium was not fully attained. As a result of larger domain deformations, maximum adventitial collagen fibre stretches also reach larger values in the untreated case of this study, with $\lambda_A^{C,\max}$ reaching 1.17 at $t = 6$, followed by a small reduction, Fig. 4.9(c). Application

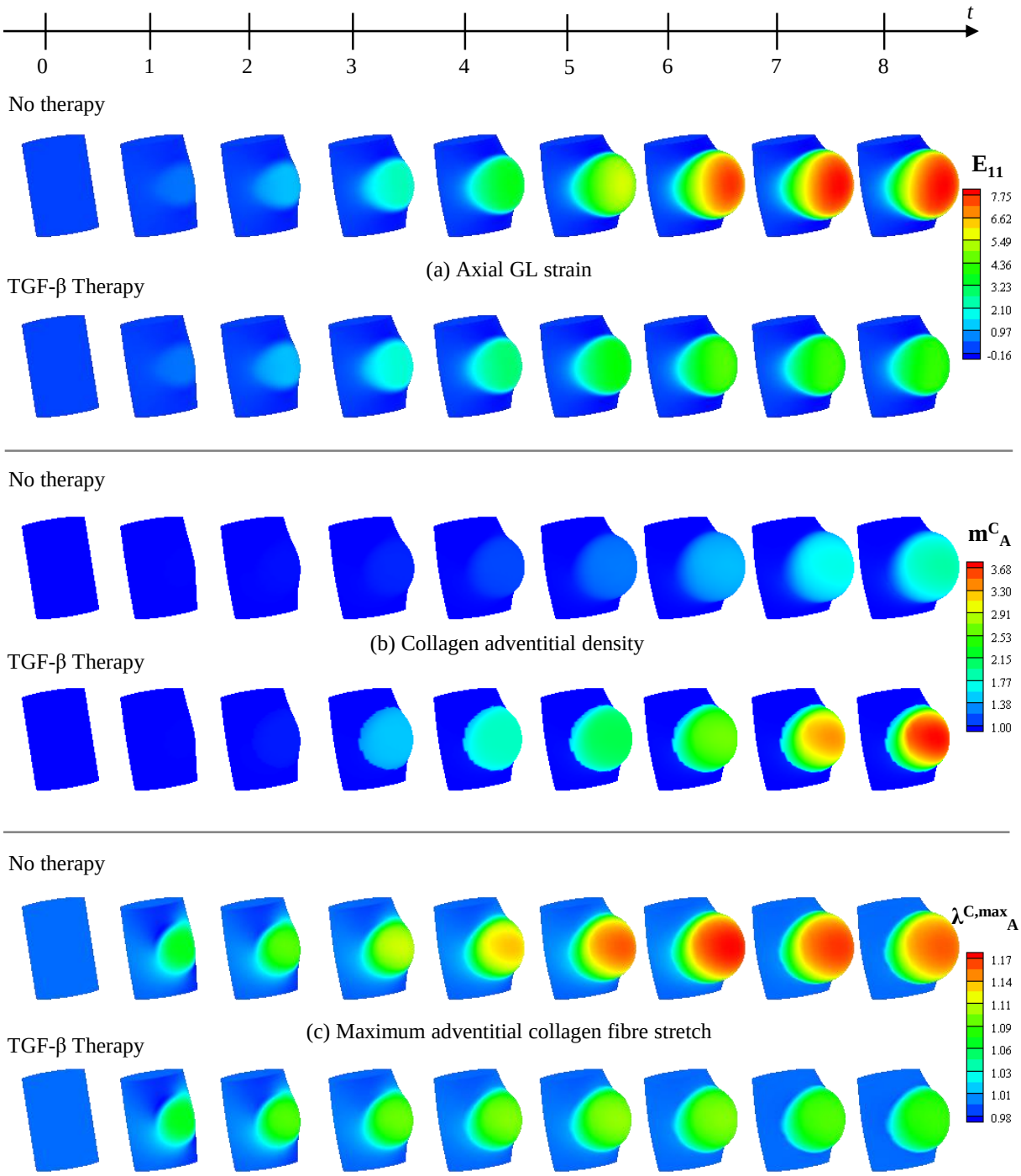

Figure 4.9: **3D CMB model investigating profibrotic therapy on very large (T_{AT} = 10) saccular aneurysms — mechanical variables.** Untreated case (*No therapy*) is contrasted with treated case (*TGF-β therapy*) for each variable. (a) Axial GL strain, (b) adventitial collagen density, and (c) maximum adventitial collagen fibre stretch.

of a TGF-β step in this study leads to final values of $\lambda_A^{C,\max}$ that are very similar to those of the previous study, which, however, correspond to a larger reduction with respect to the untreated case (7% here, and only 5% previously).

Fig. 4.10 shows arterial wall geometry and GL axial (E_{11}, *left*) and circumferential (E_{22}, *right*) strains for untreated (a) and treated (b) cases at $t = 8$. This figure makes clear the large reduction in saccular aneurysm size at the end of simulation in treated *vs.* untreated cases, whose surface

is less strained in both axial and circumferential directions. The effects of TGF-β treatment on arterial wall evolution were more significant for larger aneurysms; this is clearly seen by comparing aneurysm geometries in Fig. 4.7 *vs.* Fig. 4.10, which show reductions of maximum values of both GL strains components following TGF-β step to be of approx. 55% here, but only 40% in the smaller aneurysm simulated in the previous study.

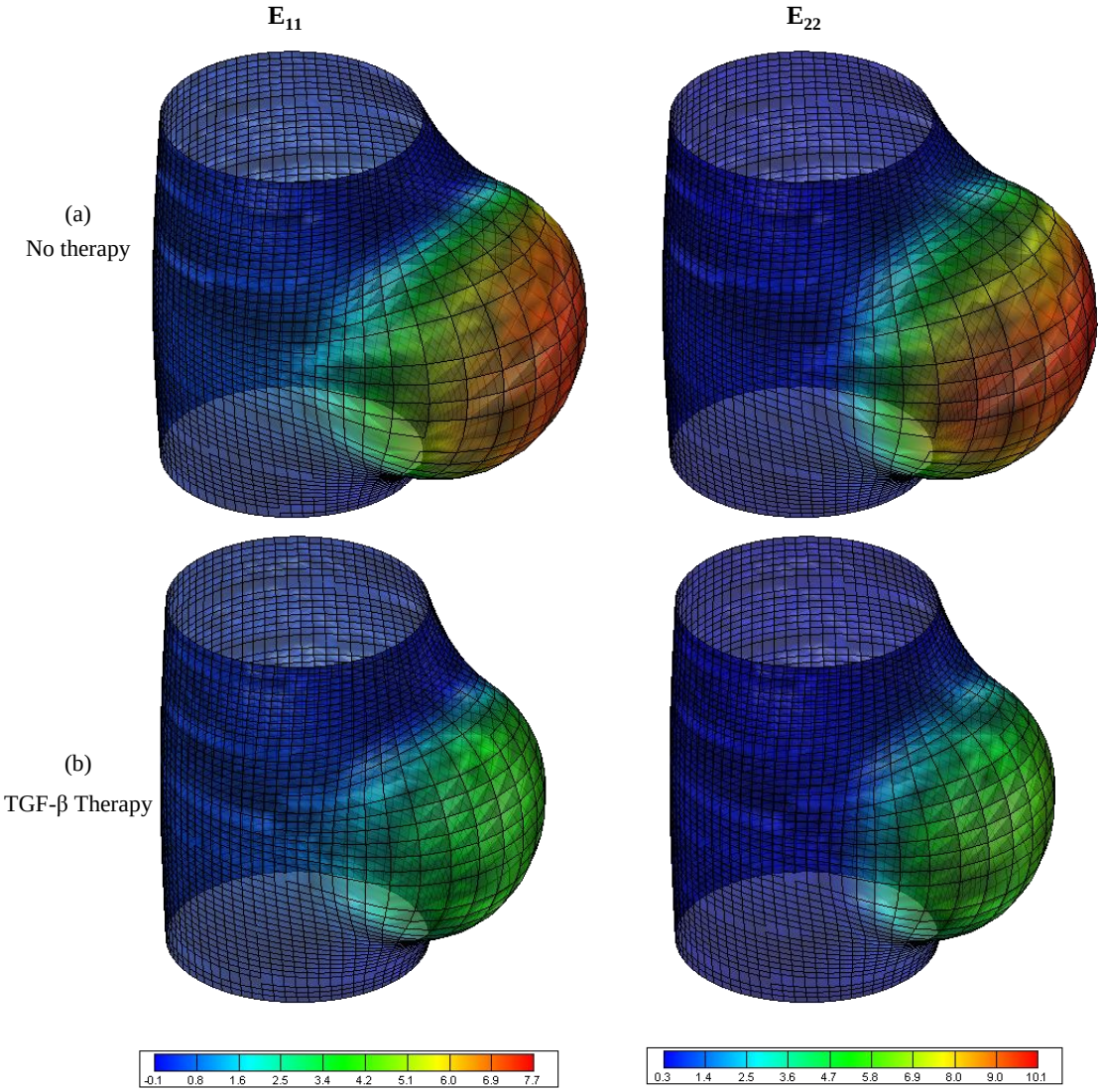

Figure 4.10: **3D CMB model investigating profibrotic therapy on very large ($T_{AT} = 10$) saccular aneurysms — geometry comparison.** Systolic geometries of untreated (a) *vs.* TGF-β "treated" (b) aneurysms at $t = 8$. Axial (*left*) and circumferential (*right*) GL strain distributions are overlaid.

4.3 Discussion

The CMB model of arterial G&R previously formulated was coupled to the 3D FEM structural solver of Watton et al.'s FSG computational framework. The arterial wall was modelled as a non-linear elastic bilayered membrane in 3D, with adventitial collagen density being for the first time

coupled to a chemo–biological model of cell–mediated collagen metabolism under the control of TGF-β signalling; moreover, evolution of both collagen recruitment and attachment stretch distributions was not prescribed, but for the first time directly computed from system dynamics. Numerical results show that the novel 3D CMB model implementation is able to simulate the heterogeneous distributions of mechanical and biomolecular variables in the complex, non–axisymmetrical geometries arising during saccular aneurysm development; this is a significant step forward from the 1D homogeneous cylindrical membrane formulation. The 3D CMB model captured the enlargement and stabilisation of small to very large aneurysms as a function of the rate of adventitial adaption to load–bearing, as well as an adventitial profibrotic response signalled by TGF-β; these results illustrate the significance of the model in coupling molecular, microstructural and cellular mechanobiological processes determining the evolution of tissue properties in complex 3D geometries.

Simulating the effects of profibrotic therapy, a step increase in active TGF-β concentration was applied at early stages of aneurysmal expansion. Aneurysms receiving this "virtual therapy" developed larger profibrotic responses, which promoted earlier stabilisation at much lower strain values. Larger aneurysms benefited more from the application of the profibrotic stimulus, in the sense that the reductions in aneurysm size and deformation following "treatment" were larger; this is a suggestive result from a clinical point of view, as aneurysm risk of rupture is commonly associated with aneurysm size and its rate of increase (Sakalihasan et al., 2005). This study is regarded as the first step towards the full integration of the CMB model of cell–mediated and TGF-β–regulated arterial G&R into the 3D multiphysics FSG loop, thus creating a 3D CMB–FSG computational framework with advanced biomechanical and mechanobiological modelling capabilities. This advanced framework is envisaged to capture vascular physiological and pathological processes that determine long–term cell–mediated and patient–specific arterial response to different classes of mechanical stimuli, as well as to investigate *in silico* novel therapeutic strategies such as pharmacological, genetic or stem cell therapies.

4.3.1 Comparison predictions 3D *vs.* 1D CMB models

So as to assess the qualitative consistency between arterial evolution predicted by the 1D *vs.* 3D model implementations, the 1D CMB model including myofibroblast differentiation (Sec. 2.2.2)

is adapted to reproduce the development of a large aneurysm as in Sec. 4.2.2 ($T_{AT} = 5$).

1D CMB model and simulation The mechanical component of the 1D CMB model is based on an axisymmetrical nonlinear elastic membrane in 1D with contributions to load–bearing from medial elastin and collagen, and adventitial collagen. The cylindrical membrane is pressurised to systolic pressure P^s and axially stretched to λ_z; the resulting force–balance equation governing mechanical equilibrium is Eq. (2.1). The signalling pathways cellular and biochemical component governing collagen metabolism is also based on the system of ODEs in Sec. 2.2.2, with the slight adaptations introduced in Sec. 4.1.2 above, Eq. (4.12)—Eq. (4.18). So as to allow for comparison with the 3D CMB implementation, remodelling of the recruitment stretch distribution is not coupled to levels of chemo–biological species (Eq. (2.46)—Eq. (2.48) with α_A^C =const.); similarly, the integral evolution laws for adaption of collagen attachment stretch distribution, Eq. (2.9)—Eq. (2.11), are not coupled to (myo)fibroblast levels (constant T_{AT} =const.), and do not include terms for narrowing or skewing ($f_{narrow}^{min}(t) = f_{skew}^{mode}(t) = 0, \forall\, t$). Elastin degradation was prescribed according to the 1D equivalent of Eq. (4.10), i.e. Eq. (2.28).

1D CMB model parameters were, with very few exceptions, equal to those used in the 3D CMB implementation in this chapter, Table 4.1. In particular, the collagen recruitment stretch remodelling rate was decreased to $\alpha = 2$ to prevent excessive domain expansion (note that in the 1D model the entire arterial circumference is perturbed, while the 3D implementation was used to model saccular aneurysm enlargement for which only part of the circumference is affected), and the elastin degradation period $\Delta t_{ED} = 2$ in Eq. (2.28) was chosen such that $m_{min}^E = 0.01$ was attained at $t = 2$ (consistent with the time course of elastin degradation in Fig. 4.5(a)). Values for the averaging time period and onset time for attachment stretch adaption ($T_{AT} = 5$, $t_0^{AT} = 3$, resp.) matched those used in the 3D study. Similarly, a default (*untreated*) simulation case was compared with a (*therapy*) simulation case where an active TGF-β step of $\beta_{step} = 0.1$ was applied at $t_{step} = 2$, as in the 3D studies. Both simulation cases were run until $t_{end} = 8$.

Fig. 4.11 displays the temporal evolution of some mechanical, microstructural, chemo–biological quantities predicted by the 1D model; the default "no therapy" simulation case is plotted in red in Fig. 4.11(a)—(c) and in Fig. 4.11(d), while the "TGF-β therapy" simulation case is plotted in green in Fig. 4.11(a)—(c) and in Fig. 4.11(e); compare the trends plotted here

with those predicted by the 3D CMB implementation for $T_{AT} = 5$, Fig. 4.5, Fig. 4.6.

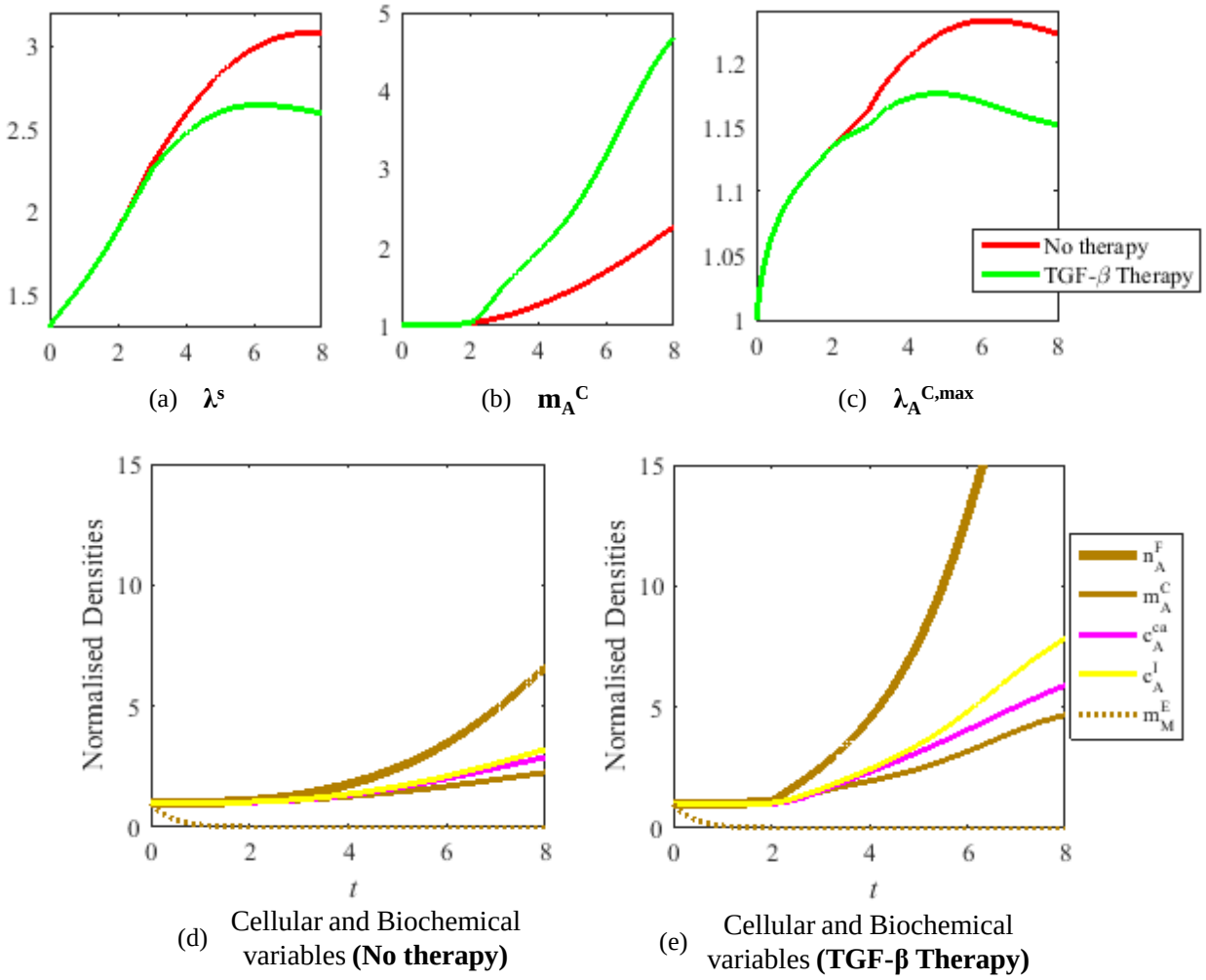

(a) $\boldsymbol{\lambda^s}$ (b) $\mathbf{m_A^C}$ (c) $\boldsymbol{\lambda_A^{C,max}}$

(d) Cellular and Biochemical variables **(No therapy)**

(e) Cellular and Biochemical variables **(TGF-β Therapy)**

Figure 4.11: **1D CMB model predictions for comparison with 3D CMB implementation.** Systolic circumferential stretch (a), adventitial collagen density (b), maximum adventitial collagen fibre stretch (c), and densities of chemo–biological variables for the no therapy (d) and TGF-β therapy (e) cases.

Simulation results Fig. 4.11(a) shows that the arterial wall expands secondary to medial elastin degradation, with (systolic) circumferential stretch λ^s stabilising for the $t > 6$; this behaviour is consistent with the evolution of 3D GL strains displayed in Fig. 4.6(a). Also consistently with 3D observations, the 1D CMB model predicts earlier stabilisation at lower stretches following the application of a TGF-β step at $t_{step} = 2$. The profibrotic nature of the applied stimulus clearly underlies system behaviour: the increase in adventitial collagen density following medial degradation is greatly boosted after exogenous TGF-β application, Fig. 4.11(b). This trend is also consistent with what was observed for the 3D implementation, Fig. 4.6(b), even if mechanobiological steady state was not yet reached by the end of the 1D simulation. Maximum values of adventitial collagen fibre stretches are predicted by the 1D CMB model to go through an initial pe-

riod of growth until $t_0^{AT} = 3$, after which attachment stretch adaption promotes peaking of $\lambda_A^{C,\max}$ followed by a small reduction, Fig. 4.11(c). The same trends are predicted by the 3D CMB implementation, Fig. 4.6(c), with initial increases that peak shortly after t_0^{AT}, and then slightly decrease (particularly visible in the treated case). Both 1D and 3D implementations predict that applying a step in active TGF-β levels promotes earlier stabilisation at lower maximum of collagen fibre stretch.

Comparing the evolution of chemo–biological species predicted by the 1D model for the untreated case, Fig. 4.11(d), it becomes clear that following degradation of medial elastin m_M^E (dashed brown curve) the adventitia develops a profibrotic response by increasing the density of fibroblasts n_A^F (thick brown curve) and regulating the levels of collagenases c_A^{ca} (magenta curve) and inhibitors n_A^I (yellow curve) secreted, such that the collagenolytic activity (collagenases:inhibitors ratio) is reduced and there is a resultant increase in the adventitial collagen density m_A^C (thin brown curve). Consistent with 3D predictions, the TGF-β therapy case, Fig. 4.11(e), displays a more intense fibrotic response characterised by larger increases in fibroblast numbers (c.f. Fig. 4.5(c)) and adventitial collagen density (c.f. Fig. 4.6(b)).

Remarks on 1D *vs.* 3D CMB model comparison The results presented above show that the trends in mechanical, microstructural, cellular and biochemical variables predicted by the 1D CMB model implementation consistently match those generated by the 3D formulation introduced in this chapter. This consistency suggests that the 1D model can be used to gain initial insight into system behaviour while requiring lower computational time (approx. one order of magnitude). However, it is important to note that absolute values and ratios of variables in treated and untreated cases as predicted by the 1D *vs.* 3D implementations may be very different (e.g. n_A^F for the treated case at $t = 8$ approx. 7.8 in 3D, and over 15 in 1D; ratio between treated and untreated cases of m_A^C at $t = 8$ of approx. 1.6 in 3D but only 1.2 in 1D). These differences are not surprising, taking into account the (a) different modes of aneurysm expansion simulated (entire cylindrical artery in 1D *vs.* saccular outpouching in 3D), and (b) different collagen architectures (single circumferentially–oriented collagen fibre families in 1D *vs.* double–helical collagen fibre families in 3D). The 1D implementation, therefore, cannot simulate the evolution of complex geometries such as saccular aneurysms, nor the heterogeneous spatial distributions of system variables that arise during arterial evolution; these, as discussed above, display very different values in different

regions (e.g. parent vessel *vs.* dome region) of the arterial wall, Sec. 4.3.2. These observations motivated the present formulation and future developments of the 3D CMB modelling framework.

4.3.2 3D CMB Model insight

Modelling strategy The 1D CMB model capturing TGF-β signalling and phenotypic regulation of adventitial fibroblast profibrotic response formulated in Chapter 2 was adapted and coupled here to the FEM structural solver of the 3D FSG loop (Watton et al., 2009a). This computational framework was then used to study the temporal evolution of surface geometry and distributions of mechanical, microstructural, cellular and biochemical quantities over saccular aneurysm development secondary to prescribed medial elastin degradation. Saccular aneurysms (SAs) are defined as permanent and irreversible vessel wall dilations that affect only part of the transverse circumference of the artery (as opposed to fusiform aneurysms, which affect the entire circumference) (Sakalihasan et al., 2011). Even though saccular aneurysms can be found in many locations along the arterial tree, they are particularly prevalent in the intracranial vasculature (80–90% of all cerebral aneurysms (Mehra et al., 2011)), which justifies model parametrisation with internal carotid artery properties. Due to their characteristic geometry, saccular aneurysm expansion cannot be described by low–dimensional mechanical models, which supports the extension of the previously formulated CMB model to 3 dimensions.

An additional capability of the 3D formulation of the CMB model implemented here is the computation of spatial distributions of mechanical, microstructural, biological and cellular variables characterising the chemo–mechano–biological condition of the wall and determining its (geometrical) evolution. Simulation results show large variations in the values of system variables in different regions of the arterial wall: comparing the central dome region *vs.* the boundary of the elastin degradation region in the very large untreated saccular aneurysms at $t = 8$ simulated in Sec. 4.2.2, adventitial collagen stretch is up to 15% different (Fig. 4.9(c)*top*), and domain circumferential GL strains are up to 300% different (Fig. 4.10(a)*right*), while the corresponding treated aneurysms display fibroblast density up to 420% different (Fig. 4.8(c)*bottom*) and adventitial collagen density up to 130% different (Fig. 4.9(b)*bottom*). The average values predicted by a homogenised 1D model would thus be significantly distant from those displayed by system variables on these two regions. In addition to extreme values, the 3D CMB implementation also

computes the spatial distribution patterns of system variables. The largest deformations were observed at the aneurysm dome (Fig. 4.10), and then gradually and smoothly decreasing towards the parent artery; biochemical and cellular (Fig. 4.8) and microstructural (Fig. 4.9) variables characterising adventitial adaptive response driven by perturbations to mechanical homoeostasis also followed the same spatial pattern. Even though these spatial distributions are very simple and do not capture the highly heterogeneous chemo–biological fields, architecture and stress–strain properties of diseased arterial walls (Frösen et al., 2012), they clearly show the potential of the model to simulate spatial distributions of system variables, which will become highly heterogeneous if spatially complex microstructure (e.g. time–evolving distribution of collagen fibre directions) or mechanobiological processes (e.g. immune cell infiltration degrading elastin) throughout disease initiation and progression are included.

In this initial study, only arterial wall solid mechanical variables (computed by FEM structural analysis) were coupled to cell–mediated arterial G&R response, with the CMB model including important mechanisms of the well–documented fibroblast–mediated adventitial G&R response (Chiquet et al., 2003); these processes are particularly relevant in the context of vascular inflammation (Maiellaro and Taylor, 2007) commonly present in many aneurysms (Frösen et al., 2004). Fluid dynamics has also been strongly correlated with immune cell infiltration and aneurysm pathology, but the exact mechanisms involved are still controversial (Sforza et al., 2012); the inclusion of such important links between resident and infiltrating cells in the arterial wall, their secretory profile and haemodynamic properties will require further CMB model development, and is thus out of the scope of this initial study.

Simulating saccular aneurysm development Simulation results for the development of saccular aneurysms (Sec. 4.2.1 and untreated cases in Sec. 4.2.2) consistently showed that loss of medial load–bearing capacity and resultant arterial wall over–straining triggered (TGF-β) mechanotransduction signalling that promoted a fibroblast–mediated adventitial profibrotic response. TGF-β–induced phenotypic changes in fibroblasts (increased fibroblast numbers, myofibroblast differentiation, increased collagen and collagenase inhibitors and decreased collagenase production per fibroblast) led to the increase in adventitial collagen mass density, reinforcing the arterial wall and promoting aneurysm stabilisation. Prescribed medial elastin degradation models the increased MMP proteolytic load secondary to immune cell infiltration observed in aneurysmal

walls (Mehra et al., 2011). All aneurysms modelled here ultimately stabilise, which corresponds to experimentally–observed unruptured aneurysms (Robertson et al., 2015). Unruptured saccular intracranial aneurysms display proliferation of mural cells and increased synthesis of collagenous matrix leading to higher tensile strength of the aneurysmal walls (Frösen et al., 2012); Robertson et al. (2015) also report increased collagen fibre density in a subset of unruptured aneurysms with higher failure stress and failure pressure. In contrast, ruptured aneurysms display strong immune cell infiltration, mural cell apoptosis and much larger collagenase (MMP-2,9) levels, jointly leading to increased wall degradation and reduced G&R capability. TGF-β signalling has been associated with arterial wall remodelling in the context of saccular cerebral aneurysm development (Frösen et al., 2006). Taken together, these experimental observations are consistent with the system behaviour predicted by the 3D CMB model, i.e. medial degradation triggering aneurysm enlargement, which reaches stability as a result of mural cell–mediated, TGF-β–regulated profibrotic response and resulting adventitial reinforcement.

In addition to collagen growth, adaption of the stretch at which newly deposited collagen fibres were attached to the matrix also had a major effect on the predicted aneurysm evolution. Modelling adventitial adaption to permanent load–bearing secondary to medial degradation, a rightward–shifting adventitial collagen attachment stretch distribution was for the first time not prescribed but rather computed as a simple running average of collagen fibre stretches. Larger averaging periods ($T_{AT} = 1, 5, 10$) corresponding to slower–adapting attachment stretches resulted in increasingly large aneurysmal geometries at later times, c.f. last time frames in Fig. 4.3(a), Fig. 4.5(a) and Fig. 4.8(a). Further computational exploration of this interesting prediction is warranted, as well as novel experimental investigation.

Investigating profibrotic TGF-β therapy The 3D CMB model was also used to investigate the effects of applying a profibrotic stimulus to enlarging saccular aneurysms, Sec. 4.2.2. The results show that the application of a step increase in active TGF-β levels boosted the development of a strong fibrotic response (in particular, increased fibroblast numbers and myofibroblast differentiation), which resulted in a much larger collagen deposition that was responsible for earlier stabilisation of smaller aneurysms with lower GL strains and collagen fibre stretches. Larger aneurysms benefited more from application of the TGF-β step, with larger reductions in aneurysmal geometries and collagen fibre stretches than observed for smaller aneurysms.

Several experimental observations support the protective role of TGF-β as a profibrotic, immunosuppressive agent against aneurysm expansion. Dai et al. (2005b) reported that overexpressing TGF-β in the walls of an animal model of abdominal aortic aneurysm (AAA) increased arterial wall cell numbers (including those expressing α-SMA, a SMC and myofibroblast marker), increased collagen levels, decreased MMP-2 collagenolytic activity, and decreased immune cell infiltration, which promoted stabilisation of otherwise enlarging aneurysms. The same group later induced endogenous TGF-β overexpression in three animal models of AAA, confirming the previous observations correlating increased TGF-β signalling with increased mural cellularity, decreased inflammation, aortic wall structural preservation and aneurysm stabilisation (Dai et al., 2011). Studies focusing on reduced TGF-β signalling also support its protective role against aneurysm expansion. The early study of Smith et al. (1999) showed that following inflatable catheter arterial injury, mural cells upregulated TGF-β expression, and that quenching TGF-β signalling by administering soluble TGF-βR2 inhibited adventitial collagen deposition and reduced α-SMA expression in the adventitia (suggesting reduced myofibroblast differentiation). Systemic neutralisation of TGF-β promoted aneurysm development following the administration of an inflammatory stimulus, leading to disruption of wall architecture and increased incidence of rupture (Wang et al., 2010). Even though TGF-β protective action against aneurysm expansion is certainly partially due to its immunosuppressor effect (Akhurst and Hata, 2012), the previous set of observations relating TGF-β signalling to (adventitial) arterial fibrosis and preservation of wall architecture support its important role as a profibrotic mediator, which is included in the CMB model.

A second interesting result is the formation of a significant myofibroblast population with large residence time in the very large aneurysm simulation case (Fig. 4.8(d)), whose latent TGF-β activation mechanism contributed to steady active TGF-β levels (Fig. 4.8(b)) well after material equilibrium was reached ($\lambda_A^{C,max}$ stabilisation in Fig. 4.9(c)) and latent TGF-β secretion was back to baseline. Myofibroblasts are highly secretory, highly contractile cells that differentiate from fibroblasts (and other cell sources) in cases of stress– or injury–triggered adventitial remodelling, such as in vascular inflammation or hypertension (Zalewski et al., 2002). Myofibroblast differentiation requires a combination of matrix loading, TGF-β signalling and the existence of a mechanically–resistive matrix (Tomasek et al., 2002); once differentiated, these cells deposit and

organise (i.e., remodel) large amounts of collagen fibres (Hinz, 2010). In addition, myofibroblasts activate latent TGF-β by a contraction–driven, integrin–mediated mechanism (Wipff et al., 2007); this mechanism was included in the CMB model (terms $r_{\beta l_7}$ and r_{β_3} in Eq. (4.16) and Eq. (4.17), resp.), and is likely to explain the time courses observed.

Common to the previous points, micro–scale cellular–biochemical interactions (TGF-β effect on fibroblast phenotype, and myofibroblast action on TGF-β activation) included in the 3D CMB model determined tissue–level properties (collagen mass density) and geometrical evolution (expansion and stabilisation); previously existing models could not straightforwardly capture these multi–scale couplings between tissue mechanics, chemistry and biology. Simulation results illustrate the potential of this type of approach, specifically in investigating the effects of pharmacological therapy on aneurysm evolution, or the contribution of certain cell populations in changing arterial wall properties. The more advanced 3D CMB model implementation allows for the spatial distributions of mechanical, biochemical and cellular variables determining arterial response to perturbation and therapeutic outcomes to be simulated in more complex and realistic geometries, thus modelling more accurately a wider range of systems such as the saccular aneurysms simulated here.

4.3.3 Limitations and future work

The work presented here focused on updating the CMB model previously formulated to 3D, and in doing so providing the multi–physics 3D fluid–solid–growth framework of Watton et al. (2011) with a better description of the chemo–biological processes underlying microstructural changes over disease progression. Several particular choices and simplifications were made, which should be revised in the future.

The chemo–biological model component of cell–mediated, TGF-β–regulated arterial G&R was coupled only to the FEM structural solver of the FSG loop. This was a natural first step, given the (1) CMB model focus on adventitial profibrotic response, and (2) significantly increased computational times necessary for simulating fluid flow, in particular pulsatile. In any case, and given that the chemo–biological model component has been fully integrated in the FSG loop, it would be fairly straightforward to extend it to capture the couplings between intraluminal haemodynamics and endomural mechanobiological processes. It is now well established

that blood flow patterns correlate with arterial wall properties and aneurysm progression (Sforza et al., 2012) and risk of rupture (Cebral et al., 2005): low wall shear stress (WSS) is associated with aneurysm progression, while complex and/or unstable flow patterns forming concentrated impingement regions are associated with rupture. Disturbed haemodynamics seem to be associated with aneurysm progression by promoting a shift in lumen endothelial cells (ECs) towards a pro–inflammatory phenotype, and increasing the adhesion and transmural migration of circulating immune cells (Sho et al., 2004; Conway and Schwartz, 2012); immune cells, in particular macrophages, are then responsible for the increase in proteolytic load responsible for extensive degradation of the wall and loss of load–bearing capacity (Frösen et al., 2012). Coupling haemodynamic metrics such as average WSS, average oscillatory shear index (OSI) or blood residence time (Xiang et al., 2011) to the levels of immune cells already included in the initial CMB formulation (Eq. (2.41) in Sec. 2.2.2.2) could be done fairly easily by modelling EC permeability to immune cell infiltration; phenomenological relations between elastin degradation and blood flow conditions have already been included in previous studies using Watton et al.'s framework, e.g. Watton et al. (2009a, 2011) and Aparício et al. (2014).

Once a fully coupled CMB–FSG computational framework is developed, two important yet more challenging extensions should be considered. First, fluxes of biochemical and cellular species between spatial elements should be modelled. The current FSG framework was not developed to compute mass transport processes, given that previously modelled elastin and collagen fibres form a structurally cohesive matrix. However, small molecules such as active TGF-β, MMP proteases and collagenase inhibitors (TIMPs) are diffusible, and (myo)fibroblast cells are motile (McAnulty, 2007), migrating along biochemical and/or stiffness gradients. Diffusion terms should thus be included in the equations (currently ODEs) governing cellular and biochemical variables, which would be numerically solved by coupling an advection–diffusion solver into the current FSG framework; the fluid–solid–growth–mass transport model formulated in 1D by Holland (2012) could be adapted for this purpose.

Second, the 3D CMB framework would benefit from integration in thick–wall models. From a mechanical point of view, late stage aneurysmal arteries often display large variations in regional wall thickness (Raghavan et al., 2006), which may lead to stress concentrations and high rupture risk. In addition, the extensive degradation of medial elastin at later stages compromises

the maintenance of residual stresses (Cardamone et al., 2009), whose homogenisation effect on transmural stress distributions (Fung, 1991) often justifies the use of average quantities and a membrane formulation (Humphrey, 2002). From a chemo–biological point of view, the 3D CMB model has the capability of predicting localised changes in fibroblast numbers and collagenase concentration, thus having the potential to predict the evolution of wall thickness at each mesh element. Given that (a) rupture takes place where wall stress exceeds wall strength, (b) wall stress is inversely correlated with wall thickness, and (c) tensile strength has been found to correlate with wall thickness in ruptured (abdominal) aneurysms (Di Martino et al., 2006), the potential of using a CMB–FSG framework to model the biology–driven localised evolution of rupture risk becomes apparent. Several thick–wall implementations of arterial G&R models can be found in the literature (Karšaj et al., 2010; Valentín et al., 2013), including one using Watton et al.'s G&R laws (Schmid et al., 2010); more recently, volumetric growth stemming from G&R of arterial wall load–bearing constituents modelled by Watton et al.'s evolution equations has been studied in a thick–wall fibre–reinforced model (Eriksson et al., 2014). Given the body of work already available in the literature, updating the CMB–FSG framework to a thick–wall formulation should be feasible in the short term.

Finally, model behaviour should be further explored by running comprehensive parameter studies. The previous results show that aneurysm development is highly dependent on the dynamics of adventitial collagen adaption to load–bearing. As such, studying the influence of parameters controlling collagen fibre dynamics such as T_{AT} (averaging period for attachment stretch computation), t_0^{AT} (onset time for attachment stretch adaption) or α (rate of collagen recruitment stretch remodelling) assumes special importance. Similarly, parameters controlling TGF-β stimulus such as t_β (stimulus time) or β_{step} (stimulus magnitude), as well as different stimulus functions and types of stimuli, should be investigated. In fitting the model to experimental data sets, the CMB model will have to be re–dimensionalised, and parameter sets capturing physiological G&R time scales (e.g. collagen fibre half–life in mature healthy arteries of approx. 60 days (Humphrey, 2002)) will have to be adopted. Moreover, all the aneurysms simulated here ended up reaching material equilibrium and stable geometry (but not necessarily chemo-mechano-biological equilibrium); in the future, simulating unstable aneurysm growth would be interesting, in particular in relation to the application of therapies (e.g. profibrotic stimuli) that may change system be-

haviour from continuous growth to stabilisation. In addition, the 3D CMB model is very well suited to study other types of aneurysms in different vascular locations, e.g. fusiform abdominal aneurysms (which have been previously simulated with the FSG loop without CMB coupling (Aparício et al., 2014)).

4.4 CONCLUSION

The 3D CMB model of arterial G&R formulated in this chapter was a natural development of the 1D formulation in Chapter 2, which can now simulate evolving heterogeneous tissue properties in complex and non–axisymmetrical geometries. The choice of a particular formulation for the chemo–biological model was based on the experimental observation that large numbers of adventitial myofibroblasts arose following mechanical perturbation, Chapter 3. This chemo–biological model was coupled to the 3D FEM–based structural solver of a fluid–solid–growth (FSG) simulation loop. To take full advantage of it, the haemodynamics computed by the CFD component of the FSG loop should be coupled to arterial wall mechanobiology by extending the existing chemo–biological model. This fully coupled 3D CMB–FSG computational framework would be able to solve solid and fluid mechanics modulating the chemo–biological mechanisms underlying arterial G&R in complex geometries, which could be applied to investigate the response of dysfunctional arteries to novel pharmacological, genetic or stem cell therapies.

CHAPTER 5

CONCLUSIONS AND FUTURE DIRECTIONS

A conceptual chemo–mechano–biological (CMB) model of cell–mediated, TGF-β–regulated arterial growth and remodelling (G&R) was formulated, informed by experimental observations and integrated into a 3–dimensional computational framework. In this chapter, key model findings of the D.Phil. work will be summarised (Sec. 5.1). Limitations and recommendations on how to address them are then presented, as well as directions for future research (Sec. 5.2).

Bidirectional interactions between vascular cell populations and the matrix they maintain determine arterial response to perturbation from homoeostasis in health and disease; this has been the subject of extensive investigation by means of experimental and theoretical models focusing on separate aspects of arterial chemo–mechano–biology, Chapter 1. In this D.Phil. project, the roles of signalling pathways and cell–mediated vascular tissue growth and remodelling (G&R) determining arterial biomechanics were investigated by a combined theoretical, experimental and computational approach.

A conceptual model of fibroblast–mediated adventitial collagen metabolism under the control of the signalling mediator transforming growth factor (TGF)-β was coupled to a 1D model of arterial mechanics, which treated the vessel wall as an internally pressurised, axially stretched bilayered nonlinear elastic membrane, Chapter 2. The coupled 1D chemo–mechano–biological (CMB) model was used to describe the evolution of mechanical, microstructural, biochemical and cellular variables characterising the wall of evolving inflammatory aneurysms, as well as to investigate *in silico* the outcomes of applying a profibrotic stimulus to enlarging aneurysms. The model was then extended to capture different aspects of arterial mechanobiology, in partic-

ular: cellular and biochemical variables influencing collagen fibre remodelling; myofibroblast differentiation and population dynamics; and vascular cell mechanical maturation. So as to guide theoretical model development, a novel mouse model of arterial mechanobiological response to perturbed TGF-β signalling was further challenged by pharmacologically–induced hypertension, Chapter 3. Arterial wall properties were quantified for different segments (ascending thoracic aorta, ATA *vs.* infrarenal abdominal aorta, IAA), different layers (media *vs.* adventitia) and at several time points (6, 12, 14 and 18 weeks). For each sample, arterial mechanics were characterised by fitting pressure–inflation, axial force–stretching biaxial mechanical testing data to a four fibre–family constitutive model; arterial collagen microstructure was visualised by Picrosirius red (PSR) histological staining; and layer–specific distributions of biomolecular and cellular markers were imaged by immunofluorescence (IF). In Chapter 4, the CMB theoretical model informed by experimental observations was extended to 3 dimensions by coupling with the FEM structural solver component of a fluid–solid–growth (FSG) computational framework. This 3D–CMB modelling framework was used to simulate the development of saccular intracranial aneurysms, as well as to investigate the couplings between the dynamics of arterial mechanics and geometry and its microstructural, biochemical and cellular properties, in particular when subject to a TGF-β profibrotic stimulus.

5.1 Main findings

5.1.1 Chapter 2: Conceptual 1D CMB model of arterial G&R

The 1D CMB model of cell–mediated, TGF-β–regulated arterial G&R was used to simulate the evolution of biomechanical, biochemical and cellular variables over aneurysmal expansion secondary to inflammation–driven medial degradation, Sec. 2.1. The model is able to capture two clinically–observed modes of aneurysm development, continuous growth *vs.* stabilisation, by varying a single parameter value governing cellular mechanotransduction. Aneurysm stabilisation is promoted by two mechanisms observed experimentally and included in the model: (a) adventitial adaption to load–bearing as a result of a rightward shift of the collagen attachment stretch distribution; and (b) profibrotic adventitial response promoted by (transient) TGF-β signalling and characterised by increased fibroblast cellularity, collagenase and collagenase inhibitor

levels and lower proteolytic activity, with the resulting collagen accumulation increasing load–bearing capacity. The application of a step increase in TGF-β levels promotes the stabilisation of otherwise growing aneurysms; this novel theoretical prediction is consistent with experimental observations from animal aneurysm models. Numerical exploration revealed that predicted system behaviour was very sensitive to parameters related to TGF-β secretion (in response to deviation from mechanical homoeostasis), activation and influence on fibroblast population dynamics, as well as to parameters related to collagen fibre recruitment stretch remodelling and attachment stretch adaption.

CMB model formulation was then extended to capture several mechanobiological processes, Sec. 2.2. Firstly, the rate of remodelling of the collagen recruitment stretch distribution was coupled to the levels of fibroblasts and collagenases mediating collagen turnover, Sec. 2.2.1. Simulation results are consistent with those of previous formulations for most parameter sets; however, large rates of recruitment stretch remodelling and/or low rates of attachment stretch adaption led to continuous growth. This behaviour resulted from a fibroblast–mediated competition between collagen growth (stabilising) *vs.* remodelling (unstabilising), favouring the latter; further theoretical and experimental investigation is warranted.

In a second extension, the CMB model was enriched with terms describing TGF-β– and strain–dependent fibroblast to myofibroblast differentiation, and terms coupling immune cell phenotype and TGF-β signalling, Sec. 2.2.2. Following the introduction of a small medial perturbation, the model predicts aneurysmal enlargement of the artery and the appearance of a population of adventitial myofibroblasts. Increasing myofibroblast permanence time by increasing differentiation rate and/or reducing apoptosis rate past critical values shifts system behaviour from stabilisation to continuous growth, which has been hypothesised (but not yet modelled or experimentally studied) in the literature. Two mechanisms were responsible for this bifurcation behaviour: excessive collagen degradation as a result of an imbalance between collagenase and collagen secretion by (highly migratory) myofibroblasts; and very fast remodelling of collagen recruitment stretch by (highly contractile) myofibroblasts.

Finally, a descriptor of vascular cell mechanical maturation was added to the CMB model. The *cell stiffness* variable (ς^{cell}) captures the formation of sub–cellular stress generating and transmitting elements under the control of mechanical and biochemical stimuli, and couples it

to cell–mediated collagen fibre recruitment stretch remodelling and attachment stretch adaption, Sec. 2.2.3. The influence of different mechanisms on the evolution of cell stiffness was numerically assessed. Simulation results show that cell and matrix stretching determine the initial evolution and final steady–state of ς^{cell}, resp., while biochemical signalling has but a transitory influence, determining peak ς^{cell} values. Different aspects of cell stiffness dynamics can thus be independently controlled by individual parameters, which encourages further development of this model component coupling sub–cellular structure to cellular mechanical function.

5.1.2 Chapter 3: *In vivo* model of arterial chemo–mechano–biology

A previously developed animal model of arterial response to post–developmental disruption of TGF-β signalling through TGF-β receptor type 2 (TGFBR2) was further challenged by pharmacologically–induced hypertension, and used to characterise thoracic and abdominal aortic mechanical, microstructural, cellular and biochemical properties at several time points. Biaxial mechanical testing and fitting to a microstructurally–motivated fibre–reinforced arterial tissue constitutive model revealed the following trends in the perturbed groups: increased arterial calibre (in particular at low pressures) and wall thickness; increased structural stiffness (correlated to increased collagen content) and decreased extensibility and distensibility; decreased biaxial material linearised stiffness, which may be due to a shift in arterial stress–strain operating point; decreased *in vivo* stretch and stored elastic energy, and increased energy dissipation ratio, which may be correlated to elastin degradation and/or increased intramural viscous dissipation. The previous trends were exaggerated when TGFBR2 disruption was combined with hypertension, which suggests a synergistic action of these two perturbations.

Layer–specific visualisation of collagen architecture by PSR histological staining, and distribution of cellular and biochemical markers by IF revealed important changes in the microstructure and chemo–biology of perturbed arteries. In particular, altered adventitial properties following perturbation point to the very important mechanoresponsive role of this layer, as well as to the existence of a communication link between the media and the adventitia: significantly increased total adventitial collagen (especially in hypertensive arteries), with evolving collagen fibre thickness and packing suggesting collagen maturation processes; elevated adventitial density of collagen and collagenase MMP-2; greatly increased adventitial cellularity, in particular of

CD45–positive immune cells and α-SMA–positive contractile myofibroblasts; increased adventitial TGF-β signalling, both in terms of extracellular TGF-β ligands, and intracellular pSMAD-2 downstream signalling mediator. In comparison, medial properties changed much less following perturbation, with small increases in infiltrating immune cells and (elastin–degrading) MMP-2 following TGFBR2 disruption suggesting inflammatory medial damage, and increased medial collagen levels 6 weeks after induction of hypertension suggesting *de novo* collagen deposition (possibly by migratory myofibroblasts). Clear differences in chemo–mechano–biological properties in each segment could also be found. IAAs tended to display smaller increases in total collagen levels than ATAs, which tended to be thicker and more densely packed, thus suggesting a more efficient G&R response to perturbation. In line with this reasoning, mechanical quantities (thickness, biaxial Cauchy stress, stored elastic energy) in IAAs deviated less from baseline values than did those in ATAs, and levels of biochemical and cellular markers either deviated less or returned faster to baseline in IAAs than in ATAs.

So as to assess the ability of the 1D CMB model formulated in Chapter 2 to describe key features of the experimental data set, a preliminary qualitative fit was attempted. The model was parametrised with IAA geometrical features, and an exogenous adventitial TGF-β source and a step increase in intraluminal pressure were applied to simulate adventitial perturbation following TGFBR2 disruption in medial VSMCs and hypertension, resp. The arterial response predicted by the 1D model was qualitatively consistent with experimental findings, in particular adventitial thickening, increased collagen and collagenase levels, transiently increased myofibroblast numbers and increased TGF-β signalling. Less consistent predictions of biaxial stretch ratios suggested that better modelling of medial layer mechanobiology was needed; conversely, the potential of the model to virtually simulate alternative experimental conditions or time scales may be useful in informing future experimental studies.

5.1.3 Chapter 4: CMB model extension to 3 dimensions

The 1D CMB model developed in Chapter 2 was extended to a 3D formulation by coupling with the FEM structural solver component of a previously developed fluid–solid–growth (FSG) computational framework. The model was used to predict the temporal evolution of arterial geometry, mechanical properties and mural distributions of chemo–biological species in the context

of saccular aneurysm (SA) development. Following prescribed medial degradation, the 3D CMB model predicts an adaptive adventitial response signalled by TGF-β and characterised by increased cellularity, myofibroblast differentiation, decreased collagenolytic activity and increased collagen secretion, jointly promoting increased adventitial collagen levels leading to arterial wall reinforcement and aneurysm stabilisation; the predicted changes are consistent with experimental observations in the walls of unruptured, mechanically–robust SAs. The changing role of the adventitia in becoming the main load–bearing layer was captured by evolving the collagen attachment stretch distribution as a function of system dynamics. The importance of collagen dynamics in determining aneurysmal enlargement and eventual stabilisation was confirmed by observing that lower rates of collagen attachment stretch adaption promoted the development of significantly larger aneurysms. The effect of applying a profibrotic "therapeutic" stimulus to the dynamics of aneurysm expansion was also investigated. The application of a step increase in active TGF-β levels on the medial degradation region boosted the adventitial profibrotic response, which resulted in earlier arrest of aneurysm growth at much lower domain strains than otherwise. The 3D CMB model also predicted that SAs with a tendency towards larger growth had comparatively larger reductions in size.

Arterial evolution predicted by the 1D *vs.* 3D implementations of the CMB model were also compared. Consistent trends were predicted by either implementation, thus suggesting that the 1D model can be initially used to gain some insight into system behaviour with reduced computational costs. However, simulation results also make clear the importance of updating model formulation to 3D. The complex, non–axisymmetrical geometries of evolving SAs could not be simulated by a 1D model. Moreover, spatial distributions of mechanical, microstructural and chemo–biological variables were predicted to evolve over time by the 3D CMB model, which illustrates the ability of this framework to describe time–dependent heterogeneous tissue properties. In addition, a large range of values was computed for system variables at different locations (e.g. centre of aneurysm dome *vs.* boundary); the average values computed by the homogenised 1D model could not adequately reflect tissue properties at specific locations, which determine vessel geometry, mechanobiological response and disease progression.

5.2 Limitations and Recommendations

5.2.1 Chapter 2: Conceptual 1D CMB model of arterial G&R

Several simplifications and particular choices were made when formulating the 1D CMB model, Sec. 2.1. Adopting a 1D representation of the arterial wall as an idealised cylindrical membrane was important to gain initial insight; however, it does not match the geometry of most human arteries, especially at later stages of disease where tortuosity and local thickness variations arise. This point was partially addressed in Chapter 4, where the CMB model was implemented in a 3D framework able to describe non–axisymmetrical arteries. For the sake of simplicity and in the absence of detailed mechanical data, particular functional forms were chosen for the pdfs describing collagen attachment and recruitment stretch distributions, the coupling of cell phenotype to deviations from mechanical homoeostasis, and the evolution equations for collagen attachment stretch adaption; in any case, model formulation is flexible enough to accommodate alternative functions once more experimental data become available.

The biochemical component of the CMB model focused on adventitial fibroblast mechanosensing and vascular matrix turnover; coupling it with models of intimal endothelial cell (transducing haemodynamics and regulating luminal permeability) and medial vascular smooth muscle cell (regulating vessel tonus by active stress generation) function available in the literature would be relatively straightforward and expand the range of mechanobiological processes captured. Furthermore, the lack of comprehensive, multi–dimensional experimental data has not allowed for model calibration and validation. To start addressing this point, mechanical, microstructural, biochemical and cellular data were generated from an animal model of signalling and mechanical perturbation, Chapter 3; additional *in vitro* and animal models should be used to generate data to assist theoretical model development.

When coupling arterial chemo–biology to the remodelling of collagen fibre reference configuration, Sec. 2.2.1, several particular choices were made: non–saturating kinetics for all cellular/biochemical species; first order kinetics for collagen and collagenase maturation; rate of collagen recruitment stretch remodelling being proportional to the ratio of fibroblast to collagen densities. Mathematical tractability was on the basis of these simplifications; further model exploration informed by experimental findings will guide future model development.

Several simplifications were also made on the conceptual description of myofibroblast differentiation, population dynamics and action on the ECM, Sec. 2.2.2. The differentiation continuum from restive fibroblasts to differentiated myofibroblasts was modelled by means of two discrete states, n_A^F and n_A^M; describing the fibroblast–myofibroblast population as a single species with evolving properties (e.g. evolving rate parameters), or alternatively introducing an intermediate "proto–myofibroblast" variable, might be important to better model the evolving mechanobiological action of these cells (e.g. migration involving matrix degradation *vs.* stationary tension generation and matrix remodelling). In addition, fibroblasts were considered to be the only cell source of myofibroblasts, and myofibroblast de–differentiation was not considered, which are appropriate choices when modelling adventitial mechanobiology in mature arteries. Application of this conceptual model to the study of other systems (e.g. wound healing, cancer) may require that these and other aspects of myofibroblast biology are included.

Cellular integration of environmental signals in determining intracellular properties (*structure*) and behaviour (*function*) influencing cell action on the matrix was modelled in Sec. 2.2.3 by introducing a *cell stiffness* variable. This variable describes the maturation of tension–generation (stress fibres) and tension–transmission (focal adhesions) sub–cellular structures; modelling these elements separately may provide important additional insight. Particularly simple functions were chosen to describe the influence of only three signals (cell / matrix stretch and TGF-β concentration) on cell mechanical maturation. In reality, many other factors influence SF and FA dynamics (e.g. local matrix stiffness), and alternative functions may better capture the coupling between environmental cues and cell mechanical state. Performing highly controlled *in vitro* experiments where mechanical or biochemical stimuli (*inputs*) were applied, and resulting cellular composition in SF and FA (e.g. by immunostaining specific markers) and cell mechanical phenotype (*output*, e.g. by traction force microscopy) were quantified would provide high–quality data for model development.

5.2.2 Chapter 3: *In vivo* model of arterial chemo–mechano–biology

Practical restrictions resulted in a number of limitations to experimental study design, methods and data processing. Limited numbers of appropriate mice (*Myh11-CreER^{T2}.Tgfbr2$^{f/f}$* male mice of strain C57BL/6 between 6 and 18 weeks of age), a tight experimental schedule and

tissue processing artefacts resulted in low sample size in some observation groups, which precluded the use of statistical analysis. Also due to the very limited number of mice available, blood pressure was measured in uninducible female mice of matching age and strain; in the future, measuring the blood pressure in male mice of each observation group just before sacrifice is recommended. Pharmacological induction of hypertension by high–salt diet supplemented with L-NAME has been chosen due to its low inflammatory component, which is nonetheless present. An ideal hypertensive stimulus should not trigger an immune response, which confounds the chemo–mechano–biological changes observed post–perturbation; in the future, antioxidants could be administered alongside L-NAME to eliminate reactive oxygen species, thus blocking downstream proinflammatory local AngII signalling.

Fits of the biaxial mechanical data to the four–fibre family microstructurally–motivated constitutive model were of reasonable quality; some undesirable features, however, were still present, especially for diseased arteries. Continuous development of better constitutive models and objective functions for non–linear regression should be pursued. Taking into account the relatively long mechanical testing protocols (hours), and the diffusible nature of some biochemical species (e.g. TGF-β ligand) being quantified, it was decided to fix, stain and quantify tissue sections adjacent to those mechanically tested. Future investigation should assess the influence of the mechanical testing protocol on the intramural distributions of diffusible species.

In addition to the cellular and biochemical species studied here, future studies should quantify additional markers: MMP-9, a proteolytic enzyme secreted by infiltrating immune cells with elastolytic and collagenolytic activities and associated with aneurysm formation; elastin, the most important load–bearing constituent of the media and whose degradation has been associated with aneurysm expansion; protease inhibitors TIMP-1,2, which form inhibitory complexes with MMP-9,2, resp.; GAGs, whose intramural accumulation has been associated with increased viscous dissipation and wall delamination; and FSP-1, a putative fibroblast–specific marker. Both PSR and IF techniques in this study quantified protein levels. Quantifying gene transcription by techniques such as *in situ hybridization* may be important to localise sources of diffusible proteins and study inter–layer communication.

The 1D CMB model of cell–mediated, TGF-β–regulated arterial G&R was adapted to predict some trends observed in the experimental data. This qualitative fit revealed that the current model

formulation requires further development to capture arterial adaption in cases when the media is not fully degraded; coupling the model with a representation of medial VSMC mechanobiology may address this need. Future CMB model formulations will require rigorous quantitative fitting to experimental data sets for model calibration and validation.

5.2.3 Chapter 4: CMB model extension to 3 dimensions

Updating the mechanical implementation of the CMB model from 1D to 3D has allowed for the simulation of arterial chemo–mechano–biological evolution in complex, non–axisymmetrical geometries. Even so, this work is but the first step towards a fully coupled 3D CMB–FSG computational framework able to simulate arterial wall solid mechanics and intraluminal haemodynamics directing vascular cell–mediated G&R adaptive response. A critical step towards this goal is to extend the chemo–biological component of the CMB model to describe mural cell response to specific haemodynamical conditions computed by the CFD component of the FSG loop. In particular, adding a variable describing endothelial cell–regulated vascular permeability to infiltrating immune cells as a function of WSS would straightforwardly couple blood flow conditions to medial degradation triggering aneurysm development.

In the current 3D CMB model formulation, no spatial dependency is included in the equations (ODEs) governing the evolution of cellular or biochemical variables. Given that both mural (myo)fibroblasts and infiltrating immune cells are motile, and that active TGF-β and many collagenases are diffusible, it is important to formulate spatially–dependent reaction–diffusion equations (PDEs), which would be numerically solved by an advection–diffusion solver. In addition, the updated CMB model treats the arterial wall as a membrane in 3D. This formulation is not appropriate to describe thick walled arteries (such as the IAAs observed in the experimental study) that undergo significant deformations (which may take place locally in complex geometries), and/or when extensive elastin degradation compromises the prestresses homogenising the transmural stress distribution. In spite of increased computational complexity, a thick–wall formulation would enable the computation of evolving thickness at each spatial element, with important implications to wall stress/strength and rupture potential.

Detailed model characterisation should be performed by running extensive numerical sensitivity studies, in particular on parameters controlling collagen recruitment stretch remodelling

and attachment stretch adaption. All aneurysms simulated eventually stabilised, which took place faster when active TGF-β was applied; in the future, alternative "therapeutic" regimes (spatially–dependent, time–varying or periodic administration of TGF-β, collagenase inhibitors, etc.) could be simulated, in particular in the context of continuously–growing, non–stabilising aneurysms. Finally, only saccular aneurysms were simulated; however, the 3D CMB model is well suited to simulate fusiform aneurysm evolution.

5.2.4 Directions for Future Research

5.2.4.1 Therapy modelling

Based on the experimental observations of Dai et al. (2005b, 2011), the potential of increasing active TGF-β levels as a profibrotic stimulus protective against continuous aneurysm enlargement was assessed in Chapter 2 and Chapter 4. As previously discussed, the current formulation of the CMB model could be used to study the effects on arterial wall mechanobiology of different TGF-β application patterns (continuous administration and/or repeated stimulation at different levels or times).

Many diseases such as fibrosis, Marphan syndrome or late–stage cancer, however, seem to be associated with elevated TGF-β signalling. A number of different therapeutic strategies has been explored, in particular pharmacological inhibition of components of the TGF-β signalling pathway such as TGF-β ligands, TGF-β receptors, TGFBR1 kinase, or attachment of SMAD-2,3/4 transcription factors to the promoter of the *TGF-β* gene (Leask, 2010; Akhurst and Hata, 2012). The unintended side effects of TGF-β signalling inhibition (including carcinogenic potential and induction of autoimmunity and inflammation) have prompted the investigation of alternative strategies to reduce TGF-β signalling, including blocking TGF-β–activating integrins (Henderson and Sheppard, 2013).

The CMB model formulated here couples TGF-β regulation of (vascular) cell phenotype to cell–mediated G&R of their surrounding matrix influencing tissue–level mechanical properties. As such, the CMB model framework has a great potential to investigate the effects of altering TGF-β signalling on the evolution of cellular phenotype and matrix properties in diseases such as fibrosis or cancer (see Sec. 5.2.4.2 below). Extending the existing cell–level model of TGF-β

profibrotic signalling to describe other TGF-β actions, and coupling it with models of downstream intracellular signalling, would enable for the outcomes of different therapeutic strategies targeting TGF-β signalling to be assessed computationally before expensive experimental testing.

5.2.4.2 Modelling TGF-β signalling in other systems

TGF-β is a pleiotropic peptide present in connective, epithelial, muscle and nervous tissue, and involved in signalling and regulation of many cellular processes including cell differentiation, phenotype, fate and matrix remodelling in health and disease (Morikawa et al., 2016). In this section, TGF-β actions on systems other than the aneurysmal mature arterial adventitia are discussed, in particular in relation to possible extensions of the CMB modelling framework to describe regulatory TGF-β signalling in these tissues.

Vascular system Altered TGF-β signalling has been reported in several vascular conditions other than arterial aneurysms. Elevated TGF-β signalling is associated with increased TIMP secretion and decreased MMP expression resulting in increased ECM deposition, which was seen to promote aneurysm stabilisation in Chapter 2 and Chapter 4; however, excessive fibrosis and wall stiffening may also result, in particular in the context of hypertension (Ruiz-Ortega et al., 2007). TGF-β profibrotic and immunosuppressive actions seem to be protective in the context of atherosclerosis: genetic and histological studies have shown that reduced TGF-β levels are associated with the development of unstable atherosclerotic plaques (Grainger, 2007), while induced overexpression of TGF-β1 in an animal model of atherosclerosis has promoted increased matrix deposition and reduced arterial inflammation, thus leading to stabilisation of atherosclerotic plaques and reduction in atherosclerotic aneurysm dilation (Frutkin et al., 2009). Given that the current CMB model was specifically developed to capture TGF-β profibrotic action on blood vessels, model adaptation to describe vascular fibrosis and atherosclerotic plaque stabilisation under the influence of TGF-β would be relatively straightforward.

Heart TGF-β promotion of fibrotic processes has also been observed in cardiac tissue. TGF-β signalling has been reported to increase following cardiac overload, and to promote cardiac fibroblast proliferation, differentiation into contractile myofibroblasts and increased deposition of stiff collagenous matrix, and cardiomyocyte hypertrophy, jointly leading to thicker and

stiffer ventricular walls associated with reduced cardiac function and progression to heart failure (Rosenkranz, 2004). Studies on the signalling pathways regulating cardiac fibrosis suggest that TGF-β cross–talks with the proinflammatory, profibrotic AngII pathway, both of which induce the expression of connective tissue growth factor (CTGF), a strong promoter of fibrosis (Leask, 2010). Once again, the current formulation of the CMB model is well equipped to describe TGF-β profibrotic action in cardiac tissue.

Skin and musculoskeletal system TGF-β has for long been recognised as an important regulator of skin microstructure and mechanical properties, in particular in the context of wound healing (Gurtner et al., 2008). In the acute phase of wound healing, TGF-β signalling strongly promotes the migration of mesenchymal cells, in particular fibroblasts, which are responsible for fast matrix deposition (Li et al., 2007). Different proportions of TGF-β isoforms seem to promote distinct types of wound resolution, with TGF-β1 and TGF-β3 traditionally associated with fibrotic scar formation and scarless wound healing, resp. (Penn et al., 2012). Sustained TGF-β signalling together with mechanical tension promote myofibroblast differentiation, cells which are responsible for late–phase wound tissue remodelling (Tomasek et al., 2002). TGF-β signalling also plays important roles in mediating cellular transduction and integration of chemo–mechanical stimuli in the musculoskeletal system (Rys et al., 2016). Mechanical loading of articular cartilage changes the micromechanical environment of chondrocyte cells, which upregulate TGF-β3 gene expression and increase matrix deposition. Disrupted TGF-β downstream intracellular signalling *via* SMAD3 has also been associated with excessive matrix degradation in the context of osteoarthritis. TGF-β signalling of deviations from mechanical homoeostasis and regulation of cellular phenotype associated with matrix G&R informed CMB model formulation, which was based on a model of collagen metabolism in wound healing; as such, CMB model adaptation to describe TGF-β mechanotransduction in the skin or the musculoskeletal system is an interesting future possibility.

Other systems TGF-β regulates a large number of physiological processes; the CMB model formulated here can be extended and coupled with biochemical/cell biology models to describe other systems whose mechanobiological response is modulated by TGF-β. TGF-β regulation of bladder wall matrix and cell properties has not been extensively characterised; however, recent

experimental results suggest that TGF-β signalling and cyclic loading induce a phenotypic shift in bladder SMCs promoting collagen secretion (Heise et al., 2012). TGF-β signalling has also been shown to promote fibrosis in non–load bearing tissues such as the liver (Fabregat et al., 2016) and the kidney, in particular in association with chronic kidney disease (Meng et al., 2016). The TGF-β profibrotic mechanisms included in the CMB model could be integrated in conceptual models of these systems. Other important mechanobiological processes regulated by TGF-β signalling are somewhat related to those modelled here, but their description would require the development of novel CMB models. Angiogenesis, myogenesis and vasculogenesis occurring during development are strongly regulated by TGF-β signalling (Dijke and Arthur, 2007; Pardali et al., 2010), which modulates vascular cell phenotype and the establishment of a cohesive vessel wall. TGF-β signalling has also been associated with cancer progression and advanced stage metastasis, which are promoted by TGF-β–mediated fibroblast recruitment, phenotypic switch towards carcinoma–associated fibroblasts, and fibroblast–endothelial interactions facilitating the penetration of tumour cells into the blood stream (Kalluri and Zeisberg, 2006).

5.3 Final Note

The work presented in this thesis is but a first step in developing conceptual models, experimental data and computational tools to better understand the extremely important yet poorly studied couplings between arterial mechanics, biochemistry and cell biology. Future knowledge and tools developed by following these lines of research will hopefully have a positive impact in clinical prognosis, management and treatment of patients suffering from connective tissue dysfunction, in particular in the cardiovascular system.

REFERENCES

ABBAS, A., LICHTMAN, A., AND PILLAI, S. *Cellular and Molecular Immunology*. Saunders, 8th edition, 2014.

AKHURST, R. J. AND HATA, A. Targeting the TGFβ signalling pathway in disease. *Nature reviews. Drug discovery*, 11(10): 790–811, October 2012. ISSN 1474-1784.

ALBERTS, B., BRAY, D., LEWIS, J., RAFF, M., ROBERTS, K., AND WATSON, J. *Molecular biology of the cell*, page 984. Garland Publishing, 3rd edition, 1994.

ALBERTS, B., JOHNSON, A., LEWIS, J., MORGAN, D., RAFF, M., ROBERTS, M., AND WALTER, P. *Molecular Biology of the Cell*. Garland Science, 6th edition, 2014.

APARÍCIO, P., MANDALTSI, A., BOAMAH, J., CHEN, H., SELIMOVIC, A., BRATBY, M., UBEROI, R., VENTIKOS, Y., AND WATTON, P. Modelling the influence of endothelial heterogeneity on the progression of arterial disease: application to abdominal aortic aneurysm evolution. *International Journal for Numerical Methods in Biomedical Engineering*, 30:563–586, 2014.

APARÍCIO, P., THOMPSON, M. S., AND WATTON, P. N. A novel chemo-mechano-biological model of arterial tissue growth and remodelling. *Journal of biomechanics*, 49(12): 2321–2330, 2016.

APPLING, W. D., O'BRIEN, W. R., JOHNSTON, D. A., AND DUVIC, M. Synergistic enhancement of type I and III collagen production in cultured fibroblasts by transforming growth factor-beta and ascorbate. *FEBS letters*, 250(2):541–4, July 1989. ISSN 0014-5793.

ATESHIAN, G. . AND HUMPHREY, J. D. Continuum mixture models of biological growth and remodeling: past successes and future opportunities. *Annual review of biomedical engineering*, 14:97–111, January 2012. ISSN 1545-4274.

AZIZ, F. AND KUIVANIEMI, H. Role of Matrix Metalloproteinase Inhibitors in Preventing Abdominal Aortic Aneurysm. *Ann Vasc Surg.*, 21(3):392–401, 2008.

BAEK, S., GLEASON, R., RAJAGOPAL, K., AND HUMPHREY, J. Theory of small on large: potential utility in computations of fluid–solid interactions in arteries. *Computer Methods in Applied Mechanics and Engineering*, 196(31):3070–3078, 2007a.

BAEK, S., RAJAGOPAL, K. R., AND HUMPHREY, J. D. Competition between radial expansion and thickening in the enlargement of an intracranial saccular aneurysm. *Journal of Elasticity*, 80(1-3):13–31, 2005. ISSN 03743535.

BAEK, S., RAJAGOPAL, K. R., AND HUMPHREY, J. D. A Theoretical Model of Enlarging Intracranial Fusiform Aneurysms. *Journal of Biomedical Engineering*, 128:142–149, 2006.

BAEK, S., VALENTIN, A., AND HUMPHREY, J. Biomechanics of cerebral vasospasm and its resolution: Ii. constitutive relations and model simulations. *Annals of Biomedical Engineering*, 35(9):1498–1509, 2007b.

BAI, Y., LEE, P.-F., HUMPHREY, J. D., AND YEH, A. T. Sequential multimodal microscopic imaging and biaxial mechanical testing of living multicomponent tissue constructs. *Annals of biomedical engineering*, pages 1–15, 2014.

BARBOUR, J. R., SPINALE, F. G., AND IKONOMIDIS, J. S. Proteinase systems and thoracic aortic aneurysm progression. *The Journal of surgical research*, 139(2):292–307, May 2007. ISSN 0022-4804.

BEAMISH, J. A., HE, P., KOTTKE-MARCHANT, K., AND MARCHANT, R. E. Molecular regulation of contractile smooth muscle cell phenotype: implications for vascular tissue engineering. *Tissue Engineering Part B: Reviews*, 16(5): 467–491, 2010.

BELLINI, C., FERRUZZI, J., ROCCABIANCA, S., DI MARTINO, E. S., AND HUMPHREY, J. D. A microstructurally motivated model of arterial wall mechanics with mechanobiological implications. *Annals of biomedical engineering*, 42 (3):488–502, March 2014. ISSN 1573-9686.

BELLINI, C., WANG, S., MILEWICZ, D. M., AND HUMPHREY, J. D. Myh11r247c/r247c mutations increase thoracic aorta vulnerability to intramural damage despite a general biomechanical adaptivity. *Journal of biomechanics*, 48(1):113–121, 2015.

BERSI, M. R., COLLINS, M. J., WILSON, E., AND HUMPHREY, J. D. Disparate Changes in the Mechanical Properties of Murine Carotid Arteries and Aorta in Response to Chronic Infusion of Angiotensin-II. *International journal of advances in engineering sciences and applied mathematics*, 4(4):228–240, December 2013. ISSN 0975-0770.

BERSI, M. R., FERRUZZI, J., EBERTH, J. F., GLEASON, R. L., AND HUMPHREY, J. D. Consistent Biomechanical Phenotyping of Common Carotid Arteries from Seven Genetic, Pharmacological, and Surgical Mouse Models. *Annals of Biomedical Engineering*, 42(6):1207–1223, 2014. ISSN 0090-6964.

Bersi, M. R., Bellini, C., Wu, J., Montaniel, K. R., Harrison, D. G., and Humphrey, J. D. Excessive adventitial remodeling leads to early aortic maladaptation in angiotensin-induced hypertension. *Hypertension*, 67(5): 890–896, 2016.

Bhowmick, N. a., Chytil, A., Plieth, D., Gorska, A. E., Dumont, N., Shappell, S., Washington, M. K., Neilson, E. G., and Moses, H. L. TGF-beta signaling in fibroblasts modulates the oncogenic potential of adjacent epithelia. *Science (New York, N.Y.)*, 303(5659): 848–851, 2004. ISSN 0036-8075.

Brew, K., Dinakarpandian, D., and Nagase, H. Tissue inhibitors of metalloproteinases: evolution, structure and function. *Biochimica et biophysica acta*, 1477(1-2):267–83, March 2000. ISSN 0006-3002.

Brophy, C. M., Marks, W. H., Reilly, J. M., and Tilson, M. D. Decreased tissue inhibitor of metalloproteinases (TIMP) in abdominal aortic aneurysm tissue: a preliminary report. *The Journal of surgical research*, 50(6): 653–7, June 1991. ISSN 0022-4804.

Burridge, K. and Chrzanowska-Wodnicka, M. Focal adhesions, contractility, and signaling. *Annual review of cell and developmental biology*, 12(1):463–519, 1996.

Cardamone, L., Valentin, A., Eberth, J., and Humphrey, J. Origin of axial prestretch and residual stress in arteries. *Biomechanics and modeling in mechanobiology*, 8(6):431–446, 2009.

Cebral, J. R., Castro, M. A., Burgess, J. E., Pergolizzi, R. S., Sheridan, M. J., and Putman, C. M. Characterization of Cerebral Aneurysms for Assessing Risk of Rupture By Using Patient-Specific Computational Hemodynamics Models. *American Journal of Neuroradiology*, 26: 2550–2559, 2005.

Chatziprodromou, I., Tricoli, A., Poulikakos, D., and Ventikos, Y. Haemodynamics and wall remodelling of a growing cerebral aneurysm: \mbox{A} computational model. *Journal of Biomechanics*, 40:412–426, 2007.

Chen, C. S., Alonso, J. L., Ostuni, E., Whitesides, G. M., and Ingber, D. E. Cell shape provides global control of focal adhesion assembly. *Biochemical and biophysical research communications*, 307(2):355–361, 2003.

Chen, H. *Intracranial Aneurysm Disease: Novel Modelling of Inception and the Microstructural Adaption of Collagen Fabric*. PhD thesis, University of Oxford, 2014.

Chen, Y.-F., Feng, J.-A., Li, P., Xing, D., Zhang, Y., Serra, R., Ambalavanan, N., Majid-Hassan, E., and Oparil, S. Dominant negative mutation of the tgf-β receptor blocks hypoxia-induced pulmonary vascular remodeling. *Journal of Applied Physiology*, 100(2):564–571, 2006.

Cheng, J. K., Stoilov, I., Mecham, R. P., and Wagenseil, J. E. A fiber-based constitutive model predicts changes in amount and organization of matrix proteins with development and disease in the mouse aorta. *Biomechanics and modeling in mechanobiology*, 12(3):497–510, 2013.

Chiquet, M., Renedo, A. S., Huber, F., and Flück, M. How do fibroblasts translate mechanical signals into changes in extracellular matrix production? *Matrix biology : journal of the International Society for Matrix Biology*, 22 (1):73–80, March 2003. ISSN 0945-053X.

Conway, D. and Schwartz, M. Lessons from the endothelial junctional mechanosensory complex. *F1000 biology reports*, 4(January):1, January 2012. ISSN 1757-594X.

Czirok, A., Zach, J., Kozel, B. A., Mecham, R. P., Davis, E. C., and Rongish, B. J. Elastic fiber macroassembly is a hierarchical, cell motion-mediated process. *Journal of cellular physiology*, 207(1):97–106, 2006.

Dai, D., Ding, Y. H., Danielson, M. a., Kadirvel, R., Lewis, D. a., Cloft, H. J., and Kallmes, D. F. Histopathologic and immunohistochemical comparison of human, rabbit, and swine aneurysms embolized with platinum coils. *AJNR. American journal of neuroradiology*, 26 (10):2560–8, 2005a. ISSN 0195-6108.

Dai, J., Losy, F., Guinault, A.-M., Pages, C., Anegon, I., Desgranges, P., Becquemin, J.-P., and Allaire, E. Overexpression of transforming growth factor-β1 stabilizes already-formed aortic aneurysms a first approach to induction of functional healing by endovascular gene therapy. *Circulation*, 112(7):1008–1015, 2005b.

Dai, J., Michineau, S., Franck, G., Desgranges, P., Becquemin, J.-P., Gervais, M., and Allaire, E. Long term stabilization of expanding aortic aneurysms by a short course of cyclosporine a through transforming growth factor-beta induction. *PloS one*, 6(12):e28903, 2011.

Dale, P., Sherratt, J., and Maini, P. A mathematical model for collagen fibre formation during foetal and adult dermal wound healing. *Proceedings of the Royal Society of London*, 263(B):653–660, 1996.

Dallon, J. C., Sherratt, J. A., and Maini, P. K. Modeling the effects of transforming growth factor-β on extracellular matrix alignment in dermal wound repair. *Wound Repair and Regeneration*, 9(4):278–286, 2001.

Dao, H. H., Lemay, J., de Champlain, J., DeBlois, D., and Moreau, P. Norepinephrine-induced aortic hyperplasia and extracellular matrix deposition are endothelin-dependent. *Journal of hypertension*, 19(11):1965–1973, 2001. ISSN 0263-6352.

Dayan, D., Hiss, Y., Hirshberg, A., Bubis, J., and Wolman, M. Are the polarization colors of picrosirius red-stained collagen determined only by the diameter of the fibers? *Histochemistry*, 93(1):27–29, 1989.

Deshpande, V. S., Mrksich, M., McMeeking, R. M., and Evans, A. G. A bio-mechanical model for coupling cell contractility with focal adhesion formation. *Journal of the Mechanics and Physics of Solids*, 56(4):1484–1510, 2008. ISSN 00225096.

Di Martino, E. S., Bohra, A., Vande Geest, J. P., Gupta, N., Makaroun, M. S., and Vorp, D. a.

Biomechanical properties of ruptured versus electively repaired abdominal aortic aneurysm wall tissue. *Journal of vascular surgery*, 43(3):570–6; discussion 576, March 2006. ISSN 0741-5214.

DIJKE, P. AND ARTHUR, H. M. Extracellular control of tgfβ signalling in vascular development and disease. *Nature reviews Molecular cell biology*, 8(11):857–869, 2007.

DOBRIN, P. B. AND MRKVICKA, R. Failure of elastin or collagen as possible critical connective tissue alterations underlying aneurysmal dilatation . PubMed Commons. *Cardiovasc Surg*, 2(4):484–488, 1994.

DOTTER, C. T., ROBERTS, D. J., AND STEINBERG, I. Aortic Length: Angiocardiographic Measurements. *Circulation*, 2 (6):915–920, December 1950. ISSN 0009-7322.

DOYLE, J. J., GERBER, E. E., AND DIETZ, H. C. Matrix-dependent perturbation of TGFβ signaling and disease. *FEBS letters*, 586(14):2003–15, July 2012. ISSN 1873-3468.

DUGINA, V., FONTAO, L., CHAPONNIER, C., VASILIEV, J., AND GABBIANI, G. Focal adhesion features during myofibroblastic differentiation are controlled by intracellular and extracellular factors. *Journal of cell science*, 114(18):3285–3296, 2001.

EBERTH, J. F., GRESHAM, V. C., REDDY, A. K., POPOVIC, N., WILSON, E., AND HUMPHREY, J. D. Importance of pulsatility in hypertensive carotid artery growth and remodeling. *Journal of Hypertension*, 27:2010–2021, 2009.

EBERTH, J. F., POPOVIC, N., GRESHAM, V. C., WILSON, E., AND HUMPHREY, J. D. Time course of carotid artery growth and remodeling in response to altered pulsatility. *American journal of physiology. Heart and circulatory physiology*, 299(6):H1875–83, December 2010. ISSN 1522-1539.

EDELSTEIN-KESHET, L. *Mathematical Models in Biology*. SIAM, 2005.

EDWARDS, B., TULLOS, H., AND NOBLE, P. Contributory Factors and Etiology of Sciatic Nerve Palsy in Total Hip Arthoplasty. *Clinical Orthopaedics and Related Research*, 212:136–141, 1987.

ERIKSSON, T., WATTON, P., LUO, X., AND VENTIKOS, Y. Modelling volumetric growth in a thick walled fibre reinforced artery. *Journal of the Mechanics and Physics of Solids*, 73:134 – 150, 2014. ISSN 0022-5096.

FABREGAT, I., MORENO-CÀCERES, J., SÁNCHEZ, A., DOOLEY, S., DEWIDAR, B., GIANNELLI, G., AND DIJKE, P. Tgf-β signalling and liver disease. *FEBS Journal*, 2016.

FERNÁNDEZ, P., PULLARKAT, P. A., AND OTT, A. A master relation defines the nonlinear viscoelasticity of single fibroblasts. *Biophysical journal*, 90(10):3796–3805, 2006.

FERRUZZI, J., BERSI, M. R., AND HUMPHREY, J. D. Biomechanical phenotyping of central arteries in health and disease: advantages of and methods for murine models. *Annals of biomedical engineering*, 41(7):1311–30, July 2013. ISSN 1573-9686.

FERRUZZI, J., BERSI, M., UMAN, S., YANAGISAWA, H., AND HUMPHREY, J. Decreased elastic energy storage, not increased material stiffness, characterizes central artery dysfunction in fibulin-5 deficiency independent of sex. *Journal of biomechanical engineering*, 137(3):031007, 2015.

FERRUZZI, J., VORP, D., AND HUMPHREY, J. On constitutive descriptors of the biaxial mechanical behaviour of human abdominal aorta and aneurysms. *Journal of the Royal Society Interface*, page rsif20100299, 2010.

FERRUZZI, J., COLLINS, M. J., YEH, A. T., AND HUMPHREY, J. D. Mechanical assessment of elastin integrity in fibrillin-1-deficient carotid arteries: implications for Marfan syndrome. *Cardiovascular research*, 92(2):287–95, nov 2011. ISSN 1755-3245.

FERRUZZI, J., MURTADA, S.-I., LI, G., JIAO, Y., UMAN, S., TING, M. Y., TELLIDES, G., AND HUMPHREY, J. D. Pharmacologically improved contractility protects against aortic dissection in mice with disrupted transforming growth factor-β signaling despite compromised extracellular matrix properties. *Arteriosclerosis, thrombosis, and vascular biology*, 36(5):919–927, 2016.

FIGUEROA, C. A., BAEK, S., TAYLOR, C. A., AND HUMPHREY, J. D. A computational framework for fluid-solid-growth modeling in cardiovascular simulations. *Computational Methods in Applied Mechanics and Engineering*, 198:3583–3602, 2009.

FORTE, A., DELLA CORTE, A., DE FEO, M., CERASUOLO, F., AND CIPOLLARO, M. Role of myofibroblasts in vascular remodelling: focus on restenosis and aneurysm. *Cardiovascular research*, 88(3):395–405, December 2010. ISSN 1755-3245.

FRÖSEN, J., PIIPPO, A., PAETAU, A., KANGASNIEMI, M., NIEMELÄ, M., HERNESNIEMI, J., AND JÄÄSKELÄINEN, J. Remodeling of saccular cerebral artery aneurysm wall is associated with rupture: histological analysis of 24 unruptured and 42 ruptured cases. *Stroke; a journal of cerebral circulation*, 35(10):2287–93, October 2004. ISSN 1524-4628.

FRÖSEN, J., PIIPPO, A., PAETAU, A., KANGASNIEMI, M., NIEMELÄ, M., HERNESNIEMI, J., AND JÄÄSKELÄINEN, J. Growth factor receptor expression and remodeling of saccular cerebral artery aneurysm walls: implications for biological therapy preventing rupture. *Neurosurgery*, 58(3): 534–541, 2006.

FRÖSEN, J., TULAMO, R., PAETAU, A., LAAKSAMO, E., KORJA, M., LAAKSO, A., NIEMELÄ, M., AND HERNESNIEMI, J. Saccular intracranial aneurysm: pathology and mechanisms. *Acta neuropathologica*, 123(6):773–86, June 2012. ISSN 1432-0533.

FRUTKIN, A. D., OTSUKA, G., STEMPIEN-OTERO, A., SESTI, C., DU, L., JAFFE, M., DICHEK, H. L., PENNINGTON, C. J., EDWARDS, D. R., NIEVES-CINTRÓN, M., ET AL. Tgf-β1 limits plaque growth, stabilizes plaque structure, and prevents aortic dilation in apolipoprotein e-null mice. *Arteriosclerosis, thrombosis, and vascular biology*, 29(9):1251–1257, 2009.

FUKUI, D., MIYAGAWA, S., SOEDA, J., TANAKA, K., URAYAMA, H., AND KAWASAKI, S. Overexpression of transforming growth factor β1 in smooth muscle cells of human abdominal aortic aneurysm. *European Journal of Vascular and Endovascular Surgery*, 25(6):540–545, 2003. ISSN 10785884.

FUNG, Y. What are the residual stresses doing in our blood vessels? *Annals of biomedical engineering*, 19(3):237–249, 1991.

FUNG, Y., FRONEK, K., AND PATITUCCI, P. Pseudoelasticity of arteries and of its mathematical expression. *Am Physiological Soc*, 1979.

GAO, F., WATANABE, M., AND MATSUZAWA, T. Stress analysis in a layered aortic arch model under pulsatile blood flow. *Biomedical engineering online*, 5:25, January 2006. ISSN 1475-925X.

GAO, F., CHAMBON, P., OFFERMANNS, S., TELLIDES, G., KONG, W., ZHANG, X., AND LI, W. Disruption of TGF-β signaling in smooth muscle cell prevents elastase-induced abdominal aortic aneurysm. *Biochemical and Biophysical Research Communications*, 454(1):137–143, 2014a. ISSN 0006291X.

GAO, F., CHAMBON, P., TELLIDES, G., KONG, W., ZHANG, X., AND LI, W. Disruption of tgf-β signaling in smooth muscle cell prevents flow-induced vascular remodeling. *Biochemical and biophysical research communications*, 454(1): 245–250, 2014b.

GARRETT, E. R. The bateman function revisited: a critical reevaluation of the quantitative expressions to characterize concentrations in the one compartment body model as a function of time with first-order invasion and first-order elimination. *Journal of pharmacokinetics and biopharmaceutics*, 22(2):103–128, 1994.

GIANNONE, G. AND SHEETZ, M. P. Substrate rigidity and force define form through tyrosine phosphatase and kinase pathways. *Trends in cell biology*, 16(4):213–223, 2006.

GLEASON, R. L., TABER, L. A., AND HUMPHREY, J. D. A \mbox{2-D} model of flow-induced alterations in the geometry, structure and properties of carotid arteries. *Journal of Biomechanical Engineering*, 126:371–381, 2004a.

GLEASON, R., GRAY, S., WILSON, E., AND HUMPHREY, J. A multiaxial computer-controlled organ culture and biomechanical device for mouse carotid arteries. *Journal of biomechanical engineering*, 126(6):787–795, 2004b.

GOEL, S. A., GUO, L.-W., SHI, X.-D., KUNDI, R., SOVINSKI, G., SEEDIAL, S., LIU, B., AND KENT, K. C. Preferential secretion of collagen type 3 versus type 1 from adventitial fibroblasts stimulated by TGF-β/Smad3-treated medial smooth muscle cells. *Cellular Signalling*, 25(4):955–960, 2013. ISSN 08986568.

GOFFIN, J. M., PITTET, P., CSUCS, G., LUSSI, J. W., MEISTER, J.-J., AND HINZ, B. Focal adhesion size controls tension-dependent recruitment of α-smooth muscle actin to stress fibers. *The Journal of cell biology*, 172(2):259–268, 2006.

GRAINGER, D. J. TGF-beta and atherosclerosis in man. *Cardiovascular research*, 74(2):213–22, May 2007. ISSN 0008-6363.

GRINNELL, F. Fibroblast biology in three-dimensional collagen matrices. *Trends in Cell Biology*, 13(5):264–269, May 2003. ISSN 09628924.

GRYTSAN, A., WATTON, P. N., AND HOLZAPFEL, G. A. A thick-walled fluid–solid-growth model of abdominal aortic aneurysm evolution: Application to a patient-specific geometry. *Journal of biomechanical engineering*, 137(3):031008, 2015.

GURTNER, G. C., WERNER, S., BARRANDON, Y., AND LONGAKER, M. T. Wound repair and regeneration. *Nature*, 453 (7193):314–321, 2008.

GUTIERREZ, J. A. AND PERR, H. A. Mechanical stretch modulates TGF-beta1 and alpha1(I) collagen expression in fetal human intestinal smooth muscle cells. *The American journal of physiology*, 277(5 Pt 1):G1074–80, November 1999. ISSN 0002-9513.

GUYTON, A. AND HALL, J. *Textbook of Medical Physiology*. Elsevier Saunders, 11th editi edition, 2006.

HABASHI, J. P., DOYLE, J. J., HOLM, T. M., AZIZ, H., SCHOENHOFF, F., BEDJA, D., CHEN, Y., MODIRI, A. N., JUDGE, D. P., AND DIETZ, H. C. Angiotensin ii type 2 receptor signaling attenuates aortic aneurysm in mice through erk antagonism. *Science*, 332(6027):361–365, 2011.

HABASHI, J. P., JUDGE, D. P., HOLM, T. M., COHN, R. D., LOEYS, B. L., COOPER, T. K., MYERS, L., KLEIN, E. C., LIU, G., CALVI, C., PODOWSKI, M., NEPTUNE, E. R., HALUSHKA, M. K., BEDJA, D., GABRIELSON, K., RIFKIN, D. B., CARTA, L., RAMIREZ, F., HUSO, D. L., AND DIETZ, H. C. Losartan, an AT1 antagonist, prevents aortic aneurysm in a mouse model of Marfan syndrome. *Science (New York, N.Y.)*, 312(5770):117–21, April 2006. ISSN 1095-9203.

HALL, J. *Guyton and Hall Textbook of Medical Physiology*. Saunders, twelfth edition, 2010.

HE, C. M. AND ROACH, M. R. The composition and mechanical properties of abdominal aortic aneurysms. *Journal of vascular surgery*, 20(1):6–13, July 1994. ISSN 0741-5214.

HEISE, R. L., PAREKH, A., JOYCE, E. M., CHANCELLOR, M. B., AND SACKS, M. S. Strain history and TGF-β1 induce urinary bladder wall smooth muscle remodeling and elastogenesis. *Biomechanics and modeling in mechanobiology*, 11(1-2):131–45, January 2012. ISSN 1617-7940.

HENDERSON, N. C. AND SHEPPARD, D. Integrin-mediated regulation of TGF-β in fibrosis. *Biochimica et Biophysica Acta - Molecular Basis of Disease*, 1832(7):891–896, 2013. ISSN 09254439.

HIBUSE, T., MAEDA, N., NAKATSUJI, H., TOCHINO, Y., FUJITA, K., KIHARA, S., FUNAHASHI, T., AND SHIMOMURA, I. The heart requires glycerol as an energy substrate through aquaporin 7, a glycerol facilitator. *Cardiovascular research*, 83(1):34–41, 2009.

HILL, M. R., DUAN, X., GIBSON, G. A., WATKINS, S., AND ROBERTSON, A. M. A theoretical and non-destructive experimental approach for direct inclusion of measured collagen orientation and recruitment into mechanical models of the artery wall. *Journal of biomechanics*, 45(5):762–71, March 2012. ISSN 1873-2380.

HINZ, B. The myofibroblast: paradigm for a mechanically active cell. *Journal of biomechanics*, 43(1):146–155, 2010.

HINZ, B. AND GABBIANI, G. Fibrosis: recent advances in myofibroblast biology and new therapeutic perspectives. *F1000 Biology Reports*, 2(November):1–5, 2010. ISSN 1757594X.

HISHIKAWA, K., NAKAKI, T., AND FUJII, T. Transforming growth factor-beta(1) induces apoptosis via connective tissue growth factor in human aortic smooth muscle cells. *European journal of pharmacology*, 385(2-3):287–90, December 1999. ISSN 0014-2999.

HO, H., SURESH, V., KANG, W., COOLING, M. T., WATTON, P. N., AND HUNTER, P. J. Multiscale Modelling of Intracranial Aneurysms : Cell Signalling , Hemodynamics and Remodelling. *IEEE Transactions on Biomedical Engineering Letters*, pages 1–4, 2010.

HOBEIKA, M. J., THOMPSON, R. W., MUHS, B. E., BROOKS, P. C., AND GAGNE, P. J. Matrix metalloproteinases in peripheral vascular disease. *Journal of vascular surgery*, 45(4):849–57, April 2007. ISSN 0741-5214.

HOLLAND, E. *Computational modelling of transport phenomena in cerebral aneurysms*. PhD thesis, University of Oxford, Oxford, 2012.

HOLZAPFEL, G. A. *Nonlinear Solid Mechanics*. Wiley, 2000.

HOLZAPFEL, G. A. Microstructure and mechanics of human aortas in health and disease. In *Biomechanics: Trends in Modeling and Simulation*, pages 157–192. Springer, 2017.

HOLZAPFEL, G. A., GASSER, T. C., AND OGDEN, R. W. A New Constitutive Framework for Arterial Wall Mechanics and a Comparative Study of Material Models. *Journal of Elasticity*, 61:1–48, 2000.

HU, J. H., WEI, H., JAFFE, M., AIRHART, N., DU, L., ANGELOV, S. N., YAN, J., ALLEN, J. K., KANG, I., WIGHT, T. N., ET AL. Postnatal deletion of the type ii transforming growth factor-β receptor in smooth muscle cells causes severe aortopathy in mice. *Arteriosclerosis, thrombosis, and vascular biology*, 35(12):2647–2656, 2015.

HUANG, A. H. AND NIKLASON, L. E. Engineering of arteries in vitro. *Cellular and molecular life sciences : CMLS*, 71 (11):2103–18, June 2014. ISSN 1420-9071.

HUMBERT, M., MORRELL, N. W., ARCHER, S. L., STENMARK, K. R., MACLEAN, M. R., LANG, I. M., CHRISTMAN, B. W., WEIR, E. K., EICKELBERG, O., VOELKEL, N. F., ET AL. Cellular and molecular pathobiology of pulmonary arterial hypertension. *Journal of the American College of Cardiology*, 43(12s1):S13–S24, 2004.

HUMPHREY, J. Remodeling of a collagenous tissue at fixed lengths. *Journal of Biomedical Engineering*, 121:591–597, 1999.

HUMPHREY, J. AND CANHAM, P. Structure, mechanical properties, and mechanics of intracranial saccular aneurysms. *Journal of Elasticity*, 61:49–81, 2000.

HUMPHREY, J. AND HOLZAPFEL, G. Mechanics, mechanobiology, and modeling of human abdominal aorta and aneurysms. *J Biomech*, 45(5):805–814, 2012.

HUMPHREY, J. D. Vascular adaptation and mechanical homeostasis at tissue, cellular, and sub-cellular levels. *Cell biochemistry and biophysics*, 50(2):53–78, January 2008a. ISSN 1085-9195.

HUMPHREY, J. D. Mechanisms of arterial remodeling in hypertension: coupled roles of wall shear and intramural stress. *Hypertension*, 52(2):195–200, August 2008b. ISSN 1524-4563.

HUMPHREY, J. D. *Cardiovascular solid mechanics: cells, tissues, and organs*. Springer Science & Business Media, 2013.

HUMPHREY, J. *Cardiovascular Solid Mechanics: Cells, Tissues, and Organs*. Springer-Verlag, 2002.

HUMPHREY, J. Possible mechanical roles of glycosaminoglycans in thoracic aortic dissection and associations with dysregulated transforming growth factor-β. *Journal of vascular research*, 50(1):1–10, 2012.

HUMPHREY, J., BAEK, S., AND NIKLASON, L. Biochemomechanics of cerebral vasospasm and its resolution: I. a new hypothesis and theoretical framework. *Annals of biomedical engineering*, 35(9):1485–1497, 2007.

HUMPHREY, J., EBERTH, J., DYE, W., AND GLEASON, R. Fundamental role of axial stress in compensatory adaptations by arteries. *Journal of biomechanics*, 42(1):1–8, 2009.

HUMPHREY, J. AND RAJAGOPAL, K. A constrained mixture model for growth and remodeling of soft tissues. *Mathematical models and methods in applied sciences*, 12(03): 407–430, 2002.

HYYTIÄINEN, M., PENTTINEN, C., AND KESKI-OJA, J. Latent TGF-beta binding proteins: extracellular matrix association and roles in TGF-beta activation. *Critical reviews in clinical laboratory sciences*, 41(3):233–64, January 2004. ISSN 1040-8363.

IWANO, M., PLIETH, D., DANOFF, T. M., XUE, C., OKADA, H., AND NEILSON, E. G. Evidence that fibroblasts derive from epithelium during tissue fibrosis. *The Journal of clinical investigation*, 110(3):341–350, 2002.

JANSSEN, B. J., DE CELLE, T., DEBETS, J. J., BROUNS, A. E., CALLAHAN, M. F., AND SMITH, T. L. Effects of anesthetics on systemic hemodynamics in mice. *American Journal of Physiology-Heart and Circulatory Physiology*, 287(4):H1618–H1624, 2004.

JEFFERY, T. AND MORRELL, N. Molecular and cellular basis of pulmonary vascular remodeling in pulmonary hypertension. *Progress in cardiovascular diseases*, 45(3):173–202, 2002.

JONES, J. A., BECK, C., BARBOUR, J. R., ZAVADZKAS, J. A., MUKHERJEE, R., SPINALE, F. G., AND IKONOMIDIS, J. S. Alterations in aortic cellular constituents during thoracic aortic aneurysm development: myofibroblast-mediated vascular remodeling. *The American journal of pathology*, 175(4):1746–56, October 2009a. ISSN 1525-2191.

JONES, J. A., SPINALE, F. G., AND IKONOMIDIS, J. S. Transforming growth factor-beta signaling in thoracic aortic aneurysm development: a paradox in pathogenesis. *Journal of vascular research*, 46(2):119–37, January 2009b. ISSN 1423-0135.

JU, X., IJAZ, T., SUN, H., LEJEUNE, W., VARGAS, G., SHILAGARD, T., RECINOS, A., MILEWICZ, D. M., BRASIER, A. R., AND TILTON, R. G. IL-6 Regulates Extracellular Matrix Remodeling Associated With Aortic Dilation in a Fibrillin-1 Hypomorphic mgR/mgR Mouse Model of Severe Marfan Syndrome. *Journal of the American Heart Association*, 3(1):e000476–e000476, 2014. ISSN 2047-9980.

JU, X., IJAZ, T., SUN, H., RAY, S., LEJEUNE, W., LEE, C., RECINOS, A., GUO, D.-C., MILEWICZ, D. M., TILTON, R. G., AND BRASIER, A. R. Interleukin-6-Signal Transducer and Activator of Transcription-3 Signaling Mediates Aortic Dissections Induced by Angiotensin II via the T-Helper Lymphocyte 17-Interleukin 17 Axis in C57BL/6 Mice. *Arteriosclerosis, Thrombosis, and Vascular Biology*, 33(7):1612–1621, 2013. ISSN 1079-5642.

KALLURI, R., NEILSON, E. G., ET AL. Epithelial-mesenchymal transition and its implications for fibrosis. *Journal of Clinical Investigation*, 112(12):1776–1784, 2003.

KALLURI, R. AND ZEISBERG, M. Fibroblasts in cancer. *Nature reviews. Cancer*, 6(5):392–401, 2006. ISSN 1474-175X.

KARŠAJ, I., SORIĆ, J., AND HUMPHREY, J. D. A 3-d framework for arterial growth and remodeling in response to altered hemodynamics. *International journal of engineering science*, 48(11):1357–1372, 2010.

KARSDAL, M. A., NIELSEN, M. J., SAND, J. M., HENRIKSEN, K., GENOVESE, F., BAY-JENSEN, A.-C., SMITH, V., ADAMKEWICZ, J. I., CHRISTIANSEN, C., AND LEEMING, D. J. Extracellular matrix remodeling: the common denominator in connective tissue diseases possibilities for evaluation and current understanding of the matrix as more than a passive architecture, but a key player in tissue failure. *Assay and drug development technologies*, 11(2):70–92, 2013.

KASAL, D. A. B., NEVES, M. F., OIGMAN, W., AND MANDARIM-DE LACERDA, C. A. Allopurinol attenuates L-NAME induced cardiomyopathy comparable to blockade of angiotensin receptor. *Histology and histopathology*, 23 (10):1241–8, 2008. ISSN 1699-5848.

KESKI-OJA, J., KOLI, K., AND VON MELCHNER, H. TGF-beta activation by traction? *Trends in cell biology*, 14(12): 657–9, December 2004. ISSN 0962-8924.

KIRK, T. Z., MARK, M. E., CHUA, C. C., CHUA, B. H., AND MAYES, M. D. Myofibroblasts from scleroderma skin synthesize elevated levels of collagen and tissue inhibitor of metalloproteinase (timp-1) with two forms of timp-1. *Journal of Biological Chemistry*, 270(7):3423–3428, 1995.

KITAMOTO, S., EGASHIRA, K., KATAOKA, C., KOYANAGI, M., KATOH, M., SHIMOKAWA, H., MORISHITA, R., KANEDA, Y., SUEISHI, K., AND TAKESHITA, A. Increased Activity of Nuclear Factor-ÂăB Participates in Cardiovascular Remodeling Induced by Chronic Inhibition of Nitric Oxide Synthesis in Rats. *Circulation*, 102(7):806–812, 2000. ISSN 0009-7322.

KOPKAN, L. AND MAJID, D. S. A. Superoxide Contributes to Development of Salt Sensitivity and Hypertension Induced by Nitric Oxide Deficiency. *Hypertension*, 46(4): 1026–1031, 2005. ISSN 0194-911X.

KROON, M. AND HOLZAPFEL, G. A. A model for saccular cerebral aneurysm growth by collagen fibre remodelling. *Journal of Theoretical Biology*, 247:775–787, 2007.

KROON, M. AND HOLZAPFEL, G. A. A theoretical model for fibroblast-controlled growth of saccular cerebral aneurysms. *Journal of Theoretical Biology*, 26:133–164, 2009.

KROON, M. AND HOLZAPFEL, G. A. Modeling of saccular aneurysm growth in a human middle cerebral artery. *Journal of biomechanical engineering*, 130(5):051012, October 2008. ISSN 0148-0731.

KUNDI, R., HOLLENBECK, S. T., YAMANOUCHI, D., HERMAN, B. C., EDLIN, R., RYER, E. J., WANG, C., TSAI, S., LIU, B., AND KENT, K. C. Arterial gene transfer of the TGF-Âă signalling protein Smad3 induces adaptive remodelling following angioplasty: a role for CTGF. *Cardiovascular Research*, 84(2):326–335, 2009. ISSN 0008-6363.

LAWRENCE, D. A. Transforming growth factor-beta: a general review. *European cytokine network*, 7(3):363–74, September 1996. ISSN 1148-5493.

LEASK, A. Potential Therapeutic Targets for Cardiac Fibrosis: TGFÂă, Angiotensin, Endothelin, CCN2, and PDGF, Partners in Fibroblast Activation. *Circulation Research*, 106 (11):1675–1680, 2010. ISSN 0009-7330.

LEASK, A. AND ABRAHAM, D. J. All in the CCN family: essential matricellular signaling modulators emerge from the bunker. *Journal of Cell Science*, 119(23):4803–4810, 2006. ISSN 0021-9533.

LEGANT, W. R., CHOI, C. K., MILLER, J. S., SHAO, L., GAO, L., BETZIG, E., AND CHEN, C. S. Multidimensional traction force microscopy reveals out-of-plane rotational moments about focal adhesions. *Proceedings of the National Academy of Sciences*, 110(3):881–886, 2013.

LI, D. L. AND ROBERTSON, A. M. A Structural Multi-Mechanism Damage Model for Cerebral Arterial Tissue. *ASME Journal of Biomechanical Engineering*, 131:101013, 2009.

LI, J., CHEN, J., AND KIRSNER, R. Pathophysiology of acute wound healing. *Clinics in dermatology*, 25(1):9–18, 2007.

LI, Q., MURAGAKI, Y., HATAMURA, I., UENO, H., AND OOSHIMA, A. Stretch-induced collagen synthesis in cultured smooth muscle cells from rabbit aortic media and a possible involvement of angiotensin II and transforming growth factor-beta. *Journal of vascular research*, 35(2):93–103, 1998. ISSN 1018-1172.

LI, W., LI, Q., JIAO, Y., QIN, L., ALI, R., ZHOU, J., FERRUZZI, J., KIM, R. W., GEIRSSON, A., DIETZ, H. C., ET AL. Tgfbr2 disruption in postnatal smooth muscle impairs aortic wall homeostasis. *The Journal of clinical investigation*, 124(2):0–0, 2014.

LINDAHL, G. E., CHAMBERS, R. C., PAPAKRIVOPOULOU, J., DAWSON, S. J., JACOBSEN, M. C., BISHOP, J. E., AND LAURENT, G. J. Activation of fibroblast procollagen alpha 1(I) transcription by mechanical strain is transforming growth factor-beta-dependent and involves increased binding of CCAAT-binding factor (CBF/NF-Y) at the proximal promoter. *The Journal of biological chemistry*, 277(8): 6153–61, February 2002. ISSN 0021-9258.

LINDSAY, M. E. AND DIETZ, H. C. Lessons on the pathogenesis of aneurysm from heritable conditions. *Nature*, 473 (7347):308–16, May 2011. ISSN 1476-4687.

LOEYS, B. L., CHEN, J., NEPTUNE, E. R., JUDGE, D. P., PODOWSKI, M., HOLM, T., MEYERS, J., LEITCH, C. C., KATSANIS, N., SHARIFI, N., XU, F. L., MYERS, L. A., SPEVAK, P. J., CAMERON, D. E., DE BACKER, J., HELLEMANS, J., CHEN, Y., DAVIS, E. C., WEBB, C. L., KRESS, W., COUCKE, P., RIFKIN, D. B., DE PAEPE, A. M., AND DIETZ, H. C. A syndrome of altered cardiovascular, craniofacial, neurocognitive and skeletal development caused by mutations in TGFBR1 or TGFBR2. *Nature genetics*, 37(3):275–81, March 2005. ISSN 1061-4036.

LOEYS, B. L. AND DIETZ, H. C. Loeys-Dietz Syndrome. *Gene Reviews*, 2008.

LOEYS, B. L., SCHWARZE, U., HOLM, T., CALLEWAERT, B. L., THOMAS, G. H., PANNU, H., DE BACKER, J. F., OSWALD, G. L., SYMOENS, S., MANOUVRIER, S., ET AL. Aneurysm syndromes caused by mutations in the tgf-β receptor. *New England Journal of Medicine*, 355(8): 788–798, 2006.

LONGO, G. M., XIONG, W., GREINER, T. C., ZHAO, Y., FIOTTI, N., AND BAXTER, B. T. Matrix metalloproteinases 2 and 9 work in concert to produce aortic aneurysms. *The Journal of Clinical Investigation*, 110(5):625–632, 2002.

LÓPEZ-CANDALES, A., HOLMES, D. R., LIAO, S., SCOTT, M. J., WICKLINE, S. A., AND THOMPSON, R. W. Decreased vascular smooth muscle cell density in medial degeneration of human abdominal aortic aneurysms. *The American journal of pathology*, 150(3):993–1007, March 1997. ISSN 0002-9440.

MAIELLARO, K. AND TAYLOR, W. R. The role of the adventitia in vascular inflammation. *Cardiovascular research*, 75 (4):640–8, September 2007. ISSN 0008-6363.

MAJESKY, M. W., LINDNER, V., TWARDZIK, D. R., SCHWARTZ, S. M., AND REIDY, M. A. Production of transforming growth factor beta 1 during repair of arterial injury. *The Journal of clinical investigation*, 88(3):904–10, September 1991. ISSN 0021-9738.

MANTOVANI, A., BISWAS, S. K., GALDIERO, M. R., SICA, A., AND LOCATI, M. Macrophage plasticity and polarization in tissue repair and remodelling. *The Journal of pathology*, 229(2):176–185, 2013.

MARTIN, P., HOPKINSON-WOOLLEY, J., AND MCCLUSKEY, J. GROWTH FACTORS WOUND AND CUTANEOUS REPAIR. *Progress in Growth Factor Research*, 4:25–44, 1992.

MCANULTY, R. J., CAMPA, J. S., CAMBREY, A. D., AND LAURENT, G. J. The effect of transforming growth factor beta on rates of procollagen synthesis and degradation in vitro. *Biochimica et biophysica acta*, 1091(2):231–5, January 1991. ISSN 0006-3002.

MCANULTY, R. Fibroblasts and myofibroblasts: Their source, function and role in disease. *International Journal of Biochemistry & Cell Biology*, 39:666–671, 2007.

MCDOUGALL, S., DALLON, J., SHERRATT, J., AND MAINI, P. Fibroblast migration and collagen deposition during dermal wound healing: mathematical modelling and clinical implications. *Philosophical Transactions of the Royal Society A: Mathematical, Physical and Engineering Sciences*, 364(1843):1385–1405, 2006.

MCGLOUGHLIN, T. *Biomechanics and Mechanobiology of Aneurysms*. Springer-Verlag, 2011.

MEHRA, M., SPILBERG, G., GOUNIS, M. J., AND WAKHLOO, A. K. Intracranial aneurysms: Clinical assessment and treatment options. In MCGLOUGHLIN, T., editor, *Biomechanics and Mechanobiology of Aneurysms*, pages 331–372. Springer, 2011.

MEHTA, P. K. AND GRIENDLING, K. K. Angiotensin II cell signaling: physiological and pathological effects in the cardiovascular system. *American Journal of Physiology - Cell Physiology*, 292(1):C82–C97, 2007. ISSN 0363-6143.

MENG, X.-M., NIKOLIC-PATERSON, D. J., AND LAN, H. Y. Tgf-[beta]: the master regulator of fibrosis. *Nature Reviews Nephrology*, 2016.

MESHEL, A. S., WEI, Q., ADELSTEIN, R. S., AND SHEETZ, M. P. Basic mechanism of three-dimensional collagen fibre transport by fibroblasts. *Nature cell biology*, 7(2):157–164, 2005.

MICHEL, J.-B., THAUNAT, O., HOUARD, X., MEILHAC, O., CALIGIURI, G., AND NICOLETTI, A. Topological determinants and consequences of adventitial responses to arterial wall injury. *Arteriosclerosis, thrombosis, and vascular biology*, 27(6):1259–68, June 2007. ISSN 1524-4636.

MONTECUCCO, F. AND MACH, F. Atherosclerosis is an inflammatory disease. *Semin Immunipathol*, 31:1–3, 2009.

MORI, T., KAWARA, S., SHINOZAKI, M., HAYASHI, N., KAKINUMA, T., IGARASHI, A., TAKIGAWA, M., NAKANISHI, T., AND TAKEHARA, K. Role and interaction of connective tissue growth factor with transforming growth factor-beta in persistent fibrosis: A mouse fibrosis model. *Journal of cellular physiology*, 181(May):153–159, 1999. ISSN 0021-9541.

MORIKAWA, M., DERYNCK, R., AND MIYAZONO, K. Tgf-β and the tgf-β family: Context-dependent roles in cell and tissue physiology. *Cold Spring Harbor perspectives in biology*, 8(5):a021873, 2016.

MUNGER, J. S. AND SHEPPARD, D. Cross Talk among TGF-β Signaling Pathways, Integrins, and the Extracellular Matrix. *Cold Spring Harbor Perspectives in Biology*, 3(11): a005017–a005017, 2011. ISSN 1943-0264.

NABEL, E., SHUM, L., POMPILI, V., YANG, Z.-Y., SAN, H., SHU, H., LIPTAY, S., GOLD, L., GORDON, D., DERYNCK, R., AND NABEL, G. Direct transfer of transforming growth factor beta1 gene into arteries stimulates fibrocellular hyperplasia. *Proc Natl Acad Sci USA*, 90:10759–10763, 1993.

NEPTUNE, E. R., FRISCHMEYER, P. A., ARKING, D. E., MYERS, L., BUNTON, T. E., GAYRAUD, B., RAMIREZ, F., SAKAI, L. Y., AND DIETZ, H. C. Dysregulation of TGF-beta activation contributes to pathogenesis in Marfan syndrome. *Nature genetics*, 33(3):407–11, March 2003. ISSN 1061-4036.

NHLBI. *Fact Book 2012*. National Heart Lung and Blood Institute, 2013.

NICOLAS, A. AND SAFRAN, S. A. Limitation of cell adhesion by the elasticity of the extracellular matrix. *Biophysical journal*, 91(1):61–73, 2006.

O'CALLAGHAN, C. J. AND WILLIAMS, B. Mechanical Strain-Induced Extracellular Matrix Production by Human Vascular Smooth Muscle Cells: Role of TGF-ï£¡ 1. *Hypertension*, 36:319–324, 2000.

PAGE-MCCAW, A., EWALD, A. J., AND WERB, Z. Matrix metalloproteinases and the regulation of tissue remodelling. *Nature reviews Molecular cell biology*, 8(3):221–233, 2007.

PALLADINO, M. A., MORRIS, R. E., STARNES, H. F., AND LEVINSON, A. D. The Transforming Growth Factor-Betas. *Annals New York Academy of Sciences*, pages 181–187, 1990.

PARDALI, E., GOUMANS, M.-J., AND TEN DIJKE, P. Signaling by members of the tgf-β family in vascular morphogenesis and disease. *Trends in cell biology*, 20(9):556–567, 2010.

PATHAK, A., MCMEEKING, R. M., EVANS, A. G., AND DESHPANDE, V. S. An Analysis of the Cooperative Mechano-Sensitive Feedback Between Intracellular Signaling, Focal Adhesion Development, and Stress Fiber Contractility. *Journal of Applied Mechanics*, 78(4):041001, 2011. ISSN 00218936.

PELLEGRIN, S. AND MELLOR, H. Actin stress fibres. *Journal of cell science*, 120(20):3491–3499, 2007.

PENN, J. W., GROBBELAAR, A. O., ROLFE, K. J., ET AL. The role of the tgf-β family in wound healing, burns and scarring: a review. *Int J Burns Trauma*, 2(1):18–28, 2012.

PHILLIPPI, J. A., PASTA, S., AND VORP, D. Biomechanics and pathobiology of aortic aneurysms. In MCGLOUGHLIN, T., editor, *Biomechanics and Mechanobiology of Aneurysms*, pages 67–118. Springer, 2011.

PICKUP, M., NOVITSKIY, S., AND MOSES, H. L. The roles of tgf [beta] in the tumour microenvironment. *Nature Reviews Cancer*, 13(11):788–799, 2013.

RAGHAVAN, M. L., KRATZBERG, J., MAGALHA, E., HANAOKA, M. M., WALKER, P., AND SIMA, E. Regional distribution of wall thickness and failure properties of human abdominal aortic aneurysm. *Journal of Biomechanics*, 39(2000):3010–3016, 2006.

RAGHAVAN, M. L. AND SIMÃO DA SILVA, E. Mechanical properties of aaa tissue. In MCGLOUGHLIN, T., editor, *Biomechanics and Mechanobiology of Aneurysms*, pages 139–162. Springer, 2011.

REGAN, E. AND AIRD, W. Dynamical systems approach to endothelial heterogeneity. *Circulation Research*, 111:110–130, 2012.

RISER, B., CORTES, P., YEE, J., SHARBA, A., ASANO, K., RODRIGUEZ-BARBERO, A., AND NARINS, R. Mechanical Mesangial Strain- and High Glucose-Induced Cell Collagen Metabolism : Role Alterations of TGF-f3. *Journal of the American Society of Nephrology*, pages 827–836, 1998.

RIZAS, K., IPPAGUNTA, N., AND TILSON III, M. D. Immune cells and molecular mediators in the pathogenesis of the abdominal aortic aneurysm. *Cardiol Rev*, 17:201–210, 2009.

ROBERTS, A. B., SPORN, M. B., ASSOIAN, R. K., SMITH, J. M., ROCHE, N. S., WAKEFIELD, L. M., HEINE, U. I., LIOTTA, L. A., FALANGA, V., AND KEHRL, J. H. Transforming growth factor type beta: rapid induction of fibrosis and angiogenesis in vivo and stimulation of collagen formation in vitro. *Proceedings of the National Academy of Sciences of the United States of America*, 83(12):4167–71, June 1986. ISSN 0027-8424.

ROBERTSON, A. M., DUAN, X., AZIZ, K. M., HILL, M. R., WATKINS, S. C., AND CEBRAL, J. R. Diversity in the strength and structure of unruptured cerebral aneurysms. *Annals of biomedical engineering*, 43(7):1502–1515, 2015.

RODRIGUEZ, E. K., HOGER, A., AND MCCULLOCH, A. D. Stress-dependent finite growth in soft elastic tissues. *Journal of biomechanics*, 27(4):455–467, 1994.

RODRIGUEZ-ITURBE, B., QUIROZ, Y., KIM, C., AND VAZIRI, N. Hypertension Induced by Aortic Coarctation Above the Renal Arteries Is Associated With Immune Cell Infiltration of the Kidneys. *American Journal of Hypertension*, 18(11):1449–1456, 2005. ISSN 08957061.

ROMER, L. H., BIRUKOV, K. G., AND GARCIA, J. G. Focal adhesions paradigm for a signaling nexus. *Circulation research*, 98(5):606–616, 2006.

ROSENKRANZ, S. TGF-beta1 and angiotensin networking in cardiac remodeling. *Cardiovascular Research*, 63(3):423–432, 2004. ISSN 00086363.

ROUILLARD, A. D. AND HOLMES, J. W. Mechanical regulation of fibroblast migration and collagen remodelling in healing myocardial infarcts. *The Journal of physiology*, 590 (Pt 18):4585–4602, 2012. ISSN 1469-7793.

RUDDY, J. M., JONES, J. A., SPINALE, F. G., AND IKONOMIDIS, J. S. Regional heterogeneity within the aorta: relevance to aneurysm disease. *The Journal of thoracic and cardiovascular surgery*, 136(5):1123–30, November 2008. ISSN 1097-685X.

RUIZ-ORTEGA, M., RODRIGUEZ-VITA, J., SANCHEZ-LOPEZ, E., CARVAJAL, G., AND EGIDO, J. TGF-β signaling in vascular fibrosis. *Cardiovascular Research*, 74(2): 196–206, 2007. ISSN 00086363.

RYS, J. P., MONTEIRO, D. A., AND ALLISTON, T. Mechanobiology of tgfβ signaling in the skeleton. *Matrix Biology*, 52:413–425, 2016.

SÁEZ, P., PEÑA, E., MARTÍNEZ, M. Á., AND KUHL, E. Mathematical modeling of collagen turnover in biological tissue. *Journal of mathematical biology*, 67(6-7):1765–1793, 2013.

SAKALIHASAN, N., LIMET, R., AND DEFAWE, O. D. Abdominal aortic aneurysm. *Lancet*, 365(9470):1577–89, 2005. ISSN 1474-547X.

SAKALIHASAN, N., KUIVANIEMI, H., NUSGENS, B., DURIEUZ, R., AND DEFRAIGNE, J.-O. Aneurysm: Epidemiology aetiology and pathophysiology. In MCGLOUGHLIN, T., editor, *Biomechanics and Mechanobiology of Aneurysms*, pages 1–33. Springer, 2011.

SAKATA, N., NABESHIMA, K., IWASAKI, H., TASHIRO, T., UESUGI, N., NAKASHIMA, O., ITO, H., KAWANAMI, T., FURUYA, K., AND KOJIMA, M. Possible involvement of myofibroblast in the development of inflammatory aortic aneurysm. *Pathology, research and practice*, 203(1):21–9, January 2007. ISSN 0344-0338.

SASTRY, S. K. AND BURRIDGE, K. Focal adhesions: a nexus for intracellular signaling and cytoskeletal dynamics. *Experimental cell research*, 261(1):25–36, 2000.

SCHMID, H., GRYTSAN, A., POSHTAN, E., WATTON, P. N., AND ITSKOV, M. Influence of differing material properties in media and adventitia on arterial adaptation - application to aneurysm formation and rupture. *Computer methods in biomechanics and biomedical engineering*, 16(1):33–53, 2013. ISSN 1476-8259.

SCHMID, H., WATTON, P. N., MAURER, M. M., WIMMER, J., WINKLER, P., WANG, Y. K., RÖHRLE, O., AND ITSKOV, M. Impact of transmural heterogeneities on arterial adaptation: application to aneurysm formation. *Biomechanics and modeling in mechanobiology*, 9(3):295–315, June 2010. ISSN 1617-7940.

SCHMIDT, M., SUN, G., STACEY, M. A., MORI, L., AND MATTOLI, S. Identification of circulating fibrocytes as precursors of bronchial myofibroblasts in asthma. *The Journal of Immunology*, 171(1):380–389, 2003.

SCHRAUWEN, J. T. C., VILANOVA, A., REZAKHANIHA, R., STERGIOPULOS, N., VAN DE VOSSE, F. N., AND BOVENDEERD, P. H. M. A method for the quantification of the pressure dependent 3D collagen configuration in the arterial adventitia. *Journal of structural biology*, 180(2):335–42, November 2012. ISSN 1095-8657.

SCHRIEFL, A. J., COLLINS, M. J., PIERCE, D. M., HOLZAPFEL, G. A., NIKLASON, L. E., AND HUMPHREY, J. D. Remodeling of intramural thrombus and collagen in an Ang-II infusion ApoE-/- model of dissecting aortic aneurysms. *Thrombosis research*, 130(3):e139–46, September 2012. ISSN 1879-2472.

SCHUSTER, N. AND KRIEGLSTEIN, K. Mechanisms of TGF-beta-mediated apoptosis. *Cell and tissue research*, 307(1): 1–14, January 2002. ISSN 0302-766X.

SFORZA, D., PUTMAL, C., AND CEBRAL, J. Computational fluid dynamics in brain aneurysms. *International Journal for Numerical Methods in Biomedical Engineering*, 28:801–808, 2012.

SHEIDAEI, A., HUNLEY, S. C., ZEINALI-DAVARANI, S., RAGUIN, L. G., AND BAEK, S. Simulation of abdominal aortic aneurysm growth with updating hemodynamic loads using a realistic geometry. *Medical engineering & physics*, 33(1):80–8, January 2011. ISSN 1873-4030.

SHEMESH, T., GEIGER, B., BERSHADSKY, A. D., AND KOZLOV, M. M. Focal adhesions as mechanosensors: a physical mechanism. *Proceedings of the National Academy of Sciences of the United States of America*, 102(35):12383–12388, 2005.

SHI, M., ZHU, J., WANG, R., CHEN, X., MI, L., WALZ, T., AND SPRINGER, T. A. Latent TGF-β structure and activation. *Nature*, 474(7351):343–9, June 2011. ISSN 1476-4687.

SHI, Y., BRIEN, J. E. O., BRIEN, O., FARD, A., AND ZALEWSKI, A. Transforming Growth Factor-β1 Expression and Myofibroblast Formation During Arterial Repair. *Arteriosclerosis, thrombosis, and vascular biology*, 16:1298–1305, 1996a.

SHI, Y., PATEL, S., NICULESCU, R., CHUNG, W., DESROCHERS, P., AND ZALEWSKI, A. Role of matrix metalloproteinases and their tissue inhibitors in the regulation of coronary cell migration. *Arteriosclerosis, thrombosis, and vascular biology*, 19(5):1150–1155, 1999.

SHI, Y., PIENIEK, M., FARD, A., O'BRIEN, J., MANNION, J. D., AND ZALEWSKI, A. Adventitial remodeling after coronary arterial injury. *Circulation*, 93(2):340–348, 1996b.

SHO, E., SHO, M., KATSUKI, H., KIMURA, H., NAKAHASHI, T. K., AND DALMAN, R. L. Hemodynamic forces regulate mural macrophage infiltration in experimental aortic aneurysms. *Experimental and molecular pathology*, 76 (2):108–116, 2004. ISSN 0014-4800.

SHOULDERS, M. D. AND RAINES, R. T. Collagen structure and stability. *Annual review of biochemistry*, 78:929–58, January 2009. ISSN 1545-4509.

SIEFERT, S. AND SARKAR, R. Matrix metalloproteinases in vascular physiology and disease. *Vascular*, 20(4):210–6, August 2012. ISSN 1708-5381.

SINCLAIR, R. AND RYAN, T. Proteolytic enzymes in wound healing: the role of enzymatic debridement. *The Australasian journal of dermatology*, 35(1):35–41, 1994. ISSN 0004-8380.

SMITH, J. D., BRYANT, S. R., COUPER, L. L., VARY, C. P., GOTWALS, P. J., KOTELIANSKY, V. E., AND LINDNER, V. Soluble transforming growth factor-beta type II receptor inhibits negative remodeling, fibroblast transdifferentiation, and intimal lesion formation but not endothelial growth. *Circulation research*, 84(10):1212–22, 1999. ISSN 0009-7330.

SPORN, M. B. AND ROBERTS, A. B. The transforming growth factor-betas: past, present, and future. *Annals of the New York Academy of Sciences*, 593:1–6, January 1990. ISSN 0077-8923.

STENMARK, K. R., FAGAN, K. A., AND FRID, M. G. Hypoxia-induced pulmonary vascular remodeling: cellular and molecular mechanisms. *Circulation research*, 99(7): 675–91, September 2006. ISSN 1524-4571.

STENMARK, K. R., NOZIK-GRAYCK, E., GERASIMOVSKAYA, E., ANWAR, A., LI, M., RIDDLE, S., AND FRID, M. The adventitia: essential role in pulmonary vascular remodeling. *Comprehensive Physiology*, 2011.

STRAUSS, B. H. AND RABINOVITCH, M. Adventitial fibroblasts: defining a role in vessel wall remodeling. *American journal of respiratory cell and molecular biology*, 22(1):1–3, 2000.

STREULI, C., SCHMIDHAUSER, C., KOBRIN, M., BISSEL, M. J., AND DERINCK, R. Extracellular Matrix Regulates Expression of TGF-beta 1 Gene. *The Journal of Cell Biology*, 120:253–260, 1993.

TAN, C. K., TAN, E. H., LUO, B., HUANG, C. L., LOO, J. S., CHOONG, C., AND TAN, N. S. SMAD3 Deficiency Promotes Inflammatory Aortic Aneurysms in Angiotensin II-Infused Mice Via Activation of iNOS. *Journal of the American Heart Association*, 2(3):e000269–e000269, 2013. ISSN 2047-9980.

THERUVATH, T. P., JONES, J. A., AND IKONOMIDIS, J. S. Matrix metalloproteinases and descending aortic aneurysms: parity, disparity, and switch. *Journal of cardiac surgery*, 27(1):81–90, January 2012. ISSN 1540-8191.

THOMPSON, R. W., CURCI, J. A., ENNIS, T. L., MAO, D., PAGANO, M. B., AND PHAM, C. T. N. Pathophysiology of abdominal aortic aneurysms: insights from the elastase-induced model in mice with different genetic backgrounds. *Annals of the New York Academy of Sciences*, 1085:59–73, November 2006. ISSN 0077-8923.

TIEU, B. C., JU, X., LEE, C., SUN, H., LEJEUNE, W., RECINOS, III, A., BRASIER, A. R., AND TILTON, R. G. Aortic Adventitial Fibroblasts Participate in Angiotensin-Induced Vascular Wall Inflammation and Remodeling. *Journal of Vascular Research*, 48(3):261–272, 2011. ISSN 1423-0135.

TOMASEK, J. J., GABBIANI, G., HINZ, B., CHAPONNIER, C., AND BROWN, R. A. Myofibroblasts and mechano-regulation of connective tissue remodelling. *Nature reviews. Molecular cell biology*, 3(5):349–63, May 2002. ISSN 1471-0072.

UDELSMAN, B. V., KHOSRAVI, R., MILLER, K. S., DEAN, E. W., BERSI, M. R., ROCCO, K., YI, T., HUMPHREY, J. D., AND BREUER, C. K. Characterization of evolving biomechanical properties of tissue engineered vascular grafts in the arterial circulation. *Journal of Biomechanics*, 47(9):2070–2079, 2014. ISSN 18732380.

USUI, M., EGASHIRA, K., KITAMOTO, S., KOYANAGI, M., KATOH, M., KATAOKA, C., SHIMOKAWA, H., AND TAKESHITA, A. Pathogenic Role of Oxidative Stress in Vascular Angiotensin-Converting Enzyme Activation in Long-Term Blockade of Nitric Oxide Synthesis in Rats. *Hypertension*, 34(4):546–551, 1999. ISSN 0194-911X.

VALENTÍN, A., HUMPHREY, J., AND HOLZAPFEL, G. A. A finite element-based constrained mixture implementation for arterial growth, remodeling, and adaptation: Theory and numerical verification. *International journal for numerical methods in biomedical engineering*, 29(8):822–849, 2013.

VAN LOON, P. Length-force and volume-pressure relationships of arteries. *Biorheology*, 14(4):181–201, 1976.

VAUGHAN, M. B., HOWARD, E. W., AND TOMASEK, J. J. Transforming growth factor-beta1 promotes the morphological and functional differentiation of the myofibroblast. *Experimental cell research*, 257(1):180–9, May 2000. ISSN 0014-4827.

VILAR, J. M., JANSEN, R., AND SANDER, C. Signal processing in the tgf-β superfamily ligand-receptor network. *PLoS Comput Biol*, 2(1):e3, 2006.

VIZÁN, P., MILLER, D. S., GORI, I., DAS, D., SCHMIERER, B., AND HILL, C. S. Controlling long-term signaling: receptor dynamics determine attenuation and refractory behavior of the tgf-Îš pathway. *Sci Signal*, 6(305), 2013.

VOLOKH, K. Y. AND VORP, D. A. A model of growth and rupture of abdominal aortic aneurysm. *Journal of Biomechanics*, 41:1015–1021, 2008.

VOLOKH, K. Prediction of arterial failure based on a microstructural bi-layer fiber–matrix model with softening. *Journal of biomechanics*, 41(2):447–453, 2008.

VORP, D. A. AND VANDE GEEST, J. P. Biomechanical determinants of abdominal aortic aneurysm rupture. *Arteriosclerosis, thrombosis, and vascular biology*, 25(8):1558–1566, 2005. ISSN 1524-4636.

WAN, W. AND GLEASON, R. L. Dysfunction in elastic fiber formation in fibulin-5 null mice abrogates the evolution in mechanical response of carotid arteries during maturation. *American Journal of Physiology-Heart and Circulatory Physiology*, 304(5):H674–H686, 2013.

WANG, Y., AIT-OUFELLA, H., HERBIN, O., BONNIN, P., RAMKHELAWON, B., TALEB, S., HUANG, J., OFFENSTADT, G., COMBADIÈRE, C., RÉNIA, L., JOHNSON, J. L., THARAUX, P.-L., TEDGUI, A., AND MALLAT, Z. TGF- β activity protects against inflammatory aortic aneurysm progression and complications in angiotensin II âĂŞ infused mice. *The Journal of Clinical Investigation*, 120(2):422–432, 2010.

WANG, Z. AND CHESLER, N. C. Role of collagen content and cross-linking in large pulmonary arterial stiffening after chronic hypoxia. *Biomechanics and modeling in mechanobiology*, 11(1-2):279–289, 2012.

WANG, Z., LAKES, R. S., EICKHOFF, J. C., AND CHESLER, N. C. Effects of collagen deposition on passive and active mechanical properties of large pulmonary arteries in hypoxic pulmonary hypertension. *Biomechanics and modeling in mechanobiology*, 12(6):1115–1125, 2013.

WARSINSKE, H. C., ASHLEY, S. L., LINDERMAN, J. J., MOORE, B. B., AND KIRSCHNER, D. E. Identifying mechanisms of homeostatic signaling in fibroblast differentiation. *Bulletin of mathematical biology*, pages 1–27, 2015.

WATTON, P. AND HILL, N. Evolving mechanical properties of a model of abdominal aortic aneurysm. *Biomechanics and Modeling in Mechanobiology*, 8:25–42, 2009.

WATTON, P. AND VENTIKOS, Y. Modelling evolution of saccular cerebral aneurysms. *The Journal of Strain Analysis for Engineering Design*, 44(5):375–389, 2009.

WATTON, P. N., HILL, N. A., AND HEIL, M. A mathematical model for the growth of the abdominal aortic aneurysm. *Biomechanics and modeling in mechanobiology*, 3(2):98–113, 2004. ISSN 1617-7959.

WATTON, P. N., SELIMOVIC, A., RABERGER, N. B., HUANG, P., HOLZAPFEL, G. A., AND VENTIKOS, Y. Modelling evolution and the evolving mechanical environment of saccular cerebral aneurysms. *Biomechanics and modeling in mechanobiology*, 10(1):109–132, 2011. ISSN 1617-7940.

WATTON, P. N., RABERGER, N. B., HOLZAPFEL, G. A., AND VENTIKOS, Y. Coupling the Hemodynamic Environment to the Evolution of Cerebral Aneurysms: Computational Framework and Numerical Examples. *Journal of Biomedical Engineering*, 131:101003–101014, 2009a.

WATTON, P. N., VENTIKOS, Y., AND HOLZAPFEL, G. A. Modelling the growth and stabilization of cerebral aneurysms. *Mathematical medicine and biology : a journal of the IMA*, 26(2):133–64, June 2009b. ISSN 1477-8602.

WATTON, P. *Mathematical modelling of the abdominal aortic aneurysm*. PhD thesis, University of Leeds, Leeds, 2002.

WEISS, A. AND ATTISANO, L. The tgfbeta superfamily signaling pathway. *Wiley Interdisciplinary Reviews: Developmental Biology*, 2(1):47–63, 2013.

WEIZSÄCKER, H. W., LAMBERT, H., AND PASCALE, K. Analysis of the passive mechanical properties of rat carotid arteries. *Journal of biomechanics*, 16(9):703–715, 1983.

WILSON, J. S., BAEK, S., AND HUMPHREY, J. D. Parametric study of effects of collagen turnover on the natural history of abdominal aortic aneurysms. *Proceedings of the Royal Society A: Mathematical, Physical and Engineering Sciences*, 469, 2013.

WIPFF, P.-J., RIFKIN, D. B., MEISTER, J.-J., AND HINZ, B. Myofibroblast contraction activates latent tgf-β1 from the extracellular matrix. *The Journal of cell biology*, 179(6): 1311–1323, 2007.

WU, J., THABET, S. R., KIRABO, A., TROTT, D. W., SALEH, M. A., XIAO, L., MADHUR, M. S., CHEN, W., AND HARRISON, D. G. Inflammation and Mechanical Stretch Promote Aortic Stiffening in Hypertension Through Activation of p38 Mitogen-Activated Protein Kinase. *Circulation Research*, 114(4):616–625, 2014. ISSN 0009-7330.

XIANG, J., NATARAJAN, S. K., TREMMEL, M., MA, D., MOCCO, J., HOPKINS, L. N., SIDDIQUI, A. H., LEVY, E. I., AND MENG, H. Hemodynamic-morphologic discriminants for intracranial aneurysm rupture. *Stroke; a journal of cerebral circulation*, 42(1):144–52, January 2011. ISSN 1524-4628.

YANG, L., SCOTT, P. G., GIUFFRE, J., SHANKOWSKY, H. A., GHAHARY, A., AND TREDGET, E. E. Peripheral Blood Fibrocytes from Burn Patients: Identification and Quantification of Fibrocytes in Adherent Cells Cultured from Peripheral Blood Mononuclear Cells. *Laboratory Investigation*, 82 (9):1183–1192, September 2002. ISSN 0023-6837.

YU, Q. AND STAMENKOVIC, I. Cell surface-localized matrix metalloproteinase-9 proteolytically activates TGF-beta and promotes tumor invasion and angiogenesis. *Genes and Development*, 14:163–176, 2000.

ZALEWSKI, A., SHI, Y., AND JOHNSON, A. G. Diverse Origin of Intimal Cells: Smooth Muscle Cells, Myofibroblasts, Fibroblasts, and Beyond? *Circulation Research*, 91(8):652–655, October 2002. ISSN 00097330.

ZI, Z. AND KLIPP, E. Constraint-based modeling and kinetic analysis of the smad dependent tgf-β signaling pathway. *PloS one*, 2(9):e936, 2007.

EXPERIMENTAL DATA TABLES AND ADDITIONAL EXPERIMENTAL PLOTS

Additional experimental data tables and plots can be found in this appendix.

PD, FL plots for IAAs. Fig. A.1, Fig. A.2 below show average load–deformation and stress–stretch plots resulting from pressure–inflation and axial force–stretching from biaxial mechanical testing of IAA segments. These data complement Fig. 3.3, Fig. 3.4 in Sec. 3.2.1.1, where the same quantities are plotted for the ATA segments.

Similarly to ATA segments, Fig. A.1(a) and Fig. A.2(a) show that IAAs from perturbed groups have larger diameters than their corresponding controls, which is particularly apparent for the *Dis+HT* group at 14wks. One other distinct feature is the significantly reduced axial stretches in *Dis+HT* vessels at 18wks, Fig. A.2(a) and (b). Both of these observations suggest that inducing hypertension in addition to disrupting TGF-β signalling through TGFBR2 has the highest impact on disturbing the system from homoeostasis. Circumferential and axial stress–stretch plots, Fig. A.1(c) and Fig. A.2(d), resp., show a general trend towards lower maximum stresses for perturbed groups in a *Ctrl* / *Dis* / *Dis+HT* stepwise fashion. Comparing these curves at different time points further reveals distinct time courses for the two perturbed groups: in the pressure–inflation test (Fig. A.1(c)), IAAs from the *Dis* group show a continuous reduction in the ranges of stress and stretch, whereas vessels in the *Dis+HT* group show similar mechanical behaviour at 14 and 18 weeks (which is much closer to *Ctrl* than *Dis* at 18wks is to control). Furthermore,

axial force–stretch curves (Fig. A.2(d)) show IAAs in the *Dis+HT* group having a much larger departure from baseline mechanical behaviour at 14wks than those in the *Dis* group, which becomes even more significant at 18wks. Trends present in the biaxial stretch plots, Fig. A.2(c), are less clear, with both perturbed groups at 18wks showing lower circumferential stretches, and the *Dis+HT* group displaying a significantly reduced range of axial stretches.

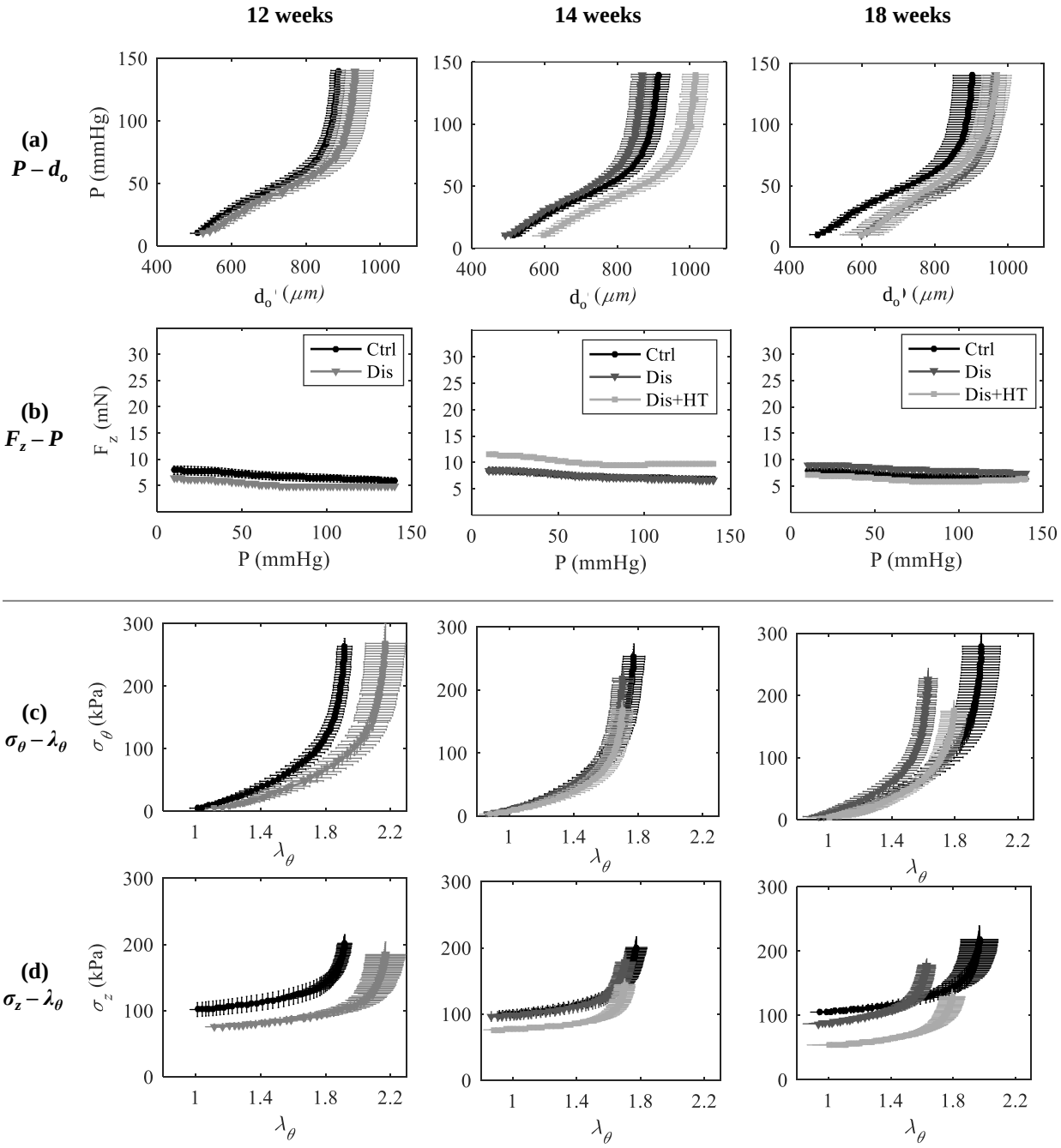

Figure A.1: **Group comparison study for IAAs subject to pressure–inflation tests.** Load–deformation and stress–stretch curves from pressure–inflation tests. Means (dots) and SEMs (horizontal and vertical bars) are depicted for each curve. Pressure–inflation tests were performed at vessel–specific $\lambda_z^{i.v.}$.

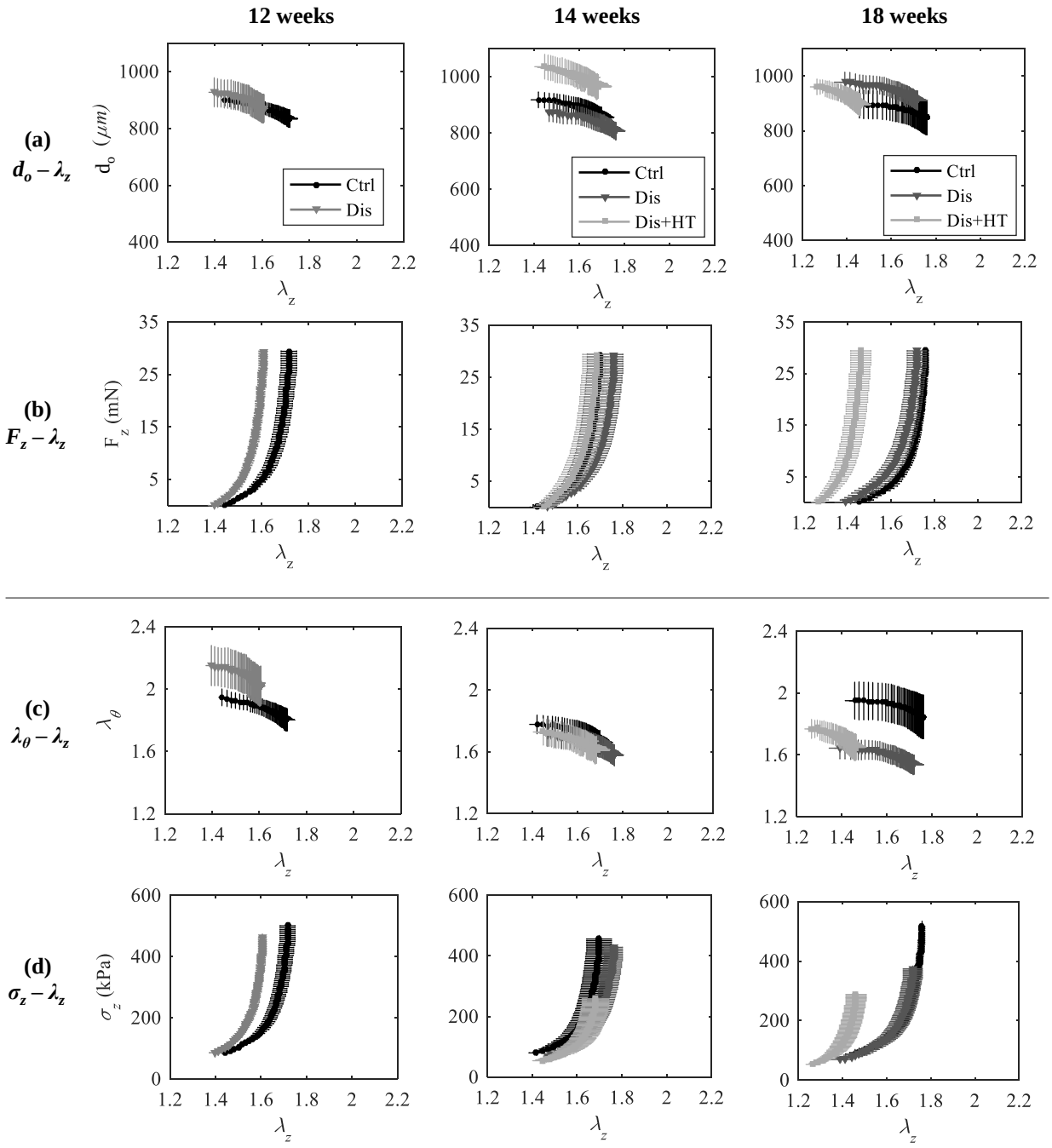

Figure A.2: **Group comparison study for IAAs subject to axial force–stretching tests.** Load–deformation and stress–stretch curves from axial force–stretching tests of IAA. Means (dots) and SEMs (horizontal and vertical bars) are depicted for each curve. Axial force–stretching tests were performed at intraluminal P=100mmHg.

Data Tables. Table A.1 displays the absolute values for the summary mechanical metrics, the normalisation of which was plotted in Sec. 3.2.1.4. Table A.2 compares some mechanical metrics for 18wks *Ctrl* segments with data presented by Ferruzzi et al. (2015). Table A.3 contains the total pixel number and distribution of pixel colours for PSR collagen staining, the normalisation of which was plotted in Sec. 3.2.2. Table A.4 displays layer–specific absolute pixel counts and area densities of the biochemical and cellular markers imaged using IF, the normalisation of which was plotted in Sec. 3.2.3.

Table A.1: **Summary mechanical variables.** Values in shaded cells were used for computation of perturbed groups fold–changes from control group. Asterisk denotes a group where the EDR could only be successfully computed for one sample.

	Control group																TGFBR2 Disruption group												TGFBR2 Disruption and Hypertension group							
Time point	6 weeks				12 weeks				14 weeks				18 weeks				12 weeks				14 weeks				18 weeks				14 weeks				18 weeks			
Segment	ATA		IAA		ATA		IAA		ATA		IAA		ATA		IAA		ATA		IAA		ATA		IAA		ATA		IAA		ATA		IAA		ATA		IAA	
Number of samples	2		3		3		3		3		3		3		3		2		2		3		3		3		3		3		2		2		2	
Metric	mean	SEM	mean	SEM	mean	SEM	mean	SEM	mean	SEM	mean	SEM	mean	SEM	mean	SEM	mean	SEM	mean	SEM	mean	SEM	mean	SEM	mean	SEM	mean	SEM	Mean	SEM	mean	SEM	mean	SEM	mean	SEM
Unloaded Dimension																																				
Outer Diameter (μm)	1071.00	4.00	567.67	12.99	1147.67	65.16	534.33	35.80	1091.00	32.58	582.67	23.02	1153.00	25.15	532.00	18.56	1394.50	16.50	512.50	2.50	1283.00	57.93	583.67	28.81	1578.33	23.00	663.67	55.74	1409.33	85.76	703.50	2.50	1616.50	98.50	627.50	42.50
Wall Thickness (μm)	113.73	7.65	77.49	6.27	107.89	3.55	87.31	0.42	104.58	0.94	85.98	2.72	98.45	1.74	88.22	3.06	147.56	3.49	96.43	6.14	133.35	2.96	94.27	6.68	151.81	11.01	94.40	6.23	184.94	7.32	136.57	3.34	170.61	3.50	113.24	7.48
Inner Diameter (μm)	843.53	19.31	412.69	20.21	931.90	70.47	359.71	36.50	881.83	33.43	410.71	27.22	956.11	25.70	355.57	21.88	1099.39	23.49	319.64	14.77	1016.29	52.52	395.12	21.05	1274.71	8.87	474.87	46.54	1039.45	77.95	430.36	9.19	1275.28	105.49	401.03	27.53
Inner Radius (μm)	421.77	9.65	206.35	10.11	465.95	35.24	179.85	18.25	440.92	16.71	205.35	13.61	478.05	12.85	177.78	10.94	549.69	11.74	159.82	7.39	508.15	26.26	197.56	10.53	637.35	4.43	237.44	23.27	519.73	38.97	215.18	4.59	637.64	52.75	200.51	13.77
H:IR ratio (%)	27.02	2.43	37.97	4.77	23.50	2.38	49.52	4.84	23.79	0.99	42.35	3.72	20.63	0.72	50.15	4.41	26.87	1.21	60.64	6.64	26.33	0.83	47.88	3.53	23.82	1.75	40.17	3.08	35.87	2.23	63.53	2.91	26.99	2.78	56.48	0.15
In Vitro Axial Length (mm)	2.83	0.08	3.61	0.11	2.71	0.12	3.79	0.37	2.37	0.10	3.91	0.22	2.76	0.23	3.79	0.78	3.02	0.22	4.27	0.39	2.61	0.12	4.55	0.07	3.20	0.23	4.20	0.19	2.51	0.13	4.78	0.13	3.46	0.17	3.43	0.66
Dimensions at MAP																																				
Outer Diameter (μm)	2101.18	36.91	873.99	16.50	2036.97	21.02	849.28	24.32	2027.52	75.92	875.16	30.62	2057.42	30.59	861.43	49.89	2162.65	7.23	895.73	49.21	2001.68	65.22	838.55	25.81	2271.18	61.62	935.69	32.81	2040.68	13.40	1004.51	42.42	2248.35	138.80	943.85	34.12
Wall Thickness (μm)	25.37	0.32	30.06	2.34	30.62	1.19	28.65	1.77	28.97	1.70	30.76	1.02	25.55	0.95	27.72	0.90	56.25	0.03	30.20	0.77	47.19	3.07	34.71	5.06	62.45	7.06	36.48	3.76	86.64	12.33	50.10	1.27	84.17	3.11	47.08	6.26
Inner Diameter (μm)	2050.43	37.56	813.88	16.99	1975.72	18.80	791.99	20.81	1969.57	78.29	813.63	32.64	2006.31	32.39	805.99	51.62	2050.15	7.17	835.33	50.74	1907.31	67.29	769.13	32.39	2146.28	70.68	862.73	27.77	1867.41	15.56	904.30	44.97	2080.00	132.58	849.68	21.60
Inner Radius (μm)	1025.22	18.78	406.94	8.49	987.86	9.40	395.99	10.40	984.79	39.15	406.81	16.32	1003.16	16.19	402.99	25.81	1025.08	3.59	417.67	25.37	953.65	33.64	384.57	16.20	1073.14	35.34	431.37	13.88	933.70	7.78	452.15	22.48	1040.00	66.29	424.84	10.80
h:ir ratio (%)	2.48	0.08	7.40	0.62	3.10	0.09	7.22	0.25	2.96	0.26	7.61	0.55	2.55	0.13	6.96	0.65	5.49	0.02	7.27	0.62	4.97	0.43	9.14	1.64	5.86	0.80	8.44	0.72	9.30	1.38	11.12	0.83	8.11	0.22	11.05	1.19
Circumferential Stretch	2.17	0.07	1.72	0.04	1.94	0.10	1.85	0.09	2.03	0.08	1.70	0.04	1.93	0.02	1.88	0.09	1.69	0.03	2.08	0.16	1.70	0.04	1.66	0.13	1.55	0.06	1.60	0.09	1.61	0.11	1.68	0.06	1.50	0.01	1.75	0.06
In Vivo Axial Stretch ratio	2.07	0.10	1.50	0.04	1.82	0.01	1.66	0.02	1.79	0.06	1.64	0.06	2.00	0.08	1.70	0.03	1.55	0.01	1.53	0.02	1.67	0.08	1.68	0.03	1.58	0.02	1.64	0.05	1.36	0.08	1.62	0.06	1.36	0.07	1.39	0.04
Cauchy Stresses at MAP																																				
Circumferential (kPa)	560.08	17.36	189.92	15.59	448.03	13.61	192.34	6.63	476.10	45.97	184.13	13.67	546.17	29.59	202.67	19.49	252.52	0.74	192.04	16.51	282.74	22.48	160.78	25.62	245.17	32.46	166.57	14.29	175.10	29.76	139.80	10.50	189.49	5.09	140.55	15.17
Axial (kPa)	509.77	5.92	249.82	20.55	381.60	19.60	279.63	7.51	410.78	43.44	269.85	4.14	475.50	9.90	283.74	20.42	198.02	3.96	219.34	0.21	232.07	14.16	212.90	26.01	169.56	18.90	198.91	14.48	113.71	23.77	159.14	4.23	111.37	6.34	141.90	17.96
Linearised Stiffness at MAP																																				
Circumferential (MPa)	3.21	0.16	2.49	0.24	3.09	0.14	1.64	0.14	3.00	0.29	1.70	0.27	3.74	0.07	1.66	0.07	4.35	0.54	1.77	0.18	2.30	0.28	1.58	0.11	3.09	0.24	1.69	0.14	1.95	0.44	1.58	0.20	1.94	0.01	1.26	0.15
Axial (MPa)	2.51	0.08	3.60	0.47	1.86	0.12	3.09	0.20	2.09	0.16	3.18	0.09	2.37	0.02	2.94	0.09	1.25	0.03	2.80	0.03	1.30	0.10	2.60	0.04	0.96	0.08	2.25	0.05	0.74	0.15	2.50	0.21	0.70	0.09	2.10	0.45
Energy Metrics																																				
Stored Energy at MAP (kPa)	169.76	10.38	39.83	2.70	118.41	6.30	50.60	2.53	129.13	15.57	49.43	2.36	152.32	6.76	56.85	5.20	48.90	1.66	40.36	2.56	64.49	5.67	42.26	7.74	39.52	6.74	39.27	4.25	25.02	5.30	32.72	0.14	26.06	0.94	26.90	4.61
Energy Dissipation Ratio (%)	4.66	0.61	8.83	0.08	3.63	0.13	6.34	0.38	3.43	0.41	6.54	0.89	3.33	0.22	6.62	0.35	4.40	0.43	8.70	0.15	5.10	0.14	6.47	1.44	5.77	0.62	7.06	0.21	5.31	0.13	4.62	–*	6.41	1.11	6.27	0.53

Table A.2: **Mechanical data comparison with previously published work.** Mechanical data characterising 18wks *Ctrl* ATAs and IAAs is compared with equivalent data presented in Ferruzzi et al. (2015) for control arteries at 20–22 weeks of age. Values in red, green and blue are over, (at least partially) within or below average±2 SEM from Ferruzzi et al.'s average data±2.

Time Point	**Aparicio data 18 weeks *Ctrl***				**[Ferruzzi2015] data (*Fbln*$^{+/+}$ control)**				**[Ferruzzi2015] data (*Fbln*$^{+/+}$ control)**			
Segment	**ATA**		**IAA**		**ATA**				**IAA**			
Number of Samples	3		3		5				5			
Metric	mean	SEM	mean	SEM	mean	SEM	mean-2 SEM	mean+2 SEM	mean	SEM	mean-2 SEM	mean+2 SEM
Unloaded Dimension												
Outer Diameter (µm)	**1153.00**	25.15	**532.00**	18.56	1090.00	22.00	1046.00	1134.00	588.00	9.00	570.00	606.00
Wall Thickness (µm)	**98.45**	1.74	**88.22**	3.06	105.00	1.00	103.00	107.00	91.00	3.00	85.00	97.00
In Vitro Axial Length (mm)	**2.76**	0.23	**3.79**	0.78	3.40	0.10	3.20	3.60	5.20	0.40	4.40	6.00
Dimensions at MAP(sys)												
Outer Diameter (µm)	**2057.42**	30.59	**861.43**	49.89	1783.00	38.00	1707.00	1859.00	929.00	16.00	897.00	961.00
Wall Thickness (µm)	**25.55**	0.95	**27.72**	0.90	35.00	0.50	34.00	36.00	30.00	2.00	26.00	34.00
In Vivo Axial Stretch	**2.00**	0.08	**1.70**	0.03	1.71	0.02	1.67	1.75	1.66	0.04	1.58	1.74
Cauchy Stresses at MAP(sys)												
Circumferential (kPa)	**546.17**	29.59	**202.67**	19.49	395.90	6.00	383.90	407.90	230.40	16.00	198.40	262.40
Axial (kPa)	**475.50**	9.90	**283.74**	20.42	377.70	4.60	368.50	386.90	275.10	13.90	247.30	302.90
Linearised Stiffness at MAP(sys)												
Circumferential (MPa)	**3.74**	0.07	**1.66**	0.07	2.57	0.10	2.37	2.77	1.86	0.15	1.56	2.16
Axial (MPa)	**2.37**	0.02	**2.94**	0.09	2.53	0.05	2.43	2.63	4.08	0.22	3.64	4.52
Energy Metrics												
Stored Energy at MAP(sys) (kPa)	**152.32**	6.76	**56.85**	5.20	108.70	1.80	105.10	112.30	61.20	5.40	50.40	72.00
Energy Dissipation Ratio (%)	**3.33**	0.22	**6.62**	0.35	1.89	0.56	0.77	3.01	5.84	0.85	4.14	7.54

Table A.3: **PSR histological staining.** Values in shaded cells were used for computation of perturbed groups fold–changes from control group.

Control group

			14 weeks				18 weeks			
			ATA		IAA		ATA		IAA	
			3		3		3		3	
			mean	SEM	mean	SEM	mean	SEM	mean	SEM
Media	Red Pixels	Number	48993.00	1021.67	53781.00	5770.93	52127.33	2929.48	48528.33	5279.39
		Percentage	48.62	1.45	61.83	4.01	47.75	1.03	53.41	1.86
	Orange Pixels	Number	36115.00	3096.80	22631.00	3507.47	39826.33	3101.01	28636.00	2092.06
		Percentage	35.61	1.45	26.10	3.78	36.36	0.48	31.75	1.72
	Red+Orange Pixels	Number	85108.00	4115.22	76412.00	5706.77	91953.67	5988.72	77164.33	7187.10
		Percentage	84.23	0.66	87.94	0.62	84.11	0.99	85.16	2.82
	Yellow Pixels	Number	3218.00	242.92	1857.00	41.62	3450.00	453.67	2299.67	185.77
		Percentage	3.18	0.09	2.15	0.10	3.13	0.22	2.57	0.28
	Green Pixels	Number	6654.00	222.88	3802.67	133.33	6767.00	929.55	4798.00	1084.45
		Percentage	6.60	0.17	4.44	0.46	6.12	0.41	5.40	1.37
	Yellow+Green Pixels	Number	9872.00	452.29	5659.67	91.73	10217.00	1375.81	7097.67	1265.45
		Percentage	9.77	0.13	6.59	0.56	9.26	0.62	7.96	1.64
	Total Pixels	Number Total	101047.67	4889.05	86811.33	5885.56	109507.00	14370.50	90468.00	6924.34
		Number R+O+Y+G	94980.00	4527.24	82071.67	5628.15	102170.67	12579.11	84262.00	6646.63
		Percentage R+O+Y+G	94.00	0.54	94.53	0.24	93.37	0.49	93.12	1.25
Adventitia	Red Pixels	Number	87840.00	1665.36	127369.33	20495.56	80067.00	7573.44	107818.33	14441.74
		Percentage	55.12	1.23	51.88	0.90	46.37	3.21	51.62	3.38
	Orange Pixels	Number	45757.00	2885.70	77562.33	9628.34	59557.33	5468.83	64877.33	12941.66
		Percentage	28.67	1.47	31.90	0.71	34.71	3.57	31.23	2.49
	Red+Orange Pixels	Number	133597.00	3781.84	204931.67	30107.24	139624.33	4771.82	172695.67	17548.18
		Percentage	83.79	1.76	83.78	0.81	81.08	0.37	82.85	1.21
	Yellow Pixels	Number	2714.67	483.10	5137.00	584.46	4606.00	457.37	4928.00	1490.58
		Percentage	1.71	0.31	2.12	0.12	2.69	0.30	2.38	0.66
	Green Pixels	Number	4738.33	1537.41	8377.67	832.97	8631.00	588.54	8774.00	2972.43
		Percentage	2.98	0.98	3.47	0.21	5.02	0.37	4.21	1.29
	Yellow+Green Pixels	Number	7453.00	2019.26	13514.67	1417.42	13237.00	1031.79	13702.00	4461.42
		Percentage	4.69	1.29	5.60	0.34	7.71	0.66	6.60	1.95
	Total Pixels	Number Total	159404.33	1879.22	244731.67	36198.25	172214.00	6092.09	208794.33	22367.47
		Number R+O+Y+G	141050.00	2301.52	218446.33	31392.40	152861.33	4956.34	186397.67	18400.43
		Percentage R+O+Y+G	88.48	0.51	89.38	0.68	88.79	1.03	89.45	1.24

TGFBR2 Disruption and Hypertension group

			14 weeks				18 weeks			
			ATA		IAA		ATA		IAA	
			2		2		2		2	
			mean	SEM	mean	SEM	mean	SEM	mean	SEM
Media	Red Pixels	Number	67049.50	24.50	60161.00	14224.00	98369.00	19280.00	141765.5	11152.50
		Percentage	68.64	5.46	79.83	4.96	59.24	6.78	88.18	7.57
	Orange Pixels	Number	20111.00	5822.00	7963.00	1778.00	39583.50	12078.50	7971.00	6524.00
		Percentage	20.11	4.33	11.47	4.42	23.00	0.04	4.93	4.02
	Red+Orange Pixels	Number	87160.5	5797.50	68124.00	12446.00	137952.50	31358.50	149736.5	4628.50
		Percentage	88.75	1.13	91.29	0.54	82.24	6.74	93.11	3.55
	Yellow Pixels	Number	1669.00	582.00	612.00	184.00	2554.00	657.00	390.50	300.50
		Percentage	1.66	0.46	0.90	0.41	1.51	0.08	0.25	0.19
	Green Pixels	Number	3881.50	1131.50	1133.50	216.50	5844.50	1137.50	891.00	711.00
		Percentage	3.89	0.85	1.63	0.58	3.52	0.41	0.55	0.44
	Yellow+Green Pixels	Number	5550.50	1713.50	1745.50	400.50	8398.50	1794.50	1281.50	1011.50
		Percentage	5.55	1.31	2.52	0.98	5.03	0.49	0.80	0.63
	Total Pixels	Number Total	98312.5	7778.50	74544.50	13192.50	172031.00	52230.00	160862.5	1163.50
		Number R+O+Y+G	92711	7511.00	69869.5	12045.50	146351	33153.00	151018	3617.00
		Percentage R+O+Y+G	94.29	0.18	93.81	0.44	87.27	7.23	93.91	2.93
Adventitia	Red Pixels	Number	229613	1706.00	228723.00	35763.00	264142.00	54819.00	391136	13998.00
		Percentage	46.61	2.11	60.83	3.97	58.23	4.43	65.47	2.31
	Orange Pixels	Number	196270.5	12204.50	110756.50	48095.50	128390.50	5354.50	138582.5	723.50
		Percentage	39.74	0.97	27.60	6.56	29.27	5.10	23.25	1.53
	Red+Orange Pixels	Number	425883.50	10498.50	339479.50	83858.50	392532.50	49464.50	529718.50	14721.50
		Percentage	86.35	1.14	88.43	2.59	87.50	0.68	88.71	3.83
	Yellow Pixels	Number	9352.00	1493.00	3084.00	858.00	5267.00	154.00	4567.50	499.50
		Percentage	1.89	0.23	0.80	0.05	1.20	0.20	0.76	0.03
	Green Pixels	Number	15392.50	503.50	3934.50	73.50	8839.50	1447.50	6272.00	1030.00
		Percentage	3.12	0.02	1.09	0.26	2.05	0.60	1.04	0.10
	Yellow+Green Pixels	Number	24744.50	1996.50	7018.50	784.50	14106.50	1601.50	10839.50	1529.50
		Percentage	5.01	0.21	1.89	0.21	3.24	0.79	1.80	0.13
	Total Pixels	Number Total	493460	18697.00	381461.50	83664.50	449092.00	59999.00	599006.5	42476.50
		Number R+O+Y+G	450628	12495.00	346498	84643.00	406639	47863.00	540558	16251.00
		Percentage R+O+Y+G	91.36	0.93	90.32	2.38	90.74	1.47	90.51	3.70

TGFBR2 Disruption group

			12 weeks				14 weeks				18 weeks			
			ATA		IAA		ATA		IAA		ATA		IAA	
			2		2		3		3		3		3	
			mean	SEM	mean	SEM	mean	SEM	mean	SEM	mean	SEM	mean	SEM
Media	Red Pixels	Number	64636.00	630.00	66796.50	699.50	51346.67	3723.53	60317.33	1866.42	38457.67	607.43	53810.33	1378.95
		Percentage	44.52	0.25	60.03	8.84	50.07	4.29	64.36	6.83	54.88	4.33	67.78	5.50
	Orange Pixels	Number	57372.00	3133.00	35036.00	12968.00	35237.00	7958.94	20599.00	4111.50	18235.33	3160.96	13013.33	3061.16
		Percentage	39.53	2.33	29.70	6.71	32.84	2.15	21.19	2.41	25.35	2.31	15.77	2.19
	Red+Orange Pixels	Number	122008.00	2503.00	101832.50	13667.50	86583.67	11404.39	80916.33	2847.35	56693.00	3170.13	66823.67	3852.59
		Percentage	84.04	2.08	89.73	2.14	82.91	2.51	85.55	4.57	80.24	2.54	83.55	3.79
	Yellow Pixels	Number	4421.00	495.00	2198.50	1149.50	3097.33	679.37	2016.00	801.13	2064.00	385.60	1146.33	317.99
		Percentage	3.05	0.33	1.82	0.73	2.89	0.18	2.01	0.65	2.86	0.30	1.37	0.23
	Green Pixels	Number	7076.00	718.00	3188.50	1878.50	6939.67	1523.89	4330.33	2098.21	5410.00	992.32	3030.00	816.62
		Percentage	4.88	0.48	2.60	1.24	6.52	0.63	4.24	1.73	7.51	0.77	3.64	0.57
	Yellow+Green Pixels	Number	11497.00	1213.00	5387.00	3028.00	10037.00	2189.93	6346.33	2895.46	7474.00	1372.07	4176.33	1134.34
		Percentage	7.92	0.80	4.42	1.97	9.41	0.78	6.25	2.38	10.37	1.05	5.01	0.79
	Total Pixels	Number Total	145191.50	623.50	113919.50	17942.50	105152.67	16406.46	95511.00	8805.21	70931.33	5617.17	80758.67	8589.76
		Number R+O+Y+G	133505.00	1290.00	107219.50	16695.50	96620.67	13424.73	87262.67	5608.65	64167.00	4459.19	71000.00	4983.70
		Percentage R+O+Y+G	91.96	1.28	94.14	0.17	92.32	1.76	91.80	2.43	90.61	1.66	88.55	3.04
Adventitia	Red Pixels	Number	104402.00	5799.00	145740.00	17256.00	105762.00	8641.08	160635.33	24031.32	111564.00	9870.30	224743.00	29300.64
		Percentage	54.53	0.78	60.11	5.94	56.16	2.32	64.51	3.38	64.61	1.67	66.90	2.62
	Orange Pixels	Number	56658.00	8716.00	57359.00	6803.00	51073.67	1318.84	59283.67	13340.01	34825.33	4849.73	67313.00	12175.09
		Percentage	29.39	2.50	23.77	3.28	27.30	1.34	23.17	2.65	19.96	0.70	19.68	1.09
	Red+Orange Pixels	Number	161060.00	14515.00	203099.00	10453.00	156835.67	8653.88	219919.00	35774.37	146389.33	14484.51	292056.00	40484.16
		Percentage	83.91	1.72	83.87	2.65	83.46	1.11	87.68	0.96	84.57	0.99	86.57	1.80
	Yellow Pixels	Number	4105.50	1.50	4349.50	1589.50	3967.00	612.02	3160.00	963.41	2924.33	700.41	3200.33	789.13
		Percentage	2.15	0.15	1.81	0.69	2.14	0.41	1.21	0.30	1.64	0.22	0.91	0.12
	Green Pixels	Number	7328.00	1483.00	7817.50	3348.50	7558.67	1226.75	4827.33	1468.41	6127.00	1758.12	4838.67	1282.47
		Percentage	3.90	1.05	3.26	1.45	4.09	0.82	1.86	0.48	3.40	0.63	1.36	0.20
	Yellow+Green Pixels	Number	11433.50	1481.50	12167.00	4938.00	11525.67	1832.61	7987.33	2430.01	9051.33	2458.54	8039.00	2068.73
		Percentage	6.05	1.20	5.07	2.14	6.22	1.23	3.07	0.78	5.03	0.85	2.27	0.31
	Total Pixels	Number Total	191679.50	13361.50	242000.00	4810.00	187829.00	9342.02	251707.00	43564.20	173499.33	19010.62	339476.67	52548.51
		Number R+O+Y+G	172493.50	13033.50	215266.00	5515.00	168361.33	7289.99	227906.33	37671.80	155440.67	16866.80	300095.00	42527.51
		Percentage R+O+Y+G	89.96	0.52	88.94	0.51	89.68	0.61	90.76	0.75	89.60	0.22	88.85	1.49

Table A.4: **Immunofluorescence quantification.** Values in shaded cells were used for computation of perturbed groups fold–changes from control group. Asterisk denotes a group where only one sample was available for IF quantification due to poor staining or sectioning artefacts.

			Control group								TGFBR2 Disruption group								TGFBR2 Disruption and Hypertension group							
		Time Point	14 weeks				18 weeks				14 weeks				18 weeks				14 weeks				18 weeks			
		Segment	ATA		IAA		ATA		IAA		ATA		IAA		ATA		IAA		ATA		IAA		ATA		IAA	
		Metric	mean	SEM	mean	SEM	mean	SEM	mean	SEM	mean	SEM	mean	SEM	mean	SEM	mean	SEM	mean	SEM	mean	SEM	mean	SEM	mean	SEM
Media	Cross Section (Segment.)	Number of samples	3		3		3		3		3		3		3		3		3		3		2		2	
		Area (μm²)	89092.40	6105.71	69959.01	2682.50	93222.00	5046.73	69591.38	1767.14	93946.93	11371.55	85897.94	10493.63	90859.26	7048.66	85715.94	11641.07	122244.17	8294.07	88798.14	3140.97	125504.83	9935.77	135290.62	3719.41
	TGF-β	Number of samples	3		3		3		3		3		3		3		2		3		2		2		1	
		Number Pixels	221538.33	7917.62	179084.67	4138.67	244668.67	10473.30	173903.67	5697.10	205010.33	10769.73	180784.00	3583.27	187217.00	31424.12	275678.50	30349.50	184183.67	13875.81	264582.00	8288.00	260724.00	30696.00	358149.00	–*
		Area Density (μm⁻²)	2.49	0.09	2.56	0.06	2.62	0.11	2.50	0.08	2.18	0.11	2.10	0.04	2.06	0.35	3.22	0.35	1.51	0.11	2.98	0.09	2.08	0.24	2.65	–*
	MMP-2	Number of samples	3		3		2		2		3		3		2		2		3		2		2		2	
		Number Pixels	135739.67	24760.07	117997.33	35152.43	135630.00	6907.00	147046.00	3802.00	209264.00	25714.61	136282.00	18765.73	129456.00	27896.00	162047.00	6420.00	195793.67	10023.38	234110.00	56582.00	319379.50	4168.50	177932.00	55762.00
		Area Density (μm⁻²)	1.52	0.28	1.69	0.50	1.45	0.07	2.11	0.05	2.23	0.27	1.59	0.22	1.42	0.31	1.89	0.07	1.60	0.08	2.64	0.64	2.54	0.03	1.32	0.41
	CD45	Number of samples	3.0000		2.0000		3.00		2.00		3.00		3.00		3.00		3.00		3.00		2.00		2.00		1.00	
		Number Pixels	51975.67	23442.69	20457.00	6399.00	28668.33	11119.14	51505.50	29020.50	68127.00	21129.99	37118.67	10761.97	13710.00	828.54	31655.33	7358.18	42133.67	11548.65	100494.00	15122.00	46922.00	15170.00	33719.00	–*
		Area Density (μm⁻²)	0.58	0.26	0.29	0.09	0.31	0.12	0.74	0.42	0.73	0.22	0.43	0.13	0.15	0.01	0.37	0.09	0.34	0.09	1.13	0.17	0.37	0.12	0.25	–*
	α-SMA	Number of samples	3		3		3		3		3		3		3		3		3		2		1		1	
		Number Pixels	237569.33	9190.36	176017.33	38966.18	175121.00	42902.05	185542.33	35292.05	250705.33	16399.52	171384.00	13587.68	268337.67	9866.27	196257.67	17635.46	280897.67	12703.46	318829.00	18675.00	375503.00	–*	234496.00	–*
		Area Density (μm⁻²)	2.67	0.10	2.52	0.56	1.88	0.46	2.67	0.51	2.67	0.17	2.00	0.16	2.95	0.11	2.29	0.21	2.30	0.10	3.59	0.21	2.99	–*	1.73	–*
	pSMAD-2	Number of samples	3		3		2		3		3		3		3		3		3		2		2		2	
		Number Pixels Mat	156514.67	14258.18	97025.00	5556.53	141136.00	20624.00	112765.00	15790.55	175025.33	25395.67	142844.33	25843.69	124835.67	15514.53	120660.00	11269.62	142919.33	33691.30	249751.00	2263.00	205277.00	20460.00	178492.50	2017.50
		Area Density Mat (μm⁻²)	1.76	0.16	1.39	0.08	1.51	0.22	1.62	0.23	1.86	0.27	1.66	0.30	1.37	0.17	1.41	0.13	1.17	0.28	2.81	0.03	1.64	0.16	1.32	0.01
		Number Pixels Nuc	35490.00	4614.77	34217.33	1804.94	35440.50	530.50	30017.33	2906.86	48540.67	1276.15	36726.00	5679.35	39880.33	1266.86	29863.67	2627.24	37732.00	7964.74	51258.50	4784.50	47586.50	6610.50	39840.50	7233.50
		Area Density Nuc (μm⁻²)	0.40	0.05	0.49	0.03	0.38	0.01	0.43	0.04	0.52	0.01	0.43	0.07	0.44	0.01	0.35	0.03	0.31	0.07	0.58	0.05	0.38	0.05	0.29	0.05
		Total Nuclei	467.00	25.24	359.67	18.52	465.50	8.50	330.33	27.83	574.33	8.09	411.00	55.87	563.00	47.29	363.33	28.26	460.00	58.18	569.00	31.00	516.50	53.50	427.00	58.00
		Nuclei Area Density (μm⁻²)	5.24E-03	2.83E-04	5.14E-03	2.65E-04	4.99E-03	9.12E-05	4.75E-03	4.00E-04	6.11E-03	8.61E-05	4.78E-03	6.50E-04	6.20E-03	5.20E-04	4.24E-03	3.30E-04	3.76E-03	4.76E-04	6.41E-03	3.49E-04	4.12E-03	4.26E-04	3.16E-03	4.29E-04
Adventitia	Cross Section (Coll. Pixels)	Number of samples	3		3		3		3		3		3		3		3		2		2		2		2	
		Area (μm²)	58680.33	957.49	90879.14	13060.02	63594.14	2061.96	77546.09	7655.04	70042.52	3032.82	94814.73	15672.41	64667.20	7017.01	124847.02	17692.51	187472.51	0.03	144151.83	35213.60	169171.99	19912.20	224885.64	6760.82
	TGF-β	Number of samples	3		3		3		3		3		3		3		2		3		2		2		1	
		Number Pixels	24461.33	1821.83	25895.00	1026.63	26386.00	2387.14	22403.67	1818.86	36461.67	1988.85	45524.00	13542.57	45782.67	1054.07	94661.00	13585.00	162077.00	12935.74	297938.00	113786.00	176378.50	15584.50	234020.00	–*
		Area Density (μm⁻²)	0.42	0.03	0.28	0.01	0.41	0.04	0.29	0.02	0.52	0.03	0.48	0.14	0.71	0.02	0.76	0.11	0.86	0.07	2.07	0.79	1.04	0.09	1.04	–*
	MMP-2	Number of samples	3		3		2		2		3		3		2		2		3		2		2		2	
		Number Pixels	23779.00	4095.88	32999.33	12179.13	17113.00	2788.00	27864.00	3896.00	45372.00	6155.62	32425.00	12899.91	41610.50	9008.50	67105.00	7091.00	177534.00	19954.88	198418.50	75168.50	227620.50	51089.50	70824.50	34545.50
		Area Density (μm⁻²)	0.41	0.07	0.36	0.13	0.27	0.04	0.36	0.05	0.65	0.09	0.34	0.14	0.64	0.14	0.54	0.06	0.95	0.11	1.38	0.52	1.35	0.30	0.31	0.15
	CD45	Number of samples	3		2		3		2		3		3		3		3		3		2		2		1	
		Number Pixels	2296.67	553.48	2112.50	719.50	979.00	168.99	5065.00	3930.00	7616.00	1747.52	9713.67	1941.48	4717.00	90.52	8180.00	450.40	47400.33	11669.73	111827.00	38124.00	30718.50	691.50	64633.00	–*
		Area Density (μm⁻²)	0.04	0.01	0.02	0.01	0.02	0.00	0.07	0.05	0.11	0.02	0.10	0.02	0.07	0.00	0.07	0.00	0.25	0.06	0.78	0.26	0.18	0.00	0.29	–*
	α-SMA	Number of samples	3		3		3		3		3		3		3		3		3		2		1		1	
		Number Pixels	4418.33	1049.60	9521.67	3792.05	5555.00	340.54	12755.67	202.66	21748.67	7712.48	10589.33	3114.76	22487.67	1562.94	23692.00	12493.16	104840.67	33645.99	122323.00	60600.00	74711.00	–*	30015.00	–*
		Area Density (μm⁻²)	0.08	0.02	0.10	0.04	0.09	0.01	0.16	0.00	0.31	0.11	0.11	0.03	0.35	0.02	0.19	0.10	0.56	0.18	0.85	0.42	0.44	–*	0.13	–*
	pSMAD-2	Number of samples	3		3		2		3		3		3		3		3		3		2		2		2	
		Number Pixels Mat	9991.67	976.63	11009.67	428.37	5048.50	236.50	10215.33	3424.07	20457.00	9569.33	29318.67	10501.47	14092.00	1998.69	19315.00	3854.82	66153.00	18908.94	147129.50	30634.50	68662.50	13810.50	42393.00	19354.00
		Area Density Mat (μm⁻²)	0.17	0.02	0.12	0.00	0.08	0.00	0.13	0.04	0.29	0.14	0.31	0.11	0.22	0.03	0.15	0.03	0.35	0.10	1.02	0.21	0.41	0.08	0.19	0.09
		Number Pixels Nuc	5697.33	628.27	7347.33	1477.58	4742.00	311.00	5960.67	2004.26	8916.33	963.27	12478.00	4159.49	9244.00	694.30	10435.00	2668.72	52867.33	6119.28	56095.00	13630.00	51695.50	5035.50	33389.00	17911.00
		Area Density Nuc (μm⁻²)	0.10	0.01	0.08	0.02	0.07	0.00	0.08	0.03	0.13	0.01	0.13	0.04	0.14	0.01	0.08	0.02	0.28	0.03	0.39	0.09	0.31	0.03	0.15	0.08
		Total Nuclei	105.67	9.53	109.00	15.59	94.00	6.00	89.00	30.60	138.00	12.12	179.33	54.76	182.33	26.67	162.00	33.50	904.67	33.23	778.50	179.50	778.00	90.00	451.00	226.00
		Nuclei Area Density (μm⁻²)	1.80E-03	1.62E-04	1.20E-03	1.72E-04	1.48E-03	9.43E-05	1.15E-03	3.95E-04	1.97E-03	1.73E-04	1.89E-03	5.77E-04	2.82E-03	4.12E-04	1.30E-03	2.68E-04	4.83E-03	1.77E-04	5.40E-03	1.25E-03	4.60E-03	5.32E-04	2.01E-03	1.00E-03